

APRIL 2018

**AJNR**

VOLUME 39 • PP 605-795

# AJNR

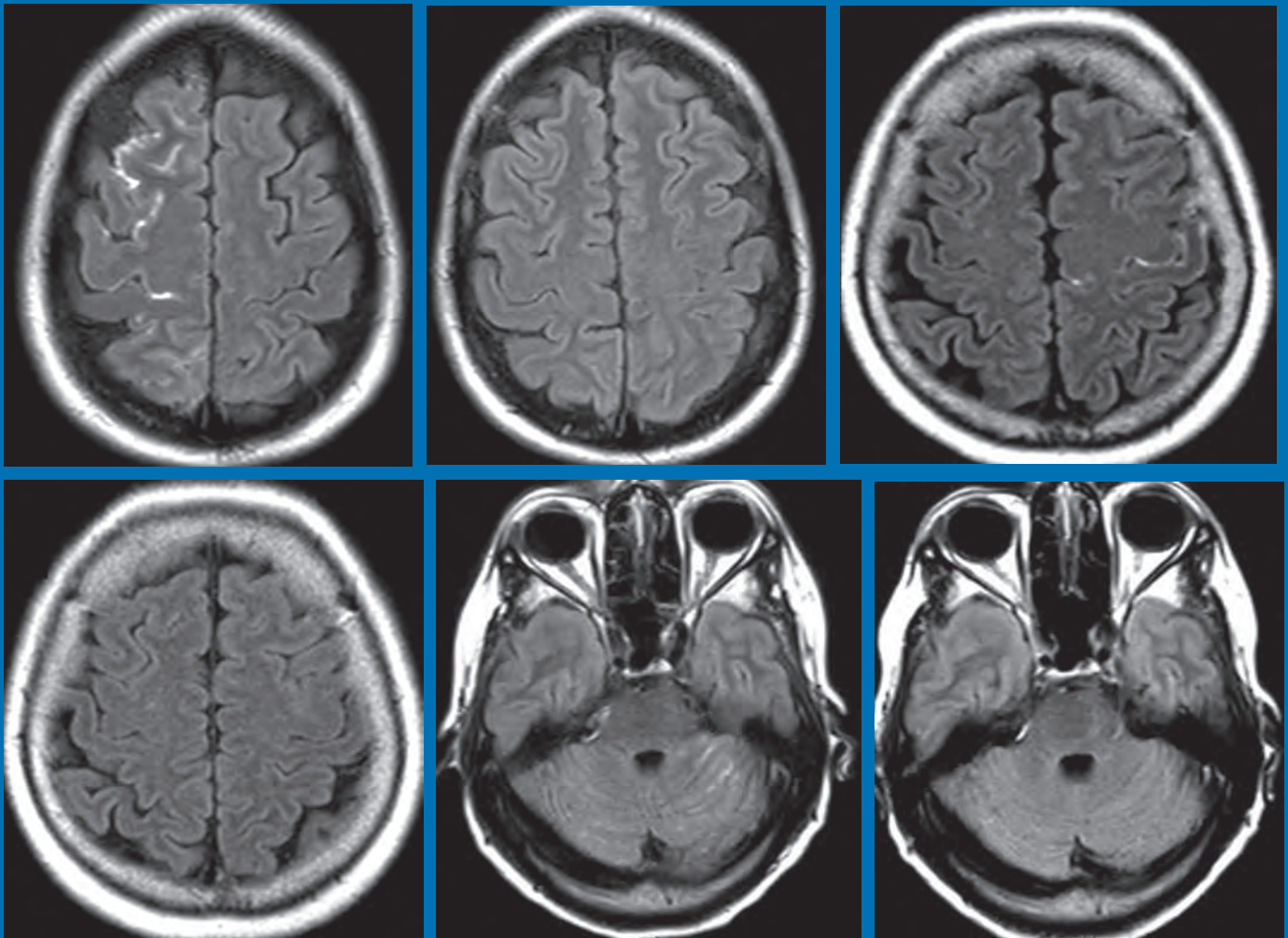
## AMERICAN JOURNAL OF NEURORADIOLOGY

APRIL 2018  
VOLUME 39  
NUMBER 4  
WWW.AJNR.ORG

THE JOURNAL OF DIAGNOSTIC AND  
INTERVENTIONAL NEURORADIOLOGY

Morphologic criteria in posttreatment head and neck carcinoma  
AQ-4 antibody–positive longitudinally extensive transverse myelitis  
Arterial spin-labeling in dural AV fistula

Official Journal ASNR • ASFNR • ASHNR • ASPNR • ASSR



# A Complete Coil Portfolio

MicroVention's comprehensive portfolio features clinically proven Hydrogel coils, which can be used exclusively or in combination with our trusted Platinum coils to treat a wide range of aneurysms and neurovascular lesions.



Aneurysm  
Therapy  
Solutions

## Breakthrough Hydrogel Technology

- Less Recurrence
- Less Retreatment
- More Progressive Occlusion

*Compared to platinum coils with comparable safety<sup>1</sup>*

### REFERENCES:

1. Taschner et al. Second-Generation Hydrogel Coils for the Endovascular Treatment of Intracranial Aneurysm; A Randomized Controlled Trial. 2018;49:00-00. DOI:10.1161/STROKEAHA.117.018707



### INDICATIONS FOR USE:

The HydroCoil® Embolic System (HES) and MicroPlex® Coil System (MCS) are intended for the endovascular embolization of intracranial aneurysms and other neurovascular abnormalities such as arteriovenous malformations and arteriovenous fistulae. The HES and MCS are also intended for vascular occlusion of blood vessels within the neurovascular system to permanently obstruct blood flow to an aneurysm or other vascular malformation and for arterial and venous embolizations in the peripheral vasculature.

The device should only be used by physicians who have undergone pre-clinical training in all aspects of HES/MCS procedures as prescribed by MicroVention.



**For more information or a product demonstration,  
contact your local MicroVention representative:**



**MicroVention Worldwide  
Innovation Center**  
35 Enterprise  
Aliso Viejo, CA 92656 USA  
MicroVention UK Limited  
MicroVention Europe, S.A.R.L.  
MicroVention Deutschland GmbH  
**microvention.com**

PH +1.714.247.8000

PH +44 (0) 191 258 6777

PH +33 (1) 39 21 77 46

PH +49 211 210 798-0

**Balt USA.**  
**The Future of Innovation is Here.**

**Introducing**



Pushing Beyond the Boundaries of  
**Softness and Speed**

**Visit [balt-usa.com](http://balt-usa.com) to learn more**

# ASNR 56<sup>th</sup> Annual Meeting & The Foundation of the ASNR Symposium 2018

June 2 - 7, 2018 | Vancouver Convention Centre East | Vancouver, B.C., CANADA



## ASNR 2018 KEYNOTE PRESENTATION *by Andy DeLaO*

The Radiology Renaissance: Shaping the Future of Healthcare

Monday, June 4, 2018 - 8:00am - 9:00am Hall A - Vancouver Convention Centre East

This keynote will highlight the changing world of radiology inside of healthcare. Radiologists at one point were referred to as the "doctor's doctor." Radiologists were the trusted advisors to help physicians from primary care to specialists such as surgeons and oncologists make clinical decisions based on imaging. As technology evolves, the role of the radiologist undergoes transformation. Today we are seeing the emergence of another technology evolution in healthcare. It presents an opportunity for radiologists to transition once again, but the choices they face today will determine the future role of radiology.



The Vancouver Convention Centre East © 2013 Vancouver Convention Centre

## Welcome and Greetings

Please join us in Vancouver, CANADA for the **56th Annual Meeting of the American Society of Neuroradiology** on June 2-7, 2018 at the Vancouver Convention Centre East. Surrounded by the coastal mountains and located on the waterfront, you can enjoy these spectacular views in the heart of downtown Vancouver. With its undeniable charm and friendly atmosphere, Vancouver is known around the world as both a popular tourist attraction and one of the best places to live. ASNR enthusiastically presents **Neuroradiology: Adding Value and Improving Healthcare** at the Symposium of the Foundation of the ASNR, as well as the common thread throughout the Annual Meeting. Implementing a value-based strategy in imaging has grasped the attention of nearly every healthcare provider; in particular with Radiologists understanding that the future will demand their imaging practices deliver better value. Value in healthcare is typically defined as those imaging strategies that yield improved outcomes, lower costs, or both. As payment transitions from a fee-for-service to a value-based system, thus creating a fundamentally different marketplace dynamic, measuring good outcomes are at the center of this changeover. At this time of uncertainty what little remains clear is that without a well-defined knowledge of their outcomes, no medical specialty will be able to succeed in the future value-based system. The Symposium will feature how Neuroradiology, in its many subspecialty areas, adds value to clinical care pathways by directing healthcare practice towards better outcomes. The annual meeting programming will continue on this theme emphasizing imaging that improves health outcomes, while considering costs, thus adding value. Our discussions will incorporate many innovative approaches to how neuroimaging currently does and will continue to improve overall healthcare performance.

As the Program Chair for ASNR 2018, it is my pleasure and honor to welcome you to Vancouver, CANADA for our annual meeting! Vancouver is known for being a very walkable city with a compact downtown core hosting many places to enjoy. So pack your comfortable walking shoes and let's tour together with our colleagues and friends!

*Pina Sanelli*

Pina C. Sanelli, MD, MPH, FACR  
ASNR 2018 Program Chair/President-Elect



ASNR 2018 ■ VANCOUVER

ASFNR ASHNR ASPNR ASSR SNIS

THE FOUNDATION OF THE ASNR



**Pina C. Sanelli, MD, MPH, FACR**

**ASNR 2018 Program Chair/President-Elect**

*Programming developed in cooperation with the...*

**American Society of Functional Neuroradiology (ASFNR)**

Max Wintermark, MD

**American Society of Head and Neck Radiology (ASHNR)**

Deborah R. Shatzkes, MD

**American Society of Pediatric Neuroradiology (ASPNR)**

Ashok Panigrahy, MD

**American Society of Spine Radiology (ASSR)**

John D. Barr, MD, FACR, FSIR, FAHA

**Society of NeuroInterventional Surgery (SNIS)**

Mahesh V. Jayaraman, MD

**ASNR Health Policy (HPC) Committee**

William D. Donovan, MD, MPH, FACR | Gregory N. Nicola, MD, FACR

**ASNR Computer Sciences & Informatics (CSI) Committee**

John L. Go, MD, FACR

**ASNR Research Scientist Programming Committee**

Dikoma C. Shungu, PhD | Timothy P.L. Roberts, PhD

**The International Hydrocephalus Imaging Working Group**

(IHIWG) / CSF Flow Group

Ari M Blitz, MD | Harold L. Reigate, MD | Bryn A. Martin, PhD

**Check out Meeting Registration/Housing!**

Please visit [2018.asnr.org](http://2018.asnr.org) for more information

**ASNR 56<sup>th</sup> Annual Meeting**

c/o American Society of Neuroradiology

800 Enterprise Drive, Suite 205

Oak Brook, Illinois 60523-4216

Phone: 630-574-0220 Fax: 630 574-0661

[2018.asnr.org](http://2018.asnr.org)



# We're Inside Every Great Neuroradiologist!

## ASNR MEMBERS RECEIVE

### *American Journal of Neuroradiology (AJNR)*

The leading neuroradiology research journal, published monthly

### *Neurographics*

Bimonthly educational journal with CME for members

### **ASNR Annual Meeting**

Discounts for members on the field's premier conference

### **eCME**

Online collection of lectures and articles with SA-CME and Category 1 credit

### **Advocacy**

Coding/reimbursement, quality standards and practice guidelines; demonstrating neuroradiology's value!

### **Networking**

Access to 5,000 peers

... And More!

**Join the leaders in neuroradiology today!**

**Learn more at [www.asnr.org/join](http://www.asnr.org/join)**

# ASNR

## American Society of Neuroradiology

800 Enterprise Dr., Suite 205, Oak Brook, IL 60523 • (630)574-0220 • [membership@asnr.org](mailto:membership@asnr.org) • [www.asnr.org](http://www.asnr.org)

## Neuroform Atlas™ Stent System

### See package insert for complete indications, contraindications, warnings and instructions for use.

**Humanitarian Device** Authorized by Federal law for use with neurovascular embolic coils in patients who are ≥ 18 years of age for the treatment of wide neck, intracranial, saccular aneurysms arising from a parent vessel with a diameter of ≥ 2 mm and ≤ 4.5 mm that are not amenable to treatment with surgical clipping. Wide neck aneurysms are defined as having a neck > 4 mm or a dome-to-neck ratio < 2. The effectiveness of this device for this use has not been demonstrated.

### INDICATIONS FOR USE

The Neuroform Atlas™ Stent System is indicated for use with neurovascular embolic coils in patients who are ≥ 18 years of age for the treatment of wide neck, intracranial, saccular aneurysms arising from a parent vessel with a diameter of ≥ 2 mm and ≤ 4.5 mm that are not amenable to treatment with surgical clipping. Wide neck aneurysms are defined as having a neck > 4 mm or a dome-to-neck ratio of < 2.

### CONTRAINDICATIONS

Patients in whom antiplatelet and/or anticoagulation therapy is contraindicated.

### POTENTIAL ADVERSE EVENTS

The potential adverse events listed below, as well as others, may be associated with the use of the Neuroform Atlas™ Stent System or with the procedure:

Allergic reaction to nital metal and medications, Aneurysm perforation or rupture, Coil herniation through stent into parent vessel, Death, Embolus, Headache, Hemorrhage, In-stent stenosis, Infection, Ischemia, Neurological deficit/intracranial sequelae, Pseudoaneurysm, Stent fracture, Stent migration/embolization, Stent misplacement, Stent thrombosis, Stroke, Transient ischemic attack, Vasospasm, Vessel occlusion or closure, Vessel perforation/rupture, Vessel dissection, Vessel trauma or damage, Vessel thrombosis, Visual impairment, and other procedural complications including but not limited to anesthetic and contrast media risks, hypotension, hypertension, access site complications.

### WARNINGS

- Contents supplied STERILE using an ethylene oxide (EO) process. Do not use if sterile barrier is damaged. If damage is found, call your Stryker Neurovascular representative.
- For single use only. Do not reuse, reprocess or resterilize. Reuse, reprocessing or resterilization may compromise the structural integrity of the device and/or lead to device failure which, in turn, may result in patient injury, illness or death. Reuse, reprocessing or resterilization may also create a risk of contamination of the device and/or cause patient infection or cross-infection, including, but not limited to, the transmission of infectious disease(s) from one patient to another. Contamination of the device may lead to injury, illness or death of the patient.
- After use, dispose of product and packaging in accordance with hospital, administrative and/or local government policy.
- This device should only be used by physicians who have received appropriate training in interventional neuroradiology or interventional radiology and preclinical training on the use of this device as established by Stryker Neurovascular.
- Select a stent size (length) to maintain a minimum of 4 mm on each side of the aneurysm neck along the parent vessel. An incorrectly sized stent may result in damage to the vessel or stent migration. Therefore, the stent is not designed to treat an aneurysm with a neck greater than 22 mm in length.
- If excessive resistance is encountered during the use of the Neuroform Atlas™ Stent System or any of its components at any time during the procedure, discontinue use of the stent system. Continuing to move the stent system against resistance may result in damage to the vessel or a system component.
- Persons allergic to nickel titanium (Nitinol) may suffer an allergic response to this stent implant.
- Purge the system carefully to avoid the accidental introduction of air into the stent system.
- Confirm there are no air bubbles trapped anywhere in the stent system.

### CAUTIONS / PRECAUTIONS

- Federal Law (USA) restricts this device to sale by or on the order of a physician.
- Use the Neuroform Atlas Stent System prior to the "Use By" date printed on the package.
- Carefully inspect the sterile package and Neuroform Atlas Stent System prior to use to verify that neither has been damaged during shipment. Do not use kinked or damaged components; contact your Stryker Neurovascular representative.
- The stent delivery microcatheter and the Neuroform Atlas Stent delivery wire should not be used to recapture the stent.
- Exercise caution when crossing the deployed stent with adjunctive devices.
- After deployment, the stent may foreshorten from up to 6.3%.
- The max OD of the coiling microcatheter should not exceed the max OD of the stent delivery microcatheter.

- Standard interventional devices with distal tips > 1.8 F may not be able to pass through the interstices of the stent.
- Safety of the Neuroform Atlas Stent System in patients below the age of 18 has not been established.
- In cases where multiple aneurysms are to be treated, start at the most distal aneurysm first.

### MAGNETIC RESONANCE IMAGING (MRI)

#### Specific Information Magnetic Resonance Conditional

Non-clinical testing and analysis have demonstrated that the Neuroform Atlas Stent is MR Conditional alone, or when overlapped with a second stent, and adjacent to a Stryker Neurovascular coil mass. A patient with the Neuroform Atlas Stent can be safely scanned immediately after placement of this implant, under the following conditions:

- Static magnetic field of 1.5 and 3.0 Tesla
- Maximum spatial gradient field up to 2500 Gauss/cm (25 Tesla/m)
- Maximum MRI system reported whole body averaged specific absorption rate of 2 W/kg (Normal Operating Mode) and head averaged specific absorption rate of 3.2 W/kg.

Under the scan conditions defined above, the Neuroform Atlas Stent is expected to produce a maximum temperature rise of 4°C after 15 minutes of continuous scanning. The Neuroform Atlas Stent should not migrate in this MRI environment.

In non-clinical testing, the image artifact caused by the device extends approximately 2 mm from the Neuroform Atlas Stent when imaged with a spin echo pulse sequence and 3 Tesla MRI System. The artifact may obscure the device lumen. It may be necessary to optimize MRI imaging parameters for the presence of this implant.

### Excelsior® XT-17™ Microcatheter

#### See package insert for complete indications, contraindications, warnings and instructions for use.

#### INTENDED USE / INDICATIONS FOR USE

Stryker Neurovascular's Excelsior XT-17 Microcatheters are intended to assist in the delivery of diagnostic agents, such as contrast media, and therapeutic agents, such as occlusion coils, into the peripheral, coronary and neuro vasculature.

### CONTRAINDICATIONS

None known.

### POTENTIAL ADVERSE EVENTS

Potential adverse events associated with the use of microcatheters or with the endovascular procedures include, but are not limited to: access site complications, allergic reaction, aneurysm perforation, aneurysm rupture, death, embolism (air, foreign body, plaque, thrombus), hematoma, hemorrhage, infection, ischemia, neurological deficits, pseudoaneurysm, stroke, transient ischemic attack, vasospasm, vessel dissection, vessel occlusion, vessel perforation, vessel rupture, vessel thrombosis

### WARNINGS

- The accessories are not intended for use inside the human body.
- Limited testing has been performed with solutions such as contrast media, saline and suspended embolic particles. The use of these microcatheters for delivery of solutions other than the types that have been tested for compatibility is not recommended. Do not use with glue or glue mixtures.
- Carefully inspect all devices prior to use. Verify shape, size and condition are suitable for the specific procedure.
- Exchange microcatheters frequently during lengthy procedures that require extensive guidewire manipulation or multiple guidewire exchanges.
- Never advance or withdraw an intravascular device against resistance until the cause of the resistance is determined by fluoroscopy. Movement of the microcatheter or guidewire against resistance could dislodge a clot, perforate a vessel wall, or damage microcatheter and guidewire. In severe cases, tip separation of the microcatheter or guidewire may occur.
- Contents supplied STERILE using an ethylene oxide (EO) process. Do not use if sterile barrier is damaged. If damage is found, call your Stryker Neurovascular representative.
- For single use only. Do not reuse, reprocess or resterilize. Reuse, reprocessing or resterilization may compromise the structural integrity of the device and/or lead to device failure which, in turn, may result in patient injury, illness or death. Reuse, reprocessing or resterilization may also create a risk of contamination of the device and/or cause patient infection or cross-infection, including, but not limited to, the transmission of infectious disease(s) from one patient to another. Contamination of the device may lead to injury, illness or death of the patient.
- After use, dispose of product and packaging in accordance with hospital, administrative and/or local government policy.
- These devices are intended for use only by physicians trained in performing endovascular procedures.
- Inspect product before use for any bends, kinks or damage. Do not use a microcatheter that has been damaged. Damaged microcatheters may rupture causing vessel trauma or tip detachment during steering maneuvers.
- The shaping mandrel is not intended for use inside the human body.

- Discontinue use of microcatheter for infusion if increased resistance is noted. Resistance indicates possible blockage. Remove and replace blocked microcatheter immediately. DO NOT attempt to clear blockage by over-pressure. Doing so may cause the microcatheter to rupture, resulting in vascular damage or patient injury.
- Do not exceed 2,070 kPa (300 psi) infusion pressure. Excessive pressure could dislodge a clot, causing thromboemboli, or could result in a ruptured microcatheter or severed tip, causing vessel injury.

### CAUTIONS / PRECAUTIONS

- To reduce the probability of coating damage in tortuous vasculature, use a guide catheter with a minimum internal diameter as specified in Table 1 above, and is recommended for use with Stryker Neurovascular hydrophilically coated microcatheters.
- To control the proper introduction, movement, positioning and removal of the microcatheter within the vascular system, users should employ standard clinical angiographic and fluoroscopic practices and techniques throughout the interventional procedure.
- Exercise care in handling of the microcatheter during a procedure to reduce the possibility of accidental breakage, bending or kinking.
- Use the product prior to the "Use By" date printed on the label.
- Limited testing indicates that Excelsior XT-17 Microcatheter is compatible with Dimethyl Sulfoxide (DMSO). The compatibility of Excelsior XT-17 Microcatheter with individual agents suspended in DMSO has not been established.
- Federal Law (USA) restricts this device to sale by or on the order of a physician.
- Wet dispenser coil or packaging tray and hydrophilically coated outer shaft of microcatheters prior to removal from packaging tray. Once the microcatheter has been wetted, do not allow to dry.
- The packaging mandrel is not intended for reuse. The packaging mandrel is not intended for use inside the human body.
- Check that all fittings are secure so that air is not introduced into guide catheter or microcatheter during continuous flush.
- In order to achieve optimal performance of Stryker Neurovascular Microcatheters and to maintain the lubricity of the Hydrolene® Coating surface, it is critical that a continuous flow of appropriate flush solution be maintained between the Stryker Neurovascular Microcatheter and guide catheter, and the microcatheter and any intraluminal device. In addition, flushing aids in preventing contrast crystal formation and/or clotting on both the intraluminal device and inside the guide catheter and/or the microcatheter lumen.
- Do not position microcatheter closer than 2.54 cm (1 in) from the steam source. Damage to the microcatheter may result.
- Excessive tightening of a hemostatic valve onto the microcatheter shaft may result in damage to the microcatheter. Removing the peel away introducer with a guidewire inserted in the crystal formation lumen might result in damage to the microcatheter shaft.
- To facilitate microcatheter handling, the proximal portion of the microcatheter does not have the hydrophilic surface. Greater resistance may be encountered when this section of the microcatheter is advanced into the RHV.

### Excelsior® SL-10™ Microcatheter

#### See package insert for complete indications, contraindications, warnings and instructions for use.

#### INTENDED USE / INDICATIONS FOR USE

Stryker Neurovascular Excelsior SL-10 Microcatheter is intended to assist in the delivery of diagnostic agents, such as contrast media, and therapeutic agents, such as occlusion coils, into the peripheral, coronary, and neurovasculature.

### CONTRAINDICATIONS

None known.

### POTENTIAL ADVERSE EVENTS

Potential adverse events associated with the use of microcatheters or with the endovascular procedures include, but are not limited to: access site complications, allergic reaction, aneurysm perforation, aneurysm rupture, death, embolism (air, foreign body, plaque, thrombus), hematoma, hemorrhage, infection, ischemia, neurological deficits, pseudoaneurysm, stroke, transient ischemic attack, vasospasm, vessel dissection, vessel perforation, vessel rupture, vessel thrombosis.

### WARNINGS

- Contents supplied STERILE using an ethylene oxide (EO) process. Do not use if sterile barrier is damaged. If damage is found, call your Stryker Neurovascular representative.
- For single patient use only. Do not reuse, reprocess or resterilize. Reuse, reprocessing or resterilization may compromise the structural integrity of the device and/or lead to device failure which, in turn, may result in patient injury, illness or death. Reuse, reprocessing or resterilization may also create a risk of contamination of the device and/or cause patient infection or cross-infection, including, but not limited to, the transmission of infectious disease(s) from one patient to another. Contamination of the device may lead to injury, illness or death of the patient.
- After use, dispose of product and packaging in accordance with hospital, administrative and/or local government policy.
- These devices are intended for use only by physicians trained in performing endovascular procedures.
- Inspect product before use for any bends, kinks or damage. Do not use a microcatheter that has been damaged. Damaged microcatheters may rupture causing vessel trauma or tip detachment during steering maneuvers.
- The shaping mandrel is not intended for use inside the human body.

- beyond the alignment marker when the fluoro-saver marker reaches the microcatheter hub.
- If the fluoro-saver marker is not visible, do not advance the coil without fluoroscopy.
- Do not rotate delivery wire during or after delivery of the coil. Rotating the Target Detachable Coil delivery wire may result in a stretched coil or premature detachment of the coil from the delivery wire, which could result in coil migration.
- Verify there is no coil loop protrusion into the parent vessel after coil placement and prior to coil detachment. Coil loop protrusion after coil placement may result in thromboembolic events if the coil is detached.
- Verify there is no movement of the coil after coil placement and prior to coil detachment. Movement of the coil after coil placement may indicate that the coil could migrate once it is detached.
- Failure to properly close the RHV compression fitting over the delivery wire before attaching the InZone® Detachment System could result in coil movement, aneurysm rupture or vessel perforation.
- Verify repeatedly that the distal shaft of the catheter is not under stress before detaching the Target Detachable Coil. Axial compression or tension forces could be stored in the 2-tip microcatheter causing the tip to move during coil delivery. Microcatheter tip movement could cause the aneurysm or vessel to rupture.
- Advancing the delivery wire beyond the microcatheter tip once the coil has been detached involves risk of aneurysm or vessel perforation.
- The long term effect of this product on extravascular tissues has not been established so care should be taken to retain this device in the intravascular space.

### CAUTIONS / PRECAUTIONS

- Federal Law (USA) restricts this device to sale by or on the order of a physician.
- Besides the number of InZone Detachment System units needed to complete the case, there must be an extra InZone Detachment System unit as backup.
- Removing the delivery wire without grasping the introducer sheath and delivery wire together may result in the detachable coil sliding out of the introducer sheath.
- Failure to remove the introducer sheath after inserting the delivery wire into the RHV the microcatheter will interrupt normal infusion of flush solution and allow back flow of blood into the microcatheter.
- Some low level overhead light near or adjacent to the patient is required to

- to injury, illness or death of the patient.
- After use, dispose of product and packaging in accordance with hospital, administrative and/or local government policy.
- **These devices are intended for use only by physicians trained in performing endovascular procedures.**
- Limited testing has been performed with solutions such as contrast media, saline and suspended embolic particles. The use of these catheters for delivery of solutions other than the types that have been tested for compatibility is not recommended. Do not use with glue or glue mixtures.
- The accessories are not intended for use inside the human body.
- Carefully inspect all devices prior to use. Verify shape, size and condition are suitable for the specific procedure.
- Exchange microcatheters frequently during lengthy procedures that require extensive guidewire manipulation or multiple guidewire exchanges.
- Never advance or withdraw an intravascular device against resistance until the cause of the resistance is determined by fluoroscopy. Movement of the microcatheter or guidewire against resistance could dislodge a clot, perforate a vessel wall, or damage microcatheter and guidewire. In severe cases, tip separation of the microcatheter or guidewire may occur.
- Inspect product before use for any bends, kinks or damage. Do not use a microcatheter that has been damaged. Damaged microcatheters may rupture causing vessel trauma or tip detachment during steering maneuvers.
- Shaping mandrel is not intended for use inside the human body.
- Discontinue use of microcatheter for infusion if increased resistance is noted. Resistance indicates possible blockage. Remove and replace blocked microcatheter immediately. DO NOT attempt to clear blockage by over-pressure. Doing so may cause the microcatheter to rupture, resulting in vascular damage or patient injury.
- Do not exceed 2,070 kPa (300 psi) infusion pressure. Excessive pressure could dislodge a clot, causing thromboemboli, or could result in a ruptured microcatheter or severed tip, causing vessel injury.

### CAUTIONS / PRECAUTIONS

- Federal Law (USA) restricts this device to sale by or on the order of a physician.
- To facilitate microcatheter handling, the proximal portion of the microcatheter does not have the hydrophilic surface. Greater resistance may be encountered when this section of the microcatheter is advanced into the RHV.
- Exercise care in handling of the microcatheter during a procedure to reduce the possibility of accidental breakage, bending or kinking.
- To reduce the probability of coating damage in tortuous vasculature, use a guide catheter with a minimum internal diameter as specified in Table 1 above, and is recommended for use with Stryker Neurovascular hydrophilically coated microcatheters.
- To control the proper introduction, movement, positioning and removal of the microcatheter within the vascular system, users should employ standard clinical angiographic and fluoroscopic practices and techniques throughout the interventional procedure.
- Flush dispenser coil of hydrophilically coated microcatheters prior to removal from dispenser coil. Once the microcatheter has been wetted, do not allow to dry. Do not reinsert the microcatheter into dispenser coil.
- Do not position microcatheter closer than 2.54 cm (1 in) from the steam source. Damage to the microcatheter may result.
- Check that all fittings are secure so that air is not introduced into guide catheter or microcatheter during continuous flush.
- In order to achieve optimal performance of Stryker Neurovascular Microcatheters and to maintain the lubricity of the Hydrolene® Coating surface, it is critical that a continuous flow of appropriate flush solution be maintained between the Stryker Neurovascular Microcatheter and guide catheter, and the microcatheter and any intraluminal device. In addition, flushing aids in preventing contrast crystal formation and/or clotting on both the intraluminal device and inside the guide catheter and/or the microcatheter lumen.
- Excessive tightening of a hemostatic valve onto the microcatheter shaft may result in damage to the microcatheter.



**Stryker Neurovascular**  
47900 Bayside Parkway  
Fremont, CA 94538

**strykerneurovascular.com**

Date of Release: NOV/2017

EX\_EN\_US

Copyright © 2017 Stryker

AP001839 v1.0 | Page 2 of 2

### Target® Detachable Coil

#### See package insert for complete indications, contraindications, warnings and instructions for use.

#### INTENDED USE / INDICATIONS FOR USE

Target Detachable Coils are intended to endovascularly obstruct or occlude blood flow in vascular abnormalities of the neurovascular and peripheral vessels.

Target Detachable Coils are indicated for endovascular embolization of:

- Intracranial aneurysms
- Other neurovascular abnormalities such as arteriovenous malformations and arteriovenous fistulae
- Arterial and venous embolizations in the peripheral vasculature

### CONTRAINDICATIONS

None known.

### POTENTIAL ADVERSE EVENTS

Potential complications include, but are not limited to: allergic reaction, aneurysm perforation and rupture, arrhythmia, death, edema, embolus, headache, hemorrhage, infection, ischemia, neurological/intracranial sequelae, post-embolization syndrome (fever, increased white blood cell count, discomfort), TIA/stroke, vasospasm, vessel occlusion or closure, vessel perforation, dissection, trauma, vessel rupture, vessel thrombosis. Other procedural complications including but not limited to: anesthetic and contrast media risks, hypotension, hypertension, access site complications.

### WARNINGS

- Contents supplied STERILE using an ethylene oxide (EO) process. Do not use if sterile barrier is damaged. If damage is found, call your Stryker Neurovascular representative.
- For single use only. Do not reuse, reprocess or resterilize. Reuse, reprocessing or resterilization may compromise the structural integrity of the device and/or lead to device failure which, in turn, may result in patient injury, illness or death. Reuse, reprocessing or resterilization may also create a risk of contamination of the device and/or cause patient infection or cross-infection, including, but not limited to, the transmission of infectious disease(s) from one patient to another. Contamination of the device may lead to injury, illness or death of the patient.
- After use, dispose of product and packaging in accordance with hospital, administrative and/or local government policy.

#### This device should only be used by physicians who have received appropriate training in interventional neuroradiology or interventional radiology and preclinical training on the use of this device as established by Stryker Neurovascular.

- Patients with hypersensitivity to 316LVM stainless steel may suffer an allergic reaction to this implant.
- MRI temperature testing was not conducted in arteriovenous malformations or fistulae and performance characteristics of the Target Detachable Coil System (Target Detachable Coils, InZone Detachment Systems, delivery systems and accessories) have not been demonstrated with other manufacturer's devices (whether coils, coil delivery devices, coil detachment systems, catheters, guidewires, and/or other accessories). Due to the potential incompatibility of non Stryker Neurovascular devices with the Target Detachable Coil System, the use of other manufacturer's devices with the Target Detachable Coil System is not recommended.
- To reduce risk of coil migration, the diameter of the first and second coil should never be less than the width of the ostium.
- In order to achieve optimal performance of the Target Detachable Coil System and to reduce the risk of thromboembolic complications, it is critical that a continuous infusion of appropriate flush solution be maintained between a) the femoral sheath and guiding catheter, b) the 2-tip microcatheter and guiding catheter, and c) the 2-tip microcatheter and Stryker Neurovascular guidewire and delivery wire. Continuous flush also reduces the potential for thrombus formation on, and crystallization of infusate around, the detachment zone of the Target Detachable Coil.
- Do not use the product after the "Use By" date specified on the package.
- Reuse of the packaging hoop or use with any coil other than the original coil may result in contamination of, or damage to, the coil.

Damaged delivery wires may cause detachment failures, vessel injury or unpredictable distal tip response during coil deployment. If a delivery wire is damaged at any point during the procedure, do not attempt to straighten or otherwise repair it. Do not proceed with deployment or detachment. Remove the entire coil and replace with undamaged product.

- Utilization of damaged coils may affect coil delivery to, and stability inside, the vessel or aneurysm, possibly resulting in coil migration and/or stretching.
- The fluoro-saver marker is designed for use with a Rotating Hemostatic Valve (RHV). If used without an RHV, the distal end of the coil may be

Copyright © 2017 Stryker

NV00018669 v2.0 | Page 2 of 2



**Stryker Neurovascular**  
47900 Bayside Parkway  
Fremont, CA 94538

**strykerneurovascular.com**

Date of Release: NOV/2017

EX\_EN\_US



LVIS®

Intraluminal Support Device

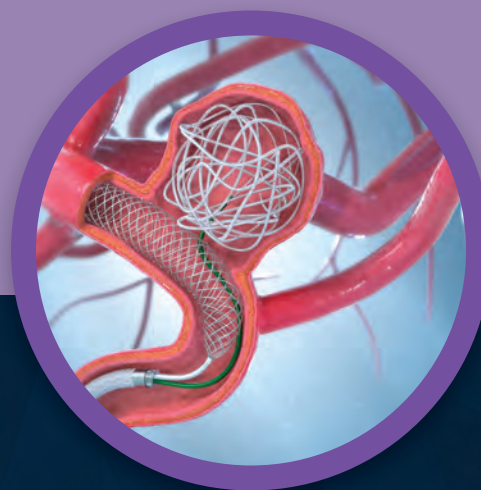
Low-profile Visualized Intرالuminal Support

## Stent Deployment. Refined.

Braided Coil Assist Stents with  
High Neck Coverage, Excellent Visibility  
and Improved Conformability\*



Aneurysm  
Therapy  
Solutions



For more information or a product demonstration,  
contact your local MicroVention representative:

MicroVention Worldwide  
Innovation Center  
35 Enterprise

Aliso Viejo, CA 92656 USA

MicroVention UK Limited

MicroVention Europe, S.A.R.L.

MicroVention Deutschland GmbH

[microvention.com](http://microvention.com)

PH +1.714.247.8000

PH +44 (0) 191 258 6777

PH +33 (1) 39 21 77 46

PH +49 211 210 798-0

*\*Humanitarian Device: Authorized by Federal Law for use with bare platinum embolic coils for the treatment of unruptured, wide neck (neck  $\geq$  4 mm or dome to neck ratio  $<$  2), intracranial, saccular aneurysms arising from a parent vessel with a diameter  $\geq$  2.5 mm and  $\leq$  4.5 mm. The effectiveness of this device for this use has not been demonstrated.*



## Smooth and stable.

Target Detachable Coils deliver consistently smooth deployment and exceptional microcatheter stability. Designed to work seamlessly together for framing, filling and finishing. Target Coils deliver the high performance you demand.

For more information, please visit [www.strykerneurovascular.com/Target](http://www.strykerneurovascular.com/Target) or contact your local Stryker sales representative.



**Target**<sup>®</sup>  
DETACHABLE COILS



## Bending expectations of conformability and stability.

**Enhanced conformability** – The hybrid cell structure is designed to enhance stent opening and conformability in bifurcations and tight curves.

**Ease of use** – All sizes of the Neuroform Atlas Stent are deliverable through Excelsior® SL-10® and Excelsior XT-17™ Microcatheters.

**Higher deployment accuracy** – The Neuroform Atlas Stent is designed to have very low foreshortening, which enables very high deployment accuracy.



## Neuroform Atlas™ STENT SYSTEM

# AJNR

## AMERICAN JOURNAL OF NEURORADIOLOGY

APRIL 2018  
VOLUME 39  
NUMBER 4  
WWW.AJNR.ORG

Publication Preview at [www.ajnr.org](http://www.ajnr.org) features articles released in advance of print. Visit [www.ajnrblog.org](http://www.ajnrblog.org) to comment on AJNR content and chat with colleagues and AJNR's News Digest at <http://ajnrndigest.org> to read the stories behind the latest research in neuroimaging.

605 PERSPECTIVES *E. Spinos*

### REVIEW ARTICLE

- 🔑 606 **Alphabet Soup: Sagittal Balance Correction Osteotomies of the Spine—What Radiologists Should Know** *T. Takahashi, et al.* SPINE

### PRACTICE PERSPECTIVES

- ☰ 612 **Revenue Increase following 2017 Multiple Procedures Payment Reduction Modification: Differential Impact on Neuroradiology—Report from an Academic Medical Center** *B.B. Noveiry, et al.*

### GENERAL CONTENTS

- ★🔑 618 **Iron-Insensitive Quantitative Assessment of Subcortical Gray Matter Demyelination in Multiple Sclerosis Using the Macromolecular Proton Fraction** *V.L. Yarnykh, et al.* ADULT BRAIN
- 🔑 626 **An Automated Statistical Technique for Counting Distinct Multiple Sclerosis Lesions** *J.D. Dworkin, et al.* ADULT BRAIN
- ★🔑 634 **Evaluation of the Sensitivity of Inhomogeneous Magnetization Transfer (ihMT) MRI for Multiple Sclerosis** *E. Van Obberghen, et al.* ADULT BRAIN
- ☰🔑 642 **Evaluation of Leptomeningeal Contrast Enhancement Using Pre- and Postcontrast Subtraction 3D-FLAIR Imaging in Multiple Sclerosis** *R. Zivadinov, et al.* ADULT BRAIN
- 🔑 648 **Brain Injury Lesion Imaging Using Preconditioned Quantitative Susceptibility Mapping without Skull Stripping** *S. Soman, et al.* ADULT BRAIN
- 654 **Utility of Repeat Head CT in Patients with Blunt Traumatic Brain Injury Presenting with Small Isolated Falcine or Tentorial Subdural Hematomas** *K.K. Devulapalli, et al.* ADULT BRAIN
- 658 **Dual-Energy CT in Hemorrhagic Progression of Cerebral Contusion: Overestimation of Hematoma Volumes on Standard 120-kV Images and Rectification with Virtual High-Energy Monochromatic Images after Contrast-Enhanced Whole-Body Imaging** *U.K. Bodanapally, et al.* ADULT BRAIN
- 🔑 663 **Prediction of the Multisegment Clot Sign on Dynamic CT Angiography of Cardioembolic Stroke** *Z. Chen, et al.* ADULT BRAIN

AJNR (Am J Neuroradiol ISSN 0195–6108) is a journal published monthly, owned and published by the American Society of Neuroradiology (ASNR), 800 Enterprise Drive, Suite 205, Oak Brook, IL 60523. Annual dues for the ASNR include \$170.00 for journal subscription. The journal is printed by Cadmus Journal Services, 5457 Twin Knolls Road, Suite 200, Columbia, MD 21045; Periodicals postage paid at Oak Brook, IL and additional mailing offices. Printed in the U.S.A. POSTMASTER: Please send address changes to American Journal of Neuroradiology, P.O. Box 3000, Denville, NJ 07834, U.S.A. Subscription rates: nonmember \$400 (\$470 foreign) print and online, \$320 online only; institutions \$460 (\$530 foreign) print and basic online, \$915 (\$980 foreign) print and extended online, \$380 online only (basic), extended online \$825; single copies are \$35 each (\$40 foreign). Indexed by PubMed/Medline, BIOSIS Previews, Current Contents (Clinical Medicine and Life Sciences), EMBASE, Google Scholar, HighWire Press, Q-Sensei, RefSeek, Science Citation Index, and SCI Expanded. Copyright © American Society of Neuroradiology.

		<b>669</b>	<b>Arterial Spin-Labeling Improves Detection of Intracranial Dural Arteriovenous Fistulas with MRI</b> <i>S.A. Amukotuwa, et al.</i>	<b>ADULT BRAIN</b>		
		<b>678</b>	<b>Early Hemodynamic Response Assessment of Stereotactic Radiosurgery for a Cerebral Arteriovenous Malformation Using 4D Flow MRI</b> <i>C.Q. Li, et al.</i>	<b>ADULT BRAIN</b>		
		<b>682</b>	<b>Quantitative Phase-Contrast MR Angiography to Measure Hemodynamic Changes in Idiopathic Intracranial Hypertension</b> <i>J. Juhász, et al.</i>	<b>ADULT BRAIN</b>		
		<b>687</b>	<b>MRI Features Can Predict 1p/19q Status in Intracranial Gliomas</b> <i>A. Lasocki, et al.</i>	<b>ADULT BRAIN</b>		
				<b>693</b>	<b>Whole-Tumor Histogram and Texture Analyses of DTI for Evaluation of IDH1-Mutation and 1p/19q-Codeletion Status in World Health Organization Grade II Gliomas</b> <i>Y.W. Park, et al.</i>	<b>ADULT BRAIN</b>
			<b>699</b>	<b>Brain Imaging in Cases with Positive Serology for Dengue with Neurologic Symptoms: A Clinicoradiologic Correlation</b> <i>H.A. Vanjare, et al.</i>	<b>ADULT BRAIN</b>	
			<b>704</b>	<b>7T Brain MRS in HIV Infection: Correlation with Cognitive Impairment and Performance on Neuropsychological Tests</b> <i>M. Mohamed, et al.</i>	<b>ADULT BRAIN</b>	
				<b>713</b>	<b>Quantification of Intracranial Aneurysm Volume Pulsation with 7T MRI</b> <i>R. Kleinloog, et al.</i>	<b>ADULT BRAIN</b> <b>INTERVENTIONAL</b>
		<b>720</b>	<b>HARMless: Transient Cortical and Sulcal Hyperintensity on Gadolinium-Enhanced FLAIR after Elective Endovascular Coiling of Intracranial Aneurysms</b> <i>S. Suthiphosuwat, et al.</i>	<b>ADULT BRAIN</b> <b>INTERVENTIONAL</b>		
		<b>727</b>	<b>Radiation Dosimetry of 3D Rotational Neuroangiography and 2D-DSA in Children</b> <i>N.A. Shkumat, et al.</i>	<b>INTERVENTIONAL</b> <b>PATIENT SAFETY</b>		
			<b>734</b>	<b>A Patient Dose-Reduction Technique for Neuroendovascular Image-Guided Interventions: Image-Quality Comparison Study</b> <i>A. Sonig, et al.</i>	<b>INTERVENTIONAL</b> <b>PATIENT SAFETY</b>	
			<b>742</b>	<b>Altered Regional Homogeneity in Chronic Insomnia Disorder with or without Cognitive Impairment</b> <i>R. Pang, et al.</i>	<b>FUNCTIONAL</b>	
			<b>748</b>	<b>MRI with DWI for the Detection of Posttreatment Head and Neck Squamous Cell Carcinoma: Why Morphologic MRI Criteria Matter</b> <i>A. Ailianou, et al.</i>	<b>HEAD &amp; NECK</b>	
		<b>756</b>	<b>Clinical Validation of a Predictive Model for the Presence of Cervical Lymph Node Metastasis in Papillary Thyroid Cancer</b> <i>N.U. Patel, et al.</i>	<b>HEAD &amp; NECK</b>		
		<b>762</b>	<b>Melanoma of the Sinonasal Tract: Value of a Septate Pattern on Precontrast T1-Weighted MR Imaging</b> <i>Y.-K. Kim, et al.</i>	<b>HEAD &amp; NECK</b>		
		<b>768</b>	<b>Intraoperative Conebeam CT for Assessment of Intracochlear Positioning of Electrode Arrays in Adult Recipients of Cochlear Implants</b> <i>H. Jia, et al.</i>	<b>HEAD &amp; NECK</b>		
		<b>775</b>	<b>Modeling Early Postnatal Brain Growth and Development with CT: Changes in the Brain Radiodensity Histogram from Birth to 2 Years</b> <i>K.A. Cauley, et al.</i>	<b>PEDIATRICS</b>		
		<b>782</b>	<b>MRI Features of Aquaporin-4 Antibody-Positive Longitudinally Extensive Transverse Myelitis: Insights into the Diagnosis of Neuromyelitis Optica Spectrum Disorders</b> <i>C.G. Chee, et al.</i>	<b>SPINE</b>		
		<b>788</b>	<b>Normal Values of Magnetic Relaxation Parameters of Spine Components with the Synthetic MRI Sequence</b> <i>M. Drake-Pérez, et al.</i>	<b>SPINE</b>		

## ONLINE FEATURES

### LETTERS

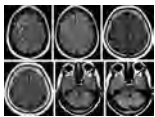
- E47** “Delayed Pial Vessels” in Multiphase CT Angiography Aid in the Detection of Arterial Occlusion in Anterior Circulation *R.-J. Singh, et al.*
- E48** *Reply* *D. Byrne, et al.*

**E49** **Neuroradiology Fellowship Case Requirements Need Reform**

*C.M. Pfeifer*

**E51** **Relationship between Ischemic Injury and Patient Outcomes after Surgical or Endovascular Treatment of Ruptured Anterior Communicating Artery Aneurysms** *S. Mugikura, et al.*

**E53** **Reply** *J.J. Heit*



Different patterns of cortical and sulcal hyperintensity on gadolinium-enhanced FLAIR: Top left image shows postcoiling Gd-enhanced FLAIR in 1 patient with resolved abnormalities on 2-month follow-up (top middle). Postcoiling of a left paraclinoid ICA aneurysm with hyperintensity along the left MCA territory in a second patient (top right), with 2-month follow-up (bottom left). Third patient s/p coiling of basilar tip aneurysm shows postprocedural hyperintensity along the left cerebellar fissures (bottom middle), with normal 2-month follow-up (bottom right).

★ Indicates Editor's Choices selection

✍ Indicates Fellows' Journal Club selection

🔑 Indicates open access to non-subscribers at [www.ajnr.org](http://www.ajnr.org)

☰ Indicates article with supplemental on-line table

🖼 Indicates article with supplemental on-line photo

📺 Indicates article with supplemental on-line video

EBM 1 Evidence-Based Medicine Level 1

EBM 2 Evidence-Based Medicine Level 2

### Official Journal:

American Society of Neuroradiology  
American Society of Functional Neuroradiology  
American Society of Head and Neck Radiology  
American Society of Pediatric Neuroradiology  
American Society of Spine Radiology

### EDITOR-IN-CHIEF

#### Jeffrey S. Ross, MD

Professor of Radiology, Department of Radiology,  
Mayo Clinic College of Medicine, Phoenix, AZ

### SENIOR EDITORS

#### Harry J. Cloft, MD, PhD

Professor of Radiology and Neurosurgery,  
Department of Radiology, Mayo Clinic College of  
Medicine, Rochester, MN

#### Thierry A.G.M. Huisman, MD

Professor of Radiology, Pediatrics, Neurology, and  
Neurosurgery, Chairman, Department of Imaging  
and Imaging Science, Johns Hopkins Bayview,  
Director, Pediatric Radiology and Pediatric  
Neuroradiology, Johns Hopkins Hospital,  
Baltimore, MD

#### Yvonne W. Lui, MD

Associate Professor of Radiology,  
Chief of Neuroradiology,  
New York University School of Medicine,  
New York, NY

#### C.D. Phillips, MD, FACR

Professor of Radiology, Weill Cornell Medical  
College, Director of Head and Neck Imaging,  
New York-Presbyterian Hospital, New York, NY

#### Pamela W. Schaefer, MD

Clinical Director of MRI and Associate Director of  
Neuroradiology, Massachusetts General Hospital,  
Boston, Massachusetts, Associate Professor,  
Radiology, Harvard Medical School, Cambridge, MA

#### Charles M. Strother, MD

Professor of Radiology, Emeritus, University of  
Wisconsin, Madison, WI

### STATISTICAL SENIOR EDITOR

#### Bryan A. Comstock, MS

Senior Biostatistician,  
Department of Biostatistics,  
University of Washington, Seattle, WA

### EDITORIAL BOARD

Ashley H. Aiken, Atlanta, GA  
Lea M. Alhilali, Phoenix, AZ  
John D. Barr, Dallas, TX  
Ari Blitz, Baltimore, MD  
Barton F. Branstetter IV, Pittsburgh, PA  
Jonathan L. Brisman, Lake Success, NY  
Julie Bykowski, San Diego, CA  
Keith Cauley, Danville, PA  
Asim F. Choudhri, Memphis, TN  
Alessandro Cianfoni, Lugano, Switzerland  
J. Matthew Debnam, Houston, TX  
Seena Dehkharghani, New York, NY  
Colin Derdeyn, Iowa City, IA  
Rahul S. Desikan, San Francisco, CA  
Yonghong Ding, Rochester, MN  
Clifford J. Eskey, Hanover, NH  
Saeed Fakhra, Phoenix, AZ  
Massimo Filippi, Milan, Italy  
Allan J. Fox, Toronto, Ontario, Canada  
Wende N. Gibbs, Los Angeles, CA  
Christine M. Glastonbury, San Francisco, CA  
John L. Go, Los Angeles, CA  
Allison Grayev, Madison, WI  
Brent Griffith, Detroit, MI  
Wan-Yuo Guo, Taipei, Taiwan  
Ajay Gupta, New York, NY  
Rakesh K. Gupta, Lucknow, India  
Lotfi Hachein-Bey, Sacramento, CA  
Christopher P. Hess, San Francisco, CA  
Andrei Holodny, New York, NY  
Benjamin Huang, Chapel Hill, NC  
George J. Hunter, Boston, MA  
Mahesh V. Jayaraman, Providence, RI  
Valerie Jewells, Chapel Hill, NC  
Christof Karmonik, Houston, TX  
Timothy J. Kaufmann, Rochester, MN  
Hillary R. Kelly, Boston, MA  
Toshibumi Kinoshita, Akita, Japan  
Kenneth F. Layton, Dallas, TX  
Michael M. Lell, Nürnberg, Germany  
Michael Lev, Boston, MA  
Karl-Olof Lovblad, Geneva, Switzerland  
Franklin A. Marden, Chicago, IL  
M. Gisele Matheus, Charleston, SC  
Joseph C. McGowan, Merion Station, PA  
Stephan Meckel, Freiburg, Germany  
Christopher J. Moran, St. Louis, MO  
Takahisa Mori, Kamakura City, Japan  
Suresh Mukherji, Ann Arbor, MI  
Amanda Murphy, Toronto, Ontario, Canada  
Alexander J. Nemeth, Chicago, IL  
Sasan Partovi, Cleveland, OH  
Laurent Pierot, Reims, France  
Jay J. Pillai, Baltimore, MD

Whitney B. Pope, Los Angeles, CA  
M. Judith Donovan Post, Miami, FL  
Tina Young Poussaint, Boston, MA  
Joana Ramalho, Lisbon, Portugal  
Otto Rapalino, Boston, MA  
Álex Rovira-Cañellas, Barcelona, Spain  
Paul M. Ruggieri, Cleveland, OH  
Zoran Rumboldt, Rovinj-Rovigno, Croatia  
Amit M. Saindane, Atlanta, GA  
Erin Simon Schwartz, Philadelphia, PA  
Lubdha M. Shah, Salt Lake City, UT  
Aseem Sharma, St. Louis, MO  
J. Keith Smith, Chapel Hill, NC  
Maria Vittoria Spampinato, Charleston, SC  
Gordon K. Sze, New Haven, CT  
Krishnamoorthy Thamburaj, Hershey, PA  
Cheng Hong Toh, Taipei, Taiwan  
Thomas A. Tomsick, Cincinnati, OH  
Aquila S. Turk, Charleston, SC  
Willem Jan van Rooij, Tilburg, Netherlands  
Arastoo Vossough, Philadelphia, PA  
Elysa Widjaja, Toronto, Ontario, Canada  
Max Wintermark, Stanford, CA  
Ronald L. Wolf, Philadelphia, PA  
Kei Yamada, Kyoto, Japan  
Carlos Zamora, Chapel Hill, NC

### EDITORIAL FELLOW

Vahe Zohrabian, New Haven, CT

### SPECIAL CONSULTANTS TO THE EDITOR

#### AJNR Blog Editor

Neil Lall, Denver, CO

#### Case of the Month Editor

Nicholas Stence, Aurora, CO

#### Case of the Week Editors

Juan Pablo Cruz, Santiago, Chile  
Sapna Rawal, Toronto, Ontario, Canada

#### Classic Case Editor

Sandy Cheng-Yu Chen, Taipei, Taiwan

#### Facebook Editor

Peter Yi Shen, Sacramento, CA

#### Health Care and Socioeconomics Editor

Pina C. Sanelli, New York, NY

#### Physics Editor

Greg Zaharchuk, Stanford, CA

#### Podcast Editor

Wende N. Gibbs, Los Angeles, CA

#### Twitter Editor

Jennifer McCarty, Atlanta, Georgia

### YOUNG PROFESSIONALS ADVISORY COMMITTEE

Asim K. Bag, Birmingham, AL  
Anna E. Nidecker, Sacramento, CA  
Peter Yi Shen, Sacramento, CA

Founding Editor  
Juan M. Taveras

Editors Emeriti

Mauricio Castillo, Robert I. Grossman,  
Michael S. Huckman, Robert M. Quencer

Managing Editor  
Karen Halm

Assistant Managing Editor

Laura Wilhelm

Digital Publications and Social Media Coordinator

Kylie Mason

Executive Director, ASNRR

Mary Beth Hepp



Title: Temple of Poseidon. This image was taken in Sounion at the tip of the Attica peninsula. It was shot with a Nikon D700 camera at ISO 400, f6.3, at 1/160 second.  
*Efstathios Spinos, MD, Peripheral & Neurovascular Interventional Radiology, Johnston-Willis Medical Center, Richmond, Virginia*

# Alphabet Soup: Sagittal Balance Correction Osteotomies of the Spine—What Radiologists Should Know

 T. Takahashi,  D. Kainth,  S. Murette, and  D. Polly



## ABSTRACT

**SUMMARY:** Global sagittal malalignment has been demonstrated to have correlation with clinical symptoms and is a key component to be restored in adult spinal deformity. In this article, various types of sagittal balance-correction osteotomies are reviewed primarily on the basis of the 3 most commonly used procedures: Smith-Petersen osteotomy, pedicle subtraction osteotomy, and vertebral column resection. Familiarity with the expected imaging appearance and commonly encountered complications seen on postoperative imaging studies following correction osteotomies is crucial for accurate image interpretation.

**ABBREVIATIONS:** BDBO = bone-disc-bone osteotomy; PSO = pedicle subtraction osteotomy; SPO = Smith-Petersen osteotomy; SVA = sagittal vertical axis; VCR = vertebral column resection

Adult spinal deformity can be either the result of progression of conditions present in childhood/adolescence or new onset secondary to degenerative changes, which is known as de novo degenerative scoliosis.<sup>1,2</sup> There are many conditions that can lead to spinal deformity, including trauma, cancer, and osteoporosis and congenital, postsurgical, and idiopathic causes. Scoliosis is defined as  $\geq 10^\circ$  of coronal spinal curvature measured by the Cobbs angle method.<sup>3</sup> In 2006, the Scoliosis Research Society published an initial attempt to classify adult spinal deformity on the basis of the King/Moe and Lenke classification systems<sup>4</sup>; however, both of these well-known classification systems were originally developed for adolescent idiopathic scoliosis, and applying this system to adult spinal deformity was found to be suboptimal. This is because the treatment of adult spinal deformity has been shown to be driven by pain and disability in contrast to adolescent idiopathic scoliosis, which is primarily driven by coronal/cos-

metic deformity.<sup>5</sup> Surgical treatment of adolescent idiopathic scoliosis depends on the curve type and magnitude and is also affected by the degree of progression, skeletal maturity, cosmesis, and pain.<sup>6</sup> An operation is typically performed for primary curves that have a Cobb angle of  $>45^\circ$ .<sup>7,8</sup> Surgeons vary in opinion regarding the levels to be fused within the general guidelines. These levels will depend on the major curve, shoulder balance, amount of correction desired, stiffness of the curve, side-bending radiographs, and clinical examination.

In recent years, sagittal spinopelvic alignment has been shown to correlate with a patient's pain and disability and is a primary determinant of health-related quality-of-life measures.<sup>9</sup> Surgical treatment of a deformity can be beneficial in the appropriately selected patient. Clinical improvement has been demonstrated in studies in which sagittal imbalance was corrected.<sup>10,11</sup> The Scoliosis Research Society Adult Deformity Committee subsequently developed a new classification system to address these pertinent features of adult spinal deformity in 2012 based on the work of Schwab et al<sup>9,12-14</sup> and Bess et al.<sup>15</sup> This classification system has shown excellent inter- and intrarater reliability on its validation study.<sup>16</sup> Spine surgeons obtain preoperative and postoperative 36-inch standing full spine radiographs in the adult patient to primarily assess the following parameters: sagittal vertical axis (SVA), pelvic incidence minus lumbar lordosis, pelvic tilt, and coronal curve type.<sup>14</sup>

Until very recently, spinopelvic alignment has not been emphasized in the radiology literature.<sup>17</sup> Glassman et al<sup>18</sup> suggested that coronal balance correction is not as important as restoration of sagittal balance. There are various surgical techniques to correct sagittal imbalance, including various types of osteotomies.

From the Departments of Radiology (T.T., S.M.), Neurosurgery (D.K.), and Orthopedic Surgery (D.P.), University of Minnesota, Minneapolis, Minnesota.

An abstract "Sagittal Balance Correction Osteotomies: What Radiologists Should Know" was presented at the American Society of Spine Radiology Annual Symposium, February 23–26, 2017; San Diego, California as an electronic poster. Part of the material was presented as an oral presentation, "Implementation of the Schwab–Scoliosis Research Society Classification for Radiographic Measurement of Adult Spinal Deformity—What the Surgeon Wants to Know?" at the American Society of Spine Radiology Annual Symposium, February 18–21, 2016; Bonita Springs, Florida, which subsequently was awarded best nonmentored diagnostic presentation.

Please address correspondence to Takashi Takahashi, MD, MS, Department of Radiology, University of Minnesota, 20 Delaware St SE, MMC 292 4, Minneapolis, MN 55455; e-mail: takas005@umn.edu

 Indicates open access to non-subscribers at [www.ajnr.org](http://www.ajnr.org)

<http://dx.doi.org/10.3174/ajnr.A5444>

Knowledge about these operations and how they appear on imaging is critical for radiologists interpreting spine imaging to optimally report the findings. The purpose of this article was to summarize the 3 most widely used types of sagittal balance-correction osteotomies: Smith-Petersen osteotomy (SPO), pedicle subtraction osteotomy (PSO), and vertebral column resection (VCR), with an additional brief discussion of their derivatives or related uncommon procedures.

### Spinopelvic Measurements

**SVA.** In the Scoliosis Research Society–Schwab Spinal Deformity Classification System evaluates global spinal alignment only in the sagittal plane by using the sagittal vertical axis. This is a measure of the horizontal distance between the C7 plumb line and the posterosuperior corner of the S1 endplate. The C7 plumb line is a vertical line drawn downward from the center of the C7 vertebral body, parallel to the vertical edge of the film.<sup>19</sup> The distance is

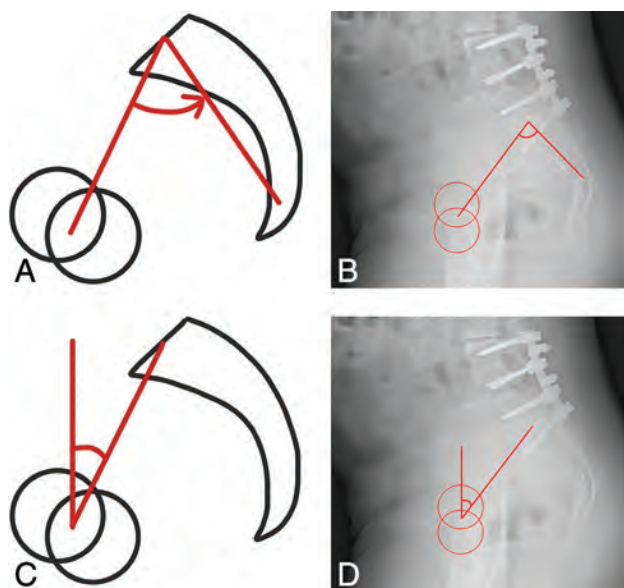


**FIG 1.** Schematic (A) and radiographic measurement (B) of pelvic incidence: an angle between a line drawn perpendicular to the middle of the superior sacral endplate and a line joining from the center of femoral heads to the center of the superior sacral endplate. Schematic (C) and radiographic measurement (D) of pelvic tilt: an angle measured between the lines connecting the center of the superior endplate of S1 to the center of femoral heads from its vertical perpendicular line.

considered positive when the C7 plumb line is located anterior to the posterosuperior corner of S1. In the pediatric population, the SVA is considered abnormal in either the positive or negative direction when it is  $>2$  cm in absolute value. However, in adult spinal deformity, only the positive direction is of clinical concern. In this classification, the C7 plumb line is considered abnormal when it is located anterior to the posterosuperior corner of the S1 vertebral body at  $>4$  cm. It is classified as positive when between 4 and 9.5 cm and very positive if  $>9.5$  cm.

**Pelvic Incidence–Lumbar Lordosis Mismatch.** Pelvic incidence is an angle between a line drawn perpendicular to the middle of the superior sacral endplate and a line joining from the center of the femoral heads to the center of the superior sacral endplate (Fig 1). This is a measure of pelvic depth and is a patient-specific parameter that determines the native sagittal contour. In the Scoliosis Research Society classification, lumbar lordosis is measured from the superior endplate of L1 to the superior endplate of S1 using the Cobbs angle technique. When pelvic incidence minus lumbar lordosis is  $\geq 10^\circ$ , a study has shown that patients had a 10 times greater risk for undergoing revision surgery if such malalignment is maintained after a lumbar fusion operation.<sup>20</sup>

**Pelvic Tilt.** Pelvic tilt is an angle measured between a line connecting the center of the superior endplate of S1 to the center of the femoral heads, relative to a vertical perpendicular line (Fig 1). This measure is used to assess pelvic version, typically retroversion, which is a compensation mechanism to maintain spinal alignment. The retroversion is manifested by an increase in the pelvic tilt angle.

### Sagittal Balance-Correction Osteotomies

The surgical correction technique of global positive sagittal balance can be considered as creation/restoration of more lordosis in the spine. In advanced cases, attaining such a goal requires osteotomies of the vertebrae. The more parts of the vertebrae resected, the more regional lordosis created (Table). There are various named osteotomies: Smith-Petersen osteotomy, pedicle subtraction osteotomy, and vertebral column resection are the paradigms of these procedures in order of increasing surgical complexity.<sup>2</sup> Recently, Schwab et al<sup>21</sup> proposed an anatomic-based spinal osteotomy classification. This approach uses grade 1 through 6 based on how much bone is resected. In this classification, a

### Summary of sagittal balance-correction osteotomy

	SPO/Ponte	PSO Category	VCR
Schwab grade	1 and 2	3 and 4	5 and 6
Resection area	Posterior element only	Included part of vertebral body	Entire vertebra
Indication	Long, gradual, rounded kyphosis, eg, Scheurmann kyphosis	Sharp, focal kyphosis with fixed disc space, ie, SPO not applicable	Sharp, focal kyphosis at thoracic vertebra Hemivertebra resection Vertebral tumor resection
Need disc space mobility?	Yes	No	No
Sharp angular kyphosis correction?	No	Yes	Yes
Thoracic spine correction?	No	No	Yes
Kyphotic curvature correction	$\sim 10^\circ$ /level	$30^\circ$ – $40^\circ$ /level	$45^\circ$ – $70^\circ$
Indicated SVA (cm)	$>6$ – $8$ cm but $<10$ cm (positive SVA)	$>10$ – $12$ cm (very positive SVA)	
Mean neurologic/overall complication rate (%) <sup>27</sup>	2.1/40.4	9.1/38.5	14.3/39

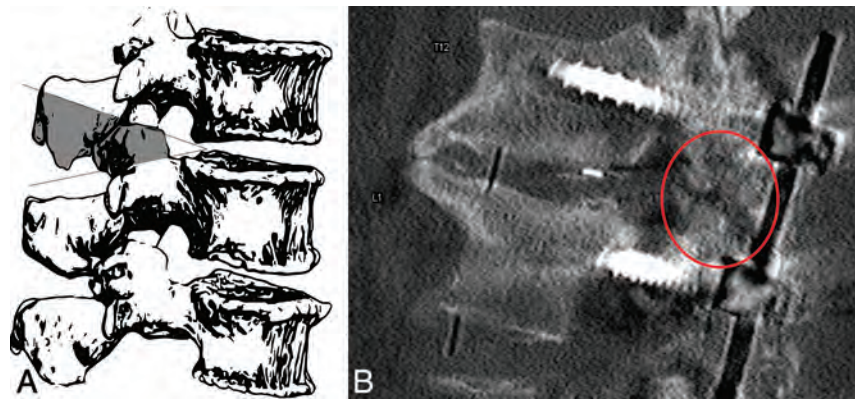


**FIG 2.** A, Schematic rendering of an SPO. Osteotomy of the posterior element, including wide resection of the facet joint. B, A 52-year-old man with a history of lumbar spinal fusion instrumentation at an outside institution who underwent sagittal correction surgery including an L3 PSO (not shown) and a T12–L1 SPO. This is a magnified image focusing on T12–L1 off the midline. The image demonstrates the T12 inferior articular facet and the L1 superior articular facet resections (*circle*) in addition to ligamentum flavum resection and bone grafts that were placed.

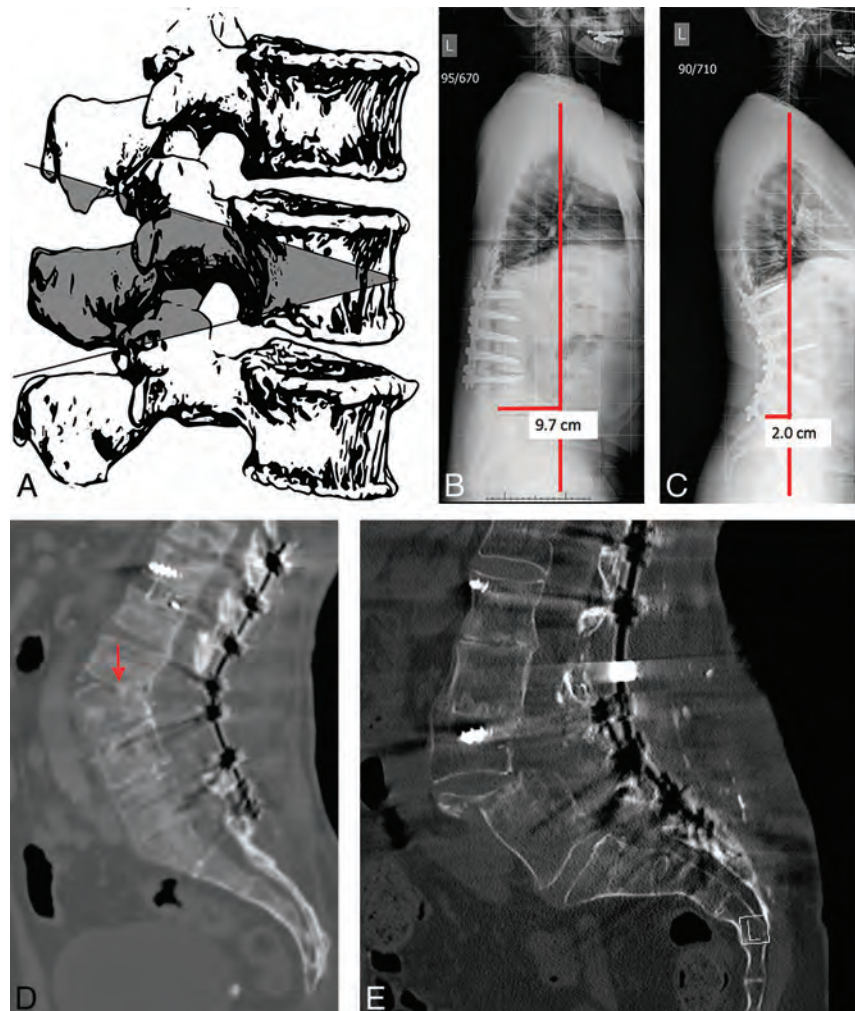


**FIG 3.** A, Schematic rendering of PSO. This is a posterior closing wedge osteotomy with resection of the posterior column, both pedicles, and part of the vertebral body. B, A 63-year-old man with prior postsurgical change of T12–L4 fusion instrumentation with very positive global sagittal imbalance (SVA = 9.7 cm). C, The same patient after L3 PSO and fusion instrumentation extension both cranially and caudally. The SVA is now within normal limits (2.0 cm). D, The same patient with a CT midsagittal bone window image demonstrating resection of the part of the L3 vertebral body extending to the superior endplate (*arrow*) with closure osteotomy at L3, consistent with pedicle subtraction osteotomy. This should not be mistaken for a posterior wedge compression fracture. E, A patient with a history of lumbar spinal fusion instrumentation, including complete intervertebral disc space fusion across L4–L5, underwent an L4 PSO and subsequently developed a fracture through the L4 vertebral body subjacent to the superior endplate, with resultant anterior subluxation of the superior fragment and L3 vertebral body relative to a dominant L4–L5 vertebral body fusion mass fragment.

modifier may be added on the basis of the surgical approach level beyond the destabilization, which is either posterior approach or combined anterior and posterior approach.

### SPO and Like Procedures

This category encompasses Schwab classification of grades 1 and 2 osteotomy categories. Grades 1 and 2 refer to partial and complete facet resection, respectively. The paradigm osteotomy under this category is the Smith-Petersen osteotomy.

**SPO.** SPO was originally described for correction of flexion deformity in rheumatoid arthritis, in which ankyloses of the articular process and the adjacent spinous processes were present.<sup>22</sup> SPO is also referred to as extension osteotomy.<sup>23</sup> It is a posterior column closing wedge osteotomy technique involving resection of the lamina, posterior ligaments, and facet joints (Fig 2). The osteotomy site is then closed by adjusting the operating table into extension or compression on posterior spinal instrumentation, resulting in posterior column shortening.

**Polysegmental Osteotomy.** Polysegmental osteotomy involves removal of the superior and inferior articular processes and the interlaminar space adjacent to the articular processes. This is performed at multiple levels to create the necessary amount of lordosis. The original SPO sometimes achieved its sagittal balance correction via destabilization of the anterior tension band, which resulted in a risk of vascular and gastrointestinal complications. Therefore, this technique was developed in an attempt to cause less disruption of the anterior column than occurred from the originally described Smith-Petersen osteotomy.<sup>24,25</sup>

**Ponte Procedure.** The Ponte procedure refers to the resection of multiple facets and spinous processes with posterior decompression along unfused regions of kyphotic deformity in Scheurmann kyphosis.<sup>25,26</sup> This technique is a more commonly used posterior column osteotomy than the originally described SPO; however, the name “SPO” has remained to describe a spectrum of posterior column osteotomies categorized generally under the grade 2 group including the Ponte procedure.<sup>25</sup> Thus, nomenclature confusion can occur at times. In this article, SPO terminology also refers to the Ponte procedure as in other literature.

In SPO, a mobile anterior disc is required for correction. SPO is generally considered when the sagittal vertical axis is 6–8 cm positive.<sup>27</sup> SPO is especially suitable for long, gradual, rounded kyphosis—that is, Scheurmann kyphosis. SPO can achieve 5°–10° of lordosis per level of correction.<sup>28</sup> It is estimated that for every 1 mm of facet resection, 1° of correction is obtained.

The benefit of SPO is that it is technically easier and safer than higher grade osteotomies. For a comparable degree of correction, 3-level SPO resulted in roughly half the blood loss compared with single-level PSO.<sup>29</sup> The disadvantage of SPO is that it provides fewer sagittal plane corrections than higher level osteotomies and may create coronal decompensation in contrast to other sagittal balance-correction osteotomies. SPO is also not suitable for sharp angular kyphosis correction. Because SPO uses the disc space as a fulcrum, this technique is inapplicable when the disc space lacks flexibility.

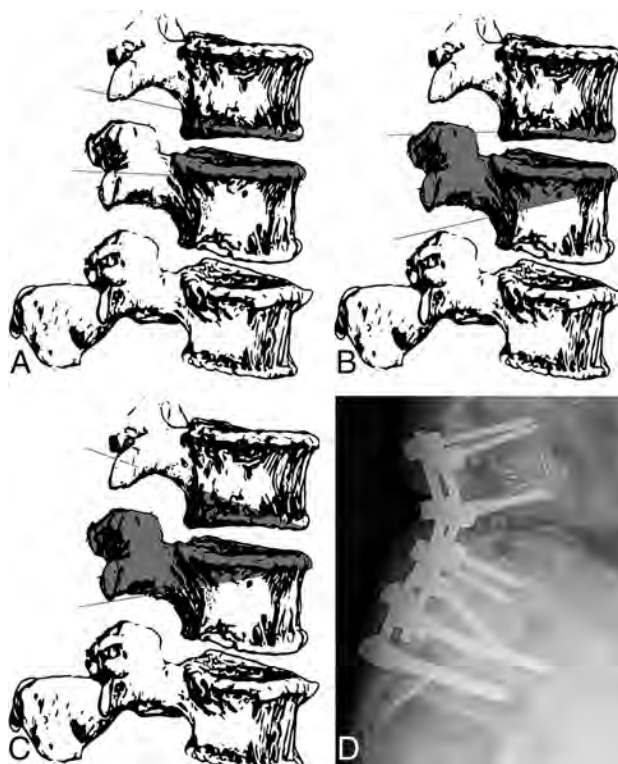


**FIG 4.** A, BDBO type 1. This osteotomy involves the resection of the inferior portion of the target vertebra, along with the disc and superior endplate below it. B, BDBO type 2, also known as extended PSO. This osteotomy extends PSO cranially to involve the disc and inferior endplate of the vertebra above it. C, BDBO type 3. Closing wedge osteotomies are performed at levels both above and below the targeted disc level, with the osteotomy extending to just inferior to the transverse processes of the both levels. D, Lateral view plain radiograph demonstrates an extended PSO (BDBO type 2) at L4 where the PSO extends into the posterior two-thirds of the superior endplate.

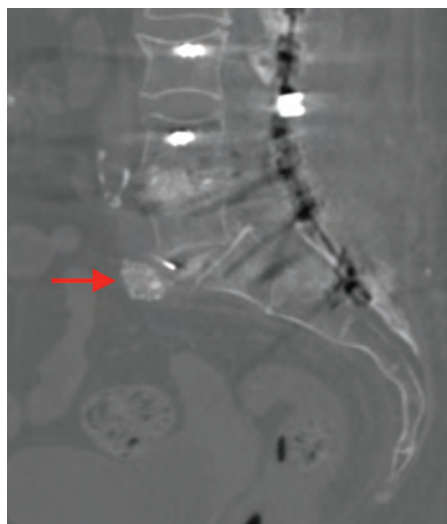


**FIG 5.** A patient with prior fusion instrumentation from L2 to the sacrum who underwent 2-level transforaminal lumbar intervertebral fusion at L3–L4 and L4–L5. There was inadvertent intraoperative anterior longitudinal ligament disruption at L5–S1. This essentially resulted in an anterior opening osteotomy effect along with a Smith-Petersen osteotomy posterior closing osteotomy (ie, X-osteotomy). There is an unintended anteriorly extruded intervertebral disc graft at this level (arrow).

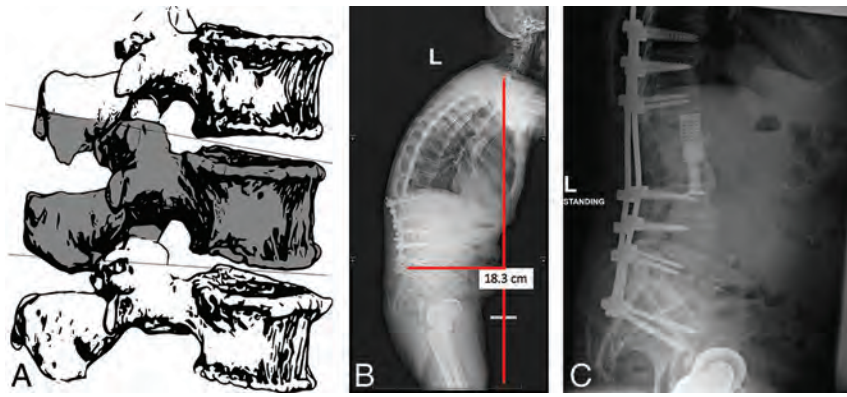


**FIG 6.** A, Schematic drawing of single-level VCR. The entire vertebral body is resected. B, A 61-year-old man with postoperative discitis/osteomyelitis with a very positive SVA (>18 cm). C, The same patient underwent 2-level (L1 and L2) VCR with extension of posterior fusion instrumentation.

### PSO and Like Procedures

In the grade 3 category of the Schwab classification, the osteotomy involves part of the posterior vertebral body and posterior elements, including the pedicles. The paradigmatic procedure of this category is a pedicle subtraction osteotomy.

**PSO.** In 1985, the pedicle subtraction osteotomy was described by Thomasen.<sup>30</sup> It was originally described for the treatment of disabling kyphosis in patients with ankylosing spondylitis. PSO is a posterior wedge-type osteotomy with resection of the posterior column, both pedicles, and part of the vertebral body, followed by closure osteotomy (Fig 3). In PSO, the anterior cortex is used as a hinge. Therefore, PSO is typically used for patients with sharp or angular kyphosis as well as at levels lacking anterior flexibility where SPO is inapplicable.<sup>25,31</sup> Analogous to the SPO, the PSO has been also referred to by various alternatives, including closing wedge osteotomy, eggshell osteotomy, and transpedicular wedge procedure.<sup>25</sup>

On imaging, PSO may be mistaken for a posterior wedge compression fracture if one is not aware of this type of surgery. PSO is generally indicated for correction of SVAs of >10–12 cm, and it can provide 30°–40° of lordosis correction on average.<sup>31,32</sup> In this technique, along with pedicle screw posterior fixation, wide laminectomies are performed at adjacent levels to protect the exiting nerve roots. Interbody fusion at levels above and below the osteotomy may be performed to avoid pseudoarthrosis.

PSO provides the main advantage of more effective focal kyphosis correction than SPO, a mean correction of 32.6° per level of PSO in contrast to 10.2° per level of SPO.<sup>25</sup> The mean neurologic complication rate is higher than that of SPO: 9.1% in PSO versus 2.1% in SPO.<sup>25</sup>

**Bone-Disc-Bone Osteotomy.** In the grade 4 category of the Schwab classification, surgical resection extends to involve a disc and its adjacent endplates. Extended PSO is a type of bone-disc-bone osteotomy (BDBO), which is categorized under this grade. There are 3 types of BDBO, with lordosis correction ranging from 35° to 60° (Fig 4).<sup>32</sup> In type 1, the inferior portion of the target vertebra, along with the disc and superior endplate below it, is involved. In type 2 or extended PSO, PSO is extended to involve

the disc and inferior endplate of the vertebra above it. In type 3, closing wedge osteotomies are performed at levels both above and below the targeted disc level, with the osteotomy extending to just inferior to the transverse processes of both levels.<sup>33</sup>

BDBO is performed when there is severe sagittal imbalance, with the apex or center of the rotational axis located at the disc space. Advantages of BDBO include a higher degree of lordosis correction beyond what SPO can provide and a decreased pseudoarthrosis rate compared with SPO. The disadvantage of BDBO is that it can create a focal angular hyperlordosis, sometimes resulting in symptomatic spinal stenosis.

**X-Osteotomy/Closing-Opening Wedge Osteotomy.** Another special form of pedicle subtraction osteotomy, which is not explicitly defined as a part of the Schwab classification, is the X-osteotomy.<sup>34</sup> This involves posterior column closing and anterior column opening; hence, it is also referred to as closing-opening wedge osteotomy. Park et al<sup>35</sup> refer to this procedure as “fish-mouth PSO,” which helps understand this procedure as indeed an extension/variation of the PSO. Closing-opening wedge osteotomy starts out as closing wedge osteotomy (ie, PSO, but in addition, the anterior wall of the vertebral body is fractured using an osteotome; Fig 5). It hinges on the middle column of the spine closing posteriorly and wedging open anteriorly, leaving an anterior column deficit, as opposed to a VCR, in which the anterior deficit is typically filled with a cage or a structural graft. PSO has a limitation due to the anatomy and morphology of the anterior cortex of the vertebral body of the apex potentially restricting the amount of attainable single-level PSO angle correction. Closing-opening wedge osteotomy may be an option in place of 2-level PSO in such situations.

**VCR.** Vertebral column resection is often used in vertebral tumor resection; however, this technique is also a form of the most extensive type of osteotomy. VCR can achieve correction of kyphotic and coronal curves, in the range of 45°–70°, depending on the case and the degree of correction required.<sup>36–39</sup> Posterior VCR is primarily used in the thoracic and thoracolumbar spine for the treatment of sharp, angular kyphotic deformity in sagittal spinal-balance correction.<sup>25</sup> In VCR, ≥1 vertebral segment is entirely resected, including the posterior elements, entire vertebral body, and the adjacent discs. In the Schwab classification system, grade 5 refers to single-level VCR and grade 6 refers to ≥2 levels of VCR (Fig 6).

The major risk of VCR is the potential for neurologic complications, either from direct injury during the operation or secondary to subsequent subluxation of the spinal column. The mean neurologic complication rate is 14.3%.<sup>25</sup> This is used only in extreme cases when there is not a good alternative.

### CONCLUSIONS

Global sagittal balance correction has shown correlation with positive clinical outcome. Some of these correction techniques, in

particular osteotomies, may appear as posterior wedge compression fractures if one is not aware of the surgical techniques. Hence, it is crucial for radiologists who read spine imaging to be familiar with these techniques and how these postoperative changes appear on imaging.

## REFERENCES

1. Birknes JK, Harrop JS, White AP, et al. **Adult degenerative scoliosis: a review.** *Neurosurgery* 2008;63:94–103 Medline
2. Youssef JA, Orndorff DO, Patty CA, et al. **Current status of adult spinal deformity.** *Global Spine J* 2013;3:51–62 CrossRef Medline
3. Aebi M. **The adult scoliosis.** *Eur Spine J* 2005;14:925–48 CrossRef Medline
4. Lowe T, Berven SH, Schwab FJ, et al. **The SRS classification for adult spinal deformity: building on the King/Moe and Lenke classification systems.** *Spine* 2006;31:S119–25 CrossRef Medline
5. Bess S, Boachie-Adjei O, Burton D, et al; International Spine Study Group. **Pain and disability determine treatment modality for older patients with adult scoliosis, while deformity guides treatment for younger patients.** *Spine* 2009;34:2186–90 CrossRef Medline
6. Agabegi SS, Kazemi N, Sturm PF, et al. **Natural history of adolescent idiopathic scoliosis in skeletally mature patients: a critical review.** *J Am Acad Orthop Surg* 2015;23:714–23 CrossRef Medline
7. Sy N, Bettany-Salnikov J, Moramarco M. **Evidence for conservative treatment of adolescent idiopathic scoliosis: update 2015 (mini-review).** *Cur Pediatr Rev* 2016;12:6–11 CrossRef Medline
8. Weinstein SL, Dolan LA, Cheng JC, et al. **Adolescent idiopathic scoliosis.** *Lancet* 2008;371:1527–37 CrossRef Medline
9. Schwab FJ, Blondel B, Bess S, et al; International Spine Study Group (ISSG). **Radiographical spinopelvic parameters and disability in the setting of adult spinal deformity: a prospective multicenter analysis.** *Spine* 2013;38:E803–12 CrossRef Medline
10. Kim YJ, Bridwell KH, Lenke LG, et al. **Results of lumbar pedicle subtraction osteotomies for fixed sagittal imbalance: a minimum 5-year follow-up study.** *Spine* 2007;32:2189–97 CrossRef Medline
11. Kiaer T, Gehrchen M. **Transpedicular closed wedge osteotomy in ankylosing spondylitis: results of surgical treatment and prospective outcome analysis.** *Eur Spine J* 2010;19:57–64 CrossRef Medline
12. Schwab FJ, Smith VA, Biserni M, et al. **Adult scoliosis: a quantitative radiographic and clinical analysis.** *Spine* 2002;27:387–92 CrossRef Medline
13. Schwab F, Farcy JP, Bridwell K, et al. **A clinical impact classification of scoliosis in the adult.** *Spine* 2006;31:2109–14 CrossRef Medline
14. Schwab F, Ungar B, Blondel B, et al. **Scoliosis Research Society-Schwab Adult Spinal Deformity Classification: a validation study.** *Spine* 2012;37:1077–82 CrossRef Medline
15. Bess S, Schwab F, Lafage V, et al. **Classifications for adult spinal deformity and use of the Scoliosis Research Society-Schwab Adult Spinal Deformity Classification.** *Neurosurg Clin North Am* 2013;24:185–93 CrossRef Medline
16. Sengupta DK. **Re: Schwab F, Ungar B, Blondel B, et al: Scoliosis Research Society-Schwab Adult Spinal Deformity Classification—a validation study—Spine 2012;37:1077–82.** *Spine (Phila Pa 1976)* 2012;37:1790 CrossRef Medline
17. Murtagh RD, Quencer RM, Uribe J. **Pelvic evaluation in thoracolumbar corrective spine surgery: how I do it.** *Radiology* 2016;278:646–56 CrossRef Medline
18. Glassman SD, Berven S, Bridwell K, et al. **Correlation of radiographic parameters and clinical symptoms in adult scoliosis.** *Spine* 2005;30:682–88 CrossRef Medline
19. Diebo BG, Varghese JJ, Lafage R, et al. **Sagittal alignment of the spine: what do you need to know?** *Clin Neurol Neurosurg* 2015;139:295–301 CrossRef Medline
20. Rothenfluh DA, Mueller DA, Rothenfluh E, et al. **Pelvic incidence-lumbar lordosis mismatch predisposes to adjacent segment disease after lumbar spinal fusion.** *Eur Spine J* 2015;24:1251–58 CrossRef Medline
21. Schwab F, Blondel B, Chay E, et al. **The comprehensive anatomical spinal osteotomy classification.** *Neurosurgery* 2014;74:112–20; discussion 120 CrossRef Medline
22. Smith-Petersen MN, Larson CB, Aufranc OE. **Osteotomy of the spine for correction of flexion deformity in rheumatoid arthritis.** *Clin Orthop Relat Res* 1969;66:6–9 Medline
23. Lu DC, Chou D. **Flatback syndrome.** *Neurosurg Clin N Am* 2007;18:289–94 CrossRef Medline
24. Sansur CA, Fu KM, Oskouian RJ Jr, et al. **Surgical management of global sagittal deformity in ankylosing spondylitis.** *Neurosurg Focus* 2008;24:E8–94 CrossRef Medline
25. Dorward IG, Lenke LG. **Osteotomies in the posterior-only treatment of complex adult spinal deformity: a comparative review.** *Neurosurg Focus* 2010;28:E4 CrossRef Medline
26. Geck MJ, Macagno A, Ponte A, et al. **The Ponte procedure: posterior only treatment of Scheuermann's kyphosis using segmental posterior shortening and pedicle screw instrumentation.** *J Spinal Disord Tech* 2007;20:586–93 CrossRef Medline
27. Kim KT, Park KJ, Lee JH. **Osteotomy of the spine to correct the spinal deformity.** *Asian Spine J* 2009;3:113–23 CrossRef Medline
28. Yang BP, Ondra SL, Chen LA, et al. **Clinical and radiographic outcomes of thoracic and lumbar pedicle subtraction osteotomy for fixed sagittal imbalance.** *J Neurosurg Spine* 2006;5:9–17 CrossRef Medline
29. Cho KJ, Bridwell KH, Lenke LG, et al. **Comparison of Smith-Petersen versus pedicle subtraction osteotomy for the correction of fixed sagittal imbalance.** *Spine (Phila Pa 1976)* 2005;30:2030–37; discussion 2038 CrossRef Medline
30. Thomasen E. **Vertebral osteotomy for correction of kyphosis in ankylosing spondylitis.** *Clin Orthop Relat Res* 1985;142:52 Medline
31. Bridwell KH. **Decision making regarding Smith-Petersen vs. pedicle subtraction osteotomy vs. vertebral column resection for spinal deformity.** *Spine* 2006;31:S171–78 CrossRef Medline
32. Enercan M, Ozturk C, Kahraman S, et al. **Osteotomies/spinal column resections in adult deformity.** *Eur Spine J* 2013;22(suppl 2):S254–64 CrossRef Medline
33. Domanic U, Talu U, Dikici F, et al. **Surgical correction of kyphosis: posterior total wedge resection osteotomy in 32 patients.** *Acta Orthop Scand* 2004;75:449–55 CrossRef Medline
34. Vaccaro AR, Rothman RH, Albert TJ. **70 posterior osteotomies: posterior Smith-Petersen, pedicle subtraction, and vertebral column resection osteotomy techniques.** In: Vaccaro AR, Rothman RH, Albert TJ, eds. *Spine Surgery.* Stuttgart: Georg Thieme Verlag; 2016:1–8
35. Park JH, Hyun SJ, Kim KJ, et al. **Comparative study between pedicle subtraction osteotomy (PSO) and closing-opening wedge osteotomy (fish-mouth PSO) for sagittal plane deformity correction.** *Spine (Phila Pa 1976)* 2017;42:E899–905 CrossRef Medline
36. Demirkiran G, Dede O, Karadeniz E, et al. **Anterior and posterior vertebral column resection versus posterior-only technique: a comparison of clinical outcomes and complications in congenital kyphoscoliosis.** *Clin Spine Surg* 2017;30:285–90 CrossRef Medline
37. Lenke LG, Newton PO, Sucato DJ, et al. **Complications after 147 consecutive vertebral column resections for severe pediatric spinal deformity: a multicenter analysis.** *Spine* 2013;38:119–32 CrossRef Medline
38. Zhang Z, Wang H, Shangguan L. **Posterior 2-level vertebral column resection for the treatment of progressive rotational dislocation in kyphoscoliotic deformities.** *World Neurosurg* 2016;88:428–32 CrossRef Medline
39. Wang Y, Xie J, Zhao Z, et al. **Perioperative major non-neurological complications in 105 patients undergoing posterior vertebral column resection procedures for severe rigid deformities.** *Spine* 2015;40:1289–96 CrossRef Medline

# Revenue Increase following 2017 Multiple Procedures Payment Reduction Modification: Differential Impact on Neuroradiology—Report from an Academic Medical Center

 B.B. Noveiry,  F.N. Varzaneh, and  D.M. Yousem



## ABSTRACT

**BACKGROUND AND PURPOSE:** The Centers for Medicare and Medicaid Services imposed a 25% professional component multiple procedure payment reduction for the professional component of advanced diagnostic imaging modalities in January 2012. In 2017, the Centers for Medicare and Medicaid Services rolled back the multiple procedure payment reduction to 5% for subsequent imaging. To evaluate the effect of this change, we analyzed 5 months of Centers for Medicare and Medicaid Services procedures at Johns Hopkins Medical Institution.

**MATERIALS AND METHODS:** We analyzed the procedure codes and reimbursement rate for studies performed between January 1 and May 31, 2017. Patients with Medicare insurance who had multiple diagnostic procedures in a day were selected. Per the Centers for Medicare and Medicaid Services guidelines, procedures with the highest price were considered fully reimbursed and subsequent studies were marked for differences between 25% (2013–2016) and 5% reduction (2017).

**RESULTS:** We included 8787 patients with 22,236 procedures (mean, 2.53 studies/day). CT, MR imaging, and ultrasound scans composed 75.9%, 21.5%, and 2.6% of all studies, with 61.2%, 54.9%, and 85.4% of the procedures of each technique subject to multiple procedure payment reduction, respectively. The projected reimbursement for these studies was \$1,666,437, which translated to a \$179,782 (12.1%) increase in revenue comparing 25%-versus-5% multiple procedure payment reduction rates for 5 months: \$128,542 for CT, \$47,802 for MR imaging, and \$3439 for ultrasound. The annual overall prorated increase in revenue would be \$431,476. The impact was maximal for neuroradiology.

**CONCLUSIONS:** With the recent favorable adjustment in multiple procedure payment reduction regulations, CT-heavy subspecialties like neuroradiology benefit the most with revenue increases. Different practice settings might experience revenue increases to a different extent, depending on the procedure and payer mix.

**ABBREVIATIONS:** ACR = American College of Radiology; ASNR = American Society of Neuroradiology; CMS = Centers for Medicare and Medicaid Services; CPT = Current Procedural Terminology; MPPR = multiple procedure payment reduction; PC = professional component; TC = technical component; US = ultrasound

The Centers for Medicare and Medicaid Services (CMS) imposed the multiple procedure payment reduction (MPPR) for certain advanced diagnostic imaging modalities (CT, MR imaging, and ultrasound [US]) in 2006 based on the Medicare Payment Advisory Commission recommendation. Initially, only the technical component (TC) of the service fee was subject to MPPR.

The TC of a service covers the cost of equipment, supplies, and nonphysician personnel. This reduction started out at 25% and applied to contiguous body parts, but in 2011, the TC MPPR was increased to 50% and became applicable to noncontiguous body parts.<sup>1</sup> Despite opposition by radiologist groups, including the American College of Radiology (ACR) and the American Society of Neuroradiology (ASNR), CMS imposed a 25% reduction in the professional component (PC) of multiple studies as part of the 2011 MPPR, which went into effect on January 1, 2012.<sup>2,3</sup> While initially this applied to multiple diagnostic imaging services administered by the same physician to the same patient during a single office visit, it was further expanded in 2013 to include all physicians practicing in the same group, irrespective of the practice setting.<sup>4</sup> In practice, this meant that if a patient underwent >1 imaging study on a single day, the highest priced procedure was reimbursed fully (100%), but any subsequent same-day imaging

Received October 6, 2017; accepted after revision December 6.

From the Departments of Medicine (B.B.N.) and Radiology (F.N.V.), Division of Body MRI, Johns Hopkins University, Baltimore, Maryland; and Department of Radiology (D.M.Y.), Division of Neuroradiology, Johns Hopkins Medical Institution, Baltimore, Maryland.

Please address correspondence to David M. Yousem, MD, MBA, Department of Radiology, Division of Neuroradiology, Johns Hopkins Medical Institution, 600 North Wolfe St, Phipps B100F, Baltimore, MD 21287; e-mail: dyousem1@jhu.edu

 Indicates article with supplemental on-line tables.

<http://dx.doi.org/10.3174/ajnr.A5555>

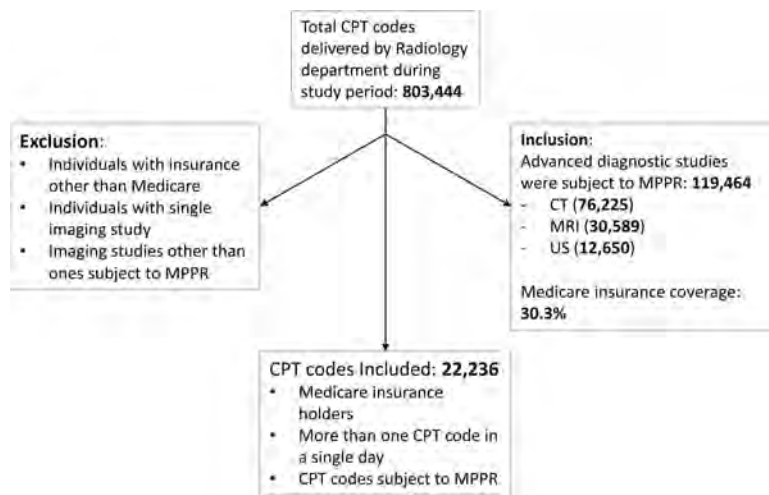


**FIGURE.** This chart illustrates the criteria for patient inclusion and exclusion.

studies would be paid at 75% of the original amount allocated by the CMS Current Procedural Terminology (CPT) codes for PC.

For example, if a patient had a brain CT, an ultrasound of the pelvis, and a cardiac MR imaging on the same day within a radiology group and 3 different radiologists reported each of those studies at 3 different office locations, Medicare would reimburse the PC of the highest priced procedure (cardiac MR imaging) fully and would only reimburse the brain CT and pelvic sonography at 75% of the full price of the subsequent studies from 2013 to 2016. This change had a large impact on neuroradiology, given the following frequent studies: 1) brain and spine CT studies in the emergency department for trauma, 2) brain and spine MRIs for multiple sclerosis, 3) CT/CTA and MR/MRA studies for strokes and aneurysms, and 4) screening cervical, thoracic, and lumbar spine studies in patients with cancer for cord compression and subarachnoid seeding.<sup>5</sup>

In 2016, the CMS was convinced to roll back the MPPR for the PC under growing pressure from the ACR, ASNR, and the American Medical Association after receiving extensive data supplied by these organizations.<sup>4,6</sup> As of January 1, 2017, the MPPR was changed to a 95% level of reimbursement for subsequent multiple body part imaging.<sup>7</sup> So, in the above instance, the brain CT and pelvic sonography PC would be paid at 95% of the full allowed reimbursement.

To evaluate the effect of this change, we analyzed the impact during 5 months of activity at Johns Hopkins Medical Institution (January to May 2017). Because our emergency department physicians often request imaging of multiple body parts for trauma and our oncologic practice uses chest, abdomen, and pelvic CT scanning to screen for and follow cancers, we hypothesized that we would see a large increase in revenue from the CMS decision.

## MATERIALS AND METHODS

The CPT codes of the procedures performed by the department of radiology at our institution between January 1, 2017, and May 31, 2017, were retrieved via our radiology billing service. Patients with Medicare insurance who had multiple diagnostic procedures in a day were selected for analysis. Patients with a single imaging and patients holding health insurance other than Medicare were excluded.

The Healthcare Common Procedure Coding System CPT codes were extracted from the CMS Web site, and the diagnostic imaging family indicator 88 (subject to the reduction of the TC diagnostic imaging [effective for services January 1, 2011 and after]) was used to retrieve procedures for which MPPR would apply.<sup>8,9</sup> TC and PC facility prices for selected imaging, for our local and national area, were extracted using modifier 26.<sup>8,9</sup> We categorized CPT codes into 4 different groups of imaging: neuroradiologic, body, musculoskeletal, and breast. Per CMS guidelines, procedures with the highest price were considered fully reimbursed and subsequent studies were marked for further calculations, either a

25% reduction (2013–2016) or a 5% (2017) reduction.

We based the calculations on Medicare reimbursement rates, not actual payments. We sought to determine the theoretic increase in revenue that could be expected through the change in MPPR for PC reimbursement. Thus, we did not explore payments received. To estimate the MPPR impact on radiology practices nationwide, we used available reports of advanced diagnostic imaging numbers in the United States. Because this project did not analyze any personal information, it was considered an institutional review board–exempt study and was in full Health Insurance Portability and Accountability Act compliance. Descriptive statistical analysis was done using Excel 2013 (Microsoft, Redmond, Washington).

## RESULTS

From January 1, 2017, to May 31, 2017, the radiology department performed 803,444 procedures. Advanced diagnostic studies subject to MPPR consisted of 14.9% of all procedures and 119,464 events (CT,  $n = 76,225$ ; MR imaging,  $n = 30,589$ ; and US,  $n = 12,650$ ). Of all patients, 30.3% had Medicare insurance coverage at our institution. After we excluded patients as defined in the “Materials and Methods” section, 8787 patients with Medicare insurance and >1 CPT code in a single day were included, undergoing procedures with 22,236 CPT codes, representing an average of 2.53 studies per day (Figure and Table 1).

The CMS has defined 121 imaging CPT codes subject to MPPR. Procedure names as shown on the CMS Web site and our institution categorization are shown in the On-line Table. For all selected CPT codes, the facility price for the PC was equal to the listing for the nonfacility limiting charge of CMS. Our local regional PC nonfacility limiting charge is 5.04% higher than the national value, on average.

Projected reimbursement after implementation of MPPR relative to full reimbursement for PC, TC, and global fees were \$1,666,436 (97.4%), \$3,206,700 (73.8%), and \$4,873,137 (80.5%), respectively. These values reflect 100% reimbursement for the first study performed plus the 2017 MPPR reduction for the PC (5%) and TC (50%) calculations.

If one applies the 25% 2013–2016 MPPR on the PC and compares that with the 5% MPPR of 2017, one finds a revenue in-

**Table 1: Advanced diagnostic imaging procedures subject to multiple procedure payment reduction performed from January to May 2017**

Modality/Imaging Category	Count (% of All Imaging)	Proportion of Imaging Category Subject to MPPR within Modality	Proportion of Imaging Modality Subject to MPPR
CT	16,874 (75.9)		61.2%
Neuroradiologic		76.4%	
Musculoskeletal		82.8%	
Body		52.3%	
MRI	4780 (21.5)		54.9%
Neuroradiologic		55.0%	
Musculoskeletal		63.8%	
Body		49.4%	
Breast		53.3%	
US	582 (2.6)		85.4%
Body		85.4%	
Total	22,236 (100)		60.5%

crease of \$179,782 (12.1%) for the 8787 patients who had multiple studies performed; this includes \$128,542 (12.1%) for CT, \$47,802 (11.6%) for MR imaging, and \$3439 (21.2%) for US.

[Highest Price CPT code + (Lower price CPT codes

$$\times 95\%) - \text{Highest Price CPT code} \\ + (\text{Lower price CPT codes} \times 75\%)]$$

One can estimate the prorated annual (12-month) revenue increase by multiplying the calculated 5-month revenue increase by the 12/5-month ratio. The prorated annual revenue increase would become \$431,476 in total (Tables 1 and 2).

A general comparison of different imaging categories and modalities and relative MPPR impact is shown in Table 2. The US technique had the highest proportion of CPT codes affected by MPPR, of which 85.4% of studies were subject to MPPR, followed by CT (61.2%) and MR imaging (54.9%); however, the total number for ultrasound was small. When we compared the different categories of CPT codes, 71.7% of musculoskeletal studies were multiple, followed by 67.9% of neuroradiologic studies, and 53.8% of body imaging.

The neuroradiology division obtained the highest increase in revenue because of the following: 1) a high rate of MPPRs overall at 67.9%, 2) higher volume of both MR imaging and CT studies, 3) higher reimbursement for MR imaging compared with CT, 4) fewer MRIs performed in the body and musculoskeletal and breast imaging designations, and 5) far fewer ultrasounds, which are reimbursed at a lower rate. Thus, although the overall rate of MPPR for neuroradiology (67.9%) was lower than for musculoskeletal studies (71.9%), the higher volume of cases subject to MPPR favored the reimbursement of neuroradiology. At the same time, body imaging, by virtue of a higher volume of MPPR CT cases than neuroradiology nearly had the same benefit in revenue (\$88,000 in neuroradiology versus \$86,000 for body), despite a lower overall rate for MPPR (53.8%) (Table 2).

The number of patients with multiple imaging in a day, their respective number of imaging scans, monetary MPPR impact, and most common imaging combinations are shown in Tables 3 and 4. Most patients (70.9%) had only 2 studies. The most common combination was abdominopelvic and thoracic CT with contrast, followed by abdominopelvic and thoracic CT without

contrast, accounting for 22.9% and 6.7% of all procedures, respectively. After the abdominopelvic CT and thoracic CT combination, the most common 2 studies performed were brain and cervical spine CT scans, commonly ordered in our emergency department. The most common 3 studies performed together were brain, maxillofacial, and cervical spine examinations, presumed to be from trauma cases in the emergency setting. These examples maximally impacted neuroradiology.

It has been reported that the total number of CT scans performed annually in the United States is around 80 million scans.<sup>10</sup> Also, in 2016, there were 121 MRIs per 1000 inhabitants,<sup>11</sup> and considering ~321 million US population,<sup>12</sup> the annual number of MR imaging studies can be estimated to be around 38.8 million per year. We could not find a report of annual studies in the United States for US, but if we assume that the proportion of advanced diagnostic imaging modalities at our institution mirrors that in the nation, we can roughly estimate 3.2 million ultrasounds performed, for a total of 122 million advanced diagnostic imaging procedures per year. If we assume that the rate of multiple procedure codes is 10% across the country (a reduction from our rate by one-third because we have a heavy emergency department/oncology practice) and if the overall Medicare payer mix is like ours at 30%, then 3.66 million studies would be affected. If we apply our added revenue of \$179,782 for 22,236 CPT codes in this study, it would yield added revenue nationally to radiology as a whole of approximately \$29.6 million.

## DISCUSSION

Our results show that depending on payer mix and procedure mix, some radiology practices may experience a major increase in reimbursement secondary to the rollback of the MPPR, with the neuroradiology portion of the practice receiving the most benefit. Those neuroradiology hospital-based practices with a higher rate of emergency department–combined trauma CT scans will likely receive a higher benefit than some outpatient imaging practices. However, neuroradiologists will also see improved revenue in MR imaging/MRA cases, complete spine MR imaging studies for metastatic disease, and neuroaxis (brain, cervical spine, thoracic spine MR) multiple sclerosis examinations.

The multiple procedures payment reduction of the CMS for the TC of certain advanced diagnostic imaging (CT, MR imaging, and ultrasound) had been justified on the basis of increased efficiency of simultaneous procedures in the same session.<sup>13</sup> MPPR was basically saying that less work is done when multiple procedures are delivered to 1 patient at a single session. This concept was followed by adjusted reimbursement (ie, decreased payment).<sup>14</sup>

The MPPR has been one of the most challenging issues between radiology communities and the CMS. Since the early introduction of the TC of the MPPR in 2006, the concept was applied to other components of radiology reimbursement and was increased

**Table 2: Different categories of advanced diagnostic imaging categories and modalities<sup>a</sup>**

	No. of Procedures	Proportion of Procedures Subject to MPPR	75% Reimbursement	95% Reimbursement	Presumed 100% Reimbursement	\$ Increase (%)	Prorated Annual Increase	\$ Deficit (%)	Prorated Annual Deficit
Imaging categories									
Neuro-radiologic	9952	67.9%	\$ 613,157	\$ 701,503	\$ 723,589	88,346 (14.4)	\$ 212,030	22,086 (3.1)	53,006
Body	11,778	53.8%	\$ 841,173	\$ 927,297	\$ 948,828	86,123 (10.2)	\$ 206,695	21,531 (2.3)	51,674
Musculoskeletal	491	71.7%	\$ 31,182	\$ 36,354	\$ 37,648	5172 (16.6)	\$ 12,412	1293 (3.4)	3103
Breast	15	53.3%	\$ 1142	\$ 1282	\$ 1318	141 (12.3)	\$ 338	35 (2.7)	84
Imaging modalities									
CT	16,874	61.2%	\$1,058,073	\$ 1,186,614	\$1,218,750	128,542 (12.1)	\$308,500	32,135 (2.6)	77,124
MRI	4780	54.9%	\$ 412,381	\$ 460,183	\$ 472,133	47,802 (11.6)	\$ 114,724	11,950 (2.5)	28,680
US	582	85.4%	\$ 16,200	\$ 19,639	\$ 20,499	3439 (21.2)	\$ 8253	860 (4.2)	2064
Total imaging	22,236	60.5%	\$1,486,654	\$1,666,437	\$ 1,711,382	179,782 (12.1)	\$ 431,476	44,946 (2.6)	107,870

<sup>a</sup> Note the new MPPR policy impact on net revenue increase and the current deficit to the full reimbursement.

**Table 3: Number of patients with multiple advanced diagnostic imagings per day, respective number of imaging procedures, and net revenue loss due to current 5% MPPR**

Procedures Count in Single Day	No. (%) of Study Patients	No. (%) of Study Procedures	Net Revenue Loss (%) due to 5% MPPR
2	6226 (70.9)	12,452 (56.0)	\$20,415 (45.4)
3	1474 (16.8)	4422 (19.9)	\$9913 (22.1)
4	648 (7.4)	2592 (11.7)	\$6734 (15.0)
≥5	439 (5.0)	2770 (12.5)	\$7884 (17.5)
Total	8787 (100)	22,236 (100)	\$44,946 (100)

from 25% to 50% applied to the TC Medicare Physician Fee Schedule, including noncontiguous body parts across different modalities.<sup>15</sup> Among different medical insurances, United Healthcare is the only major insurance company that implemented the MPPR besides the CMS.<sup>16</sup>

In 2011, the Medicare Payment Advisory Commission proposed a 50% PC MPPR inclusion in the Medicare Physician Fee Schedule, which caused stiff ACR and radiologist opposition. The Medicare Payment Advisory Commission justified this huge cut in revenue with the rationale that radiologists do not perform some reporting activities twice for multiple studies within 1 report, such as reviewing medical history, reviewing the final report, and following up with the ordering physician.<sup>15</sup> While one might understand that a single injection of contrast to a person in a CT scanner that included chest, abdomen, and pelvis in 1 session should have some reduction in the TC, this amount of PC MPPR was undermining the independent interpretation of images by radiologists, particularly across subspecialties of radiology. The ACR and ASNR argued that sometimes 1 clinical history does not pertain to all body parts (eg, brain versus chest). If the radiology group had different subspecialized radiologists interpreting different imaging modalities that are not collocated, the rationale proposed by Medicare Payment Advisory Commission was lacking.

The idea that there were “efficiencies” to justify reducing the TC by 50% on an ultrasound study performed in one building from a CT scan performed in another site on the same day seemed unreasonable to most radiologists. The application of this logic to the professional component rather than restricting it to the technical component of a CPT code also rankled radiology and the ASNR leadership. The PC of the CPT code is supposed to reimburse physician work, practice expense, and professional liability insurance.<sup>17</sup> It was unclear how multiple procedures in 1 day would have any effect on professional liability insurance costs and even on practice expenses.

However, the result was a 25% PC reduction as of January 1, 2012.<sup>1,14,18</sup> In 2013, this was further expanded, so the 25% PC MPPR would apply to all radiologists in the same group practice interpreting multiple imaging studies from the same patient on the same day, irrespective of practice setting.<sup>1,4,18</sup> The impact of this was not inconsequential. Chiao et al<sup>5</sup> found that the PC MPPR unevenly affected different divisions of radiology, with thoracic imaging losing the most percentage and neuroradiology losing the most absolute revenue relative to other divisions.<sup>5</sup>

For >4 years the ACR and ASNR lobbied Congress and provided scientific data from well-performed peer-reviewed published studies regarding the impact of performing multiple studies on the same patient. Allen et al<sup>19</sup> found that the maximum estimated percentage work reduction when multiple services were performed by the same physician in the same session was small, ranging from 4.3% to 8.2%, with a mean of 5.9% ± 1.5%, substantially less than the 25% PC MPPR that was in place at the time of the publication.

Duzak et al<sup>20</sup> found that the potential work reduction for same-session, same-technique services rendered by different physicians in the same group practice was even smaller, ranging from 1.4% to 2.7%, with a mean of 1.8% ± 0.6%.

Thus, after the initial series of unsuccessful negotiations in 2006 and 2011, the ACR, ASNR, and other radiology advocacy groups were able to convince the CMS in August 2016 to release a new decision, the MPPR rollback, which decreased the reduction in PC reimbursement from 25% to 5%.<sup>21,22</sup> The TC MPPR remained at the previous 50% level.

The impact of the 25% reductions on the field of neuroradiology was noted by the leaders in the profession. These consequences for neuroradiologists in private and academic settings included not just reduced revenue but downstream effects. First, divisional self-sufficiency was harmed. By sharply decreasing the revenue of certain divisions, the PC MPPR unintentionally but ominously impaired the financial health of these divisions. The revenue needed to support clinical fellows dropped. In academic medical centers, this impairment could have resulted in fewer dollars available for hiring new faculty, fellow support, research initiatives, and discretionary funds. Second, interdivisional relationships could be impaired. If certain divisions are seen as being subsidized by others, they may be perceived as “weak” or a drain on resources. Finally, the perception of “profitable” and “unprofitable” divisions may reach radiology residents, who are sensitive to issues of financial stability and well-being as they consider job prospects. Although the PC MPPR is certainly a minor factor

**Table 4: Most common combinations of diagnostic imaging**

First Image	Second Image	Third Image	Fourth Image	Percentage of Study Imaging
CT abdomen & pelvis w/contrast	CT thorax w/dye			22.9
CT abdomen & pelvis w/o contrast	CT thorax w/o dye			6.7
CT neck spine w/o dye	CT head/brain w/o dye			4.6
CT angio abdomen & pelvis w/o & w/dye	CT angiography chest			2.5
MRI brain stem w/o & w/dye	MR angiography head w/o dye			1.7
MRI brain stem w/o & w/dye	MRI orbit/face/neck w/o & w/dye			1.5
CT maxillofacial w/o dye	CT head/brain w/o dye			1.4
CT neck spine w/o dye	CT maxillofacial w/o dye	CT head/brain w/o dye		1.2
CT abdomen & pelvis w/o contrast	CT thorax w/o dye	CT head/brain w/o dye		1.2
CT thorax w/o dye	CT head/brain w/o dye			1.2
CT head/brain w/o dye	CT head/brain w/o dye			1.1
CT abdomen & pelvis w/contrast	CT abdomen & pelvis w/contrast	CT thorax w/dye	CT thorax w/dye	1.1
CT thorax w/o dye	CT maxillofacial w/o dye			0.9
MRI brain stem w/o dye	MR angiography head w/o dye			0.8
CT angiography head	CT angiography neck			0.8
CT soft-tissue neck w/dye	CT thorax w/dye			0.8
CT abdomen & pelvis w/contrast	CT thorax w/dye	CT head/brain w/o dye		0.8
CT abdomen & pelvis w/contrast	CT soft-tissue neck w/dye	CT thorax w/dye		0.7
CT abdomen & pelvis w/contrast	CT thorax w/dye	CT neck spine w/o dye	CT head/brain w/o dye	0.7
CT abdomen & pelvis w/contrast	CT angiography chest			0.7
MRI brain stem w/o & w/dye	MR angiography neck w/o & w/dye	MR angiography head w/o dye		0.6

**Note:**—w/o indicates without; w/o & w/, without and with; w/, with; angio, angiography.

overall, particularly now at a 5% reduction, it could conceivably have influenced resident decision-making regarding subspecialty fellowship training, resulting in fewer residents choosing to pursue certain subspecialty fellowships. In summary, the PC MPPR could have substantial unintended consequences on neuroradiology that were not considered by the CMS before the policy was adopted but were apparent to the neuroradiology community.<sup>5</sup>

On the basis of our categorization and the change in rate from 25% to 5% of MPPR, the impact on different divisions of radiology has decreased substantially. However, we have found that the revenue of the neuroradiology division and CT scanning as a technique are most affected.

During the study, 30.3% of patients who received radiology services were covered by Medicare at our institution. This MPPR policy will affect centers accordingly with more or less of a Medicare payer mix. Private insurance companies, such as United Healthcare, might mirror the changes regulated by Medicare and further decrease practice revenue.

Although we could not find a report to compare our institution count of modalities with those of other institutions, our estimates indicate that MPPR might impact a considerable portion of advanced diagnostic imaging studies for radiology practices across the United States.

There are certain limitations in this report. First, the study took place in a tertiary care academic medical center with a primary trauma center. Our study reflects the effect on an academic setting, with a high number of patients and many emergent requests for advanced diagnostic imaging, often leading to multiple studies per day. Also, it is more common in our hospital-dominated practice setting to have multiple procedures in the same day for a patient than in an outpatient center-dominated practice.

Another limitation in our results is that our numbers reflect the projected reimbursement amount, not the actual amount because the collection rate varies across CMS geographic areas and copay deductions. We also admit that since United Healthcare is not disclosing its Physician Fee Schedule the way CMS does, we

could not analyze the revenue impact on United Healthcare patients.

## CONCLUSIONS

Our results indicate that with recent favorable adjustments in MPPR regulations, the overall prorated increase in revenue at our academic medical center (\$431,476) will impact CT-heavy subspecialties the most, especially body imaging and neuroradiology. The CT volume, coupled with high MR imaging reimbursement rates, will lead to beneficial changes in neuroradiology practices. Large practices can expect increased revenue based on the analysis we have made and the number of cases affected. Depending on overall volume and payer mix, other practices may see more or less impact.

Disclosures: David M. Yousem—UNRELATED: Expert Testimony: medicolegal consulting expert witness; Payment for Lectures Including Service on Speakers Bureaus: American College of Radiology Education Center courses; Patents (Planned, Pending or Issued): peer review software; Royalties: Elsevier for 5 published books; Payment for Development of Educational Presentations: www.CMEInfo.com DVD course.\* \*Money paid to the institution.

## REFERENCES

1. Rehani B, Basu P, Ellenbogen PH, et al. **The threat to radiologists from the multiple-procedure payment reduction.** *J Am Coll Radiol* 2013;10:237–38 CrossRef Medline
2. Hackney DB. The Centers for Medicare & Medicaid Services (CMS) issues new proposals. 2011. <https://www.asnr.org/the-center-for-medicare-medicoid-services-cms-issues-new-proposals/>. Accessed November 20, 2017
3. ASNR. Procedure payment reduction (MPPR) policy to the professional component of advanced imaging service. 2011. <https://www.asnr.org/procedure-payment-reduction-mppr-policy-to-the-professional-component-of-advanced-imaging-service/>. November 20, 2017.
4. ACR. Professional Component Multiple Procedure Payment Reduction. Oppose Further Application of a Multiple Procedure Payment Reduction to the Professional Component of Diagnostic Imaging Services. Advocacy, Legislative Issue; 2016. <https://www.acr.org/Advocacy-and-Economics/Legislative-Issues/MPPR>. Accessed June 11, 2017
5. Chiao D, Monceaux S, Krishnaraj A, et al. **Impact of the professional**

- component MPPR policy on interdivisional finances in an academic radiology department.** *J Am Coll Radiol* 2016;13:274-78 CrossRef Medline
6. Schaefer PW. ASNR Comments on Proposed CMS Rule Applying MPPR to Group Practices. American Society of Neuroradiology. 2012. <https://www.asnr.org/asnr-comments-on-proposed-cms-rule-applying-mppr-to-group-practices/>. Accessed November 20, 2017
  7. Medicare Learning Network. **Multiple Procedure Payment Reduction (MPPR) on the professional component (PC) of certain diagnostic imaging procedures.** *mln Matters* 2016:2
  8. CMS. Medicare Physician Fee Schedule Look-up Tool. 2017. <https://www.cms.gov/apps/physician-fee-schedule/overview.aspx>. Accessed June 13, 2017
  9. CMS. Medicare Claims Processing Manual-Chapter 23: Fee Schedule Administration and Coding Requirements. 2017. <https://www.cms.gov/Regulations-and-Guidance/Guidance/Manuals/Downloads/clm104c23.pdf>. Accessed June 13, 2017
  10. CBS This Morning. Report: many medical imaging tests performed in U.S. are unnecessary. 2015. <https://www.cbsnews.com/news/many-medical-imaging-tests-performed-in-u-s-are-unnecessary/>. Accessed September 27, 2017
  11. Organisation for Economic Co-operation and Development. Magnetic resonance imaging (MRI) exams total, per 1000 inhabitants. 2016. <https://www.reportlinker.com/data/series/OKS-cBWFxQM>. Accessed September 27, 2017
  12. United States Census-Bureau. U.S. and World Population Clock. 2017. <https://www.census.gov/popclock/>. Accessed September 27, 2017
  13. United States Government Accounting Office. Medicare Physician Payments: Fees Could Better Reflect Efficiencies Achieved When Services Are Provided Together. 2009. <https://www.gao.gov/products/GAO-09-647>. Accessed September 27, 2017
  14. ACR. PC MPPR Rollback Enacted in the Consolidated Appropriations Act of 2016. 2016. <https://www.acr.org/Advocacy/Legislative-Issues/MPPR>. Accessed August 24, 2017
  15. MedPAC. June 2011 Report to the Congress: Medicare and the Health Care Delivery System. 2011. [http://medpac.gov/docs/default-source/reports/Jun11\\_EntireReport.pdf](http://medpac.gov/docs/default-source/reports/Jun11_EntireReport.pdf). Accessed August 24, 2017
  16. UnitedHealthCare. Network bulletin: important updates from United Healthcare to health care professionals and facilities. 2016. [https://www.unitedhealthcareonline.com/ccmcontent/ProviderII/UHC/en-US/Assets/ProviderStaticFiles/ProviderStaticFilesPdf/News/July-Network-Bulletin-PCA-1-002206\\_2016.pdf](https://www.unitedhealthcareonline.com/ccmcontent/ProviderII/UHC/en-US/Assets/ProviderStaticFiles/ProviderStaticFilesPdf/News/July-Network-Bulletin-PCA-1-002206_2016.pdf). Accessed August 24, 2017
  17. ACR. Medicare Physician Fee Schedule.
  18. Medicare Learning Network. How to Use the Searchable Medicare Physician Fee Schedule Booklet (April 2016). ICN 901344 ed; 2017. [https://www.cms.gov/Outreach-and-Education/Medicare-Learning-Network-MLN/MLNProducts/downloads/How\\_to\\_MPPFS\\_Booklet\\_ICN901344.pdf](https://www.cms.gov/Outreach-and-Education/Medicare-Learning-Network-MLN/MLNProducts/downloads/How_to_MPPFS_Booklet_ICN901344.pdf). Accessed August 24, 2017
  19. Allen B Jr, Donovan WD, McGinty G, et al. **Professional component payment reductions for diagnostic imaging examinations when more than one service is rendered by the same provider in the same session: an analysis of relevant payment policy.** *J Am Coll Radiol* 2011;8:610–16 CrossRef Medline
  20. Duszak R Jr, Silva E 3rd, Kim AJ, et al. **Professional efficiencies for diagnostic imaging services rendered by different physicians: analysis of recent Medicare multiple procedure payment reduction policy.** *J Am Coll Radiol* 2013;10:682–88 CrossRef Medline
  21. ACR. Frequently Asked Questions on the PC MPPR and Digital Radiography policy within H.R. 2029, the Consolidated Appropriations Act of 2016. 2016. <https://www.acr.org/Advocacy-and-Economics/Legislative-Issues/MPPR/FAQ>. Accessed August 24, 2017
  22. CMS Department of Health & Human Services. Multiple Procedure Payment Reduction (MPPR) on the Professional Component (PC) of Certain Diagnostic Imaging Procedures. 2016. <https://www.cms.gov/Regulations-and-Guidance/Guidance/Transmittals/Downloads/R3578CP.pdf>. Accessed August 24, 2017

# Iron-Insensitive Quantitative Assessment of Subcortical Gray Matter Demyelination in Multiple Sclerosis Using the Macromolecular Proton Fraction

V.L. Yarnykh, E.P. Krutenkova, G. Aitmagambetova, P. Repovic, A. Mayadev, P. Qian, L.K. Jung Henson, B. Gangadharan, and J.D. Bowen



## ABSTRACT

**BACKGROUND AND PURPOSE:** Fast macromolecular proton fraction mapping is a recent quantitative MR imaging method for myelin assessment. The objectives of this study were to evaluate the macromolecular proton fraction as a measure of demyelination in subcortical GM structures in multiple sclerosis and assess a potential relationship between demyelination and excess iron deposition using the macromolecular proton fraction and T2\* mapping.

**MATERIALS AND METHODS:** Macromolecular proton fraction and T2\* maps were obtained from 12 healthy controls, 18 patients with relapsing-remitting MS, and 12 patients with secondary-progressive MS using 3T MR imaging. Parameter values in the caudate nucleus, globus pallidus, putamen, substantia nigra, and thalamus were compared between groups and correlated to clinical data.

**RESULTS:** The macromolecular proton fraction in all subcortical structures and T2\* in the globus pallidus, putamen, and caudate nucleus demonstrated a significant monotonic decrease from controls to patients with relapsing-remitting MS and from those with relapsing-remitting MS to patients with secondary-progressive MS. The macromolecular proton fraction in all subcortical structures significantly correlated with the Expanded Disability Status Scale and MS Functional Composite scores with absolute Pearson correlation coefficient ( $r$ ) values in a range of 0.4–0.6. Significant correlations ( $r = -0.4$  to  $-0.6$ ) were also identified between the macromolecular proton fraction and the 9-Hole Peg Test, indicating a potential relationship with nigrostriatal pathway damage. Among T2\* values, weak significant correlations with clinical variables were found only in the putamen. The macromolecular proton fraction did not correlate with T2\* in any of the studied anatomic structures.

**CONCLUSIONS:** The macromolecular proton fraction provides an iron-insensitive measure of demyelination. Myelin loss in subcortical GM structures in MS is unrelated to excess iron deposition. Subcortical GM demyelination is more closely associated with the disease phenotype and disability than iron overload.

**ABBREVIATIONS:** CN = caudate nucleus; EDSS = Expanded Disability Status Scale; GP = globus pallidus; MPF = macromolecular proton fraction; MT = magnetization transfer; NAWM = normal-appearing WM; PASAT3 = Paced Auditory Serial Addition Test with 3-second interstimulus intervals; RRMS = relapsing-remitting multiple sclerosis; SN = substantia nigra; SPMS = secondary-progressive multiple sclerosis

Demyelination represents a global pathologic factor underlying neural tissue damage in MS and affecting the entire CNS. Demyelination manifests as both macroscopic MS lesion formation and microscopic changes in normal-appearing WM (NAWM) and

GM.<sup>1,2</sup> Widespread demyelination in subcortical GM structures in MS has been established in pathologic studies.<sup>2–4</sup> While common pathologic features of neural tissue injury in MS include inflammation, demyelination, and neurodegeneration, a specific aspect of subcortical GM pathology is excessive iron accumulation in oligodendrocytes and, to a lesser extent, in neurons, microglia, and astrocytes, compared with the rest of the GM and WM.<sup>4</sup>

Although the clinical and pathogenetic roles of excess iron deposition in the subcortical GM structures are currently debatable,<sup>5</sup> this phenomenon represents a common neuroradiologic

Received September 29, 2017; accepted after revision November 28.

From the Department of Radiology (V.L.Y.), University of Washington, Seattle, Washington; Research Institute of Biology and Biophysics (E.P.K., G.A., V.L.Y.), Tomsk State University, Tomsk, Russian Federation; Multiple Sclerosis Center (P.R., A.M., P.Q., L.K.J.H., B.G., J.D.B.), Swedish Neuroscience Institute, Seattle, Washington; and Piedmont Henry Hospital (L.K.J.H.), Stockbridge, Georgia.

Data acquisition was supported by the National Institutes of Health (grant R21EB009908) and National Multiple Sclerosis Society (grant RG 4864A1/1). Data analysis was performed under support from the Ministry of Education and Science of the Russian Federation within the State Assignment Project No. 18.2583.2017/4.6.

Paper previously presented in part at: Annual Meeting of the American Neurological Association, September 27–29, 2015; Chicago, Illinois. Abstract S514.

Please address correspondence to Vasily L. Yarnykh, PhD, Department of Radiology, University of Washington, 850 Republican St, Room 255, Seattle, WA 98109; e-mail: yarnykh@uw.edu; @yarnykh

Indicates open access to non-subscribers at www.ajnr.org

<http://dx.doi.org/10.3174/ajnr.A5542>

sign in MS, manifest as abnormal hypointensity on T2-weighted images.<sup>6</sup> Numerous studies involving iron-sensitive quantitative imaging techniques, such as T2, T2\*, magnetic susceptibility, and magnetic field correlation mapping have demonstrated abnormally increased iron content in deep GM in MS.<sup>7-10</sup> At the same time, quantitative assessment of subcortical GM demyelination is currently unavailable. The reason is the interplay between the effects of myelin and iron on tissue relaxation properties. Particularly, methods for quantitative or semiquantitative myelin imaging based on single- or multicomponent T1, T2, and T2\* relaxation models<sup>11-14</sup> are inapplicable to anatomic regions with a large and/or highly variable iron content. Similarly, a parameter frequently associated with myelination, magnetization transfer (MT) ratio, is not representative of changes in myelination in the presence of paramagnetic ions because it is subjected to the compounded effects of cross-relaxation and T1.<sup>15</sup>

A new quantitative myelin imaging method, fast macromolecular proton fraction (MPF) mapping,<sup>16-19</sup> offers the possibility of assessing demyelination in iron-rich anatomic structures due to the insensitivity of MPF to changes in relaxation properties of tissues caused by paramagnetic ions. MPF is a key parameter determining the MT effect in tissues and defined within the 2-pool model of MT as a relative number of macromolecular protons involved into cross-relaxation with water protons.<sup>16</sup> A number of animal studies have demonstrated close associations between MPF and myelin content in both WM and GM,<sup>20-24</sup> thus supporting clinical applications of this parameter as a myelin biomarker. It has been demonstrated that MPF measurements are practically insensitive to large variations in T1 caused by a paramagnetic contrast agent in an animal tumor model.<sup>25</sup> The recently developed single-point MPF mapping method has enabled reconstruction of MPF maps in isolation from other 2-pool model parameters based on a single MT-weighted image<sup>16,17</sup> and has shown promise as a fast clinical quantitative myelin imaging approach in MS<sup>18</sup> and mild traumatic brain injury<sup>19</sup> studies. Due to the insensitivity of MPF to changes in tissue relaxation associated with paramagnetic ions, fast MPF mapping offers the possibility of *in vivo* studies of demyelination in iron-rich brain structures without the confounding effect of iron deposition. The goals of this study were to compare the MPF in subcortical GM structures between healthy controls and patients with MS with different disease phenotypes, assess a potential relationship between MPF and T2\* as measures of demyelination and iron deposition in deep GM, and evaluate associations of the above quantitative imaging metrics with common clinical disability scales and tests of motor and cognitive function in MS.

## MATERIALS AND METHODS

### Study Population

We analyzed the data of a previously reported prospective cross-sectional case-control study.<sup>18</sup> The study was approved by the institutional review board at the University of Washington, and written informed consent was obtained from all participants. The study population included 18 patients with relapsing-remitting MS (RRMS) (12 women; mean age,  $48.2 \pm 10.8$  years; range, 30–62 years; mean Expanded Disability Status Scale [EDSS] score,  $2.9 \pm 1.8$ ; range, 1.0–6.5), 12 patients with secondary-

progressive MS (SPMS) (7 women; mean age,  $56.0 \pm 6.8$  years; range, 42–67 years; mean EDSS score,  $6.7 \pm 0.8$ ; range, 5.5–8.0), and 12 healthy controls (6 women; mean age,  $41.1 \pm 8.9$  years; range, 28–57 years). Available clinical data for patients with MS included the EDSS score, disease duration, the Multiple Sclerosis Functional Composite<sup>26</sup> score, and its component test scores (25-Foot Timed Walk Test, 9-Hole Peg Test, and Paced Auditory Serial Addition Test with 3-second interstimulus intervals [PASAT3]). Detailed characteristics of the study population can be found elsewhere.<sup>18</sup> Note that data from 12 of 14 initially reported<sup>18</sup> healthy controls were used in this study because T2\* maps were unavailable for 2 participants.

### MR Imaging Protocol

Images were acquired using a 3T MR imaging scanner (Achieva; Philips Healthcare, Best, the Netherlands) with a transmit-receive head coil. A fast 3D whole-brain MPF mapping protocol<sup>18</sup> included gradient-echo sequences with and without off-resonance MT saturation, variable flip angle T1 mapping,<sup>27</sup> and B0<sup>28</sup> and B1<sup>27,29</sup> field mapping. 2D T2-weighted FLAIR images were acquired for lesion segmentation. Parameters of the above imaging sequences are detailed elsewhere.<sup>18</sup> Additionally, whole-brain T2\* mapping was performed using a 3D multiple gradient-echo sequence with 8 echoes: TR = 37.5 ms, first TE = 2.3 ms, echo spacing = 3.2 ms, flip angle = 10°, FOV =  $240 \times 180 \times 184$  mm<sup>3</sup>, matrix =  $160 \times 160 \times 46$ , resolution =  $1.5 \times 1.5 \times 4$  mm<sup>3</sup> (interpolated to  $1 \times 1 \times 2$  mm<sup>3</sup>), and scan time = 3 minutes 25 seconds. The MPF and T2\* mapping scans were obtained in the axial plane with the same spatial resolution and coverage.

### Image Processing and Analysis

MPF maps were reconstructed with the single-point algorithm<sup>16</sup> using in-house-written C-language software as detailed in the earlier study.<sup>18</sup> T2\* maps were reconstructed by the voxel-based monoexponential 2-parameter fit of a squared noise-corrected signal<sup>30</sup> using in-house-written C-language software. Noise-correction factors for each dataset were determined from averaged SDs in 4 ROIs placed in the areas free from the signal and artifacts.

The head of caudate nucleus (CN), globus pallidus (GP), putamen, substantia nigra (SN), and thalamus were outlined manually on MPF maps using ImageJ software (National Institutes of Health, Bethesda, Maryland). T2\* measurements were performed in ROIs transferred from MPF maps. Parameter values for each subject were obtained by averaging bilateral measurements on the 3 adjacent cross-sections. ROI measurements were performed by 2 operators blinded to clinical information and then averaged. Examples of ROI placement corresponding to the above subcortical anatomic structures are provided in Figs 1 and 2. The results of brain segmentation into WM (NAWM for patients with MS), GM, and MS lesions were available from the previous study.<sup>18</sup>

### Statistical Analysis

The normality of data within subject groups was assessed using the Shapiro-Wilk test. No significant deviations from the normal distribution were detected, and parametric analyses were used thereafter. Interoperator variability was assessed by the coefficient of variation and intraclass correlation coefficient. Mean parametric

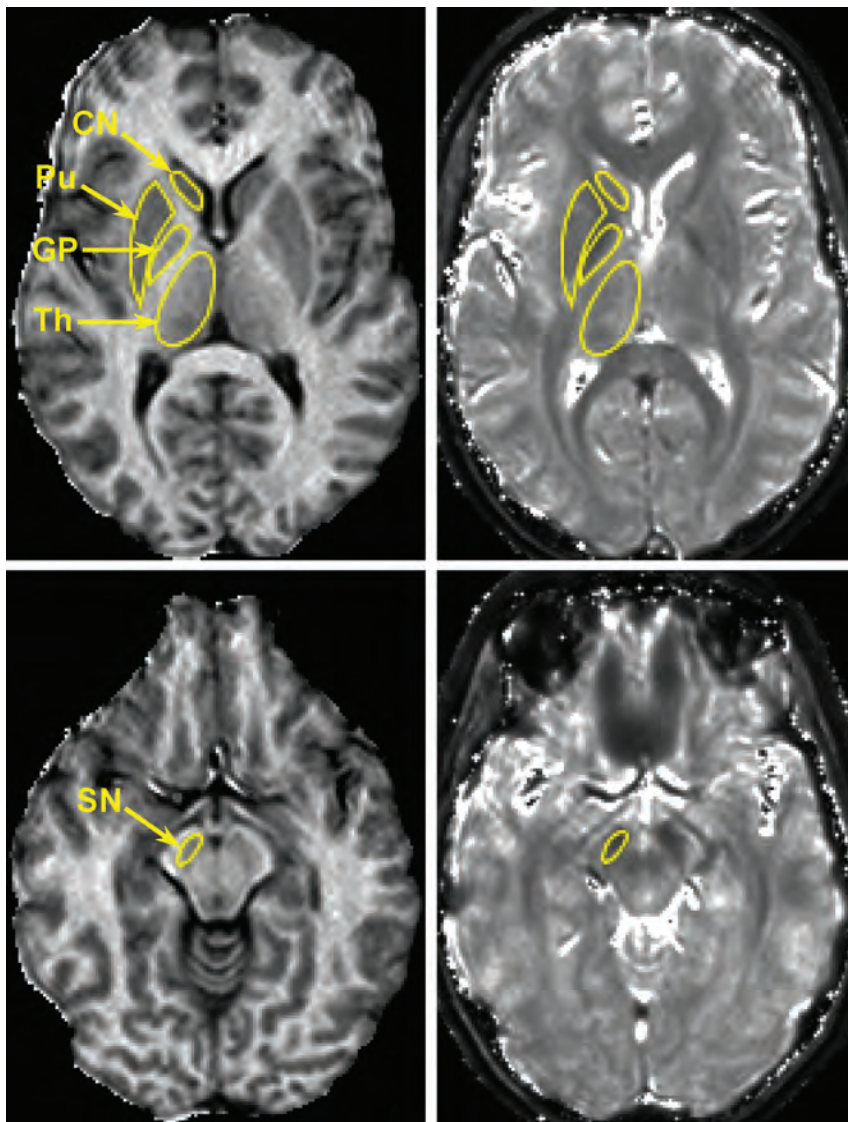


**FIG 1.** Representative cross-sections of 3D MPF (left) and T2\* (right) maps obtained from a healthy female control subject (37 years of age) with superimposed ROIs corresponding to the head of caudate nucleus, globus pallidus, putamen (Pu), substantia nigra, and thalamus (Th). MPF and T2\* maps are presented with gray-scale windows corresponding to the MPF range of 0%–20% and the T2\* range of 0–100 ms.

ter values in subcortical structures were compared among the 3 subject groups (controls, RRMS, and SPMS) using 1-way ANOVA followed by post hoc pair-wise tests with the Fisher least significant difference correction for multiple comparisons. Associations between imaging and clinical data were investigated using bivariate linear regression and the Pearson correlation coefficient ( $r$ ). The Shapiro-Wilk test was used to assess the normality of regression residuals, and appropriate transformations were used to correct for significant deviations from the normal distribution if detected. Additionally, multivariate regression models were tested using a stepwise variable elimination procedure to identify which of the previously reported<sup>18</sup> whole-brain imaging variables (MPF in NAWM, GM, and lesions, and lesion volume) or their combinations could better explain quantitative measurements in the basal ganglia. Two-tailed tests were used in all analyses.  $P$  values  $< .05$  indicated significant differences. All statistical analyses were performed using SPSS software (IBM, Armonk, New York) except

for intraclass correlation coefficient calculations, which were performed in MedCalc (MedCalc Software, Mariakerke, Belgium). Data are presented as mean  $\pm$  SD where applicable.

## RESULTS

### MPF and T2\* Measurements in the Basal Ganglia

MPF maps enabled clear anatomic definition of subcortical GM structures based on their hypointensity relative to surrounding WM in all cases (Figs 1 and 2). The appearance of these structures on T2\* maps was frequently obscured by the blooming effect, especially in the cases with excessive iron deposition (Fig 2). Manual MPF measurements were highly consistent between observers, with a coefficient of variation of  $< 2.5\%$  and an intraclass correlation coefficient of  $> 0.9$  (Table 1). T2\* measurements demonstrated higher variability with a coefficient of variation in the range of 1.8%–10.3%, but they still had excellent overall agreement (intraclass correlation coefficient  $\geq 0.8$ , Table 1).

Mean MPF and T2\* measurements in the subcortical GM structures of the study participant groups are summarized in Table 2. Monotonic trends of a decrease in both MPF and T2\* from controls to patients with RRMS and from patients with RRMS to those with SPMS were observed in all subcortical structures except for T2\* in the thalamus. ANOVA revealed the significance of these trends for all variables except for T2\* in the SN. Pair-wise comparisons identified significant differences among all 3 groups for the MPF in the GP and

putamen. In the CN and SN, the MPF was not significantly different between patients with RRMS and controls, but a significant decrease was found in the SPMS group compared with both controls and patients with RRMS. The MPF in the thalamus was significantly lower in both MS phenotypes compared with controls, but the difference between patients with RRMS and SPMS did not reach significance. T2\* in the GP, putamen, and CN was significantly shortened in patients with SPMS compared with controls. Additionally, T2\* in the CN was significantly shorter in the RRMS group relative to controls. A significant difference in T2\* between the RRMS and SPMS groups was found only in the putamen.

### Associations of MPF and T2\* in the Basal Ganglia with Clinical Status in MS

Correlations between quantitative imaging measures in the subcortical GM structures and clinical variables in patients with MS

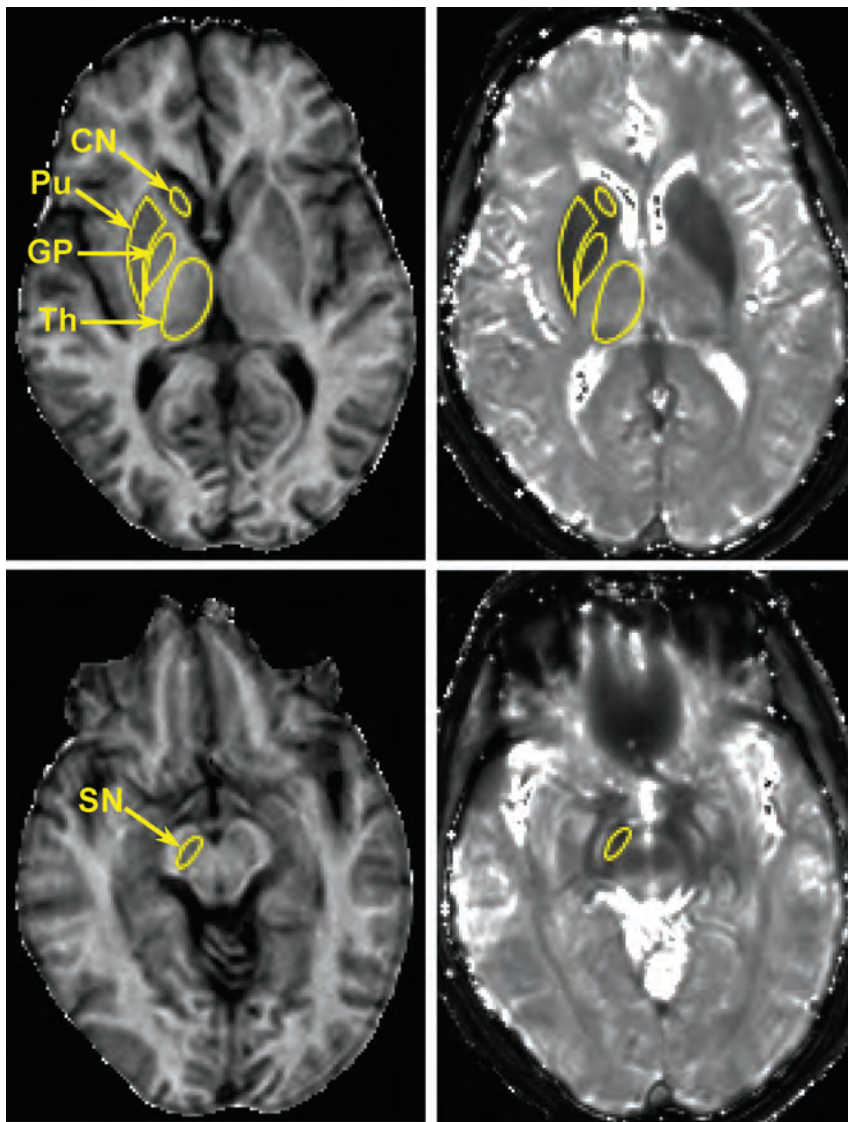


**FIG 2.** Representative cross-sections of 3D MPF (left) and T2\* (right) maps obtained from a female patient with SPMS (62 years of age; EDSS score, 5.5) with superimposed ROIs corresponding to the head of caudate nucleus, globus pallidus, putamen (Pu), substantia nigra, and thalamus (Th). MPF and T2\* maps are presented with gray-scale windows corresponding to the MPF range of 0%–20% and the T2\* range of 0–100 ms.

**Table 1: Coefficients of variation and intraclass correlation coefficients for interobserver agreement in MPF and T2\* measurements in the subcortical GM structures**

Variable	CoV (%)	ICC
MPF (CN)	1.4	0.97
MPF (GP)	1.1	0.98
MPF (putamen)	2.0	0.94
MPF (SN)	2.5	0.92
MPF (thalamus)	1.8	0.91
T2* (CN)	4.8	0.91
T2* (GP)	6.5	0.86
T2* (putamen)	2.8	0.98
T2* (SN)	10.3	0.80
T2* (thalamus)	1.8	0.95

**Note:**—CoV indicates coefficient of variation; ICC, intraclass correlation coefficient.

are listed in Table 3. Plots of selected correlations are presented in Fig 3. MPF in all subcortical structures significantly positively correlated with the Multiple Sclerosis Functional Composite and

negatively with the EDSS scores, as well as with the 9-Hole Peg Test. For other Multiple Sclerosis Functional Composite components, significant correlations of moderate strength were found for MPF in the GP and putamen (with 25-Foot Timed Walk and PASAT3 tests) and SN (with PASAT3). The MPF in the putamen, SN, and thalamus also correlated with the disease duration. Moderate significant correlations with patients' ages were found for MPF in all structures except the putamen.

Among T2\* measurements, weak-but-significant correlations with EDSS, the 25-Foot Timed Walk Test, disease duration, and age were identified for the putamen. T2\* values in other structures did not significantly correlate with clinical variables (Table 3).

### Correlations among Imaging Variables

Correlations between MPF and T2\* in the subcortical GM structures are summarized in Table 4. Correlations of both measures with global MPF measurements in brain tissues and lesion volume reported earlier for the same population<sup>18</sup> are provided in Table 5. No significant correlations between MPF and T2\* in the investigated structures were found in either patients with MS or controls taken separately. In the combined sample, weak-but-significant positive correlations were found in the GP and putamen, which are likely driven by the global group differences (a decrease of both MPF and T2\* in patients with MS).

The MPF in all subcortical structures demonstrated moderate-to-strong correlations with whole-brain MPF in NAWM and GM (Table 5). The MPF in the GP and SN also showed moderate correlations with MPF in MS lesions. T2\* in all structures did not correlate with any global imaging variable. Lesion volume did not correlate with any quantitative imaging variables except for a marginally significant ( $P = .04$ ) correlation with MPF in the putamen. Inclusion of global imaging variables into multivariate regression models (data not shown) did not improve the explanation of any of the subcortical GM measures. MPF in WM remained a single significant predictor of MPF in all examined structures in stepwise analyses.

### DISCUSSION

Being naturally rich in iron, subcortical GM structures represent an extremely difficult target to study demyelination by conventional and quantitative MR imaging because signal changes asso-

ciated with myelin loss can be easily obscured by the variable paramagnetic effect of iron. The clinical role of demyelination in the subcortical nuclei in MS has not been established to date, and the evidence of myelin loss in these structures is based on post-mortem studies.<sup>2-4</sup> Application of the MPF as an iron-insensitive myelin biomarker enabled in vivo confirmation of earlier pathologic findings of significant demyelination of subcortical GM in MS.<sup>2-4</sup> Furthermore, significant correlations between MPF in subcortical GM and clinical scales and the capability of MPF to discriminate the disease phenotypes indicate the clinical relevance of this parameter. The trends of demyelination in the basal ganglia and thalamus found in this study have common features with global demyelination in both NAWM and GM because correlations of MPF in subcortical GM structures with global MPF values in NAWM and GM are rather similar. At the same time, these correlations are not very strong and explain only 30%–40% of data dispersion within either univariate or multivariate models. In view of good interobserver agreement and low variability in MPF measurements,<sup>17,24</sup> this observation cannot be completely attributed to measurement noise.

The correlations between MPF in subcortical GM structures and disability scales appeared systematically weaker than those for cortical GM and more similar in strength to the correlations for NAWM reported earlier for the same patient population.<sup>18</sup> In contrast to global NAWM and GM values,<sup>18</sup> the MPF in the 2

structures (CN and SN) also showed no significant differences between patients with RRMS and controls. Notably, the MPF in the basal ganglia showed the strongest correlations with the 9-Hole Peg Test scores compared with other clinical tests (Table 3). Because this test measures the fine motor function of the upper extremities, our observation may indicate that demyelination detected by MPF in the CN, GP, putamen, and SN reflects the damage to the nigrostriatal pathway, which functionally manifests as motor impairment. Taken together, the above observations suggest that the subcortical GM structures may not follow a uniform trajectory of myelin loss in MS and that demyelination in different nuclei may have different clinical significances.

The absence of significant correlations between MPF and T2\* in the subcortical GM structures in patients with MS found in this study suggests that demyelination and excess iron deposition in subcortical GM represent unrelated pathologic processes with different clinical relevance. Literature data about the clinical significance of iron accumulation in subcortical GM in MS are controversial.<sup>5-10</sup> Our results are in agreement with multiple reports of a significant increase of the iron load in the basal ganglia in MS based on quantitative iron-sensitive MR imaging measures or T2 hypointensity.<sup>6-10</sup> However, similar to this study, published cross-sectional correlations between MR imaging-based iron measures and clinical scales were moderate to insignificant.<sup>6-10</sup> On the other hand, there is some evidence of a higher clinical

relevance of excess iron deposition in the deep GM in the longitudinal aspect.<sup>31,32</sup> A possible pathogenetic role of iron in MS is associated with its cytotoxic effect, causing oxidative stress and mitochondrial injury.<sup>5</sup> The cytotoxicity of iron is mainly attributed to its reactive ferrous oxidative form that may result from free ferric iron released into the extracellular space as a result of oligodendrocyte and myelin obliteration.<sup>4,5</sup>

On the other hand, the paramagnetic effect responsible for shortening tissue magnetic relaxation times is primarily

**Table 2: Mean group MPF and T2\* in the subcortical GM structures<sup>a</sup>**

Variable	Controls (Mean)	Patients with RRMS (Mean)	Patients with SPMS (Mean)	ANOVA F (P)
MPF (CN) (%)	7.23 ± 0.41	7.02 ± 0.35	6.75 ± 0.28 <sup>bc</sup>	5.7 (.007)
MPF (GP) (%)	10.23 ± 0.27	9.84 ± 0.45 <sup>b</sup>	9.39 ± 0.47 <sup>bc</sup>	12.6 (<.001)
MPF (putamen) (%)	7.62 ± 0.24	7.34 ± 0.32 <sup>b</sup>	7.03 ± 0.43 <sup>bc</sup>	9.1 (.001)
MPF (SN) (%)	9.36 ± 0.64	9.25 ± 0.45	8.81 ± 0.48 <sup>bc</sup>	3.9 (.029)
MPF (thalamus) (%)	10.05 ± 0.37	9.72 ± 0.41 <sup>b</sup>	9.47 ± 0.20 <sup>b</sup>	8.2 (.001)
T2* (CN) (ms)	49.28 ± 3.44	45.79 ± 4.18 <sup>b</sup>	44.16 ± 5.93 <sup>b</sup>	4.0 (.027)
T2* (GP) (ms)	29.04 ± 2.72	27.55 ± 2.94	25.30 ± 3.29 <sup>b</sup>	4.8 (.014)
T2* (putamen) (ms)	42.36 ± 3.08	41.04 ± 4.89	36.87 ± 6.16 <sup>bc</sup>	4.2 (.022)
T2* (SN) (ms)	29.54 ± 3.99	28.17 ± 4.78	27.17 ± 3.77	0.9 (.41)
T2* (thalamus) (ms)	46.46 ± 2.17	46.78 ± 2.88	46.59 ± 3.22	0.1 (.95)

<sup>a</sup> The least significant difference correction for multiple comparisons was used.

<sup>b</sup> Significantly different from control subjects ( $P < .05$ ).

<sup>c</sup> Significantly different from patients with RRMS ( $P < .05$ ).

**Table 3: Correlations between quantitative imaging measures in the subcortical GM structures and clinical variables in patients with MS<sup>a</sup>**

Basal Ganglia Variable	Clinical Variable						
	Age	Disease Duration	EDSS Score	MSFC Score	25FTW Score	9HPT Score	PASAT3 Score
MPF (CN)	-0.42 <sup>b</sup>	-0.34	-0.52 <sup>c</sup>	0.39 <sup>b</sup>	-0.29	-0.40 <sup>b</sup>	0.34
MPF (GP)	-0.41 <sup>b</sup>	-0.26	-0.56 <sup>c</sup>	0.47 <sup>c</sup>	-0.42 <sup>b</sup>	-0.51 <sup>c</sup>	0.40 <sup>b</sup>
MPF (putamen)	-0.30	-0.53 <sup>c</sup>	-0.52 <sup>c</sup>	0.57 <sup>c</sup>	-0.49 <sup>c</sup>	-0.60 <sup>c</sup>	0.44 <sup>b</sup>
MPF (SN)	-0.47 <sup>c</sup>	-0.40 <sup>b</sup>	-0.55 <sup>c</sup>	0.53 <sup>c</sup>	-0.36	-0.59 <sup>c</sup>	0.48 <sup>c</sup>
MPF (thalamus)	-0.44 <sup>b</sup>	-0.37 <sup>b</sup>	-0.54 <sup>c</sup>	0.48 <sup>c</sup>	-0.34	-0.52 <sup>c</sup>	0.32
T2* (CN)	-0.24	-0.25	-0.14	0.15	-0.16	-0.19	0.13
T2* (GP)	-0.19	-0.15	-0.33	0.17	-0.16	-0.23	0.25
T2* (putamen)	-0.37 <sup>b</sup>	-0.41 <sup>b</sup>	-0.43 <sup>b</sup>	0.27	-0.41 <sup>b</sup>	-0.29	0.14
T2* (SN)	-0.04	0.14	-0.16	-0.24	-0.02	0.24	-0.25
T2* (thalamus)	-0.11	-0.02	-0.23	-0.05	-0.09	0.05	-0.04

**Note:**—25FTW indicates the 25-Foot Timed Walk Test; 9HPT, 9-Hole Peg Test; MSFC, Multiple Sclerosis Functional Composite.

<sup>a</sup> Data are Pearson correlation coefficients. To correct for deviations from normal distribution, we applied the Box-Cox transformation to the 25FTW and 9HPT scores with the power of -0.5.

<sup>b</sup> .01 ≤  $P < .05$ .

<sup>c</sup>  $P < .01$ .

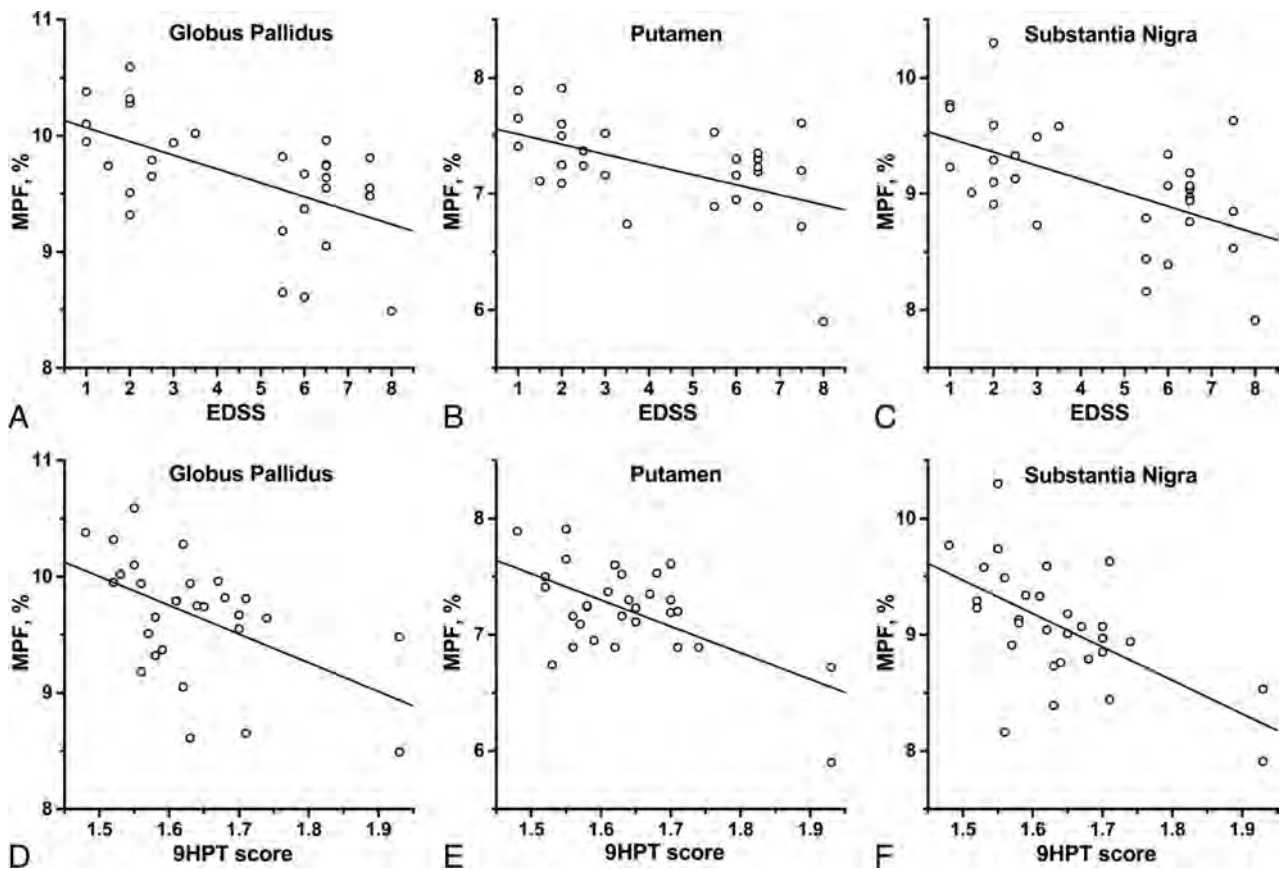


**FIG 3.** Scatterplots of correlations between clinical variables (EDSS [A–C] and 9-Hole Peg Test score [D–F]) and the MPF in the GP (A and D), putamen (B and E), and SN (C and F). Lines represent linear regression plots. Correlation coefficients are given in Table 3. The 9-Hole Peg Test scores were Box-Cox transformed with the power of  $-0.5$ .

**Table 4: Correlations between MPF and T2\* in the subcortical GM structures**

Structure	Controls (n = 12), r(P)	Patients with MS (n = 30), r(P)	Controls and Patients (n = 42), r(P)
CN	-0.54 (.07)	0.14 (.47)	0.13 (.43)
GP	-0.07 (.83)	0.26 (.16)	0.34 (.03)
Putamen	0.16 (.62)	0.35 (.06)	0.40 (.008)
SN	-0.40 (.20)	-0.22 (.24)	-0.22 (.17)
Thalamus	-0.27 (.40)	0.11 (.57)	0.02 (.99)

caused by ferric iron bound to ferritin,<sup>33</sup> a protein enabling iron storage and transport in a nontoxic form.<sup>4,5</sup> Thus, a visible effect of iron accumulation due to formation of a superparamagnetic ferritin complex may not be indicative of the actual flux of iron from damaged myelin and oligodendrocytes, as well as the free iron concentration in the extracellular space determining the potential for oxidative stress. Furthermore, excess iron deposition into the ferritin storage in the basal ganglia may provide a protective homeostatic mechanism against iron-related oxidative tissue injury.<sup>5</sup> In summary, our results do not suggest a direct relationship between demyelination and iron deposition in the deep GM in MS, while further investigations of the dynamics of these processes in longitudinal studies may provide more insight.

This study demonstrates a general methodology enabling quantitative assessment of myelin loss in subcortical GM. The fact that MPF and T2\* do not correlate in the sample characterized by high disease-related variability of both parameters confirms the

**Table 5: Correlations between quantitative imaging measures in the subcortical GM structures and global imaging variables in patients with MS<sup>a</sup>**

Basal Ganglia Variable	Global Imaging Variable			
	MPF in NAWM	MPF in GM	MPF in Lesions	Lesion Volume
MPF (CN)	0.54 <sup>b</sup>	0.43 <sup>c</sup>	0.05	-0.36
MPF (GP)	0.63 <sup>b</sup>	0.59 <sup>b</sup>	0.52 <sup>b</sup>	-0.30
MPF (putamen)	0.56 <sup>b</sup>	0.51 <sup>b</sup>	0.32	-0.37 <sup>c</sup>
MPF (SN)	0.63 <sup>b</sup>	0.50 <sup>b</sup>	0.45 <sup>c</sup>	-0.31
MPF (thalamus)	0.55 <sup>b</sup>	0.39 <sup>c</sup>	0.19	-0.24
T2* (CN)	0.01	0.14	0.08	0.09
T2* (GP)	0.05	0.29	0.15	-0.04
T2* (putamen)	0.19	0.30	0.14	0.02
T2* (SN)	-0.28	-0.12	-0.08	0.11
T2* (thalamus)	-0.07	0.02	0.16	0.13

<sup>a</sup> Data are Pearson correlation coefficients. To correct for deviations from normal distribution, we applied the Box-Cox transformation to the lesion volume with the power of 0.5.

<sup>b</sup>  $P < .01$ .

<sup>c</sup>  $.01 \leq P < .05$ .

independence of the MPF measured by the single-point method of the iron content. Hypothetically, one might expect that high iron concentrations could affect MPF measurements through unaccounted errors caused by the direct saturation effect. More specifically, single-point MPF mapping is based on the assumption about the constant product of the measured  $R1 = 1/T1$  and  $T2$  of free water protons defined within the 2-pool model of MT.<sup>16</sup> This product is used within the MPF reconstruction algorithm<sup>16</sup> as a

constraint for the term associated with direct saturation of water protons and may be tissue-dependent. However, in agreement with the theory,<sup>16</sup> the use of a sufficiently high offset frequency (4 kHz) in the MPF mapping protocols<sup>18</sup> makes potential MPF errors associated with the variability of R1 and T2 of free water protons in tissues practically negligible, as evidenced by both the absence of correlations between MPF and T2\* and visual hypointensity of the basal ganglia on MPF maps observed even in cases of very high iron load (Fig 2). Accordingly, this study confirms that MPF provides a robust myelin biomarker that can be applied to studies of iron-rich brain structures in a variety of pathologic conditions associated with excess iron deposition such as Parkinson, Alzheimer, and other neurodegenerative diseases.<sup>33,34</sup>

This study has several limitations. First, due to the cross-sectional design, the results of this study should be considered preliminary and the value of both demyelination and iron deposition in the basal ganglia in the aspects of disease prognosis and treatment monitoring remains to be investigated. Second, our interpretation of T2\* values in terms of iron load may be an oversimplification because this parameter is affected by various pathologic factors, including demyelination and changes in tissue water content and perfusion.<sup>33,35,36</sup> Particularly, demyelination may cause elongation of T2\* values, a trend opposite to the effect caused by iron accumulation.<sup>35</sup> However, iron remains the dominant factor determining T2\* in brain tissues, even with a low background iron content.<sup>35,36</sup> Third, while myelin content has been established as the main histologic determinant of MPF in brain tissues,<sup>21,24</sup> minor effects of other pathologic factors, such as inflammation, gliosis, and loss of neuronal arborization, on this parameter cannot be completely excluded. Fourth, we did not use a contrast agent due to the research nature of the imaging protocol and safety considerations. Thus, future studies involving contrast enhancement are needed to investigate a potential relationship between subcortical GM demyelination and active inflammation. Finally, parametric maps used in this study were obtained with relatively low resolution (1.5 mm<sup>2</sup> in-plane). Accordingly, the observed associations may be, to some extent, affected by changes in surrounding WM due to the partial volume effect.

## CONCLUSIONS

This study demonstrated that the fast MPF mapping method enables accurate quantitative assessment of demyelination in iron-rich subcortical GM structures and provides an iron-insensitive imaging biomarker of myelin. Our results confirm earlier histologic findings of demyelination in the basal ganglia in MS and suggest that the loss of myelin in subcortical GM is associated with disability and motor impairment and is unrelated to excess iron deposition.

Disclosures: Vasily L. Yarnykh—RELATED: Grant: National Institutes of Health, National Multiple Sclerosis Society, Ministry of Education and Science of the Russian Federation, Comments: National Institutes of Health grant R21EB009908, National Multiple Sclerosis Society grant RG4864A1/1, Ministry of Education and Science of the Russian Federation State Assignment Project No. 18.2583.2017/4.6.\* Elena P. Krutenkova—RELATED: Grant: Ministry of Education and Science of the Russian Federation, Comments: Ministry of Education and Science of the Russian Federation State Assignment Project No. 18.2583.2017/4.6.\* Gulsum Aitmagambetova—RELATED: Grant: Ministry of Education and Science of the Russian Federation, Comments: Ministry of Education and Science of the Russian Federation State Assignment Project No. 18.2583.2017/4.6.\* Pavle Repovic—RELATED: Grant: National

Institutes of Health, National Multiple Sclerosis Society, Comments: National Institutes of Health grant R21EB009908, National Multiple Sclerosis Society grant RG4864A1/1\*; UNRELATED: Grants/Grants Pending: Novartis\*; Payment for Lectures Including Service on Speakers Bureaus: Acorda Therapeutics, Biogen Idec, Genentech, Genzyme, EMD Serono, Novartis, Pfizer, Teva Pharmaceutical Industries.\* Peiqing Qian—RELATED: Grant: National Institutes of Health grant R21EB009908, National Multiple Sclerosis Society grant RG4864A1/1\*. Beena Gangadharan—RELATED: Grant: National Institutes of Health grant R21EB009908, National Multiple Sclerosis Society grant RG4864A1/1\*. James D. Bowen—RELATED: Grant: National Institutes of Health grant R21EB009908, National Multiple Sclerosis Society grant RG4864A1/1.\* \*Money paid to the institution.

## REFERENCES

- Lassmann H, Brück W, Lucchinetti CF. **The immunopathology of multiple sclerosis: an overview.** *Brain Pathol* 2007;17:210–18 CrossRef Medline
- Gilmore CP, Donaldson I, Bö L, et al. **Regional variations in the extent and pattern of grey matter demyelination in multiple sclerosis: a comparison between the cerebral cortex, cerebellar cortex, deep grey matter nuclei and the spinal cord.** *J Neurol Neurosurg Psychiatry* 2009;80:182–87 CrossRef Medline
- Vercellino M, Masera S, Lorenzatti M, et al. **Demyelination, inflammation, and neurodegeneration in multiple sclerosis deep grey matter.** *J Neuropathol Exp Neurol* 2009;68:489–502 CrossRef Medline
- Haider L, Simeonidou C, Steinberger G, et al. **Multiple sclerosis deep grey matter: the relation between demyelination, neurodegeneration, inflammation and iron.** *J Neurol Neurosurg Psychiatry* 2014;85:1386–95 CrossRef Medline
- Stephenson E, Nathoo N, Mahjoub Y, et al. **Iron in multiple sclerosis: roles in neurodegeneration and repair.** *Nat Rev Neurol* 2014;10:459–68 CrossRef Medline
- Bakshi R, Benedict RH, Bermel RA, et al. **T2 hypointensity in the deep gray matter of patients with multiple sclerosis: a quantitative resonance imaging study.** *Arch Neurol* 2002;59:62–68 CrossRef Medline
- Ge Y, Jensen JH, Lu H, et al. **Quantitative assessment of iron accumulation in the deep gray matter of multiple sclerosis by magnetic field correlation imaging.** *AJNR Am J Neuroradiol* 2007;28:1639–44 CrossRef Medline
- Burgetova A, Seidl Z, Krasensky J, et al. **Multiple sclerosis and the accumulation of iron in the basal ganglia: quantitative assessment of brain iron using MRI t(2) relaxometry.** *Eur Neurol* 2010;63:136–43 CrossRef Medline
- Khalil M, Langkammer C, Ropele S, et al. **Determinants of brain iron in multiple sclerosis: a quantitative 3T MRI study.** *Neurology* 2011;77:1691–97 CrossRef Medline
- Rudko DA, Solovey I, Gati JS, et al. **Multiple sclerosis: improved identification of disease-relevant changes in gray and white matter by using susceptibility-based MR imaging.** *Radiology* 2014;272:851–64 CrossRef Medline
- MacKay A, Whittall K, Adler J, et al. **In vivo visualization of myelin water in brain by magnetic resonance.** *Magn Reson Med* 1994;31:673–77 CrossRef Medline
- Deoni SCL, Rutt BK, Arun T, et al. **Gleaning multicomponent T1 and T2 information from steady-state imaging data.** *Magn Reson Med* 2008;60:1372–87 CrossRef Medline
- Hwang D, Kim DH, Du YP. **In vivo multi-slice mapping of myelin water content using T2\* decay.** *Neuroimage* 2010;52:198–204 CrossRef Medline
- Glasser MF, Van Essen DC. **Mapping human cortical areas in vivo based on myelin content as revealed by T1- and T2-weighted MRI.** *J Neurosci* 2011;31:11597–616 CrossRef Medline
- Yarnykh VL. **Pulsed Z-spectroscopic imaging of cross-relaxation parameters in tissues for human MRI: theory and clinical applications.** *Magn Reson Med* 2002;47:929–39 CrossRef Medline
- Yarnykh VL. **Fast macromolecular proton fraction mapping from a single off-resonance magnetization transfer measurement.** *Magn Reson Med* 2012;68:166–78 CrossRef Medline
- Yarnykh VL. **Time-efficient, high-resolution, whole brain three-di-**

- dimensional macromolecular proton fraction mapping. *Magn Reson Med* 2016;75:2100–06 CrossRef Medline
18. Yarnykh VL, Bowen JD, Samsonov A, et al. **Fast whole-brain three-dimensional macromolecular proton fraction mapping in multiple sclerosis.** *Radiology* 2015;274:210–20 CrossRef Medline
  19. Petrie EC, Cross DJ, Yarnykh VL, et al. **Neuroimaging, behavioral, and psychological sequelae of repetitive combined blast/impact mild traumatic brain injury in Iraq and Afghanistan war veterans.** *J Neurotrauma* 2014;31:425–36 CrossRef Medline
  20. Ou X, Sun SW, Liang HF, et al. **The MT pool size ratio and the DTI radial diffusivity may reflect the myelination in shiverer and control mice.** *NMR Biomed* 2009;22:480–87 CrossRef Medline
  21. Underhill HR, Rostomily RC, Mikheev AM, et al. **Fast bound pool fraction imaging of the in vivo rat brain: association with myelin content and validation in the C6 glioma model.** *Neuroimage* 2011;54:2052–65 CrossRef Medline
  22. Thiessen JD, Zhang Y, Zhang H, et al. **Quantitative MRI and ultrastructural examination of the cuprizone mouse model of demyelination.** *NMR Biomed* 2013;26:1562–81 CrossRef Medline
  23. Turati L, Moscatelli M, Mastropietro A, et al. **In vivo quantitative magnetization transfer imaging correlates with histology during de- and remyelination in cuprizone-treated mice.** *NMR Biomed* 2015;28:327–37 CrossRef Medline
  24. Khodanovich MY, Sorokina IV, Glazacheva VY, et al. **Histological validation of fast macromolecular proton fraction mapping as a quantitative myelin imaging method in the cuprizone demyelination model.** *Sci Rep* 2017;7:46686 CrossRef Medline
  25. Li K, Li H, Zhang XY, et al. **Influence of water compartmentation and heterogeneous relaxation on quantitative magnetization transfer imaging in rodent brain tumors.** *Magn Reson Med* 2016;76:635–44 CrossRef Medline
  26. Fischer JS, Rudick RA, Cutter GR, et al. **The Multiple Sclerosis Functional Composite Measure (MSFC): an integrated approach to MS clinical outcome assessment—National MS Society Clinical Outcomes Assessment Task Force.** *Mult Scler* 1999;5:244–50 Medline
  27. Yarnykh VL. **Optimal radiofrequency and gradient spoiling for improved accuracy of T1 and B1 measurements using fast steady-state techniques.** *Magn Reson Med* 2010;63:1610–26 CrossRef Medline
  28. Skinner TE, Glover GH. **An extended two-point Dixon algorithm for calculating separate water, fat, and B0 images.** *Magn Reson Med* 1997;37:628–30 CrossRef Medline
  29. Yarnykh VL. **Actual flip-angle imaging in the pulsed steady state: a method for rapid three-dimensional mapping of the transmitted radiofrequency field.** *Magn Reson Med* 2007;57:192–200 CrossRef Medline
  30. Miller AJ, Joseph PM. **The use of power images to perform quantitative analysis on low SNR MR images.** *Magn Reson Imaging* 1993;11:1051–56 CrossRef Medline
  31. Neema M, Arora A, Healy BC, et al. **Deep gray matter involvement on brain MRI scans is associated with clinical progression in multiple sclerosis.** *J Neuroimaging* 2009;19:3–8 CrossRef Medline
  32. Walsh AJ, Blevins G, Lebel RM, et al. **Longitudinal MR imaging of iron in multiple sclerosis: an imaging marker of disease.** *Radiology* 2014;270:186–96 CrossRef Medline
  33. Haacke EM, Cheng NY, House MJ, et al. **Imaging iron stores in the brain using magnetic resonance imaging.** *Magn Reson Imaging* 2005;23:1–25 CrossRef Medline
  34. Sadrzadeh SM, Saffari Y. **Iron and brain disorders.** *Am J Clin Pathol* 2004;121(Suppl):S64–70 Medline
  35. Stüber C, Morawski M, Schäfer A, et al. **Myelin and iron concentration in the human brain: a quantitative study of MRI contrast.** *Neuroimage* 2014;93(Pt 1):95–106 CrossRef Medline
  36. Sun H, Walsh AJ, Lebel RM, et al. **Validation of quantitative susceptibility mapping with Perls' iron staining for subcortical gray matter.** *Neuroimage* 2015;105:486–92 CrossRef Medline

# An Automated Statistical Technique for Counting Distinct Multiple Sclerosis Lesions

J.D. Dworkin, K.A. Linn, I. Oguz, G.M. Fleishman, R. Bakshi, G. Nair, P.A. Calabresi, R.G. Henry, J. Oh, N. Papinutto, D. Pelletier, W. Rooney, W. Stern, N.L. Sicotte, D.S. Reich, R.T. Shinohara, and the North American Imaging in Multiple Sclerosis Cooperative



## ABSTRACT

**BACKGROUND AND PURPOSE:** Lesion load is a common biomarker in multiple sclerosis, yet it has historically shown modest association with clinical outcome. Lesion count, which encapsulates the natural history of lesion formation and is thought to provide complementary information, is difficult to assess in patients with confluent (ie, spatially overlapping) lesions. We introduce a statistical technique for cross-sectionally counting pathologically distinct lesions.

**MATERIALS AND METHODS:** MR imaging was used to assess the probability of a lesion at each location. The texture of this map was quantified using a novel technique, and clusters resembling the center of a lesion were counted. Validity compared with a criterion standard count was demonstrated in 60 subjects observed longitudinally, and reliability was determined using 14 scans of a clinically stable subject acquired at 7 sites.

**RESULTS:** The proposed count and the criterion standard count were highly correlated ( $r = 0.97, P < .001$ ) and not significantly different ( $t_{59} = -.83, P = .41$ ), and the variability of the proposed count across repeat scans was equivalent to that of lesion load. After accounting for lesion load and age, lesion count was negatively associated ( $t_{58} = -2.73, P < .01$ ) with the Expanded Disability Status Scale. Average lesion size had a higher association with the Expanded Disability Status Scale ( $r = 0.35, P < .01$ ) than lesion load ( $r = 0.10, P = .44$ ) or lesion count ( $r = -.12, P = .36$ ) alone.

**CONCLUSIONS:** This study introduces a novel technique for counting pathologically distinct lesions using cross-sectional data and demonstrates its ability to recover obscured longitudinal information. The proposed count allows more accurate estimation of lesion size, which correlated more closely with disability scores than either lesion load or lesion count alone.

**ABBREVIATIONS:**  $C_C$  = count based on the standard connected-components technique;  $C_C$  = criterion standard count;  $C_P$  = count based on the technique proposed in this study; CV = coefficient of variation; EDSS = Expanded Disability Status Scale;  $EDSS_{avg}$  = average of the EDSS scores over all visits for each subject in the National Institute of Neurological Disorders and Stroke longitudinal study; NAIMS = North American Imaging in Multiple Sclerosis; OASIS = Automated Statistical Inference for Segmentation

Multiple sclerosis is a neuroinflammatory disorder characterized by demyelinating lesions that occur in the central nervous system. MR imaging is the most commonly used method to observe these lesions, especially in the white matter of the brain.<sup>1</sup>

The presence of new lesions on MR imaging is often considered an important clinical marker of disease activity, yet MR imaging-based measures of disease severity have been elusive.<sup>2</sup> The total lesion burden in the white matter or “lesion load”—measured as volume or volume fraction of brain size—is often used in the

Received October 30, 2017; accepted after revision December 10.

From the Departments of Biostatistics, Epidemiology, and Informatics (J.D.D., K.A.L., R.T.S.), and Radiology (I.O., G.M.F.), Perelman School of Medicine, University of Pennsylvania, Philadelphia, Pennsylvania; Laboratory for Neuroimaging Research (R.B.), Partners Multiple Sclerosis Center, Ann Romney Center for Neurologic Diseases, and Departments of Neurology (R.B.) and Radiology (R.B.), Brigham and Women's Hospital, Harvard Medical School, Boston, Massachusetts; Translational Neuroradiology Section (G.N., D.S.R.), National Institute of Neurological Disorders and Stroke, National Institutes of Health, Bethesda, Maryland; Department of Neurology (P.A.C., J.O., D.S.R.), the Johns Hopkins University School of Medicine, Baltimore, Maryland; Department of Neurology (R.G.H., N.P., W.S.), University of California, San Francisco, San Francisco, California; Keenan Research Centre for Biomedical Science (J.O.), St. Michael's Hospital, University of Toronto, Toronto, Ontario, Canada; Department of Neurology (D.P.), Keck School of Medicine, University of Southern California, Los Angeles, California; Advanced Imaging Research Center (W.R.), Oregon Health & Science University,

Portland, Oregon; and Department of Neurology (N.L.S.), Cedars-Sinai Medical Center, Los Angeles, California. A complete list of the NAIMS participants is provided in the acknowledgment section.

This work was supported in part by the National Institutes of Health grants R01 NS085211, R21 NS093349, R01 NS094456, and R01 NS060910 from the National Institute of Neurological Disorders and Stroke. The study was also supported by the Intramural Research Program of the National Institute of Neurological Disorders and Stroke and the Race to Erase MS Foundation.

The content of this article is solely the responsibility of the authors and does not necessarily represent the official views of the funding agencies.

Please address correspondence to Jordan D. Dworkin, 218 Blockley Hall, 423 Guardian Dr, Philadelphia, PA 19104; e-mail: jdwor@pennmedicine.upenn.edu; @jddwor

Indicates open access to non-subscribers at www.ajnr.org

<http://dx.doi.org/10.3174/ajnr.A5556>

study of MS, typically as a measure of disease severity<sup>3</sup> and as a clinical trial outcome.<sup>4</sup> However, lesion load has consistently shown a surprisingly weak association with clinical measures of disease severity, calling into question its usefulness as a surrogate and reinforcing the need for further development of MR imaging outcomes for MS.<sup>2,5</sup>

In past years, several clinical studies have discussed the number of lesions in a patient's brain as a possible outcome of interest.<sup>6-8</sup> In these studies, baseline lesion count has been shown to be correlated with the Expanded Disability Status Scale (EDSS) and changes in lesion count have been shown to be correlated with changes in the EDSS. However, obtaining an accurate count of biologically distinct lesions in the brain can be costly and logistically challenging, typically requiring expert review or automated analysis of scans obtained at frequent follow-up visits. This process is especially difficult in patients with a high lesion load and many confluent lesions.<sup>9</sup>

Confluent lesions commonly occur when pathologically distinct lesions (ie, lesions that arise due to spatially separate sources of structural damage in the brain, usually separated in time) occur near each other and create a larger connected region of lesion tissue. Depending on the level of lesion burden, confluent lesions can range from 2 overlapping lesions with a single connecting edge to dozens of connected lesions spanning large stretches of white matter. The existence of such confluent tissue can make it difficult or impossible to estimate the number of distinct lesions in the brain at any given visit. A patient must be scanned regularly, with temporality of appearance serving to separate spatially confluent lesions, to obtain accurate lesion counts. However, MR imaging scans are extremely costly, which can make regular follow-up visits infeasible. Additionally, in patients with a great deal of disease activity, even monthly or bimonthly scans can produce multiple new lesions that overlap in space.<sup>10,11</sup> These considerations render lesion counts unavailable or inaccurate in most clinical settings in which patients are typically scanned yearly or twice yearly.

To address this issue, the current study introduces a statistical analysis technique for obtaining valid and reliable estimates of lesion counts from a single cross-sectional MR imaging study. This fully automated method uses cutting-edge statistical models for segmenting lesion tissue and well-demonstrated mathematic methods for quantifying texture to obtain the number and location of temporally distinct white matter lesions. Additionally, this study provides evidence that the derived lesion counts are associated with clinical measures of disease severity, independent of total lesion volume.

## MATERIALS AND METHODS

### Proposed Lesion-Count Algorithm

To obtain the lesion-count estimate in a given subject, we performed the following steps: First, a map of lesion probability at each voxel in the brain was obtained using preprocessed and coregistered MR imaging volumes from a single visit. Depending on the automated segmentation method used, a combination of T1-weighted, fluid-attenuated inversion recovery, T2-weighted, and proton density volumes would be required for probability estimation. A threshold was then applied to the prob-

ability map to create a binary mask of regions considered lesion tissue.

With the probability map, the texture of the lesion tissue was quantified to find regions that exhibited the properties expected of the center of a single lesion. Texture was quantified using the eigenvalues of the Hessian matrix. The Hessian matrix was calculated for the intensity of the lesion probability map at every voxel in the lesion mask, with a gradient window of 1 voxel in each direction. In the context of a 3D image, the Hessian matrix describes the second-order variation in image intensity in the local neighborhood around a voxel. When applied to a lesion probability map, the eigenvalues of the Hessian matrix at each voxel represent the 3 primary directions of change in lesion probability at that voxel.

Thus, voxels in the center of a lesion would be expected to have a negative eigenvalue, implying a decrease in probability, in all directions. This follows from the commonly accepted pathology of MS lesions, in which initial damage to a vein causes residual inflammation to spread outward from the vein in a relatively ovoid fashion, with less damage occurring around the periphery of the visible lesion.<sup>12</sup> Therefore, voxels are eliminated if any of the 3 eigenvalues are positive; the elimination indicates that the voxel is less likely to be a lesion than its surroundings in at least 1 direction. The remaining voxels with 3 negative eigenvalues are clustered by location, and connected clusters (operationalized as the centers of distinct lesions) are counted. Figure 1 provides an example of this technique.

### Data and Preprocessing

**Validation and Clinical-Radiologic Association.** Sixty subjects diagnosed with MS were scanned between 2000 and 2008 monthly for  $\leq 5.5$  years (mean,  $2.2 \pm 1.2$  years) as part of a natural history study at the National Institute of Neurological Disorders and Stroke in Bethesda, Maryland. The subjects ranged from 18 to 60 years of age, with a mean age of  $38 \pm 9$  years. Of the 60 subjects, 38 were women and 22 were men. Most subjects ( $n = 44$ ) were diagnosed with relapsing-remitting MS; 13 had secondary-progressive MS; 1 had primary-progressive MS; and 2 were unspecified. Each subject was either untreated or treated with a variety of disease-modifying therapies during the observation period, including both FDA-approved (various preparations of interferon- $\beta$ ) and experimental therapies.

Details of the image acquisition and preprocessing have been previously published<sup>13</sup> and are briefly summarized in this section. Whole-brain 2D FLAIR, proton density, T2, and 3D T1-weighted volumes were acquired on a 1.5T MR imaging scanner (Signa Excite HDxt; GE Healthcare, Milwaukee, Wisconsin). The 2D FLAIR, proton density, and T2 volumes were acquired using fast-spin-echo sequences, and the 3D T1 volume was acquired using a gradient-echo sequence. All scanning parameters were clinically optimized for each acquired image. Each subject was scanned over multiple visits, and subjects' images at each visit were rigidly coregistered longitudinally and across sequences to a template space.<sup>14</sup>

All images were N4 bias-corrected, and FLAIR, T2, and proton density volumes for each subject were interpolated and rigidly coregistered to the T1 volume in isotropic 1-mm<sup>3</sup> space.<sup>15</sup> Extra-

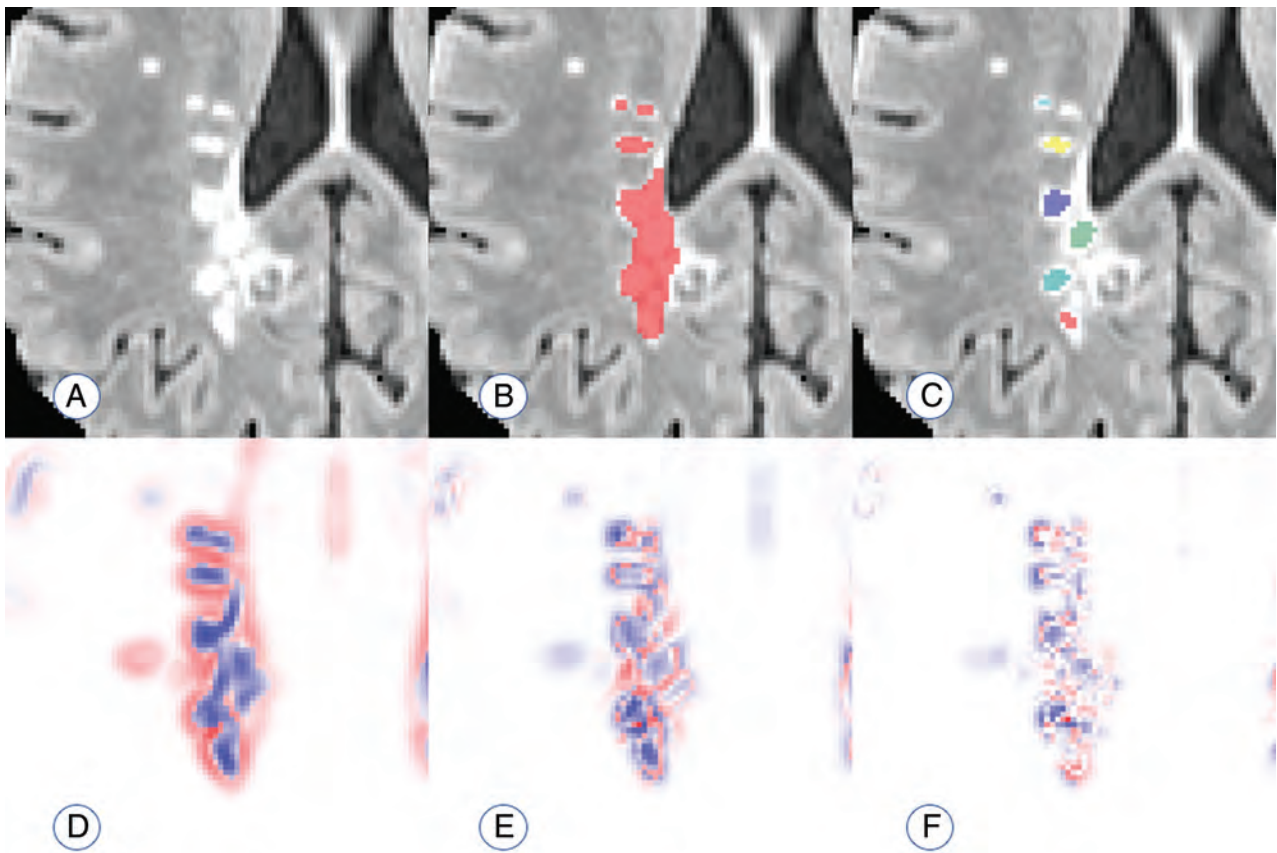


**FIG 1.** Visualization of the performance of the proposed count. *A*, An example of a region with confluent lesion tissue. *B*, Connected-components method finds 1 confluent lesion in the *highlighted region*. *C*, The proposed method finds 6 distinct lesion centers in the *highlighted region* on the visualized axial slice. *D–F*, Maps of the 3 Hessian eigenvalues used to quantify lesion texture and find distinct lesion centers (red represents positive eigenvalues; blue represents negative eigenvalues).

cerebral voxels were removed using the T1 volume via a skull-stripping procedure,<sup>16</sup> and intensity normalization<sup>17</sup> of the volumes based on *z* scoring was applied. Studies were manually quality-controlled by a researcher with >5 years' experience with structural MR imaging, and studies with analysis-limiting motion or other artifacts were removed. Following preprocessing and quality control, automatic lesion segmentation was performed on coregistered T1, T2, FLAIR, and proton density volumes using the Automated Statistical Inference for Segmentation (OASIS) model<sup>18</sup> to produce a lesion probability map for each subject. A conservative threshold of 30% was applied to the probability maps to create binary lesion masks.

**Reliability.** To test reliability, also referred to as repeatability, we analyzed data from a 45-year-old man diagnosed with clinically stable relapsing-remitting MS. This patient was imaged at 7 sites in the United States as part of a pilot study for the North American Imaging in Multiple Sclerosis (NAIMS) Cooperative. He was characterized as having mild-to-moderate physical disability, which was stable between the first and last visits, and had no clinical relapses or radiologic changes during the study.<sup>19</sup>

Details of the image acquisition have been previously published<sup>19</sup> and are briefly summarized in this section. Whole-brain 3D high-resolution FLAIR, T2, and T1-weighted volumes were acquired on 7 3T MR imaging scanners across the United States (4 Skyra, 2 Tim Trios, 1 Verio; Siemens, Erlangen, Germany). A

standardized high-resolution scanning protocol was developed through a consensus agreement in the NAIMS Cooperative and was used to the extent possible (allowing for different scanner types and software versions) for each scan. The participant was scanned twice on the same day at each site and was removed and repositioned between scan and rescan.

All images were N4 bias-corrected, and the subject's images at each scan were rigidly coregistered across sequences to the T1 volume in isotropic 1-mm<sup>3</sup> space.<sup>15</sup> Extracerebral voxels were removed using the T1 volume via a skull-stripping procedure,<sup>20</sup> and intensity normalization<sup>17</sup> of the volumes based on *z* scoring was applied. Following preprocessing, automatic lesion segmentation was performed on coregistered T1, T2, and FLAIR volumes using an extension of the OASIS model<sup>21</sup> to produce a lesion-probability map for each scan session. A conservative threshold of 30% was applied to the probability maps to create binary lesion masks.

### Statistical Analysis

**Validation.** Using the longitudinal nature of the data, we developed a criterion standard count of lesions that appeared during the study for validation. A state-of-the-art technique for segmenting new lesions since a previous visit<sup>22</sup> was applied at each visit after baseline, resulting in the number and location of new lesions at each visit for every patient. For the criterion standard count, segmented regions containing lesions separated in space or time

were considered distinct. For example, if a large contiguous region at the end of a study consisted of 1 lesion that appeared at the sixth visit and 1 lesion that appeared at the eighth visit, these would be considered 2 lesions in the criterion standard count.

The criterion standard count, henceforth referred to as  $C_G$ , was compared with 2 counts obtained cross-sectionally at the final observation for each patient. The first,  $C_p$ , is the count based on the technique proposed in this study.  $C_p$  was obtained by applying the algorithm described in the “Proposed Lesion-Count Algorithm” section to the images obtained at each patient’s final visit, then restricting the count to the number of lesion centers contained in the lesion voxels determined to have appeared during the study. Most important, this restriction means that  $C_p$  represents a subset of the total number of lesions in a subject’s scan and is distinct from the full lesion count later described in the context of the clinical-radiologic analysis. This limitation was implemented to make direct comparison between  $C_p$  and  $C_G$  possible because a criterion standard count can only be obtained for lesions that appeared during the study.

The second cross-sectional count,  $C_C$ , refers to a count based on the standard connected-components technique.  $C_C$  was obtained by performing lesion segmentation on the images obtained at each patient’s final visit, thresholding at a probability of 30%, and labeling lesions as distinct if they were separated in space.  $C_C$  was then restricted to the number of unique lesion labels contained in the lesion voxels known to have appeared during the study, to facilitate comparison with  $C_p$  and  $C_G$ .

Comparison among  $C_G$ ,  $C_C$ , and  $C_p$  occurred in 2 ways: First, to compare the linear correspondence between the criterion standard and the different counting techniques, we compared the correlation between  $C_G$  and  $C_p$  with that of  $C_G$  and  $C_C$ . Then, to determine whether the counts themselves differed meaningfully from the criterion standard, paired  $t$  tests were run for  $C_G$  and  $C_p$ , as well as  $C_G$  and  $C_C$ .

**Reliability.** Determination of the reliability of the proposed counting method was based on the coefficient of variation (CV) of the counts obtained from the 14 repeat scans. Because the typical connected-components technique for counting automatically or manually segmented lesions yields a stable-but-invalid estimate of the true count, there is no current criterion standard CV for a lesion count. Thus, the CV of the proposed count was compared with a commonly used outcome measure for MS: total cerebral lesion volume (“lesion load”).

This comparison took place in 2 contexts. The first represented a fully automated version of the proposed count, in which variation may arise from false-negatives in the segmentation mask, false-positives in the segmentation mask, thresholding of the segmentation mask, and changes in the Hessian structure of the segmentation mask. This coefficient was compared with the CV of the automated lesion load, as determined by the segmentation method.

The second context represented a manually supplemented version of the count, in which a mask of lesion tissue was provided by an expert rater<sup>19</sup> and the count was obtained using the segmentation probability map within the manual lesion tissue mask. In this case, variation in the count arises solely due to changes in the Hessian structure of the segmentation mask and changes in the

manual segmentation. This coefficient was compared with the CV of the manually obtained lesion load.

**Clinical-Radiologic Association.** Because the Expanded Disability Status Scale score is known to be noisy, a more stable measure of neurologic disability was created by averaging the EDSS scores over all visits for each subject in the National Institute of Neurological Disorders and Stroke longitudinal study,<sup>13</sup> hereby referred to as the  $EDSS_{avg}$ . One subject had no EDSS information across all follow-ups and was excluded from this analysis. Using the OASIS lesion probability maps,<sup>18</sup> we obtained the lesion load at the final visit for each subject using a probability threshold of 30%. Then, using the lesion-count technique described in the “Proposed Lesion-Count Algorithm” section, we obtained a full count of white matter lesions at the final visit for each subject. Most important, the counts obtained for the clinical-radiologic analysis are distinct from the  $C_p$  measure described in the “Validation” section because these counts represent the application of the proposed method to the entire brain, while  $C_p$  represents the application of the proposed method to only lesion tissue that appeared during the longitudinal study.

To determine the clinical relevance of the proposed lesion count independent of other potentially confounding variables, we created a linear regression model for  $EDSS_{avg}$ , with age, lesion load, and lesion count as predictors. The added statistical contribution of the lesion count was quantified using a Wald test, which is inferentially identical to a likelihood ratio test in this context, and its added clinical contribution was quantified by the increase in the adjusted  $R^2$  of the model. In this context,  $R^2$  gives the amount of variation in  $EDSS_{avg}$  explained by the model. Additionally, the Pearson correlations with  $EDSS_{avg}$  were calculated for lesion load and lesion count and a new variable we refer to as “average lesion size” (defined as lesion load divided by lesion count).

## RESULTS

### Validation

The temporally informed criterion standard count of new lesions appearing during the study,  $C_G$ , ranged from 0 to 75 among the 60 subjects, with a median of 4 (interquartile range, 1–12). The connected-components count,  $C_C$ , ranged from 0 to 14 with a median of 2 (interquartile range, 1–5). The proposed count,  $C_p$ , ranged from 0 to 60 with a median of 4 (interquartile range, 1–15). Figure 2 provides an example of these counting techniques.

The correlation between  $C_p$  and  $C_G$  was 0.97, compared with the correlation of 0.67 between  $C_C$  and  $C_G$ . Figure 3 shows the scatterplots for the 2 linear associations, along with the line demonstrating a 1-to-1 relationship. The paired  $t$  test comparing  $C_C$  and  $C_G$  yielded a highly significant result ( $t_{59} = 4.19$ ,  $P < .001$ ), with  $C_G$  being 6.9 lesions larger than  $C_C$  on average (95% CI, 3.6–10.2). The paired  $t$  test comparing  $C_p$  and  $C_G$  did not find a significant difference between the counts ( $t_{59} = -.83$ ,  $P = .41$ ), with  $C_p$  being 0.4 lesions larger than  $C_G$  on average (95% CI,  $-1.3$ –0.5).

### Reliability

For the fully automated count, the coefficient of variation was 0.19, compared with a CV of 0.22 for the automated lesion load.

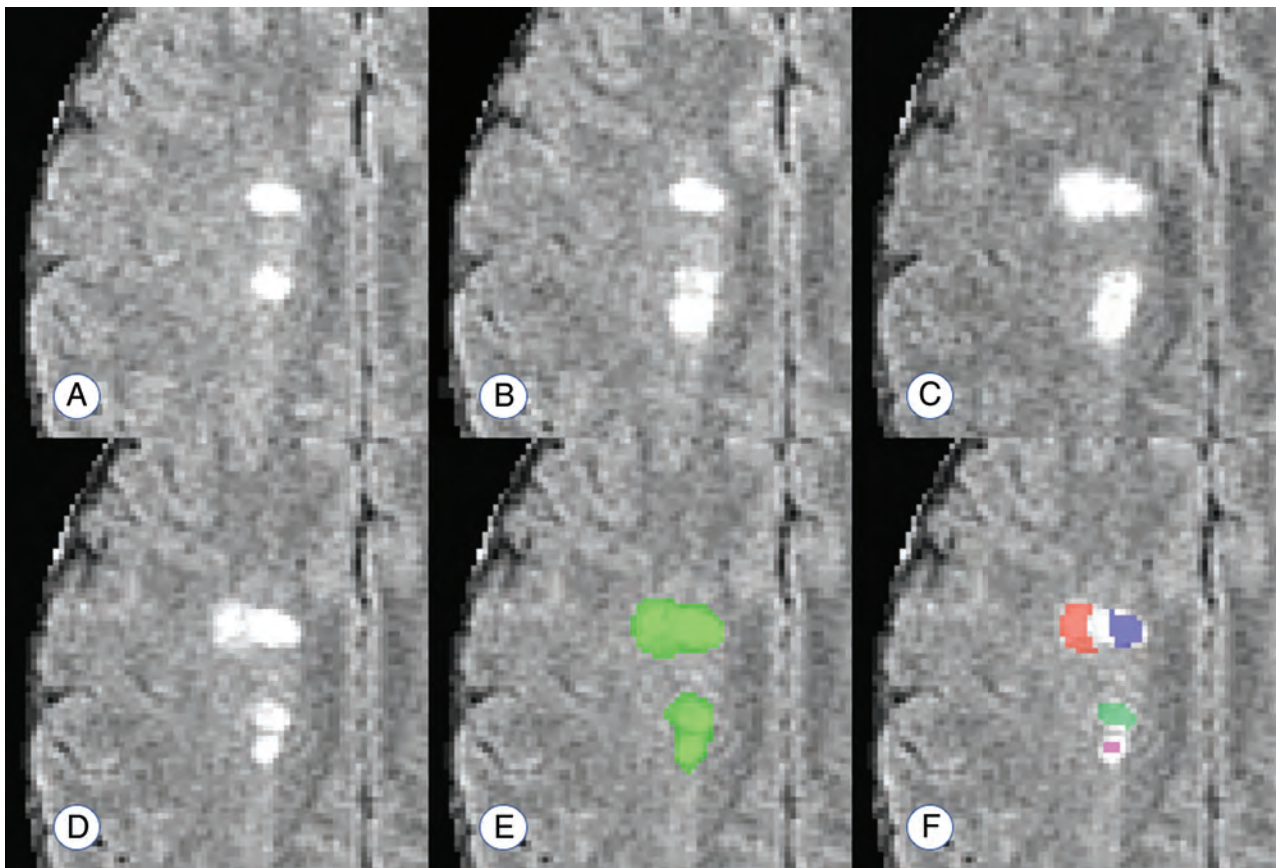


**FIG 2.** Example of the lesion counts in a region with 4 apparently distinct lesions, 2 of which develop with observable temporal separation. *A–D*, Development of 2 new and temporally distinct lesions. *E* and *F*, The performance of a connected-components count and the proposed count, respectively. The connected-components method finds 1 confluent lesion in the visualized space (connected in an adjacent plane), and the proposed method finds 4 distinct lesion centers. Days from scan in *A*: 28 days (*B*); 91 days (*C*); 252 days (*D–F*).

Using the manual segmentation as a mask, we reduced the CV for the lesion count to 0.12, compared with a CV of 0.10 for the manual lesion load. In 1 case, automated lesion segmentation was discovered to have failed; this failure created a probability map with a drastically different Hessian structure and large regions of false-positive segmentation. With this scan removed, the CV of the fully automated lesion count remained at 0.19 and the CV of the manual segmentation-based lesion count dropped to  $<0.06$ , suggesting that the proposed count has equivalent or lower variability than the current clinical standard of lesion load.

#### Clinical-Radiologic Association

If we accounted for lesion load and age, the proposed lesion count was negatively associated with  $EDSS_{avg}$  ( $t_{58} = -2.73$ ,  $P < .01$ ); this finding suggests that for a given lesion load and age, a higher count is associated with lower disease severity. The inclusion of lesion count in the model explains an additional 10% of the variance in  $EDSS_{avg}$  compared with a model with only age and lesion load, providing support to the hypothesis that the proposed count contains disease information independent of other commonly used measures.

The Pearson correlation between lesion load and  $EDSS_{avg}$  was small and did not reach significance ( $r = 0.10$ ,  $P = .44$ ); the same was true of the correlation between lesion count and  $EDSS_{avg}$  ( $r = -.12$ ,  $P = .36$ ). However, average lesion size was significantly

correlated with  $EDSS_{avg}$  ( $r = 0.35$ ,  $P < .01$ ); this correlation indicated that larger lesions were associated with higher disability.

#### DISCUSSION

In this article, we introduce a novel technique for obtaining cross-sectional counts of pathologically distinct lesions and demonstrate it to be a valid, reliable, and clinically meaningful biomarker for MS disease status. Using information contained in the Hessian structure of lesion probability maps produced by automated segmentation methods, this technique counts distinct lesions by identifying regions that resemble the physiologic traits of distinct lesion centers.

The validity of this measure was established by comparing counts obtained at a single time point with criterion standard counts that incorporated temporal information on lesion development. The proposed count had a correlation of 0.97 with the criterion standard count, indicating the very strong validity of this measure. A count obtained using the connected-components method had only a 0.67 correlation with the criterion standard and appeared to strongly underestimate the number of lesions in individuals who developed  $>1$  or 2 lesions per year during the study. This underestimation manifested in a highly significant difference between the connected-components counts and the criterion standard counts in a paired  $t$  test, whereas no difference was found between the

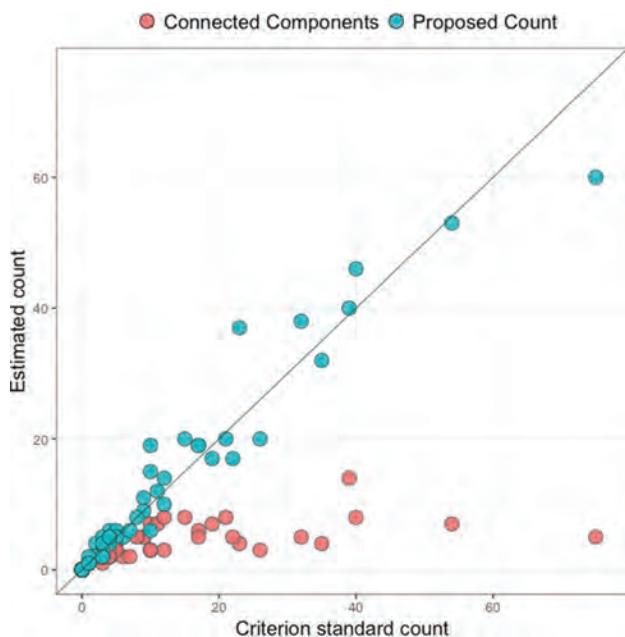


**FIG 3.** Scatterplot for the comparison between the criterion standard count and the connected-components count and the comparison between the criterion standard count and the proposed count. The *diagonal line* represents a 1-to-1 relationship, *red points* represent the connected-components count, and *blue points* represent the proposed count.

proposed counts and the criterion standard counts. These findings demonstrate that the proposed technique yields a count consistent with the natural history of lesion formation.

Reliability was considered using a rich set of data from the NAIMS Cooperative.<sup>19,23</sup> In the NAIMS pilot study,<sup>24</sup> a clinically and radiologically stable subject was scanned 2 times at each of 7 different sites across the United States. The lesion count was obtained for all 14 scans of this subject, and the coefficient of variation of the counts was compared with that of lesion load in 2 contexts, to judge the reliability of the proposed measure. In the fully automated comparison, lesion count had a slightly lower CV than lesion load. This finding indicates that across repeat scans of the same brain, automated lesion count is a less variable measure than automated lesion load. In the manually supplemented comparison, lesion count had a slightly higher CV than lesion load, implying that manually obtained lesion load is a slightly less variable measure than semiautomated lesion count. On inspection, there appeared to be 1 scan in which automated lesion segmentation failed, producing an abnormal Hessian structure within the manually segmented lesion mask. With this scan removed, the CV of the semiautomated lesion count dropped to slightly more than half that of the manual lesion load. This result suggests that when automated lesion-segmentation methods perform as expected, the semiautomated lesion count is appreciably more reliable than the manual lesion load, a widely used measure of disease severity.

Clinically, the lesion-count measure appears to be a potentially important addition to commonly used radiologic biomarkers for MS. In a model accounting for lesion load and age, lesion count was highly significantly associated with EDSS. Most interesting, this association was negative, indicating that for subjects

who have similar lesion loads, better outcomes are associated with more (and smaller) lesions rather than fewer (and larger) lesions. This finding lends support to the idea that neither the number of lesions nor the amount of tissue damage alone captures all relevant clinical information and instead suggests that they should be considered together. One way to conceptualize the combination of these metrics is average lesion size, which taps into the degree to which the brain can halt the growth of lesions and encourage lesional recovery<sup>13,25,26</sup> after incidence.

To investigate this concept more directly, we created a measure of average lesion size by dividing lesion load by lesion count. Pearson correlations with EDSS were then compared for the 3 biomarkers: lesion load, lesion count, and average lesion size. These findings provided further support for the combined importance of lesion load and lesion count, with both showing small and nonsignificant associations with EDSS. However, average lesion size showed a significant positive association with EDSS, consistent with the notion that the ability of the brain to slow or stop lesion growth is clinically relevant. These findings point to the importance of considering lesion count in MS research and provide further evidence of the validity of the proposed counting technique.

A limitation of the current study is the possibility of alternate explanations of confluence that are not accounted for in the design of the proposed count. It has been hypothesized that confluent lesions may occasionally occur as a result of the growth of older lesions or the expansion of pathologic processes. Future research should consider the degree to which this technique does or does not characterize these types of confluence as pathologically distinct lesions. Additionally, the current analyses do not account for the possibility of vascular comorbidity, which is a common and notable occurrence in patients with MS. Future work should investigate the performance of this algorithm in the presence of vascular lesions.

The lesion-count method presented in this article has several appealing features, including its low computational burden and its easy and flexible implementation. Computationally, the counting algorithm takes less than a minute to run once probability maps are obtained. The speed of the full technique varies depending on the lesion-segmentation method used but took approximately 25 minutes per subject as presented in this study. In terms of implementation, this method can be quickly and easily coded in any program capable of calculating the Hessian structure of a 3D image, a feature included in most image-processing packages. It can also be used with any lesion-segmentation method that yields a probability map; thus, it may be added to almost any pipeline regardless of the preferred segmentation algorithm.

## CONCLUSIONS

This article introduces a novel and reliable fully automated method for counting pathologically distinct lesions using images obtained at a single time point, allowing an accurate reconstruction of the natural history of lesion formation without longitudinal data. Lesion count was found to be significantly associated with EDSS, independent of potential confounders such as lesion load and age, and the results suggest that individuals with more

small lesions may have better clinical outcomes than those with fewer large lesions. This study also demonstrates the importance of obtaining both lesion count and lesion load by using them to construct a new MS biomarker, average lesion size, and showing that average lesion size has a significantly larger association with EDSS than both lesion load and lesion count. With further study, this technique and the findings it produces could set the stage for new lesion-level considerations in research and treatment of MS.

## ACKNOWLEDGMENTS

The authors would like to thank Blake Dewey, the Neuroimmunology Branch clinical group, and the technicians at the National Institutes of Health who were instrumental in helping to collect and process the validation and clinical-radiologic data. Additionally, the following is a full list of individuals who contributed to the collection and processing of the NAIMS data used in the reliability analysis described in this article: Brigham and Women's Hospital, Harvard Medical School (Boston, Massachusetts): Rohit Bakshi, Renxin Chu, Gloria Kim, Shahamat Tauhid, Subhash Tummala, Fawad Yousuf; Cedars-Sinai Medical Center (Los Angeles, California): Nancy L. Sicotte, Henry M. Jackson; Foundation for the Advancement of Military Medicine (Bethesda, Maryland): Dzung Pham, Snehashis Roy; National Institutes of Health (Bethesda, Maryland): Frances Andrada, Irene C.M. Cortese, Jennifer Dwyer, Rosalind Hayden, Haneefa Muhammad, Govind Nair, Joan Ohayon, Daniel S. Reich, Pascal Sati, Chevaz Thomas; Johns Hopkins (Baltimore, Maryland): Peter A. Calabresi, Sandra Cassard, Jiwon Oh; Oregon Health & Science University (Portland, Oregon): William Rooney, Daniel Schwartz, Ian Tagge; University of California (San Francisco, California): Roland G. Henry, Nico Papinutto, William Stern, Alyssa Zhu; University of Pennsylvania (Philadelphia, Pennsylvania): Christos Davatzikos, Jimit Doshi, Guray Erus, Kristin Linn, Russell Shinohara; University of Toronto (Toronto, Ontario, Canada): Jiwon Oh; Yale University (New Haven, Connecticut): R. Todd Constable, Daniel Pelletier.

Disclosures: Jordan D. Dworkin—RELATED: Grant: National Institutes of Health.\* Kristin A. Linn—UNRELATED: Payment for Development of Educational Presentations: Institute of Electrical and Electronics Engineers. Ipek Oguz—RELATED: Grant: National Institutes of Health.\* Rohit Bakshi—UNRELATED: Consultancy: EMD Serono, Genentech, Sanofi Genzyme, Novartis; Grants/Grants Pending: Biogen, EMD Serono, Novartis, Sanofi Genzyme.\* Peter A. Calabresi—UNRELATED: Consultancy: Biogen, Disarm Therapeutics; Grants/Grants Pending: Genzyme, Annexon Bio, MedImmune\*; Royalties: Cambridge Press, Comments: book on optical coherence tomography. Roland G. Henry—UNRELATED: Consultancy: Roche, MedDay; Grants/Grants Pending: Roche, Genentech, MedDay\*; Payment for Lectures Including Service on Speakers Bureaus: Sanofi-Genzyme. Daniel Pelletier—UNRELATED: Consultancy: Genzyme Sanofi, Biogen, Novartis, Actelion, Genentech. William Rooney—UNRELATED: Employment: Oregon Health & Science University; Grants/Grants Pending: National Institutes of Health\*; Payment for Lectures Including Service on Speakers Bureaus: Teva Pharmaceutical Industries; Patents (Planned, Pending or Issued): Pending: US 20150141804 A1, US 20150087967 A1; Issued: US 7286867 B2, US 9619875 B2.\* Nancy L. Sicotte—RELATED: Grant: Race to Erase MS.\* Russell T. Shinohara—RELATED: Grant: National Institutes of Health\*; UNRELATED: Board Membership: Genentech, Comments: Scientific Advisory Board member; Expert testimony: Roche, Comments: legal consulting; Payment for Lectures Including Service on Speakers Bureaus: National Institutes of Health, National Multiple Sclerosis Society.\* \*Money paid to the institution.

## REFERENCES

- Radü EW, Sahraian MA, eds. *MRI Atlas of MS Lesions*. Berlin: Springer-Verlag; 2008
- Barkhof F. **The clinico-radiological paradox in multiple sclerosis revisited**. *Curr Opin Neurol* 2002;15:239–45 CrossRef Medline
- Popescu V, Agosta F, Hulst HE, et al; MAGNIMS Study Group. **Brain atrophy and lesion load predict long term disability in multiple sclerosis**. *J Neurol Neurosurg Psychiatry* 2013;84:1082–91 CrossRef Medline
- Calabresi PA, Radue EW, Goodin D, et al. **Safety and efficacy of fingolimod in patients with relapsing-remitting multiple sclerosis (FREEDOMS II): a double-blind, randomised, placebo-controlled, phase 3 trial**. *Lancet Neurol* 2014;13:545–56 CrossRef Medline
- Thompson AJ, Kermode AG, MacManus DG, et al. **Patterns of disease activity in multiple sclerosis: clinical and magnetic resonance imaging study**. *BMJ*. 1990;300:631–34 CrossRef Medline
- Brex PA, Ciccarelli O, O'Riordan JI, et al. **A longitudinal study of abnormalities on MRI and disability from multiple sclerosis**. *N Engl J Med* 2002;346:158–64 CrossRef Medline
- Khoury SJ, Guttman CR, Orav EJ, et al. **Longitudinal MRI in multiple sclerosis: correlation between disability and lesion burden**. *Neurology* 1994;44:2120–24 CrossRef Medline
- Rudick RA, Lee JC, Simon J, et al. **Significance of T2 lesions in multiple sclerosis: a 13-year longitudinal study**. *Ann Neurol* 2006;60:236–42 CrossRef Medline
- Zivadinov R, Zorzon M, De Masi R, et al. **Effect of intravenous methylprednisolone on the number, size and confluence of plaques in relapsing-remitting multiple sclerosis**. *J Neurol Sci* 2008;267:28–35 CrossRef Medline
- Harris JO, Frank JA, Patronas N, et al. **Serial gadolinium-enhanced magnetic resonance imaging scans in patients with early, relapsing-remitting multiple sclerosis: implications for clinical trials and natural history**. *Ann Neurol* 1991;29:548–55 CrossRef Medline
- Guttman CR, Rousset M, Roch JA, et al. **Multiple sclerosis lesion formation and early evolution revisited: a weekly high-resolution magnetic resonance imaging study**. *Mult Scler J* 2016;22:761–69 CrossRef Medline
- Gaitán MI, Shea CD, Evangelou IE, et al. **Evolution of the blood-brain barrier in newly forming multiple sclerosis lesions**. *Ann Neurol* 2011;70:22–29 CrossRef Medline
- Sweeney EM, Shinohara RT, Dewey BE, et al. **Relating multi-sequence longitudinal intensity profiles and clinical covariates in incident multiple sclerosis lesions**. *Neuroimage Clin* 2016;10:1–17 CrossRef Medline
- Fonov V, Evans AC, Botteron K, et al; Brain Development Cooperative Group. **Unbiased average age-appropriate atlases for pediatric studies**. *Neuroimage* 2011;54:313–27 CrossRef Medline
- Avants B, Tustison N, Song G, et al. *ANTS: Advanced Open-Source Normalization Tools for Neuroanatomy*. Philadelphia: Penn Image Computing and Science Laboratory; 2009
- Carass A, Wheeler MB, Cuzzocreo J, et al. **A joint registration and segmentation approach to skull stripping**. In: *Proceedings of the 4th IEEE International Symposium on Biomedical Imaging: From Nano to Macro*, Arlington, Virginia. April 12–15, 2007:656–59. [http://ieeexplore.ieee.org/xpls/abs\\_all.jsp?arnumber=4193371](http://ieeexplore.ieee.org/xpls/abs_all.jsp?arnumber=4193371). Accessed April 1, 2016
- Shinohara RT, Sweeney EM, Goldsmith J, et al; Australian Imaging Biomarkers Lifestyle Flagship Study of Ageing, Alzheimer's Disease Neuroimaging Initiative. **Statistical normalization techniques for magnetic resonance imaging**. *Neuroimage Clin* 2014;6:9–19 CrossRef Medline
- Sweeney EM, Shinohara RT, Shiee N, et al. **OASIS is Automated Statistical Inference for Segmentation, with applications to multiple sclerosis lesion segmentation in MRI**. *Neuroimage Clin* 2013;2:402–13 CrossRef Medline
- Shinohara RT, Oh J, Nair G, et al; NAIMS Cooperative. **Volumetric analysis from a harmonized multisite brain MRI study of a single subject with multiple sclerosis**. *AJNR Am J Neuroradiol* 2017;38:1501–09 CrossRef Medline
- Jenkinson M, Pechaud M, Smith S. **BET2: MR-based estimation of brain, skull and scalp surfaces**. Oxford: Oxford Centre for

Functional Magnetic Resonance Imaging of the Brain (fMRIB); 2005. <http://mickaelpechaud.free.fr/these/HBM05.pdf>. Accessed June 13, 2016

21. Valcarcel AN, Linn KA, Vandekar SN, et al. MIMoSA: a method for inter-modal segmentation analysis. June 15, 2017. bioRxiv 150284 CrossRef
22. Sweeney EM, Shinohara RT, Shea CD, et al. **Automatic lesion incidence estimation and detection in multiple sclerosis using multi-sequence longitudinal MRI.** *AJNR Am J Neuroradiol* 2013;34:68–73 CrossRef Medline
23. Papinutto N, Bakshi R, Bischof A, et al; North American Imaging in Multiple Sclerosis Cooperative (NAIMS). **Gradient nonlinearity effects on upper cervical spinal cord area measurement from 3D T1-weighted brain MRI acquisitions.** *Magn Reson Med* 2018;79:1595–601 CrossRef Medline
24. Oh J, Bakshi R, Calabresi PA; NAIMS Cooperative Steering Committee. **The NAIMS cooperative pilot project: Design, implementation and future directions.** *Mult Scler* 2017 Oct 1. [Epub ahead of print] CrossRef Medline
25. Meier DS, Guttman CR. **Time-series analysis of MRI intensity patterns in multiple sclerosis.** *Neuroimage* 2003;20:1193–209 CrossRef Medline
26. Meier DS, Guttman CR. **MRI time series modeling of MS lesion development.** *Neuroimage* 2006;32:531–37 CrossRef Medline

# Evaluation of the Sensitivity of Inhomogeneous Magnetization Transfer (ihMT) MRI for Multiple Sclerosis

E. Van Obberghen, S. Mchinda, A. le Troter, V.H. Prevost, P. Viout, M. Guye, G. Varma, D.C. Alsop, J.-P. Ranjeva, J. Pelletier, O. Girard, and G. Duhamel



## ABSTRACT

**BACKGROUND AND PURPOSE:** Inhomogeneous magnetization transfer is a new endogenous MR imaging contrast mechanism that has demonstrated high specificity for myelin. Here, we tested the hypothesis that inhomogeneous magnetization transfer is sensitive to pathology in a population of patients with relapsing-remitting MS in a way that both differs from and complements conventional magnetization transfer.

**MATERIALS AND METHODS:** Twenty-five patients with relapsing-remitting MS and 20 healthy volunteers were enrolled in a prospective MR imaging research study, whose protocol included anatomic imaging, standard magnetization transfer, and inhomogeneous magnetization transfer imaging. Magnetization transfer and inhomogeneous magnetization transfer ratios measured in normal-appearing brain tissue and in MS lesions of patients were compared with values measured in control subjects. The potential association of inhomogeneous magnetization transfer ratio variations with the clinical scores (Expanded Disability Status Scale) of patients was further evaluated.

**RESULTS:** The magnetization transfer ratio and inhomogeneous magnetization transfer ratio measured in the thalami and frontal, occipital, and temporal WM of patients with MS were lower compared with those of controls ( $P < .05$ ). The mean inhomogeneous magnetization transfer ratio measured in lesions was lower than that in normal-appearing WM ( $P < .05$ ). Significant ( $P < .05$ ) negative correlations were found between the clinical scores and inhomogeneous magnetization transfer ratio measured in normal-appearing WM structures. Weaker nonsignificant correlation trends were found for the magnetization transfer ratio.

**CONCLUSIONS:** The sensitivity of the inhomogeneous magnetization transfer technique for MS was highlighted by the reduction in the inhomogeneous magnetization transfer ratio in MS lesions and in normal-appearing WM of patients compared with controls. Stronger correlations with the Expanded Disability Status Scale score were obtained with the inhomogeneous magnetization transfer ratio compared with the standard magnetization transfer ratio, which may be explained by the higher specificity of inhomogeneous magnetization transfer for myelin.

**ABBREVIATIONS:** CC = corpus callosum; EDSS = Expanded Disability Status Scale; FWM = frontal WM; IC = internal capsule; ihMT = inhomogeneous magnetization transfer; ihMTR = inhomogeneous magnetization transfer ratio; MT = magnetization transfer; MTR = magnetization transfer ratio; OCCWM = occipital WM; RRMS = relapsing-remitting MS; TEMPWM = temporal WM

Multiple sclerosis is a chronic inflammatory, demyelinating autoimmune disease of the central nervous system. Whereas edema, inflammation, and axonal loss are part of the

pathologic processes of MS, demyelination stands out as a major contributor to its pathogenesis. Hence, obtaining a precise in vivo assessment of myelin content is urgently needed, especially considering the recent advances in our understanding of the molecular and cellular mechanisms regulating de- and re-myelination and the emergence of new therapies to promote re-myelination. The ability of MR imaging to produce contrasts sensitive to different tissues, combined with its noninvasiveness, has propelled it to a technique of choice for in vivo imaging. Direct imaging of

Received October 4, 2017; accepted after revision December 22.

From Aix-Marseille Université (E.V.O., S.M., A.I.T., V.H.P., P.V., M.G., J.-P.R., J.P., O.G., G.D.), Centre de Résonance Magnétique Biologique et Médicale (CRMBM), UMR 7339 Centre National de Recherche Scientifique (CNRS), Marseille, France; Department of Radiology (G.V., D.C.A.), Division of MR Research, Beth Israel Deaconess Medical Center, Harvard Medical School, Boston, Massachusetts; and Aix-Marseille University (J.P.), Assistance Publique des Hôpitaux de Marseille (APHM), Hôpital de La Timone, Pôle de Neurosciences Cliniques, Service de Neurologie, Marseille, France.

V.H.P. received support from A\*MIDEX ANR (Agence Nationale de la Recherche, n° ANR11-IDEX-0001-02), the Investissements d'Avenir program of the French Government. S.M. received support from l'Association pour la recherche sur la sclérose en plaques (ARSEP), 2015 and l'institut pour la recherche sur la moelle épinière et l'encéphale (IRME), 2016.

Please address correspondence to Guillaume Duhamel, PhD, Aix-Marseille Université, Centre de Résonance Magnétique Biologique et Médicale, CRMBM-CEMEREM, UMR 7339 CNRS, Faculté de Médecine, 27 Boulevard Jean Moulin, 13005 Marseille, France; e-mail: guillaume.duhamel@univ-amu.fr

Indicates open access to non-subscribers at [www.ajnr.org](http://www.ajnr.org)

<http://dx.doi.org/10.3174/ajnr.A5563>

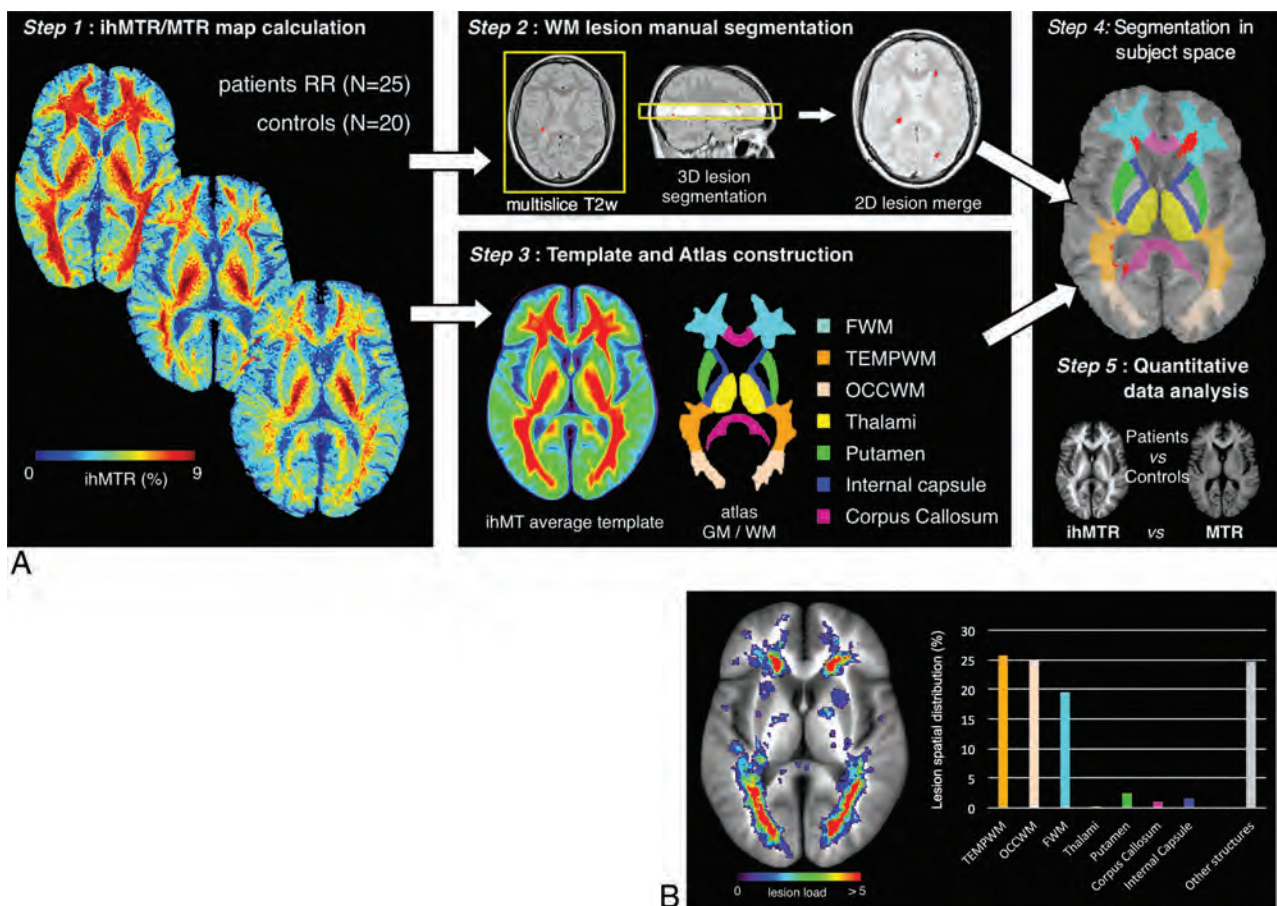


**FIG 1.** A, Postprocessing pipeline. Step 1: Quantitative MTR and ihMTR map calculation for controls and patients with RRMS. Step 2: Manual segmentation of WM lesions on the multislice  $T_{2w}$  images and reslicing to the single-slice 2D ihMT reference space. Step 3: Construction of the ihMT average template by realignment of the ihMT images of the control and RRMS subjects into a new common reference space. Construction of the ihMT atlas was based on the ihMT average template by manual segmentation of frontal, temporal, and occipital WM, internal capsule, corpus callosum, thalami, and putamen. Step 4: Automatic segmentation of individual ihMT images by projection of the ihMT atlas onto the individual native space of each control and patient. Individual lesion masks obtained in step 2 were removed from the ihMT atlas to generate normal-appearing tissue ROIs. Step 5: Quantitative measurement of ihMTR and MTR in the ROIs and lesions. B, Lesion-load map calculated over all the patients with RRMS and superimposed over the ihMT average template. The histogram shows the percentage of lesions within each brain structure.

myelin is, however, challenged by the MR imaging properties of the nonaqueous protons in the phospholipid bilayers that make up myelin. They produce a broad resonance spectrum spanning several kilohertz and leading to transverse relaxation times on the order of a few tens of microseconds, which correspond to a signal decay too fast to be detected directly. Advanced MR imaging techniques such as diffusion tensor imaging, myelin water fraction,<sup>1</sup> and magnetization transfer (MT)<sup>2,3</sup> have thus been developed and their associated metrics have been shown to correlate, to some extent, with myelin content, thus providing an indirect assessment of myelin-related information.

The MT technique has been particularly used in clinical MS research studies, and its sensitivity for the pathology has been widely demonstrated.<sup>4-7</sup> However, the MT signal is not specific to myelin, and other mechanisms involved in this complex disease (eg, inflammation, axonal loss) also contribute to the changes in MT metrics, thus preventing a complete understanding of myelin damage and repair in MS. The development of myelin-specific MR imaging techniques remains thus an active and highly focused area of research in which novel approaches are being sought. One promising example is the recently described inhomogeneous

magnetization transfer (ihMT) technique,<sup>8</sup> which can be envisioned as a method to image, *in vivo*, the dipolar order (characterized by a dipolar relaxation time constant) underlying broad tissue macromolecular lines.<sup>9-11</sup> The long dipolar relaxation time values associated with myelinated structures compared with others<sup>12,13</sup> allow the ihMT technique to more selectively isolate the contribution of the myelin dipolar order within the broad MT signal, thereby providing higher specificity for myelinated structures.<sup>14</sup> Studies performed on control subjects have shown exquisite contrast for CNS myelin-containing tissues,<sup>15,16</sup> but the value of ihMT in clinical applications has yet to be demonstrated.

The current study aimed to provide preliminary evidence for the utility of ihMT in multiple sclerosis. We hypothesized that due to its strong specificity for myelin, ihMT should be sensitive to MS pathology and provide complementary information relative to the non-myelin-specific standard MT technique.

## MATERIALS AND METHODS

### Subjects

All subjects provided informed consent to participate in this prospective research study, which received the approval of the local

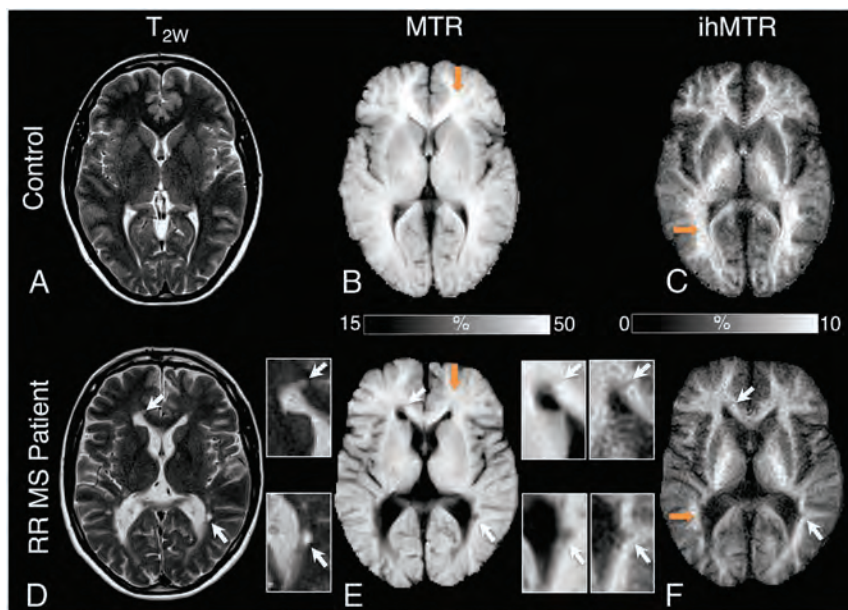


**FIG 2.** Representative anatomic  $T_{2w}$  images (A and D) and MTR (B and E) and ihMTR (C and F) maps obtained on a control subject and a patient with RRMS after step 1 of the postprocessing procedure. Decrease of MTR and ihMTR signals is clear in patients (E and F) relative to controls (B and C) in the FWM and OCCWM (orange arrows). Brain areas encompassing lesions (white arrows) are shown in inserts for each technique.  $T_{2w}$  hyperintensities and MTR/ihMTR hypointensities are clearly visible in lesions.

research ethics committee (CPP Sud Méditerranée 1). Twenty-five patients with relapsing-remitting MS (RRMS) (20:5 women/men; mean age, 42/41 years; age range, 28–53 years; mean disease duration, 11/9 years; disease duration range, 1–22 years; 10 patients under disease-modifying treatment at the time of MR examinations; 9 patients with acute relapses at the time of MR imaging examinations) and 20 matched healthy volunteers (14:6 women/men; mean age, 42/39 years; age range, 28–57 years) were enrolled in this 1-year study. The exclusion criteria were alcohol or other drug abuse, history of psychiatric diseases, or any neurologic diseases other than MS. All patients underwent a standard neurologic examination by certified neurologists, and disability was assessed by the Kurtzke Expanded Disability Status Scale (EDSS)<sup>17</sup> (mean group EDSS, 1.7; EDSS range, 0–6.5).

### MR Imaging Acquisition

MR imaging examinations were performed on a 1.5T MR imaging system (Avanto; Siemens, Erlangen, Germany). The protocol included a 3D-FLAIR sequence (TR/TE/TI = 6000/333/2200 ms, FOV = 256 × 256 × 176 mm<sup>3</sup>, matrix = 256 × 256 × 176, isotropic spatial resolution = 1 mm<sup>3</sup>); a  $T_{2w}$  multi-TE sequence (TR = 2600 ms, TEs = 14/85 ms, 44 contiguous axial slices [3-mm thick] parallel to the anterior/posterior commissure line, FOV = 256 × 256 mm<sup>2</sup>, matrix = 256 × 256, spatial resolution = 1.0 × 1.0 × 3.0 mm<sup>3</sup>); and an axial 2D-pulsed-ihMT HASTE sequence<sup>15</sup> (circular polarized mode, TR/TE = 3000/21 ms, 789-Hz/pixel readout bandwidth, echo spacing = 3.52 ms, 120° spin-echo refocusing angle for limitation of the radiofrequency specific absorption rate, FOV = 256 × 256 mm<sup>2</sup>, matrix = 256 × 256, single slice of 9-mm thick, spatial resolution = 1.0 × 1.0 × 9.0 mm<sup>3</sup>). The slice was common to all subjects and chosen parallel to the anterior/posterior commissure line, midventricle to intercept the thalami. The ihMT preparation used the fol-

lowing parameters, optimized for brain studies at 1.5T<sup>15</sup>: frequency-offset,  $|\Delta f| = 7$  kHz; pulse width/interpulse delay, PW/ $\Delta t = 0.5/1$  ms; duration of saturation,  $\tau = 700$  ms; intensity of saturation over the whole presaturation phase,  $B_{1,RMS} = 7.0$   $\mu$ T. The 4 MT-prepared images required to generate the ihMT contrast (Equation 1) were averaged 20 times (20 NEX) corresponding to 4 minutes 15 seconds of acquisition time.

### Postprocessing

The entire postprocessing procedure is summarized in Fig 1:

Step 1: Quantitative magnetization transfer ratio (MTR) and inhomogeneous magnetization transfer ratio (ihMTR) map calculation. Magnitude MT-weighted images derived from the ihMT sequence were processed using Matlab (Version R2012; MathWorks, Natick, Massachusetts) custom routines to generate, for all subjects (controls and patients), the composite ihMT images and the quantitative ihMT and MT ratios as

defined by Girard et al<sup>15</sup> and Prevost et al<sup>18</sup>:

$$1) \quad \text{ihMT} = (\text{MT}^+ + \text{MT}^- - \text{MT}^{+-} - \text{MT}^{-+}),$$

$$\text{ihMTR} = \text{ihMT}/S_0,$$

$$\text{MTR} = 1 - \text{MT}^+/S_0.$$

( $\text{MT}^+$ ,  $\text{MT}^-$ ) and ( $\text{MT}^{+-}$ ,  $\text{MT}^{-+}$ ) correspond to MT-weighted images obtained with radiofrequency saturation at a single frequency offset ( $+\Delta f$  or  $-\Delta f$ , Fig 2A of Girard et al<sup>15</sup>) and dual frequency offset ( $\pm\Delta f$ , Fig 2B of Girard et al<sup>15</sup>), respectively.  $S_0$  is the signal measured with the radiofrequency saturation power set to zero.

Step 2: Manual segmentation of WM lesions in the ihMT space. Following a procedure commonly used in clinical trials, segmentation of MS lesions (characterized by T2-hyperintensities) was performed on  $T_{2w}$  images. For each patient, MS lesions were manually delineated on the 3-mm-thick  $T_{2w}$  images contained within the single 9-mm-thick ihMT image, using FSLView 3.2.0 (<http://www.fmrib.ox.ac.uk/fsl/fslview>). Note that FLAIR images were used as a secondary reference to improve the accuracy of the lesion location. The resulting 3D mask of lesions was resliced in the single-slice ihMT reference space, and voxels were considered lesions if at least 1 voxel was labeled as a lesion in the  $T_{2w}$  images.

Step 3: ihMT template and atlas construction. ihMT images of all control subjects and patients were realigned into a new common reference space by a 2D nonlinear registration using a symmetric group-wise normalization procedure<sup>19,20</sup> and further averaged to create a specific ihMT average template. Note that combining images of both patients and controls allowed optimization of the group-wise registration procedure by minimization

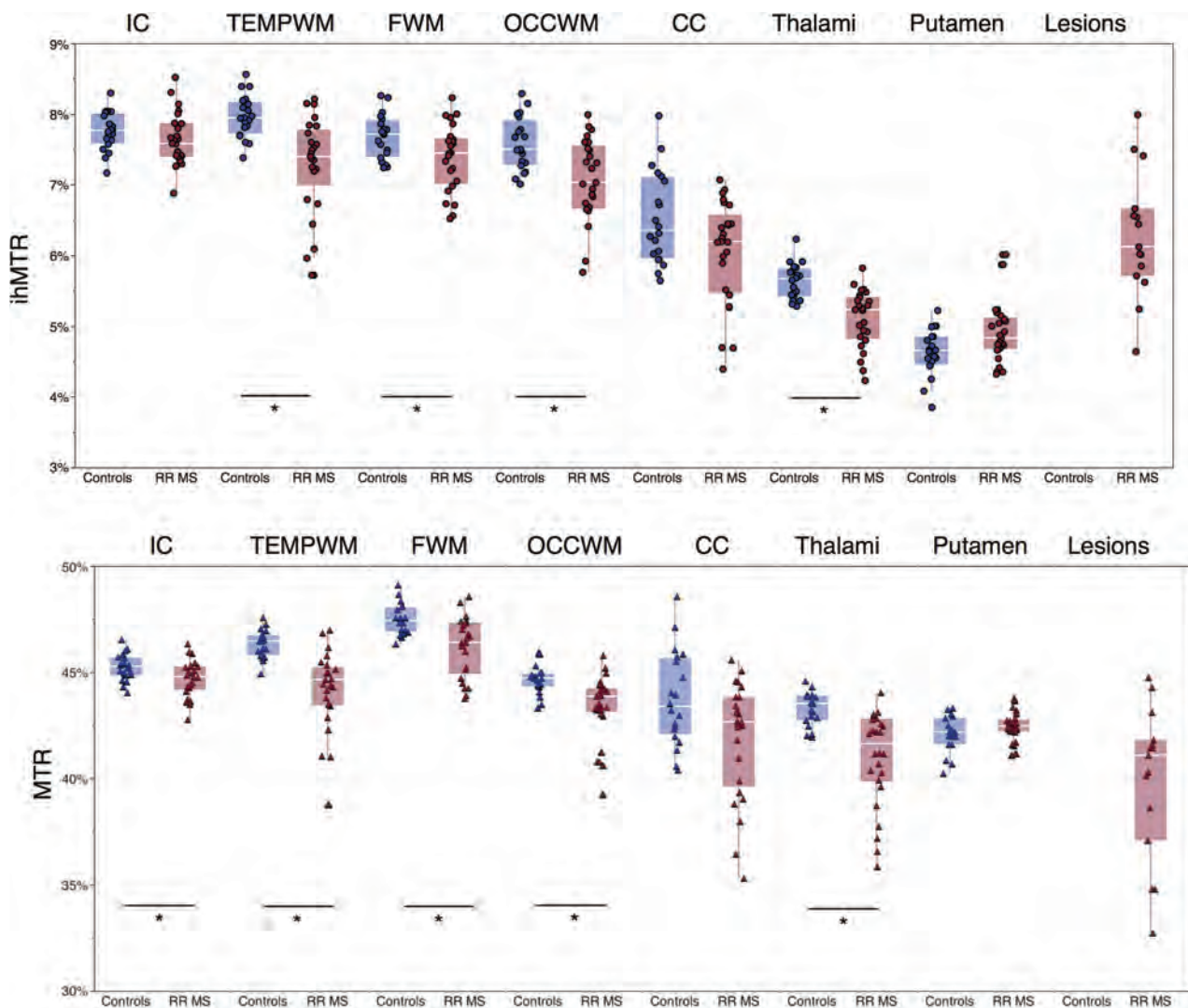


**FIG 3.** Mean MTR and ihMTR values measured in the 7 ROIs of the ihMT atlas (TEMPWM, FWM, OCCWM, CC, thalami, and putamen) for each control (blue markers) and patient with RRMS (pink markers). For patients, mean values measured in lesions are also reported. Boxplots indicate the median, upper and lower quartiles, and the minimum and maximum values excluding outliers. The asterisk indicates a significant difference ( $P < .05$ ) in values between controls and patients (comparison assessed by the nonparametric Wilcoxon rank test [ $\alpha = .05$ ] corrected by the Holm-Bonferroni method for multiple comparisons [ $m = 7$  brain structures]).

of image deformations from all individual subjects, especially the patients, to the common average template. Seven brain structures, including frontal, temporal, and occipital WM (FWM, TEMPWM, OCCWM), internal capsule (IC), corpus callosum (CC), thalami, and putamen were manually segmented on the ihMT average template by experienced clinical researchers (E.V.O. and J.P., with more than 10 years of experience in brain anatomy) using FSLView 3.2.0, to create a single 2D ihMT atlas. Note that partial volume effects induced by the large slice thickness of the ihMT images prevented accurate measurement in other finer brain structures.

**Step 4: Segmentation in subject space.** The ihMT atlas was automatically transformed into the individual native space of each subject (controls and patients) using inverse deformation fields estimated by the nonlinear process described in step 3. For each patient, the lesion mask derived in step 2 was removed from the ihMT atlas to generate normal-appearing tissue ROIs and enable calculation of normal-appearing tissue metrics.

**Step 5: Quantitative data analysis.** Mean ihMTR and MTR values were calculated in the 7 ROIs and in lesions.

### Statistics

All statistical analyses were performed using JMP software (Version 9.0.1; SAS Institute, Cary, North Carolina). Three analyses were performed to identify diffuse and focal microstructural damage in patients with MS using ihMT and MT:

1) ihMTR and MTR values extracted from the 7 ROIs were compared between patients and controls using a nonparametric Wilcoxon rank test ( $\alpha = .05$ ) corrected for multiple comparisons ( $m = 7$  ROIs) by the Holm-Bonferroni procedure.

2) ihMTR and MTR values measured in MS lesions were compared with values measured in the 7 normal-appearing tissue ROIs across all patients using a Kruskal-Wallis test corrected for multiple comparisons using the Steel-Dwass procedure.<sup>21</sup>

3) Computation and comparison of  $z$  scores (a measure of how many SDs below or above the population mean a raw

data value is) were used to assess the sensitivity of ihMT and MT to microstructural damage. The ihMTR and MTR z scores of patients with RRMS relative to control subjects were calculated for each of the 7 ROIs according to the following equation:

$$Z \text{ Score}(X)_{ROI}^{\text{patient},i} = \left( \frac{X_{ROI}^{\text{patient},i} - \mu^{\text{controls}}}{\sigma^{\text{controls}}} \right)_{ROI}$$

where  $X$  represents the value of ihMTR or MTR,  $\mu^{\text{controls}}$  and  $\sigma^{\text{controls}}$  represent the control group mean and SD of  $X$  values. Mean ihMTR and MTR z scores calculated over the patients with RRMS were compared using a nonparametric Wilcoxon rank test ( $\alpha = .05$ ).

Finally, the potential of ihMT to provide complementary information relative to standard MT was evaluated by the analysis of correlations between MTR and ihMTR values measured in the normal-appearing tissue ROIs with the EDSS clinical scores of patients with RRMS, using a statistical nonparametric Spearman rank test ( $\alpha = .05$ ) corrected for multiple comparison ( $m = 6$  ROIs) by the Holm-Bonferroni procedure.

**Mean ihMTR and MTR values calculated in the 7 ROIs of the ihMT atlas and in lesions<sup>a</sup>**

Brain Structure	ihMTR (%)		MTR (%)	
	Controls	Patients	Controls	Patients
IC	7.8 ± 0.3 <i>P</i> = .16	7.6 ± 0.4	45.2 ± 0.6 <i>P</i> = .02 <sup>b</sup>	44.7 ± 0.8
TEMPWM	8.0 ± 0.3 <i>P</i> < .001 <sup>b</sup>	7.3 ± 0.7	46.3 ± 0.6 <i>P</i> < .001 <sup>b</sup>	44.2 ± 1.9
FWM	7.7 ± 0.3 <i>P</i> = .01 <sup>b</sup>	7.4 ± 0.5	47.5 ± 0.7 <i>P</i> = .01 <sup>b</sup>	46.2 ± 1.4
OCCWM	7.6 ± 0.4 <i>P</i> = .004 <sup>b</sup>	7.0 ± 0.6	44.6 ± 0.7 <i>P</i> = .005 <sup>b</sup>	43.4 ± 1.5
CC	6.5 ± 0.6 <i>P</i> = .09	6.0 ± 0.7	43.7 ± 2.2 <i>P</i> = .07	41.9 ± 2.7
Thalami	5.6 ± 0.2 <i>P</i> < .001 <sup>b</sup>	5.1 ± 0.4	43.3 ± 0.8 <i>P</i> < .001 <sup>b</sup>	41.0 ± 2.2
Putamen	4.6 ± 0.3 <i>P</i> = .03	4.9 ± 0.4	42.0 ± 0.8 <i>P</i> = .09	42.4 ± 0.7
Lesions	NA	6.3 ± 0.9 <sup>c</sup>	NA	39.9 ± 3.6 <sup>c</sup>

**Note:**—NA indicates not applicable.

<sup>a</sup> ihMTR and MTR data are expressed as mean value ± SD. Between-group comparison (*P* value): comparison of mean ihMTR and MTR between patients with RRMS and controls was assessed by the nonparametric Wilcoxon rank test ( $\alpha = .05$ ) corrected by the Holm-Bonferroni method for multiple comparisons ( $m = 7$  brain structures). <sup>b</sup> Statistically significant.

<sup>c</sup> Within-patient group: ihMTR and MTR values in lesions statistically different (Kruskal-Wallis test corrected for multiple comparisons using the Steel-Dwass procedure) from values in all normal-appearing WM structures ( $P < .05$ ) except the corpus callosum ( $P > .5$ ).

**RESULTS**

**Sensitivity of ihMT to Microstructural Damage in MS**

On qualitative examination, the ihMTR and MTR maps of patients with MS exhibited focal hypointense areas in WM brain structures. This is illustrated in Fig 2 in a patient with reduced MTR and ihMTR in the FWM and OCCWM compared with a control subject. As shown in Fig 3 and in the Table, apart from the putamen, quantitative ihMTR and MTR values measured in patients with MS were lower compared with those of controls in the structures of the ihMT atlas (by trend in the IC and CC for ihMTR and in the CC for MTR; significant elsewhere). Additionally and despite pronounced partial volume effects, lesions (indicated by white arrows on Fig 2) could be identified on both ihMTR and MTR maps and exhibited hypointensities compared with the surrounding normal-appearing tissue.

More generally, mean ihMTR and MTR values measured in lesions, which were distributed among the main WM structures of the ihMT atlas structures (Fig 1B), were lower than those in normal-appearing WM structures (not significant in the CC,  $P = .7$ ; significant in the IC, TEMPWM, FWM, and OCCWM;  $P < .05$ ).

Mean patient ihMTR and MTR z scores were close to or lower than  $-2$  in WM structures (Fig 4). A tendency for lower z score values was observed with MTR compared with ihMTR in normal-appearing WM, but this was not significant ( $P > .1$ ).

**Correlation of ihMT with Clinical Disability**

Typical ihMTR and MTR maps of patients with MS with various values of EDSS are shown in Fig 5. Significant ( $P \leq .05$ ) negative correlations were found between the EDSS scores and ihMTR values measured in all normal-appearing WM structures (except OCCWM) and the thalami. Weaker, nonsignificant trends were found for MTR values (Fig 6).

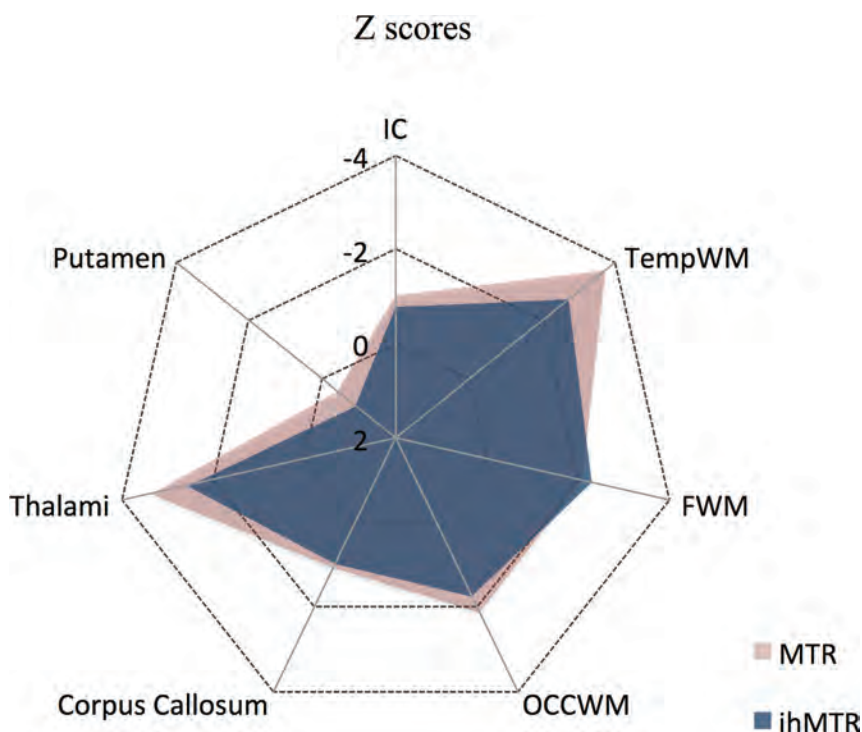


**FIG 4.** Radar plot of mean ihMTR and MTR z scores of patients with RRMS relative to control subjects calculated for each brain structure of the ihMT atlas. A tendency (not significant,  $P > .1$ ) for lower values was observed with MTR compared with ihMTR in the IC, TEMPWM, OCCWM, CC, and thalami.

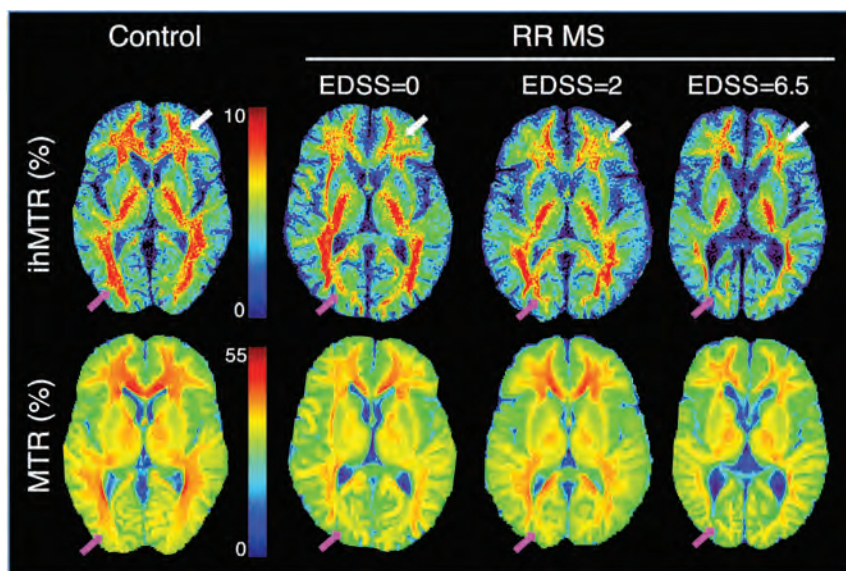


**FIG 5.** Representative ihMTR and MTR maps obtained after step 1 of the postprocessing procedure for a control subject and for patients with RRMS with various values of EDSS. Progressive loss of signal with increasing EDSS is noticed in occipital WM for both MTR and ihMTR (pink arrows). In frontal WM though, the decrease in values is more apparent with ihMTR (white arrows).

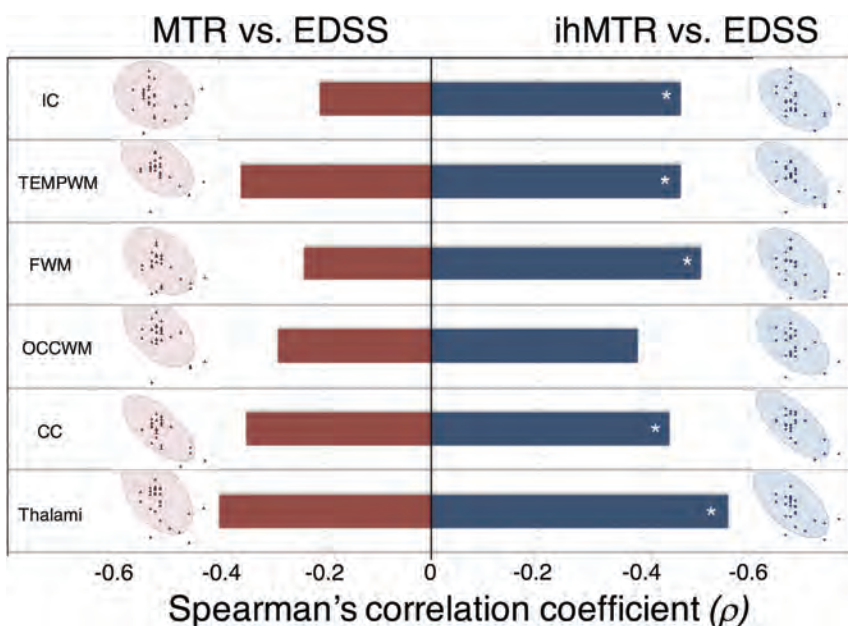


**FIG 6.** Correlation analysis of ihMTR versus EDSS scores of patients with RRMS. Mean MTR (pink markers) and ihMTR (blue markers) values measured in each structure of the ihMT atlas plotted as a function of the EDSS score and the density ellipses ( $\alpha = .95$ ) are shown. Bar plots indicate the Spearman correlation coefficient: The asterisk indicates statistically significant ( $\alpha = .05$ , corrected by the Holm-Bonferroni method for multiple comparisons [ $m = 6$  brain structures]). For ihMTR, significant negative correlations with EDSS were obtained in all structures (except the OCCWM); conversely, for the MTR, only a trend for low negative correlations with EDSS was obtained in all structures.

## DISCUSSION

One of the key findings of this first report of ihMT in a clinical context is the significant reduction of ihMT signal in patients with multiple sclerosis compared with controls, hence demonstrating the sensitivity of this new technique for MS-related physiopathologic processes. Of additional interest, our results also highlighted a correlation of ihMT metrics with clinical disability, whereas MT

metrics did not. This finding validates the hypothesis that ihMT and conventional MT provide complementary information. Combined, these results, albeit preliminary, support the use of ihMT in further clinical studies because its higher specificity for myelin could be advantageously used in the assessment of patients with MS.

In numerous studies,<sup>22</sup> including the present report, conventional MT has been shown to be sensitive to tissue disorders in MS through changes in MTRs (lower MTR values in MS lesions, subtle significant diffuse decrease in MTR in normal-appearing tissue in patients). Similarly, the significant changes obtained in ihMTR values along with the ihMTR z score intensities are key findings supporting the sensitivity of ihMT for the MS pathology.

The association between clinical disability and conventional MT is debatable. Whereas some studies have reported significant correlations between EDSS and MTR histogram features of normal-appearing brain tissue,<sup>23,24</sup> others have suggested that the MTR of lesions in white matter, rather than in normal-appearing tissue, relates to the disability in patients with MS.<sup>4,25</sup> Most important, correlations between MTR and clinical outcomes were predominantly detected for the highest EDSS (>3) scores.<sup>25-27</sup> Hence, the trend for a negative correlation of MTR in normal-appearing tissue with the EDSS score (not significant) observed in our study is in agreement with these general findings. Overall, these controversial reports reflect confounding contributions to the standard MT signal induced by its sensitivity to multiple pathophysiologic mechanisms underlying MS,<sup>28</sup> which limits its ability to relate clinical deficits to underlying regional pathology. Conversely, the potential of ihMT to derive metrics that more faithfully reflect the severity of the disease was apparent from the stronger significant correlations of ihMTR with EDSS. More generally, the

lower sensitivity of ihMTR to the normal-appearing WM difference from controls but higher correlation with disability could suggest that ihMT is primarily detecting myelin changes that are more closely linked to disability, while MTR primarily detects inflammation-linked edema, one of the causes of normal-appearing WM changes in MS.<sup>28</sup> Hence, the combined use of these 2

contrasts and other myelin-sensitive modalities, such as diffusion MR imaging, in further studies may help disentangle the complex pathologic mechanisms occurring in MS.

Caution is advised, however, in drawing definitive conclusions because this preliminary study has some limitations. First, the cohort of patients was rather small and heterogeneous regarding disease duration and clinical status; these features may have mitigated the expected MTR and ihMTR variations. This relatively low number of patients may also explain why, though statistically significant, the correlations of ihMT and EDSS did not appear visually highly convincing. A stronger relationship between ihMTR variations and demyelination/remyelination processes might be established by focusing on the early onset of the disease following the detection of active lesions and by monitoring the ihMT parameters at different stages (inflammation, demyelination, remyelination, gliosis). Also, looking at potential correlations between ihMT metrics and clinical scores (eg, Multiple Sclerosis Functional Composite score) that assess other functional aspects of the disease than those assessed by EDSS should be considered in further studies to establish a more comprehensive relationship between ihMT- and MS-related impairment.

From a technical perspective, despite the care taken in the atlas construction, partial volume effects produced by the large slice thickness induced measurement bias, which may have led to underestimation of the variations of MTR and ihMTR in demyelinated lesions. Finally, the findings of this study could not be generalized at this stage because the single-slice ihMT approach did not allow whole-brain coverage. Hence, although the main objective of this study, demonstration of the sensitivity of ihMT for MS pathology, has been met, the technique must be improved to overcome these important technical limitations and make ihMT a practical tool applicable in daily clinical practice. In this context, the recently proposed sensitivity-enhanced 3D ihMT technique, which permits full brain coverage at an improved spatial resolution (1.5-mm isotropic) in 15 minutes<sup>29</sup> is very promising. Hence, combining 3D-ihMT with other imaging modalities (MT and DTI for inflammation and axonal loss evaluation) would be a useful tool for assessment of myelin impairment and for more accurate characterization of the complex MS disease mechanisms.

## CONCLUSIONS

Results obtained in this preliminary investigation demonstrate the sensitivity of the ihMT technique for MS, characterized by significant reduction in ihMTR values in both demyelinated lesions and normal-appearing tissue of patients with RRMS. Stronger correlations with disability were obtained with ihMT compared with standard MT, which confirmed the complementarity of both techniques and may be explained by the higher specificity of ihMT for myelin. Our results warrant further exploration, which, if performed with the recently proposed 3D sensitivity-enhanced ihMT approach, could make ihMT a propitious asset for in vivo assessment of myelin status in MS.

Disclosures: Samira Mchinda—RELATED: Grant: Institut pour la Recherche sur la Moelle épinière et l'Encéphale (IRME) 2016, Association pour la Recherche sur la Sclérose en Plaques (ARSEP) 2015.\* David C. Alsop—UNRELATED: Grants/Grants Pending: GE Healthcare. Comments: I receive research support from GE Healthcare to advance perfusion imaging and magnetization transfer imaging methods\*; Royal-

ties: I receive postmarket royalties through my institution for licensing of inventions related to perfusion MRI. These technologies have been licensed by GE Healthcare, Philips Healthcare, Siemens, Hitachi Medical, and Animage Technology.\* Jean Pelletier—UNRELATED: Board Membership: Biogen, Novartis, Merck, Roche, Teva Pharmaceutical Industries, MedDay\*; Grants/Grants Pending: Biogen, Novartis, Merck, MedDay\*; Travel/Accommodations/Meeting Expenses Unrelated to Activities Listed: Biogen, Novartis, Merck, Roche, Teva Pharmaceutical Industries, MedDay. Olivier Girard—RELATED: Grant: ARSEP 2015. Comments: supporting MRI costs\*; UNRELATED: Employment: Aix-Marseille University. Comments: full-time research engineer; Grants/Grants Pending: ARSEP, Agence Nationale de la Recherche, SATT Sud Est\*; Patents (Planned, Pending or Issued). Comments: patent pending, no license or financial interest up to now. Guillaume Duhamel—RELATED: Grant: IRME 2016, ARSEP 2015. \*Money paid to institution.

## REFERENCES

1. MacKay A, Whittall K, Adler J, et al. **In vivo visualization of myelin water in brain by magnetic resonance.** *Magn Reson Med* 1994;31:673–77 CrossRef Medline
2. Henkelman RM, Stanisz GJ, Graham SJ. **Magnetization transfer in MRI: a review.** *NMR Biomed* 2001;14:57–64 CrossRef Medline
3. Sled JG, Pike GB. **Quantitative imaging of magnetization transfer exchange and relaxation properties in vivo using MRI.** *Magn Reson Med* 2001;46:923–31 CrossRef Medline
4. Gass A, Barker GJ, Kidd D, et al. **Correlation of magnetization transfer ratio with clinical disability in multiple sclerosis.** *Ann Neurol* 1994;36:62–67 CrossRef Medline
5. Rocca MA, Mastrorardo G, Rodegher M, et al. **Long-term changes of magnetization transfer–derived measures from patients with relapsing-remitting and secondary progressive multiple sclerosis.** *AJNR Am J Neuroradiol* 1999;20:821–27 Medline
6. Schmierer K, Scaravilli F, Altmann DR, et al. **Magnetization transfer ratio and myelin in postmortem multiple sclerosis brain.** *Ann Neurol* 2004;56:407–15 CrossRef Medline
7. Filippi M, Campi A, Dousset V, et al. **A magnetization transfer imaging study of normal-appearing white matter in multiple sclerosis.** *Neurology* 1995;45(3 Pt 1):478–82 CrossRef Medline
8. Varma G, Duhamel G, de Bazelaire C, et al. **Magnetization transfer from inhomogeneously broadened lines: a potential marker for myelin.** *Magn Reson Med* 2015;73:614–22 CrossRef Medline
9. Varma G, Girard OM, Prevost VH, et al. **Interpretation of magnetization transfer from inhomogeneously broadened lines (ihMT) in tissues as a dipolar order effect within motion restricted molecules.** *J Magn Reson* 2015;260:67–76 CrossRef Medline
10. Swanson SD, Malyarenko DI, Fabiilli ML, et al. **Molecular, dynamic, and structural origin of inhomogeneous magnetization transfer in lipid membranes.** *Magn Reson Med* 2017;77:1318–28 CrossRef Medline
11. Manning AP, Chang KL, MacKay AL, et al. **The physical mechanism of “inhomogeneous” magnetization transfer MRI.** *J Magn Reson* 2017;274:125–36 CrossRef Medline
12. Varma G, Girard OM, Prevost VH, et al. **In vivo measurement of a new source of contrast, the dipolar relaxation time,  $T_{1D}$ , using a modified inhomogeneous magnetization transfer (ihMT) sequence.** *Magn Reson Med* 2017;78:1362–72 CrossRef Medline
13. Prevost VH, Girard OM, Mchinda S, et al. **Optimization of inhomogeneous magnetization transfer (ihMT) MRI contrast for preclinical studies using dipolar relaxation time ( $T_{1D}$ ) filtering.** *NMR Biomed* 2017;30:e3706 CrossRef
14. Prevost VH, Girard OM, Cayre M, et al. **Validation of inhomogeneous magnetization transfer (ihMT) as a myelin biomarker.** In: *Proceedings of the Annual Meeting and Exhibition of the International Society for Magnetic Resonance in Medicine*, Honolulu, Hawaii. April 22–24, 2017:1498
15. Girard OM, Prevost VH, Varma G, et al. **Magnetization transfer from inhomogeneously broadened lines (ihMT): experimental optimization of saturation parameters for human brain imaging at 1.5 Tesla.** *Magn Reson Med* 2015;73:2111–21 CrossRef Medline
16. Girard OM, Callot V, Prevost VH, et al. **Magnetization transfer from inhomogeneously broadened lines (ihMT): improved imaging**

- strategy for spinal cord applications. *Magn Reson Med* 2017;77:581–91 CrossRef Medline
17. Kurtzke JF. **Rating neurologic impairment in multiple sclerosis: an expanded disability status scale (EDSS).** *Neurology* 1983;33:1444–52 CrossRef Medline
  18. Prevost VH, Girard OM, Varma G, et al. **Minimizing the effects of magnetization transfer asymmetry on inhomogeneous magnetization transfer (ihMT) at ultra-high magnetic field (11.75 T).** *MAGMA* 2016;29:699–709 CrossRef Medline
  19. Avants BB, Tustison NJ, Song G, et al. **A reproducible evaluation of ANTs similarity metric performance in brain image registration.** *Neuroimage* 2011;54:2033–44 CrossRef Medline
  20. Wu G, Jia H, Wang Q, et al. **Emergence of groupwise registration in MR brain study.** In: Liang H, Bronzino JD, Peterson DR, eds. *Biosignal Processing: Principles and Practices*. Boca Raton, Florida: CRC Press; 2012: chap 5
  21. Neuhäuser M, Bretz F. **Nonparametric all-pairs multiple comparisons.** *Biom J* 2001;43:571–80
  22. Filippi M, Agosta F. **Magnetization transfer MRI in multiple sclerosis.** *J Neuroimaging* 2007;17:22S–26S. CrossRef Medline
  23. Traboulsee A, Dehmeshki J, Peters KR, et al. **Disability in multiple sclerosis is related to normal appearing brain tissue MTR histogram abnormalities.** *Mult Scler* 2003;9:566–73 CrossRef Medline
  24. Vrenken H, Pouwels PJ, Ropele S, et al. **Magnetization transfer ratio measurement in multiple sclerosis normal-appearing brain tissue: limited differences with controls but relationships with clinical and MR measures of disease.** *Mult Scler* 2007;13:708–16 CrossRef Medline
  25. Amann M, Papadopoulou A, Andelova M, et al. **Magnetization transfer ratio in lesions rather than normal-appearing brain relates to disability in patients with multiple sclerosis.** *J Neurol* 2015;262:1909–17 CrossRef Medline
  26. De Stefano N. **Brain damage as detected by magnetization transfer imaging is less pronounced in benign than in early relapsing multiple sclerosis.** *Brain* 2006;129:2008–16 CrossRef Medline
  27. Santos AC, Narayanan S, de Stefano N, et al. **Magnetization transfer can predict clinical evolution in patients with multiple sclerosis.** *J Neurol* 2002;249:662–68 CrossRef Medline
  28. Moll NM, Rietsch AM, Thomas S, et al. **Multiple sclerosis normal-appearing white matter: pathology-imaging correlations.** *Ann Neurol* 2011;70:764–73 CrossRef Medline
  29. Mchinda S, Varma G, Prevost VH, et al. **Whole brain inhomogeneous magnetization transfer (ihMT) imaging: sensitivity enhancement within a steady-state gradient echo sequence.** *Magn Reson Med* 2017 Sep 23. [Epub ahead of print] CrossRef Medline

# Evaluation of Leptomeningeal Contrast Enhancement Using Pre-and Postcontrast Subtraction 3D-FLAIR Imaging in Multiple Sclerosis

R. Zivadinov, D.P. Ramasamy, J. Hagemeyer, C. Kolb, N. Bergsland, F. Schweser, M.G. Dwyer, B. Weinstock-Guttman, and D. Hojnacki



## ABSTRACT

**BACKGROUND AND PURPOSE:** Leptomeningeal contrast enhancement is found in patients with multiple sclerosis, though reported rates have varied. The use of 3D-fluid-attenuated inversion recovery pre- and postcontrast subtraction imaging may more accurately determine the frequency of leptomeningeal contrast enhancement. The purpose of this study was to investigate the frequency of leptomeningeal contrast enhancement using the pre- and postcontrast subtraction approach and to evaluate 3 different methods of assessing the presence of leptomeningeal contrast enhancement.

**MATERIALS AND METHODS:** We enrolled 258 consecutive patients with MS (212 with relapsing-remitting MS, 32 with secondary progressive MS, and 14 with clinically isolated syndrome) who underwent both pre- and 10-minute postcontrast 3D-FLAIR sequences after a single dose of gadolinium injection on 3T MR imaging. The analysis included leptomeningeal contrast-enhancement evaluation on 3D-FLAIR postcontrast images in native space (method A), on pre- and postcontrast 3D-FLAIR images in native space (method B), and on pre-/postcontrast 3D-FLAIR coregistered and subtracted images (method C, used as the criterion standard).

**RESULTS:** In total, 51 (19.7%) patients with MS showed the presence of leptomeningeal contrast enhancement using method A; 39 (15.1%), using method B; and 39 (15.1%), using method C ( $P = .002$ ). Compared with method C as the criterion standard, method A showed 89.8% sensitivity and 92.7% specificity, while method B showed 84.6% sensitivity and 97.3% specificity ( $P < .001$ ) at the patient level. Reproducibility was the highest using method C ( $\kappa$  agreement,  $r = 0.88$ ,  $P < .001$ ). The mean time to analyze the 3D-FLAIR images was significantly lower with method C compared with methods A and B ( $P < .001$ ).

**CONCLUSIONS:** 3D-FLAIR postcontrast imaging offers a sensitive method for detecting leptomeningeal contrast enhancement in patients with MS. However, the use of subtraction imaging helped avoid false-positive cases, decreased reading time, and increased the accuracy of leptomeningeal contrast-enhancement foci detection in a clinical routine.

**ABBREVIATIONS:** CE = contrast enhancement; CIS = clinically isolated syndrome; Gd = gadolinium; LM = leptomeningeal; LV = lesion volume; NPV = negative predictive value; PPV = positive predictive value; RR = relapsing-remitting; SP = secondary-progressive

Persistent leptomeningeal (LM) inflammation in the form of ectopic lymphoid follicle-like structures<sup>1-4</sup> is associated with development of subpial cortical lesions in patients with multiple sclerosis.<sup>2-8</sup>

Use of 3D-fluid-attenuated-inversion recovery MR imaging acquired 10 minutes post-contrast administration of gadolinium (Gd) has been recently proposed as a novel in vivo potential biomarker for the detection of persistent LM inflammation. It has been hypothesized that trapped contrast enhancement (CE) within the subarachnoid space of patients with MS<sup>8-10</sup> and subjects in their prodromal disease stage<sup>11</sup> is indicative of LM inflammation and can be visualized by 3D-FLAIR postcontrast MR imaging.

However, at this time, to our knowledge, there are no currently available consensus guidelines regarding the most sensitive and specific approach for the detection of LM CE in patients with MS

Received September 13, 2017; accepted after revision November 28.

From the Department of Neurology (R.Z., D.P.R., J.H., N.B., F.S., M.G.D.), Buffalo Neuroimaging Analysis Center, Jacobs School of Medicine and Biomedical Sciences; Translational Imaging Center at Clinical Translational Science Institute (B.W.-G.); and Department of Neurology (R.Z., C.K., D.H.), Jacobs Comprehensive MS Treatment and Research Center, University at Buffalo, State University of New York, Buffalo, New York.

This work was funded by the internal funds of the Buffalo Neuroimaging Analysis Center, Department of Neurology, Jacobs School of Medicine and Biomedical Sciences, University at Buffalo, State University of New York.

Please address correspondence to Robert Zivadinov, MD, PhD, FAAN, FEAN, FANA, Buffalo Neuroimaging Analysis Center, Translational Imaging Center at Clinical Translational Science Institute, University at Buffalo, State University of New York, 100 High St, Buffalo, NY 14203; e-mail: rzivadinov@bnac.net

Indicates article with supplemental on-line tables.

Indicates article with supplemental on-line photos.

<http://dx.doi.org/10.3174/ajnr.A5541>

in vivo, so imaging of LM CE cannot be translated immediately to the clinical routine. Given the uncertainty in the literature as to the frequency of LM CE in patients with MS with different field strengths, pulse sequences, Gd-based protocols, and analysis methods,<sup>9,10,12-14</sup> there is an urgent need to determine LM CE prevalence using different validation techniques. In previous studies, the estimates of LM CE frequency ranged from <1% to 90%. For example, using 3T MR imaging, Absinta et al<sup>9</sup> showed that LM CE was detected in 74 of 299 (25%) examined patients with MS, compared with 1 of 37 (2.7%) healthy subjects. Using 7T MR imaging, Harrison et al<sup>14</sup> showed that 26 of 29 (90%) participants with MS had at least 1 foci of LM CE, suggesting that LM CE detection may be more prevalent using ultra-high-field MR imaging, which is also more in line with findings from histopathologic studies.<sup>8</sup>

In previous LM CE imaging studies, detection of LM CE was performed on pre- and/or postcontrast native space images, not oriented and sliced in exactly the same way, which could complicate their comparison and increase the likelihood of detection of false-positive findings.<sup>9-13</sup>

The purpose of this study was to investigate the frequency of LM CE using the pre- and postcontrast 3D-FLAIR subtraction approach and to evaluate 3 different methods of assessing the presence of LM CE in consecutively enrolled patients with MS consisting of relapsing-remitting (RR) and secondary-progressive (SP) MS disease subtypes and in patients with clinically isolated syndrome (CIS) who were recruited in a clinical routine.

## MATERIALS AND METHODS

### Study Population

The study consisted of 258 consecutive patients with MS (212 with RRMS, 32 with SPMS, and 14 with CIS) who were enrolled and underwent both pre- and 10-minute postcontrast 3D-FLAIR sequences after a single dose of Gd injection on 3T MR imaging.

The inclusion criteria for this retrospective study of LM CE in MS were the following: 1) patients with CIS, RRMS, or SPMS; 2) 18–75 years of age; 3) undergoing pre- and postcontrast 3D-FLAIR sequences 10 minutes after a single dose of Gd injection using a standardized 3T MR imaging protocol; and 4) physical/neurologic examination within 30 days from MR imaging. Exclusion criteria were the following: 1) the presence of relapse and steroid treatment within the 30 days preceding study entry, 2) pre-existing medical conditions known to be associated with brain pathology (cerebrovascular disease, positive history of substance abuse), or 3) pregnancy.

All subjects were assessed with physical and neurologic examinations. The study data collection was approved by the local institutional review board of the University at Buffalo.

### MR Imaging Acquisition and Analysis

Subjects were examined with a 3T Signa Excite HD 12.0 scanner (GE Healthcare, Milwaukee, Wisconsin) using an 8-channel head and neck coil that did not undergo major hardware or software upgrades during the study.

The presence and frequency of LM CE were assessed using a 3D-FLAIR for enhanced lesion detection (3D-FLAIRE) sequence.<sup>10,15</sup> The pre- and post-3D-FLAIR sequences were ac-

quired before and 10 minutes after an intravenous bolus of 0.1 mmol/kg of gadolinium-DTPA injection in a sagittal acquisition with TR/TI/TE = 9000/2420/600 ms, acquisition matrix = 256 × 192, voxel size = 1.0 × 1.3 × 1.3 mm<sup>3</sup>, frequency direction = inferior to superior.<sup>16</sup> The sequence uses variable flip angles so that the effective TE of 600 ms for the sequence was equal to a TE of 110 ms for a conventional spin-echo sequence<sup>10,15</sup> and was 12 minutes 22 seconds long. A spin-echo 2D-T1WI was acquired using a 256 × 192 matrix and 256 × 192 mm<sup>2</sup> FOV, resulting in a nominal in-plane resolution of 1 × 1 mm<sup>2</sup> and 48 gapless 3-mm-thick slices with TE/TR = 16/600 ms before and 5 minutes after Gd injection, for detection of T1 hypointense and hyperintense (Gd) lesions, and each was 4 minutes 34 seconds long.

The 3D-FLAIR postcontrast image was rigidly registered to the 3D-FLAIR precontrast image.<sup>17</sup> The 3D-FLAIR precontrast image was then voxelwise subtracted from the coregistered 3D-FLAIR postcontrast image, yielding a subtraction map, which was subsequently smoothed with a Gaussian kernel of 0.5 mm (Figure).

MR imaging analysts were blinded to the subject's cohort and physical and neurologic conditions. The images were examined first on 3D-FLAIR postcontrast images in native space (method A, On-line Fig 1), pre- and postcontrast 3D-FLAIR images in native space (method B, On-line Fig 1), and pre/postcontrast 3D-FLAIR coregistered and subtracted images (method C, Figure) in a randomized manner to avoid potential practice effects. A 4-week delay was introduced for all 3 methods to further reduce potential recall bias. Additional analysis was conducted a posteriori to examine the concordance of all 3 methods. The LM CE foci were compared side by side in an unblinded manner to determine discordant cases (true-positive, true-negative, false-positive, and false-negative), determined by methods A and B compared with method C.

The LM CE analysis was performed by 2 experienced neuroimagers (D.P.R. and D.H. with >15 years of reading experience) fully blinded to other imaging modalities of the individual subject examinations. An additional expert neuroimager (R.Z. with >15 years of reading experience) served on a panel to reach a consensus when there were discrepancies by the 2 readers. The unblinded comparison was performed by a consensus of all 3 readers. The mean time to analyze the 3D-FLAIR images for the 3 methods included only the operator time for inspection of the images.

The reproducibility for detection of LM CE was obtained by 2 raters in 30 patients with MS for methods A, B, and C, using a similar approach as previously reported.<sup>10</sup>

LM CE foci were defined as signal intensity within the subarachnoid space that was substantially greater than that of brain parenchyma. The images were reviewed using Jim software (<http://www.xinapse.com/home.php>) in the sagittal plane of the original acquisition and in additional coronal and axial views (On-line Fig 1). LM CE was evaluated according to aspect (focal or diffuse), location (within a sulcus or overlying the brain convexity, along a dural fissure, or traversing several of these areas), shape (nodular, linear, or platelike), cerebral hemisphere (right or left), tentorium (supra- or infratentorial), and lobe (frontal, parietal, temporal, and occipital) as previously reported.<sup>9,10</sup>

T2-, T1-, and Gd lesion volume (LV) and number were calculated using a reliable semiautomated edge-detection contouring/

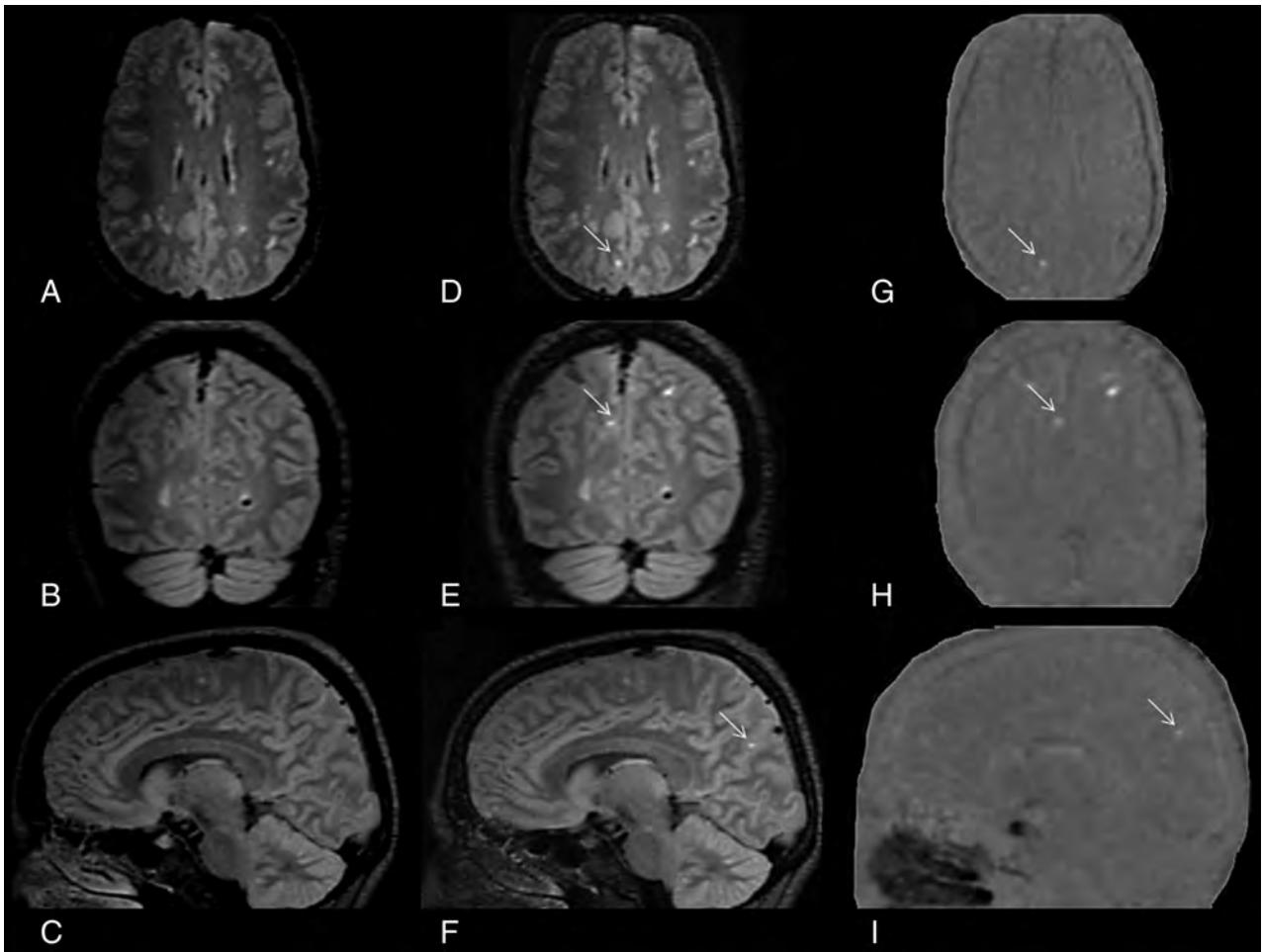


**FIGURE.** Detection of leptomeningeal contrast-enhancement foci using subtraction images. A–C, Coregistered 3D-FLAIR precontrast images in all 3 orthogonal planes. D–F, The corresponding coregistered 3D-FLAIR postcontrast images in all 3 orthogonal planes. G–I, The corresponding pre-/postcontrast 3D-FLAIR subtraction images in all 3 orthogonal planes. A patient with relapsing-remitting multiple sclerosis has a true LM CE in the right parietal region that was easily spotted with the aid of pre-/postcontrast 3D-FLAIR subtraction images, which otherwise would have been undetected.

thresholding technique on 3D-FLAIR and 2D-T1 pre- and post-contrast examinations, respectively.<sup>18</sup>

### Statistical Analysis

Statistical analysis was performed using the Statistical Package for the Social Sciences, Version 21.0 (IBM, Armonk, New York). Differences in the categorical variables between the groups were analyzed using the  $\chi^2$  test. Differences in clinical and MR imaging variables between the groups were tested using the Student *t* test and analysis of variance for continuous variables, the Mann-Whitney rank sum test and Kruskal-Wallis test for ordinal measures, and the  $\chi^2$  test for categorical measures. The Cohen  $\kappa$  agreement was used to test the reproducibility for detection of LM CE foci among the 3 raters.

The differences among the 3 assessment methods were tested using repeat analysis of variance for continuous measures and the Cochran Q for categorical measures.

Sensitivity, specificity, positive predictive value (PPV), and negative predictive value (NPV) with 95% confidence intervals were calculated among the 3 assessment methods at the patient level, using the coregistered, pre-/postcontrast 3D-FLAIR subtraction images (method C, Figure) as the criterion standard.

A nominal *P* value of  $< .05$  was considered statistically significant using 2-tailed tests.

### RESULTS

#### Demographic, Clinical, and MR Imaging Characteristics at Baseline

Table 1 shows demographic, clinical, and MR imaging characteristics between patients with MS with or without the presence of LM CE in various disease subtypes, according to the method C classification. Patients positive for RRMS LM CE were older ( $P = .047$ ), had an older age at onset ( $P = .045$ ), were more disabled ( $P = .01$ ), and had higher T2-LV ( $P < .001$ ) and T1-LV ( $P = .002$ ). No differences in demographic, clinical, and MR imaging characteristics were found between patients positive and negative for SPMS and CIS LM CE.

#### Comparison of LM CE Characteristics Using the 3 Different Assessment Methods

On-line Table 1 shows LM CE characteristics and regional distribution, according to assessment methods A, B, or C.

In total, 51 (19.8%) patients showed the presence of LM CE using method A; 39 (15.1%), using Method B; and 39 (15.1%),

**Table 1: Demographic, clinical, and basic MRI characteristics in patients with multiple sclerosis with and without leptomeningeal contrast enhancement, according to the method C classification**

Demographic and Clinical Characteristics	RR (n = 212)			SP (n = 32)			CIS (n = 14)		
	Negative for LM CE (n = 179)	Positive for LM CE (n = 33)	P Value <sup>a</sup>	Negative for LM CE (n = 27)	Positive for LM CE (n = 5)	P Value <sup>a</sup>	Negative for LM CE (n = 13)	Positive for LM CE (n = 1)	P Value <sup>a</sup>
Female (No.) (%)	138 (77.1)	23 (69.7)	.361	22 (81.5)	4 (80.0)	.938	10 (76.9)	0 (0)	.286
Age (mean) (SD) (yr)	46.8 (12.4)	51.3 (9.8)	.047 <sup>b</sup>	56.8 (8.3)	60.6 (7.6)	.348	43.4 (12.6)	32.0 (-)	.401
Age of onset (mean) (SD) (yr)	32.3 (11.5)	36.6 (9.8)	.045 <sup>b</sup>	31.4 (10.4)	40.0 (5.4)	.086	37.8 (11.8)	32.0 (-)	.999
Disease duration, (mean) (SD) (yr)	14.5 (9.2)	14.7 (9.1)	.916	25.4 (12.9)	20.8 (5.6)	.441	5.4 (6.1)	0 (-)	.645
EDSS (median) (IQR)	2.5 (1.5–3.5)	3.0 (2.0–4.5)	.010 <sup>b</sup>	6.0 (6.0–7.0)	6.5 (3.5–7.5)	.658	1.5 (1.0–2.0)	1.5 (1.5–1.5)	.999
DMT (No.) (%)									
Interferon	38 (21.3)	8 (24.4)	.220	3 (11.1)	1 (20.0)	.845	6 (46.2)	0 (0)	.160
Glatiramer acetate	29 (16.2)	6 (18.2)		2 (7.4)	1 (20.0)		0 (0)	0 (0)	
Natalizumab	22 (12.3)	5 (15.2)		1 (3.7)	1 (20.0)		1 (7.7)	0 (0)	
Rituximab	3 (1.7)	1 (3.0)		0 (0)	0 (0)		0 (0)	0 (0)	
Fingolimod	7 (3.9)	5 (15.2)		0 (0)	0 (0)		0 (0)	0 (0)	
Dimethyl fumarate	30 (16.8)	2 (6.1)		1 (3.7)	0 (0)		0 (0)	0 (0)	
Teriflunomide	7 (3.9)	1 (3.0)		6 (22.2)	1 (20.0)		0 (0)	0 (0)	
IVIg	6 (3.3)	0 (0)		2 (7.4)	0 (0)		1 (7.7)	0 (0)	
Other DMT <sup>c</sup>	3 (1.7)	1 (0)		1 (3.7)	0 (0)		0 (0)	1 (100)	
Combination	13 (7.3)	1 (3.0)		2 (7.4)	0 (0)		1 (7.7)	0 (0)	
No DMT	19 (10.6)	4 (12.1)		9 (33.3)	1 (20.0)		4 (30.8)	0 (0)	
T2-LV (mean) (SD)	8.86 (10.42)	16.62 (12.11)	<.001 <sup>b</sup>	15.19 (17.22)	14.38 (11.53)	.920	5.79 (7.34)	1.38 (-)	.574
TI-LV (mean) (SD)	2.55 (4.82)	5.65 (8.25)	.002 <sup>b</sup>	5.69 (8.62)	5.45 (4.62)	.579	1.87 (4.01)	0.25 (-)	.704
Gd-LN (mean) (SD)	0.15 (0.61)	0.55 (1.55)	.290	1.37 (4.77)	0 (0)	.725	0.31 (0.86)	1 (-)	.286
Gd-LV (mean) (SD)	0.01 (0.05)	0.05 (0.17)	.282	0.20 (0.72)	0 (0)	.725	0.02 (0.06)	0.08 (-)	.286

**Note:**—LN indicates lesion number; —, indicates not available; DMT, disease modifying therapy; EDSS, Expanded Disability Status Scale; IQR, interquartile range; IVIG, intravenous immunoglobulin.

<sup>a</sup> P values represent positive and negative LM CE group comparisons. The P values were derived using the  $\chi^2$  test, Fisher exact test, Student t test, analysis of variance, Mann-Whitney U test, and Kruskal-Wallis test.

<sup>b</sup> Significant P value < .05.

<sup>c</sup> Other DMT therapies included intravenous methylprednisolone, intravenous immunoglobulin, mitoxantrone, and mycophenolate mofetil.

using method C ( $P = .002$ ). There were more multiple LM CE foci detected using method A, compared with methods B and C ( $P = .013$ ), and the mean number of LM CE foci was the highest with method A ( $P = .001$ ). All LM CEs were focal, and most were detected on brain convexities (Figure and On-line Fig 1). Most of the LM CE foci were nodular, and there were no hemispheric differences. All LM CE foci were supratentorial, except 1 infratentorial foci detected with method A.

On-line Table 2 shows comparisons of patients with RRMS and SPMS according to assessment methods A, B, and C for the detection of LM CE foci. In total, 44 (20.8%) patients with RRMS showed the presence of LM CE using method A; 35 (16.5%), using method B, and 33 (15.6%), using method C ( $P = .004$ ). The figures were 5 (15.6%) for method A, 3 (9.4%) for method B, and 5 (15.6%) for method C ( $P =$  not significant) in patients with SPMS. In patients with RRMS, there were more multiple LM CE foci detected using method A compared with methods B and C ( $P = .05$ ), and the mean number of LM CE foci was the highest with method A ( $P = .004$ ). No significant differences among the 3 methods were detected in patients with SPMS.

The mean time to analyze the 3D-FLAIR images was significantly lower with method C, compared with methods A and B ( $P < .001$ , On-line Table 1). In patients with both RRMS ( $P < .001$ ) and SPMS ( $P = .049$ ), the mean time to analyze the 3D-FLAIR images was significantly lower with method C, compared with methods A and B ( $P < .001$ , On-line Table 2).

### Reproducibility of Leptomeningeal Contrast-Enhancement Assessment Using the 3 Different Assessment Methods

The Cohen  $\kappa$  agreement for the presence of LM CE foci (yes/no) was 0.72,  $P < .001$ , for method A; 0.81,  $P < .001$ , for method B; and 0.88,  $P < .001$ , for method C.

### A Posteriori Unblinded Concordance Analysis of the 3 Different Assessment Methods

In total, 75 LM CE foci were detected with method A, 55 with method B, and 61 with method C ( $P = .001$ , On-line Table 1). Compared with the criterion standard (method C), 51 of 75 observed LM CE foci were classified as true-positive; 24, as false-positive; 0, as true-negative; and 10, as false-negative using method A. This calculation yielded a sensitivity of 83.6% (95% CI, 71.4%–91.4%). Compared with the criterion standard (method C), 48 of 55 observed LM CE foci were classified as true-positive; 7, as false-positive; 17, as true-negative; and 13, as false-negative using method B. This yielded a sensitivity of 78.7% (95% CI, 70%–87.8%) and a specificity of 70.8% (95% CI, 48.8%–87.7%).

### Comparison of Sensitivity, Specificity, and Positive and Negative Predictive Values in Patients Using Method C as the Reference

Table 2 shows the sensitivity, specificity, PPV, and NPV with 95% CIs between methods A and B using method C as the reference in total patients with MS and according to the disease subtypes. In the total study sample, method A showed 89.8% sensitivity, 92.7% specificity, 68.6% PPV, and 98.1% NPV ( $P < .001$ ), while method B showed 84.6% sensitivity, 97.3% specificity, 84.6% PPV, and 97.3% NPV ( $P < .001$ ). The differences in the 3 methods were significant for patients with both RRMS and SPMS, but not for CIS.

### DISCUSSION

The main finding of this retrospective, observational study is that the frequency of LM CE foci is lower using the 3D-FLAIR subtraction approach compared with the postcontrast-alone approach. The 3D-FLAIR subtraction approach helped to avoid LM CE false-positive cases of patients with MS followed in a clinical

**Table 2: Sensitivity, specificity, and positive and negative predictive values in patients using method C as the reference for detection of leptomeningeal contrast-enhancement foci<sup>a</sup>**

	Sensitivity	Specificity	PPV	NPV	P Value
Total study sample					
Method A LM CE presence	89.8% (74.8–96.7)	92.7% (88.2–95.6)	68.6% (53.9–80.5)	98.1% (94.8–99.4)	<.001 <sup>b</sup>
Method B LM CE presence	84.6% (68.8–93.6)	97.3% (93.8–98.8)	84.6% (68.8–93.6)	97.3% (93.9–98.9)	<.001 <sup>b</sup>
CIS-only sample					
Method A LM CE presence	100% (5.5–100)	82.3% (62.1–99.6)	50% (2.7–97.3)	100% (69.9–100)	.143
Method B LM CE presence	100% (5.5–100)	100% (71.6–100)	100% (54.7–97.2)	100% (71.6–100)	.071
RR-only sample					
Method A LM CE presence	90.1% (74.5–97.6)	92.2% (86.9–95.5)	68.2% (52.3–80.9)	98.2% (94.5–99.5)	<.001 <sup>b</sup>
Method B LM CE presence	87.9% (70.9–96.0)	96.7% (92.5–98.6)	82.9% (65.7–92.8)	97.7% (93.9–99.3)	<.001 <sup>b</sup>
SP-only sample					
Method A LM CE presence	96.3% (79.1–99.8)	96.3% (79.1–99.8)	80% (29.9–98.9)	96.3% (79.1–99.8)	<.001 <sup>b</sup>
Method B LM CE presence	60% (17.0–92.7)	100% (84.9–100)	100% (30.9–100)	93.1% (75.7–98.7)	.002

<sup>a</sup> Method A assessment was performed using postcontrast 3D-FLAIR images in native space; method B, using pre- and postcontrast 3D-FLAIR images in native space; and method C, using the coregistered, pre-/postcontrast 3D-FLAIR subtracted images. Data are presented as sensitivity, specificity, PPV, and NPV. In parenthesis are 95% confidence intervals. P Value refers to the significance of the contingency table (Fisher exact test).

<sup>b</sup> Significant.

routine. No LM CE frequency differences were found between patients with RRMS and SPMS followed in the clinical routine.

The reproducibility of LM CE foci assessment was the highest using the pre-/postcontrast subtraction approach. There was also a shorter time needed for LM CE foci analysis using 3D-FLAIR pre-/postcontrast subtraction images, which may lead to a more widespread adoption of this new imaging biomarker in MS clinical routine.

The true prevalence of LM CE in patients with CIS and MS is not well-established. In one of the first studies of LM CE in MS that included 299 patients with MS,<sup>9</sup> 25% of patients with MS presented with LM CE, while in another study of 50 patients with MS, the prevalence was 50%.<sup>10</sup> Both of those studies used 3T MR imaging and high-resolution 3D-FLAIR imaging acquired at least 10 minutes after contrast injection. Another study<sup>14</sup> that examined 29 patients with MS on 7T MR imaging using high-resolution 3D-FLAIR acquired approximately 20 minutes postcontrast injection showed 90% LM CE prevalence. The only MS study that showed <1% prevalence used 3T MR imaging with low-resolution 2D-FLAIR images acquired approximately 10 minutes postinjection.<sup>13</sup>

The current study is one of the first studies in the clinical routine in which 258 consecutive patients with MS were enrolled to undergo pre- and postcontrast 3D-FLAIR imaging, coregistered and subtracted. The sensitivity, specificity, PPV, and NPV among the 3 assessment LM CE methods were different at the patient level. The subtraction approach was particularly useful in depicting false-positive and false-negative LM CE foci due to various reasons such as partial voluming of brain parenchyma and blood vessels (On-line Fig 2). The a posteriori unblinded concordance analysis of the 3 different assessment methods found 24 false-positive and 10 false-negative LM CE foci using the postcontrast-alone approach, and 7 false-positive, 17 true-negative, and 13 false-negative foci using the pre- and postcontrast approach. The false-positive LM CE foci characteristics included focal aspect and nodular shape and were located predominantly in the supratentorial sulci of the frontal and temporal lobes. Therefore, we recommend using the subtraction approach for easier detection of LM CE mimics, such as meningeal blood vessels, large subarachnoid veins, and high signal intensity areas in regions adja-

cent to dural venous sinuses and basal meninges related to CSF enhancement.<sup>9,10,12</sup>

In the present study of consecutive clinical routine patients with MS, we found that LM CE frequency was substantially lower compared with that in the previous studies.<sup>9,10,12,14</sup> With the pre-/postcontrast 3D-FLAIR subtraction approach, the LM CE frequency was 15.6% in patients with RRMS and 15.6% in those with SPMS, and we found only 1 patient with CIS presenting with LM CE foci. Consequently, we did not confirm findings from previous studies indicating that LM CE prevalence is significantly increased in patients with SPMS compared with those with RRMS.<sup>9,10</sup> Therefore, the frequency of LM CE foci may be substantially lower in clinical routine in patients with MS imaged on a 3T scanner using a pre-/postcontrast 3D-FLAIR subtraction approach.

On modern 1.5T and 3T scanners, the 3D-FLAIR acquisition takes approximately 5–7 minutes. Adding postcontrast 3D-FLAIR for the detection of LM CE increases the acquisition time in a clinical routine. The current Consortium of Multiple Sclerosis Centers MR imaging protocol guidelines include the 3D-FLAIR precontrast examination in core recommended sequences,<sup>19</sup> because it has been shown that 3D-FLAIR detects significantly more lesions in patients with MS compared with 2D T2-based pulse sequences, especially in the infratentorial and cortical regions.<sup>15,20,21</sup>

If the detection of LM CE foci is to become part of the clinical routine MR imaging reading assessment in MS, it should be done in the least amount of time possible and in the most accurate way. The subtraction approach had an approximately 18% shorter time for detection of LM CE foci with respect to the postcontrast-only approach and 31% shorter time compared with pre- and postcontrast-only approach, with an average of slightly above 2 minutes used per examination, including inspection of the source images. Patients with MS without LM CE foci could be identified in <1 minute using the subtraction approach without the use of the source images. We believe this is a reasonable amount of time to add to the reading burden of expert MS neuroimagers with high reproducibility among the raters. Most important, our findings suggest that the subtraction approach could be sufficiently accurate for fast screening of LM CE in clinical routine in patients

with MS. The allocated time measured just the reading component of pre-/postcontrast 3D-FLAIR subtraction images in all 3 orthogonal planes and did not take into account the running of the algorithm for creation of the images themselves. However, we anticipate that the algorithm applied in this study can be run fully automatically at the MR imaging scanner workstation or a console in <1 minute, producing corresponding per-slice images.

The strength of the study is the use of a large cohort of patients with MS consecutively enrolled in a clinical routine and a careful methodologic approach for the detection of LM CE foci. The limitation of the study includes lack of longitudinal serial imaging in these patients with MS, which is underway in our center. In addition, the subtraction approach for detection of LM CE should be also validated using cases without MS and independent MS cohorts in future studies.

## CONCLUSIONS

The frequency of LM CE foci is lower using the pre-/post-3D-FLAIR subtraction approach, compared with the postcontrast alone approach. No LM CE frequency differences were found between patients with RRMS and SPMS in a clinical routine. Use of subtraction imaging helped to avoid false-positive cases, decreased reading time, and increased the accuracy of LM CE foci detection in a clinical routine.

Disclosures: Robert Zivadinov—UNRELATED: Consultancy: Sanofi Genzyme, Novartis, EMD Serono; Grants/Grants Pending: Sanofi Genzyme, Novartis, IMS Health\*; Payment for Lectures Including Service on Speakers Bureaus: Sanofi Genzyme, Novartis, EMD Serono. Michael G. Dwyer—UNRELATED: Consultancy: Claret Medical; Grants/Grants Pending: Novartis.\* Bianca Weinstock-Guttman—UNRELATED: Board Membership: Biogen Idec, Teva Pharmaceutical Industries, EMD Serono, Sanofi Genzyme, Genentech, Novartis; Consultancy: Biogen Idec, Teva Pharmaceutical Industries, EMD Serono, Sanofi Genzyme, Genentech, Novartis; Grants/Grants Pending: Biogen Idec, Teva Pharmaceutical Industries, EMD Serono, Sanofi Genzyme, Genentech, Novartis\*; Payment for Lectures Including Service on Speakers Bureaus: Biogen, Teva Pharmaceutical Industries, Novartis, Genentech. David Hojnacki—UNRELATED: Consultancy: Biogen, Teva Pharmaceutical Industries, Genentech, Serono; Payment for Lectures Including Service on Speakers Bureaus: Biogen, Teva Pharmaceutical Industries, Genentech, Serono. \*Money paid to the institution.

## REFERENCES

- Popescu BF, Lucchinetti CF. **Meningeal and cortical grey matter pathology in multiple sclerosis.** *BMC Neurol* 2012;12:11 CrossRef Medline
- Magliozzi R, Howell O, Vora A, et al. **Meningeal B-cell follicles in secondary progressive multiple sclerosis associate with early onset of disease and severe cortical pathology.** *Brain* 2007;130:1089–104 Medline
- Magliozzi R, Howell OW, Reeves C, et al. **A gradient of neuronal loss and meningeal inflammation in multiple sclerosis.** *Ann Neurol* 2010;68:477–93 CrossRef Medline
- Serafini B, Rosicarelli B, Magliozzi R, et al. **Detection of ectopic B-cell follicles with germinal centers in the meninges of patients with secondary progressive multiple sclerosis.** *Brain Pathol* 2004;14:164–74 CrossRef Medline

- Lucchinetti CF, Popescu BF, Bunyan RF, et al. **Inflammatory cortical demyelination in early multiple sclerosis.** *N Engl J Med* 2011;365:2188–97 CrossRef Medline
- Choi SR, Howell OW, Carassiti D, et al. **Meningeal inflammation plays a role in the pathology of primary progressive multiple sclerosis.** *Brain* 2012;135:2925–37 CrossRef Medline
- Howell OW, Reeves CA, Nicholas R, et al. **Meningeal inflammation is widespread and linked to cortical pathology in multiple sclerosis.** *Brain* 2011;134:2755–71 CrossRef Medline
- Zurawski J, Lassmann H, Bakshi R. **Use of magnetic resonance imaging to visualize leptomeningeal inflammation in patients with multiple sclerosis: a review.** *JAMA Neurol* 2017;74:100–09 CrossRef Medline
- Absinta M, Vuolo L, Rao A, et al. **Gadolinium-based MRI characterization of leptomeningeal inflammation in multiple sclerosis.** *Neurology* 2015;85:18–28 CrossRef Medline
- Zivadinov R, Ramasamy DP, Vaneckova M, et al. **Leptomeningeal contrast enhancement is associated with progression of cortical atrophy in MS: a retrospective, pilot, observational longitudinal study.** *Mult Scler* 2017;23:1336–45 CrossRef Medline
- Xia Z, Steele SU, Bakshi A, et al. **Assessment of early evidence of multiple sclerosis in a prospective study of asymptomatic high-risk family members.** *JAMA Neurol* 2017;74:293–300 CrossRef Medline
- Absinta M, Cortese IC, Vuolo L, et al. **Leptomeningeal gadolinium enhancement across the spectrum of chronic neuroinflammatory diseases.** *Neurology* 2017;88:1439–44 CrossRef Medline
- Eisele P, Griebel M, Szabo K, et al. **Investigation of leptomeningeal enhancement in MS: a postcontrast FLAIR MRI study.** *Neurology* 2015;84:770–75 CrossRef Medline
- Harrison DM, Wang KY, Fiol J, et al. **Leptomeningeal enhancement at 7T in multiple sclerosis: frequency, morphology, and relationship to cortical volume.** *J Neuroimaging* 2017;27:461–68 CrossRef Medline
- Polak P, Magnano C, Zivadinov R, et al. **3D FLAIRE: 3D fluid attenuated inversion recovery for enhanced detection of lesions in multiple sclerosis.** *Magn Reson Med* 2012;68:874–81 CrossRef Medline
- Busse RF, Hariharan H, Vu A, et al. **Fast spin echo sequences with very long echo trains: design of variable refocusing flip angle schedules and generation of clinical T2 contrast.** *Magn Reson Med* 2006;55:1030–37 CrossRef Medline
- Jenkinson M, Bannister P, Brady M, et al. **Improved optimization for the robust and accurate linear registration and motion correction of brain images.** *Neuroimage* 2002;17:825–41 CrossRef Medline
- Zivadinov R, Heininen-Brown M, Schirda CV, et al. **Abnormal subcortical deep-gray matter susceptibility-weighted imaging filtered phase measurements in patients with multiple sclerosis: a case-control study.** *Neuroimage* 2012;59:331–39 CrossRef Medline
- Traboulsee A, Simon JH, Stone L, et al. **Revised Recommendations of the Consortium of MS Centers Task Force for a Standardized MRI Protocol and Clinical Guidelines for the Diagnosis and Follow-Up of Multiple Sclerosis.** *AJNR Am J Neuroradiol* 2016;37:394–401 CrossRef Medline
- Bink A, Schmitt M, Gaa J, et al. **Detection of lesions in multiple sclerosis by 2D FLAIR and single-slab 3D FLAIR sequences at 3.0 T: initial results.** *Eur Radiol* 2006;16:1104–10 CrossRef Medline
- Moraal B, Roosendaal SD, Pouwels PJ, et al. **Multi-contrast, isotropic, single-slab 3D MR imaging in multiple sclerosis.** *Eur Radiol* 2008;18:2311–20 CrossRef Medline

# Brain Injury Lesion Imaging Using Preconditioned Quantitative Susceptibility Mapping without Skull Stripping

 S. Soman,  Z. Liu,  G. Kim,  U. Nemeč,  S.J. Holdsworth,  K. Main,  B. Lee,  S. Kolakowsky-Hayner,  M. Selim,  A.J. Furst,  P. Massaband,  J. Yesavage,  M.M. Adamson,  P. Spincemallie,  M. Moseley, and  Y. Wang



## ABSTRACT

**BACKGROUND AND PURPOSE:** Identifying cerebral microhemorrhage burden can aid in the diagnosis and management of traumatic brain injury, stroke, hypertension, and cerebral amyloid angiopathy. MR imaging susceptibility-based methods are more sensitive than CT for detecting cerebral microhemorrhage, but methods other than quantitative susceptibility mapping provide results that vary with field strength and TE, require additional phase maps to distinguish blood from calcification, and depict cerebral microhemorrhages as bloom artifacts. Quantitative susceptibility mapping provides universal quantification of tissue magnetic property without these constraints but traditionally requires a mask generated by skull-stripping, which can pose challenges at tissue interphases. We evaluated the preconditioned quantitative susceptibility mapping MR imaging method, which does not require skull-stripping, for improved depiction of brain parenchyma and pathology.

**MATERIALS AND METHODS:** Fifty-six subjects underwent brain MR imaging with a 3D multiecho gradient recalled echo acquisition. Mask-based quantitative susceptibility mapping images were created using a commonly used mask-based quantitative susceptibility mapping method, and preconditioned quantitative susceptibility images were made using precondition-based total field inversion. All images were reviewed by a neuroradiologist and a radiology resident.

**RESULTS:** Ten subjects (18%), all with traumatic brain injury, demonstrated blood products on 3D gradient recalled echo imaging. All lesions were visible on preconditioned quantitative susceptibility mapping, while 6 were not visible on mask-based quantitative susceptibility mapping. Thirty-one subjects (55%) demonstrated brain parenchyma and/or lesions that were visible on preconditioned quantitative susceptibility mapping but not on mask-based quantitative susceptibility mapping. Six subjects (11%) demonstrated pons artifacts on preconditioned quantitative susceptibility mapping and mask-based quantitative susceptibility mapping; they were worse on preconditioned quantitative susceptibility mapping.

**CONCLUSIONS:** Preconditioned quantitative susceptibility mapping MR imaging can bring the benefits of quantitative susceptibility mapping imaging to clinical practice without the limitations of mask-based quantitative susceptibility mapping, especially for evaluating cerebral microhemorrhage-associated pathologies, such as traumatic brain injury.

**ABBREVIATIONS:** CMH = cerebral microhemorrhage; GRE = gradient recalled-echo; mQSM = mask-based QSM; pQSM = preconditioned QSM; QSM = quantitative susceptibility mapping; TBI = traumatic brain injury

Multiple diseases, including traumatic brain injury (TBI),<sup>1,2</sup> stroke,<sup>3,4</sup> hypertension, and cerebral amyloid angiopathy<sup>5</sup> require assessment of cerebral microhemorrhage (CMH) for diagnosis and/or management. However, the choice of neuroimag-

ing technique can provide very different assessments of CMH burden. While knowledge of CMH burden and distribution should inform risk stratification and treatment choices, variabil-

Received August 18, 2017; accepted after revision December 4.

From the Departments of Radiology (S.S., G.K., B.L.) and Neurology (M.S.), Beth Israel Deaconess Medical Center, Harvard Medical School, Boston, Massachusetts; Department of Biomedical Engineering (Z.L., Y.W.), Cornell University, New York, New York; Department of Biomedical Imaging and Image-Guided Therapy (U.N.), Medical University of Vienna, Vienna, Austria; Departments of Radiology (S.J.H., P.M., M.M.), Psychiatry and Behavioral Sciences (A.J.F., J.Y., M.M.A.), and Neurosurgery (M.M.A.), Stanford University, Stanford, California; Research Division, Defense and Veterans Brain Injury Center (K.M.), General Dynamics Health Solutions, Silver Spring, Maryland; Department of Rehabilitation Medicine (S.K.-H.), Icahn School of Medicine at Mount Sinai, New York, New York; Departments of Psychiatry (A.J.F., J.Y.) and Radiology (P.M.) and Defense and Veterans Brain Injury Center (M.M.A.),

VA Palo Alto Health Care System, Palo Alto, California; and Department of Radiology (P.S., Y.W.), Weil Cornell Medical College, New York, New York.

Paper previously presented, in part, at Annual Meeting of the American Society of Neuroradiology and the Foundation of the ASNR Symposium, April 22–27, 2017; Long Beach, California; and International Society for Magnetic Resonance in Medicine Annual Meeting and Exhibition, April 22–27, 2017; Honolulu, Hawaii.

This study was funded by the War Related Illness and Injury Study Center, National Institutes of Health ROI EB013443, ROI NS090464, ROI NS095562, ROI CA181566, and ROI CA178007.

Please address correspondence to Salil Soman, MD, Rosenberg B90A, 1 Deaconess Rd, Boston, MA 02215; e-mail: sal@alum.mit.edu

 Indicates open access to non-subscribers at [www.ajnr.org](http://www.ajnr.org)

<http://dx.doi.org/10.3174/ajnr.A5550>

**Table 1: Subject demographics across Ohio TBI Scores<sup>23</sup> (n = 56)**

Ohio TBI Score	Sex		Age (yr)			Blood on GRE	Nonvisualized Brain	
	Male	Female	Mean Age	SD	Age Range		on mQSM	on pQSM
All	34	22	42.1	14.42778	20–74	10	31	5
1 (none)	13	9	41.7	14.6878	20–74	1	13	3
2 (mild)	2	2	44.0	15.71623	27–58	1	3	0
3 (mild)	8	5	47.0	14.94434	30–71	4	8	1
4 (moderate)	2	1	45.7	13.50309	32–59	0	1	0
5 (severe)	9	5	37.9	13.96621	23–64	4	5	1
Correlation across TBI severity	$\chi^2 = 0.17, P = .98^a$		ANOVA $F(3,52) = 0.74, P = .53$			$P = .11^b$	$\chi^2 = 2.20, P = .53^a$	$P = .88^b$
Correlation with blood products on 3D GRE	$\chi^2 = 0.04, P = .86^a$		$P = .49^c$			–	$\chi^2 = 2.99, P = .08^a$	$P = .10^b$

<sup>a</sup>  $\chi^2$  test.<sup>b</sup> Fisher exact test.<sup>c</sup> Student *t* test.

ity in CMH assessment based on the choice of neuroimaging method produces uncertainty about how this information should be used to inform patient management.<sup>6</sup> This ambiguity signals the need for an easy-to-implement, sensitive, and specific method to identify CMHs.

Susceptibility-based (T2\*) MR imaging methods (2D gradient recalled-echo[GRE], 3D GRE, susceptibility-weighted imaging, quantitative susceptibility mapping [QSM]) are more sensitive than CT for CMH detection.<sup>7,8</sup> However, all these MR imaging CMH evaluation methods, other than QSM,<sup>9–13</sup> will depict CMHs as bloom artifacts instead of as actual lesion size.<sup>14</sup> They also have an appearance that varies on the basis of MR imaging field strength and scan parameters<sup>9,15–18</sup> and require an additional phase map to distinguish blood products (diamagnetic) from calcium<sup>19</sup> (paramagnetic). Also, QSM distinguishes calcium from blood products better than susceptibility-weighted imaging.<sup>20</sup> QSM estimates the intrinsic susceptibility distribution of tissue by deconvolving the blooming in the GRE phase.<sup>21</sup>

Most QSM methods, however, use a mask (mQSM) to remove the phase of low-magnitude signal to avoid singularities and streaking artifacts (mainly in the noise). The mask may either include high-susceptibility regions shown as hypointense blooming artifacts on GRE or mask out regions of brain parenchyma. Selecting a brain mask can be challenging, especially near the brain boundary, where large tissue-air or tissue-bone susceptibility differences can cause substantial signal loss on the magnitude images used to define the mask.<sup>21</sup> This signal loss can be made even worse when hemorrhage is near the boundary. Using a mask for mQSM that is too small can include noisy phase information and lead to streaking, while a mask that is too large results in nonvisualized brain. Erosion of the brain mask can especially prevent visualization of important structures at the brain boundaries. Although numerous skull-stripping algorithms can be applied to generate an optimal mask for any individual case, there is no one automated method that will uniformly generate the optimal mask for all cases. Even optimal masks can be made suboptimal after application of extreme intensity masking by some algorithms, which can lead to nonvisualized CMHs. These mask issues can result in variable portions of brain nonvisualization, impeding the application of mQSM methods in clinical practice.

A potential solution to this problem is application of the pre-conditioned QSM (pQSM) method with total field inversion,<sup>22</sup>

which produces whole-head quantitative susceptibility maps without skull-stripping, reduces the error propagation associated with imprecise background field removal, and suppresses streaking artifacts in intracerebral hemorrhage on QSM images.<sup>22</sup> pQSM calculates tissue-susceptibility values for the entire FOV (including the otherwise hypointense areas). We hypothesize that removing the need for a brain mask will enable pQSM imaging to generate robust brain susceptibility imaging, which can more reliably identify brain parenchyma and characterize CMHs relative to mQSM. To test this hypothesis, we evaluated the visualized brain parenchyma and lesions generated from a single multiecho 3D GRE MR image in a cohort of patients with TBI and controls, comparing the images of the resulting three 3D GRE magnitude images (each at a different TE), mQSM using a standard mask method,<sup>23</sup> and pQSM.

## MATERIALS AND METHODS

### Subjects

Under an institutional review board protocol approved by the VA Palo Alto Health Care System and Stanford University, subjects with a history of TBI and control subjects without TBI were recruited through the Santa Clara Valley Medical Center, VA Palo Alto Health Care System, and surrounding communities. All subjects were evaluated for a history of prior TBI using the Ohio State University Traumatic Brain Injury Identification Method score (Ohio TBI score), which was then used to classify subjects as having no, mild, moderate, or severe TBI.<sup>24</sup> Subjects also underwent neuroimaging.

A total of 81 subjects were recruited, of which only 63 subjects could tolerate the entire MR imaging protocol to undergo multiecho 3D GRE for QSM imaging. Of these 63 subjects, mQSM and pQSM images could only be produced for 56 subjects (89%) due to erroneous lines of *k*-space present in the raw data files. Subjects' ages, sex, and TBI demographic information are summarized in Table 1. There was no significant difference between non-TBI subjects and TBI subgroups (mild, moderate, or severe, as defined from the Ohio TBI score<sup>24</sup>) for age (1-way ANOVA,  $F(3,52) = 0.74, P = .53$ ) or sex ( $\chi^2 = 0.17, P = .98$ , Table 1).

### Image Acquisition

Images were obtained with a Discovery MR750 3T MR imaging scanner (GE Healthcare, Milwaukee, Wisconsin), using a 3D

multishot multiecho EPI acquisition (TR = 98 ms; echoes = 3; TE = 14.3–19.7/33.1–46.99/51.8–74.28 ms; matrix = 224 × 224; resolution = 1 × 1 × 1 mm<sup>3</sup>), and a 3D fast-spoiled gradient-recalled acquisition (TR/TE/TI = 9.5/3.8/900 ms, resolution = 1 × 1 × 1 mm<sup>3</sup>) using an 8-channel Signa head coil (GE Healthcare). Multicoil phase reconstruction was performed using the method of Bernstein et al.<sup>25</sup> Magnitude 3D GRE images were produced automatically with the MR imaging scanner. mQSM images were created with the MEDI toolbox using the default mask (genmask.m).<sup>23</sup> pQSM images were created using the method described by Liu et al.<sup>22,26</sup>

### Image Interpretation

The images derived from the 3D multiecho GRE (the three 3D GRE magnitude volumes—each at 1 of 3 TE values [TE = 14.3–19.7/33.1–46.99/51.8–74.28 ms], the mQSM, and pQSM) and the T1-weighted fast-spoiled gradient-recalled images were examined by a neuroradiologist and a radiology resident, evaluating the presence of lesions and absent/distorted brain parenchyma, blinded to patient TBI status. Images were reviewed in 4 sessions (the T1 images were available for all sessions): 1) the three 3D GRE magnitude volumes, 2) the three 3D GRE volumes and mQSM, 3) the three 3D GRE volumes and pQSM images, and 4) all images. For each subject, consensus reading by the neuroradiologist and radiology resident resulting in scores of yes or no were created for the image pair attributes listed in Tables 1 and 2.

**Table 2: 3D GRE, mQSM, and pQSM image review results (n = 56)**

Feature	Count	%
Blood products		
3D GRE	10	18
mQSM	4	7
pQSM	10	18
Nonvisualized brain tissue on		
mQSM, pQSM visible	31	55
mQSM and pQSM, less on pQSM	5	9
pQSM, mQSM visible	0	0
Pons probable artifacts, more visible on		
pQSM	6	11
mQSM	0	0

### Statistics

The Student *t* test, ANOVA, and  $\chi^2$  statistics with contingency tables were used to calculate statistical differences between groups on the following variables: age, sex, a history of TBI, blood on 3D GRE, and tissue missing on mQSM that was preserved on pQSM. The Fisher exact test was performed on the detection of blood on pQSM that was not seen on mQSM and blood on mQSM that was preserved on pQSM.

### RESULTS

Subjects with blood products did not show a significant difference from those without regarding age ( $P = .49$ ), sex ( $\chi^2 = 0.04, P = .86$ , Table 1), or TBI severity ( $P = .11$ ). Ten subjects demonstrated blood products on at least 1 of the three 3D GRE volumes in the occipital, temporal, parietal, or frontal lobes, as well as the basal ganglia or cerebellum (Figs 1–3). Nine of these 10 subjects had a history of TBI.

Of the 10 subjects with blood on a 3D GRE image, these cases had pQSM images depicting those lesions, but only 4 of these lesions were visible on the mQSM images, due to nonvisualized brain parenchyma, which was a statistically significant difference ( $P < .01$ ).

Thirty-one subjects (55%) demonstrated brain parenchyma (some containing lesions) preserved on pQSM but eroded on mQSM due to masking. Five subjects (9%) demonstrated areas of more nonvisualized brain parenchyma on mQSM compared with that same region on pQSM images ( $P = .88$ , Table 1 and Fig 3). In subjects in whom there was brain parenchyma nonvisualization on mQSM or pQSM, none demonstrated greater areas of nonvisualized brain parenchyma on pQSM relative to mQSM images. Overall, there was more brain parenchyma visualization on pQSM images compared with corre-

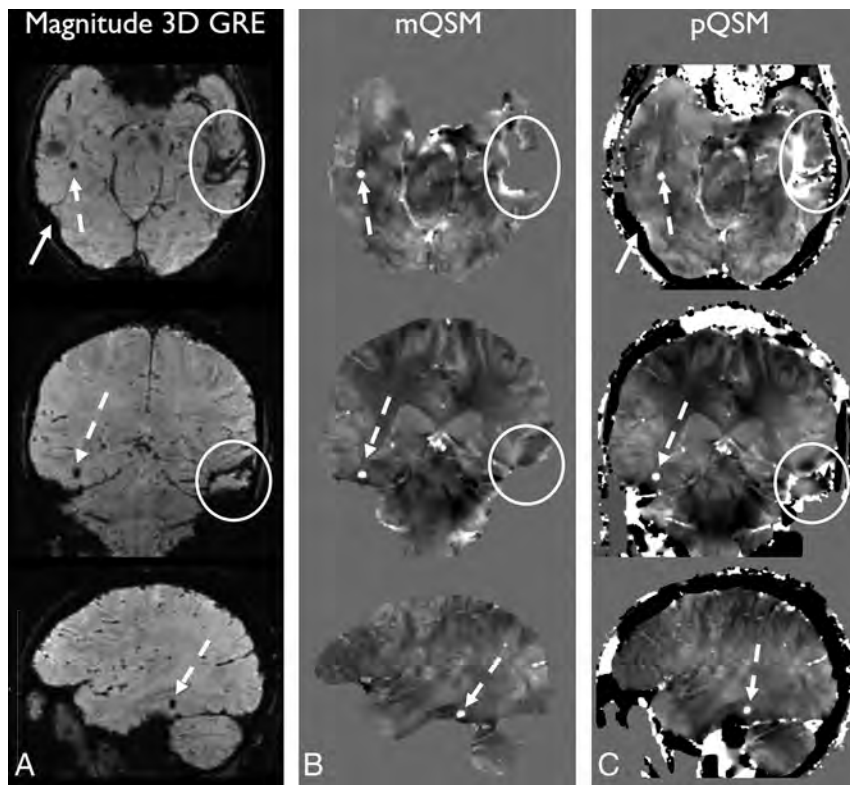


**FIG 1.** Paramagnetic right temporal hemorrhage is hypointense on magnitude 3D GRE (TE = 17.3 ms) (A) and hyperintense on mQSM (B) and pQSM (C) images (white dashed arrows). The diamagnetic calcification in bone (white solid arrows) is mostly hypointense on 3D GRE (A) and pQSM (C) and not present on mQSM (B) secondary to masking. Some areas of hyperintensity within the bone may represent diamagnetic structures, such as veins or artifacts. Left temporal lobe parenchyma next to hemorrhage is eroded on the mQSM (B), but preserved on magnitude and pQSM (C) images (white circles).

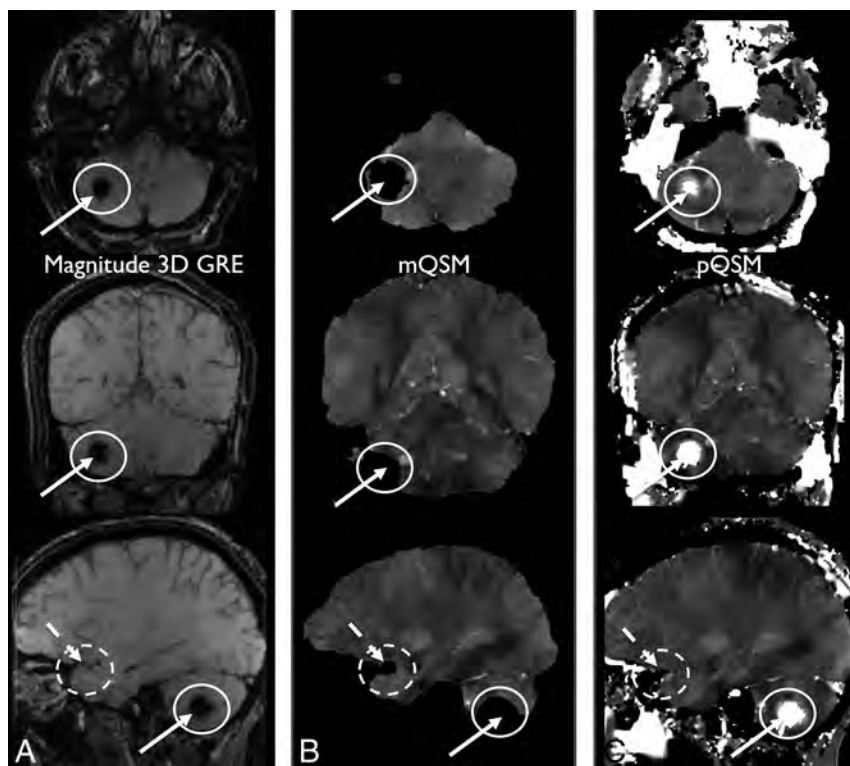


**FIG 2.** Right cerebellar hemorrhage is hypointense on magnitude 3D GRE (TE = 14.3 ms) (A). This part of the cerebellar parenchyma has been eroded on mQSM (B) and so is not visible due to masking. The same anatomy is preserved on pQSM (C), and hemorrhage is demonstrated (white solid arrows and circles). Additionally, an absent section of the right temporal brain parenchyma on mQSM (B) is partially preserved on the pQSM (C) relative to the 3D GRE image (A) (white dashed arrows and dashed circles). Note areas of black pixels within the white dashed circles on the mQSM and pQSM images (B and C) that correspond to brain tissue seen on 3D GRE image (A) indicate areas of nonvisualized brain.



**FIG 3.** Magnitude 3D GRE (TE = 14.3 ms) (A), mQSM (B), and pQSM (C) images demonstrating partial pQSM image depiction relative to mQSM. An area of the right inferior frontal lobe present on the 3D GRE image is present on the pQSM image and absent on mQSM image (black solid arrows). An adjacent inferior frontal lobe is present on the 3D GRE image, distorted on the pQSM image, and absent on the mQSM (white dashed arrows).

sponding mQSM images. The differences in parenchymal depiction on pQSM compared with mQSM were statistically significant ( $P < .01$ ). There was not a statistically significant difference in age ( $P = .76$ ), sex ( $\chi^2 = 0.04, P = .84$ ), TBI severity ( $\chi^2 = 2.20, P = .5$ , Table 1), or the presence of blood products on 3D GRE ( $\chi^2 = 2.99, P = .08$ , Table 1) for cases demonstrating nonvisualized brain parenchyma on mQSM relative to cases that did not. Six subjects (11%) demonstrated mQSM and pQSM pons hypointensity with no corresponding 3D GRE finding suggestive of artifacts, all larger on pQSM than on corresponding mQSM images (Fig 4).

## DISCUSSION

This report shows that pQSM can depict more brain parenchyma than masked-based QSM using the same acquisition data. Com-

paring these images generated from a single multiecho 3D GRE scan allowed evaluation of imaging features while holding other acquisition parameters constant (eg, field strength, flip angle, sampled TEs, and so forth.). Additionally, our results demonstrate that some of these areas of brain visible on pQSM but not present on mQSM contained clinically relevant pathology, such as CMHs. This difference in brain depiction is consistent with the expectation that variations in skull-stripping performance and variations of intensity that threshold-based masking algorithms use, especially near hemorrhages (as demonstrated in Figs 2 and 3), can result in areas of nonvisualized brain on mQSM methods. This contrasts with pQSM, which uses magnitude information to differentiate weak from strong sources of susceptibility over the entire head for reconstruction. Instead of splitting the QSM problem into background field removal and local field fitting (in which errors are propagated from the first into the second), preconditioned QSM solves them together. Demonstration of better preservation of brain parenchyma in pQSM compared with mQSM in subjects was independent of age, sex, and the presence of hemorrhage or history of prior trauma; this finding suggests generalizability across patients. The preservation of anatomic landmarks, such as skull margins, on pQSM images also has the potential to aid in clinical interpretation. The feature of preserving skull and scalp in pQSM may also allow better depiction of calvarial and skin masses if challenges regarding scalp SNR and implementation of a robust water/fat separation algorithm can be managed.

Like other neuroimaging studies evaluating cerebral microhemorrhage presence, this study used an accepted GRE imaging sequence as the reference standard for CMH presence.<sup>8,15,27,28</sup> Here, the 3 echoes of the 3D GRE magnitude images were used as ground truth for the presence of CMHs, given that direct pathologic correlation was not possible (as is the case in many clinical imaging studies). Across the 3 TE volumes, more subtle susceptibility changes are likely to be visible at higher TEs, but often with corresponding increased artifacts. The three 3D GRE magnitude whole-brain volumes were each interpreted as they would be clinically for the presence of a lesion across the 3 TEs. However, in routine clinical practice, only 1 volume would likely be reviewed, leaving the possibility that smaller or subtler CMHs may have

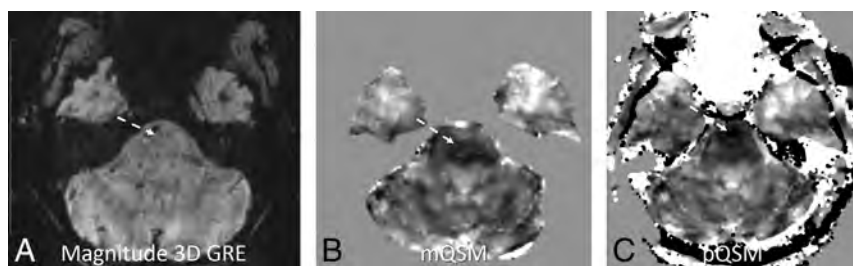


**FIG 4.** pQSM (C) demonstrates worse nonspecific diffuse low signal in the pons compared with mQSM (B), with no corresponding abnormality on the magnitude 3D GRE (TE = 41.8 ms) image (A) (white dashed arrows). Note that areas of hypointensity are in different positions within the pons.

been visible at a longer TE, which is not the case for QSM-based images. Also, reviewing those magnitude images without phase maps would leave room for doubt as to whether the lesions were blood products or calcification, as is often the case in current clinical practice. Because the pQSM images did not show any lesions that did not appear on at least 1 of the 3D GRE images, no false-positives were encountered.

While our work found pQSM to always depict more brain parenchyma than mQSM, there was still omission of some brain areas on pQSM relative to at least 1 of the 3 TE 3D GRE images. These areas of pQSM failure may be related to the magnitude image of the first echo (14.3–19.7 ms in this study) not being sufficiently short, impacting the ability of pQSM to differentiate strong and weak sources. At this level of first TE, the cortex might already experience  $R2^*$  decay due to field inhomogeneity at air/tissue interfaces. QSM may only reduce blooming artifacts to the amount in the first echo. Future work should study the ability of a shorter first TE to remedy this problem. The instances in which pQSM demonstrates brain parenchyma more than mQSM, but with some distortion or some nonvisualized brain tissue, do raise the concern about whether it is better to not demonstrate tissue at all rather than show it with distortion. Future work incorporating lower TE information should consider this question as well.

Overall, the osseous structures on QSM appear hypointense, compatible with paramagnetic calcification. However, some hyperintense areas in bone were noted (Figs 1–4). These findings may be related to intraosseous venous structures or artifacts (because, in the case of skull bone, there is little local phase signal to aid in identifying its susceptibility value). Although the current implementation of pQSM is not optimized for bone, improvement could be made by acquiring the first echo at an earlier TE, similar to acquisitions such as ultrashort TE, to more reliably characterize bone properties.

This study did not evaluate the quantitative aspects of pQSM. Although QSM is a quantitative method, current clinically used susceptibility-based neuroimaging methods are interpreted solely on a qualitative basis, assessing hypointense foci, with the occasional addition of phase maps to distinguish blood from calcification. Future work could assess the additional clinical value of mQSM/pQSM quantitative lesion analysis.

Limitations of this study include the small sample size of patients with hemorrhage. While this work did not clearly demonstrate instances of CMHs visible on pQSM or mQSM that were not seen on 3D GRE images, only 10 (18%) subjects had CMHs,

despite having 34 subjects (61%) with a history of TBI. Future studies would benefit from larger subject cohorts, with more subjects demonstrating susceptibility-based pathologies, such as CMHs. An additional limitation is that categorization of brain loss in the current study was performed by only 2 readers providing a consensus read, and subsequent studies would benefit from using an automated or multireader evaluation. The 6 cases (11%) in which pQSM demonstrated greater pontine tissue contrast relative to mQSM, with no definite cor-

responding anatomic or pathologic finding on 3D GRE images (Fig 4), also represent an important area for future evaluation. Further investigation of pQSM specificity for CMH evaluation would also advance defining the clinical role that pQSM can play in managing patients in whom identifying CMHs is clinically relevant.

## CONCLUSIONS

pQSM can improve the evaluation of CMH-associated pathologies, such as TBI.

Disclosures: Stephanie Kolakowsky-Hayner—UNRELATED: Consultancy: Gerson Lehrman Group, Comments: various consulting calls related to brain injury rehabilitation; Employment: Ichan School of Medicine at Mount Sinai, Comments: current employer; Grants/Grants Pending: National Institute on Disability, Independent Living, and Rehabilitation Research, Comments: TBI Model Systems Grant, Spinal Cord Injury Model Systems Grant, Spinal Cord Injury Model Systems Collaborative Grant\*; Payment for Lectures Including Service on Speakers Bureaus: Brain Injury Association of Virginia, Comments: stipend for keynote; Royalties: Lash and Associates, Comments: Tip Card Royalties; Travel/Accommodations/Meeting Expenses Unrelated to Activities Listed: Paralyzed Veterans of America, Comments: conference scholarship. Maheen M. Adamson—RELATED: Grant: VA Office of Public Health (War Related Illness and Injury Study Center)\*; Support for Travel to Meetings for the Study or Other Purposes: VA Office of Public Health (War Related Illness and Injury Study Center)\*. Pascal Spincemallie—RELATED: Grant: National Institutes of Health, Comments: R01CA181566, includes salary support\*; Support for Travel to Meetings for the Study or Other Purposes: National Institutes of Health, Comments: R01CA181566\*; UNRELATED: Patents (Planned, Pending or Issued): US 8781197\*. Yi Wang—RELATED: Grant: National Institutes of Health, Comments: R01CA178007, R01NS090464, R01NS095562\*; UNRELATED: Patents (Planned, Pending or Issued): Cornell University, Comments: I am one of the inventors on QSM technology\*; Stock/Stock Options: Medimagetric, Comments: Medimagetric is working with Cornell on commercializing QSM technology.\* Magdy Selim—UNRELATED: Grants/Grants Pending: National Institute of Neurological Disorders and Stroke, American Heart Association\*; Royalties: Oxford University Press, Cambridge University Press. \*Money paid to the institution.

## REFERENCES

1. Xi G, Keep RF, Hoff JT. **Mechanisms of brain injury after intracerebral haemorrhage.** *Lancet Neurol* 2006;5:53–63 CrossRef Medline
2. Greenberg SM, Vernooij MW, Cordonnier C, et al; Microbleed Study Group. **Cerebral microbleeds: a guide to detection and interpretation.** *Lancet Neurol* 2009;8:165–74 CrossRef Medline
3. Akoudad S, Portegies ML, Koudstaal PJ, et al. **Cerebral microbleeds are associated with an increased risk of stroke: the Rotterdam Study.** *Circulation* 2015;132:509–16 CrossRef Medline
4. Charidimou A, Kakar P, Fox Z, et al. **Cerebral microbleeds and recurrent stroke risk: systematic review and meta-analysis of prospective ischemic stroke and transient ischemic attack cohorts.** *Stroke* 2013;44:995–1001 CrossRef Medline
5. Mehndiratta P, Manjila S, Ostergard T, et al. **Cerebral amyloid angi-**

- opathy-associated intracerebral hemorrhage: pathology and management. *Neurosurg Focus* 2012;32:E7 CrossRef Medline
6. Jouvent E, Puy L, Chabriat H. **Cerebral microhemorrhages: significance, associations, diagnosis, and treatment.** *Curr Treat Options Neurol* 2016;18:35 CrossRef Medline
  7. Mittl RL, Grossman RI, Hiehle JF, et al. **Prevalence of MR evidence of diffuse axonal injury in patients with mild head injury and normal head CT findings.** *AJNR Am J Neuroradiol* 1994;15:1583–89 Medline
  8. Kidwell CS, Chalela JA, Saver JL, et al. **Comparison of MRI and CT for detection of acute intracerebral hemorrhage.** *JAMA* 2004;292:1823–30 CrossRef Medline
  9. de Rochefort L, Liu T, Kressler B, et al. **Quantitative susceptibility map reconstruction from MR phase data using Bayesian regularization: validation and application to brain imaging.** *Magn Reson Med* 2010;63:194–206 CrossRef Medline
  10. Haacke EM, Tang J, Neelavalli J, et al. **Susceptibility mapping as a means to visualize veins and quantify oxygen saturation.** *J Magn Reson Imaging* 2010;32:663–76 CrossRef Medline
  11. Liu T, Xu W, Spincemaille P, et al. **Accuracy of the morphology enabled dipole inversion (MEDI) algorithm for quantitative susceptibility mapping in MRI.** *IEEE Trans Med Imaging* 2012;31:816–24 CrossRef Medline
  12. Schweser F, Sommer K, Deistung A, et al. **Quantitative susceptibility mapping for investigating subtle susceptibility variations in the human brain.** *Neuroimage* 2012;62:2083–100 CrossRef Medline
  13. Neelavalli J, Cheng YC, Jiang J, et al. **Removing background phase variations in susceptibility-weighted imaging using a fast, forward-field calculation.** *J Magn Reson Imaging* 2009;29:937–48 CrossRef Medline
  14. Liu T, Surapaneni K, Lou M, et al. **Cerebral microbleeds: burden assessment by using quantitative susceptibility mapping.** *Radiology* 2012;262:269–78 CrossRef Medline
  15. Nandigam RN, Viswanathan A, Delgado P, et al. **MR imaging detection of cerebral microbleeds: effect of susceptibility-weighted imaging, section thickness, and field strength.** *AJNR Am J Neuroradiol* 2009;30:338–43 Medline
  16. Soman S, Bregni JA, Bilgic B, et al. **Susceptibility-based neuroimaging: standard methods, clinical applications, and future directions.** *Curr Radiol Rep* 2017;5 pii: 11 CrossRef Medline
  17. Schweser F, Deistung A, Lehr BW, et al. **Differentiation between diamagnetic and paramagnetic cerebral lesions based on magnetic susceptibility mapping.** *Med Phys* 2010;37:5165–78 CrossRef Medline
  18. Li J, Chang S, Liu T, et al. **Reducing the object orientation dependence of susceptibility effects in gradient echo MRI through quantitative susceptibility mapping.** *Magn Reson Med* 2012;68:1563–69 CrossRef Medline
  19. Chen W, Zhu W, Kovanlikaya I, et al. **Intracranial calcifications and hemorrhages: characterization with quantitative susceptibility mapping.** *Radiology* 2014;270:496–505 CrossRef Medline
  20. Ciraci S, Gumus K, Doganay S, et al. **Diagnosis of intracranial calcification and hemorrhage in pediatric patients: comparison of quantitative susceptibility mapping and phase images of susceptibility-weighted imaging.** *Diagn Interv Imaging* 2017;98:707–14 CrossRef Medline
  21. Wang Y, Liu T. **Quantitative susceptibility mapping (QSM): decoding MRI data for a tissue magnetic biomarker.** *Magn Reson Med* 2015;73:82–101 CrossRef Medline
  22. Liu Z, Kee Y, Zhou D, et al. **Preconditioned total field inversion (TFI) method for quantitative susceptibility mapping.** *Magn Reson Med* 2017;78:303–15 CrossRef Medline
  23. Liu J, Liu T, de Rochefort L, et al. **Morphology enabled dipole inversion for quantitative susceptibility mapping using structural consistency between the magnitude image and the susceptibility map.** *Neuroimage* 2012;59:2560–68 CrossRef Medline
  24. Rapp PE, Rosenberg BM, Keyser DO, et al. **Patient characterization protocols for psychophysiological studies of traumatic brain injury and post-TBI psychiatric disorders.** *Front Neurol* 2013;4:91 CrossRef Medline
  25. Bernstein MA, Grgic M, Brosnan TJ, et al. **Reconstructions of phase contrast, phased array multicoil data.** *Magn Reson Med* 1994;32:330–34 CrossRef Medline
  26. Liu Z, Wen Y, Spincemaille P, et al. **Optimization of preconditioned total field inversion for whole head QSM and cardiac QSM.** In: *Proceedings of the International Society for Magnetic Resonance in Medicine Annual Meeting and Exhibition*, Honolulu, Hawaii. April 22–27, 2017
  27. Vernooij MW, Ikram MA, Wielopolski PA, et al. **Cerebral microbleeds: accelerated 3D T2\*-weighted GRE MR imaging versus conventional 2D T2\*-weighted GRE MR imaging for detection.** *Radiology* 2008;248:272–77 CrossRef Medline
  28. Soman S, Holdsworth SJ, Barnes PD, et al. **Improved T2\* imaging without increase in scan time: SWI processing of 2D gradient echo.** *AJNR Am J Neuroradiol* 2013;34:2092–97 CrossRef Medline

# Utility of Repeat Head CT in Patients with Blunt Traumatic Brain Injury Presenting with Small Isolated Falcine or Tentorial Subdural Hematomas

K.K. Devulapalli, J.F. Talbott, J. Narvid, A. Gean, B. Rehani, G. Manley, A. Uzelac, E. Yuh, and M.C. Huang

## ABSTRACT

**BACKGROUND AND PURPOSE:** In blunt traumatic brain injury with isolated falcotentorial subdural hematoma not amenable to neurosurgical intervention, the routinely performed, nonvalidated practice of serial head CT scans frequently necessitates increased hospital resources and exposure to ionizing radiation. The study goal was to evaluate clinical and imaging features of isolated falcotentorial subdural hematoma at presentation and short-term follow-up.

**MATERIALS AND METHODS:** We performed a retrospective analysis of patients presenting to a level 1 trauma center from January 2013 to March 2015 undergoing initial and short-term follow-up CT with initial findings positive for isolated subdural hematoma along the falx and/or tentorium. Patients with penetrating trauma, other sites of intracranial hemorrhage, or depressed skull fractures were excluded. Patient sex, age, Glasgow Coma Scale score, and anticoagulation history were obtained through review of the electronic medical records.

**RESULTS:** Eighty patients met the inclusion criteria (53 males; 27 females; median age, 61 years). Of subdural hematomas, 57.1% were falcine, 33.8% were tentorial, and 9.1% were mixed. The mean initial Glasgow Coma Scale score was 14.2 (range, 6–15). Isolated falcotentorial subdural hematomas were small (mean, 2.8 mm; range, 1–8 mm) without mass effect and significant change on follow-up CT (mean, 2.7 mm; range, 0–8 mm;  $P = .06$ ), with an average follow-up time of 10.3 hours (range, 3.9–192 hours). All repeat CTs demonstrated no change or decreased size of the initial subdural hematoma. No new intracranial hemorrhages were seen on follow-up CT.

**CONCLUSIONS:** Isolated falcotentorial subdural hematomas in blunt traumatic brain injury average 2.8 mm in thickness and do not increase in size on short-term follow-up CT. Present data suggest that repeat CT in patients with mild traumatic brain injury with isolated falcotentorial subdural hematoma may not be necessary.

**ABBREVIATIONS:** GCS = Glasgow Coma Scale; SDH = subdural hematoma; TBI = traumatic brain injury

Traumatic brain injury (TBI) is a common neurologic injury affecting 1.7 million Americans each year.<sup>1</sup> Up to 30% of all patients with TBI develop acute subdural hematomas (SDHs), with a higher prevalence in those patients sustaining more severe injuries.<sup>2–4</sup> While the relative distribution of SDH by location has not been well-studied, 1 retrospective series of 646 patients found 73.9% of SDHs located along the cerebral convexity, whereas 14%, and 11% were falcine or tentorial, respectively.<sup>5</sup> Convexity

SDH is often accompanied by other intracranial injuries and more frequently requires operative intervention.<sup>6,7</sup> Little, however, has been reported regarding the natural history of isolated falcine and tentorial SDH. Several reported studies suggest that these categorizations of SDH tend to occur in isolation with mild TBI and can be managed nonoperatively.<sup>5,8,9</sup>

Noncontrast CT remains an essential imaging technique in the assessment of TBI, given its sensitivity in the detection of acute intracranial hemorrhage. Many patients experiencing convexity SDH in the setting of TBI undergo initial CT in addition to repeat evaluations. In the absence of specific guidelines and data on falcine and tentorial SDH, these patients also often undergo repeat noncontrast head CT evaluation. Given the paucity of data on falcine and tentorial SDH in TBI, the purpose of this study was to evaluate clinical and imaging features of isolated falcine and tentorial SDH at presentation and short-term follow-up. We hypothesized that in this patient population, repeat imaging demon-

Received May 4, 2017; accepted after revision November 30.

From the Department of Radiology and Biomedical Imaging (K.K.D., J.F.T., J.N., A.G., B.R., A.U., E.Y.), University of California, San Francisco and Zuckerberg San Francisco General Hospital, San Francisco, California; Department of Neurological Surgery (G.M., M.C.H.), Zuckerberg San Francisco General Hospital, San Francisco, California; and Department of Neurological Surgery (J.F.T., G.M., E.Y., M.C.H.), Brain and Spinal Injury Center, San Francisco, California.

Please address correspondence to Jason Talbott, MD, PhD, Department of Radiology and Biomedical Imaging, University of California, San Francisco, 400 Parnassus Ave, San Francisco, CA 94110; e-mail: Jason.talbott@ucsf.edu

<http://dx.doi.org/10.3174/ajnr.A5557>

strates no significant change from baseline and may be of little if any clinical utility.

## MATERIALS AND METHODS

A retrospective analysis of the PACS data base of adult patients presenting to a level 1 trauma center between January 2013 and March 2015 who underwent CT within 24 hours of presentation to the emergency department was performed. Imaging reports were queried with 4 separate searches using the words “subdural hematoma” in conjunction with the terms “falx,” “falxine,” “tentorium,” and “tentorial.” Patients with other sites of intracranial hemorrhage, brain contusion, or depressed skull fractures were excluded. Additionally, patients were excluded if there was no history of TBI. Finally, patients were excluded if a repeat CT scan was not performed within 7 days of emergency department presentation to exclude potential confounding repeat trauma. Clinical information, including sex, age, and history of anticoagulation; Glasgow Coma Scale (GCS) score at presentation and discharge; international normalized ratio; platelet count; and admission level of care was obtained through a review of electronic medical records. Mild TBI was defined as a GCS score of 13–15 on presentation. The Zuckerberg San Francisco General Hospital institutional review board approved this study with a waiver of informed consent.

All imaging was assessed by reviewers K.K.D. (fourth-year radiology resident) and J.F.T. (subspecialty trained and board-certified neuroradiologist with 4 years of attending experience). The thickest dimension of the SDH measured perpendicular to the plane of the tentorium and/or falx on initial and repeat head CT as evaluated in the axial, sagittal, and coronal planes was measured. Hemorrhage location was categorized as falxine, tentorial, or falcotentorial on the basis of location on the initial CT scan. (Figs 1 and 2).

Outcome measures included the number of patients with an increase in size of the SDH on repeat imaging and the difference in mean SDH size between the initial and repeat scans. Descriptive statistics of continuous and categorical variables in addition to comparative analysis of means using a paired sample *t* test were performed using JASP, Version 0.8.0.1 ([www.jasp-stats.org](http://www.jasp-stats.org)). *P* < .05 was considered statistically significant.

## RESULTS

According to an internal Department of Neurosurgery data base maintained at our institution, the neurosurgery service evaluated 1798 cases of TBI. Of these, 1414 had a GCS score of  $\geq 13$ , one hundred forty-five had a GCS score of 9–12, and 239 had a GCS score of  $\leq 8$ . Of 98 patients identified in our PACS query with imaging reports of falxine and/or tentorial subdural hematomas, 80 adult patients were identified as having isolated falxine or tentorial SDH with repeat imaging performed within 7 days of the initial presentation. Eleven patients were excluded due to lack of follow-up imaging, 4 patients were excluded because of multi-compartmental intracranial hemorrhage, 2 patients were excluded on the basis of equivocal findings for hemorrhage on initial CT, and 1 patient was excluded secondary to an equivocal history of TBI.

Demographic and clinical data are presented in Table 1. The

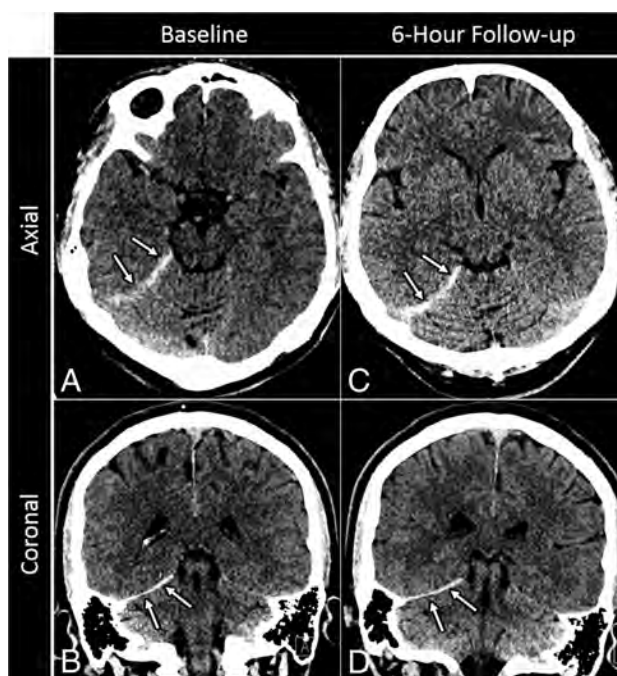


**FIG 1.** Sample isolated tentorial SDH. A 78-year-old man who presented after a fall. Baseline axial (A) and coronal (B) images from a noncontrast head CT reveal a small, 3-mm-thick acute subdural hematoma along the right tentorium (arrows) without associated mass effect. Axial (C) and coronal (D) images from a noncontrast follow-up CT performed 6 hours later reveal no new hemorrhage or interval change in size of the initial tentorial SDH (arrows).

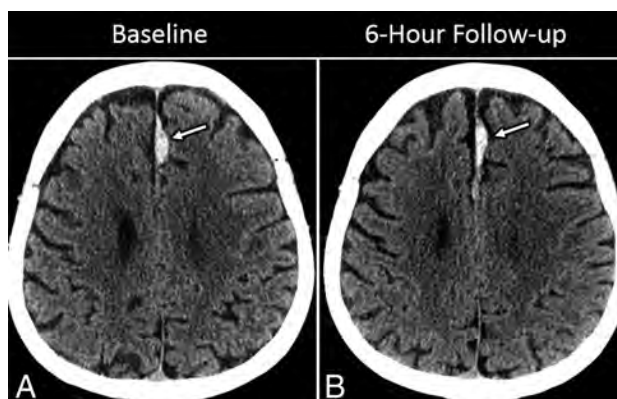


**FIG 2.** Sample isolated falxine SDH. A 65-year-old man with headache after a fall. Axial image (A) from an initial noncontrast head CT shows a lobulated and relatively focal acute high-density SDH along the left side of the anterior falx (arrow). On follow-up CT (B), there has been some mild local redistribution of acute SDH without significant interval change in the overall size or maximal thickness of the hematoma (arrow).

median age was 61.0 years, with a male predominance (66.3%). Seventy-four patients (92.5%) presented with an initial GCS score of 13–15, with an initial mean GCS score of 14.2 (range, 6–15). The mean discharge GCS score was 14.9 (range, 13–15). Overall, 69 patients (86.3%) were admitted to the hospital for SDH management. All patients were managed nonoperatively.

Six patients (7.5%) were anticoagulated, and an additional 10 (12.5%) were on antiplatelet therapy. The average international normalized ratio for anticoagulated patients was  $2.9 \pm 1.1$  (range, 1.5–4.9).

**Table 1: Patient characteristics**

Variable	
Age (median) (range) (yr)	61 (18–97)
Male/female	53:27
INR (mean) (range)	
All patients with INR within 24 hr of injury ( <i>n</i> = 78)	1.18 (0.8–4.9)
All anticoagulated patients ( <i>n</i> = 6)	2.92 (1.5–4.9)
Platelet count (mean) (range)	234.2 (83–437)
Initial GCS score (mean) (range)	14.2 (6–15.0)
GCS 13–15	74
GCS ≤12	6
Anticoagulation (No.)	
Warfarin (Coumadin)	5
Rivaroxaban	1
Antiplatelet therapy (No.)	
Aspirin	7
Clopidogrel	3
Disposition (No.)	
Discharged	11
Neurologic ICU	36
Other service	33

**Note:**—INR indicates international normalized ratio; ICU, intensive care unit.

**Table 2: Imaging data**

Variable	No.
SDH location	
Falcine	47 (57.1%)
Tentorial	26 (33.8%)
Falcotentorial	7 (9.1%)
Time interval from initial to repeat CT (mean) (range) (hr)	10.3 (3.9–192)
SDH expansion	
Yes	0
No	80
SDH size (mean) (range) (mm)	
Initial	2.8 ± 1.6 (1–8)
Follow-up	2.7 ± 1.6 (0–8)

The average time between the initial and repeat examinations was 10.3 hours (Table 2). All 80 patients (100%) experienced either no change or a decrease in size of the SDH on repeat imaging. There was no statistically significant difference in average SDH size between the initial and follow-up imaging (2.7 versus 1.6 mm, *P* = .17). Subgroup analysis of 69 patients with mild TBI also did not yield any statistically significant difference in the mean SDH size between initial and follow-up imaging (2.5 versus 2.4 mm, *P* = .12). No significant difference was noted between the mean SDH size between initial and follow-up imaging in 6 patients with a GCS score of <13 (2.5 versus 2.5 mm).

A single patient with mild TBI experienced clinical deterioration after initial head CT related to polytrauma. This 77-year-old woman was admitted following pedestrian-versus-automobile injury with a GCS score of 14 in the field and 15 on the initial emergency department assessment. The initial head CT showed a 4-mm isolated falcine SDH without additional acute findings. This patient also had multiple rib fractures and became acutely hypotensive (blood pressure equal to 84 systolic and 51 diastolic) in the emergency department after the initial head CT, with a significant drop in hematocrit secondary to hemothorax (28.7% compared with 37.4% on admission), ultimately requiring intubation and chest tube placement. Subsequent repeat head CT demonstrated a temporal contusion and subarachnoid hemor-

rhage, which was unchanged on subsequent head CT performed 6 hours later. This patient was managed nonoperatively and discharged after a 7-day hospitalization without further imaging.

## DISCUSSION

Our findings demonstrate that isolated falcine and tentorial SDHs tend to be small (mean size, 2.8 mm thick) and do not increase on repeat CT examinations. To the authors' knowledge, this is the largest study to date to assess short-term repeat imaging in patients with isolated falcine or tentorial SDH.

Most published literature regarding isolated falcine and tentorial SDH is limited to case reports and series,<sup>10–13</sup> except for 2 relatively recent retrospective studies. Sweis et al<sup>8</sup> reported clinical features and outcomes of 27 patients with isolated falcine or tentorial SDH. They reported favorable clinical outcomes without short hospital stays and no need for surgical intervention. A more recent study by Howard et al<sup>9</sup> reported both imaging and clinical outcomes of 65 patients with isolated falcine and tentorial SDH, noting no significant change in SDH size on repeat imaging. Present data build on these studies and further support the conclusion that repeat CT in patients with TBI with isolated falcine or tentorial SDH may not be necessary.

There are several limitations to the current study. First, the retrospective approach may subject the current analysis to inherent observation bias. Second, only 6 patients in the current analysis presented with a GCS score of <13, which may make the overall results less generalizable to this subgroup. Finally, the cohort studied includes only 16 patients receiving antiplatelet and/or anticoagulation medication, of whom 6 patients received anticoagulation with an average international normalized ratio of 2.9. Howard et al<sup>9</sup> also found similar findings of lack of SDH expansion in 12 patients receiving antiplatelet and/or anticoagulation medication. Sweis et al<sup>8</sup> reported no change in clinical outcomes in 3 patients with isolated falcotentorial SDH receiving warfarin anticoagulation. Additional studies with significantly larger numbers of anticoagulated patients are needed to more conclusively define the natural history of isolated falcine and tentorial SDH in patients with a history of anticoagulation or coagulopathy and to inform recommendations regarding repeat imaging in this subgroup of patients.

## CONCLUSIONS

Our study suggests that most patients with blunt TBI, especially those with mild TBI presenting with isolated tentorial or falcine SDH, may not require routine repeat head CT examinations in the absence of clinical deterioration. Repeat examinations in this group of patients may result in unnecessary cost and increased length of hospital stay. The decision to repeat imaging should be based on clinical suspicion of worsening hemorrhage, with repeat imaging being reserved for those patients with new focal neurologic deficits, acute changes in mental status, or other complications of polytrauma such as hypotension.

**Disclosures:** Geoff Manley—UNRELATED: Grant: National Institutes of Health and Department of Defense, Comments: research funding for traumatic brain injury studies.\* Jason Talbott—UNRELATED: Consultancy: StemCells Inc, Comments: member of data-monitoring committee for stem cell clinical trial. This study has

concluded, and I am no longer involved; *Expert Testimony*: Tindall Bennett and Shoup. \*Money paid to the institution.

## REFERENCES

1. Wintermark M, Sanelli PC, Anzai Y, et al. **Imaging evidence and recommendations for traumatic brain injury: advanced neuro- and neurovascular imaging techniques.** *AJNR Am J Neuroradiol* 2015;36:E1–11 CrossRef Medline
2. Massaro F, Lanotte M, Faccani G, et al. **One hundred and twenty-seven cases of acute subdural haematoma operated on: correlation between CT scan findings and outcome.** *Acta Neurochir (Wien)* 1996;138:185–91 CrossRef Medline
3. McKhann GM II, Copass MK, Winn RH. **Prehospital care of the head-injured patient.** In: Narayan RK, Wilberger JE, Povlishock JT, ed. *Neurotrauma*. New York: McGraw-Hill; 1996:103–18
4. Meyer SH, Chestnut M. **Posttraumatic extra-axial mass lesions: subdural and extradural hematoma.** In: Tindall GT, Cooper PR, Barrow DL, eds. *The Practice of Neurosurgery*. Baltimore: Williams and Wilkins; 1996:1443–60
5. Bajsarowicz P, Prakash I, Lamroueux J, et al. **Nonsurgical acute traumatic subdural hematoma: what is the risk?** *J Neurosurg* 2015; 123:1176–83 CrossRef Medline
6. Karibe H, Hayashi T, Hirano T, et al. **Surgical management of traumatic acute subdural hematoma in adults: a review.** *Neurol Med Chir (Tokyo)* 2014;54:887–94 CrossRef Medline
7. Bullock MR, Chesnut R, Ghajar J, et al; Surgical Management of Traumatic Brain Injury Author Group. **Surgical management of acute subdural hematomas.** *Neurosurgery* 2006;58:S16–24; discussion Si–iv Medline
8. Sweis RT, Ouyang B, Lopez GA, et al. **Falcine and tentorial subdural hematomas may not routinely require transfer to a tertiary care center.** *J Emerg Med* 2015;49:679–85 CrossRef Medline
9. Howard BM, Rindler R, Holland CM, et al. **Management and outcomes of isolated tentorial and parafalcine “smear” subdural hematomas at a level-1 trauma center: necessity of high acuity care.** *J Neurotrauma* 2017;34:128–36 CrossRef Medline
10. Bartels RH, Verhagen WI, Prick MR, et al. **Interhemispheric subdural hematoma in adults: case reports and a review of the literature.** *Neurosurgery* 1995;36:210–14 Medline
11. Takeuchi S, Takasato Y, Massoka H, et al. **Traumatic peritentorial subdural hematomas: a study of 32 cases.** *Turk Neurosurg* 2012;22: 305–08 CrossRef Medline
12. Want Y, Wang C, Cai S, et al. **Surgical management of traumatic interhemispheric subdural hematoma.** *Turk Neurosurg* 2014;24: 228–33 CrossRef Medline
13. Vaz R, Duarte F, Oliveria J, et al. **Traumatic interhemispheric, subdural haematomas.** *Acta Neurochir* 1991;111:128–31 CrossRef Medline

# Dual-Energy CT in Hemorrhagic Progression of Cerebral Contusion: Overestimation of Hematoma Volumes on Standard 120-kV Images and Rectification with Virtual High-Energy Monochromatic Images after Contrast-Enhanced Whole-Body Imaging

U.K. Bodanapally, K. Shanmuganathan, G. Issa, D. Dreizin, G. Li, K. Sudini, and T.R. Fleiter

## ABSTRACT

**BACKGROUND AND PURPOSE:** In patients with hemorrhagic contusions, hematoma volumes are overestimated on follow-up standard 120-kV images obtained after contrast-enhanced whole-body CT. We aimed to retrospectively determine hemorrhagic progression of contusion rates on 120-kV and 190-keV images derived from dual-energy CT and the magnitude of hematoma volume overestimation.

**MATERIALS AND METHODS:** We retrospectively analyzed admission and follow-up CT studies in 40 patients with hemorrhagic contusions. After annotating the contusions, we measured volumes from admission and follow-up 120-kV and 190-keV images using semiautomated 3D segmentation. Bland-Altman analysis was used for hematoma volume comparison.

**RESULTS:** On 120-kV images, hemorrhagic progression of contusions was detected in 24 of the 40 patients, while only 17 patients had hemorrhagic progression of contusions on 190-keV images ( $P = .008$ ). Hematoma volumes were systematically overestimated on follow-up 120-kV images (9.68 versus 8 mm<sup>3</sup>; mean difference, 1.68 mm<sup>3</sup>; standard error, 0.37;  $P < .001$ ) compared with 190-keV images. There was no significant difference in volumes between admission 120-kV and 190-keV images. Mean and median percentages of overestimation were 29% (95% CI, 18–39) and 22% (quartile 3 – quartile 1 = 36.8), respectively.

**CONCLUSIONS:** The 120-kV images, which are comparable with single-energy CT images, significantly overestimated the hematoma volumes, hence the rate of hemorrhagic progression of contusions, after contrast-enhanced whole-body CT. Hence, follow-up of hemorrhagic contusions should be performed on dual-energy CT, and 190-keV images should be used for the assessment of hematoma volumes.

**ABBREVIATIONS:** DECT = dual-energy CT; HPC = hemorrhagic progression of contusion; SECT = single-energy CT; WBCT = whole-body CT

Approximately 6 million patients with head and neck trauma are seen annually in the emergency departments of North America.<sup>1</sup> One of the most severe types of traumatic brain injury is cerebral hemorrhagic contusion.<sup>2</sup> Hemorrhagic contusions are usually complicated by secondary injury, resulting in hemorrhagic progression of contusion (HPC), which is designated as enlargement of the existing hemorrhagic contusions or appearance of new lesions.<sup>2</sup> Several authors have reported rates of HPC in 38%–59% of cases.<sup>3–8</sup> HPC is a progressive injury that results in irreversible loss of brain tissue with significant increase in morbidity

and mortality.<sup>3</sup> Noncontrast head CT is the diagnostic method used to assess patients with hemorrhagic contusions and HPC.<sup>3</sup>

There is increasing availability of dual-energy CT (DECT) technology in major academic and level 1 trauma centers. We have included a high-monochromatic (190-keV) image set in our routine head CT protocol at the University of Maryland Shock Trauma Center and Adult Emergency Department due to its potential to positively affect the display of cortical contusions and subdural hematomas by decreasing the beam-hardening artifacts from cranial bones.<sup>9–11</sup> Mixed 120-kV images derived from dual-energy data mirror typical single-energy CT (SECT) images used in clinical practice. We have frequently observed higher hemorrhagic contusion volumes on follow-up 120-kV compared with 190-keV images (Fig 1A, -B). This discrepancy was seen in patients after admission contrast-enhanced whole-body CT (WBCT) imaging, which has become a widely used technique for the work-up of the patient with blunt polytrauma.<sup>12</sup>

Studies have shown an increase in capillary endothelial permeability in contusions and surrounding parenchyma.<sup>2</sup> We hypoth-

Received September 8, 2017; accepted after revision December 11.

From the Department of Diagnostic Radiology and Nuclear Medicine (U.K.B., K.S., G.I., D.D., G.L., T.R.F.), R Adams Cowley Shock Trauma Center, University of Maryland Medical Center, Baltimore, Maryland; and Department of Environmental Health Sciences (K.S.), Bloomberg School of Public Health, Johns Hopkins University, Baltimore, Maryland.

Please address correspondence to Uttam K. Bodanapally, MBBS, Department of Radiology, R Adams Cowley Shock Trauma Center, 22 S Greene St, University of Maryland Medical Center, Baltimore, MD 21201; e-mail: ubodanapally@umm.edu

<http://dx.doi.org/10.3174/ajnr.A5558>

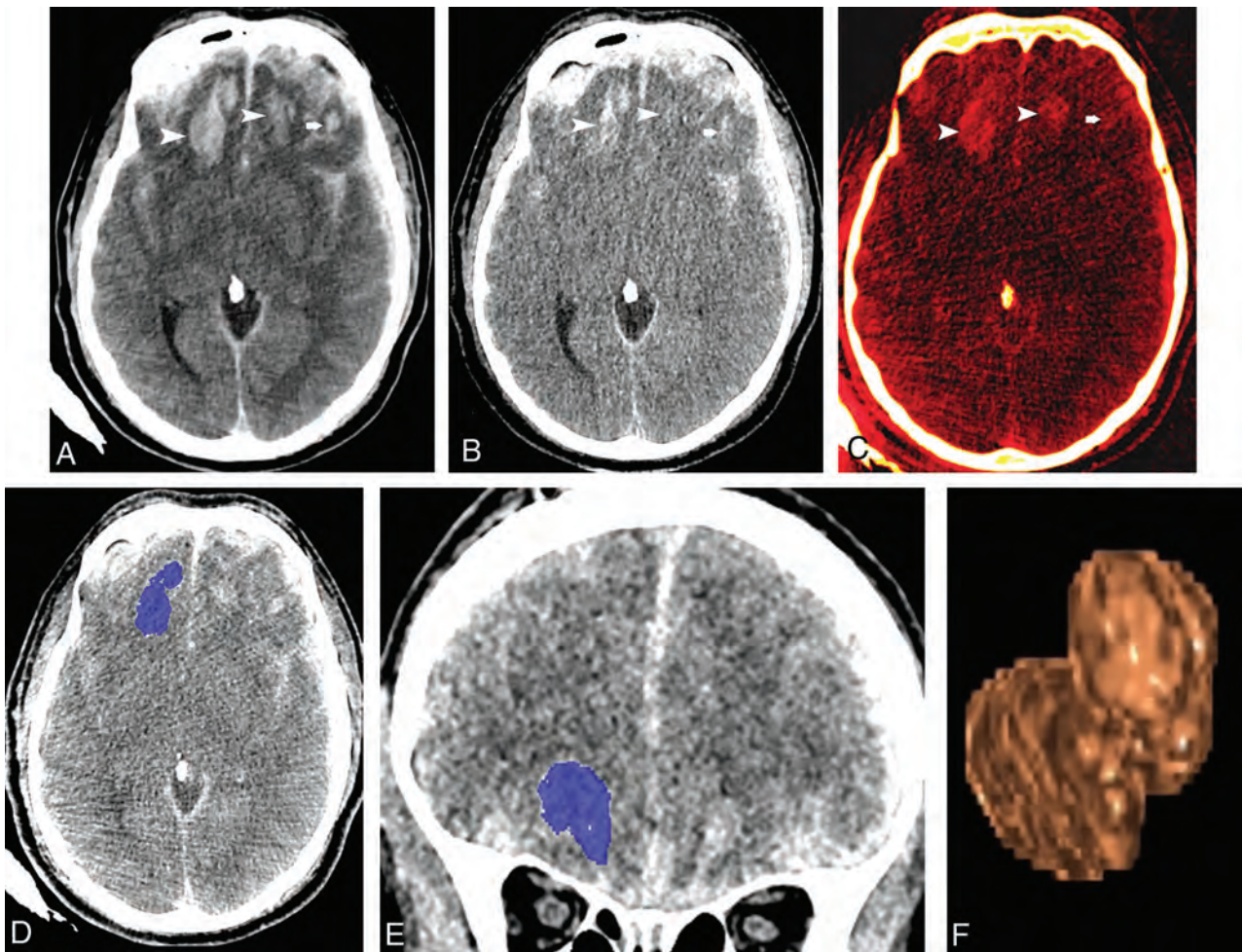


**FIG 1.** A 55-year-old man with traumatic brain injury sustained after an assault. *A*, Follow-up axial 120-kV image shows hemorrhagic contusions in both frontal lobes (*arrowheads* and *arrow*). *B*, Virtual high-monochromatic image (190-keV) shows significantly smaller hemorrhagic contusions compared with the 120-kV images due to negligible attenuation contribution from leaked iodinated contrast (*arrowheads* and *arrow*). *C*, Iodine overlay image shows contrast staining of the hemorrhagic contusions (*arrowheads* and *arrow*). Axial (*D*) and coronal (*E*) CT images demonstrate the ROIs drawn by 3D segmentation on the thin-client server. *F*, Segmented volume-rendered image of the hemorrhagic contusion.

esized that the discrepancy in measured volumes on follow-up noncontrast head CT is caused by retained iodinated contrast that leaks into the parenchyma through the permeable endothelium in the epicenter and penumbra of the contusions after admission contrast-enhanced WBCT (Fig 1C). The high attenuation of the leaked iodine resembles that of hematoma on 120-kV images, resulting in volume overestimation.<sup>13-15</sup> The linear attenuation of iodine shows a dramatic decrease along the spectrum of monochromatic energy, therefore greatly reducing the attenuation contribution of iodine at 190 keV, while at the same time, maintaining the attenuation of hematoma relatively constant.<sup>16,17</sup> Hence, at clinically relevant tissue iodine concentrations, the attenuation contribution of iodine tends to be negligible at 190 keV and demonstrates only the attenuation resulting from hematoma, thus allowing true measurement of hematoma volume.<sup>13,16,17</sup> This phenomenon needs to be substantiated in a systematic study. We aimed to retrospectively determine HPC rates on 120-kV and 190-keV images derived from DECT data and the magnitude of hematoma volume overestimation on follow-up 120-kV images in patients after admission contrast-enhanced WBCT.

## MATERIALS AND METHODS

This retrospective study was Health Insurance Portability and Accountability Act-compliant, and permission was obtained from University of Maryland, Baltimore institutional review board. Informed consent was waived. Consecutive series of patients referred to the trauma resuscitation unit were eligible. The inclusion criteria were the following: 1) a history of blunt trauma with acquisition of noncontrast head DECT followed by contrast-enhanced WBCT, as a part of diagnostic work-up of blunt polytrauma, between May 15, 2016, and September 10, 2016, with a confirmed diagnosis of hemorrhagic contusion on admission CT; 2) acquisition of follow-up noncontrast head DECT within 3 days of admission CT; and 3) 18 years of age or older. Patients were excluded if the mechanism of injury was penetrating trauma or if they underwent surgical interventions to address their contusions.

## Subjects

A search of our radiology information system data base from the designated period yielded 171 patients with initial and at least 1 follow-up study performed on a DECT scanner. A radiologist

with 11 years of experience reviewed the initial and follow-up DECT studies to select all the patients with hemorrhagic contusions ( $n = 40$ ) that constituted the study group. The mean age of the final cohort was 38.4 years (range, 18–73 years), with 26 men and 14 women.

### Reference Standard

HPC is defined as an enlargement of  $\geq 30\%$  of the original hematoma volume on follow-up CT studies as suggested by Alahmadi et al.<sup>18</sup>

### Imaging Technique

Admission WBCT and follow-up head examinations were performed on a DECT scanner (Somatom Force; Siemens, Erlangen, Germany). WBCT involves a noncontrast head CT followed by contrast-enhanced CT of the neck, chest, abdomen, and pelvis. The studies were performed after injection of 100 mL of iodinated contrast media (iohexol, Omnipaque 300; GE Healthcare, Piscataway, New Jersey) using a biphasic injection with 60 mL injected at 5 mL/s and 40 mL injected at 4 mL/s. The contrast injection was followed by a 50-mL saline injection at 4 mL/s.

DECT head images were obtained with the x-ray tubes at 80 kV and Sn150kV (150 kV + tin filter). Scan parameters were as follows: rotation time, 0.5 seconds; pitch, 0.55. The reference milliampere-second was 273 for the Sn150kV and 410 for the 80-kV tube. Original dual-energy datasets were reconstructed with an increment of 1 mm and a slice thickness of 1 mm. Automatic reconstruction of 120-kV-equivalent mixed-DECT images at 5-mm slice thickness and 5-mm intervals using an adaptive iterative reconstruction algorithm (ADMIRE, Siemens) with a strength value of 3 was performed and sent to the PACS at the time of the study. Automatic tube current modulation (CARE Dose4D; Siemens) was used in all patients.

### Image Analysis of DECT

DECT data from admission and follow-up head CTs were processed to derive 190-keV image sets at 5-mm slice thickness and 5-mm intervals on a workstation (syngo.via, Version VB10B; Siemens) and sent to the PACS. Both 120-kV and 190-keV image sets from the PACS (5-mm slice thickness, 5-mm intervals) were loaded onto the thin-client server at our institution (IntelliSpace Portal; Philips Healthcare, Best, the Netherlands) to facilitate hematoma volume measurements. Hence, 4 image sets were used for volume measurements in each patient (ie, 120-kV, 190-keV image sets [from the admission study] and 120-kV, 190-keV [from the follow-up study]). Reviewer 1 annotated the hemorrhagic contusions that were meant for volume measurements. In patients with multiple contusions, the largest lesion was used for measurement. Reviewer 2 (third-year radiology resident) measured the volumes of the hemorrhagic contusions in each patient. Measurements were randomly performed regarding patient order and the order of the image sets to avoid potential preconceived bias. Volumes were measured using semiautomated 3D segmentation. An ROI was drawn on axial slices with the use of coronal and sagittal slices to exclude unwanted surrounding brain tissue from the ROIs (Fig 1D–F).<sup>19</sup>

### Statistical Analysis

Statistical analysis was performed by K.S. using statistical software (JMP 12 software; SAS Institute, Cary, North Carolina). Contingency analysis was used to compare dichotomous variables. The McNemar test was used to compare the frequencies of HPC on 120-kV and 190-keV images. For comparison of hematoma volumes obtained by 120-kV and 190-keV, Bland-Altman analysis was performed. To determine the correlation of volume measurements on both image sets, we calculated the Pearson correlation coefficient. The Wilcoxon signed rank test was used to test the potential differences between the median values obtained by both methods. Regression analysis was performed to identify the best predictor of the percentage of hematoma volume overestimation. The following formulas were used to calculate the different variables: Percentage of Hematoma Overestimation =  $100 (\text{Volume on Follow-Up 120-kV} - \text{Volume on Follow-Up 190-keV}) / (\text{Volume on Follow-Up 190-keV})$ ; Percentage of Hemorrhagic Progression on 190 keV =  $100 (\text{Volume of Hematoma on Follow-Up 190-keV} - \text{Volume on Admission 190-keV}) / (\text{Volume on Admission 190-keV})$ ; similarly, the percentage of hemorrhagic progression on 120 kV =  $100 (\text{Volume of Hematoma on Follow-Up 120-kV} - \text{Volume on Admission 120-kV}) / (\text{Volume on Admission 120-kV})$ . A  $P$  value of  $< .05$  was considered significant.

### RESULTS

The median time to follow-up noncontrast head CT was 6 hours (quartile 3 – quartile 1 = 4.75 hours) after admission contrast-enhanced WBCT. On follow-up 120-kV images, HPC was detected in 24 of the 40 patients (60%), with HPC defined as an enlargement of  $\geq 30\%$  of the original hematoma volume. On 190-keV images, HPC was detected in only 17 of the 40 patients (43%). The McNemar test showed that HPC was more frequently observed on 120-kV images with a test result of 7 ( $P = .008$ ).

Bland-Altman analysis showed that hematoma volumes were systematically overestimated on follow-up 120-kV images (9.68 versus 8 mm<sup>3</sup>; mean difference, 1.68 mm<sup>3</sup>; standard error, 0.37;  $P < .001$ ) compared with 190-keV images (Fig 2). There was no significant difference in the measured volumes between admission 120-kV and 190-keV images (6.11 versus 6.07 mm<sup>3</sup>; mean difference, 0.045 mm<sup>3</sup>; standard error, 0.05;  $P = .22$ ). The Pearson correlation coefficient for hematoma volumes determined by 120-kV and 190-keV was  $r = 0.999$  ( $P < .001$ ) for admission head CTs and  $r = 0.98$  ( $P < .001$ ) for follow-up head CTs. The mean percentage of hematoma volume overestimation on follow-up 120-kV images was  $29\% \pm 32\%$  (95% CI, 18%–39%), and the median was 22% (quartile 3 – quartile 1 = 36.8).

Regression analysis was performed using the hematoma volume on admission CT (190-keV), hematoma volume on follow-up CT (190-keV), time to follow-up, absolute volume of hemorrhagic progression (190-keV), and percentage of hemorrhagic progression as independent variables with percentage of hematoma overestimation as a dependent variable. The percentage of HPC was the best predictor of the percentage of hematoma volume overestimation ( $\beta = 16.4$ ; 95% CI, 9.91–22.97; standard error, 3.2;  $P < .001$ ).

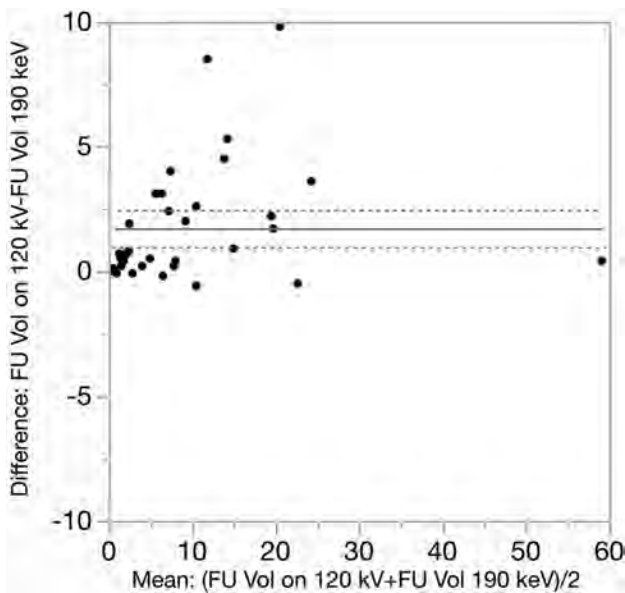


**FIG 2.** Bland-Altman plots of the hematoma volume overestimation on follow-up 120-kV images compared with 190-keV images. *Horizontal lines* represent the mean volume overestimation (*solid line*) and limits of agreement (*dashed lines*). FU indicates follow-up; Vol, volume.

## DISCUSSION

The major findings from our study in patients after admission contrast-enhanced WBCT are the following: 1) follow-up 120-kV head CT images, which are akin to SECT images, significantly overestimate the hematoma volume and hence the rate of HPC, 2) mean and median percentages of hematoma volume overestimations were 29% and 22%, respectively, and 3) the best predictor of percentage of volume overestimation was the percentage of hemorrhagic progression on follow-up CT (ie, the magnitude of overestimation is proportional to the magnitude of HPC).

Our study demonstrated that the true occurrence of HPC in patients after contrast-enhanced WBCT, as measured from the 190-keV images, was 43%. This number is similar to the 45% that was reported in conservatively managed patients by Alahmadi et al,<sup>18</sup> who had similar selection criteria and cutoff values for progression. However, the rate increased to 60% if measured on 120-kV images (images comparable with SECT images) because there were 7 patients (18%) who were wrongly diagnosed with HPC. This higher rate of HPC is caused by “pseudohematoma.” We describe pseudohematoma as the volume of nonhemorrhagic hyperattenuating brain parenchyma caused by iodinated contrast leak from the permeable capillary endothelium. The leaked contrast from the bolus administered during the admission WBCT is retained in the brain parenchyma and would be seen in the follow-up studies as an area of hyperattenuation on 120-kV images, simulating a hematoma. The exact duration of this parenchymal contrast retention has not yet been analyzed and reported.

The attenuation contribution of iodine is negligible at the higher end of the monochromatic energy spectrum.<sup>13,16,17</sup> Hence, 190-keV images demonstrate the actual hematoma size by displaying attenuation contributed predominantly by hematoma. It was recently demonstrated that virtual noncontrast images are comparable with 190-keV images in minimizing the attenuation

contribution of iodine to negligible levels.<sup>13</sup> Hence, virtual non-contrast images, if used in place of 190-keV images, may have yielded similar results in obtaining true hematoma volumes. Enhancement of cerebral contusion on contrast-enhanced SECT was described by Huang et al<sup>20</sup>; however, the authors did not describe how they were able to differentiate the hyperattenuation caused by iodinated contrast from that of the hematoma.

Cerebral contusions can be divided into 3 distinct regions: 1) epicenter, 2) penumbra, and 3) paratenumbra.<sup>2</sup> The epicenter receives the peak energy from impact, and surrounding regions receive progressively less energy with distance. Energy deposited in the epicenter is sufficient to fracture capillaries, resulting in an immediate hemorrhagic lesion. In the penumbra and paratenumbra, the energy is not enough to fracture the capillaries but activates the mechanosensitive molecular processes that will lead to the delayed structural failure of capillaries.<sup>21,22</sup> Animal studies have shown that the mechanosensitive molecular process begins with transcriptional up-regulation, followed by opening of the sulfonyleurea receptor 1 (SUR1) SUR1-regulated channel.<sup>2,21</sup> Opening the channel has been linked to gradual oncotic cell swelling and death of the endothelial cells, resulting in increased capillary permeability, and progression to capillary fragmentation. Increased permeability results in vasogenic edema, while capillary fragmentation results in extravasation of blood, contributing to HPC. HPC rates are directly related to the degree of endothelial damage and capillary fragmentation. The penumbra and paratenumbra usually manifest as vasogenic edema on CT because of increased permeability of the damaged endothelium.<sup>2</sup> However, after contrast administration, enhancement of the parenchyma in the penumbra and paratenumbra results from the leak of iodinated agents through the same damaged endothelium, resulting in pseudohematoma.<sup>20</sup> The phenomenon of HPC rates being proportional to the degree of capillary disruption caused by the mechanosensitive molecular process likely explains our other finding (ie, the magnitude of overestimation of hematoma is proportional to the magnitude of HPC because both are directly related to the degree of endothelial damage and capillary fragmentation).

Several authors have reported HPC as the reason for an operation, sometimes in up to 20% of patients.<sup>3-8</sup> Studies have also reported that patients with progression of injury on a repeat CT underwent more frequent interventions related to intracranial pressure management changes, ventriculostomy placement or adjustment, addition of antiseizure medication, repeat CT, intensive care unit observation, delay in extubation, and initiation of thromboprophylaxis, even in patients with stable or improved Glasgow Coma Scale scores.<sup>12,18,23-25</sup> Similarly, Alahmadi et al<sup>18</sup> reported a significant association between radiographic progression of contusions and the need for neurosurgical interventions, even though the mean Glasgow Coma Scale score and mean change in Glasgow Coma Scale score during the hospital course showed no difference.<sup>18</sup> Hence, an accurate assessment of HPC has important clinical implications in preventing unnecessary interventions and radiation from follow-up imaging.

Using strict criteria in describing HPC, including indicating whether there was prior contrast administration, and detailing image sets used for measurement (SECT, 120 kV, or 190 keV)

would minimize potential errors in identifying contusion progression. Health care providers should account for overestimation of hematoma volumes if the follow-up studies were performed on SECT. We also suggest that future research articles describe in detail the imaging techniques in their methods section, because contrast-enhanced WBCT has become a widely used technique for the work-up of the patient with blunt polytrauma.

### Limitations

Our study has several limitations. It is a retrospective single-center design, which introduces selection and institutional bias. The cohort comprised only those patients who underwent WBCT studies at the time of admission. Thus, these data may not be generalizable to all trauma patients who may have undergone focused imaging of the head. A lack of consistent protocol for follow-up CTs (though most scans were obtained within 9 hours) may have affected the values. Finally, we excluded patients who underwent neurosurgical interventions. Those patients may differ in the severity of endothelial damage and hence have a different magnitude of iodine leak and hematoma volume overestimation.

### CONCLUSIONS

Mixed 120-kV images from DECT and by extension the SECT images overestimate hematoma volumes, hence the HPC rates on follow-up head CTs, in patients after contrast-enhanced WBCT. Our study demonstrates that it is important to perform follow-up of cerebral contusions on a DECT scanner and use high-monochromatic (190-keV) images in patients after contrast-enhanced WBCT to accurately estimate HPC.

Disclosures: Uttam K. Bodanapally—UNRELATED: Payment for Lectures Including Service on Speakers Bureaus: Siemens, Comments: talk on the role of "Dual-Energy CT in Patients with Traumatic Brain Injury" at the American Society of Head and Neck Radiology Annual Meeting in Las Vegas, September 17, 2017; Travel/Accommodations/Meeting Expenses Unrelated to Activities Listed: Siemens, Comments: talk on the role of "Dual-Energy CT in Patients with Traumatic Brain Injury" at American Society of Head and Neck Radiology Annual Meeting in Las Vegas, September 17, 2017. David Dreizin—UNRELATED: Grants/Grants Pending: Radiological Society of North American research scholar grant, Siemens.\* \*Money paid to the institution.

### REFERENCES

1. Stiell IG, Clement CM, Grimshaw JM, et al. A prospective cluster-randomized trial to implement the Canadian CT Head Rule in emergency departments. *CMAJ* 2010;182:1527–32 CrossRef Medline
2. Kurland D, Hong C, Aarabi B, et al. Hemorrhagic progression of a contusion after traumatic brain injury: a review. *J Neurotrauma* 2012;29:19–31 CrossRef Medline
3. Bodanapally UK, Sours C, Zhuo J, et al. Imaging of traumatic brain injury. *Radiol Clin North Am* 2015;53:695–715 CrossRef Medline
4. Chang EF, Meeker M, Holland MC. Acute traumatic intraparenchymal hemorrhage: risk factors for progression in the early post-injury period. *Neurosurgery* 2006;58:647–56; discussion 647–56 CrossRef Medline
5. Lobato R, Gomez P, Alday R, et al. Sequential computerized tomography changes and related final outcome in severe head injury patients. *Acta Neurochir* 1997;139:385–91 CrossRef Medline
6. Servadei F, Nanni A, Nasi MT, et al. Evolving brain lesions in the first 12 hours after head injury analysis of 37 comatose patients. *Neurosurgery* 1995;37:899–904 CrossRef Medline

7. Miller JD, Butterworth JF, Gudeman SK, et al. Further experience in the management of severe head injury. *J Neurosurg* 1981;54:289–99 CrossRef Medline
8. Cepeda S, Gómez PA, Castaño-Leon AM, et al. Traumatic intracerebral hemorrhage: risk factors associated with progression. *J Neurotrauma* 2015;32:1246–53 CrossRef Medline
9. Yu L, Leng S, McCollough CH. Dual-energy CT-based monochromatic imaging. *Am J Roentgenol* 2012;199(5 Suppl):S9–15 CrossRef Medline
10. Wu X, Langan DA, Xu D, et al. Monochromatic CT image representation via fast switching dual kVp. *Proc SPIE* 2009;7258:725845
11. Matsumoto K, Jinzaki M, Tanami Y, et al. Virtual monochromatic spectral imaging with fast kilovoltage switching: improved image quality as compared with that obtained with conventional 120-kVp CT. *Radiology* 2011;259:257–62 CrossRef Medline
12. Gunn ML, Kool DR, Lehnert BE. Improving outcomes in the patient with polytrauma: a review of the role of whole-body computed tomography. *Radiol Clin North Am* 2015;53:639–56 CrossRef Medline
13. Bodanapally UK, Dreizin D, Issa G, et al. Dual-energy CT in enhancing subdural effusions that masquerade as subdural hematomas: diagnosis with virtual high-monochromatic (190-keV) images. *AJNR Am J Neuroradiol* 2017;38:1946–52 CrossRef Medline
14. Gupta R, Phan CM, Leidecker C, et al. Evaluation of dual-energy CT for differentiating intracerebral hemorrhage from iodinated contrast material staining. *Radiology* 2010;257:205–11 CrossRef Medline
15. Phan CM, Yoo AJ, Hirsch JA, et al. Differentiation of hemorrhage from iodinated contrast in different intracranial compartments using dual-energy head CT. *AJNR Am J Neuroradiol* 2012;33:1088–94 CrossRef Medline
16. Postma AA, Das M, Stadler AA, et al. Dual-energy CT: what the neuroradiologist should know. *Curr Radiol Rep* 2015;3:16 CrossRef Medline
17. Potter CA, Sodickson AD. Dual-energy CT in emergency neuroimaging: added value and novel applications. *Radiographics* 2016;36:2186–98 CrossRef Medline
18. Alahmadi H, Vachhrajani S, Cusimano MD. The natural history of brain contusion: an analysis of radiological and clinical progression. *J Neurosurg* 2010;112:1139–45 CrossRef Medline
19. Bodanapally UK, Addis H, Dreizin D, et al. Prognostic predictors of visual outcome in open globe injury: emphasis on facial CT findings. *AJNR Am J Neuroradiol* 2017;38:1013–18 CrossRef Medline
20. Huang AP, Lee CW, Hsieh HJ, et al. Early parenchymal contrast extravasation predicts subsequent hemorrhage progression, clinical deterioration, and need for surgery in patients with traumatic cerebral contusion. *J Trauma* 2011;71:1593–99 CrossRef Medline
21. Simard JM, Kilbourne M, Tsybalyuk O, et al. Key role of sulfonylurea receptor 1 in progressive secondary hemorrhage after brain contusion. *J Neurotrauma* 2009;26:2257–67 CrossRef Medline
22. Patel AD, Gerzanich V, Geng Z, et al. Glibenclamide reduces hippocampal injury and preserves rapid spatial learning in a model of traumatic brain injury. *J Neuropathol Exp Neurol* 2010;69:1177–90 CrossRef Medline
23. Wang MC, Linnau KF, Tirschwell DL, et al. Utility of repeat head computed tomography after blunt head trauma: a systematic review. *J Trauma* 2006;61:226–33 CrossRef Medline
24. Lee TT, Aldana P, Kirton O, et al. Follow-up computerized tomography (CT) scans in moderate and severe head injuries: correlation with Glasgow Coma Scores (GCS), and complication rate. *Acta Neurochir* 1997;139:1042–47; discussion 1047–48 CrossRef Medline
25. Givner A, Gurney J, O'Connor D, et al. Reimaging in pediatric neurotrauma: factors associated with progression of intracranial injury. *J Pediatr Surg* 2002;37:381–85 CrossRef Medline

# Prediction of the Multisegment Clot Sign on Dynamic CT Angiography of Cardioembolic Stroke

Z. Chen, F. Shi, M. Zhang, X. Gong, L. Lin, and M. Lou



## ABSTRACT

**BACKGROUND AND PURPOSE:** The multisegment clot sign has been observed at the site of large-artery occlusion in patients with acute ischemic stroke. This study aimed to assess its occurrence rate and relationship with stroke etiologies in patients with acute intracranial large-artery occlusion.

**MATERIALS AND METHODS:** We included consecutive patients with acute ischemic stroke who had acute intracranial large-artery occlusion and underwent perfusion CT within 8 hours after stroke onset. The multisegment clot sign was assessed on dynamic CT angiography derived from perfusion CT. The stroke etiologies were defined by the international Trial of Org 10172 in Acute Stroke Treatment criteria. Poisson regression analyses and diagnostic testing were used to investigate the relationship between the multisegment clot sign and stroke etiologies.

**RESULTS:** Finally, 194 patients with intracranial large-artery occlusion were enrolled. According to the Trial of Org 10172 in Acute Stroke Treatment criteria, 110 (56.7%) patients were diagnosed with cardioembolism; 43 (22.2%), with large-artery atherosclerosis; and 41 (21.1%), with undetermined etiology. The multisegment clot sign was found in 74 (38%) patients. Poisson regression analysis showed that the presence of the multisegment clot sign was significantly higher in patients with cardioembolism than in those with large-artery atherosclerosis (52.7% versus 9.3%; prevalence ratio, 1.53; 95% confidence interval, 1.03–2.90;  $P = .037$ ). For determined etiologies, the sensitivity, specificity, and positive and negative predictive values of the multisegment clot sign for predicting cardioembolism were 52.7%, 90.7%, 93.5%, and 42.9%, respectively.

**CONCLUSIONS:** The presence of the multisegment clot sign on dynamic CTA specifically indicates intracranial large-artery occlusion caused by an embolism from a cardiac source, which may be useful for acute management and secondary prevention of stroke.

**ABBREVIATIONS:** CE = cardioembolism; LAA = large-artery atherosclerosis; LAO = intracranial large-artery occlusion; MSC = multisegment clot; TOAST = Trial of Org 10172 in Acute Stroke Treatment

Intracranial large-artery occlusion (LAO) is a common cause of acute ischemic stroke and may cause severe disability and mortality.<sup>1</sup> LAO is estimated to account for 20%–50% of ischemic stroke and varies in different populations.<sup>2</sup> Endovascular therapy

has been recommended as a standard treatment for acute proximal cerebral LAO.<sup>3</sup> Recently, the success of endovascular therapy has been reported to be affected by the sources of the vessel occlusion.<sup>4</sup> Cardioembolism (CE) and large-artery atherosclerosis (LAA) are the 2 common causes of LAO. However, differentiating these 2 etiologies is often challenging, especially in an acute clinical scenario where a quick treatment decision must be made after acute ischemic stroke.<sup>5</sup>

Attempts have been made to address this challenge by implementing advanced brain imaging. Recent MR imaging studies suggest that both the 2-layered susceptibility vessel sign on T2\*-weighted images and the overestimation ratio of the susceptibility vessel sign can predict CE.<sup>6,7</sup> Another study showed that the

Received August 1, 2017; accepted after revision December 3.

From the Department of Neurology (Z.C., F.S., M.Z., X.G., M.L.), the Second Affiliated Hospital of Zhejiang University, School of Medicine, Hangzhou, China; Zhejiang University Brain Research Institute (M.L.), Hangzhou, China; and School of Medicine and Public Health (L.L.), University of Newcastle, New South Wales, Australia.

Zhicai Chen and Feina Shi contributed equally to this work.

This work was supported by the National Natural Science Foundation of China (81622017, 81601017, 81400946), the National Key Research and Development Program of China (2016YFC1301500), Fundamental Research Funds for the Central Universities (2017XZZX002-09), and the Natural Science Foundation of Zhejiang Province (LQ16H090003).

The perfusion analysis software (MISStar) used in this study was provided to the site as part of the involvement in the International Stroke Perfusion Imaging Registry (INSPIRE, a study funded by the National Health and Medical Research Council of Australia).

Please address correspondence to Min Lou, MD, PhD, Department of Neurology, the Second Affiliated Hospital of Zhejiang University, School of Medicine, No. 88 Jiefang Rd, Hangzhou, China, 310009; e-mail: lm99@zju.edu.cn

Indicates open access to non-subscribers at www.ajnr.org

<http://dx.doi.org/10.3174/ajnr.A5549>

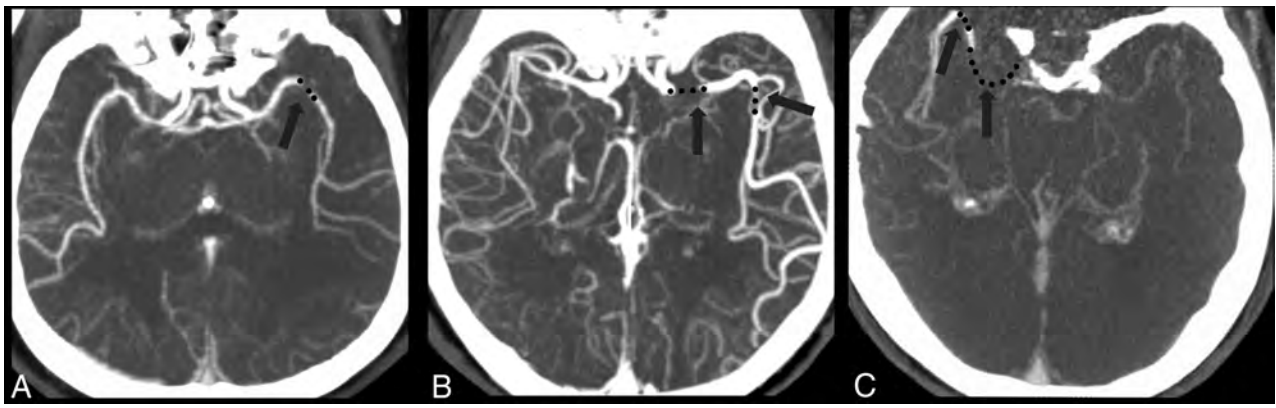


**FIGURE.** Examples of the multisegment clot sign on dynamic CT angiography derived from CT perfusion. *A*, One patient with LAA had 1 clot (black dot) presenting as 1 segment in the middle cerebral artery, which was categorized as a 1-segment clot. *B*, One patient with CE had 2 segments of the clot on a delayed phase of dynamic CTA, which was categorized as a multisegment clot. *C*, Another patient with CE had 2 segments of the clot on a late delayed phase of dynamic CTA, which was also categorized as a multisegment clot.

branching-site occlusion on digital subtraction angiography was highly associated with CE.<sup>4</sup> Because CT is available in most emergency departments of comprehensive stroke centers, perfusion CT is routinely performed before reperfusion treatment. Given that DSA is an invasive procedure and MR imaging has its contraindications, dynamic CT angiography derived from CTP is a more ideal and convenient technique, which can provide dynamic angiographic and parenchymal information. Therefore, it is worthwhile to investigate its role in predicting CE.

Recently, on the basis of dynamic CTA derived from CTP, which uses the extended image-acquisition time span, we noticed a phenomenon of 1 clot presenting as multiple segments. Because pathology studies have shown that the clot from CE has a higher proportion of red blood cells than LAA clots and is more prone to dissociate itself into multiple segments,<sup>8</sup> we thought that the presence of this sign might be associated with cardiac-origin clots.

In the present study, we introduce the definition of the multisegment clot (MSC) sign on dynamic CTA and aim to evaluate the association between the MSC sign and stroke etiologies.

## MATERIALS AND METHODS

### Patients

This study was approved by the human ethics committee of the Second Affiliated Hospital of Zhejiang University, School of Medicine. We retrospectively reviewed our prospectively collected data base for consecutive patients with acute ischemic stroke who received thrombolytic therapy with or without endovascular therapy between May 2009 to March 2016. We enrolled patients under the following conditions: 1) They underwent CTP within 8 hours after stroke onset, 2) had occlusion of the internal carotid artery or middle cerebral artery up to the proximal M2 segment, and 3) had acute ischemic stroke with CE, LAA, or undetermined etiology. Patients who had poor image quality because of motion artifacts or incomplete images were excluded.

### Clinical Data

Baseline clinical variables were recorded, including demographics, risk factors (smoking, hypertension, diabetes mellitus, hyperlipidemia, or a history of stroke/TIA or atrial fibrillation), prior antiplatelet usage, prior warfarin (Coumadin) use, onset-to-im-

aging time, baseline National Institutes of Health Stroke Scale score, and laboratory and radiologic data. The stroke etiologies were determined according to the Trial of Org 10172 in Acute Stroke Treatment (TOAST).<sup>5</sup> CE needed to fit evidence of cardiac disease that has a potential for embolism and no evidence of stenosis of  $\geq 50\%$  on relevant intracranial or extracranial large arteries.<sup>5</sup> LAA needed to fit clinical and brain imaging findings of either severe ( $>50\%$ ) stenosis or occlusion of a major brain artery or branch cortical artery, presumably due to atherosclerosis, and no potential sources of cardiogenic embolism. Undetermined etiology included the following: 1)  $\geq 2$  potential causes of stroke, or 2) no likely etiology determined despite an extensive evaluation, or 3) no cause found due to inadequate evaluation.<sup>5</sup>

### Imaging Protocol

Baseline CTP was performed on a 64-slice CT scanner (Somatom Definition Flash; Siemens, Erlangen, Germany), including an NCCT scan (120 kV, 320 mA, contiguous 5-mm axial slices, 7-second acquisition time) and volume CTP (100 mm in the z-axis, 4-second delay after the start of contrast medium injection, 74.5-second total imaging duration, 80 kV, 120 mA, 1.5-mm slice thickness,  $32 \times 1.2$  mm collimation). Volume CTP consisted of 26 consecutive spiral acquisitions of the brain. All 26 scans were divided into 4 parts: 1) 2 scans with 3-second cycle time; 2) 15 scans with 1.5-second cycle time; 3) 4 scans with 3-second cycle time; and 4) 5 scans with 6-second cycle time. Axial slice coverage was 150 mm. A 60-mL bolus of contrast medium, Imeron (iopamidol; Bracco, Milan, Italy), with a single injection at a flow rate of 6 mL/s was followed by a 20-mL saline chaser at 6 mL/s.

### Assessment of the MSC Sign

Thick-slab reformatted dynamic CTA images were reconstructed from CTP source images in axial, coronal, and sagittal planes with a 30-mm-thick maximum intensity projection on an Advantage Windows Workstation (GE Healthcare, Milwaukee, Wisconsin). The MSC sign was defined as  $>1$  occlusion site on 26-phase dynamic CTA, including angiographic information of both the early and late phases (Figure). We assessed the MSC sign on all 26 phases by adjusting the planes forward and backward on dynamic CTA to ensure every occlusion site. Two experienced neurologists

blinded to the patient information assessed the MSC sign with rater discrepancies settled by consensus discussion.

### Statistical Analysis

The patients were trichotomized according to the TOAST criteria or dichotomized according to the presence of the MSC sign. The  $\kappa$  statistic value was used to assess intraobserver and interobserver variability for evaluating the MSC sign. Clinical characteristics and imaging profiles were summarized by medians with interquartile range for continuous variables, and percentages for categorical variables. For continuous variables, the Mann-Whitney *U* test was used to compare difference between 2 groups, and the Kruskal-Wallis test was used to compare difference among 3

groups. For categorical variables, the  $\chi^2$  test was used to compare differences among groups. Variables with a *P* < .2 in univariate regression analyses were included in Poisson regression or a binary logistic regression model. Diagnostic parameters, including sensitivity, specificity, and positive and negative predictive values, were calculated to assess the prognosis of the MSC sign in differentiating CE from other etiologies. All statistical analyses were performed using SPSS, Version 22.0 (IBM, Armonk, New York) and STATA 14.0 (StataCorp, College Station, Texas). A *P* value < .05 was considered statistically significant.

### RESULTS

A total of 194 patients were finally included (112 men; median age, 73 years; interquartile range, 60–80 years; median baseline NIHSS score, 13; interquartile range, 8–17). Among them, 110 (56.7%) were in the CE group, 43 (22.2%) were in the LAA group, and 41 (21.1%) were in the undetermined etiology group. The MSC sign was identified in 74 (38%) patients. The intraobserver and interobserver  $\kappa$  values for the detection of the MSC sign were 0.989 and 0.956, respectively.

Table 1 shows that patients with the MSC sign had lower blood glucose levels (*P* = .017), lower leukocyte counts (*P* = .028), and higher rates of cardioembolism (78.4% versus 43.3%, *P* < .001) compared with those without the MSC sign. Besides, patients with the MSC sign were inclined to be older (*P* = .097) and have lower rates of diabetes mellitus (*P* = .072). Moreover, atrial fibrillation was a significant independent predictor of the presence of the MSC sign after adjusting for age, onset to imaging time, blood glucose levels, leukocyte counts, hypertension, and diabetes mellitus in

**Table 1: Comparison of baseline characteristics between patients with and without the MSC sign<sup>a</sup>**

	No MSC (n = 120)	MSC (n = 74)	P Value
Age (yr)	70 (60–79)	76 (63–80)	.097
Male sex (No.) (%)	71 (59.2%)	41 (55.4%)	.606
Baseline NIHSS score	13 (7–16)	13 (9–17)	.217
Systolic BP (mm Hg)	149 (133–162)	150 (137–169)	.288
Diastolic BP (mm Hg)	80 (71–90)	79 (71–94)	.975
Onset-to-imaging time (min)	185 (115–236)	152 (92–223)	.105
Laboratory data			
Glucose (mg/dL)	7.10 (6.28–8.30)	6.60 (5.78–7.36)	.017
Leukocytes (10E9/L)	8.30 (6.60–10.53)	7.10 (5.75–9.25)	.028
Percentage of neutrophils	75.75 (64.63–83.40)	74.70 (61.50–84.65)	.874
Platelets (10E9/L)	183 (145–216)	171 (130–209)	.305
Risk factors			
Smoking (No.) (%)	42 (35.0%)	23 (31.1%)	.574
Hypertension (No.) (%)	73 (60.8%)	52 (70.3%)	.182
Diabetes mellitus (No.) (%)	27 (22.5%)	9 (12.2%)	.072
Hyperlipidemia (No.) (%)	46 (38.3%)	27 (36.5%)	.796
History of stroke/TIA (No.) (%)	21 (17.5%)	11 (14.9%)	.631
Atrial fibrillation (No.) (%)	53 (44.2%)	56 (75.7%)	<.001
Prior antiplatelet use (No.) (%)	19 (15.8%)	14 (18.9%)	.578
Prior Coumadin use (No.) (%)	4 (3.3%)	6 (8.1%)	.260
Stroke etiologies			
CE (No.) (%)	52 (43.3%)	58 (78.4%)	<.001
LAA (No.) (%)	39 (32.5%)	4 (5.4%)	<.001
Undetermined etiology (No.) (%)	29 (24.2%)	12 (16.2%)	.188

**Note:**—BP indicates blood pressure.

<sup>a</sup> Data are expressed as median (Q1–Q3) for continuous variables.

**Table 2: Comparison of baseline characteristics among the 3 groups**

	CE (n = 110)	LAA (n = 43)	Undetermined Etiology (n = 41)	P <sup>a</sup>	P <sup>b</sup>
Age (yr)	74 (66–80)	67 (56–79)	63 (59–79)	.016	.016
Male sex (No.) (%)	52 (47.3%)	32 (74.4%)	28 (68.3%)	.003	.002
Baseline NIHSS score	14 (10–18)	10 (5–14)	14 (9–18)	.002	.001
Systolic BP (mm Hg)	150 (133–168)	154 (138–164)	144 (129–155)	.172	.450
Diastolic BP (mm Hg)	79 (71–94)	80 (72–93)	78 (68–89)	.370	.955
Onset-to-imaging time (min)	154 (92–225)	163 (112–230)	197 (134–262)	.128	.540
Prior antiplatelet use (No.) (%)	19 (17.3%)	6 (14.0%)	8 (19.5%)	.790	.618
Risk factors					
Smoking (No.) (%)	28 (25.5%)	21 (48.8%)	16 (39.0%)	.016	.005
Hypertension (No.) (%)	73 (66.4%)	29 (67.4%)	23 (56.1%)	.451	.899
Diabetes mellitus (No.) (%)	20 (18.2%)	11 (25.6%)	5 (12.2%)	.285	.306
Hyperlipidemia (No.) (%)	41 (37.3%)	15 (34.9%)	17 (41.5%)	.818	.783
History of stroke/TIA (No.) (%)	19 (17.3%)	9 (20.9%)	4 (9.8%)	.365	.599
Atrial fibrillation (No.) (%)	98 (89.1%)	0 (0.0%)	11 (26.8%)	<.001	<.001
MSC sign (No.) (%)	58 (52.7%)	4 (9.3%)	12 (29.3%)	<.001	<.001

**Note:**—BP indicates blood pressure.

<sup>a</sup> Data are expressed as median (Q1–Q3) for continuous variables among the 3 groups.

<sup>b</sup> Data are expressed as median (Q1–Q3) for continuous variables between CE and LAA.

the binary logistic regression model (odds ratio, 3.704; 95% CI, 1.761–7.790;  $P = .001$ ). The area under the curve generated from the final regression model to predict the presence of MSC sign was 0.72.

Table 2 shows the clinical and image characteristics of the 3 groups. Univariate analysis showed that age, sex, baseline NIHSS score, smoking, atrial fibrillation, and the presence of the MSC sign were significantly different among the 3 groups. Patients with CE were older and had lower proportions of men and current smokers and higher baseline NIHSS scores compared with those with LAA ( $P < .05$ ). Moreover, the rate of the MSC sign was higher in patients with CE than in those with LAA or undetermined etiology (52.7%, 9.3%, and 29.3%, respectively;  $P < .001$ ).

Thus, age, sex, smoking, baseline NIHSS score, systolic blood pressure, onset-to-imaging time, and the MSC sign were included in the Poisson regression model to select predictors of CE stroke. It revealed that the presence of the MSC sign (prevalence ratio, 1.53; 95% CI, 1.03–2.90;  $P = .037$ ) was independently associated with CE after adjustment compared with the LAA (Table 3). The area under the curve generated from the final model based on Poisson regression was 0.84. However, the presence of the MSC sign could not independently predict CE from undetermined etiology after adjustment for age, sex, smoking, baseline NIHSS score, systolic blood pressure, and onset-to-imaging time (prevalence ratio, 1.19; 95% CI, 0.80–1.76;  $P = .393$ ) (Table 4).

Among patients with determined etiologies, there were 110 patients with CE and 43 with LAA. The sensitivity, specificity, and positive and negative predictive values of the MSC sign for predicting CE were 52.7%, 90.7%, 93.5%, and 42.9%, respectively (Table 5).

**Table 3: Poisson regression for differentiating CE from LAA**

Variables	PR (95% CI)	P Value
Age	1.01 (0.99–1.02)	.453
Baseline NIHSS score	1.02 (0.99–1.05)	.195
Male	0.86 (0.53–1.40)	.552
Smoking	0.83 (0.48–1.43)	.499
Systolic BP	1.00 (0.99–1.01)	.550
Onset-to-imaging time	1.00 (1.00–1.00)	.984
MSC sign	1.53 (1.03–2.90)	.037

Note:—PR indicates prevalence ratio; BP, blood pressure.

**Table 4: Poisson regression for differentiating CE from undetermined etiology**

Variables	PR (95% CI)	P Values
Age	1.00 (0.99–1.02)	.602
Baseline NIHSS score	1.00 (0.97–1.04)	.784
Male sex	0.84 (0.53–1.34)	.472
Smoking	0.94 (0.55–1.60)	.818
Systolic BP	1.00 (1.00–1.00)	.776
Onset-to-imaging time	1.00 (1.00–1.00)	.373
MSC sign	1.19 (0.80–1.76)	.393

Note:—PR indicates prevalence ratio; BP, blood pressure.

**Table 5: Diagnostic testing of the multisegment clot sign for predicting cardioembolism with or without excluding patients with undetermined etiology**

	Sensitivity (%)	Specificity (%)	Positive Predictive Value (%)	Negative Predictive Value (%)	Accuracy
All patients ( $n = 194$ )	52.7	81.0	78.4	56.7	64.9
Excluding UE ( $n = 153$ )	52.7	90.7	93.5	42.9	63.4

Note:—UE indicates undetermined etiology.

## DISCUSSION

Our study indicates that conditions of patients with acute LAO with the MSC sign are more likely due to CE rather than LAA. In the current study, the MSC sign was detected in more than half of the patients with CE, and this sign predicted CE with high specificity and a positive predictive value of 90.7% and 93.5%, respectively.

The sensitivity (52.7%) and the specificity (90.7%) of the MSC sign to predict stroke etiologies were similar to the previously reported 2-layered susceptibility vessel sign on T2\*WI, and that previous study included only patients with CE and LAA.<sup>6</sup> The sensitivity of the MSC sign to predict CE is not high, while the MSC sign exhibited a higher specificity for CE. Thus, we cannot exclude CE in the patients without the MSC sign. However, the high specificity and positive predictive value showed the usefulness of the MSC sign for diagnosing CE, even in patients without known atrial fibrillation.

The underlying mechanism of the MSC sign may be related to clot size, hemodynamic features, and the clot composition. A previous study showed that the CE clot had a larger size and longer walking pathway to occlusion site compared with an LAA clot, which might increase the risk of CE clot collisions on the vessel wall, resulting in splitting of the clot.<sup>9</sup> In addition, the CE clot has the hemodynamic feature of passing through high-pressure gradient areas such as a mitral or aortic valve after discharging from a cardiac chamber,<sup>10</sup> while beyond the site of stenosis, the blood flow velocity of an LAA clot is relatively slow. This difference may make it easier for the CE clot to divide into pieces than the LAA clot.<sup>10</sup> Clot composition may also play a role. A CE clot has a high proportion of erythrocytes, while an LAA clot contains a high composition of fibrin.<sup>11–13</sup> Moreover, different from a CE clot, an atherothrombotic clot usually consists of an exterior meshwork of fibrin and platelet aggregates and an interior close-packed array of compressed polyhedral erythrocytes.<sup>14,15</sup> As a result, the contrast agent penetrates into the space between separated segments due to clot permeability or collateral circulation and is presented as the MSC sign on dynamic CTA.

Currently, guidelines recommend endovascular therapy for patients with acute LAO, while different devices and combined therapy have been introduced when treating patients with different etiologies.<sup>16</sup> Rapid identification of the etiology is crucial for emergent management. With a short acquisition time and wide use of CTP, the assessment of the MSC sign is quick and easy. By providing interventionists with additional information about occlusion etiology, the MSC sign may help decision-making for endovascular procedures and even advance the secondary prevention strategy.<sup>17,18</sup> The etiology of acute LAO seems related to stent retriever refractoriness and some other complications, such as inadvertent detachment, stent retrievers getting stuck, and frequent reocclusions.<sup>19–22</sup> The presence of truncal-site occlusion

reflecting intracranial atherosclerosis was associated with a lower chance of stent retriever success, and these patients more frequently required adjunctive therapies, such as stent placement or use of glycoprotein IIb/IIIa inhibitors.<sup>4</sup> Failure of stroke intervention was associated with longer procedural times and delayed recanalization, resulting in larger infarct volumes and worse neurologic outcomes.<sup>23</sup> Thus, those patients may require greater monitoring for stroke progression and edema development in the postprocedure period.<sup>24</sup> Therefore, stroke etiology provides potentially useful information for neurologists and neurointerventionists involved in acute ischemic stroke treatment.

In the present study, 12 (29.3%) patients in the undetermined etiology group presented with the MSC sign, which could not differentiate CE from undetermined etiology. A previous histologic study found that the features of the clots in patients with undetermined etiology were like those of cardiogenic thrombi.<sup>25</sup> Therefore, the presence of the MSC sign in patients with acute ischemic stroke with inexplicit etiology during this hospitalization indicates the importance of the search for the cardiac sources. Anticoagulation is highly effective for reduction of recurrent stroke among patients with atrial fibrillation.<sup>26</sup> Our findings suggest that anticoagulation should be considered among patients with the MSC sign.

In clinical practice, CTP is used to provide information about infarct core and penumbra. The advantage of evaluating the MSC sign on dynamic CTA is no additional x-ray exposure and contrast medium usage because it is derived from CTP. CT scanners are more widely available than MR imaging scanners and are commonly located in emergency departments of local hospitals.<sup>27</sup> In addition, it is reported that early arterial imaging can overestimate clot length while a late-phase CTA can more accurately delineate the distal thrombus extent.<sup>27</sup> The “delayed-vessel sign” on multiphase CTA refers to the presence of an artery distal to the point of occlusion that is absent or poorly opacified on the early angiographic phases but becomes more opacified and denser on the late phases, which can rapidly indicate the presence of an ipsilateral vessel occlusion.<sup>28</sup> Moreover, compared with MR imaging, dynamic CTA is less commonly influenced by motion and denture artifacts.

There are several limitations to this study. First, it is a retrospective study, though data were prospectively collected using a stroke registry and CTP protocol. A potential risk of selection bias might exist. Second, the sensitivity of the MSC sign was not high, so we cannot exclude CE in our patients without the MSC sign. Third, it was difficult to assess the thrombi beyond the M2 segment; this issue makes the MSC sign less positive. Fourth, the LAA group did not include patients with potential vulnerable plaque despite <50% stenosis, such as those with carotid intraplaque hemorrhage or enhancing intracranial atherosclerotic plaque.<sup>29</sup> Finally, we did not make the histologic comparison of the clots between patients with and without the MSC sign, lacking the information about the nature of different clots.

## CONCLUSIONS

The presence of the multisegment clot sign on dynamic CTA specifically indicates the cause of CE in patients with acute LAO. In

clinical practice, this sign may be helpful for acute management and secondary prevention of ischemic stroke.

Disclosures: Zhicai Chen—RELATED: Grant: National Natural Science Foundation of China (81601017) and Zhejiang Provincial Natural Science Foundation of China (LQ16H090003).\* Min Lou—RELATED: Grant: National Natural Science Foundation of China (81622017 and 81471170) and National Key Research and Development Program of China (2016YFC1301500).\* \*Money paid to the institution.

## REFERENCES

1. Saver JL, Jahan R, Levy EI, et al; SWIFT Trialists. **Solitaire flow restoration device versus the Merci retriever in patients with acute ischaemic stroke (SWIFT): a randomised, parallel-group, non-inferiority trial.** *Lancet* 2012;380:1241–49 CrossRef Medline
2. Gorelick PB, Wong KS, Bae HJ, et al. **Large artery intracranial occlusive disease: a large worldwide burden but a relatively neglected frontier.** *Stroke* 2008;39:2396–99 CrossRef Medline
3. Powers WJ, Derdeyn CP, Biller J, et al; American Heart Association Stroke Council. **2015 American Heart Association/American Stroke Association Focused Update of the 2013 Guidelines for the Early Management of Patients with Acute Ischemic Stroke Regarding Endovascular Treatment: A Guideline for Healthcare Professionals from the American Heart Association/American Stroke Association.** *Stroke* 2015;46:3020–35 CrossRef Medline
4. Baek JH, Kim BM, Kim DJ, et al. **Importance of truncal-type occlusion in stentriever-based thrombectomy for acute stroke.** *Neurology* 2016;87:1542–50 CrossRef Medline
5. Adams HP, Bendixen BH, Kappelle LJ, et al. **Classification of subtype of acute ischemic stroke: definitions for use in a multicenter clinical trial—TOAST. Trial of Org 10172 in Acute Stroke Treatment.** *Stroke* 1993;24:35–41 CrossRef Medline
6. Yamamoto N, Satomi J, Tada Y, et al. **Two-layered susceptibility vessel sign on 3-Tesla T2\*-weighted imaging is a predictive biomarker of stroke subtype.** *Stroke* 2015;46:269–71 CrossRef Medline
7. Zhang R, Zhou Y, Liu C, et al. **Overestimation of susceptibility vessel sign: a predictive marker of stroke cause.** *Stroke* 2017;48:1993–96 CrossRef Medline
8. Kaesmacher J, Boeckh-Behrens T, Simon S, et al. **Risk of thrombus fragmentation during endovascular stroke treatment.** *AJNR Am J Neuroradiol* 2017;38:991–98 CrossRef
9. Hart RG, Halperin JL. **Atrial fibrillation and stroke: concepts and controversies.** *Stroke* 2001;32:803–08 CrossRef Medline
10. Jung JM, Kwon SU, Lee JH, et al. **Difference in infarct volume and patterns between cardioembolism and internal carotid artery disease: focus on the degree of cardioembolic risk and carotid stenosis.** *Cerebrovasc Dis* 2010;29:490–96 CrossRef Medline
11. Kang DW, Jeong HG, Kim DY, et al. **Prediction of stroke subtype and recanalization using susceptibility vessel sign on susceptibility-weighted magnetic resonance imaging.** *Stroke* 2017;48:1554–59 CrossRef Medline
12. Kim SK, Yoon W, Kim TS, et al. **Histologic analysis of retrieved clots in acute ischemic stroke: correlation with stroke etiology and gradient-echo MRI.** *AJNR Am J Neuroradiol* 2015;36:1756–62 CrossRef Medline
13. Sato Y, Ishibashi-Ueda H, Iwakiri T, et al. **Thrombus components in cardioembolic and atherothrombotic strokes.** *Thromb Res* 2012; 130:278–80 CrossRef Medline
14. Tutwiler V, Peshkova AD, Andrianova IA, et al. **Contraction of blood clots is impaired in acute ischemic stroke.** *Arterioscler Thromb Vasc Biol* 2017;37:271–79 CrossRef Medline
15. Cines DB, Lebedeva T, Nagaswami C, et al. **Clot contraction: compression of erythrocytes into tightly packed polyhedra and redistribution of platelets and fibrin.** *Blood* 2014;123:1596–603 CrossRef Medline
16. Behme D, Molina CA, Selim MH, et al. **Emergent carotid stenting after thrombectomy in patients with tandem lesions.** *Stroke* 2017; 48:1126–28 CrossRef Medline
17. Campbell BC, Christensen S, Levi CR, et al. **Comparison of com-**

- puted tomography perfusion and magnetic resonance imaging perfusion-diffusion mismatch in ischemic stroke. *Stroke* 2012;43:2648–53 CrossRef Medline
18. Payabvash S, Souza LC, Kamalian S, et al. **Location-weighted CTP analysis predicts early motor improvement in stroke: a preliminary study.** *Neurology* 2012;78:1853–59 CrossRef Medline
  19. Matias-Guiu JA, Serna-Candel C, Matias-Guiu J. **Stroke etiology determines effectiveness of retrievable stents.** *J Neurointerv Surg* 2014;6:e11 CrossRef Medline
  20. Toyoda K, Koga M, Hayakawa M, et al. **Acute reperfusion therapy and stroke care in Asia after successful endovascular trials.** *Stroke* 2015;46:1474–81 CrossRef Medline
  21. Gascou G, Lobotesis K, Machi P, et al. **Stent retrievers in acute ischemic stroke: complications and failures during the perioperative period.** *AJNR Am J Neuroradiol* 2014;35:734–40 CrossRef Medline
  22. Kang DH, Kim YW, Hwang YH, et al. **Instant reocclusion following mechanical thrombectomy of in situ thromboocclusion and the role of low-dose intra-arterial tirofiban.** *Cerebrovasc Dis* 2014;37:350–55 CrossRef Medline
  23. Khatri P, Abruzzo T, Yeatts SD, et al; IMS I and II Investigators. **Good clinical outcome after ischemic stroke with successful revascularization is time-dependent.** *Neurology* 2009;73:1066–72 CrossRef Medline
  24. Chaturvedi S, Campbell B. **Predicting failure of acute stroke intervention.** *Neurology* 2016;87:1528–29 CrossRef Medline
  25. Ahn SH, Hong R, Choo IS, et al. **Histologic features of acute thrombi retrieved from stroke patients during mechanical reperfusion therapy.** *Int J Stroke* 2016;11:1036–44 CrossRef Medline
  26. Ruff CT, Giugliano RP, Braunwald E, et al. **Comparison of the efficacy and safety of new oral anticoagulants with warfarin in patients with atrial fibrillation: a meta-analysis of randomised trials.** *Lancet* 2014;383:955–62 CrossRef Medline
  27. Mortimer AM, Simpson E, Bradley MD, et al. **Computed tomography angiography in hyperacute ischemic stroke: prognostic implications and role in decision-making.** *Stroke* 2013;44:1480–88 CrossRef Medline
  28. Byrne D, Sugrue G, Stanley E, et al. **Improved detection of anterior circulation occlusions: the “delayed vessel sign” on multiphase CT angiography.** *AJNR Am J Neuroradiol* 2017;38:1911–16 CrossRef Medline
  29. Rai S, Thaler DE, Salehi P, et al. **More to atherosclerosis than stenosis: symptomatic carotid artery with intraplaque hemorrhage.** *Stroke* 2017;48:e104–07 CrossRef Medline

# Arterial Spin-Labeling Improves Detection of Intracranial Dural Arteriovenous Fistulas with MRI

S.A. Amukotuwa, M.P. Marks, G. Zaharchuk, F. Calamante, R. Bammer, and N. Fischbein



## ABSTRACT

**BACKGROUND AND PURPOSE:** Intracranial dural arteriovenous fistulas carry a risk of substantial neurologic complications but can be difficult to detect on structural MR imaging and TOF-MRA. The purpose of this study was to assess the accuracy and added value of 3D pseudocontinuous arterial spin-labeling MR imaging for the detection of these lesions.

**MATERIALS AND METHODS:** This retrospective study included 39 patients with a dural arteriovenous fistula and 117 controls who had undergone both DSA and MR imaging with pseudocontinuous arterial spin-labeling. Two neuroradiologists blinded to the DSA results independently assessed MR imaging with and without pseudocontinuous arterial spin-labeling. They recorded specific signs, including venous arterial spin-labeling signal, and the likelihood of a dural arteriovenous fistula using a 5-point Likert scale. Logistic regression and receiver operating characteristic analyses were performed to determine the accuracy of specific signs and the added value of pseudocontinuous arterial spin-labeling. Interobserver agreement was determined by using  $\kappa$  statistics.

**RESULTS:** Identification of the venous arterial spin-labeling signal had a high sensitivity (94%) and specificity (88%) for the presence of a dural arteriovenous fistula. Receiver operating characteristic analysis showed significant improvement in diagnostic performance with the addition of pseudocontinuous arterial spin-labeling in comparison with structural MR imaging ( $\Delta$ area under the receiver operating characteristic curve = 0.179) and a trend toward significant improvement in comparison with structural MR imaging with time-of-flight MRA ( $\Delta$ area under the receiver operating characteristic curve = 0.043). Interobserver agreement for the presence of a dural arteriovenous fistula improved substantially and was almost perfect with the addition of pseudocontinuous arterial spin-labeling ( $\kappa$  = 0.92).

**CONCLUSIONS:** Venous arterial spin-labeling signal has high sensitivity and specificity for the presence of a dural arteriovenous fistula, and the addition of pseudocontinuous arterial spin-labeling increases confidence in the diagnosis of this entity on MR imaging.

**ABBREVIATIONS:** ASL = arterial spin-labeling; AUC = area under the ROC curve; DAVF = dural arteriovenous fistula; NCH = nodular and/or curvilinear hyperintensities; NPV = negative predictive value; pCASL = pseudocontinuous ASL; PPV = positive predictive value; ROC = receiver operating characteristic; sMRI = structural MRI

Dural arteriovenous fistulas (DAVFs) are intracranial arteriovenous shunting lesions characterized by direct connection between dural arteries and either a dural sinus or cortical vein.<sup>1,2</sup> The consequent increase in blood flow and pressure in draining veins can lead to complications, including cerebral edema, ischemia, and hemorrhage.<sup>2</sup> The criterion standard for the diagnosis

of a DAVF, catheter-based DSA, is invasive, uses ionizing radiation, and carries a small-but-significant risk of permanent neurologic injury.<sup>3</sup>

The clinical presentation of DAVFs is nonspecific and broad, ranging from asymptomatic to pulsatile tinnitus, seizures, altered mental status, and/or intracranial hemorrhage.<sup>4</sup> In some of these patients, an alternative etiology for the presentation is not identified by standard noninvasive imaging methods, and there remains clinical suspicion for a DAVF. A sensitive noninvasive imaging method for the detection of DAVFs would help avoid exposing such patients to the risks (and cost) of diagnostic DSA. 3D TOF-MRA, time-resolved contrast-enhanced MRA, and CTA tech-

Received April 20, 2017; accepted after revision December 26.

From the Department of Radiology (S.A.A., M.P.M., G.Z., R.B., N.F.), Stanford University, Stanford, California; and Florey Department of Neuroscience and Mental Health (S.A.A., F.C.), University of Melbourne, Melbourne, Victoria, Australia.

Drs Amukotuwa and Bammer are supported by National Institutes of Health (National Institute of Biomedical Imaging and Bioengineering) grants 3R01EB002711-06S1 and 5R21EB021029. Dr Calamante is supported by the National Health and Medical Research Council of Australia, grant APP1117724.

Please address correspondence to Shalini A. Amukotuwa, MB, BS, Stanford University, Stanford, California; and Florey Department of Neuroscience and Mental Health, University of Melbourne, Melbourne, VIC, Australia 3052; e-mail: samukotuwa@gmail.com

Indicates open access to non-subscribers at [www.ajnr.org](http://www.ajnr.org)

Indicates article with supplemental on-line tables.

<http://dx.doi.org/10.3174/ajnr.A5570>

niques have been shown to have a high sensitivity and specificity for the identification of DAVFs.<sup>5-10</sup> The diagnosis of DAVFs in daily practice on these conventional imaging studies remains a challenge, however. Unlike AVMs, which often have a conspicuous nidus surrounded by brain tissue, DAVFs often manifest only subtle findings on structural imaging.<sup>4,11</sup> An easily applicable imaging method that increases the conspicuity of DAVFs would therefore be valuable.

Arterial spin-labeling (ASL) is a completely noninvasive MR imaging technique that is now widely available on clinical MR imaging scanners. ASL signal is not observed in cerebral veins under normal conditions due to T1 decay during capillary transit and exchange with the extravascular space of labeled blood-water protons.<sup>11,12</sup> In conditions with arteriovenous shunting such as DAVFs, rapid transit of labeled blood directly from feeding arteries to draining veins results in high signal in venous structures.<sup>11,12</sup> This venous ASL signal is a conspicuous finding that can alert the reader to the presence of shunting. Conventional sequences can then be more closely scrutinized for structural signs of a DAVF. Preliminary studies indicate that ASL improves the detection of small intracranial shunting lesions and increases the reader's diagnostic confidence.<sup>11</sup> These prior investigations, however, included AVMs and only a few DAVFs.<sup>11,12</sup>

The purpose of this case-control study was to assess the value of an MR imaging protocol augmented with 3D pseudocontinuous ASL (pCASL) for the detection of DAVFs and to determine whether reader accuracy and confidence are improved over MR imaging with conventional structural sequences and TOF-MRA.

## MATERIALS AND METHODS

### Patient Population

This retrospective study was approved by our institutional review board.

Thirty-nine patients (15 females, 24 males, 8–86 years of age; mean age, 55 years) with a DAVF and 117 controls (51 females, 66 males, 4 months to 80 years of age; mean age, 50 years) who underwent both DSA and MR imaging with 3D pCASL at our institution between June 1, 2009, (pCASL was used in routine brain MR imaging protocols from this date) and September 30, 2014, were included. To develop our study population, we searched reports of consecutive cerebral DSAs performed during this time for the terms “DAVF,” “dural AVF,” “arteriovenous fistula,” “fistula,” and “carotid cavernous.” This search yielded 792 patients: 139 consecutive patients with a DAVF and 653 patients with no DAVF.

**Patients with DAVFs.** Fifty-six of 139 patients with a DAVF diagnosed on DSA also had an MR imaging with 3D pCASL. One patient was excluded due to markedly motion-degraded images; and 16, due to angiographically complete treatment of the fistula before the MR imaging. Of the 39 patients included in the study, MR imaging and DSA were performed before any treatment of the fistula in 26 patients and following partial treatment (with DSA evidence of residual shunting) in 13. Fistula Cognard grades<sup>13</sup> were the following: I ( $n = 10$ ), IIa ( $n = 7$ ), IIb ( $n = 7$ ), II a + b ( $n = 8$ ), III ( $n = 6$ ), and IV ( $n = 1$ ). Fistula locations were the following: transverse and/or sigmoid sinus ( $n = 14$ ), marginal sinus ( $n = 2$ ), superior sagittal sinus ( $n = 3$ ), torcula herophili ( $n = 1$ ),

vein of Galen ( $n = 3$ ), sphenoparietal sinus ( $n = 1$ ), cavernous sinus ( $n = 8$ ), cortical vein ( $n = 6$ , two infratentorial), and tentorium cerebelli ( $n = 1$ ). Clinical presentations were the following: intracranial hemorrhage ( $n = 15$ ), pulsatile tinnitus ( $n = 9$ ), chemosis/proptosis ( $n = 6$ ), cranial nerve VI palsy ( $n = 2$ ), seizures ( $n = 2$ ), dementia ( $n = 1$ ), and follow-up of previous dural venous sinus thrombosis ( $n = 2$ ) and meningioma resection ( $n = 2$ ).

**Controls.** Six hundred fifty-three patients who had undergone DSA due to a clinical presentation (eg, pulsatile tinnitus or intracranial hemorrhage of unclear origin) potentially attributable to an intracranial vascular malformation did not have a DAVF. Patients with an AVM (which is also associated with arteriovenous shunting) on DSA were excluded. Two hundred nineteen of these patients had an MR imaging with pCASL, and 117 of these patients (3 times the number of cases) were randomly selected as controls.

In patients with multiple imaging studies, the DSA and MR imaging examinations temporally closest to each other were selected (mean time interval, 46 days for the control group and 57 days for the DAVF group).

### Imaging Methods

In 68 subjects (16 patients, 52 controls), MRIs were performed on a 3T scanner (Discovery 750w; GE Healthcare, Milwaukee, Wisconsin); and in 88 subjects (23 patients and 65 controls), on a 1.5T scanner (Signa HDx; GE Healthcare).

3D pCASL imaging (TR/TE, 4800/9.5 ms [1.5T], 5000/10.5 ms [3T]; 24-cm FOV) with background suppression was implemented using a labeling period of 1500 ms, a postlabel delay of 2000 ms, the labeling plane at the level of the foramen magnum, and a segmented 3D stack-of-spirals FSE readout (spiral arms: 6 [1.5T]; 8 [3T]). In-plane spatial resolution was 3–4 mm, and through-plane spatial resolution was 4–6 mm, yielding 24–40 slices. Scan time was 3 minutes 30 seconds–6 minutes. No vascular crusher gradients were used. This acquisition complies with the consensus recommendations of the ASL community.<sup>14</sup> The presence of venous ASL signal was assessed on the label-control subtraction images and required no postprocessing.

3D multislab TOF-MRA (1.5T: TR/TE, 30/2.9 ms; FOV, 22 cm; matrix, 320 × 192; 1.4-mm slice thickness; 3T: TR/TE, 22/2.5 ms; FOV = 24 cm; matrix = 512 × 288; 1.2-mm slice thickness) was performed in 147 patients (36 patients and 111 controls).

All 156 MR imaging examinations also included the following sequences: sagittal T1-weighted (1.5T: TR/TE, 600/15 ms; 3T: TR/TE/TI, 1800/6.7/920 ms) and axial T2-weighted FSE (TR/TE, 4800/84 ms [1.5T]; 4000/100 ms [3T]); T2\*-weighted gradient recalled-echo (TR/TE, 600/30 ms [1.5T]; 600/15 ms [3T]); T2-weighted FLAIR (TR/TE/TI, 8802/110/2200 ms [1.5T]; 9000/143/2300 ms [3T]); and diffusion-weighted ( $b = 1000$  s/mm<sup>2</sup>; TR/TE, 6000/70 ms [1.5T], 5000/83 ms [3T]) imaging performed with a 24-cm FOV, 5-mm slice thickness.

Catheter-based DSA for the clinical work-up of the DAVF was performed by 1 of 3 interventional neuroradiologists (with 5, 12, and >20 years' experience respectively) in a dedicated biplane neuroangiography suite (Axiom Artis; Siemens, Erlangen, Germany). Imaging included, at minimum, anteroposterior and lat-

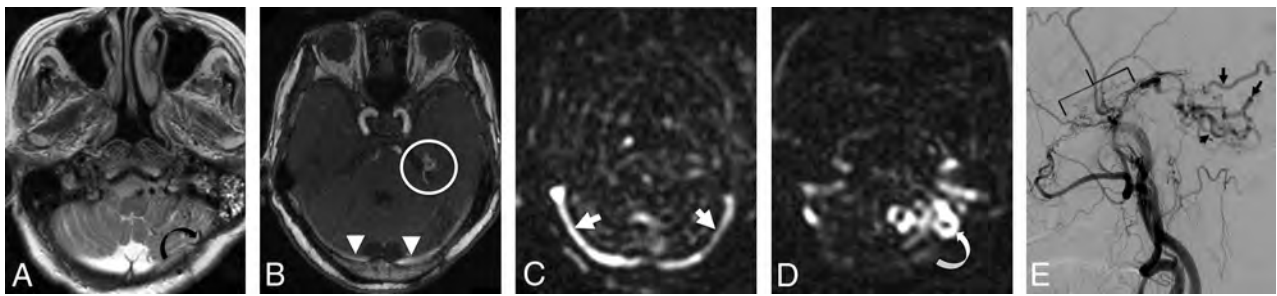


**FIG 1.** A 79-year-old woman presenting with ataxia. *A*, T2-weighted imaging demonstrates tortuous and ectatic pial veins (*curved black arrow*) along the inferior surface of the left cerebellar hemisphere. *B*, MIP TOF-MRA image demonstrates nodular and curvilinear hyperintensities immediately superior to the left petrous apex, representing a left tentorial fistula (*white circle*) and high signal in the transverse sinuses (*white arrowheads*). *C*, pCASL image shows venous ASL signal in the transverse sinuses (*white arrows*) due to shunting. *D*, More inferiorly, venous ASL signal is seen in draining pial veins (*white curved arrow*). *E*, DSA image following left external carotid artery injection confirms a Cognard type IV left tentorial DAVF (*bracket*) with a middle meningeal artery supply and drainage directly into ectatic cerebellar cortical veins (*black arrows*).

eral views obtained following selective injection with iodinated contrast medium (iohexol, Omnipaque 300; GE Healthcare, Piscataway, New Jersey) of the internal carotid, external carotid, and/or vertebral artery supplying the DAVF.

CTA was not included in this evaluation because it is not routinely performed for the evaluation of suspected DAVFs at our institution and it was therefore inconsistently available in the patients in the study population.

### Image Interpretation

**MR Imaging.** MRIs were independently reviewed in random order by 2 neuroradiologists (with 20 years' and 5 years' postfellowship experience) blinded to the clinical data and DSA findings. Review of nonenhanced CT performed before MR imaging was not permitted because it was unavailable in many patients with DAVFs ( $n = 31$ ).

The readers rated the likelihood of a DAVF on a 5-point Likert scale (1, very unlikely; 2, unlikely; 3, equally likely and unlikely; 4, likely; and 5, very likely) based on sequences presented to them. The reads were performed in 2 separate sittings, with and without pCASL, 2 months apart to negate the effects of memory and learning:

**First Sitting.** pCASL was omitted.

**Step 1.** Structural sequences (T1- and T2-weighted imaging, FLAIR, and gradient recalled-echo) were reviewed first to establish the baseline accuracy of MR imaging for identification of DAVFs. We recorded the presence or absence of each of the following signs: intracranial hemorrhage; white matter T2 hyperintensity with mass effect (edema); abnormal vessels (abnormal clusters of flow voids, serpiginous and/or dilated leptomeningeal or medullary vessels, and/or venous pouches) (Fig 1A); and enlarged (reader's subjective impression) dural venous sinuses. DAVFs in the cavernous sinus may produce characteristic features suggestive of this diagnosis; therefore, we specifically recorded these signs: cavernous sinus enlargement, superior ophthalmic vein enlargement, proptosis, and/or orbital edema. The overall likelihood of a DAVF was then rated on the 5-point Likert scale.

**Step 2.** In the 147 patients in whom TOF-MRA was performed, source images and MIPs were assessed next. The following signs

were recorded as present or absent: hyperintense (signal higher than that of suppressed background tissue and similar to that within arteries) dural venous sinus (Fig 1B) or cortical vein; nodular and/or curvilinear hyperintense structures<sup>5</sup> (NCH) adjacent to a dural venous sinus, representing the fistula itself (Fig 1B); increased number or size of arteries near a dural venous sinus; and/or enlargement of external carotid artery branches.<sup>5,6</sup> The overall likelihood of a DAVF based on TOF-MRA and structural features was rated on the 5-point Likert scale.

**Second Sitting.** pCASL was first reviewed in conjunction with anatomic sequences. The presence or absence of venous ASL signal, defined as the presence of high signal intensity on pCASL images within a dural venous sinus (Fig 1C), deep venous structure, and/or cortical vein (Fig 1D) was recorded. TOF-MRA (source and MIP images) was subsequently reviewed, and the overall likelihood of a DAVF based on all sequences was rated.

The presence of a DAVF on angiography was considered the criterion standard. When there was discordance between the findings on MR imaging and angiography, the DSA and MR imaging were reviewed, in consensus, by the 2 neuroradiologists and an experienced neurointerventional radiologist.

### Statistical Analysis

All statistical analyses were performed using SPSS (SPSS Statistics 24.0.0.1, 64 bit; IBM, Armonk, New York) and MedCalc Statistical Software, Version 17.2, 64 bit (MedCalc Software, Mariakerke, Belgium).

To test the added value of pCASL, we performed sensitivity and specificity analyses (individual reader and pooled) for the following: 1) conventional structural MR imaging (sMRI) alone; 2) structural MR imaging and TOF-MRA (sMRI/MRA); 3) structural MR imaging, TOF-MRA, and pCASL (sMRI/MRA/pCASL) using receiver operating characteristic (ROC) analyses by nonparametric estimation of the area-under-the-ROC-curve (AUC) and subsequent pair-wise comparisons using the DeLong algorithm.

Sensitivity, specificity, positive predictive value (PPV), and negative predictive value (NPV) for individual imaging features were computed using the readers' classification tables, with the reference standard being the presence or absence of a DAVF. The likelihood of a DAVF (on DSA) based on the identification of an

**Table 1: Individual imaging features—univariate binary logistic regression analysis on DSA and interreader agreement**

Imaging Feature	OR	SE	Wald Test	P	Sensitivity (95% CI) (%)	Specificity (95% CI) (%)	PPV (95% CI) (%)	NPV (95% CI) (%)	Interobserver Agreement ( $\kappa$ ) (95% CI)
Structural MRI									
ICH	0.18	1.32	37.84	.001	37.2 (26.5–47.9)	23.1 (17.7–28.5)	13.9 (9.2–18.6)	52.4 (43.0–62.1)	0.99 (0.97–1.00)
Vasogenic edema or gliosis	0.36	1.37	10.59	.001	20.8 (11.7–58.1)	58.1 (51.8–64.4)	14.0 (7.7–20.4)	69.0 (62.6–75.5)	1.00 (1.00–1.00)
Abnormal vessels	5.57	1.32	37.24	.001	59.0 (48.1–69.9)	79.5 (74.3–84.7)	48.9 (38.8–59.0)	85.3 (80.6–90.0)	0.73 (0.67–0.79)
Enlarged sinus	2.58	1.36	9.50	.002	31.2 (20.8–41.5)	79.9 (73.9–85.8)	40.7 (28.1–53.2)	72.4 (66.1–78.7)	0.69 (0.61–0.76)
Enlarged SOV	3.68	1.62	7.36	.007	12.7 (5.3–20.0)	96.2 (93.7–98.6)	52.6 (30.2–75.1)	76.5 (71.7–81.4)	0.83 (0.74–0.93)
Cavernous sinus enlargement	34.80	2.14	21.85	.001	23.1 (13.7–32.4)	99.2 (98.0–100.3)	90.0 (76.9–103.2)	79.5 (74.8–84.1)	0.89 (0.82–0.97)
Orbital edema/proptosis	12.26	2.23	10.38	.001	10.3 (3.5–17.0)	99.2 (98.0–100.3)	80.0 (55.2–104.8)	76.8 (72.1–81.6)	1.00 (1.00–1.00)
Time-of-flight MRA									
NCH	114.70	1.88	56.75	.001	61.1 (49.9–72.4)	98.7 (97.1–100.2)	93.6 (86.6–100.6)	88.7 (84.7–92.6)	0.87 (0.82–0.93)
Abnormal vessels	6.00	1.34	37.28	.001	59.7 (48.4–71.1)	80.2 (74.9–85.4)	49.4 (38.9–59.9)	86.0 (81.3–90.7)	0.38 (0.30–0.46)
Venous signal	20.75	1.47	60.96	.001	87.5 (79.9–95.1)	74.8 (69.1–80.5)	52.9 (44.0–61.9)	94.9 (91.6–98.1)	0.87 (0.83–0.91)
Enlarged extracranial arteries	17.81	1.41	70.98	.001	62.5 (51.3–73.7)	91.4 (87.8–95.1)	70.3 (59.1–81.5)	88.3 (84.1–92.4)	0.76 (0.69–0.83)
ASL									
Venous ASL signal	103.20	1.65	84.95	.001	93.6 (88.2–99.0)	87.6 (83.4–91.8)	71.5 (62.8–80.3)	97.6 (95.6–99.7)	0.94 (0.9–0.97)

**Note:**—SOV indicates superior ophthalmic vein; SE, standard error; ICH, intracerebral hemorrhage.

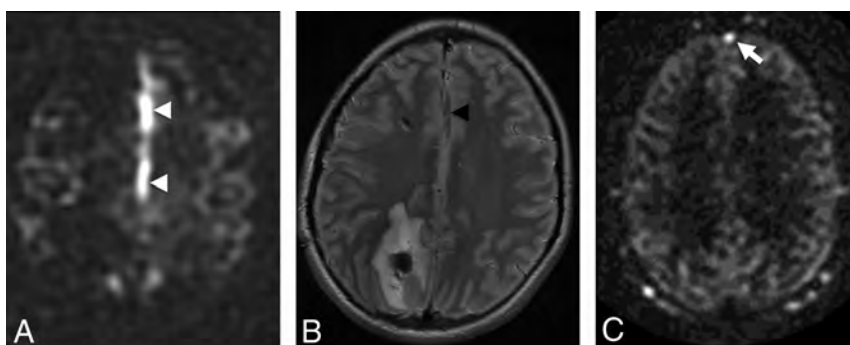


**FIG 2.** False-positive venous ASL signal in 2 patients. A, ASL signal in the A3 branches of the anterior cerebral arteries (*white arrowheads*) was mistaken for venous ASL signal in a 15-year-old male patient who presented with a right parietal parenchymal hematoma. B, T2-weighted images show localization of this signal to the anterior cerebral arteries (*black arrowhead*). C, ASL signal in the anterior aspect of the superior sagittal sinus in a 70-year-old man with subarachnoid hemorrhage (*white arrow*). This patient had no evidence of a DAVF or shunting on DSA.

individual imaging feature was determined using univariate binary logistic regression. A likelihood ratio test between multivariate binary logistic regression models was performed to determine whether the addition of the venous ASL signal feature yielded a stronger association with the presence of a DAVF than structural features alone or structural-plus-TOF-MRA features.

Interobserver agreement between readers was assessed using the Cohen  $\kappa$  statistic for specific imaging features and a linear weighted  $\kappa$  statistic for the likelihood of a DAVF. A  $\kappa$  of at least 0.61 (substantial agreement) was made a prerequisite to pool reader scores for subsequent analysis.

## RESULTS

### Individual Imaging Features

Venous ASL signal had the highest sensitivity (94%; 95% CI 88%–99%) and NPV (98%; 95% CI, 96%–100%) for DAVFs of all the investigated specific features (Table 1). Venous ASL signal and other signs of DAVFs were not visible even on post hoc review of 2 false-negative cases. Both were low-flow DAVFs (1 incidentally detected tentorial fistula in a patient undergoing DSA for evaluation of aneurysmal subarachnoid hemorrhage and 1 low-flow cavernous sinus DAVF).

Nodular and/or curvilinear hyperintensities on TOF-MRA (Fig 1B) had a much lower sensitivity (61%; 95% CI, 50%–72%). Of the 36 patients with a fistula who had undergone TOF-MRA,

the fistula was located above the TOF-MRA slab in 3 on post hoc analysis. Of the 33 patients whose fistula was located within the TOF-MRA slab, NCH were not identified in 9 (reader 1) and 13 (reader 2) patients, and they were absent in 7 patients (21%) on post hoc review. Three were Cognard III fistulas with a single feeding artery.

Univariate binary logistic regression analyses found extremely high odds ratios for both venous ASL signal (103) and NCH (114), reflecting their high specificity. There were a number of false-positives for venous ASL signal in our cohort; therefore, its specificity (88%; 95% CI, 83%–92%) was lower

than that of NCH (99%; 95% CI, 97%–100%). On post hoc review of these 16 false-positive cases, cortical vein ASL signal was evident in 4 and dural venous sinus ASL signal was seen in 11. A definite cause for this ASL signal such as an AVM, hypervascular tumor, or subacute stroke could not be discerned on review of these patients' clinical histories and follow-up imaging, including DSAs. In 3 patients, the cortical vein ASL signal was observed immediately adjacent to a parenchymal hematoma, and we hypothesize that the hematoma may have compressed and obscured (on DSA and conventional MR imaging) a small parenchymal AVM. The other most likely explanation for venous ASL signal in these cases, as well as in 7 of the patients with dural sinus ASL signal, is seizure incited by parenchymal hematoma. In the 4 remaining patients, mild ASL signal in the anterior superior sagittal sinus (Fig 2C) was not associated with parenchymal hematoma, and this is likely a normal variant.

There may have been a small underlying AVM in each of these cases, obscured and compressed by hematoma, hence occult on DSA and structural MR imaging. Alternatively, subclinical seizures incited by hematoma would also account for the venous ASL signal.

Arterial transit artifact<sup>15</sup> was mistaken for venous ASL signal in 1 control (Fig 2A). Venous hyperintensity on TOF-MRA had a lower specificity (75%; 95% CI, 69%–80%) than venous ASL sig-

nal due to a greater number of false-positives (26 for reader 1 and 30 for reader 2).

Structural imaging signs of a fistula were of high specificity but low sensitivity and NPV. Although signs of a cavernous sinus DAVF had high specificity and odds ratios, fistulas in this location were too sparsely represented in our study cohort to draw meaningful conclusions related to these findings.

Agreement between the readers was almost perfect ( $\kappa > 0.81$ ) for all individual features except 3 TOF-MRA parameters: enlarged sinus, enlarged extracranial arteries, and abnormal vessels (Table 1). Only fair agreement ( $\kappa > 0.21$ ) was reached on the latter.

### Overall Assessment

The ROC plots (Fig 3), their corresponding AUCs, and the substantial differences in the AUCs demonstrate improvement in diagnostic performance for the detection of DAVFs with the addition of pCASL (Table 2). Diagnostic performance significantly improved with the addition of TOF-MRA to sMRI (pooled  $\Delta$ AUC, 0.14;  $P < .01$ ). The addition of pCASL significantly improved diagnostic performance over sMRI (pooled  $\Delta$ AUC, 0.179;  $P < .01$ ). Improvement in diagnostic performance with the addition of pCASL to sMRI/TOF-MRA reached statistical significance for reader 2 but not reader 1 (whose excellent diagnostic performance on sMRI and TOF-MRA left little room for improvement). When reader performance was pooled, a trend toward improvement was seen (with only 11% probability that the observed improvement in the detection of DAVFs was due to chance).

These ROC analysis findings were corroborated by the multivariate binary logistic regression models indicating a significant contribution to diagnostic performance from the addition of TOF-MRA and pCASL features to sMRI (Table 3 and On-line Tables 1 and 2). If we applied a  $P = .5$  classification threshold (Table 4), sensitivity was poor for sMRI (33%; 95% CI, 22%–44%), improved if TOF-MRA was added (sensitivity, 76%; 95% CI, 66%–86%), and increased further with pCASL (sensitivity, 89%; 95% CI, 81%–96%) at comparably high specificity (On-line Table 2). When used in combination, sMRI, MRA, and pCASL yielded a high NPV of 96.4% (95% CI, 93.9%–98.9%), which is crucial if MR imaging is to be used as a screening tool.

Incremental improvement in reader confidence in the presence or absence of a DAVF with the addition of pCASL is illustrated in Fig 4.

Interobserver agreement was good for structural imaging alone ( $\kappa = 0.62$ ; 95% CI,  $-1.0$ – $1.0$ ) and improved with the addition of TOF-MRA ( $\kappa = 0.72$ ; 95% CI,  $-1.0$ – $1.0$ ). It improved substantially and was almost perfect with the addition of pCASL ( $\kappa = 0.92$ ; 95% CI,  $-0.23$ – $1.0$ ).

In 4 cases, a DAVF was present on DSA but was considered unlikely on MR imaging until pCASL was reviewed. In 1 case, the fistula was located outside the TOF-MRA slab. In the remaining 3 cases, the fistula was not visible on TOF-MRA despite being located within the slab, and other MRA signs were also absent. Two of these cases were partially treated fistulas with low residual flow on DSA.

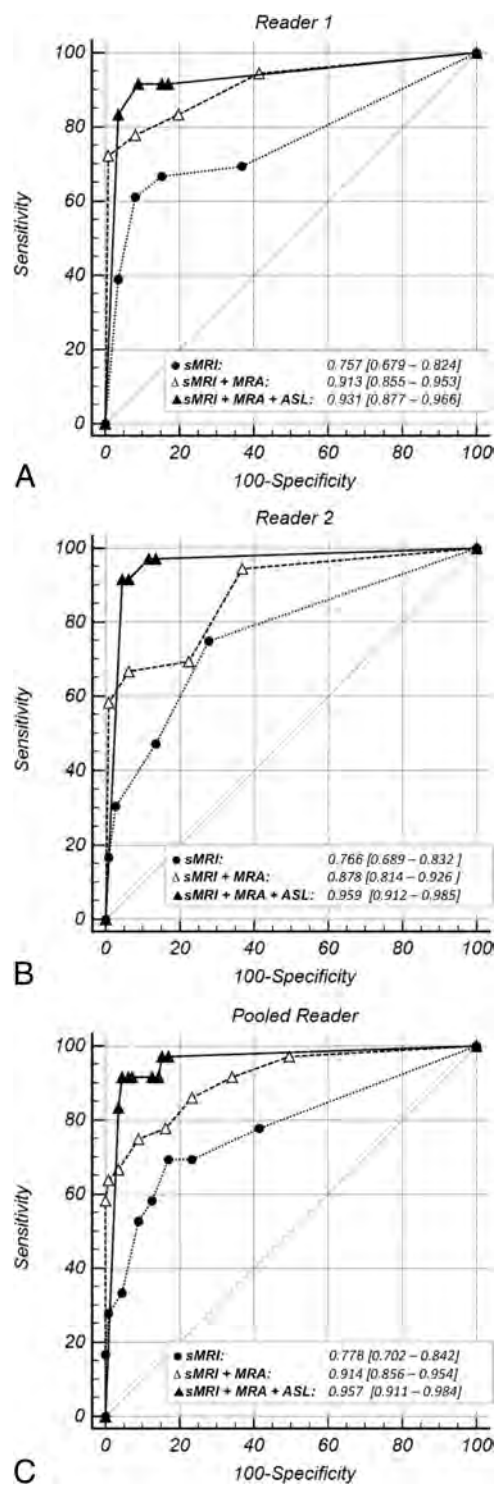


**FIG 3.** ROC curves for each reader's individual diagnostic performance (A and B) and their pooled diagnostic performance (C) with each of the following: structural MR imaging (dotted line), structural MR imaging and TOF-MRA (sMRI + MRA, dashed line), and structural MR imaging with TOF-MRA and pCASL (sMRI + MRA + pCASL, solid line). The light gray diagonal is the line of no discrimination. The triangle and dot symbols on the curve indicate true-positive rate/false-positive rate pairs computed at different discrimination thresholds. With the addition of TOF-MRA and then pCASL to structural MR imaging, the ROC curve becomes more well-rounded with an incrementally higher AUC. This indicates increased diagnostic sensitivity for detection of a DAVF at a set specificity.

**Table 2: Pair-wise comparison of ROC curves**

Reader, Diagnostic Instrument	$\Delta$ AUC	SE	95% CI	z	P
<b>Reader 1</b>					
sMRI vs sMRI + MRA	0.156	0.046	0.066–0.247	3.381	<.01
sMRI vs sMRI + MRA + pCASL	0.174	0.047	0.082–0.266	3.701	<.01
sMRI + MRA vs sMRI+MRA + pCASL	0.018	0.028	–0.036–0.072	0.644	.52
<b>Reader 2</b>					
sMRI vs sMRI + MRA	0.112	0.044	0.027–0.197	2.581	<.01
sMRI vs sMRI + MRA + pCASL	0.193	0.043	0.108–0.277	4.475	<.01
sMRI + MRA vs sMRI + MRA + pCASL	0.081	0.030	0.022–0.140	2.675	<.01
<b>Pooled Readers 1 + 2</b>					
sMRI vs sMRI + MRA	0.136	0.042	0.053–0.219	3.208	<.01
sMRI vs sMRI + MRA + pCASL	0.179	0.045	0.091–0.267	3.965	<.01
sMRI + MRA vs sMRI + MRA + pCASL	0.043	0.027	–0.009–0.100	1.615	.11

**Table 3: Pair-wise likelihood ratio tests for the multivariate models**

Reader, Diagnostic Instrument	-2LL	$\chi^2$	P	$\Delta$ df
sMRI	260.18			
sMRI + MRA	117.09			
sMRI + MRA + ASL	84.23			
(sMRI) vs (sMRI + MRA)		143.09	<.001 <sup>a</sup>	4
(sMRI + MRA) vs (sMRI + MRA + ASL)		32.86	<.001 <sup>a</sup>	1
(sMRI) vs (sMRI + MRA + ASL)		175.95	<.001 <sup>a</sup>	8

**Note:**—LL indicates log likelihood.

<sup>a</sup> Significance ( $P < .001$ )—that is, that the null hypothesis (difference in  $-2LLs = 0$ ) is rejected and that the  $-2LLs$  are different.

## DISCUSSION

This case-control study confirmed that venous ASL signal has a high sensitivity and specificity and an even higher NPV than previously reported<sup>11</sup> for detecting the presence of an intracranial DAVF. Identification of venous ASL signal improves the diagnostic accuracy and increases confidence in the presence or absence of a DAVF. We have previously shown that MR imaging with pCASL can be used to accurately determine the grade of a DAVF.<sup>16</sup> In this study, we investigated the clinical utility of pCASL for detection of DAVFs.

A reliable noninvasive technique for detection of DAVFs can improve patient triage, expedite referral for treatment, and decrease the number of DSAs a patient with a DAVF undergoes by allowing diagnostic and therapeutic angiography to be performed at the same session. Perfect or almost perfect sensitivity and NPV are requisite, given that failure to detect a DAVF has a greater potential for adverse consequences than a false-positive. Unfortunately, conventional structural MR imaging is unreliable for the diagnosis of DAVF as seen in this study. TOF-MRA was also less sensitive than previously reported. For example, nodular/curvilinear hyperintensities have been previously reported to be 100% sensitive,<sup>5</sup> but these were absent even on post hoc review in 21% of DAVFs. Three were high-grade fistulas with a single feeding artery draining directly into a nonectatic cortical vein that would not be expected to manifest as nodular/curvilinear hyperintensities.

Venous ASL signal had a higher sensitivity for the presence of a DAVF than structural or TOF-MRA signs. There were only 2 cases in which the venous ASL signal was absent. The high conspicuity of the venous ASL signal against the relatively flat background of normal ASL signal makes it easy to detect when present. Nulling of static tissue signal by background suppression and subtraction of control from label images produces a high contrast-to-

noise ratio with only labeled blood giving rise to signal on pCASL images.<sup>15,16</sup> One hundred percent of the voxel is occupied by labeled blood in a draining vein in comparison with 2%–5% in a tissue voxel.<sup>16</sup> There is also greater T1 decay of signal of labeled blood by the time it reaches the tissue in comparison with labeled blood shunted directly into venous structures. Consequently, there is a large contrast differential between the draining veins of a DAVF and adjacent brain parenchyma.<sup>16</sup> Absence of ASL signal in arteries under normal conditions also enhances the conspicuity of the venous ASL signal. Conversely, high signal is seen in normal arteries on both TOF-MRA and contrast-enhanced MRA. A hyperintense cortical vein may therefore be dismissed or misclassified as an artery on these sequences.

pCASL is likely to be particularly beneficial to less experienced readers: The junior reader in this study had a lower sensitivity for detection of DAVFs on sMRI and TOF-MRA and demonstrated greater improvement in diagnostic performance following the addition of pCASL. The readers' confidence and agreement regarding the presence or absence of a DAVF also improved following review of pCASL. Interreader agreement for venous ASL signal was higher than for TOF-MRA signs. These findings suggest that venous ASL signal is not only easier to detect but can also be interpreted with greater certainty. Even when present, findings on structural sequences and TOF-MRA are often subtle and equivocal, requiring scrutiny of images and high diagnostic skill to identify and interpret; this has relevance in routine clinical practice, in which there is a broad range of reader experience levels and more likelihood that an unsuspected positive case will be mixed in with many negative cases. The high conspicuity of venous ASL signal may also enable detection of unsuspected DAVFs.

Venous ASL signal also had a high specificity for the presence of a DAVF. Theoretically, high signal is absent in venous structures on pCASL under normal conditions due to T1 decay of labeled blood during the time it takes to pass through the tissue capillary bed.<sup>11,12</sup> The shorter time that labeled blood takes to reach veins when shunted directly precludes significant T1 decay. Venous ASL signal is therefore seen in conditions with arteriovenous shunting, including hypervascular tumors, seizures, stroke, and AVMs.<sup>11,12</sup> False-positive cases of venous ASL signal in this study were likely due to one of these alternative causes of shunting, such as seizure or an occult AVM obscured by hematoma. Four control patients with mild ASL signal in the anterior aspect of the superior sagittal sinus lacked a plausible alternative cause of shunting. The authors have observed mild ASL signal in

**Table 4: Classification tables for the multivariate binary logistic regression models<sup>a</sup>**

MRI Sequences	Sensitivity (95% CI) (%)	Specificity (95% CI) (%)	PPV (95% CI) (%)	NPV (95% CI) (%)
Structural MRI alone	32.9 (22.3–43.5)	97.0 (94.8–99.2)	78.1 (63.8–92.5)	81.7 (77.1–86.2)
Structural MRI and TOF-MRA	75.7 (65.7–85.8)	98.7 (97.1–100.2)	94.6 (88.8–100.5)	92.8 (89.5–96.1)
Structural MRI, TOF-MRA and pCASL	88.6 (81.1–96.0)	96.4 (93.9–98.9)	88.5 (81.1–96.0)	96.4 (93.9–98.9)

<sup>a</sup> Classification table generated for a probability value of  $P = .05$  for each of the 3 multivariate models.

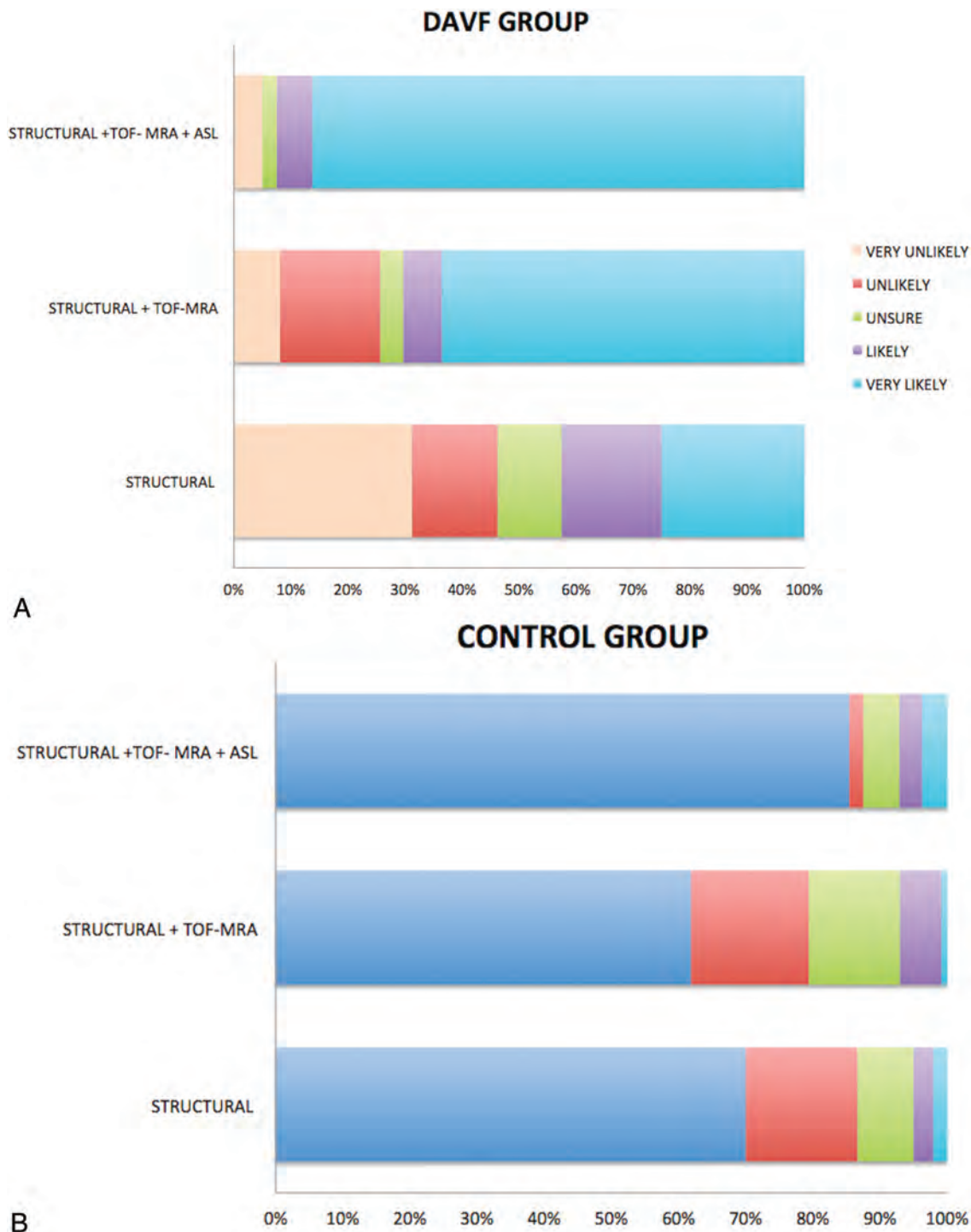


**FIG 4.** Distribution of Likert scale scores for patients with (A) and without (B) a DAVF on structural MR imaging alone, structural MR imaging with TOF-MRA (sMRI/MRA), and structural MR imaging with both TOF-MRA and pCASL (sMRI/MRA/pCASL). A, In the DAVF group, there is a marked incremental increase in reader accuracy and confidence in the presence of a DAVF—with a higher percentage considered “very likely” to have a DAVF—with the addition of pCASL. B, In the control group, reader accuracy and confidence in the absence of a DAVF decrease with the addition of TOF-MRA to sMRI due to a high number of false-positives for venous hyperintensity on TOF-MRA. Reader certainty as to the absence of a fistula increased (and was highest) following review of pCASL.

this location in other patients without a shunting lesion. Readers should be cognizant of this potential normal variant.

Another advantage of pCASL is whole-brain coverage in a reasonable scan time. Despite technologic advances such as 3T and parallel imaging, coverage of TOF-MRA often does not extend to the vertex due to clinical time constraints. DAVFs located superior to the imaged slabs may therefore be missed.

Venous ASL signal was absent in 2 low-flow DAVFs, likely due to an inadequate volume of shunted blood to produce perceptible signal in draining veins. Two other low-flow fistulas were detected on pCASL but missed on TOF-MRA (likely due to signal saturation). There were too few<sup>4</sup> low-flow DAVFs in this study to draw meaningful conclusions regarding this population. Long-label long-delay pCASL may allow detection of these low-flow fistulas, because more labeled blood would be present in draining veins at a later imaging.<sup>15</sup>

Another potential pitfall of pCASL is high signal in arterial structures in conditions with delayed transit of labeled blood such as steno-occlusive disease.<sup>11,15</sup> Cognizance of this arterial transit artifact<sup>15</sup> (Fig 2A) and careful cross-reference with other sequences are necessary to avoid false-positives.

Contrast-enhanced MRA has been reported to be accurate for the detection of DAVFs.<sup>5,7,17</sup> The diagnosis requires identification of early venous filling, which is likely more challenging than identification of the conspicuous venous ASL sign, given the compromise between spatial and temporal resolution required to perform clinical contrast-enhanced MRA; even with highly constrained reconstruction techniques, spatial and temporal resolution is much lower than that of DSA.<sup>18</sup> Contrast-enhanced MRA also requires administration of gadolinium-based contrast, adding to the cost. Gadolinium is also associated with a risk of nephrotoxicity, nephrogenic systemic fibrosis, and deposition. Other advanced techniques for detection and characterization of DAVFs such as 4D ASL-based MRA<sup>18</sup> are still research tools not available for clinical use.

pCASL is also available on both 1.5T and 3T clinical units and is feasible within the constraints of everyday clinical practice. Given its utility for detection of intracranial shunting, we recommend its routine inclusion in the MR imaging protocol for patients with intracranial hemorrhage and pulsatile tinnitus. It should also be added to the protocol for those patients with clinical or noninvasive imaging findings raising suspicion for a DAVF.

The major limitation of this study is the small number of low-flow DAVFs, which may potentially be occult on pCASL. Its retrospective nature also limited us to reviewing routine MR images obtained at our institution. Prospective enrollment would enable inclusion and comparative assessment of CTA, contrast-enhanced MRA, and alternative ASL techniques (eg, long-label long-delay, which may be more sensitive for shunting).

## CONCLUSIONS

Venous ASL signal has high sensitivity and specificity for the presence of a DAVF; hence, its identification increases confidence in the presence or absence of a DAVF on noninvasive imaging. It is also a highly conspicuous finding that is easy to detect and has the potential to increase diagnostic performance, particularly of less

experienced readers. False-positives can occur and are likely due to alternative causes of intracranial shunting. False-negatives also occur, with some small and low-flow fistulas occult on MR imaging with pCASL so that sensitivity is imperfect compared with the criterion standard of DSA. We therefore do not advocate replacing DSA for the screening of DAVFs at this stage if clinical suspicion of a DAVF is high, but MR imaging with pCASL can help refine triage and expedite management by increasing confidence in the diagnosis.

## ACKNOWLEDGMENTS

The authors would like to thank Dr Jarrett Rosenberg for his feedback on the statistical analyses.

Disclosures: Shalini A. Amukotuwa—RELATED: Grant: National Institute of Biomedical Imaging and Bioengineering. Comments: grant numbers 5R21EB021029, 3R01EB002711-06S1.\* Fernando Calamante—RELATED: Grant: National Health and Medical Research Council of Australia; UNRELATED: Grant: Australian Research Council; Payment for Lectures Including Service on Speakers Bureaus: Siemens.\* Greg Zaharchuk—UNRELATED: Grants/Grants Pending: GE Healthcare, National Institutes of Health. Roland Bammer—RELATED: Grant: National Institute of Biomedical Imaging and Bioengineering. Comments: grant numbers 5R21EB021029, 3R01EB002711-06S1\*; Support for Travel to Meetings for the Study or Other Purposes: National Institutes of Health (National Institute of Biomedical Imaging and Bioengineering).\* \*Money paid to the institution.

## REFERENCES

1. Newton TH, Cronqvist S. **Involvement of dural arteries in intracranial arteriovenous malformations.** *Radiology* 1969;93:1071–78 CrossRef Medline
2. Cognard C, Casasco A, Toevl M, et al. **Dural arteriovenous fistulas as a cause of intracranial hypertension due to impairment of cranial venous outflow.** *J Neurol Neurosurg Psychiatry* 1998;65:308–16 CrossRef Medline
3. Cloft HJ, Joseph GJ, Dion JE. **Risk of cerebral angiography in patients with subarachnoid hemorrhage, cerebral aneurysm, and arteriovenous malformation: a meta-analysis.** *Stroke* 1999;30:317–20 CrossRef Medline
4. Miller TR, Gandhi D. **Intracranial dural arteriovenous fistulae: clinical presentation and management strategies.** *Stroke* 2015;46:2017–25 CrossRef Medline
5. Noguchi K, Melhem ER, Kanazawa T, et al. **Intracranial dural arteriovenous fistulas: evaluation with combined 3D time-of-flight MR angiography and MR digital subtraction angiography.** *AJR Am J Roentgenol* 2004;182:183–90 CrossRef Medline
6. Kwon BJ, Han MH, Kang HS, et al. **MR imaging findings of intracranial dural arteriovenous fistulas: relations with venous drainage patterns.** *AJNR Am J Neuroradiol* 2005;26:2500–07 Medline
7. Meckel S, Maier M, Ruiz DS, et al. **MR angiography of dural arteriovenous fistulas: diagnosis and follow-up after treatment using a time-resolved 3D contrast-enhanced technique.** *AJNR Am J Neuroradiol* 2007;28:877–84 Medline
8. Farb RI, Agid R, Willinsky RA, et al. **Cranial dural arteriovenous fistula: diagnosis and classification with time-resolved MR angiography at 3T.** *AJNR Am J Neuroradiol* 2009;30:1546–51 CrossRef Medline
9. Nishimura S, Hirai T, Sasao A, et al. **Evaluation of dural arteriovenous fistulas with 4D contrast-enhanced MR angiography at 3T.** *AJNR Am J Neuroradiol* 2010;31:80–85 CrossRef Medline
10. Brouwer PA, Bosman T, van Walderveen MA, et al. **Dynamic 320-section CT angiography in cranial arteriovenous shunting lesions.** *AJNR Am J Neuroradiol* 2010;31:767–70 CrossRef Medline
11. Le TT, Fischbein NJ, André JB, et al. **Identification of venous signal on arterial spin labeling improves diagnosis of dural arteriovenous fistulas and small arteriovenous malformations.** *AJNR Am J Neuroradiol* 2012;33:61–68 CrossRef Medline

12. Wolf RL, Wang J, Detre JA, et al. **Arteriovenous shunt visualization in arteriovenous malformations with arterial spin-labeling MR imaging.** *AJNR Am J Neuroradiol* 2008;29:681–87 CrossRef Medline
13. Cognard C, Gobin YP, Pierot L, et al. **Cerebral dural arteriovenous fistulas: clinical and angiographic correlation with a revised classification of venous drainage.** *Radiology* 1995;194:671–80 CrossRef Medline
14. Alsop DC, Detre JA, Golay X, et al. **Recommended implementation of arterial spin-labeled perfusion MRI for clinical applications: a consensus of the ISMRM perfusion study group and the European consortium for ASL in dementia.** *Magn Reson Med* 2015;73:102–16 CrossRef Medline
15. Amukotuwa SA, Yu C, Zaharchuk G. **3D pseudocontinuous arterial spin labeling in routine clinical practice: a review of clinically significant artifacts.** *J Magn Reson Imaging* 2016;43:11–27 CrossRef Medline
16. Amukotuwa SA, Heit JJ, Marks MP, et al. **Detection of cortical venous drainage and determination of the Borden type of dural arteriovenous fistula by means of 3D pseudocontinuous arterial spin-labeling MRI.** *AJR Am J Roentgenol* 2016;207:163–69 CrossRef Medline
17. Clark Z, Johnson KM, Wu Y, et al. **Accelerated time-resolved contrast-enhanced magnetic resonance angiography of dural arteriovenous fistulas using highly constrained reconstruction of sparse cerebrovascular data sets.** *Invest Radiol* 2016;51:365–71 CrossRef Medline
18. Iryo Y, Hirai T, Kai Y, et al. **Intracranial dural arteriovenous fistulas: evaluation with 3-T four-dimensional MR angiography using arterial spin labeling.** *Radiology* 2014;271:193–99 CrossRef Medline

# Early Hemodynamic Response Assessment of Stereotactic Radiosurgery for a Cerebral Arteriovenous Malformation Using 4D Flow MRI

C.Q. Li, A. Hsiao, J. Hattangadi-Gluth, J. Handwerker, and N. Farid



## ABSTRACT

**SUMMARY:** Brain AVMs treated with stereotactic radiosurgery typically demonstrate a minimum latency period of 1–3 years between treatment and nidus obliteration. Assessment of treatment response is usually limited to evaluation of AVM nidus structural changes using conventional MR imaging and MRA techniques. This report describes the use of 4D Flow MRI to also measure radiation-induced hemodynamic changes in a Spetzler-Martin grade III AVM, which were detectable as early as 6 months after treatment.

**ABBREVIATION:** SRS = stereotactic radiosurgery

Stereotactic radiosurgery (SRS) is an effective treatment option for brain arteriovenous malformations that are not amenable to microsurgical resection or endovascular embolization. Nidus obliteration is thought to result from radiation-induced endothelial cell proliferation causing progressive vessel wall thickening and eventual occlusion.<sup>1</sup> When successful, this process typically results in a latency period of 1–3 years between treatment and nidus obliteration,<sup>2</sup> though the nidus can persist in approximately 20% of AVMs even 5 years after treatment.<sup>3</sup>

Although MR imaging and MRA have widely supplanted DSA as the mainstay modalities for following AVMs posttreatment, prior studies evaluating their ability to assess the response to SRS have only examined AVM structure, specifically nidus volume.<sup>4–8</sup> Advanced MRA techniques capable of measuring intracranial flow dynamics, such as 4D Flow MRI (<https://www.arterys.com/4d-flow>), have not yet been leveraged to study SRS treatment effects on AVMs.<sup>9</sup>

4D Flow MRI acquires time-resolved phase-contrast data with 3D velocity-encoding throughout the cardiac cycle, pro-

ducing a 4D dataset of velocity vectors. This 4D dataset can be retrospectively analyzed to measure flow in any direction, as well as to calculate numerous other fluid dynamic metrics such as velocity, pressure gradients, vorticity, wall shear stress, turbulence, and so forth.<sup>10</sup> Flow vectors can also be rendered in 3D in various display formats for qualitative visualization.<sup>11</sup>

We report imaging and hemodynamic data from serial 4D Flow MRI of a Spetzler-Martin grade III AVM treated with SRS as a proof-of-concept application of 4D Flow, and we compare this technique with traditional MR imaging/MRA.

## MATERIALS AND METHODS

A 19-year-old man was diagnosed with an unruptured 3.5 × 2.9 × 2.5 cm Spetzler-Martin grade III AVM in the medial left temporal lobe on a trauma work-up. Conventional angiography showed primary arterial supply from the left MCA with secondary contribution from the left posterior cerebral artery (Fig 1A, -B). Venous drainage was solely via the left basal vein of Rosenthal (Fig 1C). The nidus was treated with single-fraction SRS to a prescription dose of 1800 cGy (mean dose, 2000 cGy; maximum, dose 2200 cGy) using a linear accelerator–based volumetric arc therapy technique. The patient experienced no acute or subacute complications.

Baseline MR imaging and serial follow-up MR imaging were performed at 1, 6, 12, and 20 months after SRS. All scans were obtained on a 3T Discovery 750 scanner (GE Healthcare, Milwaukee, Wisconsin), including simple 4-point-encoded 4D Flow MRI with variable-density Poisson disc undersampling,<sup>11,12</sup> with E-SPiRiT (eigenvector-based iTerative Self-consistent Parallel Imaging Reconstruction) combined parallel imaging and compressed-sensing image reconstruction.<sup>13,14</sup>

Received August 28, 2017; accepted after revision November 13.

From the Department of Radiology (C.Q.L., A.H., J.H., N.F.), University of California, San Diego, San Diego, California; and Department of Radiation Medicine and Applied Sciences (J.H.-G.), University of California, San Diego, La Jolla, California.

Paper previously presented at: Annual Meeting of the American Society of Neuro-radiology and the Foundation of the ASNR Symposium, April 22–27, 2017; Long Beach, California.

Please address correspondence to Charles Q. Li, MD, Department of Radiology, University of California, San Diego, 200 W Arbor Dr, MC 8756, San Diego, CA 92103; e-mail: charlesqli@alummi.ucsd.edu



Indicates article with supplemental on-line video.

<http://dx.doi.org/10.3174/ajnr.A5535>

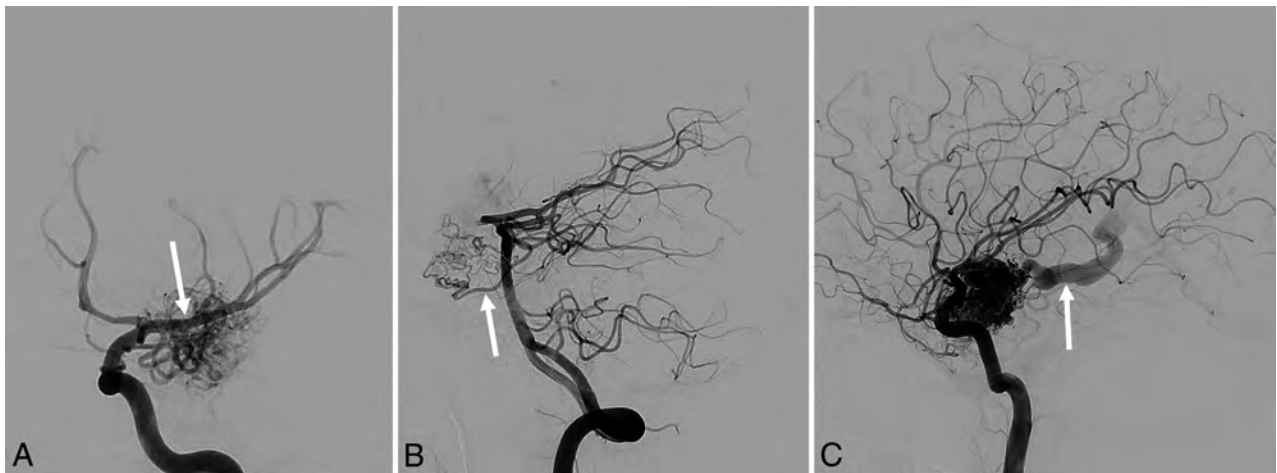


**FIG 1.** Conventional angiography of a left temporal lobe AVM. Early arterial phases show primarily MCA supply (arrow) on a left frontal oblique left ICA injection (A), with secondary posterior cerebral artery supply via a small branch artery (arrow) on a lateral left vertebral artery injection (B). Late arterial phase (C) shows early opacification of the left basal vein of Rosenthal, the exclusive venous drainage (arrow).

#### 4D Flow MRI acquisition parameters

Parameter	
Contrast volume	15–20 mL of gadobenic acid
Voxel size	1.12 × 0.98 × 1.60 to 1.16 × 1.02 × 1.80 mm
Flip angle	15°
TR	4.96–5.05 sec
TE	2.40–2.57 ms
Scan time	7 min 45 sec to 9 min 3 sec
Velocity encoding	100–200 cm/s
Bandwidth	62 kHz

The combination of variable-density Poisson undersampling and E-SPiRiT reconstruction provides the mechanism for compressed sensing, which preserves signal to noise while reducing 4D Flow acquisition time. The parallel imaging acceleration factor was 3.6 overall (1.8 in phase-encode and 2.0 in slice-encode directions). Additional specific acquisition parameters are listed in the Table. At each time point, blood flow (liters/minute) was measured in bilateral distal ICAs, bilateral proximal MCAs, and the draining left basal vein of Rosenthal.

#### RESULTS

In the 20 months following SRS, the patient's left temporal lobe AVM nidus gradually decreased in size from approximately  $3.5 \times 2.9 \times 2.5$  cm to  $2.0 \times 1.5 \times 1.3$  cm, as measured on 3D time-of-flight MRA. Time-resolved color-coded 3D volumetric renderings of 4D Flow velocity data demonstrated visibly decreasing flow velocity in the left MCA, the dominant arterial supply, denoted by decreasing red and yellow velocity vectors and increasing green velocity vectors (Fig 2). Video renderings of 4D Flow data collected throughout the cardiac cycle are available in the On-line Videos.

Blood flow measurements performed using 4D Flow data initially showed asymmetrically greater flow to the left MCA and ICA compared with the contralateral side 1 month posttreatment, which began to normalize by the 6-month follow-up examination. In contrast, flow in the right anterior circulation slightly increased between the 1- and 6-month follow-ups.

By the 20-month follow-up scan, flow in the left MCA and ICA

had decreased by 51% (0.51 to 0.25 L/min) and 34% (0.59 to 0.39 L/min) compared with initial values, respectively, while the net change in right MCA and ICA flow was <11% (Fig 3A). Blood flow in the draining vein also decreased with time, from 0.25 to 0.07 L/min by the 20-month follow-up, a net reduction of 80% (Fig 3B).

#### DISCUSSION

Treatment response following SRS therapy for AVMs is most commonly assessed with conventional MR imaging and MRA techniques, which are tailored to evaluate brain parenchyma and vascular anatomy. This case of a patient with an unruptured AVM treated with curative SRS demonstrates the ability of 4D Flow MRI to quantify radiation therapy-induced hemodynamic changes that are not captured by traditional anatomic imaging modalities.

While radiation-induced endothelial hyperproliferation typically results in a 1- to 3-year latency period between SRS and AVM nidus obliteration, we quantified a decrease in blood flow through a left temporal lobe AVM as early as 6 months after treatment, previously unreported using MRA techniques. We also quantified an increase in flow to the contralateral anterior circulation at the 6-month follow-up, which may suggest reversal of a left-to-right steal phenomenon as flow to the AVM decreased.<sup>15</sup> These findings underscore the ability of 4D Flow MRI to quantify flow dynamics across the entire brain in 1 scan and represent the first application of this technique in the evaluation of SRS treatment effects on AVMs.<sup>16</sup>

Future studies will follow cohorts of patients to explore the relationship between flow dynamics measured by 4D Flow MRI and long-term outcomes, such as hemorrhage risk, length of latency period, and rate of eventual obliteration. Additional hemodynamic measures, such as intravascular pressure gradients, turbulence, and wall shear stress can be examined as well. Flow-mapping capabilities could evaluate changes in flow connectivity in complex AVMs with multiple feeding and draining vessels and perhaps help to further optimize SRS treatment targets.<sup>17</sup>

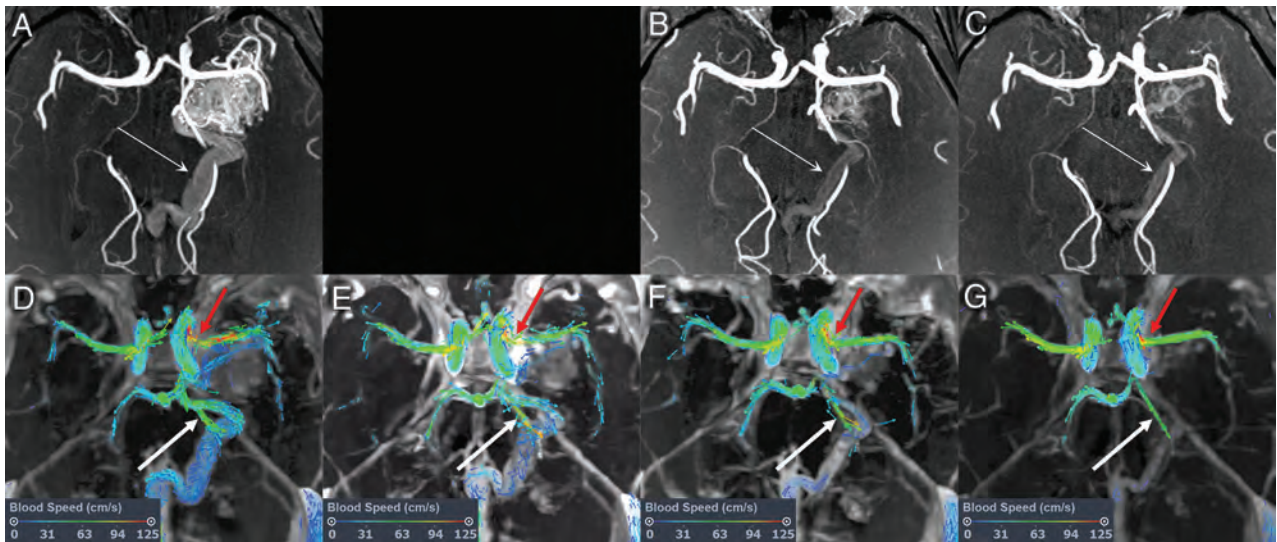


**FIG 2.** Conventional 3D time-of-flight MRA (upper row) and 4D Flow MRI (lower row) during a 20-month follow-up course after SRS. Scans were acquired at 1 (A and D), 6 (E), 12 (B and F), and 20 (C and G) months following SRS (MRA was not performed at the 6-month follow-up). Conventional sequences show a gradual decrease in size of the left temporal lobe AVM nidus, with decreasing distention of the draining vein (thin white arrow). 4D Flow MRI 1 month after SRS (D) shows asymmetrically greater flow in the left MCA (thick red arrow) and posterior cerebral artery feeding vessels (thick white arrow), as well as in the distended draining vein. The left MCA flow velocity gradually decreases with time (D–G).

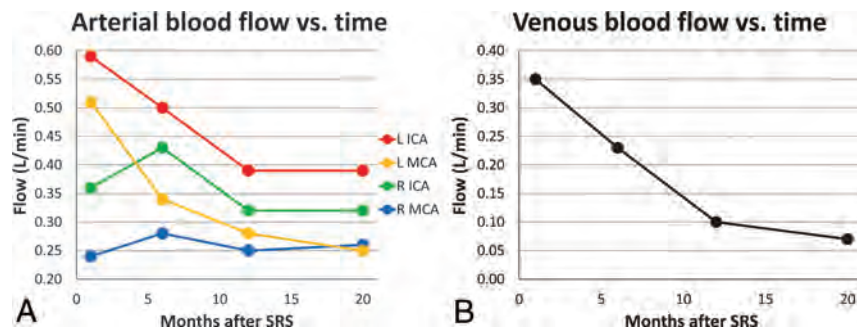


**FIG 3.** Blood flow in the anterior circulation (A) and draining vein (B) measured by 4D Flow over a 20-month follow-up after SRS. At the 6-month follow-up, arterial flow decreased most dramatically in the left MCA. Flow in the left MCA, left ICA, and draining vein continued to decrease throughout the posttreatment course.

Disclosures: Albert Hsiao—UNRELATED: Consultancy: Arterys; Grants/Grants Pending: GE Healthcare\*; Patents (Planned, Pending or Issued): Stanford University; Royalties: Stanford University; Stock/Stock Options: Arterys\*. \*Money paid to the institution.

## REFERENCES

- Lunsford LD, Kondziolka D, Flickinger JC, et al. Stereotactic radiosurgery for arteriovenous malformations of the brain. *J Neurosurg* 1991;75:512–24 CrossRef Medline
- van Beijnum J, van der Worp HB, Buis DR, et al. Treatment of brain arteriovenous malformations: a systematic review and meta-analysis. *JAMA* 2011;306:2011–19 CrossRef Medline
- Kano H, Kondziolka D, Flickinger JC, et al. Stereotactic radiosurgery for arteriovenous malformations, Part 3: outcome predictors and risks after repeat radiosurgery. *J Neurosurg* 2012;116:21–32 CrossRef Medline
- O'Connor TE, Friedman WA. Magnetic resonance imaging assessment of cerebral arteriovenous malformation obliteration after stereotactic radiosurgery. *Neurosurgery* 2013;73:761–66 CrossRef Medline
- Pollock BE, Kondziolka D, Flickinger JC, et al. Magnetic resonance imaging: an accurate method to evaluate arteriovenous malformations after stereotactic radiosurgery. *J Neurosurg* 1996;85:1044–49 CrossRef Medline
- Kihlström L, Guo WY, Karlsson B, et al. Magnetic resonance imaging of obliterated arteriovenous malformations up to 23 years after radiosurgery. *J Neurosurg* 1997;86:589–93 CrossRef Medline
- Buis DR, Bot JC, Barkhof F, et al. The predictive value of 3D time-of-flight MR angiography in assessment of brain arteriovenous malformation obliteration after radiosurgery. *AJNR Am J Neuroradiol* 2012;33:232–38 CrossRef Medline
- Lee CC, Reardon MA, Ball BZ, et al. The predictive value of magnetic resonance imaging in evaluating intracranial arteriovenous malformation obliteration after stereotactic radiosurgery. *J Neurosurg* 2015;123:136–44 CrossRef Medline
- Pereira VM, Delattre B, Brina O, et al. 4D flow MRI in neuroradiology: techniques and applications. *Top Magn Reson Imaging* 2016;25:81–87 CrossRef Medline
- Markl M, Frydrychowicz A, Kozerke S, et al. 4D flow MRI. *J Magn Reson Imaging* 2012;36:1015–36 CrossRef Medline
- Hsiao A, Lustig M, Alley MT, et al. Evaluation of valvular insufficiency and shunts with parallel-imaging compressed-sensing 4D phase-contrast MR imaging with stereoscopic 3D velocity-fusion volume-rendered visualization. *Radiology* 2012;265:87–95 CrossRef Medline
- Hsiao A, Alley MT, Massaband P, et al. Improved cardiovascular

- flow quantification with time-resolved volumetric phase-contrast MRI.** *Pediatr Radiol* 2011;41:711–20 CrossRef Medline
13. Uecker M, Lai P, Murphy MJ, et al. **ESPIRiT—an eigenvalue approach to autocalibrating parallel MRI: where SENSE meets GRAPPA.** *Magn Reson Med* 2014;71:990–1001 CrossRef Medline
14. Murphy M, Alley M, Demmel J, et al. **Fast  $\ell_1$ -SPIRiT compressed sensing parallel imaging MRI: scalable parallel implementation and clinically feasible runtime.** *IEEE Trans Med Imaging* 2012;31:1250–62 CrossRef Medline
15. Homan RW, Devous MD Sr, Stokely EM, et al. **Quantification of intracerebral steal in patients with arteriovenous malformation.** *Arch Neurol* 1986;43:779–85 CrossRef Medline
16. Ansari SA, Schnell S, Carroll T, et al. **Intracranial 4D flow MRI: toward individualized assessment of arteriovenous malformation hemodynamics and treatment-induced changes.** *AJNR Am J Neuroradiol* 2013;34:1922–28 CrossRef Medline
17. Wu C, Schnell S, Markl M, et al. **Combined DSA and 4D flow demonstrate overt alterations of vascular geometry and hemodynamics in an unusually complex cerebral AVM.** *Clin Neuroradiol* 2016;26:471–75 CrossRef Medline

# Quantitative Phase-Contrast MR Angiography to Measure Hemodynamic Changes in Idiopathic Intracranial Hypertension

J. Juhász, T. Lindner, C. Riedel, N.G. Margraf, O. Jansen, and A. Rohr

## ABSTRACT

**BACKGROUND AND PURPOSE:** Idiopathic intracranial hypertension is a syndrome of raised intracranial pressure of unknown etiology. Few MR imaging–based studies have investigated arterial and venous blood flow in these patients. Results are inconclusive, and to our knowledge, no comparison of the hemodynamic parameters before and after CSF pressure reduction has been published. The aim of this study was to assess the short-term effects of normalizing CSF pressure on intracranial flow to better understand the pathophysiology of idiopathic intracranial hypertension.

**MATERIALS AND METHODS:** In this study, we performed quantitative MR imaging–derived flow measurements of brain-supplying arteries and draining veins/dural sinuses to visualize hemodynamic changes in patients with idiopathic intracranial hypertension before and after therapy by lumbar puncture in comparison with a healthy control group.

**RESULTS:** We found differences in patients before and after lumbar puncture in the calculated resistance and pulsatility indices in the superior sagittal sinus. Venous pulsatility showed a negative correlation with CSF pressure in untreated patients. Additionally, there was a trend toward lower flow in the superior sagittal sinus in patients compared with healthy controls. Flow in the internal jugular veins was significantly reduced by lumbar puncture, and the resistance and pulsatility indices differed in patients and controls. The arterial flow was not influenced by pressure normalization.

**CONCLUSIONS:** The results of the present study indicate that venous but not arterial blood flow differs in patients compared with controls and that calculating resistance and pulsatility indices may contribute to assessing short-term hemodynamic changes in patients with diagnosed idiopathic intracranial hypertension before and after CSF diversion.

**ABBREVIATIONS:** BA = basilar artery; IIH = idiopathic intracranial hypertension; IJV = internal jugular veins; LP = lumbar puncture; PI = pulsatility index; RI = resistance index; SS = straight sinus; SSS = superior sagittal sinus

Idiopathic intracranial hypertension (IIH), also known as pseudotumor cerebri, is a syndrome of raised intracranial pressure of unknown etiology.<sup>1</sup> Clinical symptoms include headache, visual impairment, nausea, and papillary edema.<sup>2,3</sup> The initial diagnosis is based on clinical assessment, evidence of increased CSF pressure as per direct measurement (ie, lumbar puncture), and cranial imaging excluding mass lesions and venous sinus thrombosis.<sup>4–6</sup> The finding of transverse sinus stenoses in most patients with IIH, easily visualized with MR venography, has raised the

question of whether IIH is caused by (or results in) impaired cranial blood flow, and studies using MR imaging flow techniques indicate that arterial hyperperfusion and abnormal venous outflow are present in patients with IIH.<sup>7,8</sup> Reducing intracranial pressure in patients with IIH may interfere with a pathologic feedback loop, in which a focal collapse of dural sinuses maintains CSF pressure at an increased level, with increased CSF pressure perpetuating collapse of the dural sinuses. To our knowledge, the short-term effects of normalization of intracranial pressure using lumbar puncture on intracranial flow properties have not been systematically studied. Our study compares MR imaging–derived blood flow properties in patients with IIH before and after normalization of CSF pressure and in healthy controls and aims to answer 2 questions: Can MR imaging flow studies help identify patients with IIH compared with healthy controls? What are the short-term effects of normalizing CSF pressure on intracranial flow (ie, does flow return to normal with treatment)?

Received April 18, 2017; accepted after revision December 29.

From the Clinic for Radiology and Neuroradiology (J.J., T.L., C.R., O.J., A.R.) and Clinic for Neurology (N.G.M.), University Hospital Schleswig-Holstein Campus Kiel, Kiel, Germany; and Neuroradiology Section (A.R.), Vancouver General Hospital, Vancouver, British Columbia, Canada.

Please address correspondence to Julia Juhász, MD, Clinic for Radiology and Neuroradiology, University Hospital Schleswig-Holstein Campus Kiel, Arnold-Heller-Str 3, 24105 Kiel, Germany; e-mail: julia.juhasz@uksh.de

<http://dx.doi.org/10.3174/ajnr.A5571>

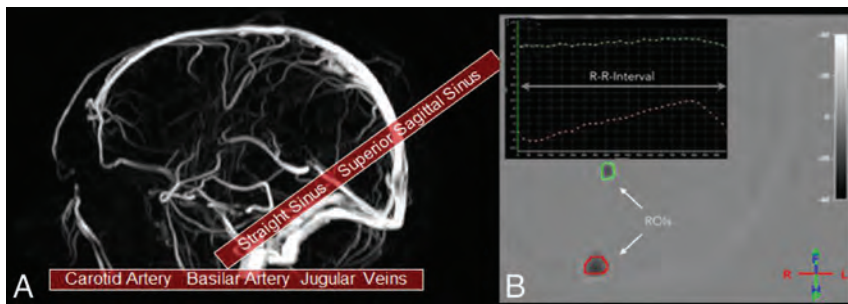


**FIG 1.** A, Slice positioning of the quantitative phase-contrast angiography measurements. Each slab was acquired twice, first with a velocity-encoding of 40 cm/s to visualize venous outflow and then with 100 cm/s to resolve arterial inflow. B, Placement of the measurement ROIs to measure flow properties in the superior sagittal sinus (red circle) and the straight sinus (green circle) with the corresponding measurement points in 1 R-R interval.

## MATERIALS AND METHODS

### Subjects

Twenty consecutive patients seen in the Department of Radiology and Neuroradiology of the UKSH Kiel (18 women, 2 men; mean age,  $34.4 \pm 13.8$  years; mean body mass index,  $35.9 \pm 8.9$  kg/m<sup>2</sup>) with a clinical diagnosis of IIH were included in the study and underwent MR imaging before lumbar puncture (LP). All patients gave written informed consent before scanning, and the study was approved by the local ethics committee. All patients had signs and symptoms of raised intracranial pressure in the presence or absence of prior medical treatment, in particular visual disturbances related to papilledema. LP revealed opening CSF pressures from 21 to >50 cm H<sub>2</sub>O (mean, 35 cm H<sub>2</sub>O) and normal CSF composition. Patients with secondary or unconfirmed disease (ie, normal CSF pressure) were excluded. The mean CSF drained was  $31.3 \pm 5.3$  mL, and the pressure was reduced to  $10.4 \pm 9.9$  cm H<sub>2</sub>O. After LP, a second MR imaging was performed on the same day.

The control group consisted of 20 volunteers (17 women, 3 men; mean age,  $34.9 \pm 11.2$  years) without neurologic disease, undergoing a single MR imaging examination. None of the controls had signs or symptoms of IIH, and none of them had sinus stenosis.

### MR Imaging and Analysis

MR imaging was performed on a 1.5T Achieva scanner (Philips Healthcare, Best, the Netherlands) using a 6-channel receive head coil. To exclude secondary causes of the symptoms, we conducted routine MR imaging, including diffusion-weighted imaging, T2-weighted imaging, and T2-weighted fluid-attenuated inversion recovery. To assess dural sinus morphology, we used 3D phase contrast angiography. To measure venous and arterial hemodynamic properties, we used retrospective 2D cardiac-triggered phase-contrast angiography. Four single-slice measurements were performed. Two were positioned across the neck to evaluate the internal jugular veins and the internal carotid arteries. The others were positioned to image the straight sinus (SS), the superior sagittal sinus (SSS), and the basilar artery (BA). Slice positioning is demonstrated in Fig 1A. Velocity-encoding was set to 40 and 100 cm/s to image venous and arterial flow, respectively. Imaging parameters for phase-contrast angiography were the following: fast-field echo imaging with  $2.2 \times 2.2$  mm voxel size; 20-mm slice thickness; FOV,  $200 \times 165$  mm; flip angle,

15°; TR/TE, 4.6/3.0 ms (venous) and 4.0/2.5 ms (arterial); sensitivity encoding factor, 2. The electrocardiography trigger had a tolerance of +10% and -20% per heartbeat.

Image analysis was conducted by ROI analysis using QFlow (Philips Healthcare). ROIs were placed by an experienced neuroradiologist (J.J.) to cover the area of the BA, SS, and SSS as well as the left and right ICAs and internal jugular veins (IJV). A representative example is shown in Fig 1B. Total arterial inflow was calculated by adding the flow in the BA to the flow in both ICAs.

Flow in the IJV represents total venous outflow. The resistance index (RI) and pulsatility index (PI) of blood flow in all vessels were determined according to the following formulas:

$$1) \quad RI = \frac{v_{\text{systolic}} - v_{\text{diastolic}}}{v_{\text{systolic}}}$$

$$2) \quad PI = \frac{v_{\text{systolic}} - v_{\text{diastolic}}}{v_{\text{mean}}}$$

where  $v_{\text{systolic}}$  describes the maximum systolic velocity;  $v_{\text{diastolic}}$ , the minimum diastolic velocity; and  $v_{\text{mean}}$ , the mean velocity. Venous sinus morphology was assessed by a senior neuroradiologist (A.R.) on the basis of standard phase-contrast imaging, with distinct transverse sinus stenoses assumed when the diameter of the transverse sinus was focally reduced to  $\geq 50\%$  on both sides, compared with the normal-appearing adjacent sinus diameter, and indistinct narrowing when there was  $< 50\%$  reduction in diameter or only unilateral narrowing. Technical parameters were the following: TR/TE, 17/7.9 ms; flip angle, 10°; FOV,  $220 \times 220$ ; velocity-encoding, 20 cm/s.

Results of flow measurements were compared using a paired *t* test for the patient group before and after lumbar puncture. A nonpaired *t* test was used to assess differences between the patient group before LP and the control group. A *P* value  $< .05$  was considered statistically significant.

## RESULTS

### Arterial Inflow

Total arterial inflow values demonstrated no significant differences in patients before versus after LP and between the patient group and the control group, nor did the RI and PI values obtained in the ICA and BA demonstrate any. Flow in the ICAs was higher and flow in the basilar artery was lower in patients than in controls, but the flow did not change after LP.

### Venous Outflow

Flow values in the SSS in patients before and after LP were lower than in healthy controls, but differences reached statistical significance only for patients after LP. Flow did not change significantly after LP. RI and PI in the SSS were lower in patients compared with controls as well as after LP. PI showed a negative correlation with CSF pressure in untreated patients.

**Table 1: Results of flow measurements, RI, and PI in the intracranial vasculature of n = 20 patients and n = 20 controls<sup>a</sup>**

Vessel	Parameter	Patients		Controls	Pre-/Post-LP (P Value)	Pre-LP/Controls (P Value)	Post-LP/Controls (P Value)
		Pre-LP	Post-LP				
SSS	RI	0.33 (±0.08)	0.26 (±0.13)	0.35 (±0.10)	.09	.21	<.04
	PI	0.39 (±0.12)	0.31 (±0.16)	0.43 (±0.18)	.09	.48	<.04
	Flow (mL/min)	454 (±133)	457 (±85)	526 (±119)	.86	.08	<.05
IJV	Flow (mL/min)	663 (±195)	564 (±216)	653 (±199)	<.01	.88	.20

<sup>a</sup> A full list of results is presented in Tables 2 and 3. Data in columns 3–5 are mean values.

**Table 2: Results of flow measurements, RI, and PI in the intracranial vasculature of n = 20 patients and n = 20 controls<sup>a</sup>**

Vessel	Patients		Controls
	Pre-LP	Post-LP	
ICA			
Flow (mL/min)	971 (±222)	969 (±199)	827 (±218)
RI	0.67 (±0.09)	0.63 (±0.08)	0.69 (±0.09)
PI	1.16 (±0.25)	1.05 (±0.20)	1.23 (±0.31)
BA			
Flow (mL/min)	219 (±87)	236 (±90)	316 (±109)
RI	0.66 (±0.10)	0.50 (±0.63)	0.62 (±0.10)
PI	1.20 (±0.32)	0.96 (±0.57)	0.99 (±0.20)
Total arterial inflow (ICA+BA)			
Flow (mL/min)	1189 (±235)	1206 (±241)	1143 (±261)
SSS			
Flow (mL/min)	454 (±133)	457 (±85)	526 (±119)
RI	0.33 (±0.08)	0.26 (±0.13)	0.35 (±0.10)
PI	0.39 (±0.12)	0.31 (±0.16)	0.43 (±0.18)
SS			
Flow (mL/min)	138 (±30)	151 (±68)	143 (±33)
RI	0.30 (±0.06)	0.30 (±0.20)	0.31 (±0.08)
PI	0.36 (±0.09)	0.35 (±0.24)	0.37 (±0.12)
IJV			
Flow (mL/min)	663 (±195)	564 (±216)	653 (±199)
RI	0.47 (±0.14)	0.29 (±0.64)	0.60 (±0.24)
PI	0.64 (±0.28)	0.48 (±0.48)	0.96 (±0.59)

<sup>a</sup> Data are mean values of patients and volunteers.

**Table 3: Corresponding P values for Table 2**

Vessel	Pre-/Post-LP (P Value)	Pre-LP/Controls (P Value)	Post-LP/Controls (P Value)
ICA			
Flow (mL/min)	.98	.05	.04
RI	.20	.66	.04
PI	.17	.50	.04
BA			
Flow (mL/min)	.21	<.01	.02
RI	.29	.16	.43
PI	.30	.21	.82
Total arterial inflow (ICA+BA)			
Flow (mL/min)	.73	.57	.44
SSS			
Flow (mL/min)	.86	.08	.05
RI	.09	.21	.04
PI	.09	.48	.04
SS			
Flow (mL/min)	.46	.59	.65
RI	.91	.73	.78
PI	.90	.79	.78
IJV			
Flow (mL/min)	<.01	.88	.20
RI	.25	.04	.05
PI	.16	.04	<.01

Flow in the IJV did not differ between patients and controls but was significantly reduced after LP in patients. RI and PI in the IJV were lower in patients before and after LP compared with

controls. Again, RI and PI were lower after LP. In the straight sinus, no differences were observed among all groups regarding flow, RI, and PI.

**Dural Sinus Stenoses**

Seventeen of 20 patients (85%) showed distinct bilateral transverse sinus narrowing on MR venograms, with the remaining 3 patients showing only mild-to-moderate narrowing. After LP, sinus narrowing normalized in 2 patients, improved in another 4 patients, but was unchanged in 11/20 patients. None of the controls showed distinct sinus narrowing.

In Table 1, a list of the most important results is presented. The results from the remaining measurements are listed in the Tables 2 and 3. Figure 2 demonstrates an example of a patient with IIH before and after LP.

**DISCUSSION**

In recent years, the value of cranial MR venography has been investigated for its potential in diagnosis and monitoring therapeutic success in patients with IIH.<sup>9</sup> While the presence of bilateral transverse sinus stenoses was found to be a strong predictor of IIH by several authors, follow-up studies are rare and have yielded conflicting results.<sup>10</sup> In some cases, resolution of sinus narrowings was observed after normalization of intracranial pressure, but others reported that sinus stenoses persisted in most patients who improved clinically on follow-up.<sup>10-13</sup> It is, however, largely accepted that sinus narrowing in patients with IIH plays a role in increasing intracranial venous and intracranial CSF pressure, and interesting theoretic models have been proposed explaining the underlying mechanisms.<sup>14-16</sup> The pathophysiology of IIH is not well-understood, and several hypotheses to explain the etiology of this disease have been published.<sup>17</sup>

Of particular interest is a model that explains increased CSF pressure being induced by a negative feedback loop: A self-limiting collapse of

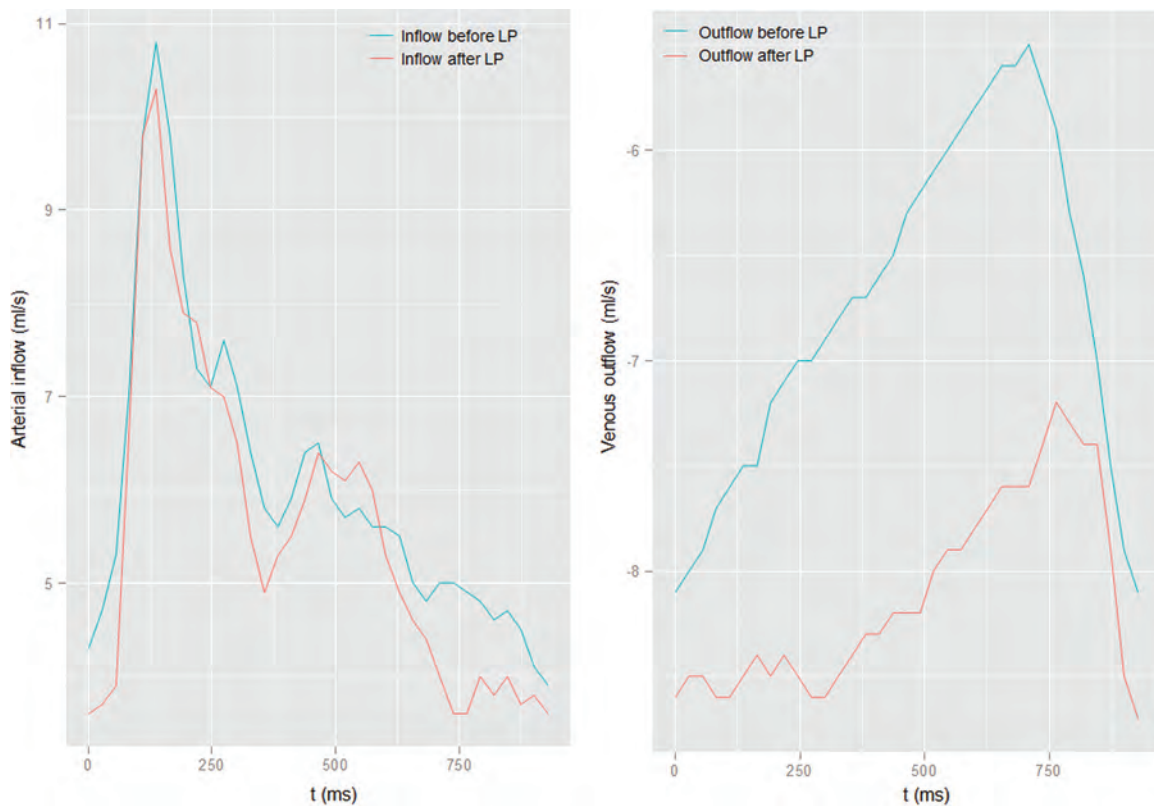


**FIG 2.** Example of the flow measurements (carotid arteries) of 1 patient showing no difference before and after LP (*left*). On the venous measurements of the SSS (*right*), a change in flow can be observed.

the transverse sinuses is presumed to result in a different equilibrium state with an increase in intracranial venous and CSF pressure, depending on the compliance of the sinus wall.<sup>18</sup>

Also, several case series have reported the success of dural sinus stent placement in these patients, further confirming the importance of dural sinus stenoses in the pathophysiology of IIH.<sup>19,20</sup> Intravascular MR imaging–based flow studies in patients with IIH could therefore be of interest in elucidating exactly which hemodynamic changes occur and have been conducted by a few authors. Hemodynamic properties studied include the total inflow and outflow rate (milliliters/minute) and flow velocity (centimeters/second) of the intracranial arterial and venous systems, respectively.<sup>7,8</sup> From these values, the resistance and pulsatility indices can be derived. MR imaging phase conventional angiography, also used in this study, is an established technique with reported error rates below 5% and a negligible intra- and interobserver variability.<sup>21–23</sup> Results by Bateman<sup>7,8</sup> indicated that transverse sinus stenoses resulted in decreased SSS outflow and probable redistribution of venous outflow via smaller collaterals. Also, increased arterial inflow was observed in at least a subset of patients with IIH, suggesting that impaired autoregulation might play a role in the etiology of IIH.<sup>7,8</sup> In our study, we wanted to re-evaluate those findings, and in particular, we wanted to find out if and how intracranial flow is influenced by normalization of intracranial pressure via LP.

Our findings indicate that total arterial inflow in patients with IIH is not significantly different from that in healthy controls. The number of patients in our study who did not show distinct sinus narrowing was too small ( $n = 3$ ) to allow subgroup analysis. Therefore, we cannot confirm that impaired autoregulation re-

sulting in hyperemia plays a role in this subset of patients with IIH, as suggested by Bateman.<sup>7,8</sup> Most interesting, compared with us and most authors, Bateman had a much higher percentage of patients with IIH who did not show sinus narrowing (50% and 58%, respectively<sup>7,8</sup>), which might have influenced his findings.

The largest intracranial sinus, the SSS, showed reduced flow compared with that in controls, possibly related to stenosis-induced outflow impairment via transverse sinuses, but this did not reach statistical significance ( $P = .08$ ), compared with reports elsewhere.<sup>7,8</sup> A reduced SSS outflow could be explained by a compensatory increased venous outflow through other venous outflow pathways. This implies that there is compensatory increased venous outflow through other venous outflow pathways that might have a higher compliance for changes in pressure. These alternative drainage pathways, however, could not be directly assessed because they are too small to be visualized with the MR imaging technique used. These small collateral venous vessels might be sensitive to pressure changes after LP, resulting in increased venous collateral outflow. This could explain why we found a decrease in flow in the IJV after LP but no change in the relatively reduced flow in the SSS.

In the literature, a correlation between elevated intracranial pressure and narrowing of the transverse sinuses has been described,<sup>13,15</sup> but resolution of sinus narrowing following the decrease of intracranial pressure by LP has been reported in only a minority of patients.<sup>13,24,25</sup> Sinus narrowing normalized in only 2 of our patients following LP though, indicating fixed stenoses in most patients, possibly due to chronic dural sinus wall changes.

It was reported that the PI in the dural sinuses of patients with IIH is lower than in healthy controls, possibly reflecting the increase in

dural sinus venous pressure that has been observed by different groups using invasive methods.<sup>21</sup> In our patient cohort, lower values of PI in the SSS of patients were found compared with controls. We found a significant negative correlation of the PI with the degree of CSF pressure, supporting the above-mentioned assumptions.

It was reported that venous pressure and flow in the SSS normalized in patients with IIH treated with transverse sinus stents. This outcome, however, does not necessarily seem to be the case in patients treated with LP. We found that SSS flow did not change and RI and PI further decreased after LP. This finding indicates that measuring RI and PI allows visualizing changes in flow dynamics after therapy that have not been seen otherwise. RI and PI could therefore serve as diagnostic markers for a successful reduction in CSF pressure in treated patients. Figure 2 shows an example of a patient having distinct changes in PI and RI in the SSS after LP.<sup>26</sup>

In this study, we only evaluated the short-term effects of reducing CSF pressure by a single LP. Follow-up studies regarding the long-term effects of a single LP (or multiple LPs), medical treatment, or dural sinus stent placement might also give added insight into pathophysiologic changes in these patients.

In this study, the correlation of intracranial pressure with arterial and venous flow parameters in patients with IIH was measured. In addition to blood flow properties, other parameters might play a role in the assessment of IIH. For a deeper understanding of this complex disease, multifactorial analysis of the whole intracranial system, including CSF flow and pulsatility and elastographic measurements of the brain tissue itself may be helpful.<sup>27,28</sup> These additional variables could potentially be used for a better understanding of the pathomechanism of IIH.

## CONCLUSIONS

Our results indicate changes in several aspects of intracranial blood flow in patients with diagnosed IIH before and shortly after CSF diversion and patients with IIH compared with controls. Venous flow measurements and calculation of resistance and pulsatility indices in combination with dural sinus imaging might provide parameters to distinguish different patient cohorts, help in therapeutic decision-making (eg, stent placement), and monitor effects of CSF-lowering therapies. However, using flow measurements alone for the diagnosis of IIH and evaluating therapeutic strategies might not be sufficient. Therefore, a larger number of patients need to be studied.

Disclosures: Nils Gerd Margraf—UNRELATED: Payment for Lectures Including Service on Speakers Bureaus: Merz Pharmaceuticals and Bayer.

## REFERENCES

- McGeeney BE, Friedman DI. **Pseudotumor cerebri pathophysiology.** *Headache* 2014;54:445–58 CrossRef Medline
- Friedman DI, Liu GT, Digre KB. **Revised diagnostic criteria for the pseudotumor cerebri syndrome in adults and children.** *Neurology* 2013;81:1159–65 CrossRef Medline
- Wall M. **Update on idiopathic intracranial hypertension.** *Neurol Clin* 2017;35:45–57 CrossRef Medline
- Kosmorsky GS. **Idiopathic intracranial hypertension: pseudotumor cerebri.** *Headache* 2014;54:389–93 CrossRef Medline
- Brodsky MC, Vaphiades M. **Magnetic resonance imaging in pseudotumor cerebri.** *Ophthalmology* 1998;105:1686–93 CrossRef Medline
- Rangel-Castilla L, Gopinath S, Robertson CS. **Management of intracranial hypertension.** *Neurol Clin* 2008;26:521–41 CrossRef Medline
- Bateman GA. **Association between arterial inflow and venous outflow in idiopathic and secondary intracranial hypertension.** *J Clin Neurosci* 2006;13:550–56; discussion 557 CrossRef Medline
- Bateman GA. **Vascular hydraulics associated with idiopathic and secondary intracranial hypertension.** *AJNR Am J Neuroradiol* 2002;23:1180–86 Medline
- Agid R, Farb RI, Willinsky RA, et al. **Idiopathic intracranial hypertension: the validity of cross-sectional neuroimaging signs.** *Neuroradiology* 2006;48:521–27 CrossRef Medline
- Kelly LP, Saindane AM, Bruce BB, et al. **Does bilateral transverse cerebral venous sinus stenosis exist in patients without increased intracranial pressure?** *Clin Neurol Neurosurg* 2013;115:1215–19 CrossRef Medline
- Wall M, Corbett JJ. **Revised diagnostic criteria for the pseudotumor cerebri syndrome in adults and children.** *Neurology* 2014;8:198–99 CrossRef Medline
- Bono F, Giliberto C, Mastrandrea C, et al. **Transverse sinus stenoses persist after normalization of the CSF pressure in IIH.** *Neurology* 2005;65:1090–93 CrossRef Medline
- Rohr A, Dörner L, Stinge R, et al. **Reversibility of venous sinus obstruction in idiopathic intracranial hypertension.** *AJNR Am J Neuroradiol* 2007;28:656–59 Medline
- Owler BK, Parker G, Halmagyi GM, et al. **Cranial venous outflow obstruction and pseudotumor cerebri syndrome.** *Adv Tech Stand Neurosurg* 2005;30:107–74 CrossRef Medline
- King JO, Mitchell PJ, Thomson KR, et al. **Manometry combined with cervical puncture in idiopathic intracranial hypertension.** *Neurology* 2002;58:26–30 CrossRef Medline
- Bateman GA. **Idiopathic intracranial hypertension: priapism of the brain?** *Med Hypotheses* 2004;63:549–52 CrossRef Medline
- Wall M. **Idiopathic intracranial hypertension (pseudotumor cerebri).** *Curr Neurol Neurosci Rep* 2008;8:87–93 CrossRef Medline
- De Simone R, Ranieri A, Montella S, et al. **The role of dural sinus stenosis in idiopathic intracranial hypertension pathogenesis: the self-limiting venous collapse feedback-loop model.** *Paininerva Med* 2014;56:201–09 Medline
- Donnet A, Metellus P, Levrier O, et al. **Endovascular treatment of idiopathic intracranial hypertension: clinical and radiologic outcome of 10 consecutive patients.** *Neurology* 2008;70:641–47 CrossRef Medline
- Ahmed RM, Wilkinson M, Parker GD, et al. **Transverse sinus stenting for idiopathic intracranial hypertension: a review of 52 patients and of model predictions.** *AJNR Am J Neuroradiol* 2011;32:1408–14 CrossRef Medline
- Evans AJ, Iwai F, Grist TA, et al. **Magnetic resonance imaging of blood flow with a phase subtraction technique: in vitro and in vivo validation.** *Invest Radiol* 1993;28:109–15 CrossRef Medline
- Laffon E, Valli N, Latrabe V, et al. **A validation of a flow quantification by MR phase mapping software.** *Eur J Radiol* 1998;27:166–72 CrossRef Medline
- Powell AJ, Maier SE, Chung T, et al. **Phase-velocity cine magnetic resonance imaging measurement of pulsatile blood flow in children and young adults: in vitro and in vivo validation.** *Pediatr Cardiol* 2000;21:104–10 CrossRef Medline
- Baryshnik DB, Farb RI. **Changes in the appearance of venous sinuses after treatment of disordered intracranial pressure.** *Neurology* 2004;62:1445–46 CrossRef Medline
- Higgins JN, Pickard JD. **Lateral sinus stenoses in idiopathic intracranial hypertension resolving after CSF diversion.** *Neurology* 2004;62:1907–08 CrossRef Medline
- Juhász J, Lindner T, Jansen O, et al. **Changes in intracranial venous hemodynamics in a patient with idiopathic intracranial hypertension after lumbar puncture precedes therapeutic success.** *J Magn Reson Imaging* 2018;47:286–88 CrossRef Medline
- Alperin N, Ranganathan S, Bagci AM, et al. **MRI evidence of impaired CSF homeostasis in obesity-associated idiopathic intracranial hypertension.** *AJNR Am J Neuroradiol* 2013;34:29–34 CrossRef Medline
- Glaser KJ, Manduca A, Ehman RL. **Review of MR elastography applications and recent developments.** *J Magn Reson Imaging* 2012;36:757–74 CrossRef Medline

# MRI Features Can Predict 1p/19q Status in Intracranial Gliomas

A. Lasocki, F. Gaillard, A. Gorelik, and M. Gonzales

## ABSTRACT

**BACKGROUND AND PURPOSE:** The 2016 revision of the *World Health Organization Classification of Tumors of the Central Nervous System* mandates codeletion of chromosomes 1p and 19q for the diagnosis of oligodendroglioma. We studied whether conventional MR imaging features could predict 1p/19q status.

**MATERIALS AND METHODS:** Patients with previous 1p/19q testing were identified through pathology department records, typically performed on the basis of an oligodendroglial component on routine histology; 69 patients met the inclusion criteria. Preoperative imaging of patients with grade II or III gliomas was retrospectively assessed by 2 neuroradiologists, blinded to the 1p/19q status. Thirteen MR imaging features were first assessed in a small initial cohort ( $n = 10$ ), after which the criteria were narrowed for the remaining patients as a validation cohort.

**RESULTS:** There was 85% agreement between radiologists for the overall prediction of 1p/19q status in the validation cohort, with an accuracy of 84%. The presence of >50% T2-FLAIR mismatch and calcification was found to be the most useful for predicting 1p/19q status. The >50% T2-FLAIR mismatch variable was demonstrated in 14 tumors and had 100% specificity for identifying a noncodeleted tumor ( $P = .001$ ), with 97% interobserver correlation. Calcification was visualized in 7 tumors, 6 of which were 1p/19q codeleted (specificity, 97%;  $P = .006$ ), with 100% interobserver correlation.

**CONCLUSIONS:** The presence of >50% T2-FLAIR mismatch is highly predictive of a noncodeleted tumor, while calcifications suggest a 1p/19q codeleted tumor. If formal 1p/19q testing is not possible, a combined MR imaging–histologic assessment may improve the diagnostic accuracy over histology alone.

**ABBREVIATIONS:** TCGA/TCIA = The Cancer Genome Atlas/The Cancer Imaging Archive; WHO = World Health Organization

The diagnostic criteria for astrocytic and oligodendroglial tumors have recently been updated by the World Health Organization (WHO), leading to a greater reliance on molecular markers over just the histologic phenotype.<sup>1</sup> An important update has been the mandating of codeletion of chromosomes 1p and 19q for the diagnosis of oligodendroglioma, in addition to the presence of a mutation in the *isocitrate dehydrogenase (IDH)* genes, either type 1 (*IDH1*) or type 2 (*IDH2*).<sup>1</sup> Thus, the previous heterogeneous

group of oligoastrocytomas, containing both neoplastic astrocytic and oligodendroglial components, has been largely abolished, with true mixed oligoastrocytomas now being rare.<sup>1</sup> As the number and importance of distinct genetic mutations increases, however, there is the potential for a substantial increase in cost. MR imaging has the potential to improve the targeting of molecular testing to those patients with a greater likelihood of a positive result.<sup>2</sup> In addition, 1p/19q testing is not readily available in many centers, and there may be insufficient tissue to perform 1p/19q testing in some cases. It is not clear how to optimize diagnosis in this context. In such situations, the WHO recommends labeling the tumor on the basis of its histologic phenotype, but with the suffix “NOS” (not otherwise specified).<sup>1</sup> This labeling essentially reverts to the prior classification, the deficiencies of which have been acknowledged.<sup>1</sup>

A conventional MR imaging feature labeled “T2-FLAIR mismatch” has been studied by Patel et al<sup>3</sup> in patients from The Cancer Genome Atlas/The Cancer Imaging Archive (TCGA/TCIA)

Received January 31, 2017; accepted after revision December 29.

From the Department of Cancer Imaging (A.L.), Peter MacCallum Cancer Centre, Melbourne, Victoria, Australia; Department of Radiology (A.L., F.G.), Melbourne EpiCentre (A.G.), and Department of Anatomical Pathology (M.G.), The Royal Melbourne Hospital, Parkville, Victoria, Australia; Monash Imaging (A.L.), Monash Health, Clayton, Victoria, Australia; and Departments of Medicine (A.G.) and Pathology (M.G.), The University of Melbourne, Parkville, Victoria, Australia.

Please address correspondence to Arián Lasocki, MD, Department of Cancer Imaging, Peter MacCallum Cancer Centre, Grattan St, Melbourne, Victoria, Australia 3000; e-mail: arian.lasocki@petermac.org

<http://dx.doi.org/10.3174/ajnr.A5572>

cohort. This feature was found in 15 of 125 cases of lower grade gliomas, all of which were 1p/19q noncodeleted. The authors subsequently validated their findings in 82 patients from their own institution, with all 10 tumors having this appearance being 1p/19q noncodeleted.<sup>3</sup> T2-FLAIR mismatch is equivalent to the MR imaging appearances of so-called “protoplasmic” astrocytomas; these tumors typically demonstrate a component with high signal on T2WI and substantial suppression on T2-FLAIR imaging.<sup>4</sup> This T2-FLAIR suppression was found in all 8 protoplasmic astrocytomas in the series by Tay et al<sup>4</sup> and occupied more than half of the tumor in 5 of their 8 cases. Although protoplasmic astrocytomas are no longer recognized as a distinct entity in the updated WHO classification, now being included within the diagnosis of diffuse astrocytoma,<sup>1</sup> this characteristic appearance provides an explanation for the correlation between T2-FLAIR mismatch and 1p/19q noncodeleted tumors.

In contrast, the presence of calcification on CT has been found to predict 1p/19q loss of heterozygosity.<sup>5</sup> Noncircumscribed borders have also been shown to correlate with 1p/19q codeletion, occurring in 92% of molecular oligodendrogliomas in a recent series by Johnson et al,<sup>6</sup> but this appearance is not specific because it was also present in 45% of noncodeleted tumors. Other conventional imaging features suggested as being typical of oligodendrogliomas include a cortical-subcortical location,<sup>7</sup> though it is not clear whether this remains true in the current molecular era. Also before the classification update, elevated CBV was a well-known feature of oligodendrogliomas related to their “chicken wire” vascularity.<sup>8</sup> CBV elevation has been associated with chromosome 1p deletion, albeit in a small cohort.<sup>9</sup> The value of CBV elevation for the differentiation between codeleted and noncodeleted tumors is limited, however, by the association with high-grade gliomas.<sup>10</sup> This limitation is of particular relevance to anaplastic gliomas but also relevant to WHO grade II tumors, due to the risk of sampling error.<sup>11</sup>

The purpose of this study was to determine whether conventional MR imaging features can be used to predict 1p/19q status in WHO grade II and III gliomas.

## MATERIALS AND METHODS

### Patient Selection

Institutional human research ethics committee approval was obtained. Patients with previous 1p/19q testing were identified through the records of the Department of Anatomical Pathology at The Royal Melbourne Hospital. Testing for 1p/19q by fluorescence in situ hybridization had been performed on samples received between August 2010 and August 2016 as previously described,<sup>12</sup> assessing 20 nuclei at 10 different sites for a total of 200 nuclei. Reference to a test signal ratio of <0.8 was regarded as indicating detection. We included WHO grade II or III gliomas with the following histologic diagnoses: astrocytoma, oligodendroglioma, oligoastrocytoma, or diffuse glioma. Testing for 1p/19q had generally been performed due to the presence of an oligodendroglial component or diagnostic uncertainty on standard histologic assessment, though testing was performed more broadly in the last few months of the study cohort (thus in a minority of patients) as a result of the updated WHO criteria. *IDH1*, *ATRX*, and *TP53* immunohistochemistry was also per-

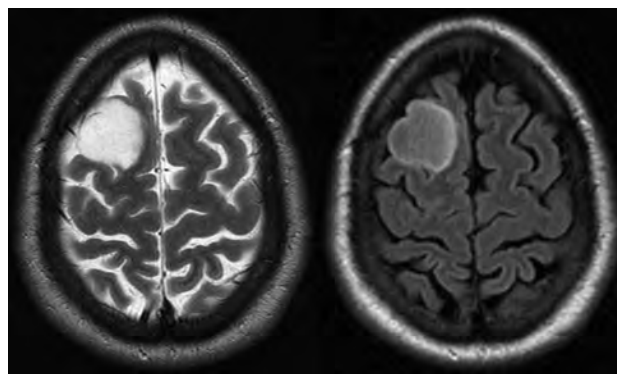


**FIG 1.** Axial T2 and FLAIR images of a patient with a low-grade right frontal lobe glioma. It is markedly T2-hyperintense, like CSF, with the majority of the tumor demonstrating substantially lower signal on the FLAIR sequence. This tumor was 1p/19q noncodeleted.

formed for all patients, but more definitive *IDH* mutation testing was not routinely available for patients with immunohistochemistry negative for *IDH1*. Histologic assessment was performed by subspecialist neuropathologists for all patients. Patients were excluded if they had a histologic diagnosis other than those listed, a WHO grade IV tumor, or no preoperative MR imaging available.

### MR Imaging Assessment

Preoperative MRIs were reviewed by 2 neuroradiologists with a subspecialty interest in neuro-oncology. MRIs were performed on several different scanners at our institution (35 at 1.5T and 12 at 3T) or incorporated from a variety of outside institutions ( $n = 22$ ). Assessment was performed in 2 stages. Initially, 10 cases thought by the study neuropathologist to be histologically characteristic of each entity (five 1p/19q codeleted and 5 noncodeleted tumors, all WHO grade II) were reviewed, assessing a larger number of conventional MR imaging features based on the Visually Accessible Rembrandt Images (VASARI) feature set.<sup>13</sup> These features were the following: lobar location; tumor laterality; cortical involvement (the percentage of the total perimeter of the tumor within the cortex); enhancement quality; proportions of enhancing tumor, non-contrast-enhancing tumor, necrosis, and edema; proportion of T2-FLAIR mismatch; cysts; T1/FLAIR ratio; definition of non-contrast-enhancing tumor margin; and calcification. Proportions were stratified as 0%, 1%–5%, 6%–33%, 34%–67%, 68%–95%, or >95%, as per the VASARI criteria.<sup>13</sup> Calcification was only considered present if it could be confidently differentiated from hemorrhage, either by CT or the phase component of susceptibility-weighted imaging when performed. T2-FLAIR mismatch was subjectively determined as the proportion of the tumor demonstrating high signal on T2WI and substantial suppression on T2-FLAIR imaging (Fig 1). Finally, an overall subjective MR imaging prediction of 1p/19q status was made on the basis of the combination of findings because at this initial stage of the evaluation, the relative specificities of each feature were not clear.

After the initial cohort of 10 patients, the cases were discussed and the imaging features included in the subsequent assessment were rationalized to those thought to be most helpful in suggesting either a 1p/19q codeleted or noncodeleted tumor, to minimize the chances of finding an association by chance alone. These fea-

tures were the presence of calcification, the extent of T2-FLAIR mismatch, and the extent of cortical involvement. The other MR imaging features were thought to have too much overlap between the 2 tumor types. Calcification was based on CT for most patients (preoperative CT was available for 40 patients and was performed within 48 hours postoperatively in another 15), supplemented by susceptibility-weighted imaging, including phase images, in 12 patients. T2-FLAIR mismatch and cortical involvement were stratified as <33%, 33%–50%, or >50%, to determine the optimal threshold for predicting 1p/19q status. As before, an overall MR imaging prediction on 1p/19q status was also made on the basis of the sequential assessment of calcification (its presence indicating a codeleted tumor), T2-FLAIR mismatch (>50% indicating a noncodeleted tumor), and substantial cortical involvement (>50% suggesting a codeleted tumor). If all 3 features were absent, the assessment was then subjective, typically considering 33%–50% T2-FLAIR mismatch or cortical involvement as a positive finding (for a noncodeleted and codeleted tumor, respectively). This assessment was performed for the remaining patients in the cohort.

### Statistical Analysis

$\kappa$  statistics were calculated to determine interobserver agreement between the 2 reviewers, and the Fisher exact test was used to determine the association between 1p/19q status and the presence of calcification and >50% T2-FLAIR mismatch. The analysis was performed by using STATA 12 (StataCorp, College Station, Texas).

## RESULTS

### Histology

Of 92 patients initially identified as having undergone 1p/19q testing, 23 were excluded (14 did not have preoperative MR imaging available for review, 4 had a grade IV tumor, and 5 had other histologic diagnoses), leaving 69 patients, comprising the initial cohort of 10 patients and the 59 patients in the validation cohort. The histologic diagnoses in the validation cohort (based on pathology department records) consisted of oligoastrocytomas ( $n = 35$ ), oligodendrogliomas ( $n = 12$ ), astrocytomas ( $n = 6$ , including 1 protoplasmic astrocytoma based on the prior WHO classification), and diffuse gliomas ( $n = 6$ ). The tumors labeled as diffuse gliomas were diagnosed after the release of the 2016 revision of the WHO classification. Forty-three tumors were WHO grade II (73%); the remaining 16 were grade III. Twenty-one of the 59 tumors (36%) in the validation cohort were 1p/19q codeleted (12 phenotypic oligoastrocytomas, 7 oligodendrogliomas, 1 astrocytoma, and 1 diffuse glioma); the remaining 38 tumors were noncodeleted (23 oligoastrocytomas, 5 oligodendrogliomas, 5 astrocytomas, and 5 diffuse gliomas).

Forty-seven patients had immunohistochemistry positive for *IDH1*. *IDH* pyrosequencing was also performed for one of the patients with immunohistochemistry negative for *IDH1*, demonstrating an R132S mutation. Five of the 10 noncodeleted tumors with immunohistochemistry negative for *IDH1* demonstrated both ATRX and TP53 mutations: 4 had mutations in either ATRX or TP53, and 1 patient had immunohistochemistry negative for both. All except 1 of the 1p/19q codeleted tumors had immuno-

histochemistry positive for *IDH1*. This tumor had the appearance of an oligodendroglioma on standard histology, with wild-type ATRX and TP3. The tumor was thus suspected of having a non-R132H *IDH* mutation, given the strong association between 1p/19q codeleted oligodendrogliomas and *IDH* mutations.<sup>14</sup>

### MR Imaging Assessment: Initial 10 Patients

The 2 radiologists agreed on the diagnosis in 9 of the 10 patients in the initial cohort, with 100% agreement with 1p/19q status in these cases. The only discrepancy was a patient with calcification (suggestive of 1p/19q codeletion) but features otherwise suggestive of a noncodeleted tumor. This tumor had 1p/19q codeletion.

### MR Imaging Assessment: Validation Cohort

There was good agreement between radiologists for the overall prediction of 1p/19q status ( $\kappa = 0.61$ ; 95% CI, 0.4–0.8;  $P < .001$ ), with both giving the same diagnosis in 50 of the 59 cases (85%). Both radiologists had 78% accuracy in predicting 1p/19q status, which improved to 84% for the 50 cases with agreement between radiologists. Interobserver correlation varied among individual MR imaging features. Calcification had 100% correlation between radiologists. The agreement between radiologists for the T2-FLAIR mismatch variable was almost perfect, with absolute agreement in 57 of 59 patients and 2 with  $\pm 1$  point difference (weighted  $\kappa = 0.88$ ; 95% CI, 0.76–1.00;  $P < .001$ ). The cortical involvement variable had poor interobserver correlation, however, at 42%, which largely accounted for the differences in the overall MR imaging prediction of 1p/19q status between the 2 readers.

Calcification was visualized in 7 tumors, 6 of which were 1p/19q codeleted ( $P = .006$ ). These consisted of 5 oligoastrocytomas, 1 oligodendroglioma, and 1 diffuse glioma based on initial phenotypic assessment. Fourteen tumors demonstrated >50% T2-FLAIR mismatch according to both readers, all noncodeleted ( $P = .001$ ). Importantly, the presence of >50% T2-FLAIR mismatch correctly identified the noncodeleted status in 2 patients when this was not suspected on initial histology (both being phenotypic oligodendrogliomas). Of the remaining 12, eight were initially labeled as oligoastrocytomas; 3, as astrocytomas; and 1, as a diffuse glioma. Of note, the 1 protoplasmic astrocytoma in this cohort did demonstrate >50% T2-FLAIR mismatch. Eleven of the 14 tumors with >50% T2-FLAIR mismatch had immunohistochemistry positive for *IDH1*, while the 3 patients with immunohistochemistry negative for *IDH1* all demonstrated both ATRX and TP53 mutations, suggesting that they had non-R132H *IDH* mutations.<sup>15</sup> Only 1 tumor had 33%–50% T2-FLAIR mismatch, also noncodeleted. Greater than 50% cortical involvement (Fig 2) was identified by both readers in 4 patients, all with 1p/19q codeletion. Only 1 patient had the presence of >1 of these 3 features: This patient had both calcification and >50% cortical involvement, both features correctly predicting 1p/19q codeletion.

Specificity was high for both the >50% T2-FLAIR mismatch variable (100% specific for predicting a noncodeleted tumor) and the presence of calcification (97% specific for predicting a codeleted tumor). The positive predictive values were also high at 100% and 86%. Sensitivity was relatively low, however, at 37% and 29%, because most tumors (38 of 59) did not have either of

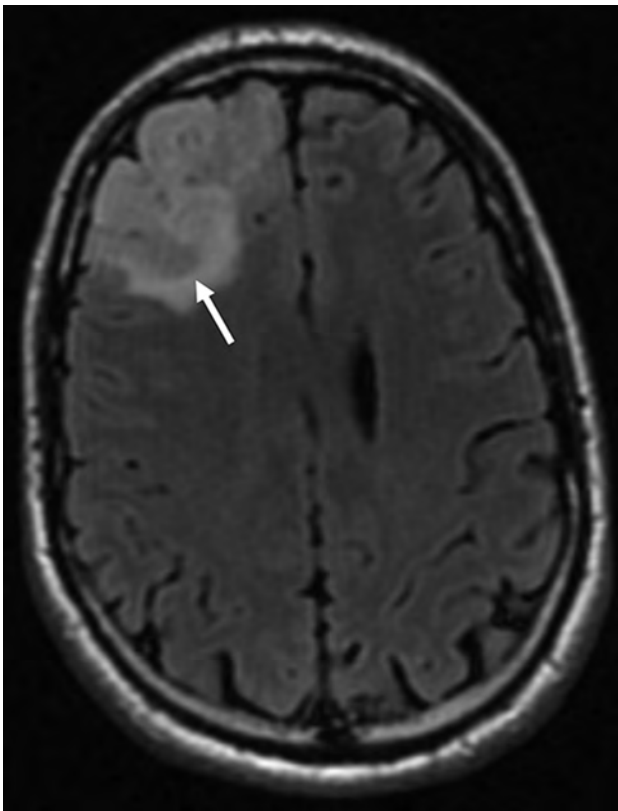


**FIG 2.** Axial FLAIR image showing a right frontal tumor with >50% cortical involvement. The margin of the expanded cortex is demonstrated by the *white arrow*. This tumor was 1p/19q codeleted.

these 2 features. Given the poor interobserver correlation for the cortical involvement variable, it was not considered appropriate to determine consensus results; thus, an overall correlation with 1p/19q status was not calculated. For 1 reader, the overall accuracy was 71% by using cut-offs of either >33% or >50% cortical involvement as predictive of 1p/19q codeletion; for the second reader, the overall accuracy was 61% and 53%, respectively. With a cutoff of >33% cortical involvement (which fared better across the 2 readers), the sensitivity and specificity were 55% and 81%, respectively, for one reader, and 78% and 50% for the other reader.

Using the presence of >50% T2-FLAIR mismatch and/or calcification to predict 1p/19q status in the 35 patients with phenotypic oligoastrocytomas decreased the number of patients with indeterminate 1p/19q status by 13 (to 22) and thus doubled the number of patients in whom 1p/19q status was predicted correctly (from 13 to 26). If these MR imaging features were used in preference to the histologic phenotype when present (in the 2 phenotypic oligodendrogliomas demonstrating >50% T2-FLAIR mismatch, as described above), 1p/19q status was correctly predicted in a further 2 patients, decreasing the number of incorrect predictions from 5 to 3.

## DISCUSSION

The simple MR imaging assessment described was overall moderately accurate for predicting 1p/19q status, but the accuracy of 82% is insufficient to replace formal 1p/19q testing for all patients. The inaccuracy is partly because, in some tumors, none of

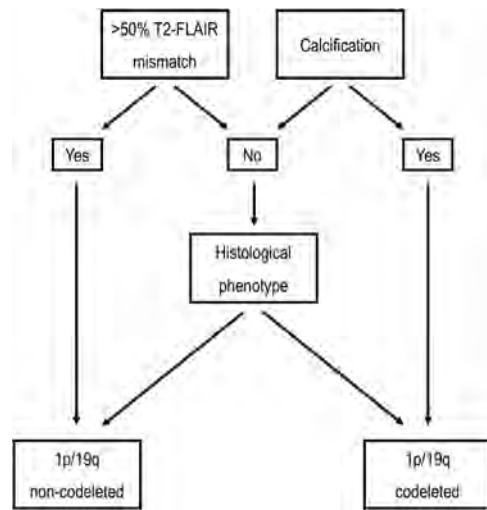


**FIG 3.** A suggested combined MR imaging–histology method of determining 1p/19q status when formal testing is not possible.

the key MR imaging features were present. More important for the clinical setting, however, a substantial proportion of tumors demonstrated MR imaging features that can predict 1p/19q status with high specificity, including in cases in which this is not expected from the histologic phenotype. Thus, >50% T2-FLAIR mismatch is strongly predictive of a noncodeleted tumor, while the tumor is likely 1p/19q-codeleted if there are calcifications. Of these 2 MR imaging features, >50% T2-FLAIR mismatch was both more sensitive and more specific than the presence of calcifications. No patients had both features, suggesting that they are mutually exclusive, at least in large part.

Histology remains a crucial first step, both to confirm the diagnosis of glioma (because these MR imaging features can also occur in other tumors and nonneoplastic conditions) and for glioma grading.<sup>14</sup> Nevertheless, once a grade II or III glioma has been diagnosed (and other differentials have been excluded), MR imaging is very useful for predicting 1p/19q status. The presence of >50% T2-FLAIR mismatch or calcification may provide a surrogate marker of 1p/19q status in cases in which formal testing cannot be performed, for example due to financial or geographic limitations. This feature would be most useful in patients with an indeterminate histologic phenotype, specifically those labeled as “oligoastrocytoma NOS” according to the updated WHO classification.<sup>1</sup> The MR imaging features may even negate the need for formal 1p/19q testing, especially if the phenotypic appearances are supportive. Figure 3 illustrates a possible combined MR imaging–histology assessment method for cases in which formal 1p/19q testing is not possible. First, the tumor is assessed for the presence of >50% T2-FLAIR mismatch or calcifications. If neither of these features is present or if the results are discordant (likely a very rare occurrence), the diagnosis reverts to the histologic phenotype. While there will be rare exceptions to this method, because not all tumors having calcifications are non-codeleted (as demonstrated by 1 patient in our cohort), our results show that this method is likely to be more accurate than using the histologic phenotype alone.

Johnson et al<sup>6</sup> have shown that noncircumscribed borders correlate with 1p/19q codeletion, but given that this appearance

was also present in 45% of noncodeleted tumors, this MR imaging feature is not sufficiently specific to predict codeletion with confidence. Rather, to predict 1p/19q status with high specificity, it may be more useful to use circumscribed borders as predictive of a noncodeleted tumor, albeit with limited sensitivity. The suggested combined assessment method could also potentially be extended to cases in which MR imaging is not available, because CT provides useful information. CT is excellent for the detection of calcifications, while the correlate of T2-FLAIR mismatch on CT is a markedly hypodense tumor. Using these features may also have some value even if formal 1p/19q testing is available. Both of the most common methods of determining 1p/19q status (fluorescence in situ hybridization and polymerase chain reaction–based microsatellite loss of heterozygosity) have been shown to occasionally produce false-positive results,<sup>16</sup> and there is also a small risk of sampling error due to the inherent heterogeneity of glial series tumors.<sup>17–19</sup> In contrast, MR imaging provides the potential to overcome this limitation due to its ability to assess the entire tumor.<sup>11</sup> A discrepancy between the MR imaging appearances and formal 1p/19q testing may thus raise the possibility of sampling error or a mixed tumor.

Dominant cortical involvement was the least useful feature in our cohort due to the high interobserver variability and low incidence. In addition, it is likely to be the least specific feature, especially in smaller tumors, because cortical involvement is also frequently present in astrocytomas.<sup>20,21</sup> These limitations of the cortical involvement variable account for some of the inaccuracies in the overall prediction of 1p/19q status. We also assessed the 2 possible thresholds of >50% or >33% for the proportions of T2-FLAIR mismatch and cortical involvement. This assessment is most relevant to T2-FLAIR mismatch, given the limitations of cortical involvement discussed above. Of the 2 thresholds, we think that >50% is the most appropriate. Only 1 tumor had 33%–50% T2-FLAIR mismatch; thus, dropping the threshold to >33% would only slightly increase the sensitivity of MR imaging assessment in identifying a noncodeleted tumor, but at the risk of decreasing the specificity and interobserver correlation.

We acknowledge the presence of selection bias because 1p/19q testing was not performed on all intracranial gliomas during this period, which was largely before the update to the WHO criteria. Because 1p/19q testing was generally performed on the basis of an oligodendroglial component on standard histologic assessment (usually an oligoastrocytoma), one may have expected a relatively large proportion of 1p/19q codeleted tumors, but the proportion of 1p/19q codeleted tumors in our cohort was similar to that in a large series described recently.<sup>15</sup> Presumably this similarity reflects a balance between the relatively small number of histologic astrocytomas and oligodendrogliomas in our cohort, which were not thought to require 1p/19q testing at the time. Also related to this selection bias, there was only 1 protoplasmic astrocytoma in our cohort (diagnosed before the recent WHO classification). Nevertheless, the substantial number of patients in our cohort with >50% T2-FLAIR mismatch suggests that this MR imaging feature is not specific to tumors labeled protoplasmic astrocytomas. This may be because a protoplasmic (or microcystic) appearance on histology occurs on a continuum, and the diagnosis was not clearly defined in the previous WHO classification,<sup>22</sup> a reason

for this entity no longer being recognized in the more recent classification.<sup>1</sup> Whatever the histologic correlate for T2-FLAIR mismatch, however, it is a very useful biomarker.

More definitive *IDH* mutation testing was not routinely available for patients with immunohistochemistry negative for *IDH1*, but the addition of ATRX and TP53 immunohistochemistry data overcomes some of this limitation, suggesting some tumors that are likely to harbor non-R132H *IDH* mutations. Our results thus somewhat support the findings of Patel et al<sup>3</sup> that substantial T2-FLAIR mismatch is specific to *IDH*-mutant astrocytomas rather than *IDH* wild-type astrocytomas, but we are unable to support this definitively. Of note, the single 1p/19q codeleted tumor with immunohistochemistry negative for *IDH1* did not demonstrate calcifications or >50% T2-FLAIR mismatch; thus, the uncertainty regarding the exact diagnosis according to the updated WHO criteria does not affect the results.

The single-institution nature of our study is a limitation, though in this context, ours is a large cohort, with the number of codeleted tumors demonstrating >50% T2-FLAIR mismatch being like that reported for the TCGA/TCIA cohort.<sup>3</sup> Our study is retrospective, and prospective validation of our results in a different cohort would be important. The targeted nature of our MR imaging assessment is also a potential limitation. We thought that it was important to focus on a small number of MR imaging features, to minimize the chance of finding an association by chance alone. Given the small size of the initial cohort, consisting of only 10 patients, it is possible that some MR imaging features that would have been useful in this context were not identified. In addition, the incidence of calcification is likely to be underestimated in our cohort. First, CTs were not available for all patients, and in patients with only a postoperative CT available, there is the potential for the component containing calcifications to have been resected (and thus not accurately identifiable on the imaging available). Second, susceptibility-weighted imaging was variably available; thus, often calcification could not be accurately differentiated from hemorrhage, in which case tumors were labeled as negative for calcification. We suspect, therefore, that our results underestimate the frequency of calcifications, and the ability of MR imaging to identify codeleted tumors may have been higher if CT and/or susceptibility-weighted imaging had been performed in all patients. This addition has the potential to further increase the value of the method we have outlined.

## CONCLUSIONS

Some MR imaging features can predict 1p/19q status with high specificity. In particular, >50% T2-FLAIR mismatch is highly predictive of a noncodeleted tumor, while calcifications suggest a 1p/19q codeleted tumor. Both features have high interobserver correlation. If formal 1p/19q testing is not possible, these MR imaging features are likely to be more specific for determining 1p/19q status than the histologic phenotype and are particularly useful in phenotypic oligoastrocytomas. We thus suggest the use of combined MR imaging–histologic assessment in such situations to optimize diagnosis.

## REFERENCES

1. Louis DN, Perry A, Reifenberger G, et al. **The 2016 World Health Organization Classification of Tumors of the Central Nervous System: a summary.** *Acta Neuropathol* 2016;131:803–20 CrossRef Medline
2. Lasocki A, Tsui A, Gaillard F, et al. **Reliability of noncontrast-enhancing tumor as a biomarker of IDH1 mutation status in glioblastoma.** *J Clin Neurosci* 2017;39:170–75 CrossRef Medline
3. Patel SH, Poisson LM, Brat DJ, et al. **T2-FLAIR mismatch, an imaging biomarker for IDH and 1p/19q status in lower-grade gliomas: a TCGA/TCIA project.** *Clin Cancer Res* 2017;23:6078–85 CrossRef Medline
4. Tay K, Tsui A, Phal P, et al. **MR imaging characteristics of protoplasma-astrocytomas.** *Neuroradiology* 2011;53:405–11 CrossRef Medline
5. Saito T, Muragaki Y, Maruyama T, et al. **Calcification on CT is a simple and valuable preoperative indicator of 1p/19q loss of heterozygosity in supratentorial brain tumors that are suspected grade II and III gliomas.** *Brain Tumor Pathol* 2016;33:175–82 CrossRef Medline
6. Johnson DR, Diehn FE, Giannini C, et al. **Genetically defined oligodendroglioma is characterized by indistinct tumor borders at MRI.** *AJNR Am J Neuroradiol* 2017;38:678–84 CrossRef Medline
7. Smits M. **Imaging of oligodendroglioma.** *Br J Radiol* 2016;89:20150857 CrossRef Medline
8. Osborne AG. *Osborne's Brain: Imaging, Pathology and Anatomy.* Salt Lake City: Amirsys; 2013:496
9. Law M, Brodsky JE, Babb J, et al. **High cerebral blood volume in human gliomas predicts deletion of chromosome 1p: preliminary results of molecular studies in gliomas with elevated perfusion.** *J Magn Reson Imaging* 2007;25:1113–19 CrossRef Medline
10. Law M, Yang S, Wang H, et al. **Glioma grading: sensitivity, specificity, and predictive values of perfusion MR imaging and proton MR spectroscopic imaging compared with conventional MR imaging.** *AJNR Am J Neuroradiol* 2003;24:1989–98 Medline
11. Lasocki A, Tsui A, Tacey MA, et al. **MRI grading versus histology: predicting survival of World Health Organization grade II–IV astrocytomas.** *AJNR Am J Neuroradiol* 2015;36:77–83 CrossRef Medline
12. Gonzales M, Dale S, Susman M, et al. **Quantitation of chromosome 1p and 19q deletions in glial tumours by interphase FISH on formalin-fixed paraffin-embedded tissue.** *J Clin Neurosci* 2006;13:96–101 CrossRef Medline
13. VASARI Research Project. <https://wiki.cancerimagingarchive.net/display/Public/VASARI+Research+Project>. Updated March 25, 2015. Accessed August 20, 2015
14. Louis DN, Ohgaki H, Wiestler OD, et al. *World Health Organization Histological Classification of Tumours of the Central Nervous System.* Lyon: International Agency for Research on Cancer; 2016
15. Brat DJ, Verhaak RG, Aldape KD, et al; Cancer Genome Atlas Research Network. **Comprehensive, integrative genomic analysis of diffuse lower-grade gliomas.** *N Engl J Med* 2015;372:2481–98 CrossRef Medline
16. Clark KH, Villano JL, Nikiforova MN, et al. **1p/19q testing has no significance in the workup of glioblastomas.** *Neuropathol Appl Neurobiol* 2013;39:706–17 CrossRef Medline
17. Ito M, Wakabayashi T, Natsume A, et al. **Genetically heterogeneous glioblastoma recurring with disappearance of 1p/19q losses: case report.** *Neurosurgery* 2007;61:E168–69; discussion E169 CrossRef Medline
18. Huse JT, Diamond EL, Wang L, et al. **Mixed glioma with molecular features of composite oligodendroglioma and astrocytoma: a true “oligoastrocytoma”?** *Acta Neuropathol* 2015;129:151–53 CrossRef Medline
19. Qu M, Olofsson T, Sigurdardottir S, et al. **Genetically distinct astrocytic and oligodendroglial components in oligoastrocytomas.** *Acta Neuropathol* 2007;113:129–36 CrossRef Medline
20. Lasocki A, Gaillard F, Tacey M, et al. **Incidence and prognostic significance of non-enhancing cortical signal abnormality in glioblastoma.** *J Med Imaging Radiat Oncol* 2016;60:66–73 CrossRef Medline
21. Tang YM, Ngai S, Stuckey S. **The solitary enhancing cerebral lesion: can FLAIR aid the differentiation between glioma and metastasis?** *AJNR Am J Neuroradiol* 2006;27:609–11 Medline
22. Louis DN, Ohgaki H, Wiestler OD, et al. *World Health Organization Histological Classification of Tumours of the Central Nervous System.* Lyon: International Agency for Research on Cancer; 2007

# Whole-Tumor Histogram and Texture Analyses of DTI for Evaluation of *IDH1*-Mutation and 1p/19q-Codeletion Status in World Health Organization Grade II Gliomas

Y.W. Park, K. Han, S.S. Ahn, Y.S. Choi, J.H. Chang, S.H. Kim, S.-G. Kang, E.H. Kim, and S.-K. Lee



## ABSTRACT

**BACKGROUND AND PURPOSE:** Prediction of the *isocitrate dehydrogenase 1* (*IDH1*)-mutation and 1p/19q-codeletion status of World Health Organization grade II gliomas preoperatively may assist in predicting prognosis and planning treatment strategies. Our aim was to characterize the histogram and texture analyses of apparent diffusion coefficient and fractional anisotropy maps to determine *IDH1*-mutation and 1p/19q-codeletion status in World Health Organization grade II gliomas.

**MATERIALS AND METHODS:** Ninety-three patients with World Health Organization grade II gliomas with known *IDH1*-mutation and 1p/19q-codeletion status (18 *IDH1* wild-type, 45 *IDH1* mutant and no 1p/19q codeletion, 30 *IDH1*-mutant and 1p/19q codeleted tumors) underwent DTI. ROIs were drawn on every section of the T2-weighted images and transferred to the ADC and the fractional anisotropy maps to derive volume-based data of the entire tumor. Histogram and texture analyses were correlated with the *IDH1*-mutation and 1p/19q-codeletion status. The predictive powers of imaging features for *IDH1* wild-type tumors and 1p/19q-codeletion status in *IDH1*-mutant subgroups were evaluated using the least absolute shrinkage and selection operator.

**RESULTS:** Various histogram and texture parameters differed significantly according to *IDH1*-mutation and 1p/19q-codeletion status. The skewness and energy of ADC, 10th and 25th percentiles, and correlation of fractional anisotropy were independent predictors of an *IDH1* wild-type in the least absolute shrinkage and selection operator. The area under the receiver operating curve for the prediction model was 0.853. The skewness and cluster shade of ADC, energy, and correlation of fractional anisotropy were independent predictors of a 1p/19q codeletion in *IDH1*-mutant tumors in the least absolute shrinkage and selection operator. The area under the receiver operating curve was 0.807.

**CONCLUSIONS:** Whole-tumor histogram and texture features of the ADC and fractional anisotropy maps are useful for predicting the *IDH1*-mutation and 1p/19q-codeletion status in World Health Organization grade II gliomas.

**ABBREVIATIONS:** FA = fractional anisotropy; GLCM = gray level co-occurrence matrices; *IDH* = *isocitrate dehydrogenase*; IDM = inverse different moment; LASSO = least absolute shrinkage and selection operator; WHO = World Health Organization

The World Health Organization (WHO) classification of gliomas was updated in 2016.<sup>1</sup> For the diagnosis of WHO grade II gliomas, the *isocitrate dehydrogenase* (*IDH*)-mutation and 1p/19q-codeletion status are used in combination with the histologic phenotype; the genotype takes precedence over the histologic

phenotype in discordant cases. The molecular subtypes of WHO grade II gliomas are divided into 3 classes: *IDH* wild-type, *IDH* mutant without 1p/19q codeletion, and *IDH* mutant with 1p/19q-codeletion.<sup>1</sup> These molecular subtypes reportedly vary in prognosis and chemosensitivity.<sup>2</sup> Patients with grade II astrocytomas and *IDH* wild-type have significantly poorer prognoses than those with *IDH*-mutant tumors; the 5-year progression-free survival and overall survival rates are 14% and 51% versus 42% and 93%, respectively.<sup>3</sup> Moreover, patients with gliomas with *IDH* mutations were more sensitive to chemoradiation therapy and had longer survival than those with the *IDH* wild-type.<sup>4</sup> Additionally,

Received October 22, 2017; accepted after revision December 29.

From the Department of Radiology (Y.W.P.), Ewha Womans University College of Medicine, Seoul, Korea; and Departments of Radiology and Research Institute of Radiological Science (Y.W.P., K.H., S.S.A., Y.S.C., S.-K.L.), Neurosurgery (J.H.C., S.-G.K., E.H.K.), and Pathology (S.H.K.), Yonsei University College of Medicine, Seoul, Korea.

This work was supported by the Basic Science Research Program through the National Research Foundation of Korea funded by the Ministry of Science, Information and Communication Technologies, and Future Planning (2017RID1A1B03030440).

Please address correspondence to Sung Soo Ahn, MD, PhD, Department of Radiology and Research Institute of Radiological Science, Yonsei University College of Medicine, 50-one Yonsei-ro, Seodaemun-gu, Seoul 120-752, Korea; e-mail: sung-soo@yuhs.ac.

Indicates open access to non-subscribers at www.ajnr.org.

Indicates article with supplemental on-line tables.

Indicates article with supplemental on-line photos.

<http://dx.doi.org/10.3174/ajnr.A5569>

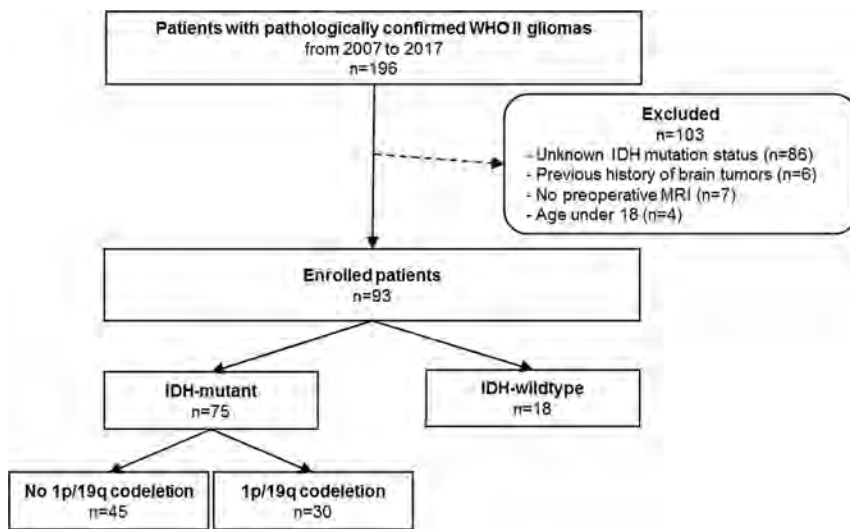


**FIGURE.** Flowchart of the study population.

1p/19q codeletion predicts therapeutic response and survival.<sup>5</sup> Thus, predicting the *IDH*-mutation and 1p/19q-codeletion status of WHO grade II gliomas preoperatively may aid in predicting prognosis and planning treatment strategies.

*IDH* mutation and 1p/19 codeletion may reflect alterations in tumor cell proliferation and microvessel density that exhibit characteristic features on ADC and fractional anisotropy (FA) parameters. The ADC is an index of tumor cellularity, reflecting tumor burden and correlating negatively with glioma grade.<sup>1,6</sup> DTI provides information about the motion of water protons at the cellular level<sup>7</sup>; the directional restriction of water diffusivity can be measured as the FA, which correlates with myelinated fiber tract integrity.<sup>8,9</sup> ADC and FA histograms may predict histologic subtypes, such as oligodendroglioma, oligoastrocytoma, and astrocytoma in WHO grade II gliomas.<sup>10,11</sup> However, these studies did not obtain molecular markers, and mean or histogram percentile values of ADC and FA have limitations in terms of evaluation of gliomas, due to the heterogeneity.<sup>12</sup> Histogram-based measures can reflect the intensity distribution of a volume of interest, but not the spatial distribution of these intensities.<sup>13</sup> On the other hand, texture analysis features show the characteristics of the entire tumor and allow noninvasive quantification of tumor features, such as tumor uniformity, heterogeneity, smoothness, randomness, and symmetry.<sup>14</sup>

To the best of our knowledge, there have been no previous reports that have comprehensively examined the whole-tumor histogram and texture features (ie, ADC and FA parameters), according to the *IDH*-mutation and 1p/19q-codeletion status of grade II gliomas. This study evaluated the role of histogram and texture analyses of ADC and FA maps based on the entire tumor volume in determining the *IDH*-mutation and 1p/19q-codeletion status of grade II gliomas, preoperatively.

## MATERIALS AND METHODS

### Patient Population

The institutional review board waived the need for obtaining informed patient consent for this retrospective study. Between January 2007 and February 2017, one hundred ninety-six patients

with pathologically diagnosed WHO grade II gliomas were included in this study. Inclusion criteria were as follows: 1) WHO grade II gliomas confirmed by histopathology; and 2) patients who underwent preoperative MR imaging, including DTI, with a b-value of 600 s/mm<sup>2</sup>. Exclusion criteria were the following: 1) an unknown *IDH*-mutation status ( $n = 86$ ), 2) patients with a previous history of brain tumor ( $n = 6$ ), 3) patients with incomplete MR imaging sequences or suboptimal images ( $n = 7$ ), and 4) patients younger than 18 years of age ( $n = 4$ ). The mean interval between the MR imaging examination and the operation was  $10.73 \pm 12.49$  days.

Immunohistochemical analysis and peptide nucleic acid–mediated clamping polymerase chain reaction were performed to detect the *IDH1* R132H mutation.<sup>15</sup> For immunohistochemistry, monoclonal antibody H09 was used, and the degree of *IDH1*-R132H staining was determined as positive in patients with any stained cells or as negative in those without any stained cells.<sup>16</sup> If immunohistochemistry results were negative for *IDH1*-R132H, we confirmed the *IDH1* status by peptide nucleic acid–mediated clamping polymerase chain reaction. Fluorescence in situ hybridization analysis was used to investigate 1p/19q codeletion.<sup>17</sup>

### MR Imaging Protocol

Preoperative MR imaging was performed with a 3T MR imaging scanner (Achieva; Philips Healthcare, Best, the Netherlands) with an 8-channel sensitivity encoding head coil. The preoperative MR imaging protocol included T1-weighted (TR/TE, 1800–2000/10–15 ms; FOV, 240 mm; section thickness, 5 mm; matrix, 256 × 256), T2-weighted (TR/TE, 2800–3000/80–100 ms; FOV, 240 mm; section thickness, 5 mm; matrix, 256 × 256), and FLAIR (TR/TE, 9000–10,000/110–125 ms; FOV, 240 mm; section thickness, 5 mm; matrix, 256 × 256) sequences. 3D contrast-enhanced T1-weighted images (TR/TE, 6.3–8.3/3.1–4 ms; FOV, 240 mm; section thickness, 1 mm; matrix, 192 × 192) were acquired after administering 0.1 mL/kg of gadolinium-based contrast material (gadobutrol, Gadovist; Bayer Schering Pharma, Berlin, Germany). Whole-brain DTI was performed with b-values of 600 and 0 s/mm<sup>2</sup>, 32 directions, and the following parameters: TR/TE, 8413.4/77 ms; FOV, 220 mm; section thickness, 2 mm; matrix, 112 × 112; acceleration factor, 2.5; and with an acquisition time of 5 minutes 20 seconds.

### Image Postprocessing: Volume Acquisition

DTI data were processed off-line with the Medical Image Processing, Analysis, and Visualization software package, Version 7.0 (National Institutes of Health; <https://mipav.cit.nih.gov/>). T2-weighted images were coregistered to ADC and FA maps using affine transformation with normalized mutual information as a cost function,<sup>18,19</sup> and the ROIs were drawn on every tumor

**Table 1: Patient characteristics according to the IDH1-mutation status and 1p/19q-codeletion status<sup>a</sup>**

	IDH1 Wild-Type (n = 18)	IDH1 Mutant without 1p/19q Codeletion (n = 45)	IDH1 Mutant with 1p/19q Codeletion (n = 30)
Age (yr) (mean)	49.57 ± 3.45	40.80 ± 1.25	45.10 ± 1.91
Sex			
Male	8 (44.4)	27 (60)	13 (43.3)
Female	10 (55.6)	18 (40)	17 (56.7)
Karnofsky performance status (mean)	88.89 ± 1.37	90.67 ± 1.12	91.00 ± 1.39
Extent of resection			
Gross total resection	7 (38.9)	29 (64.5)	15 (50)
Subtotal/partial resection	7 (38.9)	14 (31.1)	14 (46.7)
Biopsy	4 (22.2)	2 (4.4)	1 (3.3)

<sup>a</sup> Unless otherwise indicated, data are presented as number of patients (%).

section on T2-weighted images using a semiautomatic method, with signal intensity thresholds as previously described.<sup>20</sup> The ROIs, were drawn by a single neuroradiologist (Y.W.P) and confirmed by another neuroradiologist (S.S.A.) and were transferred to ADC and FA maps.

### Histogram and Texture Analysis of ADC and FA

**First-Order Statistics Including Histogram Parameters.** ADC and FA histogram parameters consisting of the mean value and SD were calculated from ROIs overlaid on ADC and FA maps. For cumulative ADC and FA histograms, the 10th, 25th, 50th, 75th, and 90th percentile ADC and FA values in the histogram were generated.<sup>10</sup> Skewness and kurtosis were also calculated.

**Second-Order Statistics via Gray Level Co-Occurrence Matrices.** Texture analysis via gray level co-occurrence matrices (GLCM) allows extraction of second-order statistical texture features from images.<sup>21</sup> Co-occurrence matrix texture considers the relationship between 2 pixels, the reference and neighboring pixel, reflecting local heterogeneity. We used the following parameters for quantitative analysis of the summation of 2D ROIs: contrast, dissimilarity, inverse different moment 1 (IDM1), homogeneity or IDM2, energy, maximum probability, entropy, mean, variance, SD, correlation, cluster shade, and cluster prominence in ADC and FA maps. Altogether, ADC and FA map features were quantified by various features, including their degrees of uniformity (IDM1, homogeneity [IDM2], angular second moment, and energy), heterogeneity (contrast, dissimilarity, variance, and SD), smoothness (correlation), randomness (entropy), and symmetry (cluster shade and prominence). To obtain rotational invariant features, we computed the co-occurrence matrix by averaging >4 uniformly distributed angular directions (0°, 45°, 90°, and 135°).

### Statistical Analysis

The differences between ADC and FA histogram parameters and IDH1-mutation status were assessed using the Student *t* test or the Mann-Whitney *U* test, according to normality test results. Because the number of significant imaging features was relatively large, compared with the number of patients when comparing the IDH1 wild-type and IDH1-mutant groups, we used the regularization method to assess the predictive power of the imaging features based on the least absolute shrinkage and selection operator (LASSO), which reduces the potential risk of overfitting or false discovery. LASSO involves penaliz-

**Table 2: Prediction model for an IDH1-mutation status in WHO grade II gliomas using the LASSO procedure**

Imaging Parameters	Adjusted OR for IDH1 Wild-Type
ADC skewness	1.04
ADC energy	1.15
FA 10th percentile	23.19
FA 25th percentile	998.91
FA correlation	0.004

ing irrelevant variables to zero and retains only useful features, thereby effectively reducing the number of variables. We used 5-fold cross-validation to find the optimal regularization parameter for LASSO. We estimated the area under the receiver operating curve to assess the predictive ability of variables by selecting significant variables based on LASSO. The 5-fold cross-validated area under the receiver operating curve is the average of the predictive areas under the receiver operating characteristic curve of 5 validation datasets generated by the cross-validation process.

The identical process was performed to evaluate correlations between ADC and FA histograms and 1p/19q-codeletion status in the IDH1-mutant subgroup.

Statistical analysis was performed using R statistical and computing software (Version 3.3.1; <http://www.r-project.org/>). Statistical significance was set at *P* < .05.

## RESULTS

The characteristics of the 93 enrolled patients with WHO grade II gliomas are summarized in Table 1. Eighteen patients had IDH1 wild-type tumors, 45 had IDH1-mutant without 1p/19q-codeletion tumors, and 30 had IDH1-mutant with 1p/19q-codeletion tumors.

### Histogram and Texture Analyses of ADC and FA Values for Determining IDH1-Mutation Status

Various histogram and texture analyses features differed significantly between the IDH1 wild-type and IDH1-mutant groups (On-line Table 1). Among these factors, 5 were independently associated with predicting the IDH1 mutation based on the LASSO procedure (Table 2). The IDH1 wild-type group had higher skewness and energy of ADC and FA 10th and 25th percentiles, whereas the IDH1-mutant group had a higher FA correlation. The area under the receiver operating curve for the optimal model was 0.853 (95% confidence interval, 0.761–0.945).

**Table 3: Prediction model for 1p/19q-codeletion status in *IDH1*-mutant WHO grade II gliomas using the LASSO procedure**

Imaging Parameters	Adjusted OR for 1p/19q Codeletion
ADC skewness	1.71
ADC cluster shade	1.00
FA energy	0.005
FA correlation	0.12

### **Histogram and Texture Analyses of ADC and FA Values for Determining 1p/19q-Codeletion Status in the *IDH1*-Mutant Group**

Various histogram and texture analysis features were significantly different according to the 1p/19q-codeletion status in the *IDH1*-mutant subgroup (On-line Table 2). Among these factors, 4 were independently associated with predicting the 1p/19q-codeletion status on the basis of the LASSO procedure (Table 3). The 1p/19q-codeletion group had higher ADC skewness and cluster shade, whereas the group without 1p/19q codeletion had higher FA energy and FA correlation. The area under the receiver operating curve for the optimal model was 0.807 (95% confidence interval, 0.649–0.965). Representative cases according to *IDH1*-mutation and 1p/19q-codeletion status are demonstrated in On-line Fig 1. On-line Fig 2 shows the heat map according to *IDH1*-mutation and 1p/19q-codeletion status, which reveals the strong relationship between significant histogram and texture features of ADC and FA maps ( $P < .05$ ) and molecular subtypes.

## **DISCUSSION**

WHO grade II gliomas are heterogeneous at both genetic and histopathologic levels, with intratumoral spatial variation<sup>22</sup>; we comprehensively analyzed the histogram and texture features of whole tumors using ADC and FA maps according to the molecular subtypes.

ADC and FA histogram analyses differ significantly according to histopathologic subtypes or molecular markers of WHO grade II/III gliomas.<sup>10,23,24</sup> However, some study groups followed the 2007 WHO classification, and texture analyses have not been performed in all studies. Spatial textures in the ADC and FA signals arise from destruction of normal anatomy by tumors, vasogenic edema, tumor cellularity, degenerative changes, or the compression of normal structures, including some that are imperceptible to human eyes. The notion that texture analysis can reveal visually imperceptible tumor information extends beyond radiology to histopathology; texture analysis (in conjunction with histopathology) has been reported to be more accurate than histopathology alone in predicting prognosis in malignant gliomas.<sup>25</sup> In WHO grade II gliomas, *IDH* wild-type tumors showed lower ADC and higher FA values than *IDH1*-mutant tumors, in agreement with our results.<sup>11,23,26</sup> Generally, increased tumor cell proliferation and angiogenesis increase tumor cellularity,<sup>27</sup> and the diffusivity of water molecules is restricted in environments with high cellular density, resulting in lower ADCs.<sup>28</sup> Therefore, this finding suggests that *IDH* mutation is associated with lower tumor cellularity<sup>29</sup> and explains why the presence of an *IDH* mutation is a favorable prognostic marker in patients with glioma.<sup>2</sup>

DTI-based FA values have received attention in the detection of glioma infiltration.<sup>30</sup> Previous studies have suggested that tu-

mors with higher FA values have higher tumor cell density and a relatively high Ki-67 index in malignant brain tumors, which indicate greater malignancy potential.<sup>30,31</sup> Therefore, the mechanisms underlying lower FAs in WHO grade II gliomas with *IDH* mutations may involve a lower rate of proliferation and aggressiveness and lower tumor cell densities of these tumors. In our study, various ADC and FA histograms and texture features differed statistically significantly according to *IDH1*-mutation status; this finding is useful for enhancing the understanding of tumor heterogeneity according to *IDH1*-mutation status. The *IDH1* wild-type group had higher skewness and energy of ADC and 10th and 25th percentiles of FA, whereas the *IDH1*-mutant group demonstrated higher FA correlation. The energy represents the orderliness of the image; when the image is highly organized, the energy values are high. Correlation is a measure of the linear dependence of gray levels on those of neighboring pixels (ie, local gray-level dependence); higher values can be obtained for similar gray-level regions. Thus, the *IDH1* wild-type group demonstrated higher ADC orderliness, whereas the *IDH1*-mutant group had a higher frequency of similar FA value regions. Few studies have analyzed the texture features of T1 contrast-enhanced or T2 FLAIR images according to the *IDH1*-mutation status of WHO grade II gliomas<sup>32,33</sup>; but none performed DTI analyses, which provide insight into the spatial distribution of the tumor cellularity and myelinated fiber tract integrity.

In a recent study, diffusion characteristics from visual assessment were significantly different according to the 1p/19q-codeletion status in *IDH1*-mutant grade II gliomas.<sup>34</sup> For further evaluation of the roles of diffusion characteristics in determining the 1p/19q-codeletion status of WHO grade II gliomas, we evaluated histogram and texture features measured quantitatively, which can be more objective. Our results demonstrate that histogram and texture features can be effective for predicting 1p/19q-codeletion status. The 1p/19q-codeletion group demonstrated higher ADC skewness, whereas the 1p/19q-intact group had higher FA energy and FA correlation. Thus, the 1p/19q-codeletion group showed more ADC asymmetry, whereas the 1p/19q-intact group had higher FA organization and more regions with similar FA values. Previous studies showed discrepant results of association between 1p/19q codeletion and ADC and/or FA features in WHO grade II gliomas,<sup>24,26,35,36</sup> which may be due to different study groups, smaller sample sizes, and different imaging analyses. Several studies included oligoastrocytic or oligodendroglial tumors based on histopathology, according to the 2007 WHO classification, regardless of *IDH*-mutation status; then the authors classified them according to 1p/19q codeletion status. Therefore, a small number of patients with *IDH* wild-type gliomas might have been included. Additionally, previous studies included fewer WHO grade II gliomas with evaluation of focal ROIs of the tumor instead of the entire tumor volume.

Because WHO grade II glioma is a heterogeneous tumor with cystic or calcified areas, ADC or FA values calculated in small ROIs cannot represent the cellular density or arrangement of the whole tumor. However, we analyzed tumors according to 1p/19q-codeletion status in an *IDH1*-mutant subgroup throughout the whole tumor volume, using comprehensive texture analyses. *IDH1*-mutant with 1p/19q-codeletion tumors showed lower

ADC and higher FA values than *IDH1*-mutant without 1p/19q-codeletion tumors. *IDH*-mutant with 1p/19q-codeletion tumors are markedly infiltrated by perineuronal satellitosis, with more persistent neurons, as seen on pathology, which may explain their higher FA values.<sup>11</sup> If the neurons are spared and the volume of invasion is less, edema should be less, which may explain the lower ADC values in such tumors.<sup>11</sup> Calcification is another pathologic finding related to differences in ADC and FA values according to the 1p/19q-codeletion status in *IDH1*-mutant tumors; microcalcifications are seen in up to 90% of *IDH*-mutant with 1p/19q codeletion tumors.<sup>11</sup> Tumors with calcifications are expected to have lower ADC values, due to lack of water movement in the calcified region.

Our study had several limitations. First, it was based on a single-center, retrospectively collected dataset. Second, prognostic markers were not analyzed because patients with WHO II gliomas have a relatively long overall survival. Further studies are needed to correlate prognostic markers, such as overall survival and progression-free survival with genotypic and imaging features. Third,  $b = 600 \text{ s/mm}^2$  was used instead of  $b = 1000 \text{ s/mm}^2$  or higher in DTI. This low  $b$ -value may have resulted in overestimation of ADC values due to perfusion effects. However, this would have little effect on analyzing the difference between molecular groups because the pixels as a whole are affected. Fourth, only *IDH1* R132H mutation was detected in our hospital, and a small proportion of *IDH2*-mutation or non-*IDH1* R132H mutation tumors was not detected. However, it has been previously reported that the predominant amino acid sequence alteration in *IDH1* mutation is R132H, accounting for 92.7% of the detected mutations in WHO grade II and III gliomas.<sup>37</sup> Fifth, this retrospective study did not investigate the direct relationship between ADC and tumor cellularity from histologic specimens. However, previous studies have proved the negative correlation between ADC and tumor cellularity.<sup>38,39</sup>

## CONCLUSIONS

Histogram and texture features of ADC and FA maps of the entire tumor volume differ according to the *IDH1*-mutation and 1p/19q-codeletion status in WHO grade II gliomas and may be helpful for predicting molecular status.

Disclosures: Sung Soo Ahn—RELATED: Grant: This research received funding from the Basic Science Research Program through the National Research Foundation of Korea funded by the Ministry of Science, Information and Communication Technologies, and Future Planning (2017R1D1A1B03030440). \* \*Money paid to the institution.

## REFERENCES

- Louis DN, Perry A, Reifenberger G, et al. **The 2016 World Health Organization classification of tumors of the central nervous system: a summary.** *Acta Neuropathol* 2016;131:803–20 CrossRef Medline
- Brat DJ, Verhaak RG, Aldape KD, et al; Genome Atlas Research Network. **Comprehensive, integrative genomic analysis of diffuse lower-grade gliomas.** *N Engl J Med* 2015;372:2481–98 CrossRef Medline
- Metellus P, Coulibaly B, Colin C, et al. **Absence of IDH mutation identifies a novel radiologic and molecular subtype of WHO grade II gliomas with dismal prognosis.** *Acta Neuropathol* 2010;120:719–29 CrossRef Medline
- Olar A, Wani KM, Alfaro-Munoz KD, et al. **IDH mutation status and role of WHO grade and mitotic index in overall survival in grade II-III diffuse gliomas.** *Acta Neuropathol* 2015;129:585–96 CrossRef Medline
- Jenkins RB, Blair H, Ballman KV, et al. **A t (1;19)(q10;p10) mediates the combined deletions of 1p and 19q and predicts a better prognosis of patients with oligodendroglioma.** *Cancer Res* 2006;66:9852–61 CrossRef Medline
- Omuro A, DeAngelis LM. **Glioblastoma and other malignant gliomas: a clinical review.** *JAMA* 2013;310:1842–50 CrossRef Medline
- Balss J, Meyer J, Mueller W, et al. **Analysis of the IDH1 codon 132 mutation in brain tumors.** *Acta Neuropathol* 2008;116:597–602 CrossRef Medline
- Chenevert TL, Brunberg JA, Pipe JG. **Anisotropic diffusion in human white matter: demonstration with MR techniques in vivo.** *Radiology* 1990;177:401–05 CrossRef Medline
- Hansen JR. **Pulsed NMR study of water mobility in muscle and brain tissue.** *Biochim Biophys Acta* 1971;230:482–86 CrossRef Medline
- Tozer DJ, Jäger HR, Danchaivijitr N, et al. **Apparent diffusion coefficient histograms may predict low-grade glioma subtype.** *NMR Biomed* 2007;20:49–57 CrossRef Medline
- Khayal IS, McKnight TR, McGue C, et al. **Apparent diffusion coefficient and fractional anisotropy of newly diagnosed grade II gliomas.** *NMR Biomed* 2009;22:449–55 CrossRef Medline
- Ryu YJ, Choi SH, Park SJ, et al. **Glioma: application of whole-tumor texture analysis of diffusion-weighted imaging for the evaluation of tumor heterogeneity.** *PLoS One* 2014;9:e108335 CrossRef Medline
- Brynnolfsson P, Nilsson D, Henriksson R, et al. **ADC texture: an imaging biomarker for high-grade glioma?** *Medical Phys* 2014;41:101903 CrossRef Medline
- Davnull F, Yip CS, Ljungqvist G, et al. **Assessment of tumor heterogeneity: an emerging imaging tool for clinical practice?** *Insights Imaging* 2012;3:573–89 CrossRef Medline
- Yan H, Parsons DW, Jin G, et al. **IDH1 and IDH2 mutations in gliomas.** *N Engl J Med* 2009;360:765–73 CrossRef Medline
- Takano S, Tian W, Matsuda M, et al. **Detection of IDH1 mutation in human gliomas: comparison of immunohistochemistry and sequencing.** *Brain Tumor Pathol* 2011;28:115–23 CrossRef Medline
- Riemenschneider MJ, Jeuken JW, Wesseling P, et al. **Molecular diagnostics of gliomas: state of the art.** *Acta Neuropathol* 2010;120:567–84 CrossRef Medline
- Cha J, Kim S, Kim HJ, et al. **Differentiation of tumor progression from pseudoprogression in patients with posttreatment glioblastoma using multiparametric histogram analysis.** *AJNR Am J Neuro-radiol* 2014;35:1309–17 CrossRef Medline
- Maes F, Collignon A, Vandermeulen D, et al. **Multimodality image registration by maximization of mutual information.** *IEEE Trans Med Imaging* 1997;16:187–98 CrossRef Medline
- Ko SB, Choi HA, Carpenter AM, et al. **Quantitative analysis of hemorrhage volume for predicting delayed cerebral ischemia after subarachnoid hemorrhage.** *Stroke* 2011;42:669–74 CrossRef Medline
- Haralick RM, Shanmugam K. **Textural features for image classification.** *IEEE Trans Syst Man Cybern* 1973;6:10–21 CrossRef
- Paulus W, Peiffer J. **Intratumoral histologic heterogeneity of gliomas: a quantitative study.** *Cancer* 1989;64:442–47 Medline
- Xiong J, Tan WL, Pan JW, et al. **Detecting isocitrate dehydrogenase gene mutations in oligodendroglial tumors using diffusion tensor imaging metrics and their correlations with proliferation and microvascular density.** *J Magn Reson Imaging* 2016;43:45–54 CrossRef Medline
- Jenkinson MD, Smith TS, Brodbelt AR, et al. **Apparent diffusion coefficients in oligodendroglial tumors characterized by genotype.** *J Magn Reson Imaging* 2007;26:1405–12 CrossRef Medline
- Zacharaki EI, Morita N, Bhatt P, et al. **Survival analysis of patients with high-grade gliomas based on data mining of imaging variables.** *AJNR Am J Neuroradiol* 2012;33:1065–71 CrossRef Medline
- Xiong J, Tan W, Wen J, et al. **Combination of diffusion tensor imaging and conventional MRI correlates with isocitrate dehydrogenase 1/2 mutations but not 1p/19q genotyping in oligodendroglial tumours.** *Eur Radiol* 2016;26:1705–15 CrossRef Medline

27. Fischer I, Gagner JP, Law M, et al. **Angiogenesis in gliomas: biology and molecular pathophysiology.** *Brain Pathol* 2005;15:297–310 Medline
28. Yamasaki F, Kurisu K, Satoh K, et al. **Apparent diffusion coefficient of human brain tumors at MR imaging.** *Radiology* 2005;235:985–91 CrossRef Medline
29. Bralten LB, Kloosterhof NK, Balvers R, et al. **IDH1 R132H decreases proliferation of glioma cell lines in vitro and in vivo.** *Ann Neurol* 2011;69:455–63 CrossRef Medline
30. Beppu T, Inoue T, Shibata Y, et al. **Fractional anisotropy value by diffusion tensor magnetic resonance imaging as a predictor of cell density and proliferation activity of glioblastomas.** *Surg Neurol* 2005;63:56–61; discussion 61 CrossRef Medline
31. Kinoshita M, Hashimoto N, Goto T, et al. **Fractional anisotropy and tumor cell density of the tumor core show positive correlation in diffusion tensor magnetic resonance imaging of malignant brain tumors.** *Neuroimage* 2008;43:29–35 CrossRef Medline
32. Yu J, Shi Z, Lian Y, et al. **Noninvasive IDH1 mutation estimation based on a quantitative radiomics approach for grade II glioma.** *Eur Radiol* 2017;27:3509–22 CrossRef Medline
33. Li Z, Wang Y, Yu J, et al. **Deep learning based radiomics (DLR) and its usage in noninvasive IDH1 prediction for low grade glioma.** *Sci Rep* 2017;7:5467 CrossRef Medline
34. Leu K, Ott GA, Lai A, et al. **Perfusion and diffusion MRI signatures in histologic and genetic subtypes of WHO grade II-III diffuse gliomas.** *J Neurooncol* 2017;134:177–88 CrossRef Medline
35. Khayal IS, Vandenberg SR, Smith KJ, et al. **MRI apparent diffusion coefficient reflects histopathologic subtype, axonal disruption, and tumor fraction in diffuse-type grade II gliomas.** *Neuro Oncol* 2011;13:1192–201 CrossRef Medline
36. Park Y, Han K, Ahn S, et al. **Prediction of IDH1-mutation and 1p/19q-codeletion status using preoperative MR imaging phenotypes in lower grade gliomas.** *AJNR Am J Neuroradiol* 2018;39:37–42 CrossRef Medline
37. Hartmann C, Meyer J, Balss J, et al. **Type and frequency of IDH1 and IDH2 mutations are related to astrocytic and oligodendroglial differentiation and age: a study of 1,010 diffuse gliomas.** *Acta Neuropathol* 2009;118:469–74 CrossRef Medline
38. Kono K, Inoue Y, Nakayama K, et al. **The role of diffusion-weighted imaging in patients with brain tumors.** *AJNR Am J Neuroradiol* 2001;22:1081–88 Medline
39. Sugahara T, Korogi Y, Kochi M, et al. **Usefulness of diffusion-weighted MRI with echo-planar technique in the evaluation of cellularity in gliomas.** *J Magn Reson Imaging* 1999;9:53–60 Medline

# Brain Imaging in Cases with Positive Serology for Dengue with Neurologic Symptoms: A Clinicoradiologic Correlation

H.A. Vanjare, P. Mannam, A.K. Mishra, R. Karuppusami, R.A.B. Carey, A.M. Abraham, W. Rose, R. Iyyadurai, and S. Mani



## ABSTRACT

**BACKGROUND AND PURPOSE:** Dengue is a common arboviral disease, which uncommonly involves the brain. There has been a recent surge in dengue cases and dengue-related deaths in tropical countries. The aim of this study was to describe brain imaging findings in patients with dengue infection having neurologic symptoms.

**MATERIALS AND METHODS:** Thirty-five patients with positive serology for dengue with CNS symptoms undergoing imaging of the brain were included in the study. Clinical, laboratory, and imaging parameters were assessed and correlated to poor outcome.

**RESULTS:** A Glasgow Coma Scale score of  $\leq 12$  at presentation, clinical classification of severe-type dengue, and the presence of acute renal failure were associated with poor outcome. Imaging parameters associated with poor outcome were involvement of the thalami and cerebellar peduncles and the presence of diffusion restriction and hemorrhagic foci in the brain parenchyma.

**CONCLUSIONS:** Although not specific, dengue infection has imaging findings that can be used to narrow down the differential list and help in prognostication.

**ABBREVIATIONS:** GCS = Glasgow Coma Scale; PRES = posterior reversible encephalopathy syndrome

Dengue is an arboviral disease found in the tropics; it is the second most common mosquito-borne disease. It is transmitted by the bite of *Aedes* mosquitoes, which are primarily found in the tropics where the mosquitoes flourish in stagnant water.<sup>1</sup> The virus has 4 different serotypes. Infection with 1 serotype (primary infection) does not provide life-long immunity from infection through other serotypes. Other serotypes can subsequently infect the same person and cause secondary infection. There has been a recent surge in dengue cases, and it has been reported from >100 countries.<sup>2</sup> Fifty million cases are estimated to occur globally per year.<sup>1</sup> Following a bite from an infected mosquito, symptoms can occur after 4–10 days of incubation with abrupt onset of fever called the “febrile phase.” Patients can have nonspecific symptoms such as myalgia, headache, skin erythema, and vomiting. Petchiae and mucosal hemorrhage can occur during this

phase. This is followed by the “critical phase,” in which capillary permeability increases, leading to hemoconcentration with associated thrombocytopenia. Significant plasma leak can occur during this phase with associated multiorgan dysfunction. Most patients gradually improve during the “recovery phase,” in which extravascular fluid is reabsorbed with improvement in platelet count. Neurologic involvement of dengue infection is uncommon and can be seen in 4%–5% of those infected, and includes encephalopathy, acute disseminated encephalomyelitis, brachial neuritis, myelitis, hypokalemic paralysis, opsoclonus myoclonus, and Guillain-Barré syndrome.<sup>3–5</sup> Dengue is known to cause encephalitis (for which the hallmark is altered sensorium and seizures); however, multiple metabolic derangements, which usually occur with dengue infection, can also lead to a similar clinical presentation (encephalopathy). Therefore, clinical distinction between dengue encephalitis and encephalopathy is often not possible. Because of rare CNS involvement in dengue, primary care physicians may be unfamiliar with its neurologic manifestations; in addition, there are insufficient data with respect to brain imaging findings in dengue infection, with most of the data published as case reports or short case series.

These cases were included from a tertiary care nongovernment medical college hospital in South India. Cases presenting to this institution are often referrals from surrounding primary and sec-

Received June 23, 2017; accepted after revision November 29.

From the Departments of Radiology (H.A.V., P.M., S.M.), Medicine (A.K.M., R.A.B.C., R.I.), Biostatistics (R.K.), Virology (A.M.A.), and Pediatrics (W.R.), Christian Medical College and Hospital, Tamil Nadu, India.

Please address correspondence to Sunithi Mani, MD, Department of Radiology, Christian Medical College and Hospital, Ida Scudder Rd, Vellore–632004, India; e-mail: sunithi.mani@cmcvellore.ac.in



Indicates article with supplemental on-line photos.



Indicates article with supplemental on-line table.

<http://dx.doi.org/10.3174/ajnr.A5544>

ondary care medical facilities where management of complicated cases is difficult. Patients seen in this hospital are from poor socioeconomic backgrounds. This causes constraint on the investigation that a physician can request because most patients are self-paid.

## **MATERIALS AND METHODS**

A single-center retrospective chart review was performed with the cases identified using the case data base of the radiology department. Thirty-five patients with acute dengue infection with symptoms suggestive of CNS involvement undergoing imaging of the brain were included in the study (duration, 2006 to 2017). Both CT and MR imaging scans were included. There were an additional 4 patients for whom there was no imaging available during the acute phase of the illness; however, follow-up imaging was available. These cases were not included in the data analysis but are described briefly.

Clinical parameters assessed were the following: age and sex of the patients; type of dengue infection (primary versus secondary); Glasgow Coma Scale (GCS) score at presentation; the presence of seizures, vomiting, and hemorrhagic manifestations (such as mucosal hemorrhage, hematemesis, hematochezia or excessive menstrual flow); the requirement of intubation and inotropic support; the presence of hospital-acquired pneumonia; the World Health Organization (2009) classification of dengue infection; the lowest documented platelet count; liver dysfunction (hyperbilirubinemia and transaminitis); deranged prothrombin time and activated partial thromboplastin time; acute renal failure; sepsis (positive blood culture); urinary tract infection; and CSF analysis if performed.

Indications for imaging were documented. MR imaging was performed on 1.5T (Magnetom Avanto; Siemens, Erlangen, Germany) or 3T (Intera Achieva; Philips Healthcare, Best, the Netherlands) scanners while CT was performed on 6-slice (Brilliance 6; Philips Healthcare) or 64-slice (Discovery 750 HD; GE Healthcare, Milwaukee, Wisconsin) scanners. Scans were reviewed by 2 radiologists with 2 and 4 years of experience in neuroradiology working simultaneously on a single workstation. Any disagreement was resolved by consensus. In the absence of consensus, images were reviewed by a neuroradiologist with 10 years' experience whose decision was considered final. Studies were assessed for the following: supratentorial white matter changes (periventricular, deep, and subcortical white matter; assessed for symmetry), infratentorial white matter (brain stem, middle cerebellar peduncles, and cerebellar white matter; assessed for symmetry), involvement of gray matter (cortical gray matter, basal ganglia, and thalami), the presence of diffusion restriction (cerebral white matter, deep gray matter, brain stem, and cerebellum), and the presence of hemorrhage (micro- [small foci of hemorrhage on CT or small foci of blooming of susceptibility-weighted images on MR imaging] and macrohemorrhage).

Final outcome was assessed and divided into good outcome for patients discharged in stable condition with no neurologic deficit versus poor outcome for death or the presence of neurologic deficits at discharge.

## **Statistical Analysis**

All the cases were divided into 2 categories of poor-versus-good outcome, and each of the clinical, laboratory, and imaging parameters was assessed individually using  $\chi^2$  and Fisher exact tests to look for any significant association with poor outcome (On-line Table). All analyses were performed using the Statistical Package for Social Sciences software, Version 21.0 (IBM, Armonk, New York). A GCS score of  $\leq 12$  at presentation, World Health Organization (2009) classification of dengue as severe type, and the presence of acute renal failure had significant association with poor outcome ( $P = .04$ ,  $.02$ , and  $.03$  respectively). Imaging parameters that had significant association with poor outcome were thalamic involvement ( $P = .005$ ), cerebellar peduncle involvement ( $P = .01$ ), the presence of diffusion restriction ( $P = .01$ ), and the presence of hemorrhage (both micro- and macrohemorrhage,  $P = .003$ ).

## **RESULTS**

Fourteen (40%) patients were children (15 years of age or younger; mean, 6.8 years) and 21 (60%) were adults (mean, 33.2 years). Clinical and laboratory parameters were assessed as described in the On-line Table. CSF analysis was performed in 6 cases. Three patients had normal CSF analysis and 2 had a marginal increase in white blood cells with normal proteins, and 1 patient had normal cells but marginally elevated proteins. CSF was not tested for the dengue antigen.

### **Type of Dengue Infection**

There were 8 cases with primary infection (positive for serum immunoglobulin M and negative for immunoglobulin G for dengue. In 1 case, both immunoglobulin M and immunoglobulin G were negative; however, the nonstructural protein 1 antigen was positive). Twenty-seven cases had secondary infection (serum immunoglobulin G—positive with or without positive serum immunoglobulin M). Of the 22 patients in whom the serum nonstructural protein 1 antigen test was available, it was positive in 9.

### **World Health Organization (2009) Classification of Dengue**

One case was classified as dengue without warning signs, 3 cases were classified as dengue with warning signs, and 31 cases were classified as severe dengue.

### **Indications for Imaging**

One case had an acute drop in sensorium, 18 cases had altered sensorium, 8 cases had altered sensorium with seizures, 5 cases had acute onset headache, and intracranial hemorrhage was suspected in 3 cases.

### **Imaging Findings**

Nine cases had both MR imaging and CT scans, 7 cases had only MR imaging, and 19 cases had only CT scans. Fifteen (42.9%) cases did not have any significant abnormality on imaging (On-line Figures 1–4).

**Table 1: White and gray matter abnormalities in different brain regions on both CT and MRI scans (35 cases)**

Patterns of Involvement	No.	%
White matter		
Cerebral white matter	14	40.0%
Symmetric	3	
Asymmetric	10	
Periventricular white matter	4	
Deep white matter	9	
Subcortical U-fibers	11	
Cerebellar white matter	11	31.4%
Peripheral	3	
Both central and peripheral	5	
Symmetric	4	
Asymmetric	7	
Middle cerebellar peduncles	8	22.9%
Basal ganglia	2	5.7%
Thalamus	9	25.7%
Symmetric	6	
Asymmetric	3	
Substantia nigra	3	8.6%
Asymmetric	1	
Symmetric	2	
Brain stem	10	28.6%

#### **Involvement of White and Gray Matter on T1-Weighted/T2-Weighted Sequences and CT**

Of the 9 patients who had both MR imaging and CT scans performed in a short interval (within 1 week), there was concordance of the imaging findings in 8 cases. One case demonstrated involvement of the substantia nigra on MR imaging, which could not be appreciated on CT.

Dengue infection is known to involve cortical gray matter, subcortical and deep white matter, the basal ganglia, thalami, brain stem, and cerebellum.<sup>6-8</sup> In 1 series, all ( $n = 8$ ) cases had involvement of the cerebellum.<sup>9</sup> In our series (Table 1), posterior structures such as the brain stem and cerebellum were more commonly involved than anterior structures such as the basal ganglia. A clear gradient was found in which there was progressive involvement of basal ganglia, thalami, brain stem, and cerebellum in an increasing order. While involvement of thalami is commonly seen in patients with Japanese encephalitis and is considered quite specific for this disease,<sup>10,11</sup> there were 9 cases (25.7%) with involvement of thalami in the current series with 1 case showing pure thalamic involvement. With respect to involvement of the cerebellum (31.4% of the cases), peripherally located structures were involved more commonly, either in isolation or in combination with central structures rather than central structures alone. Involvement of cerebral white matter was also found in 40% of the cases. Again, a superficial-to-deep gradient was observed in which subcortical white matter was involved more commonly than deep white matter. Cerebral white matter involvement was found to be predominantly asymmetric.

#### **Involvement of the Substantia Nigra**

Viral encephalitis is very rarely known to involve the substantia nigra with Parkinsonism-like late clinical presentation.<sup>12</sup> Encephalitis related to West Nile virus, Murray Valley encephalitis, Epstein-Barr virus, and, more commonly, Japanese encephalitis is known to involve the substantia nigra as an exception rather than a rule.<sup>13-16</sup> In the current series, 3 cases were found to have substantia nigra involvement.

**Table 2: Diffusion restriction in cases with MRI scans (16 cases)**

Patterns	No.	%
Diffusion restriction present	11	68.8%
Cerebral white matter involvement	7	43.8%
Deep gray matter involvement	8	50.0%
Brain stem involvement	6	37.5%
Cerebellar involvement	6	37.5%

#### **Diffusion Restriction**

Eleven (68.8%) of the 16 patients who underwent MR imaging had focal areas of diffusion restriction. Areas of diffusion restriction were found to involve both gray and white matter in both supra- and infratentorial regions (Table 2). In 1 case, there was diffusion restriction involving the head of the bilateral hippocampi, while 1 case had focal splenial hyperintensity with associated diffusion restriction. In patients with thalamic involvement, thalami were symmetrically swollen, with T2-weighted hyperintensity and central diffusion restriction.

Diffusion restriction is known to be involved in cases with viral encephalitis with studies describing areas of diffusion restriction in cytomegalovirus, herpes simplex, influenza, enterovirus 71-related encephalitis, and John Cunningham virus-related progressive multifocal leukoencephalopathy among others.<sup>17-21</sup> There are few data with respect to diffusion restriction with dengue infection, with case reports describing the presence of diffusion restriction in the thalami, splenium of the corpus callosum,<sup>22</sup> and pons.<sup>23</sup>

Acute arterial territory strokes have been described as a rare complication in dengue infection.<sup>24</sup> In the current series, there was 1 case for which only follow-up imaging was available, showing chronic lacunar infarcts in the bilateral basal ganglia region.

#### **Microhemorrhages**

Of the 10 cases, 8 had MR imaging scans in which microhemorrhages were seen as small foci of blooming on susceptibility-weighted images, while they were seen as high-density foci on CT. Microhemorrhages were seen involving the thalami in 5 cases, the pons in 4 cases, and the cerebral and cerebellar white matter in 2 cases each. Six patients who had microhemorrhages on MR imaging also underwent CT at close intervals (within 1 week). Microhemorrhages could not be appreciated on these CT scans.

#### **Macrohemorrhages**

Macrohemorrhage was found in 3 cases on CT. In the first case, there was acute intraventricular hemorrhage with a normal platelet count at the time of imaging. In the second case, there was acute left cerebellar hematoma with posteriorly located subdural hemorrhage along the posterior fossa and extension along bilateral tentorial leaves. In the third case, there was acute right cerebellar hematoma with associated right parietal subdural hemorrhage extending along the tentorium. Both cases with acute cerebellar hematoma had low platelet counts (5000 and 29,000/mm<sup>3</sup>) at the time of imaging.

Dengue encephalitis with associated acute hemorrhage is termed "dengue hemorrhagic encephalitis." These hemorrhages can be tiny or large and intra- or extra-axial. Hemorrhages are known to rarely occur in the basal ganglia, pituitary gland, pons, cerebellum, and subdural or intraventricular locations or may

present as multiple small intraparenchymal hemorrhagic foci.<sup>25-28</sup> In the current series, there were 13 (37.1%) cases with hemorrhages, the pattern suggestive of posterior predominance (involvement of thalami, pons, and cerebellar white matter).

### **Posterior Reversible Encephalopathy Syndrome**

Two patients had white matter edema involving the bilateral occipital and parietal regions in a fairly symmetric distribution with associated increases in blood pressure during their hospital stay suggestive of posterior reversible encephalopathy syndrome (PRES). The presence of PRES in a case with dengue infection has been described previously.<sup>29</sup>

### **Outcome following an Acute Episode**

Poor outcome was seen in 21 patients. There were 9 deaths in the hospital, 2 patients were discharged at their request in a critical state for end-of-life care at home, 4 patients had decreased sensorium at discharge (1 of whom had gaze palsy), 6 patients were alert at discharge with varying deficits (1 right hemiparesis, 1 ataxia, 2 swallowing dysfunctions requiring nasogastric feeding, 1 truncal weakness, and 1 patient with psychiatric symptoms in the form of anger outbursts, irritability, memory deficits, and delusions of infidelity causing loss of employment on follow-up). Of the 15 cases with normal findings on imaging studies, 9 cases had good outcome and 6 cases had poor outcome.

### **Cause of Death**

No postmortem examination was performed. All the cases had multiorgan dysfunction with 3 cases documented with disseminated intravascular coagulation.

### **Follow-Up Imaging**

Follow-up imaging was available in 6 cases at mean interval of 4.7 months. On the initial scans, swelling and T2-weighted hyperintensity were seen in the pons in 5 cases; the cerebellum in 4 cases; the thalami in 3 cases; and periventricular, deep, and subcortical U-fibers in 2 cases each with cortical gray matter involvement in 1 case. On follow-up imaging, the swelling in these regions had resolved with volume loss and residual gliotic changes. In 1 case with symmetric involvement of the substantia nigra and another case with cortical gray matter involvement, no residual gliotic changes could be appreciated.

Additionally, in 4 cases (not included in data analysis) only follow-up imaging was available. The first case was a 2-year-old boy admitted with severe dengue infection. At discharge, he had regression of developmental milestones in the form of partial loss of head control and required support to sit. MRI at 1 month after the acute episode demonstrated chronic lacunar infarcts in the bilateral caudate nuclei, left lentiform nucleus, and anterior limb of the left internal capsule. The second case was a 4-year-old boy admitted with severe dengue infection. At discharge, he had swallowing dysfunction and required feeding via a nasogastric tube. One month after the acute episode, MRI scan showed normal imaging findings. The third and fourth patients, 18 and 22 years of age respectively, were both admitted with severe dengue but were discharged in stable condition with no neurologic deficits. MR imaging was performed at 2 months and 2 weeks, respectively, for

both the patients after the acute episode. Findings of these scans were normal.

## **DISCUSSION**

Dengue is an RNA virus and has come into prominence due to the high social and economic cost associated with the infections it causes, especially because it involves underdeveloped parts of the world.<sup>30</sup> Although dengue virus causes multisystem disease, which can lead to multiorgan dysfunction, it rarely has neurologic manifestation. Neurologic involvement is of concern because of long-term sequelae that can be seen in such cases.

Following a bite by an infected mosquito, the dengue virus can replicate in lymph nodes, muscles, and fibroblasts. Macrophages can also be infected. The virus can access the brain parenchyma either by disruption of the blood-brain barrier or secondary to movement of the infected macrophage from peripheral blood into the CSF or brain parenchyma.<sup>31</sup> Postmortem studies have isolated the dengue antigen from the brain tissue.<sup>32</sup> The actual mechanism of brain injury is still debated and can be attributed to direct viral invasion, metabolic imbalance, hemorrhagic diathesis, or postinfection autoimmunity.<sup>31</sup> Current research is limited by the lack of a good animal model. Therefore, in vivo imaging studies can help further our understanding.

A large proportion of cases in the current series did not have any significant abnormal findings on their cranial scans (15 cases, 42.9%). The apparent lack of correlation between CNS symptoms and normal imaging findings could be related to metabolic derangement that was present in these cases.

Among the cases with abnormal brain imaging findings, this study demonstrates involvement of important brain structures such as the brain stem, cerebellum, thalami, and cerebral white matter, which could explain the significant morbidity (12 cases, 34.3%) and mortality (9 cases, 25.7%). The imaging findings in this series can also be seen in other Flavivirus infections such as Japanese encephalitis, West Nile virus encephalitis, and Murray valley virus encephalitis, suggestive of similar pathophysiology.<sup>10-14</sup>

Therefore, although accurate identification of dengue-related brain changes cannot be made purely on the basis of imaging findings, the differential diagnosis can be significantly reduced. With the additional input of typical clinical presentation, thrombocytopenia, and local prevalence of the disease, one cannot only suggest the possibility of dengue infection but can also help in prognosis based on involvement of the thalami and cerebellar peduncles, and the presence of diffusion restriction and intraparenchymal hemorrhage.

### **Limitations**

This was a retrospective study with selection bias because only very sick individuals with CNS symptoms underwent imaging of the brain. Therefore, the results can be extrapolated to only a small similar subgroup of patients.

## **CONCLUSIONS**

Although imaging findings are not unique, in the presence of CNS symptoms, dengue infection has radiological findings that can be used to narrow down the differential diagnosis list and help in prognostication. Development of an animal model will help to

better understand the pathophysiology of CNS involvement in dengue infection. This could also help in the development of neuroprotective measures.

## REFERENCES

1. Dengue: Guidelines for Diagnosis, Treatment, Prevention and Control. Geneva: World Health Organization; 2009 (WHO Guidelines Approved by the Guidelines Review Committee). <http://www.ncbi.nlm.nih.gov/books/NBK143157/>. Accessed April 18, 2017
2. WHO. Epidemiology. Dengue control. <http://www.who.int/denguecontrol/epidemiology/en/>. Accessed November 13, 2017
3. Solomon T, Dung NM, Vaughn DW, et al. **Neurological manifestations of dengue infection.** *Lancet* 2000;355:1053–59 CrossRef
4. Pancharoen C, Thisyakorn U. **Neurological manifestations in dengue patients.** *Southeast Asian J Trop Med Public Health* 2001;32:341–45 Medline
5. Verma R, Sharma P, Garg RK, et al. **Neurological complications of dengue fever: experience from a tertiary center of north India.** *Ann Indian Acad Neurol* 2011;14:272–78 CrossRef Medline
6. Bhoi SK, Naik S, Kumar S, et al. **Cranial imaging findings in dengue virus infection.** *J Neurol Sci* 2014;342:36–41 CrossRef Medline
7. Kamble R, Peruvamba JN, Kovoor J, et al. **Bilateral thalamic involvement in dengue infection.** *Neurol India* 2007;55:418–19 CrossRef Medline
8. Wasay M, Channa R, Jumani M, et al. **Encephalitis and myelitis associated with dengue viral infection clinical and neuroimaging features.** *Clin Neurol Neurosurg* 2008;110:635–40 CrossRef Medline
9. Hegde V, Aziz Z, Kumar S, et al. **Dengue encephalitis with predominant cerebellar involvement: report of eight cases with MR and CT imaging features.** *Eur Radiol* 2015;25:719–25 CrossRef Medline
10. Basumatary LJ, Raja D, Bhuyan D, et al. **Clinical and radiological spectrum of Japanese encephalitis.** *J Neurol Sci* 2013;325:15–21 CrossRef Medline
11. Misra UK, Kalita J. **Overview: Japanese encephalitis.** *Prog Neurobiol* 2010;91:108–20 CrossRef Medline
12. Rebai I, Ben Rhouma H, Kraoua I, et al. **Postencephalitic parkinsonism and selective involvement of substantia nigra in childhood.** *Brain Dev* 2015;37:153–57 CrossRef Medline
13. Bosanko CM, Gilroy J, Wang AM, et al. **West Nile virus encephalitis involving the substantia nigra: neuroimaging and pathologic findings with literature review.** *Arch Neurol* 2003;60:1448–52 CrossRef Medline
14. Einsiedel L, Kat E, Ravindran J, et al. **MR findings in Murray Valley encephalitis.** *AJNR Am J Neuroradiol* 2003;24:1379–82 Medline
15. Çelik T, Çelik Ü, Tolunay O, et al. **Epstein-Barr virus encephalitis with substantia nigra involvement.** *J Pediatr Neurosci* 2015;10:401–03 CrossRef Medline
16. Ogata A, Tashiro K, Pradhan S. **Parkinsonism due to predominant involvement of substantia nigra in Japanese encephalitis.** *Neurology* 2000;55:602 Medline
17. Renard T, Dumas-Duport B, Auffray-Calvier E, et al. **Cytomegalovirus encephalitis: undescribed diffusion-weighted imaging characteristics—original aspects of cases extracted from a retrospective study, and from literature review.** *J Neuroradiol* 2016;43:371–77 CrossRef Medline
18. Sener RN. **Herpes simplex encephalitis: diffusion MR imaging findings.** *Comput Med Imaging Graph* 2001;25:391–97 CrossRef Medline
19. Bulakbasi N, Kocaoglu M, Tayfun C, et al. **Transient splenic lesion of the corpus callosum in clinically mild influenza-associated encephalitis/encephalopathy.** *AJNR Am J Neuroradiol* 2006;27:1983–86 Medline
20. Lian Z, Huang B, He S, et al. **Diffusion-weighted imaging in the diagnosis of enterovirus 71 encephalitis.** *Acta Radiol* 2012;53:208–13 Medline
21. Barata Tavares J, Geraldo AF, Neto L, et al. **Diffusion-weighted MR imaging characterization of progressive multifocal leucoencephalopathy (PML) lesions [in Portuguese].** *Acta Med Port* 2012;25(Suppl 1):34–37 Medline
22. Pal S, Sen K, Biswas NM, et al. **Clinico-radiological profile and outcome of dengue patients with central nervous system manifestations: a case series in an Eastern India tertiary care hospital.** *J Neurosci Rural Pract* 2016;7:114–24 CrossRef Medline
23. Mehta A, Mahale RR, Javali M, et al. **Diffusion restriction in pons resembling “reverse moustache” in dengue encephalitis.** *Neurol India* 2014;62:683–84 CrossRef Medline
24. Mathew S, Pandian JD. **Stroke in patients with dengue.** *J Stroke Cerebrovasc Dis* 2010;19:253–56 CrossRef Medline
25. Kumar R, Prakash O, Sharma BS. **Intracranial hemorrhage in dengue fever: management and outcome: a series of 5 cases and review of literature.** *Surg Neurol* 2009;72:429–33; discussion 433 CrossRef Medline
26. Kumar V, Kataria R, Mehta VS. **Dengue hemorrhagic fever: a rare cause of pituitary tumor hemorrhage and reversible vision loss.** *Indian J Ophthalmol* 2011;59:311–12 CrossRef Medline
27. Kumar R, Prakash O, Sharma BS. **Dengue hemorrhagic fever: a rare presentation as atypical acute subdural hematoma.** *Pediatr Neurosurg* 2008;44:490–92 CrossRef Medline
28. de Souza LJ, Martins AL, Paravidini PC, et al. **Hemorrhagic encephalopathy in dengue shock syndrome: a case report.** *Braz J Infect Dis* 2005;9:257–61 Medline
29. Sohoni CA. **Bilateral symmetrical parieto occipital involvement in dengue infection.** *Ann Indian Acad Neurol* 2015;18:358–59 CrossRef Medline
30. Dengue: Guidelines for Diagnosis, Treatment, Prevention and Control: New Edition. Epidemiology, Burden of Disease and Transmission. <https://www.ncbi.nlm.nih.gov/books/NBK143159/>. Accessed November 14, 2017
31. Puccioni-Sohler M, Rosadas C. **Advances and new insights in the neuropathogenesis of dengue infection.** *Arq Neuropsiquiatr* 2015;73:698–703 CrossRef Medline
32. Bhoopat L, Bhamarapravati N, Attasiri C, et al. **Immunohistochemical characterization of a new monoclonal antibody reactive with dengue virus-infected cells in frozen tissue using immunoperoxidase technique.** *Asian Pac J Allergy Immunol* 1996;14:107–13 Medline

# 7T Brain MRS in HIV Infection: Correlation with Cognitive Impairment and Performance on Neuropsychological Tests

M. Mohamed, P.B. Barker, R.L. Skolasky, and N. Sacktor



## ABSTRACT

**BACKGROUND AND PURPOSE:** Validated neuroimaging markers of HIV-associated neurocognitive disorder in patients on antiretroviral therapy are urgently needed for clinical trials. The purpose of this study was to explore the relationship between cognitive impairment and brain metabolism in older subjects with HIV infection. It was hypothesized that MR spectroscopy measurements related to neuronal health and function (particularly *N*-acetylaspartate and glutamate) would be lower in HIV-positive subjects with worse cognitive performance.

**MATERIALS AND METHODS:** Forty-five HIV-positive patients (mean age, 58.9 ± 5.3 years; 33 men) underwent detailed neuropsychological testing and brain MR spectroscopy at 7T. Twenty-four subjects were classified as having asymptomatic cognitive impairment, and 21 were classified as having symptomatic cognitive impairment. Single-voxel proton MR spectra were acquired from 5 brain regions and quantified using LCModel software. Brain metabolites and neuropsychological test results were compared using nonparametric statistics and Pearson correlation coefficients.

**RESULTS:** Differences in brain metabolites were found between symptomatic and asymptomatic subjects, with the main findings being lower measures of *N*-acetylaspartate in the frontal white matter, posterior cingulate cortex, and precuneus. In the precuneus, glutamate was also lower in the symptomatic group. In the frontal white matter, precuneus, and posterior cingulate cortex, NAA and glutamate measurements showed significant positive correlation with better performance on neuropsychological tests.

**CONCLUSIONS:** Compared with asymptomatic subjects, symptomatic HIV-positive subjects had lower levels of NAA and glutamate, most notably in the frontal white matter, which also correlated with performance on neuropsychological tests. High-field MR spectroscopy offers insight into the pathophysiology associated with cognitive impairment in HIV and may be useful as a quantitative outcome measure in future treatment trials.

**ABBREVIATIONS:** cART = combined antiretroviral therapy; FWM = frontal white matter; Glu = glutamate; HAND = HIV-associated neurocognitive disorder; PC = precuneus; PCC = posterior cingulate cortex; tNAA = NAA + *N*-acetyl aspartylglutamate

Human immunodeficiency virus-associated neurocognitive disorder (HAND) is characterized by cognitive, behavioral, and motor dysfunction, which impacts daily functioning<sup>1-3</sup> and is predictive of poor survival in patients.<sup>4</sup> Combination antiretrovi-

ral therapy (cART) can improve cognitive performance and brain metabolism in some patients with HAND.<sup>2,5,6</sup> However, many antiretroviral drugs do not penetrate well into the central nervous system,<sup>7</sup> and neurocognitive deficits are reversed in many but not all patients.<sup>8,9</sup> The prevalence of HAND in HIV positive (HIV+) individuals with advanced infection remains around 45%–50%, and patients are now surviving for years with HIV infection and HAND as chronic conditions.<sup>10,11</sup> Advanced age is an important risk factor for HAND; for instance, in the Hawaii Aging with HIV cohort, HIV+ individuals older than 50 years of age were twice as likely to have dementia compared with HIV+ individuals who were 20–39 years of age.<sup>12,13</sup> Because HIV+ individuals are now living longer as a result of cART, the proportion of HIV+ individuals older than 50 years of age has increased.

There is some evidence that HIV+ subjects may develop cognitive decline earlier than the HIV-negative (HIV-) population (ie, more rapid aging). For the quantitative assessment of neuro-

Received August 3, 2017; accepted after revision December 1.

From the Russell H. Morgan Department of Radiology and Radiological Science (M.M., P.B.B.) and Departments of Neurology (R.L.S., N.S.), Orthopedic Surgery (R.L.S.), and Psychiatry and Behavioral Sciences (P.B.B.), Johns Hopkins University School of Medicine, Baltimore, Maryland; and F.M. Kirby Center for Functional Brain Imaging (P.B.B.), Kennedy Krieger Institute, Baltimore, Maryland.

This work was funded by National Institutes of Health grants RO1NS081196, P41EB015909, and P30MH075673.

Please address correspondence to Mona A. Mohamed, MD, Department of Radiology, Johns Hopkins University School of Medicine, 600 N Wolfe St, Park Building, Third Floor, 367G, Baltimore, MD 21287; e-mail: mnourell@jhmi.edu

Indicates open access to non-subscribers at www.ajnr.org

Indicates article with supplemental on-line table.

<http://dx.doi.org/10.3174/ajnr.A5547>

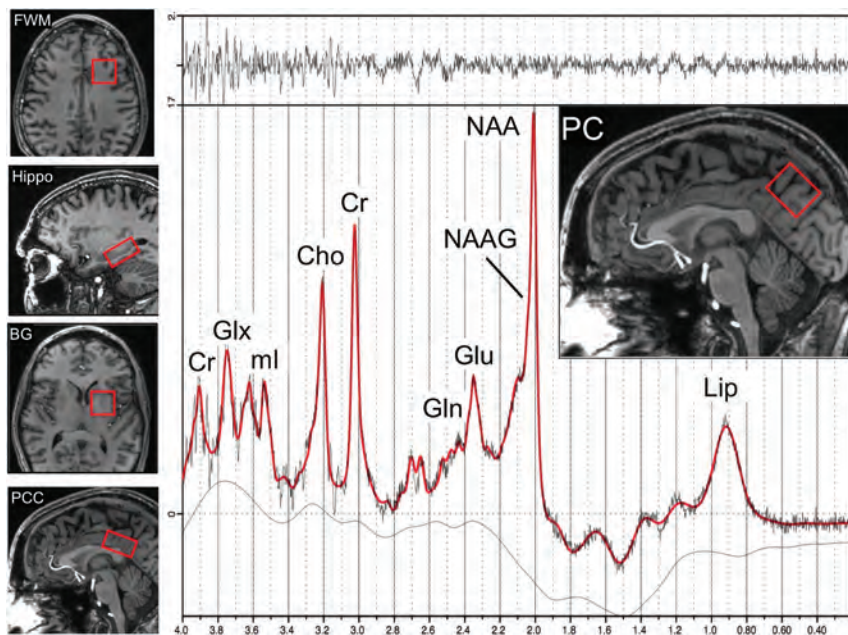


**FIG 1.** Examples of the 5 voxel locations used for brain MR spectroscopy in the left frontal white matter, left hippocampus (Hippo), left basal ganglia (BG), mesial posterior cingulate cortex, and mesial precuneus. An example of a spectrum from the PC in a 55-year-old HIV+ subject is shown, including results from the LCMoDel analysis (red curve). Signals are assigned to lipids (Lip), *N*-acetylaspartate, *N*-acetyl aspartylglutamate (NAAG), glutamate, glutamine (Gln), creatine, choline, myo-inositol (ml), and Glx (the sum of Glu and Gln). The top trace is the difference between the original data and the results of the curve fit.

logic involvement in older HIV+ individuals, it is important to develop and validate noninvasive imaging tools that are sensitive to changes in cognitive and behavioral statuses, which, for instance, may be of use as quantitative measures in future treatment trials. Measurements of regional brain metabolism may also shed some light on the neurobiology of brain aging and cognitive decline in the older HIV+ population.

Proton MR spectroscopy (MR spectroscopy) is a noninvasive technique that gives information on brain pathophysiology through measurement of brain metabolite levels.<sup>14</sup> The most common observations in HIV+ subjects are increased levels of choline<sup>15</sup> and mIns,<sup>16</sup> thought to reflect inflammation and microglial proliferation, and decreased levels of *N*-acetylaspartate and glutamate,<sup>17-19</sup> believed to be due to neuronal injury or dysfunction.<sup>15,20-22</sup> Metabolic abnormalities may be observed in regions of the brain with normal appearance on conventional MR imaging, even in subjects who are neurologically asymptomatic, and increase with increasing degrees of neurologic involvement.<sup>23</sup> Thus, MR spectroscopy has been proposed as suitable tool for monitoring the degree of HIV involvement in the brain and the effects of therapy.<sup>24,25</sup>

MR spectroscopy at field strengths of 1.5T, 3T, and 4T<sup>6,18,26-28</sup> has been extensively used to investigate neurologic involvement in HIV+ subjects. Higher magnetic field strengths (such as 7T) allow increased sensitivity and chemical shift dispersion and more reliable determination of brain metabolites, particularly for some of the smaller and overlapping signals in the spectrum, such as glutamate and glutamine.<sup>29,30</sup>

The current study was undertaken to investigate the utility of 7T MR spectroscopy in evaluating a cohort of older HIV+ pa-

tients with varying degrees of neurocognitive impairment. It was hypothesized that differences in brain metabolites reflecting neuronal and glial cell populations would be observed between older HIV+ individuals with and without cognitive impairment. For analysis, patients were classified either as “asymptomatic” (ie, either cognitively healthy or having asymptomatic neurocognitive impairment) or “symptomatic” (HAND, including those with either a mild neurocognitive disorder or HIV-associated dementia).

## MATERIALS AND METHODS

### Participants and Clinical Testing

The study was approved the local institutional review board, and all subjects gave written informed consent. HIV+ individuals were recruited at the Institute for Clinical and Translational Research at Johns Hopkins Hospital in Baltimore, Maryland, from 2013 to 2016. Inclusion criteria were adults who were HIV-positive, older than 50 years of age, and had the ability to provide written informed consent and to ambulate at the

first clinic visit. Patients were excluded if they had a history of or current opportunistic central nervous system infection, schizophrenia, affective disorder, or psychiatric diseases, which could be a confounder for cognitive impairment, or chronic neurologic disorders such as brain infarction, hemorrhage, epilepsy, and multiple sclerosis. Active substance abusers or opiate users were excluded, defined as any history of illicit drug use within 3 months preceding the baseline visit, established by subject history and urine toxicology screens. Any contraindication for 7T MR imaging (metal in the body, claustrophobia, inner ear disorder) was also an exclusion criterion.

As described above, subjects were stratified by neurocognitive disorder status using the revised American Academy of Neurology “Frascati” criteria.<sup>31</sup> All subjects underwent detailed neurologic, neuropsychological, laboratory, and functional assessments. Clinical assessments included standardized questionnaires that assessed demographic information, including primary language; reading abilities; medical, psychiatric, and neurologic history; and a neurologic examination. Serum CD4 T-cell counts and HIV RNA levels via quantitative polymerase chain reaction in the plasma and CSF were obtained. Depression symptomatology was rated using the Center for Epidemiological Studies Depression Scale.<sup>32</sup> Hepatitis C viral status was obtained via clinical history and evaluation of laboratory findings for hepatitis C virus antibodies.

Measures of functional performance included the Karnofsky Performance Scale, a questionnaire for instrumental activities of daily living, and a questionnaire for physical quality of life measures.<sup>1-3,33-35</sup> Neuropsychological testing included the Trail-

Making Test, Color Trails Test, Grooved Pegboard Test, Digit Symbol Test, Stroop Test, Rey Complex Figure Test, and Hopkins Verbal Learning Test.<sup>36-38</sup> Raw scores on each neuropsychological test were converted to *z* scores using published normative data.<sup>31</sup>

### MR Imaging and Spectroscopy

All studies were performed on a 7T scanner (Achieva; Philips Healthcare, Best, the Netherlands) equipped with a 32-channel receive head coil and quadrature transmit coil (Nova Medical, Wilmington, Massachusetts). Brain MR imaging consisted of lo-

### Subject demographics in the 2 HIV+ groups: asymptomatic neurocognitive impairment and symptomatic HIV-associated neurocognitive disorder<sup>a</sup>

	ANI	HAND	P Value
No.	24	21	—
Age (yr)	59.6 ± 5.7	58.2 ± 5.0	.378
Male sex (No.) (%)	17 (71%)	16 (76%)	.764
Education (yr)	14.9 ± 3.0	14.0 ± 2.7	.263
Race (% African American)	12 (50%)	13 (62%)	.655
Duration of infection (yr)	19.9 ± 9.0	19.2 ± 9.4	.790
CES-D	7.7 ± 6.8	11.0 ± 11.7	.253
HART Est IQ <sup>b</sup>	112.9 ± 12.8	103.7 ± 12.9	.022
CD4 cell count (cells/mm <sup>3</sup> )	674 ± 281	676 ± 375	.988
Plasma HIV RNA (Log <sup>10</sup> copies/mL) <sup>c</sup>	1.6 ± 0.1	2.3 ± 1.4	.569

**Note:**—ANI indicates asymptomatic neurocognitive impairment; CES-D = Center for Epidemiological Studies Depression Scale; HART Est IQ = Hopkins Adult Reading Test estimated intelligence quotient.

<sup>a</sup> Values given are mean ± SD unless otherwise indicated.

<sup>b</sup> Significant (*P* < .05).

<sup>c</sup> Plasma HIV RNA only among those with detectable viral load (*n* = 2 ANI and *n* = 3 HAND).

calizer images and a 3D T1-weighted MPRAGE scan with 1.2-mm isotropic voxel size. Single-voxel Stimulated Echo Acquisition Mode (STEAM) spectra (TR/TE/mixing time = 3000/14/25 ms) were acquired from the left frontal white matter (FWM), left basal ganglia, mesial precuneus (PC), mesial posterior cingulate cortex (PCC), and left hippocampus with and without variable power and optimized relaxation water suppression. These regions were chosen on the basis of prior studies that have indicated that the regions are involved in HIV infection and aging.<sup>10,39-41</sup> The voxel sizes ranged from 8 to 15 mL (Fig 1). The hippocampal voxel was carefully angulated parallel to the long axis of the hippocampus and had dimensions of 1.5 × 1.5 × 3.5 cm to minimize partial volume contributions from surrounding tissues. Eighty acquisitions had water suppression, and 2 were unsuppressed, to give a total scan time per region of 4 minutes 6 seconds. Before the acquisition of each region, field inhomogeneity was corrected up to second order using the FASTMAP (fast, automatic shimming technique by mapping along projections) localized shimming technique,<sup>42</sup> and localized power optimization<sup>43</sup> was also performed (transmit *B*<sub>1</sub> = 15 μT).

Spectra were analyzed using a basis set designed for the 7T STEAM sequence incorporated in the LCModel software package (<http://www.lcmodel.com/>)<sup>44</sup> and quantified in approximately millimolar concentrations (referred to here as institutional units because relaxation time corrections were not performed) relative to the unsuppressed water signal. Ratios relative to creatine were also calculated. We did not perform any volumetric morphome-

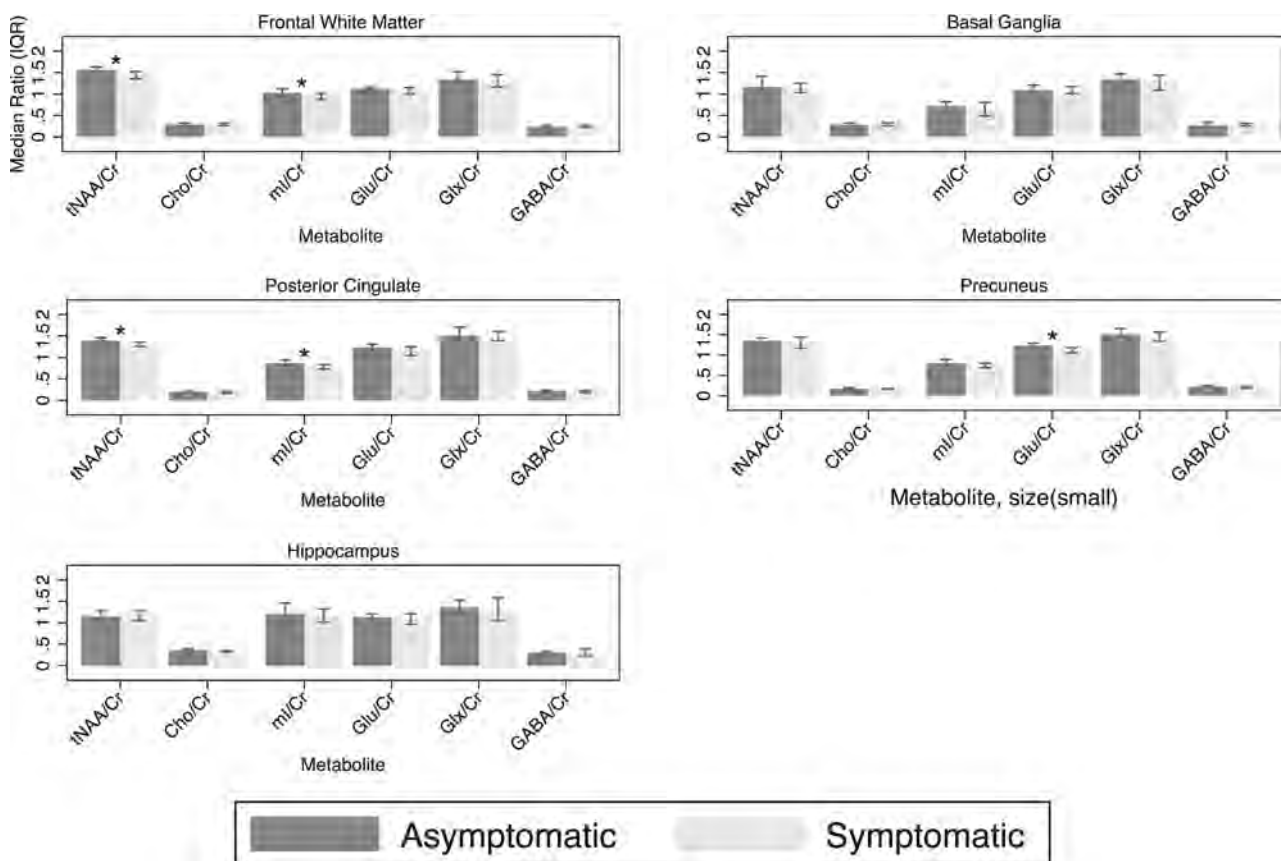


**FIG 2.** Metabolite ratios for the frontal white matter, posterior cingulate, precuneus, basal ganglia, and hippocampal voxels. Asterisk indicates significant; GABA,  $\gamma$ -aminobutyric acid; IQR, interquartile range; ml, myoinositol.

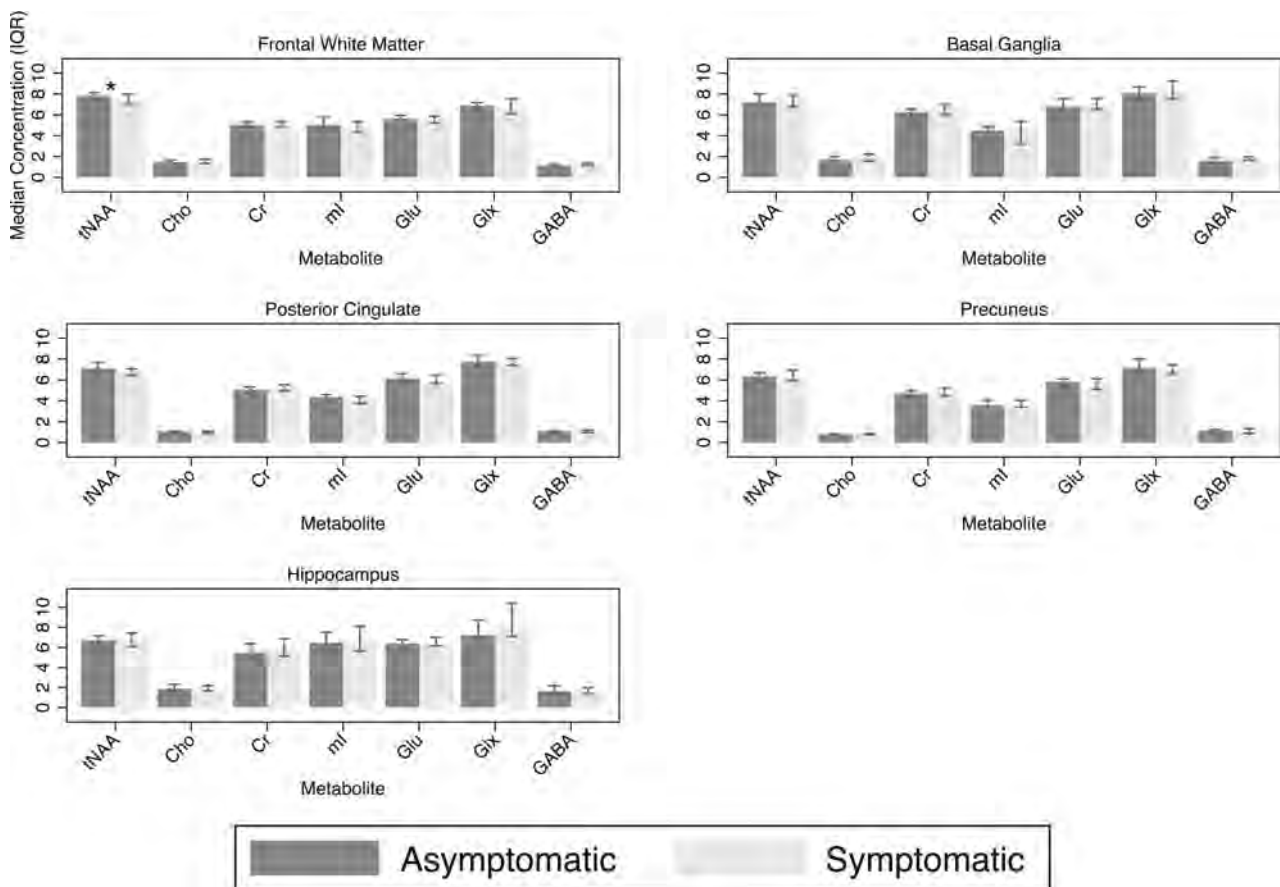


**FIG 3.** Metabolite concentrations in institutional units for the frontal white matter, posterior cingulate, precuneus, basal ganglia, and hippocampal voxels. Asterisk indicates significant, GABA,  $\gamma$ -aminobutyric acid; IQR, interquartile range; ml, myoinositol.

try because we reported metabolite ratios in addition to metabolite concentrations. The LCModel basis set contained 20 different metabolites and the standard LCModel macromolecule peaks. Concentration and ratio values were only included for statistical analysis if their Cramér-Rao lower bounds were  $\leq 20\%$ .<sup>44</sup> A representative PC spectrum is shown from 1 subject in Fig 1.

### Statistical Analysis

The objective of the current study was to compare metabolite concentration and ratio values between older HIV+ patients who were either asymptomatic or symptomatic for neurocognitive impairment. With the Shapiro-Wilk test, the data were not normally distributed; therefore, we present the data as median and interquartile range (interquartile range, 25th and 75th percentiles). Between-group comparisons were made using the nonparametric median test. Pearson correlation coefficients were calculated between metabolite values and concentrations and neurocognitive tests.

### RESULTS

Forty-five subjects (mean age,  $58.9 \pm 5.3$  years; 33 [73%] men) were enrolled. All patients were receiving cART. Twenty-four subjects were classified as asymptomatic, and 21, as symptomatic. Patient demographics are given in the Table. There were no significant group differences in age, education, sex, race, CD4 count, or plasma HIV RNA between groups. The estimated intelligence

quotient was significantly lower in the symptomatic group (103.7 versus 112.9, respectively,  $P = .02$ ). Apart from some small white matter hyperintensities in 2 individuals, which were avoided during MR spectroscopy voxel placement, there were no significant T2WI or FLAIR lesions or other abnormalities in any of the subjects in this study.

In the frontal white matter, the median NAA/Cr ratio was lower in the symptomatic group compared with the asymptomatic group (1.21 versus 1.30, respectively;  $P = .005$ ), and NAA + N-acetyl aspartylglutamate (tNAA)/Cr (1.46 versus 1.56, respectively;  $P = .005$ ) and the median mIns/Cr (0.97 versus 1.03, respectively;  $P = .02$ ) (Fig 2). There was also a trend toward lower FWM tNAA concentration in the symptomatic group compared with the asymptomatic group (7.46 versus 7.81 mmol/L, respectively;  $P = .06$ ) (Fig 3). In the posterior cingulate cortex, the median NAA/Cr was also significantly lower in the symptomatic group (1.16 versus 1.21, respectively;  $P = .01$ ), as was the median tNAA/Cr (1.32 versus 1.40, respectively;  $P = .02$ ) and median mIns/Cr (0.78 versus 0.87, respectively;  $P = .002$ ) (Fig 2). In the precuneus, the median NAA/Cr was also significantly lower in the symptomatic group (1.14 versus 1.23, respectively;  $P = .02$ ), as was median glutamate/Cr (Glu/Cr) (1.12 versus 1.24, respectively;  $P = .01$ ) (Fig 2). There were no significant differences between groups in basal ganglia and hippocampus metabolite concentrations or ratios.

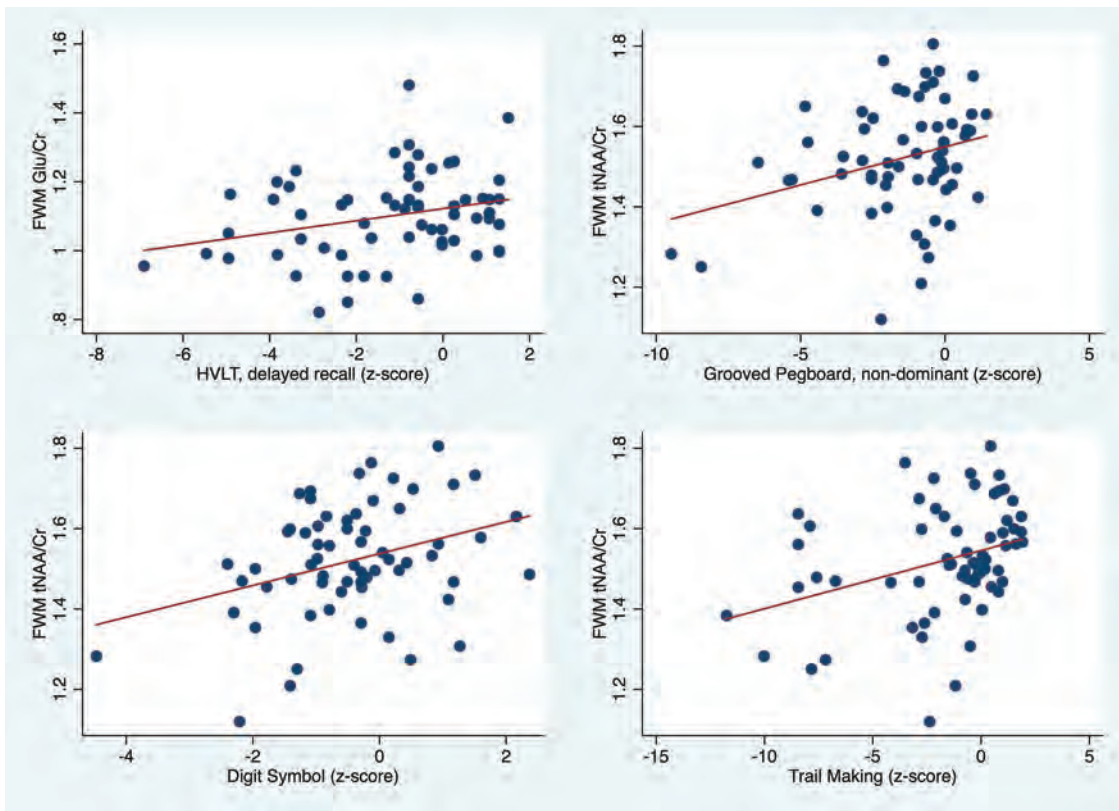


**FIG 4.** Scatterplots showing significant positive correlations of FWM Glu/Cr with the Hopkins Verbal Learning Test (HVLT) delayed recall, and FWM tNAA/Cr with the Grooved Pegboard non-dominant hand, Digit Symbol, and Trail-Making Test B z scores.

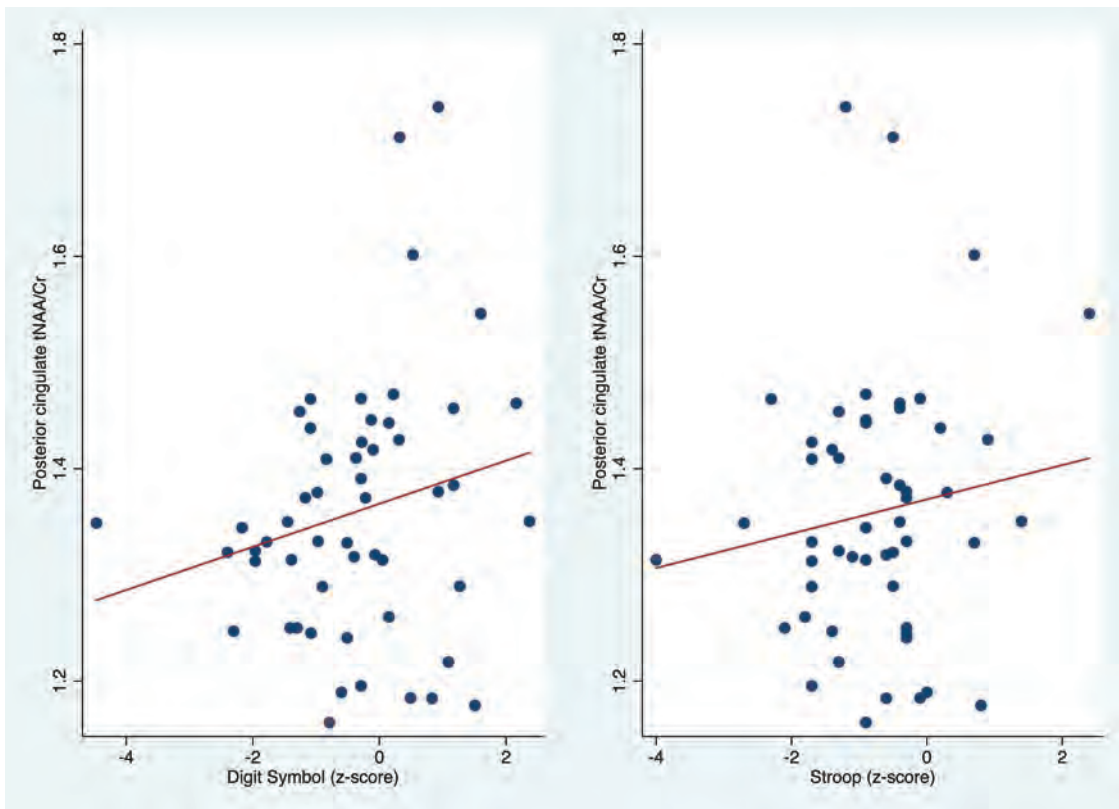


**FIG 5.** Scatterplots showing significant positive correlation of the posterior cingulate tNAA/Cr with the Digit Symbol and Stroop test z scores.

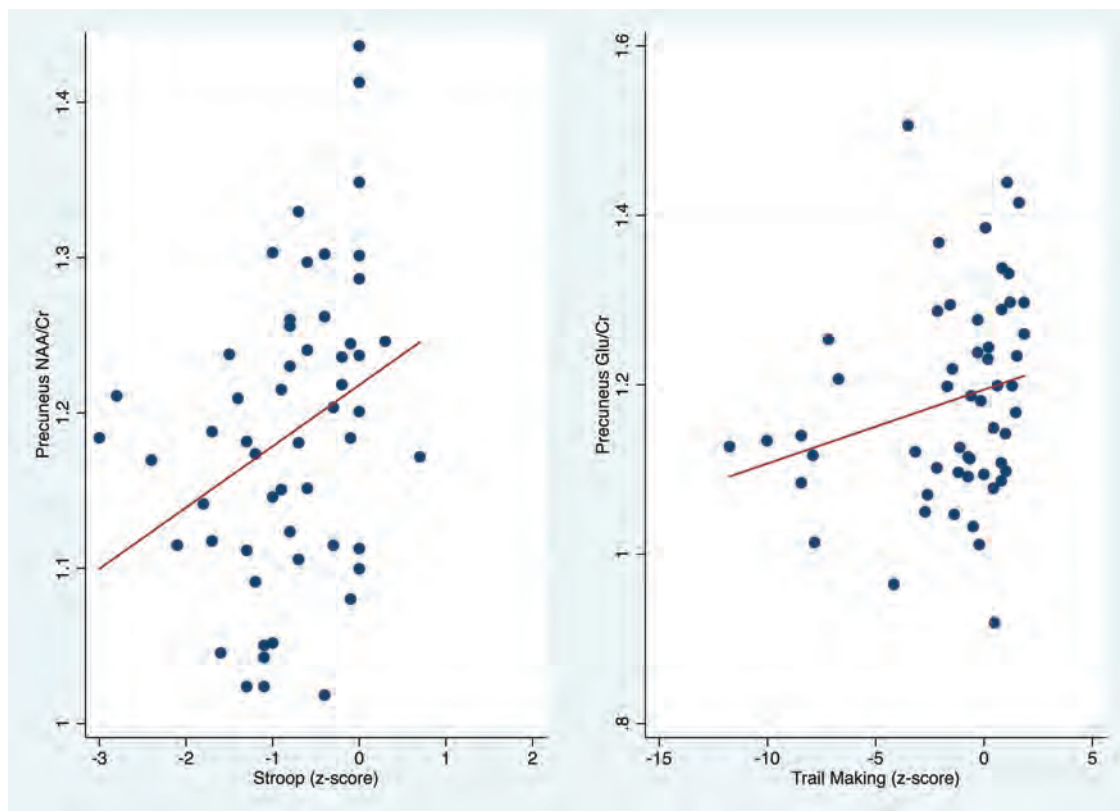


**FIG 6.** Scatterplots showing significant positive correlation of the precuneus NAA/Cr and Glu/Cr with Stroop test and Trail-Making Part B z scores, respectively.

Regarding correlations between MR spectroscopy results and neuropsychological tests (On-line Table and Figs 4–6), lower FWM tNAA/Cr was associated with worse performance on measures of executive function, fine motor, and psychomotor speed (Trail-Making Test, Part B; Grooved Pegboard Test non-dominant hand; and the Digit Symbol test ( $P = .005, .01, \text{ and } .001$ , respectively). Furthermore, lower FWM Glu/Cr was associated with lower performance on delayed recall on the Hopkins Verbal Learning Test ( $P = .02$ ) (Fig 4). Lower tNAA/Cr in the posterior cingulate was associated with worse performance on tests of psychomotor speed (Digit Symbol and Stroop Test;  $P = .02$  and  $.04$ , respectively) (Fig 5). Lower precuneus NAA/Cr was associated with worse performance on the Stroop Test, a test of processing speed ( $P = .04$ ); while precuneus Glu/Cr decreases were associated with worse performance in the Trail-Making Test, Part B, a measure of executive functioning ( $P = .04$ ) (Fig 6).

## DISCUSSION

The main finding of this study is that 7T MR spectroscopy could find significant differences in metabolite levels between symptomatic and asymptomatic HIV+ subjects, with the primary result being lower levels of tNAA (or the ratio tNAA/Cr) in the frontal white matter, posterior cingulate, and precuneus. Glu/Cr was also lower in the precuneus in the symptomatic group. In addition, significant correlations were found between FWM measures of tNAA (and tNAA/Cr) and Glu (and Glu/Cr, Glx, and Glx/Cr) and multiple neuropsychological test scores. Posterior cingulate cortex and precuneus measures of NAA and Glu also correlated with performance on the Digit Symbol and Stroop

tests. Overall, these results suggest that MR spectroscopy measurements of NAA and glutamate in these brain regions reflect neuroaxonal loss or dysfunction, which correlates with worse performance on neuropsychological tests.

Decreased NAA and Glx (Glu + glutamine) concentrations in HIV infection are well-established from MR spectroscopy studies at lower field strengths; for instance, in 1 study, long TEs performed at 1.5T revealed decreased levels of NAA/Cr in the parieto-occipital white matter in asymptomatic HIV+ men compared with healthy controls.<sup>45</sup> MR spectroscopic imaging studies also performed at long TEs found progressive declines in NAA from HIV-negative controls to asymptomatic and then symptomatic HIV+ patient groups in multiple gray and white matter regions.<sup>6,18,46</sup> NAA was also found to increase after initiation of cART.<sup>6,46</sup> Previous 3T studies have also reported decreasing Glx concentrations (or Glx/Cr ratios) with increasing symptomatology in HIV infection<sup>17,18</sup> and decreased levels compared with HIV-negative controls.<sup>19</sup> Although some 3T studies have used the technique of the TE-averaged point-resolved spectroscopy sequence<sup>19</sup> to selectively detect Glu, generally it can be difficult to reliably separate Glu from glutamine using conventional MR spectroscopy. Prior studies comparing 7T with lower field strengths have shown improved ability at 7T to quantify Glu and glutamine<sup>43</sup>; the current study at 7T confirms that only significant HIV-associated correlations are found for Glu, with no significant associations found for glutamine. NAA and Glu are known to be primarily located in neurons and have been shown in previous studies of various pathologies to decrease when neuronal damage

occurs. The mechanisms by which neuronal damage occurs in HIV infection are complicated, but it is believed that infiltration of infected macrophages and lymphocytes results in inflammation, astrocytosis, oxidative stress, and synaptodendritic injury.<sup>47</sup>

Several studies performed at 1.5 and 3T have reported increased mIns in HIV infection and symptomatic HIV+ subjects compared with asymptomatic subjects.<sup>6,19</sup> The current study is consistent with these findings. Previous studies at lower field strengths, and usually in younger cohorts of subjects, have generally reported increased levels of mIns in HIV+ subjects compared with HIV- controls, with higher mIns in symptomatic HIV+ subjects compared with asymptomatic subjects.<sup>18,48</sup> The current study did not find strong differences in mIns (or mIns/Cr) between asymptomatic and symptomatic groups in most brain regions, with the exception of slightly lower mIns/Cr in the FWM in the symptomatic group (ie, in the opposite direction to prior findings).<sup>18,49</sup> There were also few significant positive correlations between high mIns and worse performance on neuropsychological tests. These findings may be due to the older nature of the HIV+ cohort studied here, with a longer disease duration, generally well-controlled viral load, and less neuroinflammation than in previous studies.

Regarding correlations between brain metabolites and neuropsychological test scores, frontal white matter test NAA and Glu measures correlated positively with measures of executive function, motor speed, and verbal and working memory, whereas posterior cingulate cortex and precuneus measures of NAA and Glu predominantly correlated with the Digit Symbol and Stroop tests, measures of working memory and information-processing speed, respectively. The precuneus and posterior cingulate cortex are both visual processing areas, and neuronal dysfunction as measured by the metabolite changes in these areas could contribute to impaired performance in neuropsychological tests, which include visuospatial processing, such as the Digit Symbol and Stroop tests. Specifically, decreased FWM Glu/Cr and Glx were correlated with verbal recall, while posterior cingulate and precuneus Glu Glu/Cr and Glx were associated with attention and working memory and information-processing speed tests. These findings are generally consistent with prior studies performed at 1.5 or 3T; for instance, in patients receiving cART, significant correlations were found between 3T measures of Glu, Glx, and NAA with performance on motor and psychomotor speed, attention, and working memory.<sup>6</sup>

A study performed at 1.5T<sup>25</sup> in HIV+ subjects (most being on cART) assessed motor skills (fine and gross), psychomotor function, information-processing speed, and verbal memory and expressed the results as a composite score NPZ-8 (the average neuropsychological z scores of 8 different neuropsychological test components). Consistent with the concept of HIV+ as a predominantly subcortical dementia, NPZ-8 scores correlated positively with NAA/Cr (and NAA/Cho and NAA/mIns) in the FWM, similar to findings in the current study. Negative correlations in that study were also found between basal ganglia mIns/Cr and NPZ-8.<sup>25</sup> Another study at 1.5T in 45 antiretroviral-naïve HIV+ subjects also found elevated frontal white matter mIns and Cho compared with HIV-negative controls, which were correlated with slow performance in fine motor (Grooved Pegboard), psychomotor

(Trail-Making Test), and executive function (Stroop) tests.<sup>50</sup> The relative lack of correlations in the current study between neuropsychological test performance and measures of Cho (only PC Cho negatively correlated with the Hopkins Verbal Learning Test delayed recall task) or mIns (PCC mIns/Cr did correlate with performance on the Stroop test) most likely reflects differences in patient populations between the current and previous studies (older HIV+ subjects, all on cART).

Compared with MR spectroscopy at lower field strengths, 7T MR spectroscopy has been shown to offer increased signal-to-noise ratios and spectral resolution; however, it also presents some technical challenges, including increased chemical shift dispersion effects, difficulty shimming, and increased radiofrequency power deposition (specific absorption rate). In this study, localized second-order shimming was used to minimize the effects of field inhomogeneity. In addition, the STEAM pulse sequence was used for spatial localization because the 90° slice-selective pulses in STEAM have excellent slice profiles and low chemical shift dispersion effects and specific absorption rate.<sup>51,52</sup> However, in the future, other sequences such as semi-LASER and/or MR spectroscopic imaging sequences may be used, which provide higher SNR, spatial resolution, and coverage.

The study also has some limitations; though subjects with overt medical or neurologic abnormalities were excluded, the older HIV+ subjects in this study may well have had varying degrees of risk factors commonly encountered in the general population, which contribute to aging and cognitive decline, such as microvascular disease, diabetes, or hypertension. All subjects were taking cART, which is known to affect brain metabolite concentrations.<sup>53</sup> Although 3D T1WIs were recorded, no volumetric analysis has been performed to date in these subjects because of intensity and contrast variations due to transmit B<sub>1</sub> inhomogeneity. However, we do not expect morphometric differences to significantly affect results because metabolite ratios (relative to Cr) are relatively insensitive to voxel composition (particularly CSF contamination). Finally, no significant changes were observed in the hippocampus in this study, despite the well-known importance of this structure for memory and other age-related cognitive dysfunction.<sup>40,54,55</sup> Lack of significant findings may be in part due to the generally lower spectral quality obtained in this region due to magnetic susceptibility effects from bone/air/tissue interfaces proximal to the anterior temporal lobe, as well as partial volume with surrounding tissue due to the small size of the hippocampus. Spectral quality was also lower in the basal ganglia because of the high iron content of the globus pallidus and putamen, which is known to increase line widths in MR spectra from this region<sup>56-58</sup>; this may have also contributed to the lack of significant group differences or neurocognitive correlations detectable in this region.

## CONCLUSIONS

In the older subject population with HIV infection, 7T MR spectroscopy measurements of NAA and Glu may be useful indicators of neuroaxonal loss or dysfunction and correlate with neuropsychological performance. Therefore, 7T MR spectroscopy may be a useful adjunct technique for monitoring disease progression or

response to therapy in future treatment trials. Other future studies are needed to track longitudinal changes with time, as well as comparisons with HIV-negative control subjects to determine whether cognitive decline and brain metabolite changes occur at a greater rate in HIV+ subjects and whether there are specific metabolic changes only associated with HIV infection in the older population.

Disclosures: Mona Mohamed—RELATED: Grant: National Institutes of Health, Comments: work supported by the National Institutes of Health grant NS081196\*. Peter B. Barker—RELATED: Grant: National Institutes of Health\*. Richard L. Skolasky—RELATED: Grant: National Institutes of Health\*; UNRELATED: Board Membership: North American Spine Society, Comments: member of the Board of Directors; Grants/Grants Pending: National Institutes of Health, Patient Centered Outcomes Research Institute (PCORI); OTHER RELATIONSHIPS: Associate Editor, *Quality of Life Research*. Ned Sacktor—RELATED: Grant: National Institutes of Health, Comments: work supported by the National Institutes of Health grant NS081196\*. \*Money paid to the institution.

## REFERENCES

- Gandhi NS, Skolasky RL, Peters KB, et al. **A comparison of performance-based measures of function in HIV-associated neurocognitive disorders.** *J Neurovirol* 2011;17:159–65 CrossRef Medline
- Kakinami L, de Bruyn G, Pronyk P, et al. **The impact of highly active antiretroviral therapy on activities of daily living in HIV-infected adults in South Africa.** *AIDS Behav* 2011;15:823–31 CrossRef Medline
- Schifitto G, Kiebertz K, McDermott MP, et al. **Clinical trials in HIV-associated cognitive impairment: cognitive and functional outcomes.** *Neurology* 2001;56:415–18 CrossRef Medline
- Vivithanaporn P, Heo G, Gamble J, et al. **Neurologic disease burden in treated HIV/AIDS predicts survival: a population-based study.** *Neurology* 2010;75:1150–58 CrossRef Medline
- Sailasuta N, Ross W, Ananworanich J, et al; RV254/SEARCH 010 protocol teams. **Change in brain magnetic resonance spectroscopy after treatment during acute HIV infection.** *PLoS One* 2012;7:e49272 CrossRef Medline
- Lentz MR, Degaonkar M, Mohamed MA, et al. **Exploring the relationship of macrophage colony-stimulating factor levels on neuroaxonal metabolism and cognition during chronic human immunodeficiency virus infection.** *J Neurovirol* 2010;16:368–76 CrossRef Medline
- Letendre S, Marquie-Beck J, Capparelli E, et al; CHARTER Group. **Validation of the CNS Penetration-Effectiveness rank for quantifying antiretroviral penetration into the central nervous system.** *Arch Neurol* 2008;65:65–70 CrossRef Medline
- Clifford DB. **HIV-associated neurocognitive disorder.** *Curr Opin Infect Dis* 2017;30:117–22 CrossRef Medline
- Tozzi V, Balestra P, Bellagamba R, et al. **Persistence of neuropsychologic deficits despite long-term highly active antiretroviral therapy in patients with HIV-related neurocognitive impairment: prevalence and risk factors.** *J Acquir Immune Defic Syndr* 2007;45:174–82 CrossRef Medline
- Harezlak J, Buchthal S, Taylor M, et al; HIV Neuroimaging Consortium. **Persistence of HIV-associated cognitive impairment, inflammation, and neuronal injury in era of highly active antiretroviral treatment.** *AIDS* 2011;25:625–33 CrossRef Medline
- Neuenburg JK, Brodt HR, Herndier BG, et al. **HIV-related neuropathology, 1985 to 1999: rising prevalence of HIV encephalopathy in the era of highly active antiretroviral therapy.** *J Acquir Immune Defic Syndr* 2002;31:171–77 CrossRef Medline
- Valcour V, Paul R, Neuhaus J, et al. **The effects of age and HIV on neuropsychological performance.** *J Int Neuropsychol Soc* 2011;17:190–95 CrossRef Medline
- Valcour V, Shikuma C, Shiramizu B, et al. **Higher frequency of dementia in older HIV-1 individuals: the Hawaii Aging with HIV-1 Cohort.** *Neurology* 2004;63:822–27 CrossRef Medline
- Van Zijl PC, Barker PB. **Magnetic resonance spectroscopy and spectroscopic imaging for the study of brain metabolism.** *Ann NY Acad Sci* 1997;820:75–96 CrossRef Medline
- Chong WK, Sweeney B, Wilkinson ID, et al. **Proton spectroscopy of the brain in HIV infection: correlation with clinical, immunologic, and MR imaging findings.** *Radiology* 1993;188:119–24 CrossRef Medline
- Chang L, Ernst T, Leonido-Yee M, et al. **Highly active antiretroviral therapy reverses brain metabolite abnormalities in mild HIV dementia.** *Neurology* 1999;53:782–89 CrossRef Medline
- Ernst T, Jiang CS, Nakama H, et al. **Lower brain glutamate is associated with cognitive deficits in HIV patients: a new mechanism for HIV-associated neurocognitive disorder.** *J Magn Reson Imaging* 2010;32:1045–53 CrossRef Medline
- Mohamed MA, Barker PB, Skolasky RL, et al. **Brain metabolism and cognitive impairment in HIV infection: a 3-T magnetic resonance spectroscopy study.** *Magn Reson Imaging* 2010;28:1251–57 CrossRef Medline
- Sailasuta N, Shriner K, Ross B. **Evidence of reduced glutamate in the frontal lobe of HIV-seropositive patients.** *NMR Biomed* 2009;22:326–31 CrossRef Medline
- Menon DK, Ainsworth JG, Cox IJ, et al. **Proton MR spectroscopy of the brain in AIDS dementia complex.** *J Comput Assist Tomogr* 1992;16:538–42 CrossRef Medline
- Meyerhoff DJ, MacKay S, Poole N, et al. **N-acetylaspartate reductions measured by 1H MRSI in cognitively impaired HIV-seropositive individuals.** *Magn Reson Imaging* 1994;12:653–59 CrossRef Medline
- Barker PB, Lee RR, McArthur JC. **AIDS dementia complex: evaluation with proton MR spectroscopic imaging.** *Radiology* 1995;195:58–64 CrossRef Medline
- Laubenberger J, Häussinger D, Bayer S, et al. **HIV-related metabolic abnormalities in the brain: depiction with proton MR spectroscopy with short echo times.** *Radiology* 1996;199:805–10 CrossRef Medline
- Navia BA, Rostasy K. **The AIDS dementia complex: clinical and basic neuroscience with implications for novel molecular therapies.** *Neurotox Res* 2005;8:3–24 CrossRef Medline
- Paul RH, Yiannoutsos CT, Miller EN, et al. **Proton MRS and neuropsychological correlates in AIDS dementia complex: evidence of subcortical specificity.** *J Neuropsychiatry Clin Neurosci* 2007;19:283–92 CrossRef Medline
- Barker PB, Hearshen DO, Boska MD. **Single-voxel proton MRS of the human brain at 1.5T and 3.0T.** *Magn Reson Med* 2001;45:765–69 CrossRef Medline
- Chang L, Ernst T, St Hillaire C, et al. **Antiretroviral treatment alters relationship between MCP-1 and neurometabolites in HIV patients.** *Antivir Ther* 2004;9:431–40 Medline
- Young AC, Yiannoutsos CT, Hegde M, et al. **Cerebral metabolite changes prior to and after antiretroviral therapy in primary HIV infection.** *Neurology* 2014;83:1592–600 CrossRef Medline
- Tkác I, Oz G, Adriani G, et al. **In vivo 1H NMR spectroscopy of the human brain at high magnetic fields: metabolite quantification at 4T vs. 7T.** *Magn Reson Med* 2009;62:868–79 CrossRef Medline
- Stephenson MC, Gunner F, Napolitano A, et al. **Applications of multi-nuclear magnetic resonance spectroscopy at 7T.** *World J Radiol* 2011;3:105–13 CrossRef Medline
- Antinori A, Arendt G, Becker JT, et al. **Updated research nosology for HIV-associated neurocognitive disorders.** *Neurology* 2007;69:1789–99 CrossRef Medline
- Radloff LS. **The use of the Center for Epidemiologic Studies Depression Scale in adolescents and young adults.** *J Youth Adolesc* 1991;20:149–66 CrossRef Medline
- Giebel CM, Challis D, Montaldi D. **The newly revised interview for deteriorations in daily living activities in dementia (R-IDDD2): distinguishing initiative from performance at assessment.** *Int Psychogeriatr* 2017;29:497–507 CrossRef Medline
- Kaur N, Belchior P, Gelinis I, et al. **Critical appraisal of questionnaires to assess functional impairment in individuals with mild**

- cognitive impairment. *Int Psychogeriatr* 2016;28:1425–39 CrossRef Medline
35. Fantoni M, Izzi I, Del Borgo C, et al. **Inter-rater reliability of a modified Karnofsky Scale of Performance Status for HIV-infected individuals.** *AIDS Patient Care STDS* 1999;13:23–28 CrossRef Medline
  36. Gaines JJ, Shapiro A, Alt M, et al. **Semantic clustering indexes for the Hopkins Verbal Learning Test-Revised: initial exploration in elder control and dementia groups.** *Appl Neuropsychol* 2006;13:213–22 CrossRef Medline
  37. Shapiro AM, Benedict RH, Schretlen D, et al. **Construct and concurrent validity of the Hopkins Verbal Learning Test-revised.** *Clin Neuropsychol* 1999;13:348–58 CrossRef Medline
  38. Woods SP, Scott JC, Conover E, et al; HIV Neurobehavioral Research Center Group. **Test-retest reliability of component process variables within the Hopkins Verbal Learning Test-Revised.** *Assessment* 2005;12:96–100 CrossRef Medline
  39. Chang L, Lee PL, Yiannoutsos CT, et al; HIV MRS Consortium. **A multicenter in vivo proton-MRS study of HIV-associated dementia and its relationship to age.** *Neuroimage* 2004;23:1336–47 CrossRef Medline
  40. Fjell AM, McEvoy L, Holland D, et al; Alzheimer's Disease Neuroimaging Initiative. **What is normal in normal aging? Effects of aging, amyloid and Alzheimer's disease on the cerebral cortex and the hippocampus.** *Prog Neurobiol* 2014;117:20–40 CrossRef Medline
  41. Driscoll I, Troncoso JC, Rudow G, et al. **Correspondence between in vivo (11)C-PiB-PET amyloid imaging and postmortem, region-matched assessment of plaques.** *Acta Neuropathol* 2012;124:823–31 CrossRef Medline
  42. Öz G, Tkáč I. **Short-echo, single-shot, full-intensity 1H MRS for neurochemical profiling at 4T: validation in the cerebellum and brainstem.** *Magn Reson Med* 2011;65:901–10 CrossRef Medline
  43. Pradhan S, Bonekamp S, Gillen JS, et al. **Comparison of single voxel brain MRS at 3T and 7T using 32-channel head coils.** *Magn Reson Imaging* 2015;33:1013–18 CrossRef Medline
  44. Provencher SW. **Estimation of metabolite concentrations from localized in vivo proton NMR spectra.** *Magn Reson Med* 1993;30:672–79 CrossRef Medline
  45. Wilkinson ID, Miller RF, Miszkil KA, et al. **Cerebral proton magnetic resonance spectroscopy in asymptomatic HIV infection.** *AIDS* 1997;11:289–95 CrossRef Medline
  46. Lentz MR, Kim WK, Kim H, et al. **Alterations in brain metabolism during the first year of HIV infection.** *J Neurovirol* 2011;17:220–29 CrossRef Medline
  47. McArthur JC, Steiner J, Sacktor N, et al. **Human immunodeficiency virus-associated neurocognitive disorders: mind the gap.** *Ann Neurol* 2010;67:699–714 CrossRef Medline
  48. Cloak CC, Chang L, Ernst T. **Increased frontal white matter diffusion is associated with glial metabolites and psychomotor slowing in HIV.** *J Neuroimmunol* 2004;157:147–52 CrossRef Medline
  49. Mohamed MA, Lentz MR, Lee V, et al. **Factor analysis of proton MR spectroscopic imaging data in HIV infection: metabolite-derived factors help identify infection and dementia.** *Radiology* 2010;254:577–86 CrossRef Medline
  50. Chang L, Ernst T, Witt MD, et al. **Relationships among brain metabolites, cognitive function, and viral loads in antiretroviral-naive HIV patients.** *Neuroimage* 2002;17:1638–48 CrossRef Medline
  51. Wijtenburg SA, Rowland LM, Edden RA, et al. **Reproducibility of brain spectroscopy at 7T using conventional localization and spectral editing techniques.** *J Magn Reson Imaging* 2013;38:460–67 CrossRef Medline
  52. Mekle R, Mlynárik V, Gambarota G, et al. **MR spectroscopy of the human brain with enhanced signal intensity at ultrashort echo times on a clinical platform at 3T and 7T.** *Magn Reson Med* 2009;61:1279–85 CrossRef Medline
  53. Sailasuta N, Ananworanich J, Lerdlum S, et al; SEARCH 011 Study Group. **Neuronal-glia markers by magnetic resonance spectroscopy in HIV before and after combination antiretroviral therapy.** *J Acquir Immune Defic Syndr* 2016;71:24–30 CrossRef Medline
  54. Castellano JF, Fletcher BR, Kelley-Bell B, et al. **Age-related memory impairment is associated with disrupted multivariate epigenetic coordination in the hippocampus.** *PLoS One* 2012;7:e33249 CrossRef Medline
  55. Castellano JF, Fletcher BR, Patzke H, et al. **Reassessing the effects of histone deacetylase inhibitors on hippocampal memory and cognitive aging.** *Hippocampus* 2014;24:1006–16 CrossRef Medline
  56. Daugherty A, Raz N. **Age-related differences in iron content of subcortical nuclei observed in vivo: a meta-analysis.** *Neuroimage* 2013;70:113–21 CrossRef Medline
  57. Haacke EM, Miao Y, Liu M, et al. **Correlation of putative iron content as represented by changes in R2\* and phase with age in deep gray matter of healthy adults.** *J Magn Reson Imaging* 2010;32:561–76 CrossRef Medline
  58. Persson N, Wu J, Zhang Q, et al. **Age and sex related differences in subcortical brain iron concentrations among healthy adults.** *Neuroimage* 2015;122:385–98 CrossRef Medline

# Quantification of Intracranial Aneurysm Volume Pulsation with 7T MRI

R. Kleinloog, J.J.M. Zwanenburg, B. Schermer, E. Krikken, Y.M. Ruigrok, P.R. Luijten, F. Visser, L. Regli, G.J.E. Rinkel, and B.H. Verweij



## ABSTRACT

**BACKGROUND AND PURPOSE:** Aneurysm volume pulsation is a potential predictor of intracranial aneurysm rupture. We evaluated whether 7T MR imaging can quantify aneurysm volume pulsation.

**MATERIALS AND METHODS:** In Stage I of the study, 10 unruptured aneurysms in 9 patients were studied using a high-resolution (0.6-mm, isotropic) 3D gradient-echo sequence with cardiac gating. Semiautomatic segmentation was used to measure aneurysm volume (in cubic millimeters) per cardiac phase. Aneurysm pulsation was defined as the relative increase in volume between the phase with the smallest volume and the phase with the largest volume. The accuracy and precision of the measured volume pulsations were addressed by digital phantom simulations and a repeat image analysis. In Stage II, the imaging protocol was optimized and 9 patients with 9 aneurysms were studied with and without administration of a contrast agent.

**RESULTS:** The mean aneurysm pulsation in Stage I was  $8\% \pm 7\%$  (range, 2%–27%), with a mean volume change of  $15 \pm 14 \text{ mm}^3$  (range, 3–51  $\text{mm}^3$ ). The mean difference in volume change for the repeat image analysis was  $2 \pm 6 \text{ mm}^3$ . The artifactual volume pulsations measured with the digital phantom simulations were of the same magnitude as the volume pulsations observed in the patient data, even after protocol optimization in Stage II.

**CONCLUSIONS:** Volume pulsation quantification with the current imaging protocol on 7T MR imaging is not accurate due to multiple imaging artifacts. Future studies should always include aneurysm-specific accuracy analysis.

**ABBREVIATIONS:** CNR = contrast-to-noise-ratio; TFE = turbo field echo

Intracranial aneurysms occur in approximately 3% of the population.<sup>1</sup> Rupture of an aneurysm results in aneurysmal sub-

arachnoid hemorrhage, which often occurs at a younger age and has a high case fatality and morbidity.<sup>2</sup> Current standard treatment consists of neurosurgical clipping or endovascular coiling and can prevent rupture but carries a 4%–8% risk of major complications, including death, depending on the age of the patient and the size and site of the aneurysm.<sup>3,4</sup> Preventive treatment should therefore ideally be restricted to those patients who have a high risk of rupture. However, prediction of the risk of rupture of intracranial aneurysms is poor. Therefore, better predictors of rupture are needed. Volume pulsation, the change in volume during the cardiac cycle, is a potential predictor of rupture.<sup>5</sup> Imaging techniques used thus far in attempts to visualize volume pulsation, such as 1.5T phase-contrast MR angiography, transcranial Doppler sonography, 3D rotational angiography, and 4D CTA, have various limitations, including limited signal-to-noise ratio,

Received May 26, 2017; accepted after revision November 30.

From the Department of Neurology and Neurosurgery (R.K., B.S., E.K., Y.M.R., L.R., G.J.E.R., B.H.V.), Brain Center Rudolf Magnus, and Department of Radiology (J.J.M.Z., P.R.L., F.V.), Utrecht University, University Medical Center Utrecht, Utrecht, the Netherlands; Department of Technical Medicine (B.S., E.K.), Faculty of Science and Technology, University of Twente, Enschede, the Netherlands; Philips Healthcare (F.V.), Best, the Netherlands; and Department of Neurosurgery (L.R.), University Hospital Zurich, Zurich, Switzerland.

R. Kleinloog was supported by a Focus en massa cardiovascular research grant by the Utrecht University, the Netherlands. Y.M. Ruigrok was supported by a clinical fellowship grant from the Netherlands Organization for Scientific Research (Project No. 40-00703-98-13533). J.J.M. Zwanenburg was supported by the European Research Council under the European Union's Seventh Framework Programme (FP7/2007-2013)/European Research Council grant agreement No. 337333.

This article has not been submitted or published elsewhere in whole or in part, except as an abstract (poster at European Stroke Conference, May 28–31, 2013; London, United Kingdom; Vasospasm, July 10–12, 2013; Lucerne, Switzerland; and Joint Annual Meeting of the International Society for Magnetic Resonance in Medicine–European Society for Magnetic Resonance in Medicine and Biology, Milan, Italy; May 10–16, 2014).

Please address correspondence to Rachel Kleinloog, MD, Brain Center Rudolf Magnus, Department of Neurology and Neurosurgery, Room G.03.232, Utrecht University, University Medical Center Utrecht, Heidelberglaan 100, 3584 CX Utrecht, the Netherlands; e-mail: rachelkleinloog@gmail.com

Indicates open access to non-subscribers at [www.ajnr.org](http://www.ajnr.org)

Indicates article with supplemental on-line tables and appendix.

Indicates article with supplemental on-line photos.

Indicates article with supplemental on-line video.

<http://dx.doi.org/10.3174/ajnr.A5546>

limited spatial resolution compared with the aneurysm volume, and/or the use of a radiation dose and/or the risk of complications.<sup>5</sup> Furthermore, a test of the accuracy and precision of the volume pulsation measurement was either lacking or studies refrained from giving an error value that could be used to interpret the pulsation results for each aneurysm. Therefore, aneurysm volume pulsation is currently not used as a predictor of rupture in clinical practice.

In this experimental study, we evaluated whether volume pulsation could be quantified on images obtained with 7T MR imaging and tested the accuracy and precision of the method.

## MATERIALS AND METHODS

Our study consisted of 2 stages. In the first stage, we tested the concept of quantification of aneurysm pulsation on images obtained with 7T MR imaging, and we tested the accuracy and repeatability of the imaging-analysis method. In the second stage, we implemented the lessons learned in Stage I to optimize the imaging protocol and accuracy of the quantification of aneurysm pulsation.

### Study Population

Patients diagnosed with saccular intradural unruptured intracranial aneurysms who were either scheduled for treatment of their aneurysm or were in follow-up for growth of their aneurysm were recruited through our outpatient clinic of the Department of Neurology and Neurosurgery of the University Medical Center Utrecht, the Netherlands, between July 2011 and December 2012 as part of an existing study focusing on imaging of the aneurysm wall (Stage I).<sup>6</sup> In Stage II, additional patients were recruited for the current study between February and April 2014. The diagnosis of the aneurysm was made either on CTA or 1.5T or 3T MRA, and the aneurysms were either incidental findings (the imaging study was for other indications), found during screening because of a positive family history of intracranial aneurysm, or symptomatic aneurysms (eg, leading to a seizure or thromboembolic event). Patients with contraindications for 7T MR imaging (eg, claustrophobia, metal objects such as dental implants or prostheses in or on the body) were excluded, as well as patients with aneurysms associated with vascular malformations other than aneurysms (eg, arteriovenous malformations). In the second stage, patients with renal insufficiency and allergy to gadolinium-based contrast agent were also excluded. This study was approved by the institutional review board of our center, and all participants gave written informed consent following guidelines equivalent to the National Institutes of Health guidelines.

### 7T MR Imaging

Imaging was performed on a 7T MR imaging scanner (Achieva; Philips Healthcare, Best, the Netherlands) with a volume transmit coil and a 32-channel receive head coil (2TX/32RX; Nova Medical, Wilmington, Massachusetts). In the first stage, the volume pulsation of the aneurysm was studied by adding a 3D turbo field echo (TFE) sequence to an existing study focusing on imaging of the aneurysm wall.<sup>6</sup> This protocol included a low-resolution T1-weighted survey sequence and a TOF sequence covering the intracranial vessels from the level of the circle of Willis and upward,

taking into account the location of the aneurysm.<sup>6</sup> It also included a previously described time-resolved 3D phase-contrast MR imaging sequence.<sup>7</sup> The following parameters were used in the 3D TFE sequence: TR/TE = 8.2/4.4 ms, flip angle = 6°, FOV = 180 × 180 × 9.6 mm, acquired spatial resolution = 0.6 × 0.6 × 0.6 mm, sensitivity encoding acceleration factor = 2.0 (right-left), and acquired temporal resolution = 90 ms interpolated to 15 cardiac phases. The sequence was synchronized to the heart with a peripheral pulse unit and retrospective cardiac gating. The scan duration was approximately 4 minutes. The TFE sequence was oriented in either a coronal or transverse orientation, depending on the location of the aneurysm in the circle of Willis and its orientation, and carefully positioned over the aneurysm as observed on a TOF and/or low-resolution T1-weighted survey. In both the TOF and the TFE sequences, flow-compensated gradients were used to prevent signal drop-out from fast-flowing blood.

With the results of Stage I, the imaging protocol was optimized. An optimized version of the TFE sequence was developed and used in the additionally recruited patients in Stage II. We increased the FOV, thereby increasing the signal-to-noise ratio and improving coverage; we shortened the TE to 2.0 ms to decrease the influence of the flow-displacement artifacts; and we used a 20° flip angle to increase the contrast-to-noise ratio (CNR) between flowing blood and static tissue. Furthermore, we performed this improved TFE sequence after administration of gadobutrol, a gadolinium-based contrast agent, to further increase the CNR and decrease the influence of intensity fluctuations due to inflow effects.

### Image Analysis

**Volume Pulsation Quantification.** Image analysis was performed with Analyze 11.0 software (AnalyzeDirect, Overland Park, Kansas), designed to automatically segment and calculate volumes. For the cardiac phases of each slice (15 phases in the first stage of the study, 18 in the second stage), the same ROI containing the aneurysm was chosen on the TFE images, using the TOF or T1-weighted survey image as a 3D reference to correctly separate the aneurysm from the parent artery. Vessel segmentation (including the aneurysm) was performed by setting a signal intensity threshold. The threshold was defined by R.K. by visual inspection of the aneurysm and its surroundings and after comparing the TFE images with the anatomy of the aneurysm on the TOF and/or low-resolution T1-weighted survey. The threshold was adjusted until the aneurysm was distinguishable from the background and at the same time had the same appearance as on the anatomic scan. The threshold was set for each aneurysm separately but was fixed for all slices and cardiac phases of each aneurysm. Thereafter, the remaining parent vessel was manually deselected (by R.K.) on each slice of the first phase of the cardiac cycle; then this deselected area was copied to the 14 (or 17 in Stage II) consecutive phases of the cardiac cycle and removed. Flow artifacts in the lumen of the aneurysm were misrecognized by the software and consequently manually included in the selection, keeping the borders of the aneurysm as selected by the software intact. Voxels selected outside the aneurysm borders due to background noise were also removed from the selection. The manual corrections were done slice by slice. If the signal in the last slice containing the aneurysm

was of low intensity due to partial volume effects, it was sometimes difficult to distinguish noise pixels from aneurysm voxels. Consequently, such a slice was excluded in all phases to limit the effect of noise on the selection. For each phase of the cardiac cycle, the total volume of the aneurysm was calculated by adding up the aneurysm volumes of all slices (segmented area  $\times$  slice thickness). Absolute volume pulsation was defined as the change in volume (in cubic millimeters) between the phase of the cardiac cycle with the smallest volume and the phase with the largest volume. Relative volume pulsation was calculated with the following formula:  $[(\text{Maximum Volume} - \text{Minimum Volume})/\text{Minimum Volume}] \times 100$ .

The size (largest diameter) of the aneurysms was measured on TOF angiography in the first stage. In the second stage, it was measured on the improved TFE. Partially thrombosed aneurysms were excluded from the image analysis.

**Repeatability of the Volume Pulsation Quantification (Stage I).** By repeating the volume measurements for the phases with the smallest and largest volumes for each aneurysm, we determined the precision of the pulsation analysis. The repeat analysis was performed by the same observer but blinded for the initial analysis with a 3-month interval between the 2 analyses. We evaluated the repeatability of the image analysis using the Bland-Altman method: The mean and SD of the difference between the results of the initial analysis and the results of the repeat analysis were calculated.<sup>8</sup> A *t* distribution with a significance level of .05 and 9 *df* (10 measured aneurysms) was used to approximate the distribution of the 95% CI. In addition, the Pearson correlation coefficient between the initial analysis and the repeat analysis was calculated. The repeatability analysis was performed only in Stage I of this study.

**Accuracy of the Volume Pulsation Quantification (Stage I).** The accuracy of the volume pulsation analysis is expected to depend on 4 different factors: the CNR (between blood and surroundings) of the images, signal intensity fluctuations in the gated TFE sequence due to inflow effects, aneurysm size, and blood flow artifacts.

#### **CNR, Signal Intensity Fluctuations, and Aneurysm Size**

To estimate the influence of CNR, signal intensity fluctuations, and aneurysm size on the calculated volume pulsations, we performed digital phantom simulations in which the 3 factors that are thought to influence the accuracy were varied. See the On-line Appendix for further details. In these simulations, the CNR was defined as

$$\text{CNR} = \frac{\text{Contrast}}{\text{Noise}} = \frac{\mu_s - \mu_{bg}}{\sigma_s},$$

with  $\mu_s$  as the mean pixel value in the phantom region, and  $\mu_{bg}$  as the mean pixel value in a background region, both averaged across the time phases in the cardiac cycle (15 in the first stage of the study and 18 in the second stage).  $\sigma_s$  is the mean of the time phase SD of each pixel in the signal phantom region. In the first digital phantom experiment, the dependence of the inaccuracy of the volume pulsation analysis of both CNR and signal fluctuations was studied. Second, the interaction of aneurysm volume with the

CNR and signal fluctuations was studied by static digital phantom simulations. Third, aneurysm-specific inaccuracy in the pulsation analysis was measured for each aneurysm in the patient study by making a pulsating digital phantom with the same volume, CNR, intensity fluctuation, and volume pulsation. The difference in the volume pulsation measured in the digital phantoms and the volume pulsation measured in the patient scans (and used as input for the phantom volume pulsation) was called the “absolute observed artifactual pulsation.”

#### **Flow-Displacement Artifacts**

In image acquisition, the timing difference between the moment of phase-encoding (right after excitation) and the moment of frequency-encoding (approximately at  $t = \text{TE}$ ) will lead to the flow-displacement artifacts.<sup>9</sup> We assessed the potential influence of these artifacts by combining the TFE images from Stage I with images containing blood flow velocity data (obtained with the time-resolved 3D phase-contrast MR imaging sequence, only available in Stage I; see the On-line Appendix for further details).

**Imaging Protocol Optimization (Stage II).** Volume pulsation quantification on images obtained with the improved TFE was analyzed with the same analysis tool used in Stage I. As in Stage I, the accuracy of the volume pulsation analysis method was addressed in the pulsating phantoms. For both the improved TFE and the gadolinium-enhanced improved TFE patient data, pulsating phantoms were made to estimate the (aneurysm-specific) inaccuracy in the pulsation. The volume pulsation measurement in the phantom was compared with the given volume pulsation. This difference yielded the absolute observed artifactual pulsation.

## **RESULTS**

An overview of the results of Stages I and II are given in the Table.

### **Stage I: Volume Pulsation Quantification, Repeatability, and Accuracy of the Analysis**

In Stage I, the mean aneurysm volume change was  $15 \pm 14 \text{ mm}^3$  (range, 3–51  $\text{mm}^3$ ), and the mean volume pulsation was  $8\% \pm 7\%$  (range, 2%–27%). The mean time between the minimum and maximum volume was 7 phases (range, 2–12 phases). The timing of the minimum and maximum volumes within the cardiac cycle was inconsistent among different patients, with the minimum volume followed by the maximum volume in some patients, while the maximum was followed by the minimum volume in others (On-line Table 1). Fig 1 shows the 15 images obtained during the cardiac cycle of 1 cross-section of an aneurysm, and this pulsating aneurysm is provided as an On-line Video. The repeatability analysis yielded a correlation coefficient of 0.95 (Fig 2). The mean of the difference between the results of the initial pulsation analysis and the results of the repeat pulsation analysis was  $2 \pm 6 \text{ mm}^3$  (95% CI, –12–15; Fig 2).

The absolute observed pulsation in a static digital phantom (used as a measure of the inaccuracy of the analysis) was found to increase quickly below a CNR of approximately 6 and increased with increasing signal intensity fluctuations (see the On-line Ap-

### Overview of the 3 different sequences used to image volume pulsation and the main results

Sequence	Stage I TFE	Stage II	
		Improved TFE	CE-Improved TFE
No. of phases in the cardiac cycle	15	18	18
No. of patients included	9	9	8 <sup>a</sup>
No. of aneurysms included	10	9	8 <sup>a</sup>
Mean size of the aneurysms (SD, range) (mm)	9 (4, 3–19)	8 (4, 2–14)	8 (4, 2–14)
Mean aneurysm volume change (SD, range) (mm <sup>3</sup> )	15 (14, 3–51)	38 (31, 2–88)	14 (9, 1–25)
Mean volume pulsation (SD, range) (%)	8 (7, 2–27)	39 (24, 14–73)	15 (11, 4–36)
Mean absolute observed artifactual pulsation (SD, range) (mm <sup>3</sup> )	2 (2, 0–5)	–	13 (9, 1–27)

Note:—CE indicates contrast-enhanced.

<sup>a</sup> In 1 patient, the image acquisition of the contrast-enhanced-improved TFE failed.

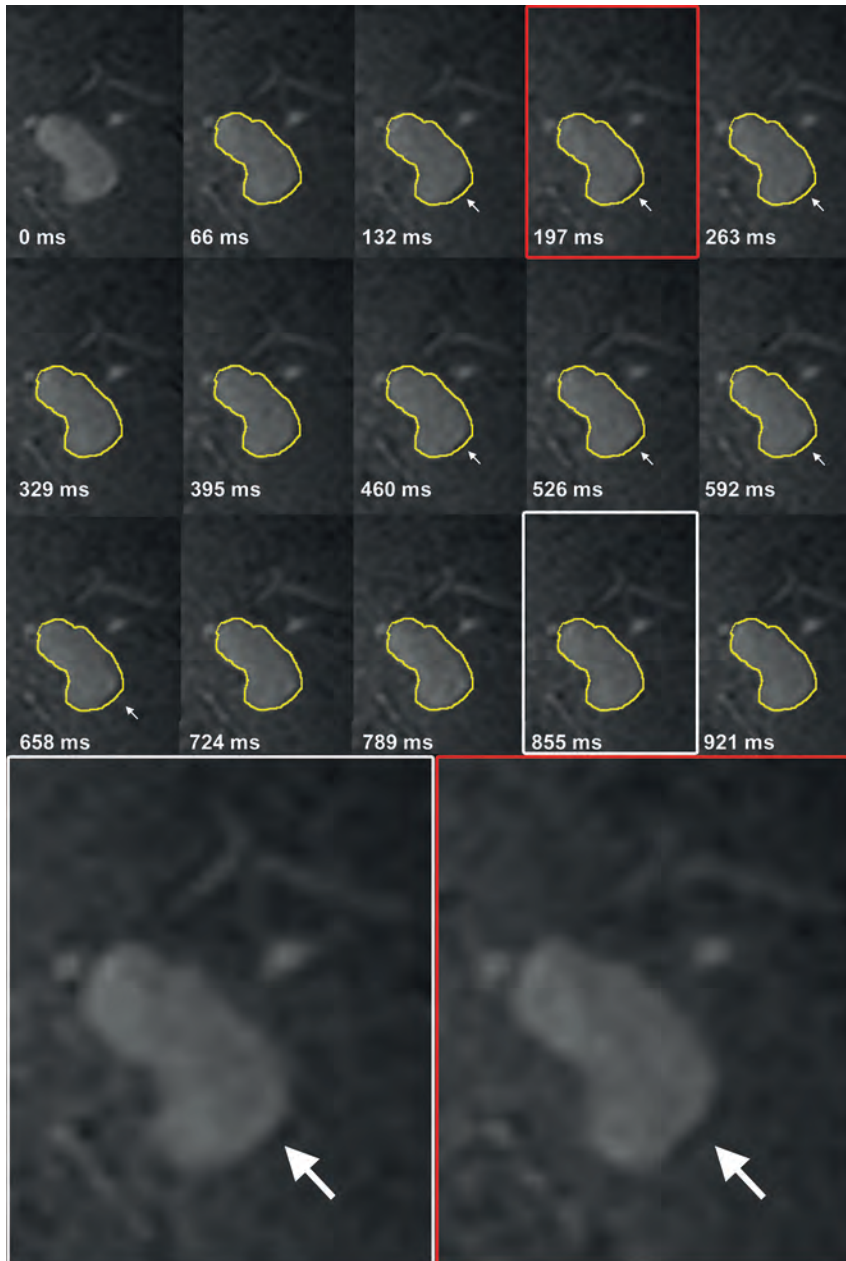


**FIG 1.** Coronal cross-section of a left middle cerebral artery aneurysm for each of the 15 phases of the cardiac cycle (heart rate, 60 beats per minute). The contour of the aneurysm at 0 ms is shown in yellow on all other time points. The white arrows indicate the area of pulsation in this cross-section. Magnification of 2 phases shows the deformation of the aneurysm at 1 side of the dome.

pendix for further details and figures). The mean CNR of aneurysms in the patient study was 5 (range, 1–8), while the mean intensity fluctuation was  $3\% \pm 1.6\%$ . Both the effects of the CNR and intensity fluctuations were size-dependent, with increasing relative inaccuracy with decreasing phantom volumes. The mean absolute observed artifactual pulsation in the pulsating digital phantoms (used as a measure for the inaccuracy of the analysis) was  $2.0 \pm 1.6 \text{ mm}^3$  (range, 0.2–5.4 mm<sup>3</sup>; On-line Tables 1 and 2). The potential pulsation observed as a result of the flow displacement artifacts depended considerably on the orientation of the acquisition. The worst case artifactual pulsation was equal to or higher than the actual pulsation measured in 4 of the 6 available patient datasets (On-line Table 3). The minimum artifactual volume pulsation was around 25% of the volume pulsation measured in the patient scans.

#### Stage II: Results after Imaging Protocol Optimization

The mean aneurysm volume change on the improved TFE was  $38 \pm 31 \text{ mm}^3$  (range, 2–88 mm<sup>3</sup>), and the mean volume pulsation was  $39\% \pm 24\%$  (range, 14%–73%). The mean aneurysm volume change on the contrast-enhanced improved TFE was  $14 \pm 9 \text{ mm}^3$  (range, 1–25 mm<sup>3</sup>), and the mean volume pulsation was  $15\% \pm 11\%$  (range, 4%–36%). The mean time between the minimum and the maximum volume was 8 phases (range, 3–14 phases) in the improved TFE and 7 phases (range, 3–13 phases) in the contrast-enhanced TFE. As in Stage I, the timing of the minimum and maximum volumes within the cardiac cycle differed among patients (On-line Table 4). The mean CNR was  $23 \pm 7$

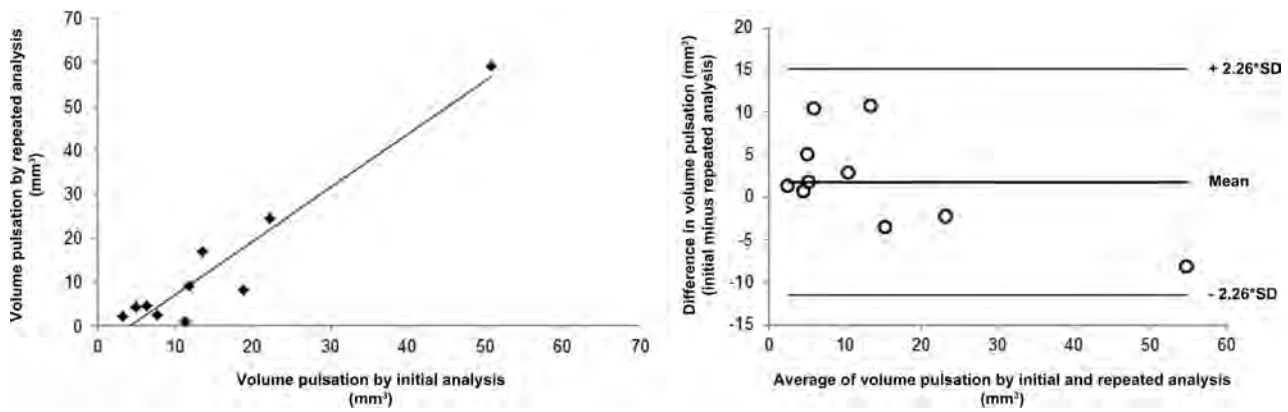


**FIG 2.** Repeatability of the image analysis method. *Left:* scatterplot showing the correlation between the measured volume pulsation obtained with the repeat image analysis versus the results from the initial analysis. *Right:* Bland-Altman plot of the same data.

in the improved TFE and  $28 \pm 8$  in the gadolinium-enhanced improved TFE, while the mean intensity fluctuation was  $23\% \pm 7\%$  in the improved TFE and  $15\% \pm 6\%$  in the gadolinium-enhanced improved TFE. The mean absolute observed artifactual pulsation in the pulsating digital phantoms (used as a measure of the inaccuracy of the analysis) was  $13 \pm 9 \text{ mm}^3$  (range, 1–27  $\text{mm}^3$ ; On-line Tables 4 and 5).

## DISCUSSION

This study shows that quantification of volume pulsation of unruptured intracranial aneurysms is currently not feasible using a semiautomatic segmentation method, even on high-resolution 7T MR images. The accuracy of the quantification of volume pulsation is influenced by the CNR, intensity fluctuations, aneurysm size, and, most important, the flow-displacement artifacts. Our study shows that the artifactual volume pulsation due to these influences is of the same magnitude as the volume pulsations observed in the patient data, even after optimization of the imaging sequences and adding contrast agent.

Three previous studies quantified pulsation in unruptured aneurysms using an electrocardiography-gated CTA.<sup>10–12</sup> Two of these studies found a volume pulsation in the range of 3%–18% with a mean of  $8\% \pm 5\%$ ,<sup>10</sup> and in the range of 1%–15% with a mean of  $5\% \pm 4\%$ ,<sup>11</sup> which compares well with our findings. The third study did not report volume pulsations but focused on the feasibility of imaging pulsation by comparing the aneurysm volume curves and random curves with the arterial pulse wave (as a measure for “true” pulsation) and found that the aneurysm volume curves showed higher similarity to the pulse wave than the random curves but only in a subset of the aneurysms under study.<sup>12</sup>

Accuracy and precision analyses were performed in all CTA studies. The first study found a mean of 8% volume pulsation in aneurysms, which was considered substantial in comparison with a 2% volume change found in bone tissue.<sup>10</sup> In the second study, a large, static phantom (a syringe filled with saline) was imaged to study the artificial volume pulsation, and it was concluded that its volume change of  $<0.248\%$  was an insignificant artifact.<sup>11</sup> However, in the current study, we showed that inaccuracy increases with decreasing phantom size; therefore, their accuracy analysis

might underestimate the artifactual pulsation because the phantom used was much larger than the aneurysms studied. The second study measured an interobserver discrepancy in the repeat measurement of 5 aneurysms of  $11.9 \pm 17.6 \text{ mm}^3$ , which was considered acceptable, given a mean expansion volume of all aneurysms of  $27.87 \pm 60.53 \text{ mm}^3$ .<sup>11</sup> The third study found an intra- and interobserver variability of around 0.5 of the postprocessing method used, which is fair. The first and second studies refrained from giving an error value that can be used to interpret the pulsation results for each aneurysm. Our study shows that the error is influenced by multiple artifacts and is aneurysm-specific, which makes it difficult to compare the accuracy of 7T MR imaging with the reported CTA accuracies. Furthermore, CTA has its own technique-specific artifacts, which should be taken into account when analyzing the accuracy of the pulsation measurement.<sup>5</sup>

We used different signal intensity–based thresholds in different aneurysms, without explicitly investigating the robustness of the aneurysm segmentation for various thresholds. Rather, we focused on the effect of signal intensity fluctuations, to give a more in-depth analysis of the behavior of the pulsation estimation as a function of the image characteristics. The segmentation depends on the actual CNR in combination with the signal intensity fluctuations. The threshold should be high enough to avoid including noise but not so high as to prevent exclusion of aneurysm pixels. If one ignored partial volume effects and assumed normally distributed noise, it is straightforward to analyze the sensitivity of the segmentation to the chosen threshold. If  $<1\%$  of the included pixels in the segmentation is allowed to be due to noise, the lower limit of the intensity threshold is approximately  $2.5 \times \text{SD}$  (where  $\text{SD} =$  the SD of the noise). Increasing the threshold further would change the volume by  $<1\%$ , provided that the threshold is not exceeding the upper limit where the aneurysm intensity will start failing to pass the threshold. Similarly, the upper limit would be  $[(1 - f) \times \text{CNR} - 2.5] \times \text{SD}$ , where  $f$  is the intensity fluctuation as a fraction of the aneurysm signal (note that  $\text{CNR} \times \text{SD}$  is the intensity of the aneurysm). From this simple reasoning, it would follow that a minimum CNR of 5 is required to allow robust segmentation without having too much noise, which matches the phantom simulations, which showed that the accuracy dropped quickly below a CNR of 6.

Nonetheless, voxels with a partial volume effect should be con-

sidered as well. They have an intensity somewhere in between the aneurysm intensity and the noise level, depending on the partial volume factor. Basically, the threshold determines how “full” a voxel should be to be counted as aneurysm voxel. In these voxels, intensity fluctuation is directly related to how many partial volume voxels will pass the intensity threshold. Thus, changing the threshold will lead to a change in (baseline) volume. However, because each partial volume fraction is equally likely to occur, the sensitivity to intensity fluctuations and to actual volume changes is not expected to depend on the chosen threshold.

This study has some limitations. First, we used a signal intensity–based threshold to segment the aneurysm volume but also showed that signal intensity fluctuations have a considerable influence on the accuracy of the volume pulsation analysis. Future studies should use an analysis method that is insensitive to signal intensity fluctuations throughout the cardiac cycle. For example, a recently published automatic segmentation method used for quantification and visualization of pulsations from electrocardiography-gated CTA data used the local deformation of image structures in all cardiac phases, which may be less dependent on the actual intensity.<sup>10</sup> With such an automated method, the effects of manual correction are also eliminated and the precision of the measurement may be increased. Second, our estimate of aneurysm-specific inaccuracy was based on patient-specific measurements of CNRs and intensity fluctuations. Although care was taken to obtain representative values, one should note that both the CNR and intensity fluctuations may be variable along the border of the aneurysm. Also, the CNR measurements were likely influenced by intensity fluctuations. Because there was no separate noise acquisition in the MR imaging protocol, we used the SD of the ROI over the cardiac cycles, which may have led to an underestimation of the actual CNR (and, thus, to a slightly worse inaccuracy than actually present). Nonetheless, the accuracy analysis shows that aneurysm-specific inaccuracies should be determined and that an increase in the signal-to-noise ratio of the images should be achieved to improve the accuracy.

Third, our restricted FOV led to incomplete imaging of the largest aneurysm of 19 mm in Stage I of the study, and the subsequent pulsation only accounts for the imaged part. We were not able to expand the FOV due to a fixed scan protocol and therefore a fixed scan time. In the second stage of this study, we were able to increase the FOV to prevent this lack of coverage. Fourth, we found quite large differences in volume pulsation in Stage II of the study compared with Stage I. This finding may be a reflection of an actual difference among aneurysms because a different sample of patients was used in Stage II, which is not optimal when investigating an optimized imaging sequence. However, the most likely explanation is the substantial increase in signal intensity fluctuations in Stage II compared with Stage I, despite the aim of increasing the CNR and decreasing intensity fluctuations. Higher signal intensity pulsation leads to a decrease in volume pulsation quantification accuracy, and this is probably an important reason why a higher pulsation was measured in the aneurysms with the improved TFE in Stage II. Furthermore, the lower volume pulsation found in the same aneurysms on the contrast-enhanced TFE compared with the improved TFE can also be explained by lower signal intensity fluctuations in the contrast-enhanced TFE. Because

lower signal intensity leads to increased accuracy of the volume pulsation quantification, the results of the contrast-enhanced TFE were considered more accurate than the results of the improved TFE. Nonetheless, the intensity pulsations with the contrast-enhanced TFE are still considerable (ranging from 7.5% to 24%), which is still too high to make the volume pulsation analysis on this sequence accurate. Last, the clinical availability of 7T MR imaging is still limited but is expected to increase in the future.

The strength of this study is the use of an advanced high-resolution imaging method to quantify pulsation in aneurysms, combined with a thorough accuracy analysis. All previous studies showed a single value for the inaccuracy, sometimes obtained from a large stable phantom. The phantom simulations in our study give insight into the relative contributions of different sources of measurement errors and their combined effect in a patient-specific way, which can stimulate future improvement on each of these aspects. An advantage of MR imaging over CTA is the lack of radiation in MR imaging. Furthermore, the ultra-high resolution of MR imaging combined with its ability to discriminate the aneurysm wall from its lumen provides a unique opportunity to search for new markers of rupture.

## CONCLUSIONS

Quantification of intracranial aneurysm pulsation seemed to be feasible with 7T MR imaging, but even after optimization of the imaging protocol, the artifactual volume pulsations as a result of intensity fluctuations, the limited CNR, aneurysm size, and the flow displacement artifact have the same magnitude as the volume pulsations observed in the patient data. The current imaging protocol on 7T MR imaging is therefore of no use in studying pulsation as a risk factor for rupture at the moment. Future studies should always include an aneurysm-specific accuracy analysis.

## ACKNOWLEDGMENTS

We acknowledge A. Zada and B. de Vries for their work on the accuracy analysis.

Disclosures: Rachel Kleinloog—*RELATED: Grant:* Focus en massa cardiovasculaire research grant by the Utrecht University, the Netherlands.\* Jaco J. Zwanenburg—*UNRELATED: Grants/Grants Pending:* European Research Council starting grant, *Comments:* Small-Vessel MRI, Grant No. 337333.\* Fredy Visser—*UNRELATED: Employment:* Philips Healthcare. \*Money paid to the institution.

## REFERENCES

1. Vlak MH, Algra A, Brandenburg R, et al. **Prevalence of unruptured intracranial aneurysms, with emphasis on sex, age, comorbidity, country, and time period: a systematic review and meta-analysis.** *Lancet Neurol* 2011;10:626–36 CrossRef Medline
2. Nieuwkamp DJ, Setz LE, Algra A, et al. **Changes in case fatality of aneurysmal subarachnoid haemorrhage over time, according to age, sex, and region: a meta-analysis.** *Lancet Neurol* 2009;8:635–42 CrossRef Medline
3. Brinjikji W, Rabinstein AA, Nasr DM, et al. **Better outcomes with treatment by coiling relative to clipping of unruptured intracranial aneurysms in the United States, 2001–2008.** *AJNR Am J Neuroradiol* 2011;32:1071–75 CrossRef Medline
4. Naggara ON, Lecler A, Oppenheim C, et al. **Endovascular treatment of intracranial unruptured aneurysms: a systematic review of the**

- literature on safety with emphasis on subgroup analyses. *Radiology* 2012;263:828–35 CrossRef Medline
5. Vanrossomme AE, Eker OF, Thiran JP, et al. **Intracranial aneurysms: wall motion analysis for prediction of rupture.** *AJNR Am J Neuroradiol* 2015;36:1796–802 CrossRef Medline
  6. Kleinloog R, Korkmaz E, Zwanenburg JJ, et al. **Visualization of the aneurysm wall: a 7.0-Tesla magnetic resonance imaging study.** *Neurosurgery* 2014;75:614–22; discussion 622 CrossRef Medline
  7. van Ooij P, Zwanenburg JJ, Visser F, et al. **Quantification and visualization of flow in the Circle of Willis: time-resolved three-dimensional phase contrast MRI at 7 T compared with 3 T.** *Magn Reson Med* 2013;69:868–76 CrossRef Medline
  8. Bland JM, Altman DG. **Applying the right statistics: analyses of measurement studies.** *Ultrasound Obstet Gynecol* 2003;22:85–93 Medline
  9. Larson TC 3rd, Kelly WM, Ehman RL, et al. **Spatial misregistration of vascular flow during MR imaging of the CNS: cause and clinical significance.** *AJNR Am J Neuroradiol* 1990;11:1041–48 Medline
  10. Firouzian A, Manniesing R, Metz CT, et al. **Quantification of intracranial aneurysm morphodynamics from ECG-gated CT angiography.** *Acad Radiol* 2013;20:52–58 CrossRef Medline
  11. Kuroda J, Kinoshita M, Tanaka H, et al. **Cardiac cycle-related volume change in unruptured cerebral aneurysms: a detailed volume quantification study using 4-dimensional CT angiography.** *Stroke* 2012;43:61–66 CrossRef Medline
  12. Illies T, Saering D, Kinoshita M, et al. **Feasibility of quantification of intracranial aneurysm pulsation with 4D CTA with manual and computer-aided post-processing.** *PLoS One* 2016;11:e0166810 CrossRef Medline

# HARMless: Transient Cortical and Sulcal Hyperintensity on Gadolinium-Enhanced FLAIR after Elective Endovascular Coiling of Intracranial Aneurysms

S. Suthiphosuwana, C.C.-T. Hsu, and A. Bharatha



## ABSTRACT

**BACKGROUND AND PURPOSE:** Cortical and sulcal hyperintensity on gadolinium-enhanced FLAIR has been increasingly recognized after iodinated contrast medium exposure during angiographic procedures. The goal of this study was to assess the relationship of cortical and sulcal hyperintensity on gadolinium-enhanced FLAIR against various variables in patients following elective endovascular treatment of intracranial aneurysms.

**MATERIALS AND METHODS:** We performed a retrospective review of 58 patients with 62 MR imaging studies performed within 72 hours following endovascular treatment of intracranial aneurysms. Patient demographics, aneurysm location, and vascular territory distribution of cortical and sulcal hyperintensity on gadolinium-enhanced FLAIR were documented. Analysis of cortical and sulcal hyperintensity on gadolinium-enhanced FLAIR with iodinated contrast medium volume, procedural duration, number of angiographic runs, and DWI lesions was performed.

**RESULTS:** Cortical and sulcal hyperintensity on gadolinium-enhanced FLAIR was found in 32/62 (51.61%) post-endovascular treatment MR imaging studies, with complete resolution of findings in all patients on the available follow-up studies (27/27). Angiographic iodinated contrast medium injection and arterial anatomy matched the vascular distribution of cortical and sulcal hyperintensity on gadolinium-enhanced FLAIR. No significant association was found between cortical and sulcal hyperintensity on gadolinium-enhanced FLAIR with iodinated contrast medium volume ( $P = .56$  value) and the presence of DWI lesions ( $P = .68$ ). However, a significant association was found with procedural time ( $P = .001$ ) and the number of angiographic runs ( $P = .019$ ). No adverse clinical outcomes were documented.

**CONCLUSIONS:** Cortical and sulcal hyperintensity on gadolinium-enhanced FLAIR is a transient observation in the arterial territory exposed to iodinated contrast medium during endovascular treatment of intracranial aneurysms. Cortical and sulcal hyperintensity on gadolinium-enhanced FLAIR is significantly associated with procedural time, and the frequency of angiographic runs suggesting a potential technical influence on the breakdown of the BBB, but no reported adverse clinical outcome or association with both iodinated contrast medium volume and DWI lesions was found. Recognition of cortical and sulcal hyperintensity on gadolinium-enhanced FLAIR as a benign incidental finding is vital to avoid unnecessary investigation.

**ABBREVIATIONS:** ACA = anterior cerebral artery; CSHF = cortical and sulcal hyperintensity on gadolinium-enhanced FLAIR; EVT = endovascular treatment; Gd-FLAIR = gadolinium-enhanced FLAIR; HARM = hyperintense acute reperfusion marker; ICM = iodinated contrast medium; IQR = interquartile range; PCA = posterior cerebral artery; VA = vertebral artery

Cortical and sulcal hyperintensity on MR imaging following a neuroangiographic procedure is an increasingly recognized clinicoradiologic phenomenon. Most data arises from the neuro-

radiology literature perhaps due to greater use of MR imaging following an angiographic procedure.<sup>1-7</sup> The FLAIR sequence is known to be particularly sensitive for the detection of various pathologic processes, including subarachnoid hemorrhage, meningitis, stroke, leptomeningeal carcinomatosis, and hyperoxygenation.<sup>6,8-11</sup> FLAIR can be acquired before or after gadolinium administration. On non-gadolinium-enhanced FLAIR, sulcal hyperintensity is the failure of nulling of normal CSF signal intensity.<sup>12</sup> Gadolinium-enhanced FLAIR (Gd-FLAIR) has the added sensitivity of the T1 shortening effect after gadolinium injection and is more sensitive in the detection of leptomeningeal pathologies.<sup>12-14</sup>

Received August 28, 2017; accepted after revision December 15.

From the Division of Diagnostic and Interventional Neuroradiology, Department of Medical Imaging (S.S., C.C.-T.H., A.B.) and Division of Neurosurgery, Department of Surgery (A.B.), St. Michael's Hospital, University of Toronto, Toronto, Ontario, Canada.

Please address correspondence to Suradech Suthiphosuwana, MD, FRCR, Department of Medical Imaging, St. Michael's Hospital, University of Toronto, 30 Bond St, Toronto, Ontario, M5B 1W8, Canada; e-mail: suradech164@gmail.com

<http://dx.doi.org/10.3174/ajnr.A5561>

Recently, cortical and sulcal hyperintensity on Gd-FLAIR (CSHF) has been observed following iodinated contrast medium (ICM) exposure, which has been hypothesized as a manifestation of blood-brain barrier impairment.<sup>7,15,16</sup> Most interestingly, CSHF has been observed following neurovascular interventions with a striking dichotomy in its clinical significance. Following acute stroke interventions, CSHF has been shown to be an imaging marker of poor prognosis, with associated reperfusion, risk of hemorrhagic transformation, and poor clinical outcome.<sup>6,17-20</sup> This phenomenon has been termed “hyperintense acute reperfusion marker (HARM)” and has been hypothesized as early disruption of the BBB in acute stroke.<sup>6,17,19,21,22</sup> Similar findings were reported on the hemodynamic changes after carotid stent placement<sup>1,3,5,23</sup> and after a cardiac bypass operation.<sup>24</sup> Most interesting, CSHF may not be strictly associated with vascular pathologies or procedures because CSHF has more recently been described in normal aging, mild cognitive impairment, or dementia. CSHF ultimately may reflect a multifactorial process leading to focal loss of BBB integrity.<sup>25,26</sup>

Based on the limited evidence from the literature, there is speculation for a causative relationship between CSHF and ICM exposure. Complex pathophysiologic processes during endovascular procedures such as hypoperfusion, hypoxia, ischemia, and reperfusion injury or direct neurotoxicity of the contrast agent<sup>1-5,19,21,22</sup> can result in transient injuries to the BBB.

At our institution, we routinely perform MR imaging with contrast-enhanced MRA in all our patients immediately post-endovascular treatment (EVT) of intracranial aneurysms as a baseline study for future comparison. We reviewed a large cohort of patients who underwent MR imaging within 72 hours after elective EVT of unruptured aneurysms and examined the associations of CSHF with ICM volume exposure, DWI lesions, duration of EVT, and number of angiographic runs.

## MATERIALS AND METHODS

### Patient Population

We retrospectively reviewed 62 consecutive postcoiling MR imaging studies in 58 consecutive patients who underwent elective treatment or re-treatment of cerebral aneurysms from July 2015 to December 2016. The institutional review board approved the study and informed consent was waived.

### Endovascular Coiling

Endovascular coiling was performed in our neuroangiography suite with Artis zee biplane neuroangiography equipment (Siemens, Erlangen, Germany). All patients underwent EVT under general anesthesia. Iohexol (Omnipaque, 300 mg I/mL; GE Healthcare, Piscataway, New Jersey) low-osmolar ICM was consistently used across the cohort.

We routinely performed a right groin approach. Contrast angiographic runs were performed using a power injector with the rate of 4 mL/s of 10-mL total volume for internal carotid artery injection and 4 mL/s of 8-mL total volume for vertebral artery (VA) injection at both the beginning and the end of the coiling procedure. For the remainder of the procedure, the angiographic runs were performed by a hand-injection technique. After EVT, all patients were re-examined and assessed for any neurologic symptoms by neurointerventionalists before discharge.

We documented the side of major arteries where endovascular maneuvering and ICM injection were performed: ICA or VA, total volume of ICM, number of angiographic runs, duration of the EVT, and duration between the end of procedure and obtaining the MR imaging scan.

### MR Imaging Techniques

All patients underwent MR imaging within 72 hours of completion of EVT of the aneurysm on a 1.5T MR imaging scanner (Achieva; Philips Healthcare, Best, the Netherlands) using a 6-channel head coil. All patients were already extubated and breathing room air at the time of the MRI (excluding hyperoxygenation as a cause for sulcal FLAIR hyperintensity). Our MR imaging protocol consisted of DWI, 3D-TOF MRA, contrast-enhanced MRA, and, last, Gd-FLAIR. Contrast-enhanced MRA was acquired after a dose of 20 mL of gadobenate dimeglumine (MultiHance, 529 mg/mL; Bracco Diagnostics, Princeton, New Jersey) was injected intravenously. The Gd-FLAIR acquisition used the following parameters: TR/TE/TI/flip angle = 11,000 ms/140 ms/2800 ms/90°, slice thickness = 5 mm, slice spacing = 6 mm, NEX = 1, matrix size = 240 × 240, FOV = 200 mm. DWI was performed with TR/TE/flip angle = 3386.71 ms/75 ms/90°, NEX = 4, slice thickness = 5 mm, slice spacing = 6 mm, matrix = 256 × 256, FOV = 230 mm, and b-values = 0 and 1000 s/mm<sup>2</sup>.

### Image Analysis

All acquired images were transferred to our PACS, and patient identity on final images for interpretation was removed to facilitate blinded analysis. Two neuroradiologists (S.S. and C.C.-T.H.) independently evaluated each study with final agreement by consensus. Gd-FLAIR was evaluated for the presence of CSHF. Findings positive for CSHF were defined as cortical or sulcal signal intensity equal to or greater than a superficial cortical vein. The location of the CSHF was documented according to conventional arterial territory: right/left anterior cerebral artery (ACA), right/left middle cerebral artery, right/left posterior cerebral artery (PCA), and right/left cerebellar hemispheres. DWI was evaluated for presence of lesions reflecting acute thromboembolic infarct, which was defined as a presence of high signal intensity focus of ≥15 mm. The number of restricted diffusion foci were graded according to Kang et al<sup>27</sup> and Kim et al<sup>28</sup>: 0 (none), I (<6 foci of diffusion restriction), and II (≥6 foci of diffusion restriction). When available, follow-up MR imaging studies 2–4 months following the index treatment were evaluated.

### Statistical Analysis

Statistical analysis was performed using SPSS (Version 22.0; IBM, Armonk, New York). Continuous variables were reported as mean ± SD or median with interquartile range (IQR) and were compared using the Student *t* test or Mann-Whitney *U* test as appropriate. The  $\chi^2$  test or Fisher exact test was performed for categorical variables. Statistical significance was defined as *P* < .05.

## RESULTS

### Patient Characteristics

Sixty-two MR imaging studies in 58 patients (40 women and 18 men) with post-elective EVT were evaluated. The age ranged from

**Table 1: Patient demographics and aneurysms**

Patient data	
No.	58
Age (mean) (range) (yr)	57.17 ± 10.94 (33–78)
Sex (No.) (%)	Female, 40 (69%)
Endovascular coiling aneurysms (No.)	62
Target aneurysm locations (N = 62)	
AComA (No.) (%)	10 (16.13)
Right ICA (No.) (%)	12 (19.35)
Left ICA (No.) (%)	8 (12.9)
Right PcomA (No.) (%)	4 (6.45)
Right MCA (No.) (%)	7 (11.29)
Left MCA (No.) (%)	2 (3.22)
BA (No.) (%)	17 (27.42)
Left VA (No.) (%)	1 (1.61)
Left PCA (No.) (%)	1 (1.61)
Endovascular coiling techniques (N = 62)	
Routine coiling (No.) (%)	23 (37.1%)
Balloon-assisted coiling (No.) (%)	29 (46.77%)
Stent-assisted coiling (No.) (%)	6 (9.68%)
Pipeline flow diverter and coiling (No.) (%)	3 (4.8%)
Balloon- and stent-assisted coiling (No.) (%)	1 (1.61%)
No. of coils (median) (range)	5 (1–32)

**Note:**—AcomA indicates anterior communicating artery; PcomA, posterior communicating artery; BA, basilar artery.

33 to 78 years with a mean of 57 years. None of these patients had SAH before or during the elective EVT. Various endovascular techniques were used for treatment of aneurysms or re-treatment for recanalized aneurysms. Of 62 EVTs, the location of the target coiling of the aneurysms was as follows: anterior communicating artery ( $n = 10$ ), right ICA ( $n = 12$ ), left ICA ( $n = 8$ ), right posterior communicating artery ( $n = 4$ ), right MCA ( $n = 7$ ), left MCA ( $n = 2$ ), basilar artery ( $n = 17$ ), left VA ( $n = 1$ ), and left PCA ( $n = 1$ ). Of the 62 EVTs, 30 studies assessed the target aneurysm via the right ICA as a major angiographic run with ICM. Thirteen studies were assessed via the left ICA. Six studies were assessed via the right VA. Thirteen studies were assessed using the left VA. Detailed data on patient demographics, aneurysm characteristics, and EVT are shown in Table 1.

### CSHF: Incidence and Location

Thirty-two MR imaging studies (51.61%) were positive for CSHF, and 30 (48.39%) were negative. No significant difference between age and sex of the patients ( $P = .77$  and  $P = .12$ , respectively) was observed between groups positive and negative for CSHF. Of 32 MR imaging studies positive for CSHF, the CSHF was found in the right ACA territory (Fig 1A) (15/32, 46.87%), right MCA territory (Fig 2B) (18/32, 56.25%), left ACA territory (Fig 1C) (4/32, 12.5%), left MCA territory (Fig 1C) (4/32, 12.5%), right PCA territory (Fig 2B) (6/32, 18.75%), left PCA territory (4/32, 12.5%), and left cerebellar hemispheric territory (2/32, 6.25%) (Fig 1E).

In the group positive for CSHF, 7 CT scans of the brain obtained immediately after EVT showed no evidence of sulcal hyperdensity. Twenty-seven follow-up MR imaging studies were performed within 2–4 months, and all demonstrated complete resolution of CSHF.

### CSHF and Site of Angiographic Injection

For the right ICA injection ( $n = 30$ ), CSHF was found in the right ACA territory (13/30, 43.33%) (Fig 1A), right MCA (Fig 2B) (18/

30, 60%), left ACA (1/30, 3.33%), and right PCA (Fig 2B) (1/30, 3.33%). The left ICA injection ( $n = 13$ ) showed that CSHF was found in the left ACA (Fig 1C) (3/13, 23.07%), left MCA (Fig 1C) (4/13, 30.77%), and right ACA (2/13, 15.38%). The right VA injection ( $n = 6$ ) demonstrated CSHF on the right PCA (1/6, 16.67%) and left PCA (1/6, 16.67%). The left VA injection ( $n = 13$ ) showed right PCA CSHF (4/13, 30.77%), left PCA CSHF (3/13, 23.08%), and left cerebellum CSHF (2/13, 15.38%) (Fig 1E).

### CSHF and ICM Volume

No significant difference in the ICM volume ( $P = .588$ ) was found between the 2 groups. The mean volume of the ICM in the group negative for CSHF was 453.33 mL (range, 200–800 mL), and in the group positive for CSHF, 431.25 mL (range, 200–800 mL). Similarly, no significant difference in the contrast volume per body weight was found between the 2 groups ( $P = .566$ ). The mean volume of contrast per body weight in the group positive for CSHF was 6.15 mL/kg (range, 1.92–11.54 mL/kg), and in the group negative for CSHF, 6.53 mL/kg (range, 3.04–12.35 mL/kg) (Table 2).

### CSHF and Procedural Time

A significant difference was found in the procedural time between the 2 groups ( $P = .001$ ). The group positive for CSHF had a longer procedural time, with a median of 2.21 hours (range, 1.07–5.13 hours) compared with the group negative for CSHF, with a median of 1.39 hours (range, 0.7–4.12 hours) (Table 2).

### CSHF and Number of Angiographic Runs

A significantly higher number of angiographic runs was documented in the group positive for CSHF ( $P = .019$ ), with a median number of 18 runs (range, 7–30 runs) and a median number of angiographic runs of 13 (range, 7–29 runs) in the group negative for CSHF group (Table 2).

### CSHF and Time from Coiling to MR Imaging

No significant differences were found between the groups positive and negative for CSHF ( $P = .87$ ). Overall the time from completion of EVT to MR imaging in all patients ranged from 3.93–64.27 hours (median, 16.16 hours). In the group positive for CSHF, the time to MR imaging ranged from 3.93 to 64.27 hours (median, 16.08 hours). In the group negative for CSHF, it ranged from 6.6 to 46.17 hours (median, 16.16 hours) (Table 2).

### CSHF and DWI Lesions

There was no significant correlation between grading of DWI lesions and the presence of CSHF ( $P = .68$ ). Twenty-two MR imaging studies (35.5%) showed no DWI lesions (grade 0): 13 studies positive for CSHF versus 9 studies negative for CSHF. Twenty-five MR imaging studies (40.3%) had grade I DWI lesions: 12 studies positive for CSHF versus 13 studies negative for CSHF. Finally, 15 MR imaging studies (24.2%) showed grade II DWI lesions: 7 in the positive for CSHF group versus 8 in the negative for CSHF group (Table 2). No large-volume confluent/territorial infarct was encountered in our series.

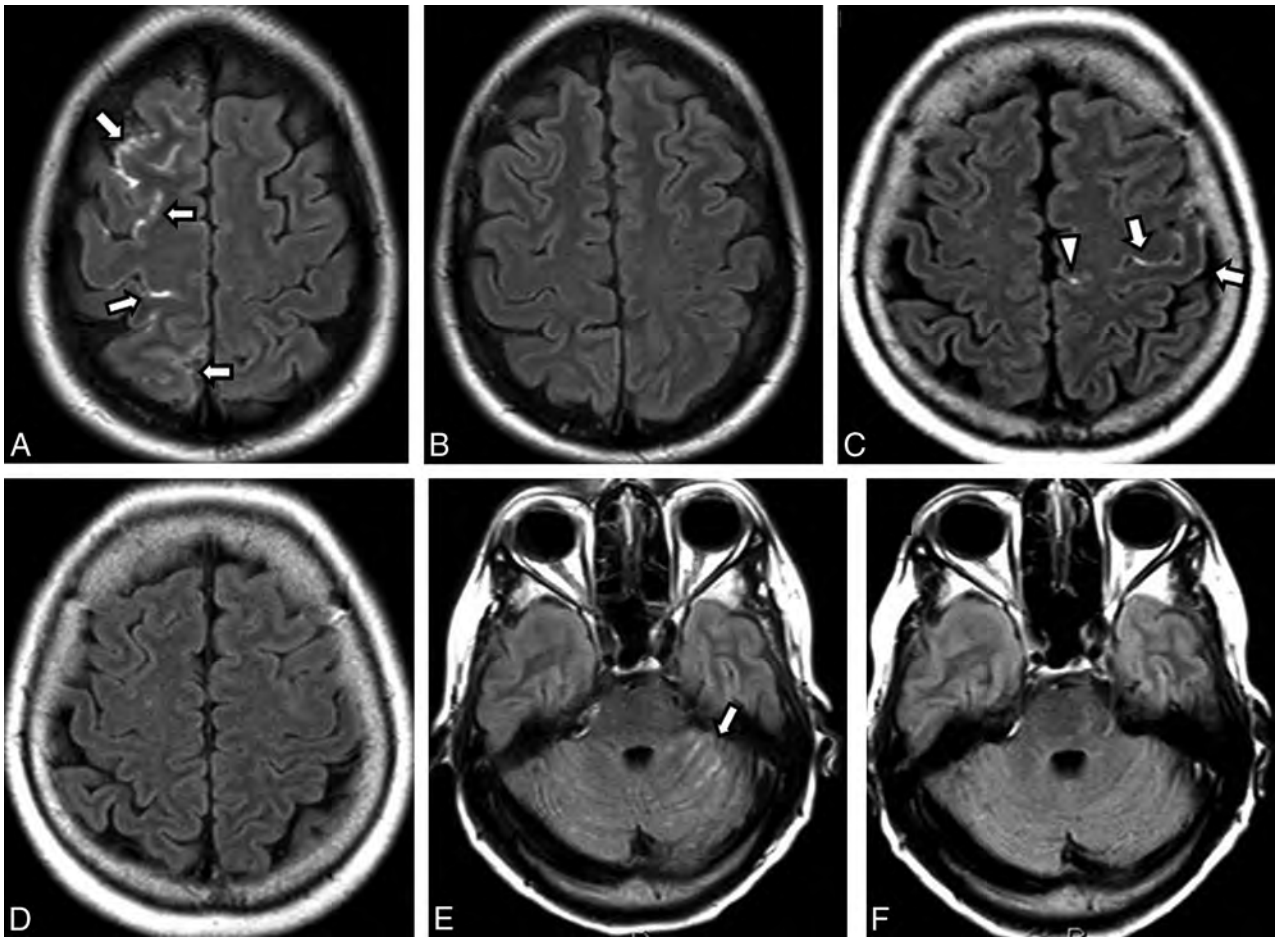


**FIG 1.** Different patterns of cortical and sulcal hyperintensity on gadolinium-enhanced FLAIR in different patients. *A* and *B*, A 49-year-old woman with a postcoiling unruptured anterior communicating artery aneurysm via a right internal carotid artery approach. *A*, Postcoiling gadolinium-enhanced FLAIR shows CSHF along the right anterior cerebral artery territory (*white arrows*). *B*, Two-month follow-up Gd-FLAIR shows no residual abnormality. *C* and *D*, A 64-year-old woman postcoiling of a left paraclinoid ICA aneurysm via a left ICA approach. *C*, Postcoiling Gd-FLAIR shows CSHF along the left middle cerebral artery territory (*white arrows*) and left ACA territory (*white arrowhead*). *D*, Two-month follow-up Gd-FLAIR shows resolution of the abnormality. *E* and *F*, A 61-year-old woman with a postcoiling basilar tip artery aneurysm via a left vertebral artery approach. *E*, Postprocedural Gd-FLAIR shows CSHF along the left cerebellar fissures (*white arrow*). *F*, Two-month follow-up Gd-FLAIR shows no residual abnormality.

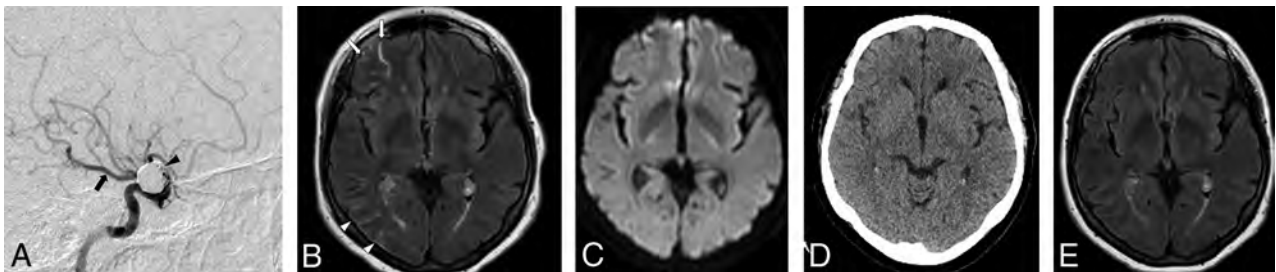


**FIG 2.** *A*, Right internal carotid artery angiographic approach for coiling of a right ophthalmic ICA aneurysm (*black arrowhead*) in a 71-year-old woman using 7.78 mL/kg of iodinated contrast volume and a procedural time of 4 hours. Note the presence of fetal origin of the right posterior cerebral artery (*black arrow*). *B*, Gadolinium-enhanced FLAIR performed at 12 hours after endovascular coiling shows cortical and sulcal hyperintensity along the right middle cerebral artery territory (*white arrows*) and the right PCA territory (*white arrowheads*). *C*, Corresponding DWI shows no diffusion restriction. *D*, A follow-up unenhanced CT scan obtained on the same date shows no evidence of subarachnoid hemorrhage. *E*, Two-month follow-up Gd-FLAIR shows no residual abnormality.

## DISCUSSION

CSHF is a radiologic phenomenon frequently observed in patients following elective EVT of unruptured aneurysms with an incidence of 51.61% (32/62 MR imaging studies). This study is the first of its kind to examine CSHF on MR imaging in a large asymp-

tomatic cohort of patients following endovascular coiling of intracranial aneurysms, to our knowledge. The phenomenon of contrast extravasation into the subarachnoid space had been described on CT immediately post-EVT of intracranial aneurysms with a reported incidence of up to 23%–49%<sup>29,30</sup>; however, in our

**Table 2: Comparison between findings negative and positive for CSHF**

Factors	Findings Negative for CSHF (n = 30)	Findings Positive for CSHF (n = 32)	Total (N = 62)	P Value
Contrast volume (mean) (mL)	453.33 ± 156.98	431.25 ± 161.52	441.93 ± 158.42	.588
Contrast volume per weight (mean) (mL/kg)	6.53 ± 2.39	6.15 ± 2.56	6.33 ± 2.46	.556
Duration of endovascular coiling procedure (median) (IQR) (hr)	1.39 (0.95–2.20)	2.21 (1.63–3.26)	1.89 (1.26–2.66)	.001
Time from coiling to MRI (median) (IQR) (hr)	16.16 (11.99–22.51)	16.08 (10.03–22.61)	16.16 (11.56–22.125)	.871
No. of angiographic runs (median) (IQR)	13 (10–17)	18 (12–22)	14 (12–20)	.019
DWI grading (No.) (%)				
0	9	13	22 (35.5%)	.68
I	13	12	25 (40.3%)	
II	8	7	15 (20.2%)	

series, subsequent CT did not show sulcal hyperdensity when performed. In addition, CSHFs were in the peripheral/cortical sulci far from the basal cisterns and hence unlikely to represent SAH or aneurysm perforation. CSHF appears to be transient, with resolution of the finding on available follow-up MR imaging. Reassuringly, no symptom or adverse clinical outcome was attributed to the observation of CSHF. The incidence of CSHF in our cohort is similar to that reported in patients following ischemic stroke therapy, which ranges from 33% to 45%.<sup>17,19,24</sup> However, the clinical significance of CSHF may be dependent on the clinical context. In the setting of acute stroke, CSHFs are known to be predictors of hemorrhagic transformation and poor clinical outcome and are termed HARMs for this particular reason.<sup>6,17–19,21,31</sup> We hypothesized that CSHF may be a radiologic manifestation of inherent vulnerability of the cerebral cortex, causing transient impairment of the BBB, allowing extravasation of gadolinium from the intravascular space into the subarachnoid space.

CSHFs in our study were observed in the arterial territories exposed to the ICM during the angiographic procedure (Figs 1 and 2).<sup>1,3,5,23</sup> In addition, when variant arterial anatomy is present, CSHF could also be seen in the vascular territory perfused by the variant vessel (Fig 2).

Our study failed to demonstrate a significant correlation between total ICM volume and CSHF. Two previous studies<sup>29,30</sup> showed a correlation between sulcal hyperdensity seen on CT and ICM volume in patients post-EVT of intracranial aneurysms. A small selective subset of patients from the study by Ozturk et al<sup>30</sup> also underwent further MR imaging evaluation after detection of sulcal hyperdensity on CT, but the MR imaging examination findings were unremarkable. In our study, we only included patients with unruptured intracranial aneurysms, hence eliminating prior subarachnoid hemorrhage as a potential confounder, whereas both prior studies included ruptured intracranial aneurysms. More important, Gd-FLAIR is far more sensitive than CT in the detection of disease of the subarachnoid space.

A small case series by Wilkinson et al<sup>1</sup> reported unilateral leptomeningeal enhancement on Gd-FLAIR in all their patients (n = 12) after carotid stent placement. Ogami et al<sup>3</sup> also reported a high incidence of 57% of this observation in a small case series (n = 21) post-carotid stent placement. The central hypothesis proposed was BBB breakdown after reperfusion or hemodynamic disturbance. In both studies, the dose of the ICM was not reported.

Contrast-induced encephalopathy is a rare complication reported after ICM exposure following diagnostic or interventional angiography. Neuroimaging findings of contrast-induced en-

cephalopathy usually show unilateral or bilateral cerebral hemispheric edema and leptomeningeal enhancement, and the affected brain parenchyma often demonstrates signal abnormality on both FLAIR and DWI.<sup>7,15,16</sup> On the basis of case reports and the small number of case series of contrast-induced encephalopathy, a speculative ICM volume threshold had been reported, which ranged from 75 to 1500 mL.<sup>15,16,32–34</sup> The average contrast volume used in our study was 441.94 mL, which is not significantly different from the reported ranges in the literature; however, no acute encephalopathy was observed in our series.

Vulnerability or injury to the brain parenchyma can weaken the BBB, making it more susceptible to permeability impairment. A measurable surrogate of parenchymal injury is DWI lesions burden indicating acute thromboembolic infarcts. The incidence of MR imaging studies with DWI lesions following endovascular coiling of unruptured aneurysms ranges between 37.3% and 54.5%,<sup>27,28,35</sup> which is similar to our reported incidence of 64.5%. Our study did not show a significant correlation between grades of DWI abnormality and CSHF. Our result is consistent with the findings of Merino et al,<sup>24</sup> which showed no significant correlation between DWI lesions and sulcal enhancement on Gd-FLAIR following cardiac bypass surgery.

Variation in angioarchitecture of the aneurysm means that a multitude of endovascular techniques are at the disposal of neurointerventionalists. A simple aneurysm may only necessitate deployment of coils, whereas larger and complex aneurysms may require assistance of a balloon microcatheter or stent. Differences in endovascular devices and techniques can have different hemodynamic impacts on the brain parenchyma but are difficult to quantify and were not addressed in this paper. Of the 4 major variables analyzed, procedural time and number of angiographic runs showed a significant correlation with CSHF. We hypothesize that perhaps it is not the total ICM volume or number of DWI lesions that correlates with weakened BBB but the frequency of contrast delivery and procedural catheter dwell time that predispose to the development of CSHF. Contrary to the HARM phenomenon following EVT of ischemic stroke, CSHF is a benign transient finding.

This study has several limitations including the retrospective nature of data collection. In addition, the MR imaging protocol does not include precontrast FLAIR; hence, we cannot unequivocally distinguish intrinsic FLAIR changes from gadolinium leak. Sometimes, we were unable to directly visualize the location of the catheter tip during angiographic runs due to technical factors, including the tip lying outside the FOV or inadequate visualiza-

tion due to poor magnification in which case we used the previous run and opacified branches to infer the location. The total ICM volume was recorded as the total number of vials used. This is a overestimation of the actual ICM injected because we anticipated contrast spillage and contrast retained within the syringes or injectors. The total ICM volume showed no significant association with CSHF; however, this is unlikely to be reflective of the local ICM volume exposure. Local concentration of ICM volume maybe a more important variable to analyze than total ICM volume, but such data would be difficult to obtain retrospectively. Last, there may be a difference in individual sensitivity to ICM.

## CONCLUSIONS

CSHF is a transient benign finding commonly seen following elective aneurysm coiling, which is observed in the vascular territory exposed to the ICM. There are statistically significant associations of CSHF with procedural time and the frequency of angiographic injections, but there is no direct relationship with total ICM volume or DWI lesions. It is vital for radiologists and clinicians to recognize CSHF because misdiagnosis can lead to unnecessary clinical concern or investigation.

## REFERENCES

1. Wilkinson ID, Griffiths PD, Hoggard N, et al. **Unilateral leptomeningeal enhancement after carotid stent insertion detected by magnetic resonance imaging.** *Stroke* 2000;31:848–51 CrossRef Medline
2. Vangosa AB, Tortora D, Modestino F, et al. **Reversible and asymptomatic gyral and subarachnoid contrast enhancement after carotid stenting.** *Neuroradiol J* 2015;28:184–86 CrossRef Medline
3. Ogami R, Nakahara T, Hamasaki O, et al. **Cerebrospinal fluid enhancement on fluid attenuated inversion recovery images after carotid artery stenting with neuroprotective balloon occlusions: hemodynamic instability and blood-brain barrier disruption.** *Cardiovasc Intervent Radiol* 2011;34:936–41 CrossRef Medline
4. Fukushima Y, Nakahara I, Ohta T, et al. **Rare complication characterized by late-onset neurological symptoms without hyperperfusion after carotid artery stenting: a report of three cases.** *Interv Neuroradiol* 2015;21:72–79 CrossRef Medline
5. Cho HJ, Kim YJ, Lee JH, et al. **Post-carotid stenting reperfusion injury with blood-brain barrier disruption on gadolinium-enhanced FLAIR MRI.** *BMC Neurol* 2014;14:178 CrossRef Medline
6. Kim EY, Kim SS, Na DG, et al. **Sulcal hyperintensity on fluid-attenuated inversion recovery imaging in acute ischemic stroke patients treated with intra-arterial thrombolysis: iodinated contrast media as its possible cause and the association with hemorrhagic transformation.** *J Comput Assist Tomogr* 2005;29:264–69 CrossRef Medline
7. Chen K, Obaid S, Guillon-Létourneau L, et al. **Iodinated contrast encephalopathy.** *Can J Neurol Sci* 2017;44:432–33 CrossRef Medline
8. Singh SK, Agris JM, Leeds NE, et al. **Intracranial leptomeningeal metastases: comparison of depiction at FLAIR and contrast-enhanced MR imaging.** *Radiology* 2000;217:50–53 CrossRef Medline
9. Taoka T, Yuh WT, White ML, et al. **Sulcal hyperintensity on fluid-attenuated inversion recovery MR images in patients without apparent cerebrospinal fluid abnormality.** *AJR Am J Roentgenol* 2001;176:519–24 CrossRef Medline
10. Frigon C, Shaw DW, Heckbert SR, et al. **Supplemental oxygen causes increased signal intensity in subarachnoid cerebrospinal fluid on brain FLAIR MR images obtained in children during general anesthesia.** *Radiology* 2004;233:51–55 CrossRef Medline
11. Iancu-Gontard D, Oppenheim C, Touze E, et al. **Evaluation of hyperintense vessels on FLAIR MRI for the diagnosis of multiple intracerebral arterial stenoses.** *Stroke* 2003;34:1886–91 CrossRef Medline
12. Morris JM, Miller GM. **Increased signal in the subarachnoid space on fluid-attenuated inversion recovery imaging associated with the clearance dynamics of gadolinium chelate: a potential diagnostic pitfall.** *AJNR Am J Neuroradiol* 2007;28:1964–67 CrossRef Medline
13. Mamourian AC, Hoopes PJ, Lewis LD. **Visualization of intravenously administered contrast material in the CSF on fluid-attenuated inversion-recovery MR images: an in vitro and animal-model investigation.** *AJNR Am J Neuroradiol* 2000;21:105–11 Medline
14. Bozzao A, Floris R, Fasoli F, et al. **Cerebrospinal fluid changes after intravenous injection of gadolinium chelate: assessment by FLAIR MR imaging.** *Eur Radiol* 2003;13:592–97 Medline
15. Guimaraens L, Vivas E, Fonnegra A, et al. **Transient encephalopathy from angiographic contrast: a rare complication in neurointerventional procedures.** *Cardiovasc Intervent Radiol* 2010;33:383–88 CrossRef Medline
16. Leong S, Fanning NF. **Persistent neurological deficit from iodinated contrast encephalopathy following intracranial aneurysm coiling: a case report and review of the literature.** *Interv Neuroradiol* 2012;18:33–41 CrossRef Medline
17. Renú A, Laredo C, Lopez-Rueda A, et al. **Vessel wall enhancement and blood-cerebrospinal fluid barrier disruption after mechanical thrombectomy in acute ischemic stroke.** *Stroke* 2017;48:651–57 CrossRef Medline
18. Latour LL, Kang DW, Ezzeddine MA, et al. **Early blood-brain barrier disruption in human focal brain ischemia.** *Ann Neurol* 2004;56:468–77 CrossRef Medline
19. Warach S, Latour LL. **Evidence of reperfusion injury, exacerbated by thrombolytic therapy, in human focal brain ischemia using a novel imaging marker of early blood-brain barrier disruption.** *Stroke* 2004;35:2659–61 CrossRef Medline
20. Mathews VP, Caldemeyer KS, Lowe MJ, et al. **Brain: gadolinium-enhanced fast fluid-attenuated inversion-recovery MR imaging.** *Radiology* 1999;211:257–63 CrossRef Medline
21. Lee KM, Kim JH, Kim E, et al. **Early stage of hyperintense acute reperfusion marker on contrast-enhanced FLAIR images in patients with acute stroke.** *AJR Am J Roentgenol* 2016;206:1272–75 CrossRef Medline
22. Köhrmann M, Struffert T, Frenzel T, et al. **The hyperintense acute reperfusion marker on fluid-attenuated inversion recovery magnetic resonance imaging is caused by gadolinium in the cerebrospinal fluid.** *Stroke* 2012;43:259–61 CrossRef Medline
23. Liu JJ, Dahlin BC, Waldau B. **Contrast encephalopathy after coiling in the setting of obstructive sleep apnoea.** *BMJ Case Rep* 2015;2015 pii: bcr2014207503 CrossRef Medline
24. Merino JG, Latour LL, Tso A, et al. **Blood-brain barrier disruption after cardiac surgery.** *AJNR Am J Neuroradiol* 2013;34:518–23 CrossRef Medline
25. Zenaro E, Piacentino G, Constantin G. **The blood-brain barrier in Alzheimer's disease.** *Neurobiol Dis* 2017;107:41–56 CrossRef Medline
26. Freeze WM, Schnerr RS, Palm WM, et al. **Pericortical enhancement on delayed postgadolinium fluid-attenuated inversion recovery images in normal aging, mild cognitive impairment, and Alzheimer disease.** *AJNR Am J Neuroradiol* 2017;38:1742–47 CrossRef Medline
27. Kang DH, Kim BM, Kim DJ, et al. **MR-DWI-positive lesions and symptomatic ischemic complications after coiling of unruptured intracranial aneurysms.** *Stroke* 2013;44:789–91 CrossRef Medline
28. Kim B, Kim K, Jeon P, et al. **Thromboembolic complications in patients with clopidogrel resistance after coil embolization for unruptured intracranial aneurysms.** *AJNR Am J Neuroradiol* 2014;35:1786–92 CrossRef Medline
29. Brisman JL, Jilani M, McKinney JS. **Contrast enhancement hyperdensity after endovascular coiling of intracranial aneurysms.** *AJNR Am J Neuroradiol* 2008;29:588–93 CrossRef Medline
30. Ozturk A, Saatci I, Pamuk AG, et al. **Focal increased cortical density in**

- immediate postembolization CT scans of patients with intracranial aneurysms.** *AJNR Am J Neuroradiol* 2006;27:1866–75 Medline
31. Lee H, Kim E, Lee KM, et al. **Clinical implications of sulcal enhancement on postcontrast fluid attenuated inversion recovery images in patients with acute stroke symptoms.** *Korean J Radiol* 2015;16:906–13 CrossRef Medline
  32. Spina R, Simon N, Markus R, et al. **Contrast-induced encephalopathy following cardiac catheterization.** *Catheter Cardiovasc Interv* 2017;90:257–68 CrossRef Medline
  33. Dangas G, Monsein LH, Lauren R, et al. **Transient contrast encephalopathy after carotid artery stenting.** *J Endovasc Ther* 2001;8:111–13 Medline
  34. Menna D, Capoccia L, Rizzo AR, et al. **An atypical case of contrast-induced encephalopathy after carotid artery stenting.** *Vascular* 2013;21:109–12 CrossRef Medline
  35. Park JC, Lee DH, Kim JK, et al. **Microembolism after endovascular coiling of unruptured cerebral aneurysms: incidence and risk factors.** *J Neurosurg* 2016;124:777–83 CrossRef Medline

# Radiation Dosimetry of 3D Rotational Neuroangiography and 2D-DSA in Children

N.A. Shkumat, M.M. Shroff, and P. Muthusami

## ABSTRACT

**BACKGROUND AND PURPOSE:** The benefit-risk assessment concerning radiation use in pediatric neuroangiography requires an extensive understanding of the doses delivered. This work evaluated the effective dose of 3D rotational angiography in a cohort of pediatric patients with complex neurovascular lesions and directly compared it with conventional 2D-biplane DSA.

**MATERIALS AND METHODS:** Thirty-three 3D rotational angiography acquisitions were acquired in 24 pediatric patients (mean age, 10.4 years). When clinically indicated, following 2D-biplane DSA, 3D rotational angiography was performed with 1 of 3 technical protocols (2 subtracted, 1 unsubtracted). The protocols consisted of 1 factory and 2 customized techniques, with images subsequently reconstructed into CT volumes for clinical management. Raw projections and quantitative dose metrics were evaluated, and the effective dose was calculated.

**RESULTS:** All 3D rotational angiography acquisitions were of diagnostic quality and assisted in patient management. The mean effective doses were 0.5, 0.12, and 0.06 mSv for the factory-subtracted, customized-subtracted, and customized-unsubtracted protocols, respectively. The mean effective dose for 2D-biplane DSA was 0.9 mSv. A direct intraprocedural comparison between 3D and 2D acquisitions indicated that customized 3D rotational angiography protocols delivered mean relative doses of 9% and 15% in unsubtracted and subtracted acquisitions, respectively, compared with biplane DSA, whereas the factory subtracted protocol delivered 68%.

**CONCLUSIONS:** In pediatric neuroangiography, the effective dose for 3D rotational angiography can be significantly lower than for 2D-biplane DSA and can be an essential adjunct in the evaluation of neurovascular lesions. Additionally, available 3D rotational angiography protocols have significant room to be tailored for effectiveness and dose optimization, depending on the clinical question.

**ABBREVIATIONS:** 3DRA = 3D rotational angiography;  $K_{a,r}$  = reference point air kerma

Angiography for the delineation of pediatric intracerebral vascular lesions can often require digital subtraction angiography at multiple angles for complete anatomic and hemodynamic assessment. To supplement existing technology, the use of 3D rotational angiography (3DRA) has increased in recent years and is now a viable imaging option available to the neuroradiologist.<sup>1-4</sup> It promises to add relevant clinical information that can increase diagnostic confidence and potentially decrease the amount of fluorography while allowing improved and more efficient intervention planning. Existing applications of 3DRA in

neuroangiography range from assessing the anatomy of arteriovenous malformations, volume-rendered vessel reformats for aneurysm treatment, CT reconstruction for hemorrhage and multiplanar reformation, and MR imaging fusion for presurgical evaluation and guidance.<sup>5-8</sup>

Although the concept of dose reduction and optimization is often described in pediatric literature, the comparison of the radiation dose between individual imaging events within a procedure is not often evaluated.<sup>9,10</sup> This practice is due to a number of factors, including the inherent variability of neuroangiographic procedures, the complexity of lesions being assessed, a wide range of body habitus, differences in technical protocols between vendors and models, operator preferences, and lack of viable patient reference models/phantoms. Previous research has evaluated the radiation dose in pediatric neuroangiography with respect to readily available, system-provided dose surrogates, though the work was not extended to effective dose, which is widely accepted as a general quantifier of radiation risk.<sup>7</sup> The correlation between

Received October 4, 2017; accepted after revision December 28.

From the Department of Diagnostic Imaging (N.A.S., M.M.S., P.M.), The Hospital for Sick Children, Toronto, Ontario, Canada; and Department of Medical Imaging (N.A.S., M.M.S., P.M.), University of Toronto, Toronto, Ontario, Canada.

Please address correspondence to Nicholas A. Shkumat, Department of Diagnostic Imaging, The Hospital for Sick Children, 555 University Ave, Suite 2175A Toronto, ON, Canada M5G 1X8; e-mail: nicholas.shkumat@sickkids.ca

<http://dx.doi.org/10.3174/ajnr.A5568>

these reference metrics and organ or effective dose is weak and has not been published for the pediatric population.<sup>11,12</sup> The effective dose for pediatric 3DRA has been investigated for applications in radiation oncology and cardiology and in adult patients and phantoms.<sup>13-17</sup> Although effective dose is an imperfect metric and not intended for use in individual patients, it can be a useful and valuable tool for the identification, assessment, and comparison of radiation burden in similar imaging scenarios. It is also an effective method of radiation dose communication throughout radiology and associated medical specialties.

With increasing use of 3DRA and advanced rotational imaging techniques, this work sought to calculate and compare the effective dose of clinical standard-of-care 2D-biplane DSA and various 3DRA protocols implemented at our institution. This research will aid in the continual assessment of the benefit-risk ratio with each application of ionizing radiation in the complex pediatric neurovascular environment.

## MATERIALS AND METHODS

Within an 18-month period, thirty-three 3D-acquisitions were performed in 24 patients requiring conventional angiography. All procedures were performed by 2 pediatric neuroradiologists (P.M. and M.M.S.) in a biplane interventional suite (Artis Q biplane; Siemens, Erlangen, Germany).

Written informed consent was obtained from parents/guardians for all procedures.

All procedures were performed with the patient under general anesthesia. Patients were catheterized via femoral artery access. Injections of iodinated contrast were delivered through a power injector, with flow rates ranging between 2.5 and 5 mL/s and total volumes ranging from 6 to 10 mL. The clinical indications for these studies are described in Table 1.

### Imaging

2D-DSA images were obtained using a 32- to 42-cm FOV with an acquisition rate of 3–6 frames/s. Acquisition length varied depending on the indication and individual hemodynamics.

Customized technical protocols were used with a target kilovolt(peak) of 70, a requested detector dose of 1200 nGy/frame, and applied copper filtration between 0.1 and 0.3 mm. Postprocessing parameters varied depending on the imaging task.

**Table 1: Patient demographics and indications**

Parameter	Value
Age (mean) (yr)	10.4 ± 5.1
Male/female	18:6
Procedure indication (No.)	
AVM	28
Intra-arterial chemotherapy	2
Aneurysm	1
Aberrant neurovasculature	1
Presurgical embolization	1

**Table 2: Technical factors for 3DRA acquisition protocols**

	Projections per Rotation		Rotations Required per Acquisition	kVp Target	Detector Dose (nGy/projection)	Filtration (mm Cu)	Half-Value Layer (mm Al)
Protocol 1 (subtracted)	133	200°	2 (mask, contrast)	70	360	0.0	2.9
Protocol 2 (subtracted)	133	200°	2 (mask, contrast)	90	200	0.3	7.1
Protocol 3 (unsubtracted)	248	200°	1 (contrast)	90	100	0.6	8.2

Following biplane imaging, a 5-second 3DRA was acquired with the patient at the isocenter and the FOV fixed at 42 cm. Three 3DRA protocols were evaluated in this article: a customized unsubtracted protocol described in previous work and 2 subtracted protocols, before and after customization.<sup>7</sup> Pathology dictated the decision to acquire subtracted or unsubtracted imaging volumes. Subtracted 3DRA is composed of 2 rotations, the first creating a “mask” volume, with the second in close succession using iodine contrast material. Together, they are referred to as the subtracted acquisition. Unsubtracted acquisitions use a single rotational volume with contrast. Select technical specifications are described in Table 2.

### Dosimetric Analysis

Effective dose was calculated through a multistep process. Quantitative radiation dose surrogates were extracted through assessment of radiation dose structured reports and information parsed from each 3DRA imaging volume. Validation of integrated radiation output systems was made with an external radiation dosimeter following the methodology specified in the American Association of Physicists in Medicine Task Group Report 190.<sup>17</sup>

Details of each projection for both 2D-DSA and 3DRA were obtained, including the following: kilovolt(peak), filtration, tube current, exposure time, source-imager distance, projection angulation, cranial-caudal angulation, milliamperes, pulse width, table position, air kerma area product, and reference point air kerma ( $K_{a,r}$ ). Attenuation of the imaging table and mattress for projections with complete interception of the FOV (namely, posterior-anterior and small angles) was accounted for in the assessment. Oblique projections with partial table attenuation were conservatively assumed to be unattenuated.

The representative effective dose was determined through Monte Carlo modeling software (PCXMC 2.0; STUK, Helsinki, Finland). The method applied was a simple application of photon transport based on stochastic simulation of interactions between x-rays and matter and the deposition of energy to organs within the imaged volume.<sup>18</sup> Mathematic hermaphrodite phantoms of 4 reference ages and sizes were used (1, 5, 10, and 15 years) to simulate each patient in this study. The age of the reference model closest to true patient age was used for each calculation.

For biplane 2D-DSA acquisitions, patient entrance air kerma was determined for precise angles (projection and craniocaudal angulation) of each stationary fluorographic run. These data with corresponding beam quality and geometric considerations, including source-to-entrance distances, were applied through the Monte Carlo simulation process to calculate the effective dose for individual posteroanterior and lateral runs. For display and discussion, each acquisition pair was summed to provide the total biplane 2D-DSA effective dose.

For 3DRA acquisitions, we determined the patient entrance air

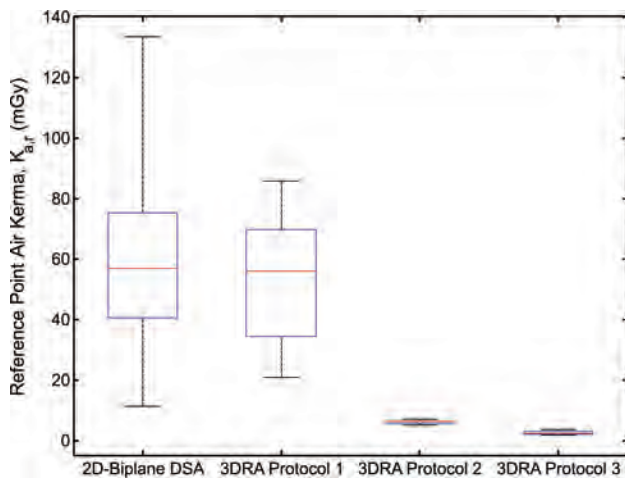


**FIG 1.** Box-and-whisker plot depicting the reference point air kerma of biplane DSA and 3DRA protocols across all patients. *Boxes* denote median, lower, and upper quartiles, with *whiskers* capturing values outside the interquartile range.

kerma for each angulation, individually accounting for changes in tube output per projection and correcting for source-to-entrance distances for each representative patient age and size. Beam collimation and FOV were assessed for each 3DRA volume and propagated into the Monte Carlo calculation model. Communication of air kerma, absorbed dose, and effective dose during each 3D acquisition indicated the summation across all projections acquired across the angular range of each rotation and the number of rotations required for the 3DRA (2 for subtracted, 1 for unsubtracted).

In all calculations, the latest tissue-weighting factors from the International Commission on Radiologic Protection Report 103 were applied in the calculation of effective dose.<sup>19</sup> Following the calculations for biplane 2D-DSA and 3DRA in the same vessel and patient, relative comparisons were made for direct assessment.

## RESULTS

Of the 33 3DRA acquisitions in this work, 12 were acquired with the conventional 3D-DSA (subtracted) protocol (referred to as protocol 1); 6, with the modified 3D-DSA (subtracted) protocol (protocol 2); and 15, with the unsubtracted protocol (protocol 3). The integrated system dosimeter in both planes was confirmed to be accurate to within 6% through external validation with a calibrated dosimetry system.

The primary quantitative radiation dose surrogate,  $K_{a,r}$  for aggregate 2D-DSA and 3DRA acquisitions, is shown in Fig 1. As evaluated in prior work, a large range is observed in biplane 2D DSA runs.<sup>7</sup> The mean and median  $K_{a,r}$  for 2D-biplane DSA were 60.1 and 56.9 mGy, respectively, with a total range of 11.5–133.5 mGy. When we evaluated 3D protocols, the mean and median air kerma for the subtracted acquisition were 52.8 and 56.0 mGy, with a range of 21.0–85.6 mGy (factory 3D-acquisition, protocol 1) and 6.4 and 6.6 mGy with a range of 5.2–7.3 mGy for the customized 3D-DSA acquisition (protocol 2). For unsubtracted 3D acquisitions (protocol 3), the mean and median air kerma were 2.7 and 2.6 mGy, with range of 1.9–3.7 mGy.

Figure 2 illustrates the considerable difference in reference

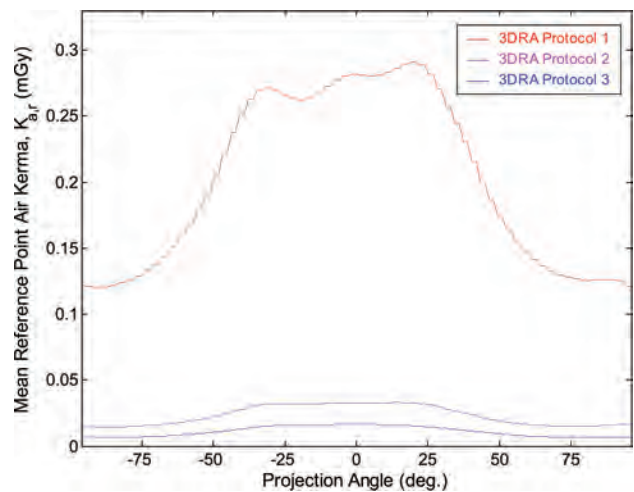


**FIG 2.** Mean reference point air kerma as a function of projection angle for 3DRA protocols 1, 2, and 3.

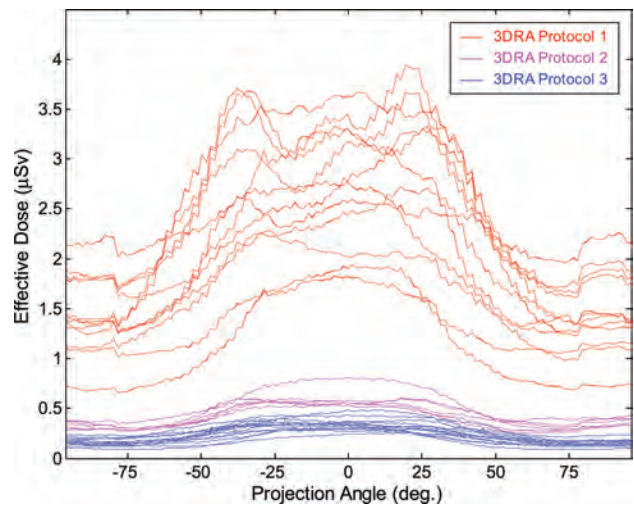


**FIG 3.** Effective dose as a function of projection angle for 3DRA protocols 1, 2, and 3. Each line indicates the effective dose for an individual rotation.

point air kerma as the tube and detector rotate about the patient in 3DRA. Each data point corresponds to the mean  $K_{a,r}$  across all patients, acquired using protocols 1, 2, and 3. The deviation in air kerma around the 200° rotation is a function of the nonuniform attenuation and thickness of the patient and the presence of table, pad, and head support. The larger relative difference observed in data from protocol 1 is due to its absence of copper filtration and reduced beam quality (half-value layer), decreasing its penetrating power and augmenting the impact of patient attenuation.

Effective dose as a function of projection angle is shown in Fig 3. All individual rotations are shown and follow a similar distribution as in Fig 2. The variation observed within each curve is indicative of deviation caused by the Monte Carlo process. The relative variability in protocol 1 was due to differences in patient head size, age, attenuation, and beam quality described earlier.

Summing across individual curves in Fig 3 determines the effective dose for each 3D rotation. These data are shown in Fig 4, aggregated across protocol and summed for subtracted

3DRA, alongside the effective dose for 2D-biplane DSA. The mean effective dose for biplane 2D imaging was 0.9 mSv, with a range of 0.2–1.7 mSv. This was significantly greater than the dose for subtracted 3DRA (factory: mean, 0.5 mSv; range, 0.3–0.7 mSv), customized subtracted (mean, 0.12 mSv; range, 0.10–0.13 mSv), and unsubtracted (mean, 0.06 mSv; range, 0.04–0.08 mSv) acquisitions. Data are summarized in Table 3.

Regarding organ dose estimates, the mean absorbed dose to the brain for biplane 2D imaging was 15 mGy, with range of 4.2–31 mGy, greater than the dose for subtracted 3DRA (factory: mean, 9.4 mGy; range, 4.1–14 mGy), customized subtracted (mean, 2.4 mGy; range, 2.1–2.7 mGy), and unsubtracted (mean, 1.2 mGy; range, 0.8–1.6 mGy) protocols. A similar relationship was calculated for active bone marrow, with mean absorbed dose estimates for 2D imaging = 2.1 mGy, subtracted 3DRA = 1.5 mGy, customized subtracted 3DRA = 0.3 mGy, and unsubtracted 3DRA = 0.2 mGy. Because the thyroid was outside the primary FOV in all acquisitions, mean doses were low, with 2D imaging

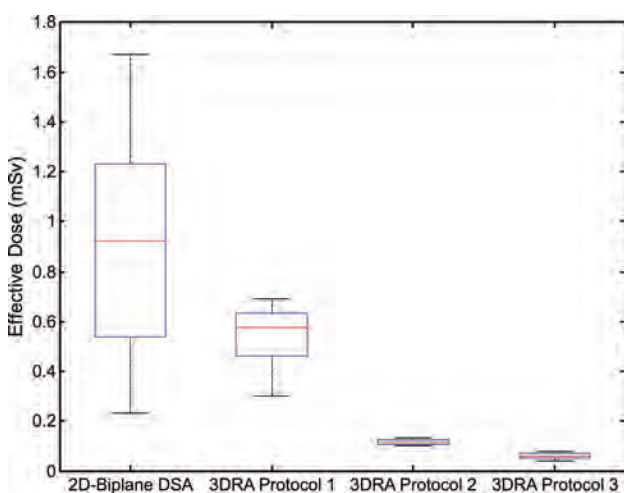


**FIG 4.** Box-and-whisker plot depicting the effective dose of biplane DSA and 3DRA protocols across all patients. Boxes denote median, lower, and upper quartiles, with whiskers capturing values outside the interquartile range.

**Table 3: Mean, median, and range of effective dose as a function of acquisition type and protocol**

	Effective Dose (mSv)		
	Mean	Median	Range
2D			
Biplane DSA	0.89	0.92	0.23–1.7
3D			
Protocol 1	0.54	0.57	0.3–0.69
Protocol 2	0.12	0.11	0.1–0.13
Protocol 3	0.06	0.06	0.04–0.08

**Table 4: Relative effective dose comparison indicating mean, median, and range for direct and normalized comparisons**

	Relative Effective Dose					
	$E_{3DRA}/E_{2D-DSA}$ (%)			$(E_{3DRA}/E_{2D-DSA})_{Normalized}$ (%)		
	Mean	Median	Range	Mean	Median	Range
Protocol 1	68	65	27–127	61	67	25–103
Protocol 2	15	13	10–24	14	13	7.4–23
Protocol 3	8.9	6.1	3.3–29	7.5	6.8	3.4–12

delivering 1.2 mGy and 3D acquisitions delivering 0.3, 0.1, and 0.06 mGy across protocols 1, 2, and 3, respectively.

One source of variability in the 2D-biplane data was the duration of each acquisition (total number of DSA frames), because it was free to vary depending on clinical needs. To account for this, the 2D data were also normalized to a run length of 60 frames (10 seconds), the median number of frames considering all DSA acquisitions (mean,  $58.4 \pm 17$  frames).

A limitation of evaluating aggregate effective doses across all subjects is that the Monte Carlo model accounted for differences in reference person (patient) age. Thus, the same 2D/3D protocol applied to a 1-year-old patient would deliver a different effective dose than that delivered to a 15-year-old patient, including adjustments for body habitus. This source of variability was removed by assessing the relative effective dose between 2D-biplane and 3D acquisitions in the same patient, in acquisitions evaluating the same vessel. This comparison delivers the formative conclusion of this work, illustrated in Table 4 and Fig 5: Customized 3DRA protocols delivered a mean of 9% (range, 3%–29%, unsubtracted) and 15% (range, 10%–24%, subtracted), the effective dose of a single 2D-biplane acquisition in the same vessel. The original subtracted protocol delivered a mean of 68%, ranging between 27% and 127% compared with 2D-biplane DSA. Figure 5 also compares the 3DRA imaging mode with normalized 2D-DSA, generalizing the results and reducing ranges to 3%–12%, 7%–22%, and 25%–103% for the customized unsubtracted, customized subtracted, and original subtracted protocols, respectively.

## DISCUSSION

Patient-centric radiation dose assessments in interventional radiology are primarily focused on the calculation of peak skin dose.<sup>20–22</sup> Although a valuable indicator of the potential for a deterministic effect (tissue reaction), skin dose is rarely the dosimetric focus in a pediatric environment due to the greater likelihood of small patient habitus and considerably lower  $K_{a,r}$  across all procedure categories. The relevant radiation concern in pediatric interventions is largely the potential stochastic effect and the current understanding that the risk in younger patients is greater than in adults.<sup>19,23</sup> Unlike in CT, quantifying the radiation burden in angiographic procedures is a difficult and protracted process. Many variables complicate dosimetry because the irradiated anatomy, geometry (positions of tubes, patient, table), acquisition type (fluoroscopy, fluorography, conebeam CT), and technical factors (choice of imaging protocol, automatic dose rate control) can vary throughout a procedure and can differ among cases.

Comparing measured and reported radiation dose surrogates is a common practice in fluoroscopic and interventional applications.<sup>24–26</sup> There is considerable utility in capturing and analyzing these metrics for use in quality programs and to establish notification and substantial radiation dose levels.<sup>27</sup> Assessing the impact of  $K_{a,r}$  and air kerma area product between interventions can be complicated as it does not account for geometric factors, colli-

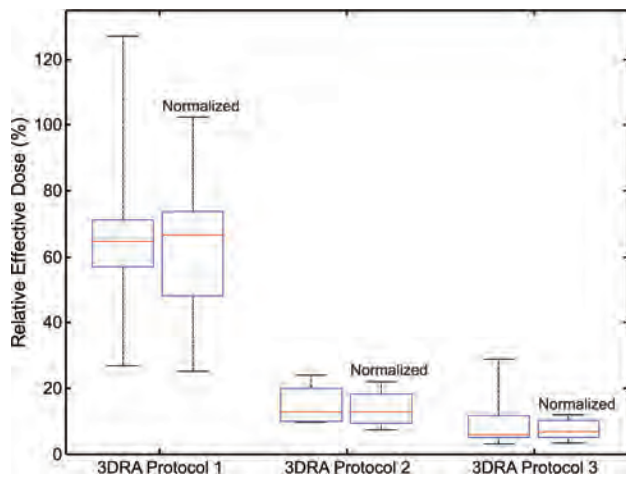


**FIG 5.** Box-and-whisker plot depicting the relative effective dose comparing 3DRA and biplane DSA acquisitions in the same patient. Relative comparison with the original 2D-DSA effective dose (*left*) and normalized DSA effective dose (*right*) for each 3DRA protocol. Boxes denote median, lower, and upper quartiles, with *whiskers* capturing values outside the interquartile range.

mation, obstacles in the path of radiation (table, pad, head support, etc) and differences in beam quality. Although these are important dosimetric metrics, they cannot provide a comprehensive assessment of radiation burden in pediatric imaging.

Effective dose is a mathematic, calculated quantity intended to act as a surrogate of risk, reflecting the detriment of a nonuniform exposure in terms of an equivalent whole-body exposure.<sup>19</sup> Because there are numerous techniques, computational steps, and variables in calculating the effective dose, values can vary by up to  $\geq 100\%$ , depending on the applied Monte Carlo model, input data, assumptions, and approximations.<sup>28</sup> Also, because estimates of biologic risk have evolved since the inception of effective dose, the concept of a “true” value is not accurate. Comparing effective doses using the same methods and calculation steps, however, allows a relative assessment of imaging events similar to those we investigated in this work. Although effective dose does not estimate the risk for individual patients, this work has value as part of an optimization process in pediatric neuroangiography. The number of significant figures described in Table 3 does not indicate precision and was not proposed to illustrate a difference in radiation risk but was intended to emphasize the dosimetric

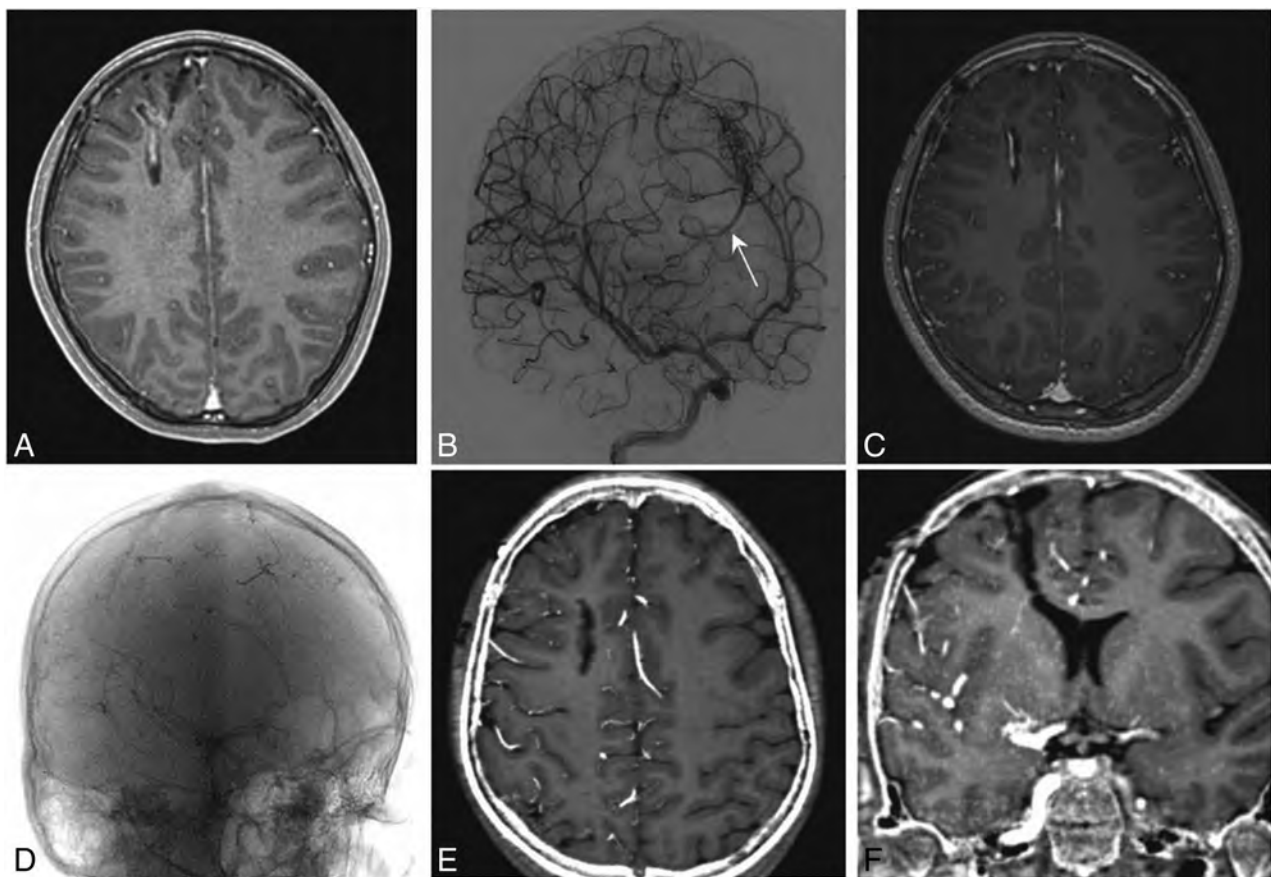


**FIG 6.** An example of the use of a 3D rotational angiographic sequence (protocol 3). A 12-year-old girl was referred from an outside institution 4 months after hemorrhage from a right frontal arteriovenous malformation. *A*, Postgadolinium axial 3D T1-weighted MR image shows the AVM nidus within a collapsed hemorrhagic cavity in the right superior frontal gyrus. *B*, Diagnostic angiography in the right internal cerebral artery in an oblique frontal projection shows the nidus fed from posterior internal frontal branches of the anterior cerebral artery, with early filling of an inferiorly draining cortical vein (*arrow*). The AVM was surgically resected, following which DSA (not shown) confirmed no residual nidus. *C*, Postgadolinium axial 3D T1-weighted MR image obtained at 6-month follow-up shows linear enhancement within the surgical cavity. Diagnostic angiography subsequently performed showed no arteriovenous shunting. *D*, 3D rotational angiography performed in the right internal cerebral artery using protocol 3 with 30% contrast concentration, subsequently reconstructed into CTA. *E* and *F*, 3D rotational angiography fused with the pregadolinium 3D T1-weighted MR imaging sequence, which confirmed no vascular structures within the surgical cavity in multiple planes.

differences in each acquisition protocol and the relative difference within specific procedures and imaging events. A similar limitation is appropriate for interpretation of the organ doses presented.

There has been a tendency to avoid performing 3DRA in children because the magnitude of its radiation use is not often fully understood. This has encouraged neuroradiologists to continue with their established standard of care (ie, multiple 2D-biplane DSA projections) in situations in which 3DRA may have been a viable and effective alternative. This work was intended to quantify and compare the dose differences between 2D and 3D acquisitions and to illustrate that the effective dose for a single 3DRA acquisition could be considerably lower than that for a typical biplane fluorographic acquisition and can be further reduced without loss of clinical utility through protocol customization. This work clearly illustrated that customized unsubtracted and subtracted 3D protocols deliver a fraction of the radiation dose delivered in a biplane 2D acquisition.

This work was one of many endeavors to better understand the application of radiation in 3D acquisitions in pediatric neuroangiographic practice. All 3DRA acquisitions reported in this article were of diagnostic quality and appropriate for clinical management of each patient, as illustrated in Fig 6. Qualitative assessments were made throughout the tuning process, and future work will measure the impact of varied 3D acquisition parameters on quantitative image quality in patients and phantoms. Although image quality is intricately linked to the conclusions of this article, the intention of this work was to determine the effective dose of customized and factory protocols acquired on patients at our institution. Additional research will evaluate the procedural impact of 3DRA in reducing the amount of fluorography in individual cases, assess the effects of varied proprietary postprocessing capabilities on quality and image acquisition, and further investigate the impact of 3DRA on patient management and outcomes.

## CONCLUSIONS

An essential responsibility of the pediatric neuroangiographer is the knowledge of radiation dose for individual actions within the interventional suite. This includes the relative magnitude of conventional DSA and 3DRA acquisition techniques. With customization of 3D acquisition protocols, the effective dose for 3DRA can be significantly lower than for 2D-biplane imaging, solidifying its place as an essential adjunct in the evaluation of neurovascular lesions.

## ACKNOWLEDGMENTS

We acknowledge Dr Timo Krings, Dr Vitor Pereira, Dr Peter Dirks, Dr James Drake, Vanessa Rea, and Evan Kitamura for their contributions to this work.

## REFERENCES

- Honarmand A, Gemmete J, Hurley M, et al. **Adjunctive value of intra-arterial cone beam CT angiography relative to DSA in the evaluation of cranial and spinal arteriovenous fistulas.** *J Neurointerv Surg* 2014;7:517–23 CrossRef Medline
- Safain M, Rahal J, Patel S, et al. **Superior performance of conebeam CT angiography in characterization of intracranial atherosclerosis.** *J Neurosurg* 2014;121:441–49 CrossRef Medline
- Schulz C, Schmitt M, Böckler D, et al. **Intraoperative contrast-enhanced cone beam computed tomography to assess technical success during endovascular aneurysm repair.** *J Vasc Surg* 2016;64:577–84 CrossRef Medline
- Patel N, Gounis M, Wakhloo A, et al. **Contrast-enhanced angiographic cone-beam CT of cerebrovascular stents: experimental optimization and clinical application.** *AJNR Am J Neuroradiol* 2011;32:137–44 CrossRef Medline
- Namba K, Niimi Y, Song J, et al. **Use of Dyna-CT angiography in neuroendovascular decision-making: a case report.** *Interv Neuroradiol* 2009;15:67–72 CrossRef Medline
- Orth R, Wallace M, Kuo M; Technology Assessment Committee of the Society of Interventional Radiology. **C-arm cone-beam CT: general principles and technical considerations for use in interventional radiology.** *J Vasc Interv Radiol* 2009;20:S538–44 CrossRef Medline
- Muthusami P, Shkumat N, Rea V, et al. **CT reconstruction and MRI fusion of 3D rotational angiography in the evaluation of pediatric cerebrovascular lesions.** *Neuroradiology* 2017;59:625–33 CrossRef Medline
- Wallace M, Kuo M, Glaiberman C, et al; Technology Assessment Committee of the Society of Interventional Radiology. **Three-dimensional C-arm cone-beam CT: applications in the interventional suite.** *J Vasc Interv Radiol* 2008;19:799–813 CrossRef Medline
- Thierry-Chef I, Simon S, Miller D. **Radiation dose and cancer risk among pediatric patients undergoing interventional neuroradiology procedures.** *Pediatr Radiol* 2006;36:159–62 CrossRef Medline
- Orbach D, Stamoulis C, Strauss K, et al. **Neurointerventions in children: radiation exposure and its import.** *AJNR Am J Neuroradiol* 2014;35:650–56 CrossRef Medline
- Wielandts J, De Buck S, Ector J, et al. **Three-dimensional cardiac rotational angiography: effective radiation dose and image quality implications.** *Europace* 2010;12:194–201 CrossRef Medline
- Peters M, Krings G, Koster M, et al. **Effective radiation dosage of three-dimensional rotational angiography in children.** *Europace* 2015;17:611–16 CrossRef Medline
- Kim S, Yoshizumi T, Frush D, et al. **Radiation dose from cone beam CT in a pediatric phantom: risk estimation of cancer incidence.** *AJR Am J Roentgenol* 2010;194:186–90 CrossRef Medline
- Wang C, Nguyen G, Toncheva G, et al. **Evaluation of patient effective dose of neurovascular imaging protocols for C-arm cone-beam CT.** *AJR Am J Roentgenol* 2014;202:1072–77 CrossRef Medline
- Wielandts J, Smans K, Ector J, et al. **Effective dose analysis of three-dimensional rotational angiography during catheter ablation procedures.** *Phys Med Biol* 2010;55:563–79 CrossRef Medline
- Bai M, Liu X, Liu B. **Effective patient dose during neuroradiological C-arm CT procedures.** *Diagn Interv Radiol* 2013;19:29–32 CrossRef Medline
- Lin P, Schueler B, Balter S, et al. **Accuracy and calibration of integrated radiation output indicators in diagnostic radiology: a report of the AAPM Imaging Physics Committee Task Group 190.** *Med Phys* 2015;42:6815–29 CrossRef Medline
- Tapiovaara M, Siiskonen T. **PCXMC: a Monte Carlo program for calculating patient doses in medical x-ray examinations.** Helsinki: STUK; 2008
- The 2007 Recommendations of the International Commission on Radiological Protection.** *Ann ICRP* 2007;37:1–332 CrossRef Medline
- Khodadadegan Y, Zhang M, Pavlicek W, et al. **Validation and initial clinical use of automatic peak skin dose localization with fluoroscopic and interventional procedures.** *Radiology* 2013;266:246–55 CrossRef Medline
- Kwon D, Little M, Miller D. **Reference air kerma and kerma-area product as estimators of peak skin dose for fluoroscopically guided interventions.** *Med Phys* 2011;38:4196–204 CrossRef Medline
- Vano E, Fernandez J, Sanchez R, et al. **Patient radiation dose management in the follow-up of potential skin injuries in neuroradiology.** *AJNR Am J Neuroradiol* 2013;34:277–82 CrossRef Medline
- Committee to Assess Health Risks from Exposure to Low Levels of Ionizing Radiation. **Health Risks from Exposure to Low Levels of Ionizing Radiation.** *Health Risks from Exposure to Low Levels of Ionizing Radiation* 2002;1–600 National Academies Press

- ing Radiation: BEIR VII Phase 2.* Washington, DC: National Academies Press; 2006
24. Chida K, Saito H, Otani H, et al. **Relationship between fluoroscopic time, dose-area product, body weight, and maximum radiation skin dose in cardiac interventional procedures.** *AJR Am J Roentgenol* 2006;186:774–78 CrossRef Medline
  25. Chida K, Ohno T, Kakizaki S, et al. **Radiation dose to the pediatric cardiac catheterization and intervention patient.** *AJR Am J Roentgenol* 2010;195:1175–79 CrossRef Medline
  26. Manica J, Borges M, Medeiros R, et al. **A comparison of radiation dose between standard and 3D angiography in congenital heart disease** [in English, Portuguese]. *Arg Bras Cardiol* 2014;103:131–37 Medline
  27. Radiation Dose Management for Fluoroscopically Guided Interventional Medical Procedures. Bethesda: National Council on Radiation Protection and Measurements. Report No. 168 2010
  28. McCollough C, Christner J, Kofler J. **How effective is effective dose as a predictor of radiation risk?** *AJR Am J Roentgenol* 2010;194:890–96 CrossRef Medline

# A Patient Dose-Reduction Technique for Neuroendovascular Image-Guided Interventions: Image-Quality Comparison Study

A. Sonig, S.V. Setlur Nagesh, V.S. Fennell, S. Gandhi, L. Rangel-Castilla, C.N. Ionita, K.V. Snyder, L.N. Hopkins, D.R. Bednarek, S. Rudin, A.H. Siddiqui, and E.I. Levy



## ABSTRACT

**BACKGROUND AND PURPOSE:** The ROI–dose-reduced intervention technique represents an extension of ROI fluoroscopy combining x-ray entrance skin dose reduction with spatially different recursive temporal filtering to reduce excessive image noise in the dose-reduced periphery in real-time. The aim of our study was to compare the image quality of simulated neurointerventions with regular and reduced radiation doses using a standard flat panel detector system.

**MATERIALS AND METHODS:** Ten 3D-printed intracranial aneurysm models were generated on the basis of a single patient vasculature derived from intracranial DSA and CTA. The incident dose to each model was reduced using a 0.7-mm-thick copper attenuator with a circular ROI hole (10-mm diameter) in the middle mounted inside the Infinix C-arm. Each model was treated twice with a primary coiling intervention using ROI-dose-reduced intervention and regular-dose intervention protocols. Eighty images acquired at various intervention stages were shown twice to 2 neurointerventionalists who independently scored imaging qualities (visibility of aneurysm-parent vessel morphology, associated vessels, and/or devices used). Dose-reduction measurements were performed using an ionization chamber.

**RESULTS:** A total integral dose reduction of 62% per frame was achieved. The mean scores for regular-dose intervention and ROI dose-reduced intervention images did not differ significantly, suggesting similar image quality. Overall intrarater agreement for all scored criteria was substantial (Kendall  $\tau = 0.62887$ ;  $P < .001$ ). Overall interrater agreement for all criteria was fair ( $\kappa = 0.2816$ ; 95% CI, 0.2060–0.3571).

**CONCLUSIONS:** Substantial dose reduction (62%) with a live peripheral image was achieved without compromising feature visibility during neuroendovascular interventions.

**ABBREVIATIONS:** DRI = dose-reduced intervention; RDI = regular-dose intervention

X-ray dose reduction during interventional radiology procedures is of paramount importance. The concept of x-ray dose reduction using ROI fluoroscopy has been previously introduced (On-line Fig 1).<sup>1–3</sup> An extension of this concept is a technique that combines dose reduction with spatially different recursive tempo-

ral filtering to reduce excessive noise in the peripheral dose-reduced region (ie, the region outside the ROI but within the FOV) and thereby restore image quality for improved visualization during an intervention.<sup>4–6</sup> Spatially different temporal filtering is a mathematic filter that reduces noise in the fluoroscopic image. Our research team has constructed 3D printed models<sup>7,8</sup> that simulate patient-specific cerebrovascular anatomy and have been used to assess neuroendovascular techniques for stroke intervention, aneurysm coiling, and parametric imaging.<sup>8–12</sup>

In this study, we applied extended ROI fluoroscopy with enhanced visualization of the peripheral field during a simulated neuroendovascular intervention using patient-specific 3D printed

Received September 14, 2017; accepted after revision December 6.

From the Departments of Neurosurgery (A.S., V.S.F., L.R.-C., C.N.I., K.V.S., L.N.H., D.R.B., S.R., A.H.S., E.I.L.), Radiology (K.V.S., L.N.H., D.R.B., S.R., A.H.S., E.I.L.), and Neurology (S.G., K.V.S.), Jacobs School of Medicine and Biomedical Sciences, University at Buffalo, State University of New York, Buffalo, New York; Department of Neurosurgery (A.S., V.S.F., S.G., L.R.-C., K.V.S., L.N.H., S.R., A.H.S., E.I.L.), Gates Vascular Institute at Kaleida Health, Buffalo, New York; Toshiba Stroke and Vascular Research Center (S.V.S.N., C.N.I., L.N.H., D.R.B., S.R., A.H.S., E.I.L.), Department of Biomedical Engineering (C.N.I., S.R.), Department of Mechanical and Aerospace Engineering (S.R.), and Department of Electrical Engineering (S.R.), University at Buffalo, State University of New York, Buffalo, New York; Buffalo Neuroimaging Analysis Center (S.G.), Buffalo, New York; and Jacobs Institute (L.N.H., A.H.S.), Buffalo, New York.

Ashish Sonig and Swetadri Vasan Setlur Nagesh are co-first authors.

Paper previously presented as an oral presentation at: Annual Meeting of the Congress of Neurological Surgeons Meeting, September 26–30, 2015; New Orleans, Louisiana.

This work was supported, in part, by National Institutes of Health grant R01EB002873 and an equipment grant from Toshiba Medical Systems Corporation.

Please address correspondence to Elad I. Levy, MD, MBA, University at Buffalo Neurosurgery, 100 High St, Suite B4, Buffalo, NY 14203; e-mail: eleyv@ubns.com

Indicates open access to non-subscribers at www.ajnr.org

Indicates article with supplemental on-line photos.

<http://dx.doi.org/10.3174/ajnr.A5552>

phantoms. The aim of our study was to compare the image quality of simulated neurointervention with regular and reduced radiation doses using a standard flat panel detector system.

## MATERIALS AND METHODS

### Dose Reduction

An x-ray beam modulated by a differential attenuator reduces the actual dose of radiation received by a patient. A 0.7-mm uniform thick copper plate<sup>13</sup> (offering 75%–80% attenuation for peak kilovoltage, ranging from 70 to 80 kV[peak]) with a central circular void of 10 mm in diameter was used as an attenuator.<sup>14</sup> This attenuator was mounted in place of an existing compensation filter inside the x-ray tube assembly of the Infinix C-arm (manufactured in 2012; Toshiba America Medical Systems, Tustin, California) and was moveable within the FOV. The mobility ensured that the circular opening could be placed over the treatment area (ie, the ROI). The ROI, which comprised 18% of the total FOV (8 inches × 8 inches in the flat panel detector), received the regular dose. The area outside the ROI (periphery) received a lower dose, thus reducing the overall dose per frame.

The regular-dose intervention (RDI) simulations were performed using the technique parameters (kilovolt[peak], milliamperere, and millisecond) calculated by the automatic exposure control of the x-ray unit. To maintain the entrance air kerma within the ROI, we manually set the exposure parameters to the same values as the RDI parameters. The ROI attenuator was moved into the FOV, with the ROI aligned over the aneurysm; then, the ROI-dose-reduced intervention (DRI) simulations were performed. The average exposure parameters for all the interventions were  $70 \pm 2$  kVp,  $50 \pm 10$  mA, and  $10 \pm 2$  ms.

The ratio of the kerma-area product with and without the dose-reduction technique was used to assess the total amount of dose reduction achieved per image. The ratio is defined as

$$\frac{KAP_{\text{dose reduced}}}{KAP_{\text{regular}}} = \frac{KAP_{\text{periphery}} \times (FOV - ROI) + K_{\text{ROI}} \times ROI}{K_{\text{ROI}} \times FOV},$$

where  $K_{\text{ROI}}$  is the entrance air kerma measured within the ROI and  $K_{\text{periphery}}$  is the entrance air kerma measured in the periphery. The air kerma was measured separately for the average exposure parameters using a 6-CC ionization chamber (TN34069; PTW Freiburg, Freiburg, Germany). The ionization chamber was placed beneath the patient table for detection of radiation in the ROI and the periphery. The measurements were repeated, and the averaged measurements were used for calculations.

### Image Enhancement

Dose reduction using an attenuator results in an image with less brightness in the periphery (ie, those regions in which the radiation dose has been reduced). For improved visualization, the initial step is to equalize the brightness of the ROI and periphery. One approach is to subtract a mask image of the ROI attenuator; this step equalizes the brightness.<sup>2,3</sup> In this study, all interventions were performed using the roadmap imaging technique. While using the ROI attenuator during roadmap generation, we registered the current position of the attenuator in the bone mask, which was then subtracted from the subsequent fluoroscopic images; this subtraction equalized brightness in the image. The pe-

riphery has excess noise due to a lower dose reaching the detector. To decrease this noise and improve the signal-to-noise ratio, we used a novel spatially different recursive temporal filtering technique.

The following equation<sup>15</sup> was used for the recursive temporal filtering technique:

$$I_{\text{current\_output}}(x, y) = I_{\text{input}}(x, y) \times (1 - \alpha) + I_{\text{previous\_output}}(x, y) \times \alpha,$$

where  $\alpha$  is the filter weight, ranging from 0 to 1;  $(x, y)$  is the spatial position of the pixel in the image;  $I_{\text{input}}$  is the current image;  $I_{\text{previous\_output}}$  is the previous noise-reduced image; and  $I_{\text{current\_output}}$  is the current noise-reduced image.

For the image pixels in the periphery, a higher filter weight of 0.7 was used to reduce the excessive noise, but this resulted in an increased image lag and loss in temporal resolution. However, for the pixels within the ROI, a lower filter weight of 0.2 was used, thus preserving temporal resolution.<sup>5,6</sup> Under these conditions, the signal-to-noise ratios in uniform regions within the ROI and in the dose-reduced periphery were similar.

### 3D Printed Model Setup

After receiving approval from our institutional review board at University at Buffalo (IRB 567513), we generated ten 3D printed aneurysm models (Objet Eden 260V PolyJet 3D printer; Stratasys, Eden Prairie, Minnesota) from 1 patient's 3D rotational intracranial DSA and CTA. Details of the additive printing process are found in earlier publications.<sup>7,8</sup> A 21-mm-thick aluminum block was placed in the FOV to simulate the attenuation offered by the cranium. For a 70- to 76-kVp input x-ray spectrum, the beam quality reaching the detector with a 21-mm aluminum block in the FOV is similar to the average beam quality with a head.<sup>16</sup>

All aneurysms underwent primary coiling, with each aneurysm treated with the same set of devices: 7F Shuttle-SL guide sheath (Cook Medical, Bloomington, Indiana), SL-10 microcatheter (Stryker Neurovascular, Kalamazoo, Michigan), 0.14-inch Synchro 14 microguidewire (Stryker Neurovascular), and 8 mm × 20 cm Target 360 soft coils (Stryker Neurovascular). A 50% dilution of iohexol solution (Omnipaque 240; GE Healthcare, Piscataway, New Jersey) was used as the contrast agent for all DSA runs. These images were acquired at a research computer station using custom-built acquisition software.

### Image Analysis

**Subjective Assessment.** Two experienced neurointerventionalists evaluated the images randomly displayed on the research station. Both were blinded to patient data and ROI status. These raters evaluated and scored the diagnostic quality of the regular DSA (ie, RDI) and DSA when the ROI was applied for dose reduction (ROI-DRI).

Each aneurysm was treated using both the ROI-DRI and the RDI protocols. For each aneurysm coiling intervention, a set of 4 images was generated at various stages of the intervention. Thus, each intervention generated 8 images (ie, 4 ROI-DRI images; Fig 1; and 4 RDI images; On-line Fig 2).

Both RDI and ROI-DRI images were acquired at the following stages of the simulated intervention:

- Angiographic run preintervention: diagnostic DSA showing aneurysm and parent vessel morphology and associated proximal and distal vasculature (Fig 1A).
- Microwire navigation: roadmap image showing the microwire

inside the aneurysm and leaving the tip of the guide catheter (Fig 1B).

- Microcatheter navigation: roadmap image showing the guide tip and microcatheter inside the aneurysm (Fig 1C).
- Postcoiling: roadmap image showing the coils inside the aneurysm and the guide catheter tip (Fig 1D).

For each defined stage, image quality was rated in 3 categories:

Unacceptable, when it was difficult to discern any of the following: vessel morphology (Table 1 angiographic run preintervention 1, 2, and 3), aneurysm morphology, and devices (guide, microcatheter, coils, microwire).

Acceptable, when it was easy to discern all the following: vessel morphology, aneurysm morphology, and devices (guide, microcatheter, coils, microwire).

High, when the discernibility was superior to the rater's experience with conventional angiography in all of the following: vessel morphology, aneurysm morphology, and devices (guide, microcatheter, coils, microwire). Table 1 lists the different criteria along with the 3 rating options presented to each rater.

Eighty images from the 10 aneurysms were acquired at the defined stages of the intervention. Each image was shown twice to the 2 neurointerventionalist raters, and each reviewed 160 images and rated 200 criteria individually. When the raters gave the same score for the same criteria, it was marked as "agreement"; otherwise, it was marked as "disagreement." A total of 400 rating responses were obtained and analyzed.

### Statistical Analysis

The Wilcoxon signed rank sum test was used to compare the scores from the neurointerventionalists' ratings of the RDI and ROI-DRI images. Intrarater

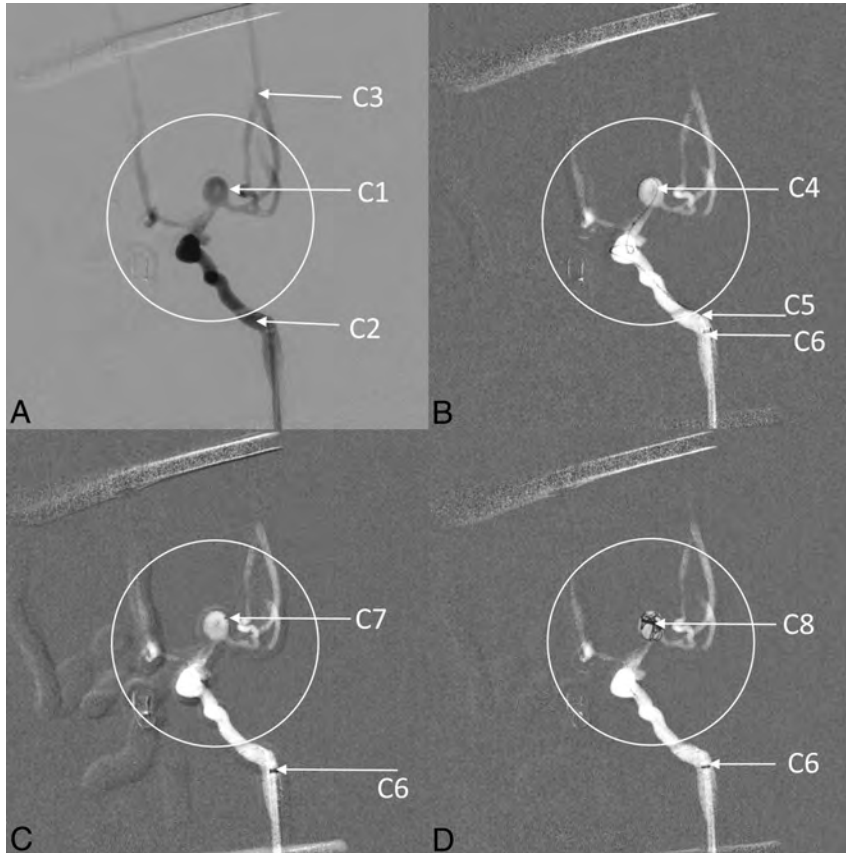


**FIG 1.** A, A single frame from an ROI–dose-reduced-intervention DSA run. Parent vessel morphology (C1), proximal vessels (C2), and distal vessels (C3) are visible (arrows). The position of the ROI is indicated by the white circular boundary. B, A single frame of the ROI-DRI fluoroscopic roadmap. The microwire is seen leaving the guide catheter (C5) and inside the aneurysm (C4). The guide catheter tip is visible (C6). C, A single frame of the ROI-DRI fluoroscopic roadmap. The guide tip is seen (C6). The distal tip of the microcatheter is seen inside the aneurysm (C7). D, A single frame of the ROI-DRI fluoroscopic roadmap. The coil is visible inside the aneurysm (C8). The guide tip is visible (C6). In comparison with the RDI images shown in On-line Fig 2, the integral dose for each of these ROI-DRI images is 38% of the integral dose of the RDI images, thus achieving an integral dose reduction of 62%.

**Table 1: Image-quality ratings<sup>a</sup>**

Timing of Image Acquisition	Visibility of	Scores Unacceptable	Scores Acceptable	Scores High
Angiographic run preintervention	1) Aneurysm-parent vessel morphology (C1)	1	2	3
	2) Proximal vessel (C2)	1	2	3
	3) Distal vessel (C3)	1	2	3
Microwire navigation	4) Microwire inside aneurysm (C4)	1	2	3
	5) Microwire leaving guide (C5)	1	2	3
	6) Guide tip (C6)	1	2	3
Microcatheter navigation	7) Distal tip of microcatheter in aneurysm (C7)	1	2	3
	8) Guide tip (C6)	1	2	3
Postcoiling	9) Coil inside aneurysm (C8)	1	2	3
	10) Guide tip (C6)	1	2	3

**Note:**—C indicates criterion.

<sup>a</sup> Used to evaluate the diagnostic quality of both standard cerebral angiograms and cerebral angiograms when the ROI was applied for x-ray dose reduction.

**Table 2: Summary statistics for scores of image quality with and without ROI-DRI application**

Visibility of	ROI-DRI Applied	Rater 1 Frequency of Scores <sup>a</sup>			Rater 2 Frequency of Scores <sup>a</sup>			Rater 1			Rater 2		
		1	2	3	1	2	3	Mean/Median	SD	P Value	Mean/Median	SD	P Value
		(C1) <sup>b</sup>	Yes	0	14	6	0	16	4	2.30/2.0	0.47	.75	2.20/2
	No	2	8	10	0	16	4	2.40/2.5	0.68		2.20/2	0.41	
(C2) <sup>b</sup>	Yes	1	9	10	0	15	5	2.45	0.60	.77	2.25	0.44	.62
	No	1	7	12	0	17	3	2.55	0.60		2.15	0.37	
(C3) <sup>b</sup>	Yes	1	13	6	1	16	3	2.25/2	0.55	1.00	2.10	0.45	1.00
	No	2	10	8	1	16	3	2.30/2	0.66		2.10	0.45	
(C4) <sup>b</sup>	Yes	1	7	12	0	13	7	2.55	0.60	1.00	2.35	0.49	.12
	No	2	6	12	0	17	3	2.50	0.69		2.15	0.37	
(C5) <sup>b</sup>	Yes	1	14	5	0	16	4	2.20/2	0.52	.53	2.20/2	0.41	.62
	No	1	17	2	2	17	1	2.05/2	0.39		1.95/2	0.39	
(C6) <sup>c</sup>	Yes	16	35	9	15	40	5	1.88/2	0.64	.09	1.83/2	0.56	.47
	No	6	46	8	12	43	5	2.03/2	0.49		1.88/2	0.52	
(C7) <sup>b</sup>	Yes	2	13	5	0	17	3	2.15/2	0.59	1.00	2.15/2	0.37	.37
	No	3	12	5	2	16	2	2.10/2	0.64		2.00/2	0.46	
(C8) <sup>b</sup>	Yes	0	7	13	0	10	10	2.65/3	0.49	.62	2.50/2.5	0.51	.5
	No	0	5	15	0	12	8	2.75/3	0.44		2.40/2.5	0.50	

<sup>a</sup> Image-quality scores: 1 = unacceptable, 2 = acceptable, 3 = high quality.

<sup>b</sup> A total of 10 aneurysms were treated. Each treated aneurysm (ROI-DRI or standard) had 1 C1/C2/C3/C4/C5/C7/C8 criterion to rate and 3 C6 criteria (because it appears thrice on the basis of the treatment stage, Table 1). Thus, 10 C1/C2/C3/C4/C5/C7/C8 criteria were rated by each rater for 10 aneurysms that were treated by either the standard or ROI-DRI approach. Because each image was shown twice to a rater, it resulted in the rating of 20 C1/C2/C3/C4/C5/C7/C8 criteria each in the ROI-DRI and standard images.

<sup>c</sup> The C6 count is 60 because the C6 criterion appears thrice on the basis of the treatment stage.

agreement was measured by Kendall  $\tau$ -b correlation coefficient, which is a nonparametric measure of association based on the number of concordances and discordances in paired observations. The paired variables were considered correlated if the correlation coefficient was close to 1 and uncorrelated if the correlation coefficient was close to zero. Interrater agreement was measured by  $\kappa$  statistics. Assessment of the degree of agreement was based on  $\kappa$  values (<0 = poor, 0.01–0.20 = slight, 0.21–0.40 = fair, 0.41–0.60 = moderate, 0.61–0.80 = substantial, 0.81–0.99 = almost perfect). Because each image was rated twice by the same reviewer, bootstrap resampling was used to calculate the  $\kappa$  statistics.

## RESULTS

In this study, the  $K_{ROI}$  was measured as an average of 0.45 mGy per frame, and the  $K_{Periphery}$  was measured as an average of 0.11 mGy per frame. The ROI area was 18% of the total FOV. The total kerma-area product with and without the dose-reduction technique was calculated as 25.44 and 66.89 mGy  $\times$  cm<sup>2</sup>, respectively. Using these values, we calculated the kerma-area product ratio with and without the dose-reduction technique to be 38%. Therefore, the integral dose per frame with the ROI attenuator was 38% of the integral dose per frame without the ROI attenuator, thus achieving an integral dose reduction of 62% per image. The air kerma in the periphery with the ROI-DRI was 20% of that in side the ROI.

The mean scores for ratings of the ROI-DRI images and RDI images were compared. None of the criteria scores were statistically different (Table 2). Visibility of the guide catheter tip was evaluated on images obtained during microwire navigation, microcatheter navigation, and postcoiling, for a total of 120 rating responses. However, no significant difference was seen (rater 1,  $P = .095$ ; rater 2,  $P = .47$ ) for ROI-DRI images versus RDI images.

## Intrarater Agreement

Tables 3 and 4 show the frequency, percentage, and Kendall  $\tau$  correlation coefficients of agreement for each rater. For visibility of the tip of the guide catheter, substantial agreement was seen in rater 1's intrarater assessment of the ROI-DRI ( $P < .001$ , Kendall  $\tau = 0.716$ ) and the RDI ( $P < .001$ , Kendall  $\tau = 0.699$ ), whereas agreement was moderate (ROI-DRI, Kendall  $\tau = 0.569$ ) to fair (RDI, Kendall  $\tau = 0.398$ ) in rater 2's assessment. For each criterion in which visibility outside the ROI (ie, periphery) was assessed (proximal vessel, distal vessel, microwire leaving the guide catheter, and guide catheter tip), intrarater agreement ranged from moderate to perfect (Tables 3 and 4). The overall intrarater agreement for raters 1 and 2 was substantial (Kendall  $\tau = 0.62887$ ,  $P$  value  $< .001$ ). For ROI images, the Kendall  $\tau$  was 0.63171 with  $P < .001$ ; and for images without ROIs, the Kendall  $\tau$  was 0.62789 with  $P < .001$  (Tables 3 and 4).

## Interrater Agreement

The  $\kappa$  characteristic ranged from  $-0.0345$  (for visibility of the aneurysm and parent vessel morphology) to 0.7 (for visibility of the coil inside the aneurysm) (Table 5). More than 50% agreement was achieved in all criteria ratings for ROI-DRI intervention cases. In cases of RDI intervention,  $>50\%$  agreement was seen in 75% of the ratings.

The overall interrater agreement for all criteria was fair ( $\kappa = 0.2816$ ; 95% CI, 0.2060–0.3571). In an analysis of the cohorts separately, the  $\kappa$  value was 0.2832 (95% CI, 0.1697–0.3967) in the ROI-DRI cohort and 0.2358 (95% CI, 0.1345–0.3371) in the RDI cohort.

## DISCUSSION

Dose reduction in x-ray image-guided interventions is of paramount concern. ROI fluoroscopy, a dose-reduction technique us-

**Table 3: Intrarater agreement relative to image-quality assessment with the Kendall  $\tau$  correlation coefficients**

Visibility of	ROI-DRI Applied	Rater 1		Rater 2		Rater 1		Rater 2	
		(f) (%)	(f) (%)	Kendall $\tau$	P Value	Kendall $\tau$	P Value		
C1	Yes	8 (80)	10 (100)	0.52381	.12	1.00000	.0027 <sup>a</sup>		
	No	10 (100)	8 (80)	1.00000	.001 <sup>a</sup>	0.37500	.2606		
C2	Yes	7 (70)	7 (70)	0.59423	.06	0.40825	.2207		
	No	5 (50)	9 (90)	0.32418	.31	0.66667	.0455 <sup>a</sup>		
C3	Yes	7 (70)	8 (80)	0.59588	.06	0.54571	.0935		
	No	10 (100)	8 (80)	1.00000	.001 <sup>a</sup>	0.54571	.0935		
C4	Yes	7 (70)	5 (50)	0.58926	.06	0.27217	.4142		
	No	6 (60)	9 (90)	0.61721	.05	0.66667	.0455 <sup>a</sup>		
C5	Yes	9 (90)	10 (100)	0.31851	.32	1.00000	.0027 <sup>a</sup>		
	No	9 (90)	7 (70)	0.72761	.02 <sup>a</sup>	0.16667	.6171		
C6	Yes	26 (86.7)	20 (66.7)	0.71659	<.001 <sup>a</sup>	0.56984	.0012 <sup>a</sup>		
	No	26 (86.7)	15 (50)	0.69942	<.001 <sup>a</sup>	0.39829	.0295 <sup>a</sup>		
C7	Yes	9 (90)	7 (70)	0.84270	.007 <sup>a</sup>	-0.16667	.6171		
	No	8 (80)	8 (80)	0.76376	.01 <sup>a</sup>	0.62554	.0528		
C8	Yes	9 (90)	8 (80)	0.80178	.01 <sup>a</sup>	0.66667	.0455 <sup>a</sup>		
	No	7 (70)	8 (80)	0.21822	.51	0.65465	.0495 <sup>a</sup>		

Note:—f indicates frequency.

<sup>a</sup> Significant.

**Table 4: Overall Kendall  $\tau$  correlation coefficients**

	Kendall $\tau$	P Value		Kendall $\tau$	P Value
Rater 1	0.70822	<.001 <sup>a</sup>	With ROI	0.69476	<.001 <sup>a</sup>
			Without ROI	0.73072	<.000 <sup>a</sup>
Rater 2	0.49899	<.001 <sup>a</sup>	With ROI	0.55057	<.000 <sup>a</sup>
			Without ROI	0.45918	<.001 <sup>a</sup>
Pooled	0.62887	<.001 <sup>a</sup>	With ROI	0.63171	<.001 <sup>a</sup>
			Without ROI	0.62789	<.001 <sup>a</sup>

<sup>a</sup> Significant.

**Table 5: Interrater agreement relative to image-quality assessment with  $\tau$  statistics with bootstrap resampling**

Visibility of	ROI-DRI Applied	Frequency	Percentage	$\kappa$	95% CI (Lower)	95% CI (Upper)
C1	Yes	16	80	0.4737	0.0438	0.9036
	No	8	40	-0.0345	-0.3341	0.2651
C2	Yes	12	60	0.2558	-0.0765	0.5881
	No	14	70	0.2040	0.2212	0.2620
C3	Yes	12	60	0.0751	-0.2676	0.4179
	No	11	55	0.1589	-0.1344	0.4521
C4	Yes	10	50	0.1111	-0.2336	0.4559
	No	9	45	0.1603	-0.0227	0.3433
C5	Yes	17	85	0.6154	0.2684	0.9623
	No	16	80	0.2523	-0.2669	0.7715
C6	Yes	31	51.67	0.0914	-0.1349	0.3177
	No	39	65	0.1656	-0.0773	0.4084
C7	Yes	10	50	-0.2195	-0.4131	-0.0259
	No	12	60	0.1667	-0.1959	0.5293
C8	Yes	17	85	0.7000	0.4014	0.9986
	No	13	65	0.3636	0.0705	0.6568

ing an x-ray beam—modulating ROI attenuator, was first presented in earlier work<sup>1</sup>; the use of this attenuator was subsequently demonstrated in an anthropomorphic phantom.<sup>2</sup> Image brightness was equalized by subtracting a preacquired mask of the attenuator. A similar concept to the ROI attenuator is the x-ray fovea introduced by Labbe et al,<sup>17</sup> which is a device that uses a semitransparent collimator with an open circular hole to reduce the dose. In that study, the authors compensated for image brightness by scaling the pixel intensity value according to the ratio of the attenuation coefficients of the attenuator in the ROI and the periphery. Comparable with these concepts was the work

by Robert et al<sup>18</sup> involving a dose-reduction technique that used an attenuator with a thin central region and a gradually increasing thickness away from the center. With this type of attenuator, only the lower spatial frequency components in the image were modulated, and brightness in the image was equalized using a high-pass spatial digital filter.

Work on variable ROI shapes was conducted by Xu et al.<sup>19</sup> They developed an ROI attenuator device made of a 16 × 16 piston array driven by stepper motors that could generate patient-specific ROIs to reduce the x-ray dose during interventions.

A 100% dose reduction in the periphery can be achieved by collimating the FOV to the ROI. In such cases, real-time imaging of the periphery is lost. During neuroendovascular interventions, visibility of the periphery is necessary. Moreover, the neurointerventionalist needs to see the position of the guide tip in the FOV. Loss of the guide catheter with difficult access can change the outcome of an intervention and add

to the risk of complications. Similarly, visibility of the distal circulation is equally important.

None of the above-mentioned techniques included noise reduction in the peripheral regions to improve image quality. A whole-image noise-reduction technique was proposed for x-ray images using a combination of temporal filtering and spatial filtering techniques based on object detection and motion.<sup>20</sup> In places where no motion was present, temporal filtering was favored, whereas a spatial blurring filter was used when motion was encountered.

In our study, a spatially different recursive temporal filtering

scheme was applied to reduce the noise in the image. A higher filter weight was used in the periphery because the noise is excessive due to less quanta reaching the detector, whereas the weight within the ROI is lower because the regular dose is reaching the detector.

Reducing the incident primary exposure to the patient in the periphery regions results in the reduction of patient skin and organ dose within the periphery region. Furthermore, reducing the primary exposure in the periphery results in reduced backscatter and thus reduced dose to the skin in the ROI. The dose reduction achieved using this technique is dependent on the size of the ROI opening and the thickness and material of the ROI attenuator. A greater reduction in dose can be achieved using either a thicker material or a smaller ROI area or both.

### **Intra- and Interrater Agreement**

The subjective assessment of 2 comparable radiographic techniques by image-quality rating scores is standard practice. This has been used for image assessment following the application of a metal artifact-reduction algorithm.<sup>21-23</sup> We used intrarater agreement, interrater agreement, and comparison of mean scores. Our hypothesis was that the use of ROI-DRI would not deteriorate image quality and would not adversely affect the clinical utility of the sequence. In our study, we found that there was no significant difference (Table 2) in the scores assigned by each rater and between the 2 raters (because every image was shown twice).

When intrarater agreement was analyzed, visibility of the guide catheter tip had the highest agreement, with significance achieved in scores assigned by both raters and in the cohorts of ROI-DRI and RDI alone. The highest agreement could be attributed to the large size of the guide catheter compared with the sizes of the microcatheters, microwire, and coils. However, this indicates that quality was not lost when the ROI was applied to standard images. Similarly, when the ROI field was analyzed, the highest agreement was seen in the visibility of the coil mass. Intrarater agreement was significant, except when the ROI was not applied (rater 1, Tables 3 and 4). This increased agreement could be due to the large size of the coil mass compared with other devices. Overall intrarater agreement was significant ( $P < .001$ ) (rater 1: ROI-DRI, Kendall  $\tau = 0.69476$ ; RDI, Kendall  $\tau = 0.73072$ ; rater 2: ROI-DRI, Kendall  $\tau = 0.55057$ ; RDI, Kendall  $\tau = 0.45918$ ).

The overall interrater agreement in our study was fair. However, when the ROI was applied, substantial significance ( $\kappa = 0.6154$  and  $0.7$ ) was attained for the criteria of microwire emerging out of the guide catheter tip and coil visibility. Better agreement between the raters in the analysis of the ROI field may be because of a reduction in scatter radiation due to the reduction of primary radiation in the periphery.

This study demonstrated a (simulated) neurointervention in a reduced-dose environment using the technique of dose reduction with a clear, real-time view of the periphery. We implemented a simple approach by replacing an existing compensation filter in the x-ray tube with a single ROI attenuator with a fixed ROI area. With this setup, we had 2 dose-reduction options available in the x-ray unit that are controlled independently by the operator/interventionist: a set of conventional 100% dose-reducing lead col-

imators and the ROI attenuator. The dose-reduction system can be integrated into other existing x-ray machines using this implementation.

The geometric magnification was kept the same for all interventions so that all comparisons were equivalent. Increasing the distance between the patient and the detector would increase the magnification and geometric unsharpness; however, the use of the ROI attenuator would not affect these image characteristics. There would be some reduction of scatter with a larger air gap resulting from increased distance between the patient and the detector, but this effect would be minimal with the ROI attenuator because the reduced size of the region of higher intensity will already have reduced scatter and improved the contrast-to-noise ratio. If the magnification were increased by increasing the source-to-image receptor distance, the exposure parameters would have to be increased to maintain the same detector exposure (hence signal to noise ratio) whether the ROI attenuator was used or not.

During neurointervention, most of the fluoroscopic time is spent on the interventional part of the procedure. The use of this novel technology is expected to reduce the total dose because during our simulations, once the aneurysm was located, the ROI attenuator was moved into the FOV and centered on the aneurysm. Then the intervention was performed, including guidance, placement, and deployment of treatment devices. In the future, neurointervention can be performed using ROI-DRI without compromising the quality of the imaging.

### **Study Limitations**

In this study, the exposure parameters for a particular aneurysm geometry were determined by the automatic exposure control while using the RDI protocol, and the same settings were manually maintained while using the ROI-DRI protocol. In earlier x-ray imaging systems with image intensifiers, the automatic exposure control signal was derived from light sensed over a central region of variable, selectable size. For stable exposure parameter tracking, the ROI attenuator would be constrained to the center of the FOV and to being larger than the sensed area. With digital flat panel detector systems, only the unattenuated region of the image with the ROI attenuator could be used to calculate automatic exposure control parameters, thus minimizing the potential for erroneous brightness selection or unstable automatic exposure-control searching behavior. With proper design, the location of this sensed area could be made to track with movement of the ROI attenuator to off the central axis locations.

In our current setup, the dose reduction for the average technique parameters was measured separately using an ionization chamber placed in the FOV. A real-time skin-dose tracking system for neurointerventional procedures was developed and is currently being used in a clinical setting to map skin doses during these procedures.<sup>24</sup> Currently, work is in progress to integrate the use of the ROI attenuator with this system.<sup>25</sup> This will allow us to measure the dose reduction achieved using our above-mentioned technique in real-time during a clinical procedure.

Ours is the initial step in the development of this technology. Neurointervention is fast evolving with newer devices. To maintain uniformity, we tested primary coiling in the current study. The visibility of stents and flow diverters needs to be further tested.

## CONCLUSIONS

Our study has shown that significant dose reduction (62%) with a live peripheral image can be achieved without compromising feature visibility at the ROI and periphery during neuroendovascular interventions.

Disclosures: Ciprian N. Ionita—*RELATED: Grant:* Toshiba Medical Systems, *Comments:* research grant; *UNRELATED: Employment:* University at Buffalo, *Comments:* Assistant Professor in the Biomedical Engineering Department; *Grants/Grants Pending:* National Institutes of Health, Medtronic, Toshiba America Medical Systems, New York State, *Comments:* research grants; *Payment for Lectures Including Service on Speakers Bureaus:* Toshiba Medical Systems. Kenneth V. Snyder—*UNRELATED: Payment for Lectures Including Service on Speakers Bureaus:* Toshiba Medical Systems and Jacobs Institute. L. Nelson Hopkins—*UNRELATED: Board Membership:* Claret Medical; *Consultancy:* Boston Scientific, Abbott, Cordis, Medtronic; *Employment:* University at Buffalo Neurosurgery, Jacobs Institute, Kaleida Health; *Payment for Lectures Including Service on Speakers Bureaus:* Memorial Healthcare System, Complete Conference Management; *Stock/Stock Options:* Boston Scientific, Claret Medical, Augmenix, Endomation, Silk Road Medical, Ostial, Apama Medical, StimSox, Photolitec, ValenTx, Atria, Ocular Therapeutix, The Stroke Project, *Comments:* financial interests, no money received. Daniel R. Bednarek—*UNRELATED: Grants/Grants Pending:* Toshiba Medical Systems\*; *Patents (Planned, Pending or Issued):* Toshiba Medical Systems, *Comments:* Joint patents have been issued but no money has been paid to the institution or self, though it may be in the future; *Royalties:* Toshiba Medical Systems, *Comments:* Royalties were paid to the institution and self for dose-tracking system technology license\*. Stephen Rudin—*RELATED: Grant:* Toshiba Medical Systems, *Comments:* for equipment support\*; *UNRELATED: Grants/Grants Pending:* National Institutes of Health, *Comments:* ROIEB002873\*; *Patents (Planned, Pending or Issued):* Toshiba Medical Systems, *Comments:* joint patent authorship; no money was involved; *Royalties:* Toshiba Medical Systems.\* Adnan H. Siddiqui—*UNRELATED: Board Membership:* Intersocietal Accreditation Commission; *Consultancy:* Codman & Shurtleff, Medtronic, GuidePoint Global Consulting, Penumbra, Stryker Neurovascular, MicroVention, W.L. Gore & Associates, Three Rivers Medical, Corindus, Amnis Therapeutics, CereVasc, Pulsar Vascular, The Stroke Project, Cerebrotech Medical Systems, Rapid Medical, Neuravi, Silk Road Medical, Rebound Therapeutics; *Stock/Stock Options:* StimMed, Valor Medical, NeuroTechnology Investors, Cardinal Health, Medina Medical Systems, Buffalo Technology Partners, International Medical Distribution Partners, Endostream Medical; *Other:* National Steering Committees: Penumbra, Separator 3D trial, Covidien (now Medtronic), SWIFT PRIME and SWIFT DIRECT trials, MicroVention, FRED trial, MicroVention, CONFIDENCE study, LARGE trial, POSITIVE trial, Penumbra, COMPASS trial, INVEST trial. Elad I. Levy—*UNRELATED: Board Membership:* American Spinal Injury Association Impairment Scale Clinical Advisory Board for Stryker Neurovascular, Advisory Board of NeXtGen Biologics, Advisory Board of MEDX, and Advisory Board for Cognition Medical Corp, *Comments:* no money paid to me; *Consultancy:* Pulsar Vascular; *Employment:* University at Buffalo Neurosurgery and the University at Buffalo, State University of New York, *Comments:* render medical/legal opinion as an expert witness, no money paid to me; all money received goes to charitable donations; *Payment for Lectures Including Service on Speakers Bureaus:* Covidien/Medtronic; *Stock/Stock Options:* Intratech Medical, NeXtGen Biologics, Neuravi/Codman Neuro, *Comments:* Neuravi, which is now Codman Neuro (Johnson & Johnson) was sold in April 2017; *Other:* Abbott Vascular, *Comments:* carotid training sessions for physicians. \*Money paid to the institution.

## ACKNOWLEDGMENTS

The authors thank Paul H. Dressel, BFA, for preparation of the illustrations, Tingting Zhuang, MA, for statistical analysis, and Debra J. Zimmer for editorial assistance.

## REFERENCES

1. Rudin S, Bednarek DR. **Region of interest fluoroscopy.** *Med Phys* 1992;19:1183–89 CrossRef Medline
2. rudin S, Bednarek DR, Kezerashvili M, et al. **Clinical application of region-of-interest techniques to radiologic imaging.** *Radiographics* 1996;16:895–902 CrossRef Medline
3. Rudin S, Guterman LR, Granger WE, et al. **Application of region-of-interest imaging techniques to neurointerventional radiology.** *Radiology* 1996;199:870–73 CrossRef Medline
4. Panse AS, Swetadri Vasan SN, Jain A, et al. **Dose reduction by moving a region of interest (ROI) beam attenuator to follow a moving ob-**
- ject of interest. *Proc SPIE Int Soc Opt Eng* 2012;8313:831355 CrossRef Medline
5. Swetadri Vasan SN, Ionita C, Bednarek DR, et al. **A novel region of interest (ROI) imaging technique for biplane imaging in interventional suites: high-resolution small field-of-view imaging in the frontal plane and dose-reduced, large field-of-view standard-resolution imaging in the lateral plane.** *Proc SPIE Int Soc Opt Eng* 2014;9033:90332F CrossRef Medline
6. Vasan SN, Pope L, Ionita CN, et al. **Dose reduction in fluoroscopic interventions using a combination of a region of interest (ROI) x-ray attenuator and spatially-different, temporally-variable temporal filtering.** *Proc SPIE Int Soc Opt Eng* 2013;8668:86683Y CrossRef Medline
7. Ionita CN, Mokin M, Varble N, et al. **Challenges and limitations of patient-specific vascular phantom fabrication using 3D PolyJet printing.** *Proc SPIE Int Soc Opt Eng* 2014;9038:90380M CrossRef Medline
8. Russ M, O'Hara R, Setlur Nagesh SV, et al. **Treatment planning for image-guided neuro-vascular interventions using patient-specific 3D printed phantoms.** *Proc SPIE Int Soc Opt Eng* 2015;9417: pii: 941726 CrossRef Medline
9. Ionita CN, Garcia VL, Bednarek DR, et al. **Effect of injection technique on temporal parametric imaging derived from digital subtraction angiography in patient specific phantoms.** *Proc SPIE Int Soc Opt Eng* 2014;9038:90380L CrossRef Medline
10. Mokin M, Ionita CN, Nagesh SV, et al. **Primary stentriever versus combined stentriever plus aspiration thrombectomy approaches: in vitro stroke model comparison.** *J Neurointerv Surg* 2015;7:453–57 CrossRef Medline
11. Mokin M, Setlur Nagesh SV, Ionita CN, et al. **Comparison of modern stroke thrombectomy approaches using an in vitro cerebrovascular occlusion model.** *AJNR Am J Neuroradiol* 2015;36:547–51 CrossRef Medline
12. Mokin M, Setlur Nagesh SV, Ionita CN, et al. **Stent retriever thrombectomy with the Cover accessory device versus proximal protection with a balloon guide catheter: in vitro stroke model comparison.** *J Neurointerv Surg* 2016;8:413–17 CrossRef Medline
13. Massoumzadeh P, Rudin S, Bednarek DR. **Filter material selection for region of interest radiologic imaging.** *Med Phys* 1998;25:161–71 CrossRef Medline
14. Setlur Nagesh S, Jain A, Ionita C, et al. **SU-D-134-03; design considerations for a dose-reducing region of interest (ROI) attenuator built in the collimator assembly of a fluoroscopic interventional C-arm.** *Med Phys* 2013;40:112 CrossRef
15. Kotre CJ, Guibelalde E. **Optimization of variable temporal averaging in digital fluoroscopy.** *Br J Radiol* 2004;77:675–78 CrossRef Medline
16. International Electrotechnical Commission. IEC 62220–1-1:2015. Medical electrical equipment - Characteristics of digital x-ray imaging devices - Part 1–1: Determination of the detective quantum efficiency - detectors used in radiographic imaging. <https://webstore.iec.ch/publication/21937>. Accessed November 16, 2017
17. Labbe MS, Chiu MY, Rzeszutarski MS, et al. **The x-ray fovea, a device for reducing x-ray dose in fluoroscopy.** *Med Phys* 1994;21:471–81 CrossRef Medline
18. Robert N, Komljenovic PT, Rowlands JA. **A filtering method for signal equalization in region-of-interest fluoroscopy.** *Med Phys* 2002; 29:736–47 CrossRef Medline
19. Xu T, Le HQ, Molloy S. **Patient-specific region-of-interest fluoroscopy device for X-ray dose reduction.** *Radiology* 2003;226:585–92 CrossRef Medline
20. Aufrichtig R, Wilson DL. **X-ray fluoroscopy spatio-temporal filtering with object detection.** *IEEE Trans Med Imaging* 1995;14:733–46 CrossRef Medline
21. Buhk JH, Groth M, Sehner S, et al. **Application of a novel metal artifact correction algorithm in flat-panel CT after coil embolization of brain aneurysms: intraindividual comparison.** *Rofa* 2013; 185:824–29 CrossRef Medline

22. Hung SC, Wu CC, Lin CJ, et al. **Artifact reduction of different metallic implants in flat detector C-arm CT.** *AJNR Am J Neuroradiol* 2014;35:1288–92 CrossRef Medline
23. van der Bom IM, Hou SY, Puri AS, et al. **Reduction of coil mass artifacts in high-resolution flat detector conebeam CT of cerebral stent-assisted coiling.** *AJNR Am J Neuroradiol* 2013;34:2163–70 CrossRef Medline
24. Rana VK, Rudin S, Bednarek DR. **A tracking system to calculate patient skin dose in real-time during neurointerventional procedures using a biplane x-ray imaging system.** *Med Phys* 2016;43:5131 CrossRef Medline
25. Vijayan S, Xiong Z, Rudin S, et al. **Calculation of the entrance skin dose distribution for fluoroscopically guided interventions using a pencil beam backscatter model.** *J Med Imaging (Bellingham)* 2017;4:031203 CrossRef Medline

# Altered Regional Homogeneity in Chronic Insomnia Disorder with or without Cognitive Impairment

R. Pang, R. Guo, X. Wu, F. Hu, M. Liu, L. Zhang, Z. Wang, and K. Li



## ABSTRACT

**BACKGROUND AND PURPOSE:** Many studies have shown that insomnia is an independent factor in cognitive impairment, but the involved neurobiological mechanisms remain unclear. We used regional homogeneity to explore the specific neurobiologic indicators of chronic insomnia disorder with mild cognitive impairment.

**MATERIALS AND METHODS:** Thirty-nine patients with insomnia were divided into a group with and without cognitive impairment; we also included a control group ( $n = 28$ ). Abnormalities in brain functional activity were identified by comparing the regional homogeneity values for each brain region among the groups.

**RESULTS:** Subjective insomnia scores were negatively correlated with cognitive impairment after controlling for age, sex, and educational effects. Regions with significant differences in regional homogeneity values in the 3 groups were concentrated in the right medial prefrontal cortex, the right superior frontal gyrus, and the left superior occipital gyrus. Meanwhile, subjective insomnia scores were negatively correlated with the strength of the decreased regional homogeneity in the right medial prefrontal cortex. The increased regional homogeneity value in the right superior frontal gyrus was positively correlated with the Montreal Cognitive Assessment score in patients.

**CONCLUSIONS:** Our results indicate that decreased regional homogeneity values in the medial prefrontal cortex and increased regional homogeneity values in the cuneus may be important neurobiologic indicators of chronic insomnia disorder and accompanying cognitive impairment. Overall, our study described the regional homogeneity of the whole brain in chronic insomnia disorder with mild cognitive impairment and could be the basis for future studies.

**ABBREVIATIONS:** BA = Brodmann area; CID = chronic insomnia disorder; MCI = mild cognitive impairment; mPFC = medial prefrontal cortex; NC = healthy control; NI = no impairment; ReHo = regional homogeneity; SFG = superior frontal gyrus

The relationship between insomnia and cognitive function has attracted considerable attention in recent years. Large-sample meta-analyses have shown that patients with insomnia have mild

or moderate dysfunction in attention, episodic memory, working memory, and executive function compared with healthy controls.<sup>1</sup> A number of neuropsychological studies have found that older patients with chronic insomnia disorder (CID) have significant deficits in cognitive function compared with individuals of the same age without insomnia symptoms.<sup>1-4</sup> Although some scholars have proposed that insomnia is associated with normal aging<sup>5</sup> or neurodegenerative changes,<sup>6,7</sup> recent research indicates that insomnia is an independent factor in cognitive impairment.<sup>8-11</sup>

Using [<sup>18</sup>F] FDG-PET, the earliest study found that the interacting neural networks of patients with insomnia were mainly distributed in the awakening, affective control, and cognitive systems.<sup>12</sup> The observed abnormalities in the hippocampus and medial prefrontal cortex (mPFC) were consistent with the clinical features of cognitive impairment in patients with insomnia and the results of neurophysiology and neuroendocrine studies, indicating that memory integration is impaired in insomnia.<sup>13-15</sup> Considering similarities in neuromodulatory factors and their

Received September 15, 2017; accepted after revision December 29.

From the Departments of Radiology (R.P., M.L., Z.W., K.L.), Neurology (R.G., L.Z.), and Acupuncture (X.W.), Dongfang Hospital, Beijing University of Chinese Medicine, Beijing, China; Department of Radiology (R.P., K.L.), Xuanwu Hospital, Capital Medical University, Beijing, China; Institute of Automation (F.H.), Chinese Academy of Sciences, Beijing, China; School of Automation (F.H.), Harbin University of Science and Technology, Harbin, China; and Beijing Key Laboratory of Magnetic Resonance Imaging and Brain Informatics (K.L.), Beijing, China.

This work was supported by a grant from Beijing University of Chinese Medicine (2017-JYB-JS-166) and grants from the National Natural Science Foundation of China (81471649, 81571648 and 81370037).

Please address correspondence to Kuncheng Li, MD, Department of Radiology, Xuanwu Hospital, Capital Medical University, Beijing, 100053, China; e-mail: cjr.likuncheng@VIP.163.com

Indicates open access to non-subscribers at [www.ajnr.org](http://www.ajnr.org)

Indicates article with supplemental on-line table.

<http://dx.doi.org/10.3174/ajnr.A5587>

mechanisms of action sites in insomnia and Alzheimer disease, a possibility that has attracted much attention from neurologists, neuroscientists, and neuroradiologists is whether insomnia and Alzheimer disease share the same pathogenesis.<sup>16,17</sup>

fMRI provides a primary method of mechanism detection in insomnia. Some researchers have explored network mechanisms underlying decreased working memory and executive dysfunction in insomnia using task-state fMRI.<sup>18–20</sup> They have found decreased activity in the frontoparietal cortex<sup>18</sup> and an abnormal frontal-striatal network during task-state in patients with insomnia.<sup>19</sup> Furthermore, the activity of the medial prefrontal lobe could be recovered following insomnia improvement.<sup>20</sup> Behavioral and fMRI studies have shown that the impairment of the executive control network in patients with CID is associated with reduced nocturnal slow-wave sleep time,<sup>21</sup> which is consistent with the impairments in the prefrontal and thalamus attention networks during sleep deprivation.<sup>13,22,23</sup> Moreover, PET and fMRI studies have yielded similar results.<sup>24,25</sup> Although the above studies suggest that insomnia may be the potential reason for cognitive impairment, the involved mechanisms in patients with insomnia remain unclear.

Compared with task-state fMRI, resting-state fMRI can be used to disregard differences in brain activation caused by inconsistencies in task performance and may be used as a reflection of the real changes within inherent brain activity and/or the endogenous neurophysiologic process of the patients' brains under the awake state. The regional homogeneity (ReHo) method can effectively evaluate resting-state brain activity across the whole brain of an individual and has good reproducibility.<sup>26,27</sup> The method has been widely used in the study of resting-state brain functional imaging for neurodegenerative diseases, emotional diseases, and cognitive function.

Several previous studies have investigated the regional spontaneous activity patterns in patients with insomnia. These studies have found that patients with insomnia have abnormal spontaneous activity in specific regions, including the insula, cingulate gyrus, fusiform gyrus, and cerebellum.<sup>28,29</sup> In addition, these altered ReHo values are associated with sleep quality and psychological scores<sup>30</sup>; these findings suggest that the abnormal ReHo values of specific regions could reflect the brain mechanism of emotional disorders in patients with insomnia. Moreover, neuroimaging studies have shown that abnormal brain regional homogeneity is an important marker of cognitive impairment in patients with Alzheimer disease<sup>31,32</sup> and could accurately reflect the severity of cognitive impairment.<sup>33</sup>

We diagnosed mild cognitive impairment (MCI) according to the Peterson MCI standard, and patients with insomnia were divided into the cognitive impairment (CID-MCI) group or the group without cognitive impairment (CID-NI). Then, we used the ReHo method to explore differences in regional spontaneous activity in the whole brain between the healthy control (NC), CID-NI, and CID-MCI groups. We hypothesized that the ReHo index would differ among the NC, CID-NI, and CID-MCI groups and that the differences in ReHo would be associated with differences in cognitive ability. A post hoc analysis was then performed to compare the ReHo index between each pair of groups. Finally, a correlation analysis was performed between the ReHo index of

the identified regions and various clinical variables in the CID-NI and CID-MCI groups to evaluate the relationship between the ReHo scores and the cognitive abilities of the CID-NI and CID-MCI groups.

## MATERIALS AND METHODS

The participants in the present study also composed the sample in a previous study of spontaneous activity measured by whole-brain functional connectivity.<sup>34</sup> All subjects met identical methodologic stringency criteria; comprehensive clinical details can be found in the prior work.<sup>34</sup>

### Participants

Patients with insomnia and volunteers were enrolled from a neurology clinic. The participants underwent a series of examinations, including a clinical interview, laboratory blood tests, and neuropsychological assessment. Consent forms were signed by the participants before the study, and the study protocol was approved by the ethics committee.

All participants underwent a complete physical and neurologic examination, standard laboratory tests, and an extensive battery of neuropsychological assessments, which included the Pittsburgh Sleep Quality Index, Insomnia Severity Index, Hamilton Anxiety Scale, Hamilton Depression Rating Scale, Mini-Mental State Examination, Montreal Cognitive Assessment, and Clinical Dementia Rating. Patients with CID also underwent polysomnography.

The diagnosis of CID met the criteria of the fifth edition of the *Diagnostic and Statistical Manual of Mental Disorders* and the third edition of the *International Classification of Sleep Disorders*.<sup>35</sup> Although chronic insomnia is not exactly equal to primary insomnia, we did not find severe anxiety and depression disorders in the included patients.

The On-line Table presents the demographic, neuropsychological, and sleep characteristics of the enrolled participants.

### Study Method

The patients with CID completed subjective and objective sleep-quality assessments (Pittsburgh Sleep Quality Index and Insomnia Severity Index scales and Polysomnography monitoring). Sleep time data were analyzed and calculated by an experienced technician and were reviewed by a neurologist. These data included total sleep time, sleep-onset latency, wake time, nonrapid eye movement slow-wave activity (S3 + S4) time and latency, and rapid eye movement sleep time and latency. The details of the neuropsychological assessments are provided in the On-line Table.

### MR Imaging Acquisition

Briefly, MR imaging was performed using a 1.5T superconductor MR imaging scanner (Intera Achieva; Philips Healthcare, Best, the Netherlands). The parameters and scanning mode of the MR imaging in this study can be found in the previously published study.<sup>34</sup>

### MR Imaging Data Preprocessing

The fMRI data were preprocessed with a method consistent with protocols in previously published studies using the BRAinNetome fMRI Toolkit (Brant; <http://brant.brainnetome.org>). The prepro-

### Regions with differences in ReHo in the CID-NI, CID-MCI, and NC groups, and their coordinates<sup>a</sup>

Brain Region	BA	Cluster Size	Voxel <i>F</i>	MNI Coordinates		
				x	y	z
R.IFG	11/47	61	15.34	16	14	-26
R.SFG	11	97	12.32	18	60	-22
R.MFG	10/11	68	16.10	34	62	-8
L.cuneus	18	88	15.78	-2	-104	12
L.SOG	31/18	63	18.87	-24	-66	22

**Note:**—R indicates right; L, left; IFG, inferior frontal gyrus; MFG, middle frontal gyrus; SOG, superior occipital gyrus; MNI, Montreal Neurological Institute.

<sup>a</sup>Voxel threshold = 60, *P* < .001, uncorrected.

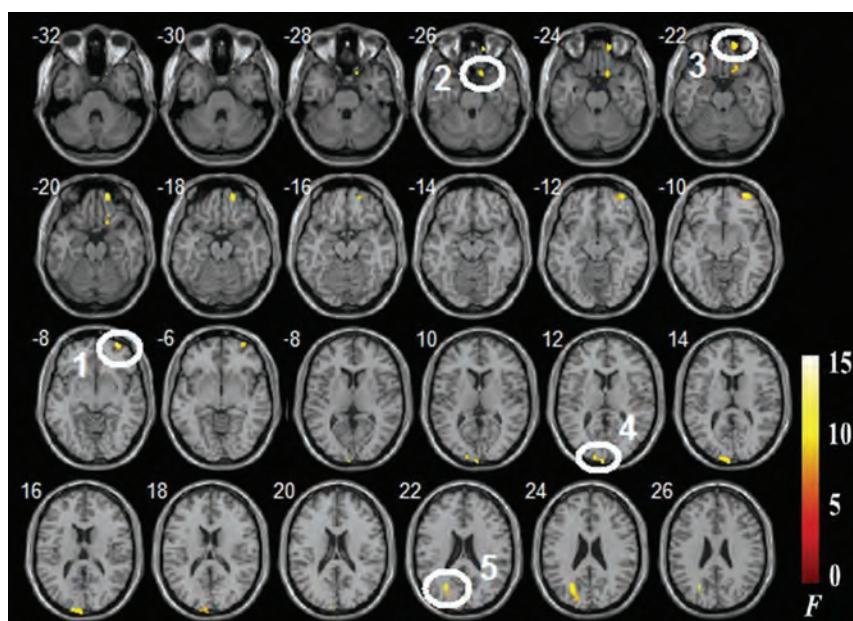


**FIG 1.** Regions with differences in regional homogeneity among the CID-NI, CID-MCI, and NC groups (voxels at least 60, *P* < .001). 1) Right inferior frontal gyrus. 2) Right superior frontal gyrus. 3) Right orbital middle frontal gyrus. 4) Left cuneus. 5) Left superior occipital gyrus.

processing steps included the following: 1) slice-timing, 2) realignment to reduce head motion, 3) normalization to a standard EPI template and reslicing to 2 × 2 × 2 mm cubic voxels, 4) denoising by regressing out several effects (6 motion parameters, linear drift, and the mean time-series of all voxels within the white matter and CSF), and 5) temporal filtering (0.01–0.08 Hz) to reduce noise.

#### Estimation of Interregional Functional Connectivity—ReHo Index

ReHo provides a fast mapping of the regional activity across the whole brain.<sup>26</sup> For each subject, the ReHo map was normalized by dividing it by the mean ReHo of the whole brain for each subject to reduce the effect of individual variability,<sup>36,37</sup> for each voxel:  $ReHo_{normalized} = ReHo(x, y, z) / Mean(ReHo)$ .

#### Statistical Analysis

A 1-way ANOVA with age and sex as covariates was performed to identify the differences among the CID-MCI, CID-NI, and NC groups. The resultant *F* value map was then thresholded using *P* < .001 (*F* = 7.76, two *df*, 60 *df* for each voxel and a cluster size of at least 60 voxels, uncorrected). Subsequently, the regions that showed significant differences were extracted as ROIs, and the

mean ReHo values were used for a post hoc analysis. Statistical comparisons of the mean ReHo values between each pair of groups were performed using a 2-sample 2-tailed *t* test at a threshold of *P* < .05.

To determine whether the ReHo index varied with disease progression in the CID-MCI and CID-NI groups, we performed correlation analyses between the ReHo index and each of the clinical variables (Mini-Mental State Examination, Pittsburgh Sleep Quality Index, and Hamilton Anxiety Scale scores). Because these analyses were exploratory in nature, we used a statistical significance level of *P* < .05 (uncorrected).

## RESULTS

### Group Differences

A 1-way ANOVA was used to determine the regions in which the ReHo index was significantly altered among the CID-NI, CID-MCI, and NC groups. We found that the ReHo index was significantly different in the following regions: the right mPFC (inferior frontal gyrus, orbital middle frontal gyrus, and Brodmann areas [BAs] 47 and 11), the right superior frontal gyrus (SFG; BA 11), the left cuneus (BA 18), and the left superior occipital gyrus (BAs 31 and 18) among the CID-NI, CID-MCI, and NC groups (Table and Fig 1).

As Fig 2 shows, the mean ReHo values in the mPFC decreased significantly (*P* < .05) in the CID-NI and CID-MCI groups compared with the NC group, while the mean ReHo values in the cuneus increased significantly (*P* < .05) in the CID-NI and CID-MCI groups compared with the NC group. In addition, the mean ReHo value in the right SFG significantly increased (*P* < .05) in the CID-NI group compared with the CID-MCI and the NC groups.

### Relationship between ReHo and Clinical Variables

As Fig 3 shows, the strength of the ReHo score was negatively correlated with the Pittsburgh Sleep Quality Index ratings (*r* = -0.35, *P* = .03) in the right inferior frontal gyrus in patients with CID. The strength of the ReHo index was positively correlated with the Montreal Cognitive Assessment ratings in the right superior frontal gyrus (*r* = 0.40, *P* = .01).

## DISCUSSION

To the best of our knowledge, this is the first study to investigate the ReHo index of brain spontaneous activity in patients with both CID-MCI and CID-NI as well as to compare them with NCs. Significant differences were found in the ReHo scores in various brain regions—that is, the right mPFC (inferior frontal gyrus,

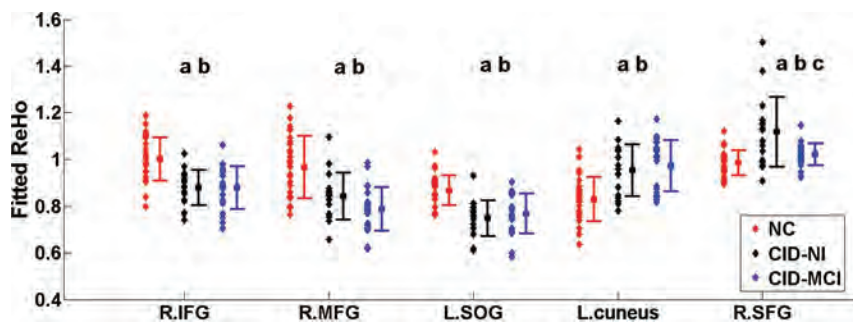


**FIG 2.** Plot of the regional homogeneity index among the CID-NI, CID-MCI, and NC groups in the identified brain regions (voxels at least 60,  $P < .001$ ). a, The ReHo index is significantly different between the NC and CID-MCI groups. b, The ReHo index is significantly different between the NC and CID-NI groups. c, The ReHo index is significantly different between the CID-MCI and CID-NI groups. R indicates right; L, left; IFG, inferior frontal gyrus; MFG, middle frontal gyrus; SOG, superior occipital gyrus.

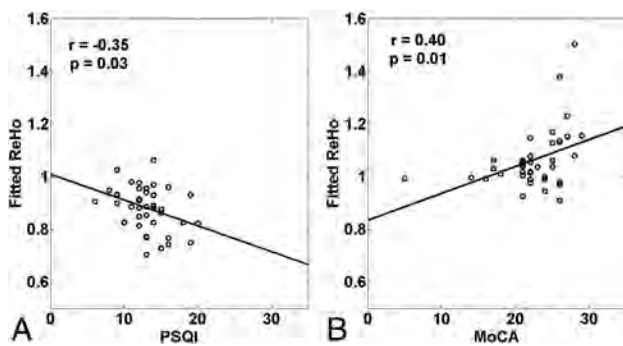


**FIG 3.** Correlations between altered regional homogeneity patterns and subjective sleep scores and cognitive scores in the chronic insomnia disorder group ( $P < .05$ ). A, Right inferior frontal gyrus. B, Right SFG. Although the 2 points in the figure (B) look like outliers, the high correlation was also obtained without them ( $r = 0.36$ ,  $P = .03$ ). PSQI indicates the Pittsburgh Sleep Quality Index; MoCA, the Montreal Cognitive Assessment.

orbital middle frontal gyrus), the right SFG, the left cuneus, and the left superior occipital gyrus among the CID-MCI, CID-NI, and NC groups (Table and Fig 1). Furthermore, the ReHo index in these identified brain regions showed a significant correlation with clinical variables in the CID groups (Fig 3).

We observed that regions with decreased ReHo were located in the right mPFC (inferior frontal gyrus, orbital middle frontal gyrus) in the CID-MCI and CID-NI groups compared with the NC group. Many studies have demonstrated that the mPFC plays a pivotal role in mediating sleep and generating nonrapid eye movement slow-wave oscillations.<sup>38-41</sup> Recent electroencephalography and fMRI studies have shown that the waking metabolism rate and reduced gray matter volumes in the medial frontal gyrus of humans are both related to aging and closely related to nighttime slow-sleep intensity.<sup>38,42</sup> Previous morphometry studies have found that patients with chronic insomnia displayed significantly reduced gray matter volumes in the orbitofrontal cortex (BAs 10 and 11) and medial frontal lobe,<sup>43,44</sup> and that the gray matter volumes in the orbitofrontal cortex are positively correlated with the severity of insomnia in patients with chronic insomnia.<sup>44</sup> Furthermore, an fMRI study found that the activity of the medial prefrontal lobe could be recovered after the insomnia improved.<sup>20</sup> All these results strengthen the evidence for insomnia-related changes in the mPFC in this study. Moreover, this

correlation was supported by the negative relationship between the ReHo index values in the right inferior frontal gyrus and scores on the Pittsburgh Sleep Quality Index (Fig 3).

Considering that the mPFC is a key region in the default mode network that characterizes autobiographic memory retrieval,<sup>45</sup> our results further suggest that ReHo values in the mPFC can reflect disrupted global cognitive function in patients with CID-MCI. Consistent with our findings, several previous studies have found decreased connectivity in the prefrontal cortex,<sup>22</sup> internal default network, and between the default network

and its negative feedback network after short-term sleep deprivation in healthy individuals.<sup>46</sup> In recent years, impaired connectivity in the default mode network has been found to be common in patients with insomnia.<sup>34,46-48</sup> Moreover, slow-wave sleep plays an important role in memory integration and storage.<sup>13-15,41,49,50</sup> Some studies have reported that structural and functional destruction in the mPFC, which is known as the major region generating slow-wave sleep oscillations, could destroy the memory systems.<sup>11,38,39</sup> In this study, the ReHo values in the right orbital middle frontal gyrus were lower in the CID-MCI than in the CID-NI group (Fig 2). This finding indicates that the coherence in the regional activity of the mPFC gives an expression of affected memory systems induced by CID. Moreover, the patients in the CID-MCI group had lower nonrapid eye movement slow-wave activity (S3 + S4) (%) and were older than the patients in the CID-NI group (On-line Table). Combined with previous experimental results, our observations suggest that the disruption of spontaneous brain activity in the mPFC due to insomnia may be accelerated with aging, or shortened nonrapid eye movement slow-wave activity (slow wave activity) and aging may synergistically disrupt certain cognitive abilities.<sup>11,39</sup> Taken together, the decreased homogeneity in the mPFC may be a characteristic alteration in the patients with CID-MCI.

We also found an increased ReHo in the left cuneus in the CID-NI and the CID-MCI groups compared with the NC group (Fig 2). Several neuroimaging studies have found abnormal metabolism and dysfunction in the occipital lobe in patients with insomnia.<sup>51,52</sup> Although these results are inconsistent, both studies reported a negative correlation between  $\gamma$  aminobutyric acid content in the occipital lobe and sleep-onset latency, which suggests that the occipital lobe plays an important role in sleep-awakening mediation. In addition, previous studies have shown that patients with insomnia displayed significantly increased ReHo in the left cuneus compared with NCs.<sup>29</sup> This conclusion is consistent with the results of our study, wherein we found that the ReHo of the left cuneus was increased in all patients with CID.

In the present study, the right SFG was the only region that could be used to distinguish the 3 groups. We found that the right SFG exhibited a significantly increased ReHo in both the CID-MCI and CID-NI groups compared with the NC group (Fig 2)

and the ReHo index values in the SFG positively correlated with Montreal Cognitive Assessment ratings. In a recent study, patients with CID showed an increased positive correlation between the left SFG and ipsilateral parahippocampal gyrus, and the connectivity strength was positively correlated with the Mini-Mental State Examination scores.<sup>34</sup> This result suggests that increased functional connectivity of the SFG could compensate for the cognitive impairment after prefrontal disconnection. In addition, 2 studies using the ReHo method have observed that patients with insomnia showed altered spontaneous activity in extensive emotional brain regions (including the insula, cingulate gyrus, fusiform gyrus, temporal lobe, cerebellum, and frontal lobe).<sup>28,29</sup> Wang et al<sup>29</sup> found that altered ReHo values (the left insula, the right middle cingulate cortex, and the right precentral gyrus) are associated with psychological scores, while Dai et al<sup>28</sup> considered the decreased ReHo values in the SFG to be a marker for cognitive and emotional dysfunction in insomnia. Moreover, the patients in the CID-NI group had both the highest ReHo values in the SFG and the most severe clinical manifestations of difficulty with sleep onset and abnormal emotions compared with the CID-MCI and NC groups; this finding is consistent with the cortical hyperarousal and emotional disorders hypothesis.<sup>53</sup> Taken together, our results further indicate that ReHo values in the right SFG can reflect the degree of difficulty with sleep onset or the hyperarousal state in patients with CID.

Some limitations should be borne in mind when interpreting the results. No regions showed significantly decreased ReHo scores in the CID-MCI group compared with the CID-NI group, while the right orbital middle frontal gyrus had a significantly more destructive tendency in the CID-MCI than in the CID-NI and NC groups (Fig 2). In addition, more data from sleep-monitoring indicators, such as nonrapid eye movement slow-wave activity and rapid eye movement sleep duration, sleep latency, and band characteristics, as well as analysis of correlations between electrophysiology and fMRI measures and cognitive ability, are required for further studies. The present study showed the brain functional changes and clinical indices of CID-MCI and CID-NI in the 2 insomnia subgroups, but not in patients with pure MCI. Further studies could consider including patients with amnesic MCI to better explain the sleep and cognitive decline effect and may help us understand the pathogenetic process that leads from insomnia to Alzheimer disease or of the aggravation of insomnia, which could explain the phenomenon of patients with insomnia having an increased incidence rate of Alzheimer disease compared with individuals without insomnia.

## CONCLUSIONS

This study is the first to examine the spontaneous brain activity of patients with CID-MCI, to our knowledge. Our results indicate that the decreased ReHo values observed in the mPFC of patients may be an important neurobiologic indicator of CID and accompanying cognitive impairment and that the enhanced local homogeneity observed in the right SFG may act as a predictor of both destruction in emotional moderation and the degree of hyperarousal state. Overall, our study describes the regional homogeneity of the whole brain in patients with CID-MCI and provides a foundation for future related studies.

## Ethical Approval and Informed Consent

This experiment was conducted on humans.

Approval: All experimental protocols were approved by the Clinical Research Ethics Committee of Dongfang Hospital of Beijing University of Chinese Medicine.

Accordance: The methods were carried out in accordance with the approved guidelines.

Informed consent: Informed consent was obtained from all participants before participation.

## ACKNOWLEDGMENTS

We thank all authors of the included studies. We especially thank Dr Yunling Zhang for his kind help and suggestions. Moreover, we would like to thank Editage (www.editage.com) for English language editing.

## REFERENCES

- Fortier-Brochu E, Beaulieu-Bonneau S, Ivers H, et al. **Insomnia and daytime cognitive performance: a meta-analysis.** *Sleep Med Rev* 2012;16:83–94 CrossRef Medline
- Naismith SL, Lewis SJ, Rogers NL. **Sleep-wake changes and cognition in neurodegenerative disease.** *Prog Brain Res* 2011;190:21–52 CrossRef Medline
- Blackwell T, Yaffe K, Laffan A, et al; Osteoporotic Fractures in Men (MrOS) Study Group. **Associations of objectively and subjectively measured sleep quality with subsequent cognitive decline in older community-dwelling men: the MrOS sleep study.** *Sleep* 2014;37:655–63 CrossRef Medline
- Lim AS, Kowgier M, Yu L, et al. **Sleep fragmentation and the risk of incident Alzheimer's disease and cognitive decline in older persons.** *Sleep* 2013;36:1027–32 CrossRef Medline
- Wolkove N, Elkholy O, Baltzan M, et al. **Sleep and aging, 1: sleep disorders commonly found in older people.** *CMAJ* 2007;176:1299–304 CrossRef Medline
- Face-Schott EF, Spencer RM. **Age-related changes in the cognitive function of sleep.** *Prog Brain Res* 2011;191:75–89 CrossRef Medline
- Hauw JJ, Hausser-Hauw C, Hasboun D, et al. **The neuropathology of sleep in human neurodegenerative diseases (in French).** *Rev Neurol (Paris)* 2008;164:669–82 CrossRef Medline
- Yaffe K, Falvey CM, Hoang T. **Connections between sleep and cognition in older adults.** *Lancet Neurol* 2014;13:1017–28 CrossRef Medline
- Potvin O, Lorrain D, Forget H, et al. **Sleep quality and 1-year incident cognitive impairment in community-dwelling older adults.** *Sleep* 2012;35:491–99 CrossRef Medline
- Branger P, Arenaza-Urquijo EM, Tomadesso C, et al. **Relationships between sleep quality and brain volume, metabolism, and amyloid deposition in late adulthood.** *Neurobiol Aging* 2016;41:107–14 CrossRef Medline
- Lucey BP, Holtzman DM. **How amyloid, sleep and memory connect.** *Nat Neurosci* 2015;18:933–34 CrossRef Medline
- Nofzinger EA. **What can neuroimaging findings tell us about sleep disorders?** *Sleep Med* 2004;31(5 Suppl 1):S16–22 Medline
- Muto V, Shaffii-Le Bourdieu AN, Matarazzo L, et al. **Influence of acute sleep loss on the neural correlates of alerting, orientating and executive attention components.** *J Sleep Res* 2012;21:648–58 CrossRef Medline
- Morin CM, Benca R. **Chronic insomnia.** *Lancet* 2012;379:1129–41 CrossRef Medline
- van Marle HJ, Hermans EJ, Qin S, et al. **The effect of exogenous cortisol during sleep on the behavioral and neural correlates of emotional memory consolidation in humans.** *Psychoneuroendocrinology* 2013;38:1639–49 CrossRef Medline
- Monti JM. **The neurotransmitters of sleep and wake, a physiological reviews series.** *Sleep Med Rev* 2013;17:313–15 CrossRef Medline

17. Spira AP, Gamaldo AA, An Y, et al. **Self-reported sleep and  $\beta$ -amyloid deposition in community-dwelling older adults.** *JAMA Neurol* 2013;70:1537–43 CrossRef Medline
18. Drummond SP, Walker M, Almklov E, et al. **Neural correlates of working memory performance in primary insomnia.** *Sleep* 2013;36:1307–16 CrossRef Medline
19. Stoffers D, Altena E, van der Werf, et al. **The caudate: a key node in the neuronal network imbalance of insomnia?** *Brain* 2014;137:610–20 CrossRef Medline
20. Altena E, Van Der Werf YD, Sanz-Arigitia EJ, et al. **Prefrontal hypoactivation and recovery in insomnia.** *Sleep* 2008;31:1271–76 Medline
21. Li Y, Liu H, Weed JG, et al. **Deficits in attention performance are associated with insufficiency of slow-wave sleep in insomnia.** *Sleep Med* 2016;24:124–30 CrossRef Medline
22. Verweij IM, Romeijn N, Smit DJ, et al. **Sleep deprivation leads to a loss of functional connectivity in frontal brain regions.** *BMC Neurosci* 2014;15:88 CrossRef Medline
23. Tomasi D, Wang RL, Telang F, et al. **Impairment of attentional networks after 1 night of sleep deprivation.** *Cereb Cortex* 2009;19:233–40 CrossRef Medline
24. Thomas M, Sing H, Belenky G, et al. **Neural basis of alertness and cognitive performance impairments during sleepiness, I: effects of 24 h of sleep deprivation on waking human regional brain activity.** *J Sleep Res* 2000;9:335–52 CrossRef Medline
25. Chee MW, Chuah LY, Venkatraman V, et al. **Functional imaging of working memory following normal sleep and after 24 and 35 h of sleep deprivation: correlations of fronto-parietal activation with performance.** *Neuroimage* 2006;31:419–28 CrossRef Medline
26. Zang Y, Jiang T, Lu Y, et al. **Regional homogeneity approach to fMRI data analysis.** *Neuroimage* 2004;22:394–400 CrossRef Medline
27. Kiviniemi V. **Endogenous brain fluctuations and diagnostic imaging.** *Hum Brain Mapp* 2008;29:810–17 CrossRef Medline
28. Dai XJ, Peng DC, Gong HH, et al. **Altered intrinsic regional brain spontaneous activity and subjective sleep quality in patients with chronic primary insomnia: a resting-state fMRI study.** *Neuropsychiatr Dis Treat* 2014;10:2163–75 CrossRef Medline
29. Wang T, Li S, Jiang G, et al. **Regional homogeneity changes in patients with primary insomnia.** *Eur Radiol* 2016;26:1292–300 CrossRef Medline
30. Dai XJ, Gong HH, Wang YX, et al. **Gender differences in brain regional homogeneity of healthy subjects after normal sleep and after sleep deprivation: a resting-state fMRI study.** *Sleep Med* 2012;13:720–27 CrossRef Medline
31. Bai F, Zhang Z, Yu H. **Default-mode network activity distinguishes amnesic type mild cognitive impairment from healthy aging: a combined structural and resting-state functional MRI study.** *Neurosci Lett* 2008;438:111–15 CrossRef Medline
32. He Y, Wang L, Zang Y, et al. **Regional coherence changes in the early stages of Alzheimer's disease: a combined structural and resting-state functional MRI study.** *Neuroimage* 2007;35:488–500 CrossRef Medline
33. Zhang Z, Liu Y, Jiang T, et al. **Altered spontaneous activity in Alzheimer's disease and mild cognitive impairment revealed by regional homogeneity.** *Neuroimage* 2012;59:1429–40 CrossRef Medline
34. Pang R, Zhan Y, Zhang Y, et al. **Aberrant functional connectivity architecture in participants with chronic insomnia disorder accompanying cognitive dysfunction: a whole-brain, data-driven analysis.** *Front Neurosci* 2017;11:259 CrossRef Medline
35. Edinger JD, Bonnet MH, Bootzin RR, et al; American Academy of Sleep Medicine Work Group. **Derivation of research diagnostic criteria for insomnia: report of an American Academy of Sleep Medicine Work Group.** *Sleep* 2004;27:1567–96 CrossRef Medline
36. Wu T, Long X, Zang Y, et al. **Regional homogeneity changes in patients with Parkinson's disease.** *Hum Brain Mapp* 2009;30:1502–10 CrossRef Medline
37. Liu C, Liu Y, Li W, et al. **Increased regional homogeneity of blood oxygen level-dependent signals in occipital cortex of early blind individuals.** *Neuroreport* 2011;22:190–94 CrossRef Medline
38. Mander BA, Rao V, Lu B, et al. **Prefrontal atrophy, disrupted NREM slow waves and impaired hippocampal-dependent memory in aging.** *Nat Neurosci* 2013;16:357–64 CrossRef Medline
39. Mander BA, Marks SM, Vogel JW, et al.  **$\beta$ -amyloid disrupts human NREM slow waves and related hippocampus-dependent memory consolidation.** *Nat Neurosci* 2015;18:1051–57 CrossRef Medline
40. Murphy M, Riedner BA, Huber R, et al. **Source modeling sleep slow waves.** *Proc Natl Acad Sci U S A* 2009;106:1608–13 CrossRef Medline
41. Mander BA, Rao V, Lu B, et al. **Impaired prefrontal sleep spindle regulation of hippocampal-dependent learning in older adults.** *Cereb Cortex* 2014;24:3301–09 CrossRef Medline
42. Wilckens KA, Aizenstein HJ, Nofzinger EA, et al. **The role of non-rapid eye movement slow-wave activity in prefrontal metabolism across young and middle-aged adults.** *J Sleep Res* 2016;25:296–306 CrossRef Medline
43. Joo EY, Noh HJ, Kim JS, et al. **Brain gray matter deficits in patients with chronic primary insomnia.** *Sleep* 2013;36:999–1007 CrossRef Medline
44. Altena E, Vrenken H, Van Der Werf YD, et al. **Reduced orbitofrontal and parietal gray matter in chronic insomnia: a voxel-based morphometric study.** *Biol Psychiatry* 2010;67:182–85 CrossRef Medline
45. Buckner RL, Andrews-Hanna JR, Schacter DL. **The brain's default network: anatomy, function, and relevance to disease.** *Ann NY Acad Sci* 2008;1124:1–38 CrossRef Medline
46. De Havas JA, Parimal S, Soon CS, et al. **Sleep deprivation reduces default mode network connectivity and anti-correlation during rest and task performance.** *Neuroimage* 2012;59:1745–51 CrossRef Medline
47. Khalsa S, Mayhew SD, Przewdzik I, et al. **Variability in cumulative habitual sleep duration predicts waking functional connectivity.** *Sleep* 2016;39:87–95 CrossRef Medline
48. Suh S, Kim H, Dang-Vu TT. **Cortical thinning and altered cortico-cortical structural covariance of the default mode network in patients with persistent insomnia symptoms.** *Sleep* 2016;39:161–71 CrossRef Medline
49. Chauvette S, Seigneur J, Timofeev I. **Sleep oscillations in the thalamocortical system induce long-term neuronal plasticity.** *Neuron* 2012;75:1105–13 CrossRef Medline
50. Steriade M, Timofeev I. **Neuronal plasticity in thalamocortical networks during sleep and waking oscillations.** *Neuron* 2003;37:563–76 CrossRef Medline
51. Winkelman JW, Buxton OM, Jensen JE, et al. **Reduced brain GABA in primary insomnia: preliminary data from 4T proton magnetic resonance spectroscopy (1H-MRS).** *Sleep* 2008;31:1499–506 CrossRef Medline
52. Morgan PT, Pace-Schott EF, Mason GF, et al. **Cortical GABA levels in primary insomnia.** *Sleep* 2012;35:807–14 CrossRef Medline
53. Killgore WD, Schwab ZJ, Kipman M, et al. **Insomnia-related complaints correlate with functional connectivity between sensory-motor regions.** *Neuroreport* 2013;24:233–40 CrossRef Medline

# MRI with DWI for the Detection of Posttreatment Head and Neck Squamous Cell Carcinoma: Why Morphologic MRI Criteria Matter

A. Ailianou, P. Mundada, T. De Perrot, M. Pusztaszieri, P.-A. Poletti, and M. Becker



## ABSTRACT

**BACKGROUND AND PURPOSE:** Although diffusion-weighted imaging combined with morphologic MRI (DWIMRI) is used to detect posttreatment recurrent and second primary head and neck squamous cell carcinoma, the diagnostic criteria used so far have not been clarified. We hypothesized that precise MRI criteria based on signal intensity patterns on T2 and contrast-enhanced T1 complement DWI and therefore improve the diagnostic performance of DWIMRI.

**MATERIALS AND METHODS:** We analyzed 1.5T MRI examinations of 100 consecutive patients treated with radiation therapy with or without additional surgery for head and neck squamous cell carcinoma. MRI examinations included morphologic sequences and DWI ( $b=0$  and  $b=1000$  s/mm<sup>2</sup>). Histology and follow-up served as the standard of reference. Two experienced readers, blinded to clinical/histologic/follow-up data, evaluated images according to clearly defined criteria for the diagnosis of recurrent head and neck squamous cell carcinoma/second primary head and neck squamous cell carcinoma occurring after treatment, post-radiation therapy inflammatory edema, and late fibrosis. DWI analysis included qualitative (visual) and quantitative evaluation with an ADC threshold.

**RESULTS:** Recurrent head and neck squamous cell carcinoma/second primary head and neck squamous cell carcinoma occurring after treatment was present in 36 patients, whereas 64 patients had post-radiation therapy lesions only. The Cohen  $\kappa$  for differentiating tumor from post-radiation therapy lesions with MRI and qualitative DWIMRI was 0.822 and 0.881, respectively. Mean ADC<sub>mean</sub> in recurrent head and neck squamous cell carcinoma/second primary head and neck squamous cell carcinoma occurring after treatment ( $1.097 \pm 0.295 \times 10^{-3}$  mm<sup>2</sup>/s) was significantly lower ( $P < .05$ ) than in post-radiation therapy inflammatory edema ( $1.754 \pm 0.343 \times 10^{-3}$  mm<sup>2</sup>/s); however, it was similar to that in late fibrosis ( $0.987 \pm 0.264 \times 10^{-3}$  mm<sup>2</sup>/s,  $P > .05$ ). Although ADCs were similar in tumors and late fibrosis, morphologic MRI criteria facilitated distinction between the 2 conditions. The sensitivity, specificity, positive and negative predictive values, and positive and negative likelihood ratios (95% CI) of DWIMRI with ADC<sub>mean</sub>  $< 1.22 \times 10^{-3}$  mm<sup>2</sup>/s and precise MRI criteria were 92.1% (83.5–100.0), 95.4% (90.3–100.0), 92.1% (83.5–100.0), 95.4% (90.2–100.0), 19.9 (6.58–60.5), and 0.08 (0.03–0.24), respectively, indicating a good diagnostic performance to rule in and rule out disease.

**CONCLUSIONS:** Adding precise morphologic MRI criteria to quantitative DWI enables reproducible and accurate detection of recurrent head and neck squamous cell carcinoma/second primary head and neck squamous cell carcinoma occurring after treatment.

**ABBREVIATIONS:** DWIMRI = combined MRI with morphologic sequences and DWI; HN = head and neck; HNSCC = head and neck squamous cell carcinoma; LR = likelihood ratio; pHNSCC = primary head and neck squamous cell carcinoma; rHNSCC = recurrent head and neck squamous cell carcinoma; RTH = radiation therapy; sHNSCC = second primary head and neck squamous cell carcinoma occurring after treatment

Squamous cell carcinoma accounts for 95% of all cancers in the head and neck (HN) region.<sup>1</sup> The aim of treatment is to provide a cure with the maximum possible preservation of organ function. Treatment options comprise radiation therapy (RTH) and/or chemotherapy and/or an operation.<sup>1,2</sup> Up to 25% of early-

stage primary head and neck squamous cell carcinomas (pHNSCCs) and up to 50% of advanced-stage tumors show treatment failure in the form of residual/recurrent HNSCC (rHNSCC), whereas 15% of patients develop second primary HN cancer (sHNSCC).<sup>2,3</sup> Early

Received July 28, 2017; accepted after revision December 2.

From the Division of Radiology (A.A., P.M., T.D.P., P.-A.P., M.B.), Department of Imaging and Medical Informatics, and Division of Clinical Pathology (M.P.), Department of Laboratory and Genetics, Geneva University Hospitals, University of Geneva, Geneva, Switzerland. Dr Ailianou is currently affiliated with the Hospital of Neuchâtel, Neuchâtel, Switzerland.

Please address correspondence to Minerva Becker, MD, Division of Radiology, Department of Imaging and Medical Informatics, Geneva University Hospitals, Rue Gabrielle-Perret-Gentil 4, 1211 Geneva 14, Switzerland; e-mail: Minerva.Becker@hcuge.ch

 Indicates article with supplemental on-line table.

 Indicates article with supplemental on-line photos.

<http://dx.doi.org/10.3174/ajnr.A5548>

detection of rHNSCC/sHNSCC prompts curative salvage treatment and may allow preservation of organ function.

RTH causes dramatic gross and microenvironmental changes in the affected soft tissues. In most cases, inflammatory edema develops, which leads to formation of fibrosis and scar tissue. Inflammatory edema and scar tissue may coexist, and they may render clinical/endoscopic evaluation challenging. Clinical/endoscopic examinations may miss a tumor under intact mucosa or may underestimate it due to its multifocal recurrence pattern. Moreover, panendoscopy is an invasive procedure requiring general anesthesia. A biopsy with negative findings does not exclude rHNSCC/sHNSCC, and multiple biopsies may increase overall morbidity.<sup>2,4,5</sup>

MRI with morphologic sequences and diffusion-weighted imaging (DWIMRI) provides anatomic, qualitative, and quantitative functional information allowing noninvasive assessment of treatment response and detection of rHNSCC/sHNSCC.<sup>5-9</sup> The imaging features of rHNSCC on morphologic MRI sequences have been scarcely addressed in the literature,<sup>1,5,7,10</sup> and several studies have focused on demonstrating the utility of DWI for the detection of recurrence.<sup>5-9,11-13</sup> However, the diagnostic performance of clearly defined morphologic MRI criteria, the interobserver reproducibility, and the impact of each technique (morphologic MRI versus combined DWI with morphologic MRI) have not been assessed in these studies. Earlier studies were rather small,<sup>6,7,13</sup> and they were based on a mix of HNSCC and other histologic tumor types<sup>7,11</sup> or included both local and nodal recurrence.<sup>6,12</sup>

The aim of this study was to evaluate the diagnostic performance of morphologic MRI with clearly defined criteria for the detection of rHNSCC/sHNSCC and to compare it with the diagnostic performance of DWI alone and of DWI combined with morphologic MRI. We likewise aimed to analyze the added value of each technique and their respective contributions to the overall diagnostic performance of DWIMRI.

## MATERIALS AND METHODS

### Patients

The institutional ethics committee approved this retrospective study, which was performed in accordance with the guidelines of the Declaration of Helsinki II. Informed consent was waived. The study population included 114 consecutive patients seen during 3.5 years in our institution. The patients underwent 1.5T MRI with morphologic MRI and DWI sequences for clinically suspected recurrence or for follow-up after RTH with or without an additional operation. Fourteen patients were excluded because of absent follow-up ( $n = 6$ ), nondiagnostic DWI ( $n = 5$ ), and nondiagnostic morphologic MRI and DWI ( $n = 3$ ). The remaining 100 patients formed the basis of the current study. The series comprised 21 women and 79 men with a median age (25 quartile–75 quartile) of 62 years (55–69 years), ranging from 18 to 89 years. The median time interval between the end of RTH and MRI was 14 months (4.5–51 months).

### Imaging Technique

The MRI protocol included imaging from the skull base to the thoracic inlet with FSE T2 and FSE T1 sequences in the axial plane, a short  $\tau$  inversion recovery sequence in the coronal plane, and axial spin-echo EPI DWI ( $b=0$  and 1000 s/mm<sup>2</sup>) with apparent

diffusion coefficient map calculation using monoexponential fitting. After administration of a gadolinium-based contrast agent, we performed T1WI  $\pm$  fat saturation in the axial, coronal, and/or sagittal plane. Sequence parameters were the following: TR/TE = 3300/106 ms, 24 slices, slice thickness = 3 mm, FOV = 230  $\times$  180 mm, matrix = 512  $\times$  416, acquisition time = 3 minutes 30 seconds; and TR/TE = 771/11 ms, 30 slices, slice thickness = 3–4 mm, FOV = 230  $\times$  230 mm, matrix = 512  $\times$  512, acquisition time = 3 minutes 56 seconds for T2- and T1-weighted acquisitions, respectively. DWI parameters were the following: TR/TE = 3200/86 ms, 40 slices, slice thickness = 3–4 mm, FOV = 230  $\times$  230 mm, matrix = 128  $\times$  128, acquisition time = 3 minutes 2 seconds.

### Evaluation of Morphologic MRI and DWI and Applied Diagnostic Criteria

Two board-certified HN radiologists (>10 years' experience in HN oncology), blinded to all clinical data (patient history, histology, and clinical/radiologic follow-up), analyzed the images separately. First, all morphologic MRIs were evaluated with the reader blinded to DWI. Then the readers evaluated morphologic MRI and DWI together (DWIMRI). After separate evaluations by each reader and assessment of interobserver variability, consensus was reached in cases of discrepant interpretations.

On the basis of the experience at our institution and according to published data,<sup>1,14,15</sup> the interpretation of morphologic MRI was performed according to the following criteria: 1) rHNSCC/sHNSCC was diagnosed in the presence of a masslike lesion with moderately high (intermediate) signal intensity on T2, low signal intensity on T1, and moderate enhancement after IV gadolinium administration; 2) post-RTH inflammatory edema was diagnosed in the presence of a diffuse lesion with high signal intensity on T2, low signal intensity on T1, and strong postcontrast enhancement; and 3) late RTH fibrosis (post-RTH scar) was diagnosed in the presence of a linear or triangular lesion with very low signal intensity on T2 (similar to or lower than that of muscle), low signal intensity on T1, and faint/absent contrast enhancement.<sup>1,14,15</sup>

DWI was assessed visually (qualitative DWI) by analyzing the signal intensity on the  $b=1000$  image and on the corresponding ADC map. The association of moderately high or very high signal on  $b=1000$  and low signal on ADC maps was interpreted as suggesting malignancy. The association of high signal on both  $b=1000$  and the ADC map (T2 shthrough) or low signal on  $b=1000$  and high signal on the ADC map was interpreted as post-RTH inflammatory edema, whereas low signal on  $b=1000$  and low signal on ADC was regarded as suggesting RTH-induced late fibrosis. Quantitative DWI analysis was based on ADC measurements in benign and malignant lesions, which was performed by drawing small ROIs on multiple slices manually, according to the recommendations in the literature.<sup>5,16,17</sup> In large, masslike lesions, ROIs were placed on the most hypointense lesion parts on the ADC maps, avoiding necrotic portions.<sup>5,16</sup>

For combined DWIMRI interpretation, whenever MRI morphology and DWI findings were concordant, the diagnosis of tumor was straightforward. Whenever morphology and DWI were discordant, on the basis of our experience, we applied the following criteria: 1) For lesions with characteristic morphologic features of late fibrosis, morphology outweighed positive DWI

**Table 1: Patient and tumor characteristics**

	Primary HNSCC	rHNSCC and sHNSCC after Treatment
Total No. of patients		100
Total No. of tumors	103	38 <sup>a</sup>
Female (No.) (%)		22 (22%)
Male (No.) (%)		78 (78%)
Mean age (yr)	59.3 ± 11.3	61.5 ± 11.1
Treatment modalities in pHNSCC (No. of patients)		NA
RTH alone	52	
Operation followed by RTH	48	
Median interval (quartile 1–quartile 3) between end of RTH and rHNSCC/sHNSCC (mo)	NA	14 (4.5–51)
Tumor location (No. of tumor sites) (%)		
Nasopharynx	7 (6.8%)	1 (2.6%)
Oral cavity	22 (21.3%)	13 (34.2%)
Oropharynx	38 (36.9%)	8 (21.1%)
Hypopharynx	12 (11.6%)	5 (13.1%)
Larynx	19 (18.5%)	6 (15.8%)
Paranasal sinuses	4 (3.9%)	2 (5.3%)
Base of the skull	0 (0%)	3 (7.9%)
Unknown primary tumor	1 (1%)	0 (0%)
T classification <sup>b</sup>		
Tx	1 (1%)	0 (0%)
Tis	1 (1%)	1 (2.6%)
T1	14 (13.6%)	3 (7.9%)
T2	30 (29.1%)	7 (18.4%)
T3	25 (24.3%)	6 (15.8%)
T4	32 (31.0%)	21 (55.3%)
N classification <sup>b</sup>		
N0	31 (30.1%)	26 (68.4%)
N1	20 (19.4%)	5 (13.2%)
N2	45 (43.7%)	6 (15.8%)
N3	6 (5.8%)	1 (2.6%)
Nx	1 (1%)	0 (0%)
M classification <sup>b</sup>		
Mx	7 (6.8%)	0 (0%)
M0	94 (91.3%)	36 (94.7%)
M1	2 (1.9%)	2 (5.3%)

**Note:**—NA indicates not applicable.

<sup>a</sup> Thirty-three rHNSCCs and 5 sHNSCCs.

<sup>b</sup> Tumor, Node, Metastasis (TNM) classification according to Union for International Cancer Control 2016.<sup>28</sup>

findings; 2) for lesions with morphology strongly suggesting rHNSCC/sHNSCC, morphology outweighed negative DWI findings; and 3) in the absence of a suspicious lesion at morphology, positive findings on DWI outweighed negative morphology. For the analysis of combined DWIMRI, we recorded the number of instances in which DWI changed the interpretation of morphologic MRI; and on the contrary, we recorded the number of instances, in which MRI changed the interpretation of DWI.

### Standard of Reference

The data extracted from the medical records were used for the validation of findings. The distinction between rHNSCC and sHNSCC was made on the basis of the interdisciplinary HN oncology tumor board reports. In rHNSCC, differentiation was made between local recurrence (at the same site as the pHNSCC or in the immediate tumor vicinity) and distant recurrence (eg, base of the skull due to perineural tumor spread). The standard of reference consisted of histology and follow-up. Histology from endoscopic biopsy and/or salvage operation and additional follow-up were available in 50 lesions (37 HNSCCs and 13 benign

lesions), whereas follow-up alone was available in 53 lesions (1 HNSCC and 52 benign lesions). Follow-up included clinical examination and cross-sectional imaging for at least 18 months after MRI. It was used to validate negative results as true-negatives in patients without biopsy and in patients with negative biopsy results. Twenty-nine patients died from disease during the follow-up with a median time interval (25th quartile–75th quartile) between MRI and death of 10 months (4–15 months). The median follow-up in the 71 surviving patients was 25 months (19–33 months).

### Statistical Analysis

Comparison between ADC<sub>mean</sub> values for tumors and benign lesions was performed with a Wilcoxon rank sum test with continuity correction. Receiver operating characteristic analysis of ADC<sub>mean</sub> values categorized according to the standard of reference was performed. An optimal cutoff value for ADC<sub>mean</sub> was calculated according to the literature.<sup>18</sup> The diagnostic performance of MRI, DWI, qualitative DWIMRI, and quantitative DWIMRI was assessed in terms of sensitivity, specificity, positive and negative predictive values, and positive and negative likelihood ratios (LR+, LR-). Percentage agreement and Cohen  $\kappa$  coefficients were used to assess interobserver reproducibility, with  $\kappa$  values of 0.21–0.40 indicating fair agreement; 0.41–0.60, moderate agreement; 0.61–0.80, substantial agreement; and 0.81–1.00, almost perfect agreement.<sup>19</sup> Comparison between sensitivities and specificities was performed with the McNemar test, whereas LRs were compared using a regression model approach.<sup>20</sup> Statistical analyses were conducted with R3.3.1 (<http://www.R-project.org>).<sup>21</sup> Statistical tests were 2-sided with a significance level of .05.

## RESULTS

### Patient and Tumor Characteristics

Patient and tumor characteristics are shown in Table 1. Post-RTH HNSCC (rHNSCC/sHNSCC) was diagnosed in 36 patients in 38 locations (tumor prevalence = 37%; 95% CI, 28%–47%; 2 patients had 2 HNSCCs each). There were 31 local rHNSCCs, 2 distant rHNSCCs (base of the skull via perineural spread), and 5 sHNSCCs in the HN region. Most post-RTH tumors ( $n = 33$ ) occurred in the same anatomic subsite as the pHNSCC ( $n = 23$ ) or at the periphery of the RTH field ( $n = 10$ ). Nevertheless, patients with oropharyngeal pHNSCC developed sHNSCC ( $n = 5$ ) more often than patients with pHNSCC originating in other HN subsites ( $P < .001$ ).

**Table 2: Diagnostic performance of morphologic MRI alone, quantitative DWI alone, qualitative DWIMRI, and quantitative DWIMRI with ADCmean <math>1.22 \times 10^{-3} \text{ mm}^2/\text{s}</math>**

	Morphologic MRI	Quantitative DWI with ADCmean <math>< 1.22</math>	Morphologic MRI with Qualitative DWI	Morphologic MRI with Quantitative DWI (ADCmean <math>< 1.22</math>)
TP (No.)	30	30	34	35
TN (No.)	52	56	59	62
FP (No.)	13	9	6	3
FN (No.)	8	8	4	3
Sensitivity (%) <sup>a</sup>	78.9	78.9	89.4	92.1
(95% CI)	(65.9–91.9)	(65.9–91.9)	(79.7–99.2)	(83.5–100.0)
Specificity (%) <sup>b</sup>	80.0	86.1	90.8	95.4
(95% CI)	(70.3–89.7)	(74.8–93.1)	(83.7–97.8)	(90.3–100.0)
PPV (%)	69.7	76.9	85.0	92.1
(95% CI)	(56.1–83.5)	(60.3–88.3)	(73.9–96.1)	(83.5–100.0)
NPV (%)	86.6	87.5	93.6	95.4
(95% CI)	(78.1–95.3)	(76.3–94.1)	(87.6–99.6)	(90.2–100.0)
LR+ <sup>c</sup>	3.94	5.70	9.69	19.9
(95% CI)	(2.36–6.59)	(3.04–10.68)	(4.48–20.9)	(6.58–60.5)
LR- <sup>d</sup>	0.26	0.24	0.11	0.08
(95% CI)	(0.14–0.49)	(0.13–0.45)	(0.04–0.29)	(0.03–0.24)

**Note:**—TP indicates true-positive; TN, true-negative; FP, false-positive; FN, false-negative; PPV, positive predictive value; NPV, negative predictive value.

<sup>a</sup> Comparison of sensitivities: MRI vs DWI:  $P = 1$ ; MRI vs qualitative DWIMRI:  $P = .10$ ; MRI vs quantitative DWIMRI:  $P = .025$ ; qualitative DWIMRI vs quantitative DWIMRI:  $P = .31$ ; DWI vs quantitative DWIMRI:  $P = .05$ .

<sup>b</sup> Comparison of specificities: MRI vs DWI:  $P = .34$ ; MRI vs qualitative DWIMRI:  $P = .05$ ; MRI vs quantitative DWIMRI:  $P = .004$ ; qualitative DWIMRI vs quantitative DWIMRI:  $P = .18$ ; DWI vs quantitative DWIMRI:  $P = .03$ .

<sup>c</sup> Comparison of LR+: MRI vs DWI:  $P = .36$ ; MRI vs qualitative DWIMRI:  $P = .03$ ; MRI vs quantitative DWIMRI:  $P = .004$ ; qualitative DWIMRI vs quantitative DWIMRI:  $P = .17$ ; DWI vs quantitative DWIMRI:  $P = .02$ .

<sup>d</sup> Comparison of LR-: MRI vs DWI:  $P = .85$ ; MRI vs qualitative DWIMRI:  $P = .06$ ; MRI vs quantitative DWIMRI:  $P = .01$ ; qualitative DWIMRI vs quantitative DWIMRI:  $P = .24$ ; DWI vs quantitative DWIMRI:  $P = .04$ .

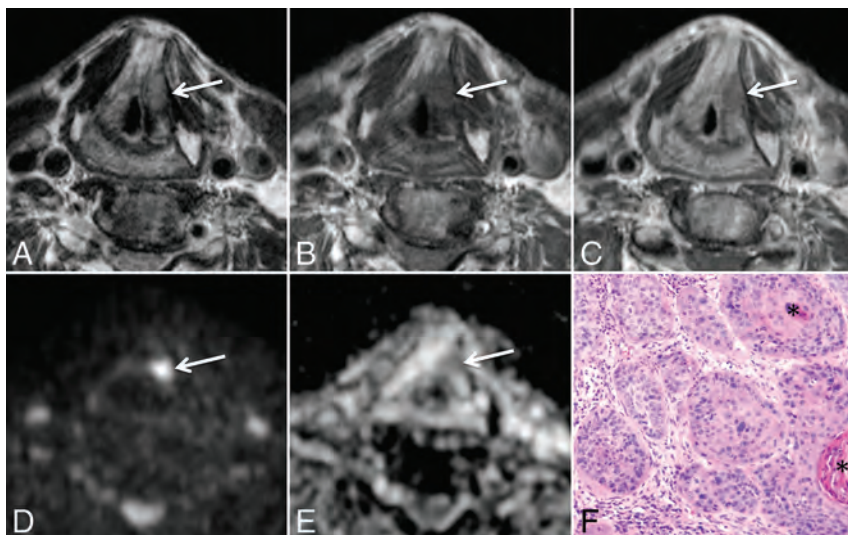


**FIG 1.** DWIMRI obtained 23 months after RTH for laryngeal squamous cell carcinoma and increasing hoarseness. Axial T2 (A), T1 (B), and contrast-enhanced T1 (C) show an oval lesion (arrows) in the left false cord and left paraglottic space with intermediate signal intensity on T2, low signal intensity on T1, and moderate contrast enhancement highly suspicious for rHNSCC. The  $b=1000$  image (D) shows high signal intensity in the lesion. ADC map (E) reveals low signal intensity compatible with restricted diffusion (arrow), further suggesting recurrence (ADCmean =  $0.798 \times 10^{-3} \text{ mm}^2/\text{s}$ ). Endoscopic biopsy confirmed rHNSCC. F, Histology (H&E, original magnification  $\times 100$ ) shows squamous cell carcinoma with areas of densely packed and loosely packed squamous cells of variable size with keratin pearls (asterisk).

### Results of Image Interpretation

Morphologic images were of good/acceptable quality in all patients. In 7 patients, DWI showed artifacts in the floor of the mouth due to dental hardware ( $n = 5$ ), tongue base ( $n = 1$ ), or lower neck ( $n = 1$ ). Because both readers considered DWI to be of acceptable quality, these patients were not excluded from analysis.

Evaluations of the 2 readers were concordant in 93/100 patients (96/103 lesions, percentage agreement = 93.2%) with MRI and in 94/100 patients (97/103 lesions, percentage agreement = 94.2%) with qualitative DWIMRI, respectively. The Cohen  $\kappa$  for differentiating tumor from post-RTH lesions with MRI and with qualitative DWIMRI was 0.822 and 0.881, respectively, indicating excellent interobserver reproducibility.<sup>19</sup> Morphologic MRI and DWI were discordant in 28 lesions. The Cohen  $\kappa$  for the 2 readers for combined DWIMRI in this subset of lesions was 0.774 (substantial interobserver reproducibility<sup>19</sup>), and the percentage agreement was 89.3%.

Results of the interpretation of MRI and DWIMRI are indicated in Table 2 for the consensus between the 2 readers. Morphologic MRI yielded 30 true-positive evaluations (Fig 1 and On-line Fig 1) and 52 true-negative evaluations (On-line Fig 2). Among the 52 true-negative evaluations, 8 fulfilled the criteria of late fibrosis due to very low signal on T2 (Figs 2 and 3). Both readers correctly identified these lesions. The 8 false-negative evaluations with MRI were caused by the following: abscess from infected osteonecrosis masking recurrence ( $n = 1$ ), in situ tumor ( $n = 1$ ), and T1 tumor ( $n = 1$ ), therefore, too small to be detected by imaging; missed tumor due to poor lesion conspicuity ( $n = 3$ ); and recurrent disease misinterpreted as

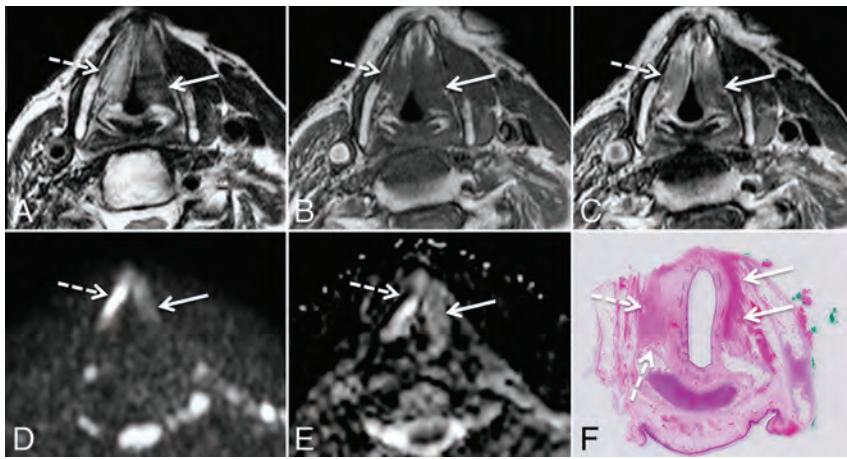


**FIG 2.** DWIMRI obtained 13 months after RTH and neck dissection for squamous cell carcinoma of the larynx and oropharynx. The patient had massive weight loss, malnutrition, and recurrent aspiration pneumonia. Endoscopy showed intact mucosa and fixed vocal cords bilaterally. Axial T2 (A), T1 (B), and contrast-enhanced T1 (C) show a triangular lesion (arrows) in the left true vocal cord with very low signal intensity on T2, low signal intensity on T1, and faint contrast enhancement suggesting post-RTH late fibrosis. In contrast, the right vocal cord (dashed arrows) displays high signal intensity on T2, low signal on T1, and enhancement. Findings on the right were interpreted as suggesting inflammatory edema. The  $b=1000$  image (D) and ADC map (E) reveal no restricted diffusion in the right vocal cord ( $ADC_{mean} = 1.643 \times 10^{-3} \text{ mm}^2/\text{s}$ ) and restricted diffusion with low ADC in the left vocal cord ( $ADC_{mean} = 1.006 \times 10^{-3} \text{ mm}^2/\text{s}$ ). Because the nonfunctional larynx was the cause of malnutrition and recurrent aspiration pneumonia, laryngectomy was performed. F, Corresponding whole-organ histologic slice (H&E) shows extensive muscle fibrosis on the left (arrows) and inflammatory edema with denervation on the right (dashed arrows).

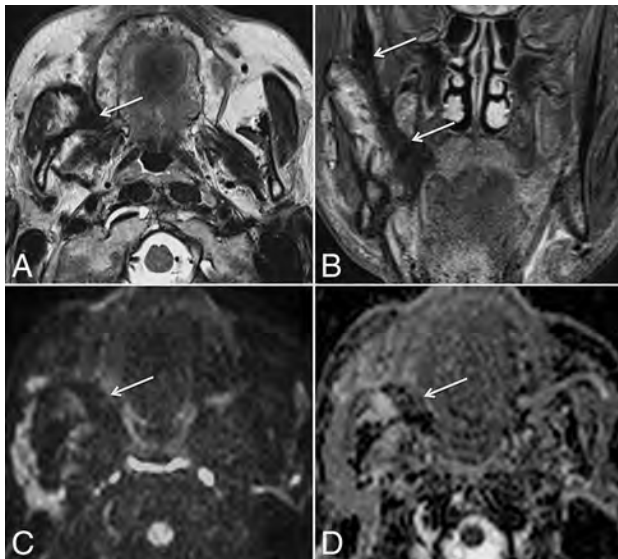


**FIG 3.** DWIMRI obtained 3 months after RTH and buccopharyngectomy for squamous cell carcinoma of the retromolar trigone. The patient had right reflex otalgia and progressing trismus. Endoscopy could not be performed. Axial T2 (A) and coronal STIR (B) images show a triangular, elongated, strongly hypointense lesion (arrows) on the right. There was no contrast enhancement (not shown). The diagnosis of benign post-RTH late fibrosis was made. The  $b=1000$  image (C) reveals low signal. ADC map (D) likewise shows low signal ( $ADC_{mean} = 0.731 \times 10^{-3} \text{ mm}^2/\text{s}$ ). Follow-up at 38 months (not shown) showed no recurrence but progressive scar retraction on MRI.

inflammation ( $n = 2$ ). Thirteen false-positive interpretations with MRI were caused by granulation tissue, which displayed similar signal intensity on T2 and enhancement similar to that of rHNSCC/sHNSCC.

Quantitative DWIMRI analysis revealed that  $ADC_{mean}$

values were significantly lower in rHNSCC/sHNSCC than in benign changes, despite overlap between both groups (mean  $ADC_{mean} = 1.097 \pm 0.295 \times 10^{-3} \text{ mm}^2/\text{s}$  versus  $1.659 \pm 0.418 \times 10^{-3} \text{ mm}^2/\text{s}$ , respectively;  $P < .001$ ). Boxplots for  $ADC_{mean}$  of benign-versus-malignant lesions are shown in Fig 4. Boxplots for  $ADC_{mean}$  in post-RTH tumors versus late fibrosis and inflammatory edema revealed that late fibrosis had  $ADC_{mean}$  values similar to those of malignant tumors (Fig 5). Mean  $ADC_{mean}$  was  $0.987 \pm 0.264 \times 10^{-3} \text{ mm}^2/\text{s}$  in post-RTH late fibrosis and  $1.097 \pm 0.295 \times 10^{-3} \text{ mm}^2/\text{s}$  in tumors, respectively ( $P > .05$ ).

The receiver operating characteristics analysis of ADC measurements (Fig 6) provided an optimal  $ADC_{mean}$  threshold of  $1.222 \times 10^{-3} \text{ mm}^2/\text{s}$  (sensitivity = 78.9%, specificity = 86.1%, positive predictive value = 76.9%, negative predictive value = 87.5%) for  $ADC_{mean}$  values only.

Results for qualitative (visual) DWIMRI and quantitative DWIMRI (with an  $ADC_{mean}$  threshold of  $< 1.22 \times 10^{-3} \text{ mm}^2/\text{s}$ ) are shown in Table 2. In comparison with morphologic MRI, qualitative and quantitative DWIMRI enabled the detection of post-RTH HNSCCs with poor morphologic conspicuity in 4 and 5 cases, respectively. Likewise, false-positive MRI interpretations were avoided with qualitative and quantitative DWIMRI in 10 and 11 instances, respectively. On the contrary, in comparison with DWI alone, morphologic MRI enabled avoiding 7 false-positive DWI evaluations due to the characteristic aspect of late fibrosis on T2 and facilitated the detection of 5 recurrent cancers, which were missed on DWI (On-line Fig 3).

### Review of the Literature

For the discussion of our results, we have performed a review of the current literature for the detection of post-RTH HNSCC with DWIMRI and have calculated the respective likelihood ratios (On-line Table).

### DISCUSSION

The studies demonstrating the utility of DWIMRI for the detection of post-RTH HNSCC (On-line Table) are based on the knowledge that high cellularity of recurrent tumors results in low  $ADC_{mean}$  values.<sup>5-9,11-13</sup> It is speculated that post-RTH tissue changes (inflammatory edema, necrosis, fibrosis) lead to high  $ADC_{mean}$  values. However, no study has examined the contribution of each post-RTH tissue change to the overall post-RTH  $ADC_{mean}$ . Literature shows that despite sparse references, post-RTH cerebral gliosis may show low  $ADC_{mean}$  and an abscess may show restricted diffusion.<sup>22</sup> Moreover, rHNSCC with cystic or necrotic components may show high  $ADC_{mean}$ . Despite this di-

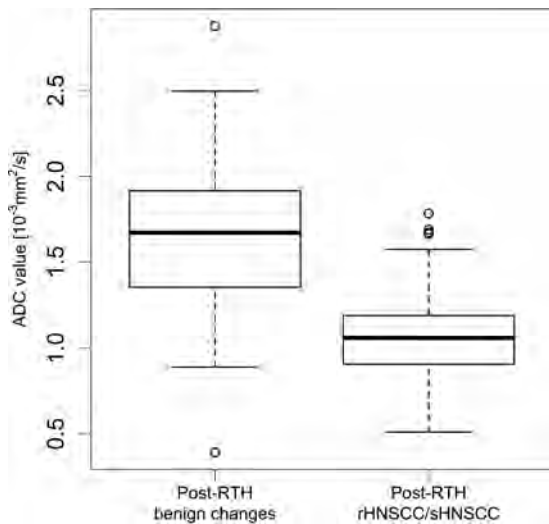


**FIG 4.** Box-and-whisker plots of ADCmean values in patients with post-RTH changes and post-RTH tumors. The *horizontal lines* represent the median values, and the bottom and the top of the box represent the 25th and 75th quartiles, respectively. Median ADCmean (25th–75th quartiles) for rHNSCC/sHNSCC =  $1.061 (0.907\text{--}1.191) \times 10^{-3} \text{ mm}^2/\text{s}$ . Median ADCmean (25th–75th quartiles) for post-RTH changes (late fibrosis and inflammatory edema together) =  $1.671 (1.3355\text{--}1.915) \times 10^{-3} \text{ mm}^2/\text{s}$ .

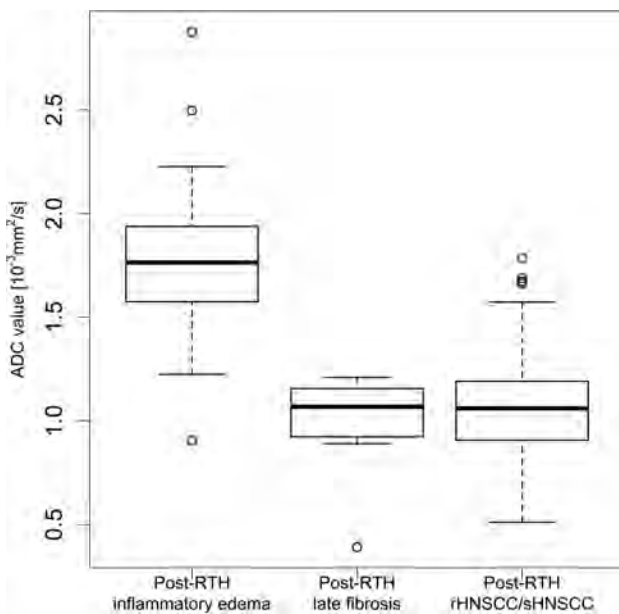


**FIG 5.** Box-and-whisker plots of ADCmean values in patients with post-RTH inflammatory edema, late fibrosis, and post-RTH HNSCCs. The *horizontal lines* represent the median values; the bottom and the top of the box represent the 25th and 75th quartiles, respectively. Median ADCmean (25th–75th quartiles) for rHNSCC/sHNSCC =  $1.061 (0.907\text{--}1.191) \times 10^{-3} \text{ mm}^2/\text{s}$ . Median ADCmean (25th–75th quartiles) for post-RTH inflammatory edema =  $1.764 (1.575\text{--}1.938) \times 10^{-3} \text{ mm}^2/\text{s}$ . Median ADCmean (25th–75th quartiles) for late fibrosis/mature scar post-RTH =  $1.068 (0.939\text{--}1.152) \times 10^{-3} \text{ mm}^2/\text{s}$ . There was no statistically significant difference between ADCmean in late fibrosis and rHNSCC/sHNSCC ( $P > .05$ ). However, there was a significant difference between ADCmean in inflammatory post-RTH edema and late fibrosis ( $P < .05$ ).

versity, in all aforementioned studies, the ADCs of various post-RTH changes were grouped together as “post-RTH ADCmean” and were compared with the ADCs of rHNSCC. This comparison

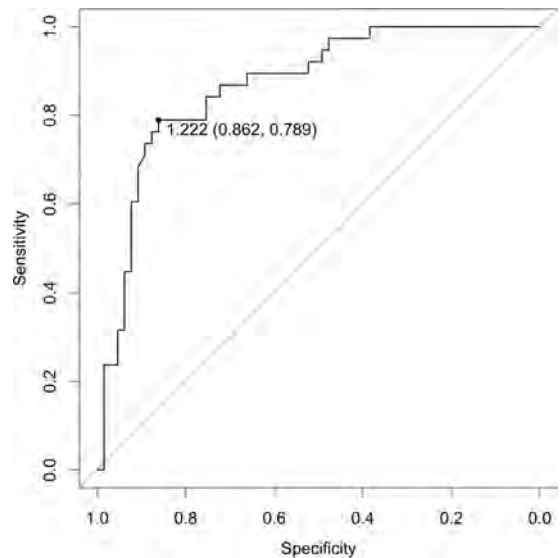


**FIG 6.** Receiver operating characteristic curve for the quantitative analysis of ADCmean values showing the area under the curve of 0.8678. A threshold of  $\text{ADC} = 1.222 \times 10^{-3} \text{ mm}^2/\text{s}$  was found (see description in the text). This threshold yielded a sensitivity of 78.9%, a specificity of 86.2%, and an accuracy of 83.5%.

showed that the ADCmean values of the 2 groups substantially overlapped. Despite the use of similar DWI sequences, the ADC thresholds obtained by these studies for differentiating rHNSCC from post-RTH changes varied from  $0.96$  to  $1.46 \times 10^{-3} \text{ mm}^2/\text{s}$ .<sup>5-8,11-13</sup>

Tshering Vogel et al<sup>5</sup> have shown that major overlap of ADC values limits the ability of quantitative DWI to differentiate rHNSCC from post-RTH changes. In their study, combined morphologic MRI and qualitative DWI could detect rHNSCC more accurately than combined morphologic MRI and quantitative DWI. However, the criteria used for morphologic analysis were neither defined nor analyzed. In our study, there was no significant difference between the ADCmean of late fibrosis and rHNSCC/sHNSCC ( $P > .05$ ). However, there was a significant difference between the ADCmean of post-RTH edema and late fibrosis ( $P < .05$ ), with virtually no overlap between these 2 values. This finding highlights the drawback of grouping ADC values of all post-RTH changes together.

Both Abdel Razek et al<sup>7</sup> and Vaid et al<sup>11</sup> reported false-positive results with DWIMRI due to late fibrosis. Other studies have not discussed the causes of false-positive cases. Although the T2 appearance of late fibrosis has been briefly addressed by some authors, its diagnostic utility as a complementary tool to DWI and its impact on the diagnostic performance have not been analyzed.<sup>1,14,23</sup> Because late fibrosis is mainly composed of densely packed collagen, ADCs tend to be low (T2 blackout effect) as opposed to RTH-induced inflammatory edema, which tends to have high ADCs. In the current study, morphologic MRI, mainly T2, enabled accurate diagnosis of late fibrosis, which otherwise may mimic rHNSCC on DWI.

Previous investigators have not compared the diagnostic performance of DWI with that of morphologic MRI. Data of the current series show that morphologic MRI with clearly defined criteria has a similar diagnostic performance to DWI alone; how-

ever, the combination of the 2 yields superior results. Careful analysis of signal intensities on morphologic MRI contributes significantly to an improved specificity of DWIMRI, whereas the overall effect on sensitivity is less pronounced.

The wide variability in sensitivity, specificity, and positive and negative predictive values of DWIMRI demonstrated by the aforementioned studies can be explained by several factors: histologic heterogeneity (HNSCC only versus HNSCC mixed with other tumor types), local recurrence only versus combined local and nodal recurrence, small sample size, varying tumor prevalence, and differences in ROI sampling.<sup>5-8,11-13</sup> Although sensitivity and specificity are not influenced by disease prevalence, they can vary depending on the disease spectrum in the study population. Disease prevalence has an important impact on the positive predictive value and a slightly weaker influence on the negative predictive value. Therefore, the use of a likelihood ratio as a measure of test accuracy overcomes the drawback of other metrics because it does not depend on disease prevalence.<sup>24</sup> Consequently, the LRs from 1 study are applicable to other studies. A LR+ of >10 indicates a good diagnostic test for ruling in the diagnosis, whereas an LR- of <0.1 indicates a good test for ruling out the diagnosis.<sup>24</sup> Results of our study show that quantitative DWIMRI was clearly superior to morphologic MRI and DWI alone because the LR+ and LR- (19.9 and 0.08, respectively) fulfilled the criteria of a good diagnostic test. Comparison with the literature further suggests that except for Vandecaveye et al,<sup>6</sup> the LR+ and LR- of quantitative DWIMRI were suboptimal in all published series; the values were similar to those of DWI alone and morphologic MRI alone in the current study.

To the best of our knowledge, except for Vaid et al,<sup>11</sup> none of the previous authors tested the interobserver reproducibility of their results regarding the assessment of post-RTH cases. In our study, the  $\kappa$  values for MRI and DWIMRI were >81%, suggesting almost perfect interobserver agreement.<sup>19</sup> Therefore, our results are reproducible, provided that experienced readers perform the image analysis. Although the guidelines for the interpretation of interrater reliability proposed by Landis and Koch<sup>19</sup> are widely used, several authors have questioned judgments about acceptable  $\kappa$  values in medical research.<sup>25</sup> The  $\kappa$  statistic was initially designed to account for raters guessing on scores. Despite this advantage, the  $\kappa$  statistic may substantially lower the estimate of agreement. Therefore, reporting both  $\kappa$  and percentage agreement may represent a good compromise.<sup>25</sup>

Our study has some limitations. It is a retrospective study of patients from a single hospital, which could have created a selection bias. Exclusion of patients who were followed up with CT and PET/CT and those with nodal recurrence only was consistent with the aim of our study and was unavoidable. To maintain homogeneity of results, we included only patients scanned on a 1.5T MRI scanner. These factors could have further added to selection bias. Another study limitation is the lack of quantitative T2 and contrast-enhanced T1 signal analysis. Although categorizing signal intensity as high, intermediate, and low may appear somewhat subjective, this visual approach is widely used in HN routine and for the assessment of tumors in other organs. Quantification of T2 and T1 requires the additional acquisition of mapping sequences to calculate relaxation maps. Quantitative information can addi-

tionally be extracted with texture/histogram analysis. This post-processing tool can be applied retrospectively to all images acquired in clinical routine.<sup>26,27</sup> However, lack of standardized software, evolving research, and variable numeric algorithms currently limit the use of these new promising tools in clinical routine.

## CONCLUSIONS

The combination of precise morphologic MRI criteria and quantitative DWI with an ADCmean <  $1.22 \times 10^{-3}$  mm<sup>2</sup> has an excellent interobserver reproducibility and yields likelihood ratios of a good diagnostic test to rule in and out post-RTH rHNSCC/sHNSCC. Our study shows that morphologic MRI criteria and DWI are complementary and contribute differently to the overall diagnostic performance of combined DWIMRI.

## REFERENCES

1. Varoquaux A, Rager O, Dulguerov P, et al. **Diffusion-weighted and PET/MR imaging after radiation therapy for malignant head and neck tumors.** *Radiographics* 2015;35:1502–27 CrossRef Medline
2. de Bree R, van der Putten L, Brouwer J, et al. **Detection of locoregional recurrent head and neck cancer after (chemo)radiotherapy using modern imaging.** *Oral Oncol* 2009;45:386–93 CrossRef Medline
3. King AD, Thoeny HC. **Functional MRI for the prediction of treatment response in head and neck squamous cell carcinoma: potential and limitations.** *Cancer Imaging* 2016;16:23 CrossRef Medline
4. Brouwer J, Bodar EJ, De Bree R, et al. **Detecting recurrent laryngeal carcinoma after radiotherapy: room for improvement.** *Eur Arch Otorhinolaryngol* 2004;261:417–22 Medline
5. Tshering Vogel DW, Zbaeren P, Geretschlaeger A, et al. **Diffusion-weighted MR imaging including bi-exponential fitting for the detection of recurrent or residual tumour after (chemo)radiotherapy for laryngeal and hypopharyngeal cancers.** *Eur Radiol* 2013;23:562–69 CrossRef Medline
6. Vandecaveye V, De Keyzer F, Nuyts S, et al. **Detection of head and neck squamous cell carcinoma with diffusion weighted MRI after (chemo)radiotherapy: correlation between radiologic and histopathologic findings.** *Int J Radiat Oncol Biol Phys* 2007;67:960–71 CrossRef Medline
7. Abdel Razek AA, Kandeel AY, Soliman N, et al. **Role of diffusion-weighted echo-planar MR imaging in differentiation of residual or recurrent head and neck tumors and posttreatment changes.** *AJNR Am J Neuroradiol* 2007;28:1146–52 CrossRef Medline
8. Hwang I, Choi SH, Kim YJ, et al. **Differentiation of recurrent tumor and posttreatment changes in head and neck squamous cell carcinoma: application of high b-value diffusion-weighted imaging.** *AJNR Am J Neuroradiol* 2013;34:2343–48 CrossRef Medline
9. King AD, Mo FK, Yu KH, et al. **Squamous cell carcinoma of the head and neck: diffusion-weighted MR imaging for prediction and monitoring of treatment response.** *Eur Radiol* 2010;20:2213–20 CrossRef Medline
10. Mukherji SK, Wolf GT. **Evaluation of head and neck squamous cell carcinoma after treatment.** *AJNR Am J Neuroradiol* 2003;24:1743–46 Medline
11. Vaid S, Chandorkar A, Atre A, et al. **Differentiating recurrent tumours from post-treatment changes in head and neck cancers: does diffusion-weighted MRI solve the eternal dilemma?** *Clin Radiol* 2017;72:74–83 CrossRef Medline
12. Desouky SS, AboSeif SS, Shama SS, et al. **Role of dynamic contrast enhanced and diffusion weighted MRI in the differentiation between post treatment changes and recurrent laryngeal cancers.** *Egypt J Radiol Nucl Med* 2015;46:379–89 CrossRef
13. Gouhar GK, El-Hariri MA. **Feasibility of diffusion weighted MR im-**

- aging in differentiating recurrent laryngeal carcinoma from radionecrosis. *Egypt J Radiol Nucl Med* 2011;42:169–75 CrossRef
14. King AD, Keung CK, Yu KH, et al. **T2-weighted MR imaging early after chemoradiotherapy to evaluate treatment response in head and neck squamous cell carcinoma.** *AJNR Am J Neuroradiol* 2013;34:1237–41 CrossRef Medline
  15. Becker M, Varoquaux AD, Combescure C, et al. **Local recurrence of squamous cell carcinoma of the head and neck after radio(chemo)therapy: diagnostic performance of FDG-PET/MRI with diffusion-weighted sequences.** *Eur Radiol* 2018;28:651–63 CrossRef Medline
  16. Thoeny HC, De Keyser F, King AD. **Diffusion-weighted MR imaging in the head and neck.** *Radiology* 2012;263:19–32 CrossRef Medline
  17. Varoquaux A, Rager O, Lovblad KO, et al. **Functional imaging of head and neck squamous cell carcinoma with diffusion-weighted MRI and FDG PET/CT: quantitative analysis of ADC and SUV.** *Eur J Nucl Med Mol Imaging* 2013;40:842–52 CrossRef Medline
  18. Perkins NJ, Schisterman EF. **The inconsistency of “optimal” cut-points obtained using two criteria based on the receiver operating characteristic curve.** *Am J Epidemiol* 2006;163:670–75 CrossRef Medline
  19. Landis JR, Koch GG. **The measurement of observer agreement for categorical data.** *Biometrics* 1977;33:159–74 CrossRef Medline
  20. Gu W, Pepe MS. **Estimating the diagnostic likelihood ratio of a continuous marker.** *Biostatistics* 2011;12:87–101 CrossRef Medline
  21. R Core Team. *R: A Language and Environment for Statistical Computing.* Vienna: R Foundation for Statistical Computing; 2017
  22. Hein PA, Eskey CJ, Dunn JF, et al. **Diffusion-weighted imaging in the follow-up of treated high-grade gliomas: tumor recurrence versus radiation injury.** *AJNR Am J Neuroradiol* 2004;25:201–09 Medline
  23. Farina D, Borghesi A, Botturi E, et al. **Treatment monitoring of paranasal sinus tumors by magnetic resonance imaging.** *Cancer Imaging* 2010;10:183–93 CrossRef Medline
  24. Šimundić AM. **Measures of diagnostic accuracy: basic definitions.** *EJIFCC* 2009;19:203–11 Medline
  25. McHugh ML. **Interrater reliability: the kappa statistic.** *Biochem Med* 2012;22:276–82 Medline
  26. Kuno H, Qureshi MM, Chapman MN, et al. **CT texture analysis potentially predicts local failure in head and neck squamous cell carcinoma treated with chemoradiotherapy.** *AJNR Am J Neuroradiol* 2017;38:2334–40 CrossRef Medline
  27. de Perrot T, Lenoir V, Domingo Ayllon M, et al. **Apparent diffusion coefficient histograms of human papillomavirus-positive and human papillomavirus-negative head and neck squamous cell carcinoma: assessment of tumor heterogeneity and comparison with histopathology.** *AJNR Am J Neuroradiol* 2017;38:2153–60 CrossRef Medline
  28. Brierley JD, Gospodarowicz MK, Wittekind C. *TNM Classification of Malignant Tumours.* 8th ed. Oxford: Wiley-Blackwell; 2017

# Clinical Validation of a Predictive Model for the Presence of Cervical Lymph Node Metastasis in Papillary Thyroid Cancer

N.U. Patel, K.E. Lind, K. McKinney, T.J. Clark, S.S. Pokharel, J.M. Meier, E.R. Stamm, K. Garg, and B. Haugen

## ABSTRACT

**BACKGROUND AND PURPOSE:** Ultrasound is a standard technique to detect lymph node metastasis in papillary thyroid cancer. Cystic changes and microcalcifications are the most specific features of metastasis, but with low sensitivity. This prospective study compared the diagnostic accuracy of a predictive model for sonographic evaluation of lymph nodes relative to the radiologist's standard assessment in detecting papillary thyroid cancer metastasis in patients after thyroidectomy.

**MATERIALS AND METHODS:** Cervical lymph node sonographic images were reported by a radiologist (R method) per standard practice. The same images were independently evaluated by another radiologist using a sonographic predictive model (M method). A test was considered positive for metastasis if the R or M method suggested lymph node biopsy. The result of lymph node biopsy or surgical pathology was used as the reference standard. We estimated relative true-positive fraction and relative false-positive fraction using log-linear models for correlated binary data for the M method compared with the R method.

**RESULTS:** A total of 237 lymph nodes in 103 patients were evaluated. Our analysis of relative true-positive fraction and relative false-positive fraction included 54 nodes with pathologic results in which at least 1 method (R or M) was positive. The M method had a higher relative true-positive fraction of 1.46 (95% CI, 1.12–1.91;  $P = .006$ ) and a lower relative false-positive fraction of 0.58 (95% CI, 0.36–0.92;  $P = .02$ ) compared with the R method.

**CONCLUSIONS:** The sonographic predictive model outperformed the standard assessment to detect lymph node metastasis in patients with papillary thyroid cancer and may reduce unnecessary biopsies.

**ABBREVIATIONS:** LN = lymph node; FNAB = fine-needle aspiration biopsy; M method = sonographic evaluation of lymph nodes using the predictive model; PTC = papillary thyroid carcinoma; R method = sonographic evaluation of the lymph node per standard clinical practice; rFPF = relative false-positive fraction; rTPF = relative true-positive fraction; Tg = thyroglobulin; US = ultrasound

Thyroid cancer represents 3.4% of all new cancer cases in the United States, with an incidence of 14.2 per 100,000 individuals per year.<sup>1</sup> The National Cancer Institute estimates 56,870 new cases of thyroid cancer and 2010 deaths due to thyroid cancer in 2017.<sup>1</sup> Its incidence has significantly increased in recent years,

attributed to increases in papillary thyroid carcinoma (PTC).<sup>2,3</sup> With a common cancer, accurate assessment for recurrence is paramount. The risk of recurrence spans from <1% in very low-risk patients to >50% in high-risk patients,<sup>4</sup> with a recurrence rate of approximately 27% for regional lymph node (LN) metastases in patients with PTC.

Evaluation of postoperative disease status can be performed with serum thyroglobulin levels (Tg), cervical ultrasound (US), iodine radioisotope scanning, contrast-enhanced neck CT, or MR imaging. Compared with diagnostic radioiodine scan or neck CT, LN evaluation by comprehensive neck ultrasound is less expensive and exposes patients to no ionizing radiation or intravenous iodinated contrast agents.

The 2015 American Thyroid Association guidelines recommend that following an operation, cervical US should be performed at 6–12 months to evaluate the thyroid bed as well as the central and lateral cervical LN compartments, with the frequency of subsequent follow-up imaging depending on the patient's risk

Received July 12, 2017; accepted after revision December 9.

From the Department of Radiology (N.U.P., K.E.L., K.M., T.J.C., S.S.P., E.R.S., J.M.M., K.G.) and Division of Endocrinology (B.H.), University of Colorado School of Medicine, Aurora, Colorado; and Department of Health Systems, Management and Policy (K.E.L.), Colorado School of Public Health, Aurora, Colorado.

This clinical trial was supported by University of Colorado Radiology Department.

This study was performed at University of Colorado Hospital at Anschutz Medical Campus in Aurora, Colorado. Name of Registry: ClinicalTrials.gov; Registration number: 14-2053.

An abstract of this study was presented at: Annual Convention of the American Institute of Ultrasound in Medicine, March 25–29, 2017; Lake Buena Vista, Florida.

Please address correspondence to Nayana U. Patel, MD, Department of Radiology, University of Colorado School of Medicine, Anschutz Medical Campus, 12401 East 17th Ave, Mail Stop L954, Aurora, CO 80045; e-mail: Nayana.patel@ucdenver.edu

<http://dx.doi.org/10.3174/ajnr.A5554>

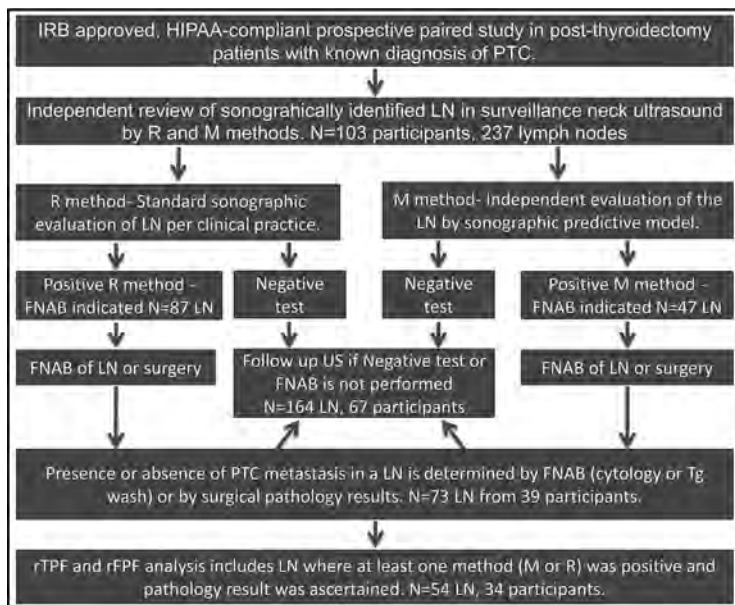


**FIGURE.** Diagram depicting the overall study design.

for disease recurrence and Tg status.<sup>4</sup> These guidelines recommend fine-needle aspiration biopsy (FNAB) of sonographically suspicious LNs of  $\geq 8$ –10 mm in the smallest diameter for evaluation of cytology, with Tg measurement in the needle washout fluid if positive results would change patient management.

Many studies report sonographic features of LNs that are associated with thyroid cancer metastasis in patients with PTC; however, some of these features are not highly sensitive. Cystic changes and microcalcifications are the most specific sonographic features of PTC LN metastasis, but with low sensitivity.<sup>5–8</sup> In the absence of these most specific sonographic features, LN selection for FNAB can be challenging. One group’s pilot data on 71 lymph nodes showed that only 32% of the abnormal or suspicious LNs by sonographic features had PTC metastasis.<sup>9</sup> A predictive model was developed in that retrospective pilot study based on sonographic markers (nonhomogeneous echo texture, microcalcification, and nodal volume). This model had a sensitivity of 65% (95% CI, 50%–78%) and a specificity of 85% (95% CI, 73%–94%) at a probability cut-point of 0.38.<sup>9</sup>

The goal of the current study was to prospectively validate this sonographic predictive model (M method) and estimate the diagnostic accuracy of the M method relative to radiologists’ standard assessments (R method) in identifying LN metastasis in a patient population with PTC after thyroidectomy. We hypothesized that the M method would have higher relative true-positive fraction (rTPF) and lower relative false-positive fraction (rFPF) compared with the R method.

## MATERIALS AND METHODS

### Study Design

The flow diagram in the Figure depicts the overall study design. We conducted a prospective study with a sample of patients at a large academic hospital (University of Colorado Hospital at Anschutz Medical Campus), recruiting patients after thyroidectomy with a known diagnosis of PTC who had a comprehensive neck sonographic examination performed at our institution from

June 2015 to December 2015. All eligible patients during this period were screened for inclusion and exclusion criteria outlined below and recruited consecutively. This study was institutional review board–approved and Health Insurance Portability and Accountability Act–compliant. Informed consent was obtained from each participant who was willing to enroll in this study.

To be eligible for the study, participants were required to have a diagnosis of PTC, be 18 years of age or older, provide informed consent to participate, and have a sonographically identified LN of at least 5 mm in the short axis for zones 3, 4, 5, 6, and 7 or at least 10 mm in the short axis for zones 1 and 2. We excluded anyone who was younger than 18 years of age, had a cancer other than papillary thyroid carcinoma, had distant

metastasis, or was unable or unwilling to provide informed consent. Each patient’s eligibility per study criteria was determined at the time of the screening US. If a patient was found eligible, then study-related information was given to the patient at the time of the US. Patients who were interested in participating in the study gave consent after the screening US or were contacted later (24–48 hours) to obtain informed consent.

Age, sex, type of PTC, and laboratory, radiology, and pathology data were abstracted from electronic medical records. Participants were followed for up to 12 months for biopsy or surgery results.

### Image Acquisition

**Neck Ultrasound Protocol.** Neck ultrasound for LN evaluation was performed using L12–5-, L17–5-, and C8–5-MHz transducers and iU22 US machines (Philips Healthcare, Best, the Netherlands). The standard neck ultrasound protocol was designed to detect, map, and characterize the lymph nodes in zones 1, 2, 3, 4, and 6. Zonal mapping of the cervical LNs was performed using anatomic landmarks.<sup>10</sup> Zone 5 was not routinely evaluated unless there was a palpable abnormality or clinical concern in that area. The C8–5 transducer was used to evaluate inferior zone 6 and zone 7 LNs.

The gray-scale ultrasound images included 3 axis dimensions of a nodule/LN if it met the size criteria:  $\geq 10$  mm in the short axis for zones 1 and 2, and  $\geq 5$  mm in the short axis in the other zones. These static gray-scale images of the lymph nodes were supplemented with a superior-to-inferior cine clip of the central compartment and right and left lateral compartments of the neck for the radiologist’s review.

Color Doppler evaluation was performed with a L12–5 or L17–5 transducer (iU22 US; Philips Healthcare) in a lymph node plane that best assessed the hilar and nonhilar flow (longitudinal or axial image). The color scale was decreased to the Nyquist limit; then, the color gain was increased to the point of color speckle and

**Table 1: Lymph node evaluation by the sonographic predictive model (features of a predicted abnormal LN)<sup>a</sup>**

Nonhomogeneous Echo Pattern	Microcalcifications	Volume (mm <sup>3</sup> )
Present	Present	Any
Absent or indeterminate	Present	≥853
Present	Absent or indeterminate	≥690
Absent or indeterminate	Absent or indeterminate	≥2538

<sup>a</sup>LN FNAB recommendation was based on the combination of features at a given volume threshold.

then decreased slightly. The following parameters were selected for color Doppler evaluation: color scale around 5 (500–800 Hz), color gain in the range of 70%–85%, and low wall filter.

### Image Analysis

**Index Test.** Neck US images were reviewed and analyzed for both M and R methods on a PACS.

**Image Analysis by the R Method.** Images from neck US were evaluated per standard clinical practice by 6 fellowship-trained radiologists with 3–20 years of experience. All radiologists involved in the standard reporting during the clinical practice underwent formal training regarding how to review and report neck US images for LN assessment. Reading radiologists reviewed all static and cine clips, evaluating multiple sonographic features described in the literature to determine whether LNs had normal or abnormal findings and if LNs required FNAB. We assessed the following features: size, shape, hilum, echo pattern, echogenicity, calcification, and color Doppler flow. Besides previous neck US for comparison, the reading radiologists also had access to other clinically relevant information, including pathology reports, risk of recurrence, serum Tg level, and abnormal findings on other imaging modalities (eg, CT or nuclear medicine radioiodine scan). The results of the R method were considered positive for metastasis if the interpreting radiologist recommended FNAB of a LN.

**Image Analysis by the M Method.** Each neck US examination was also independently evaluated by a radiologist with 10 years of experience who was not involved with and was blinded to the results of the US clinical read (R method). All static and compartment-based cine clips were reviewed for LN evaluation. LN FNAB was recommended only if the LN met sonographic feature combinations as described in the predictive model summarized in Table 1.<sup>9</sup> Node volume was calculated by an ellipsoid formula using 3 axis node dimensions. The results of the M method were considered positive for metastasis if they indicated FNAB of a LN.

**Fine-Needle Aspiration Biopsy.** At our institution, it is standard to perform compartment-based LN FNAB to assist surgeons in planning for a compartmental LN dissection operation.

FNAB of the LN positive by the R or M method was subsequently performed under US guidance per standard technique after obtaining informed consent. If the patient had multiple LNs positive by the R or M method, then the most suspicious LN in each separate compartment (central, right lateral, left lateral) was selected for FNAB. Two-to-four samples were obtained from the selected LN using a 25-ga needle for cytology and Tg wash. PTC metastasis was confirmed by positive cytology. LN samples were

examined by cytopathologists with 3–15 years of experience. If LN cytology was negative for PTC metastasis, fine-needle aspiration Tg wash was performed to determine the presence or absence of PTC metastasis.<sup>11</sup> Fine-needle aspiration Tg wash of <1 ng/mL was considered negative for PTC metastasis.<sup>12,13</sup> Results of FNAB (cytology and fine-needle aspiration Tg wash if cytology was inconclusive or inadequate) of the LNs were used as the reference standard to determine the presence or absence of PTC metastasis. Surgical pathology of the LN from the same level compartment-based surgical dissection was used as a secondary reference standard if positive LNs by the R or M method did not undergo FNAB.

**Follow-Up Neck US Examinations.** Follow-up neck ultrasound examinations were reviewed for LNs that were identified in the index US test but did not undergo FNAB or surgical resection for definite diagnosis (inclusive of positive and negative LNs by the R and M methods). The US images were evaluated to determine whether the LN was stable (unchanged in size and appearance), not suspicious (not seen on follow-up US, became normal in appearance, or smaller), or suspicious (became abnormal in appearance or increased in size).

### Statistical Design

We calculated descriptive statistics for all variables of interest, including means, medians, and SDs for continuous variables and frequencies and percentages for categorical variables.

A common problem when validating screening tests is missing data, which creates verification bias. This bias occurs when only screen-positives for cancer are referred for the reference standard test, which often happens when the reference standard is invasive. Because performing biopsies on patients who were negative with the R and M methods would be unethical, reference standard data are missing for these patients. With these data missing, classic measures of test accuracy, including sensitivity and specificity, cannot be correctly calculated. However, there are other meaningful accuracy measures that can be calculated in studies facing verification bias. Because patients who had a positive M method or R method test were referred for biopsy or an operation, we could calculate the proportion of true-positives and false-positives for each method. Furthermore, we could compare the performance of the M and R methods on these measures.

To compare the M method with the R method, we estimated the relative true-positive fraction and relative false-positive fraction using log-linear models for correlated binary data.<sup>14</sup> This approach is specifically designed to handle incomplete outcome data in instances in which screen-negatives for cancer never get the reference standard test. We fit separate models for rTPF and rFPF, with the binary outcomes of metastatic disease (determined from LN FNAB or surgical pathology results) positive and negative, respectively. The primary predictor in each model was an indicator variable equal to 1 for records corresponding to the M method and equal to zero for records corresponding to the R method. We used a backward stepwise model-building approach. We first evaluated potential tests by sex interactions, to determine whether the performance of the tests varied by patient sex; then, we evaluated sex main effects in the absence of interaction, with a plan to drop sex main effects if nonsignificant. Covariates were retained at an  $\alpha$  level of .20.<sup>15</sup>

**Table 2: Patient characteristics (N = 103)**

Variable	Mean (SD)	Median	Min, Max
Age (yr)	51.17 (13.49)	51.0	23, 78
Time since PTC diagnosis (yr)	6.07 (5.35)	4.5	0.23, 30.48

Note:—Min indicates minimum; Max, maximum.

As a secondary analysis, we evaluated the association between follow-up US examinations and M and R method results on the index US for the patients (and nodes) that did not undergo biopsy or surgery but had US follow-up performed later. We categorized the US follow-up examination results for LN into 3 groups: suspicious, not suspicious, or stable relative to the index US. To evaluate the association between the follow-up US results and results of R and M methods, we used a Fisher exact test for R and M methods separately (ie, we tested for an association between the 3-level category of follow-up US results and the binary result of the R or M method).

We used a type I error rate of 0.05 for all statistical tests. All analyses were conducted using SAS 9.4 (SAS Institute, Cary, North Carolina).

## RESULTS

A total of 105 participants after thyroidectomy were enrolled in the study from June 2015 to December 2015; two participants were excluded because one patient had medullary and papillary thyroid carcinoma diagnoses and the other participant had distant metastasis in the lungs, yielding a final study sample of 103 patients after thyroidectomy with diagnosis of papillary thyroid carcinoma. Staging information could be retrieved from electronic medical records in 66 participants ( $n = 103$ ): 46 with stage I; five with stage II; eight with stage III; and 7 with stage IV thyroid cancer. These 103 participants had 237 LNs evaluated by both the R and M methods. Forty-seven LNs were positive by the M method and 87 LNs were positive by R method.

Thirty-nine of the 103 participants had LN biopsy or an operation (37 had LN FNAB, and 2 had a compartment-based LN dissection operation). The median time between the index US and LN biopsy was 28 days for the subset of the participants (28 of 37) who had biopsy of the LNs (positive by the R or M method). Nine of 37 participants had LN biopsy recommended by the R or M method but chose not to undergo repeat biopsy because they already had the same LN biopsied before the index US. Of the 164 LNs without pathology results, 105 LNs from 67 patients had follow-up US examinations available for comparison (the time interval from the index US test ranged from 90 to 560 days; 7/67 [10.45%] had the follow-up US at <6 months; 12/67 [17.91%], at 6–9 months; 19/67 [28.36%], at 9–12 months; and 29/67 [43.28%], at >12 months).

Participant characteristics are presented in Tables 2 and 3. Most participants (73.79%) were women, and most patients had 1–3 nodes identified by US. Twenty-one of the 39 participants who underwent LN biopsy or surgical resection had 33 lymph nodes positive for metastasis. LN metastasis was commonly seen in zone 6 (17/33) followed by zone 4 (8/33) and zone 3 (5/33). Serum Tg information within 1 month of the index US was found in electronic medical records in 28 of 39 participants. Of 18 participants with LN metastasis, only 8 had elevated serum Tg levels (defined as >1.0 ng/mL).

**Table 3: Patient characteristics (N = 103)**

	Frequency (%)
Women	76 (73.79%)
Biopsy or operation performed	39 (37.86%)
Positive for LN metastasis	21 (53.85%)
No. of LNs evaluated on US	
1	30 (29.13%)
2	36 (34.95%)
3	21 (20.39%)
4	11 (10.68%)
5	4 (3.88%)
8	1 (0.97%)

**Table 4: Frequencies of patient level (N = 103 participants) and lymph node level (N = 237 LNs) M and R method results<sup>a</sup>**

	Biopsy Positive for Metastasis	Biopsy Negative for Metastasis	Not Biopsied	Total
Person level				
Total participants	21	18	64	103
M				
Positive	17	6	13	36
Negative	4	12	51	67
R				
Positive	19	13	17	49
Negative	2	5	47	54
Lymph node level				
Total lymph nodes	33	40	164	237
M				
Positive	21	9	17	47
Negative	12	31	147	190
R				
Positive	24	26	37	87
Negative	9	14	127	150

<sup>a</sup> For person level results, biopsy positive for metastasis indicates that the patient had at least 1 LN positive for metastasis, and positive M or R method indicates that the patient had at least 1 LN called positive by the respective method.

**Table 5: LN pathology results by R and M method**

Results	Method	
	+R Method	-R Method
Positive for metastasis (33 LNs)		
+M method	17	4
-M method	7	5
Negative for metastasis (40 LNs)		
+M method	6	3
-M method	20	11

**Table 6: Relative true-positive and relative false-positive rates for the M method compared with the R method (n = 54 LNs with pathology results in which at least 1 method, R or M, had positive findings)**

	Estimate (SE)	95% CI	P Value
rTPF M method	1.46 (0.20)	1.12–1.91	.01
rFPF M method	0.58 (0.14)	0.36–0.92	.02

Note:—SE, indicates standard error.

Lymph node level and patient level results are presented in Table 4. Table 5 presents the frequencies of R and M method positivity for the subsets of lymph nodes positive and negative for metastasis, respectively. The analysis of rTPF and rFPF includes 54 LNs with pathology results from 34 patients in whom at least 1 method (R or M) was positive for LN metastasis (Table 6). LNs with pathology results but negative by both methods (R and M) were excluded in the analysis of rTPF and rFPF. Model-based

**Table 7: M and R method results compared with follow-up neck ultrasound examination for interval change in lymph nodes without pathology results (n = 105)**

M and R Methods	Suspicious	Not Suspicious	Stable	P Value <sup>a</sup>
+M method	0	5	5	.66
−M method	4	33	58	
+R method	2	11	18	.74
−R method	2	27	45	

<sup>a</sup> Fisher exact test.

estimates of rTPF and rPPF are presented in Table 6. Compared with the R method, the M method had a higher rTPF of 1.46 (95% CI, 1.12–1.91;  $P = .01$ ) and a lower rPPF of 0.58 (95% CI, 0.36–0.92;  $P = .02$ ). There were not significant interactions between method and sex or the main effects of sex for either outcome ( $P > .05$  for each); thus, these parameters were dropped from the final models for both outcomes. Table 7 presents the M and R method results by follow-up US comparison and reports the results of the Fisher exact tests. The index R and M method results were not associated with suspicious findings at follow-up US examination ( $P = .74$  and  $P = .66$ , respectively).

## DISCUSSION

This study demonstrated that the sonographic predictive model (M method) outperforms the current standard of care (R method) in identifying PTC nodal metastasis in patients after thyroidectomy. The M method has higher true-positive rates and lower false-positive rates compared with the R method, providing evidence that using this model in clinical practice to determine the need for LN FNAB may more accurately identify patients who should undergo FNAB.

Also in our study, we followed LNs identified in the index US that did not undergo FNAB or surgical resection. We did not find an association between R or M method results and whether follow-up US revealed suspicious change in the LN, but this finding is not surprising given the typical indolent course of the disease and low incidence of abnormal nodes during the follow-up period. In keeping with this, of 95 nodes negative by the M method on the index US, only 4.21% (4/95 nodes) changed to the suspicious category on follow-up US examination, suggesting that 95.79% (91/95) of M method–negative nodes were either benign or had less aggressive PTC metastasis. These patients might be managed nonsurgically with active surveillance because surgical complications are typically higher with repeat surgery in the same compartment.

The predictive model (M method) can help achieve the ultimate goal of screening cervical LNs with neck sonography in the intermediate-to-high risk patient population with PTC, by improving detection of LN recurrence. Also, the M method may improve the role of surveillance neck sonography in a patient population with low-risk PTC that can be monitored for local recurrence with less aggressive strategies.

This study had several strengths, including the use of reference standard pathology results, prospective design, and analytic methods unbiased when reference standard results were incomplete. Although most patients did not have R or M method–positive nodes, thereby precluding valid estimates of sensitivity and specificity, the study design and analytic methods used in this

study are a valid and ethical alternative to complete ascertainment of reference standard results.

There are several limitations of our study. The predictive model (Table 1) is based on sonographic features only and does not take into account the risk of recurrence and serum Tg level. In low- and intermediate-risk patients, the risk of lymph node recurrence is low (<2%) in patients with undetectable serum Tg levels and is much higher in those with detectable/elevated serum Tg levels.<sup>4</sup> One of the reading radiologists for the R method was also 1 of the 2 radiologists performing LN FNAB. Our study is prospective but is of a small cohort from a single institution, limiting generalizability of the results. Also, the diagnostic performance of the predictive model in prethyroidectomy assessment of cervical lymph node metastasis in PTC is uncertain because our study included only patients after thyroidectomy; another study is needed to determine whether our results are generalizable to other patient groups.

Several studies in the literature have discussed the predictors of metastatic disease in differentiated thyroid cancer, though there were no other studies applying a sonographic predictive model for the population of patients with PTC. Other studies have noted the size, central location, echo pattern, and Doppler flow or abnormal enhancement on CT as predictors of metastatic disease: Alzahrani et al<sup>16</sup> found the size (7.5 mm) and central location of cervical LNs as the most important predictors of the presence of metastatic disease. In the study by Aribaş et al,<sup>17</sup> central location and hypoechogenicity with loss of hilum in the lateral neck were predictors of malignancy. Chammas et al<sup>18</sup> found that an altered vascularization (resistive index of 0.77 as a cutoff value), a short axis of  $\geq 0.9$  cm, an abnormal hilum, and a heterogeneous echotexture were the most accurate sonographic predictors of LN malignancy, with a diagnostic accuracy near 80%. However, pulse Doppler evaluation of a LN to obtain the resistive index can be time-consuming and requires additional technical skill. Liu et al<sup>19</sup> developed a scoring system and mathematic model using CT to diagnose metastatic central compartment nodes in PTC.<sup>19</sup> Using 4 risk factors of LN metastasis on CT, including cystic or necrotic change, abnormal enhancement, nodal grouping  $\geq 2$ , and nodal area  $\geq 30.00$  mm<sup>2</sup>, this method had a sensitivity and specificity of 68.8% and 85.9%, respectively, but it has the downside of exposing patients to ionizing radiation and an iodinated contrast agent.

## CONCLUSIONS

The sonographic predictive model demonstrated higher true-positive rates and lower false-positive rates compared with radiologists' standard assessment of LNs to detect PTC metastasis in patients after thyroidectomy. Incorporation of this sonographic predictive model in clinical practice may improve the diagnostic accuracy in detecting PTC nodal metastasis and thereby reduce the number of unnecessary LN FNABs, especially in low-risk patients with PTC. A large multi-institutional study is needed to further validate this sonographic predictive model.

## ACKNOWLEDGMENTS

The authors gratefully acknowledge the time and insight shared by the 2015 Radiological Society of North America clinical trial

methodology workshop faculty to help design the research method for this clinical trial. The authors also acknowledge the support and assistance provided by the research coordinators of the Radiology Department at the University of Colorado.

Disclosures: Nayana U. Patel—UNRELATED: Consultancy: 3DBiopsy. Sajal S. Pokharel—UNRELATED: Board Membership: 3DBiopsy. Comments: scientific advisory board member for this company developing prostate biopsy tools.\* Bryan Haugen—UNRELATED: Consultancy: Eisai. Comments: to develop a slide deck for thyroid cancer management; Payment for Lectures Including Service on Speakers Bureaus: Eisai. Comments: talks at the Endocrine Society and American Association of Clinical Endocrinologists meetings; Payment for Development of Educational Presentations: Eisai. \*Money paid to the institution.

## REFERENCES

1. National Cancer Institute. Cancer Stat Facts: Thyroid Cancer. <http://seer.cancer.gov/statfacts/html/thyro.html>. Accessed April 20, 2017
2. Davies L, Welch HG. **Current thyroid cancer trends in the United States.** *JAMA Otolaryngol Head Neck Surg* 2014;140:317–22 CrossRef Medline
3. Enewold L, Zhu K, Ron E, et al. **Rising thyroid cancer incidence in the United States by demographic and tumor characteristics, 1980–2005.** *Cancer Epidemiol Biomarkers Prev* 2009;18:784–91 CrossRef Medline
4. Haugen BR, Alexander EK, Bible KC, et al. **2015 American Thyroid Association Management Guidelines for Adult Patients with Thyroid Nodules and Differentiated Thyroid Cancer: The American Thyroid Association Guidelines Task Force on Thyroid Nodules and Differentiated Thyroid Cancer.** *Thyroid* 2016;26:1–133 CrossRef Medline
5. Rosário P, Tavares W, Borges M, et al. **Ultrasonographic differentiation of cervical lymph nodes in patients with papillary thyroid carcinoma after thyroidectomy and radioiodine ablation: a prospective study.** *Endocr Pract* 2014;20:293–98 CrossRef Medline
6. Leboulleux S, Girard E, Rose M, et al. **Ultrasound criteria of malignancy for cervical lymph nodes in patients followed up for differentiated thyroid cancer.** *J Clin Endocrinol Metab* 2007;92:3590–94 CrossRef Medline
7. Landry CS, Grubbs EG, Busaidy NL, et al. **Cystic lymph nodes in the lateral neck as indicators of metastatic papillary thyroid cancer.** *Endocr Pract* 2011;17:240–44 CrossRef Medline
8. Sohn YM, Kwak JY, Kim EK, et al. **Diagnostic approach for evaluation of lymph node metastasis from thyroid cancer using ultrasound and fine-needle aspiration biopsy.** *AJR Am J Roentgenol* 2010;194:38–43 CrossRef Medline
9. Patel NU, McKinney K, Kreidler SM, et al. **Ultrasound-based clinical prediction rule model for detecting papillary thyroid cancer in cervical lymph nodes: a pilot study.** *J Clin Ultrasound* 2016;44:143–51 CrossRef Medline
10. Som PM, Curtin HD, Mancuso AA. **Imaging-based nodal classification for evaluation of neck metastatic adenopathy.** *AJR Am J Roentgenol* 2000;174:837–44 CrossRef Medline
11. Torres MR, Nóbrega Neto SH, Rosas RJ, et al. **Thyroglobulin in the washout fluid of lymph-node biopsy: what is its role in the follow-up of differentiated thyroid carcinoma?** *Thyroid* 2014;24:7–18 CrossRef Medline
12. Snozek CL, Chambers EP, Reading CC, et al. **Serum thyroglobulin, high-resolution ultrasound, and lymph node thyroglobulin in diagnosis of differentiated thyroid carcinoma nodal metastases.** *J Clin Endocrinol Metab* 2007;92:4278–81 CrossRef Medline
13. Moon JH, Kim YI, Lim JA, et al. **Thyroglobulin in washout fluid from lymph node fine-needle aspiration biopsy in papillary thyroid cancer: large-scale validation of the cutoff value to determine malignancy and evaluation of discrepant results.** *J Clin Endocrinol Metab* 2013;98:1061–68 CrossRef Medline
14. Pepe MS, Alonzo TA. **Comparing disease screening tests when true disease status is ascertained only for screen positives.** *Biostatistics* 2001;2:249–60 CrossRef Medline
15. Mickey RM, Greenland S. **The impact of confounder selection criteria on effect estimation.** *Am J Epidemiol* 1989;129:125–37 CrossRef Medline
16. Alzahrani AS, Alsuhaibani H, Salam SA, et al. **Diagnostic accuracy of high-resolution neck ultrasonography in the follow-up of differentiated thyroid cancer: a prospective study.** *Endocr Pract* 2005;11:165–71 CrossRef Medline
17. Aribaş BK, Arda K, Çiledağ N, et al. **Predictive factors for detecting malignancy in central and lateral cervical lymph nodes in papillary carcinoma of the thyroid.** *Asia Pac J Clin Oncol* 2011;7:307–14 CrossRef Medline
18. Chammas MC, Macedo TA, Lo VW, et al. **Predicting malignant neck lymphadenopathy using color duplex sonography based on multivariate analysis.** *J Clin Ultrasound* 2016;44:587–94 CrossRef Medline
19. Liu T, Su X, Chen W, et al. **A mathematical model using computed tomography for the diagnosis of metastatic central compartment lymph nodes in papillary thyroid carcinoma.** *Eur Radiol* 2014;24:2827–34 CrossRef Medline

# Melanoma of the Sinonasal Tract: Value of a Septate Pattern on Precontrast T1-Weighted MR Imaging

Y.-K. Kim, J.W. Choi, H.-J. Kim, H.Y. Kim, G.M. Park, Y.-H. Ko, J. Cha, and S.T. Kim

## ABSTRACT

**BACKGROUND AND PURPOSE:** Various tumors of the sinonasal tract can exhibit high signal intensity on T1WI. The purpose of this study was to determine the value of a septate pattern on precontrast T1WI for diagnosing sinonasal melanoma.

**MATERIALS AND METHODS:** Retrospectively, 3 observers independently reviewed MR images of 31 histologically proved sinonasal melanomas with special attention to the presence or absence of a septate pattern on precontrast T1WI, defined as alternating hyperintense and hypointense striations on precontrast T1WI. For comparison, we evaluated the prevalence of a septate pattern on precontrast T1WI in 106 nonmelanomatous sinonasal malignant tumors with 16 different histologic types. We also tried to identify the histopathologic features responsible for the septate pattern on precontrast T1WI.

**RESULTS:** Twenty-seven (87.1%) of 31 sinonasal melanomas showed hyperintense foci on T1WI, among which a septate pattern on precontrast T1WI was seen in 23 (74.2%), while 22 (20.8%) of 106 nonmelanomatous malignant tumors demonstrated hyperintense foci on T1WI, among which only 3 (2.8%) showed a septate pattern on precontrast T1WI. The sensitivity, specificity, positive predictive value, negative predictive value, and accuracy of a septate pattern on precontrast T1WI for the diagnosis of sinonasal melanoma were 74%, 97%, 88%, 93%, and 92%, respectively. Although limited due to the retrospective nature, 4 of 23 histologically reviewed sinonasal melanomas revealed an uneven distribution of melanin with alternating melanin and fibrous bands within the tumors.

**CONCLUSIONS:** A septate pattern on precontrast T1WI might be an adjunctive imaging finding for the diagnosis of sinonasal melanoma. This might be attributed histologically to an uneven distribution of melanin and hemorrhage within the tumors.

**ABBREVIATIONS:** SNM = sinonasal melanoma; TI-SP = septate pattern on precontrast T1-weighted MR imaging

Melanoma of the sinonasal tract roughly accounts for <1% of all melanomas and up to 4% of all sinonasal malignancies.<sup>1-5</sup> According to the Surveillance, Epidemiology, and End Results data base, the approximate incidence of mucosal melanoma of the head and neck was 0.6–1.2 cases per million persons per year from 1987 to 2009 in the United States.<sup>6</sup> Of these, 72.6% of patients had disease in the sinonasal location.<sup>6</sup> The incidence of

mucosal melanoma appears to be increasing, especially in the sinonasal tract.<sup>6,7</sup>

Previous studies described high signal intensity on T1WI and low signal intensity on T2WI as the characteristic MR imaging features of melanoma. The signal characteristics on MR images are attributed to the paramagnetic properties of melanin pigment.<sup>8-13</sup> However, several substances besides melanin, such as hemorrhage, high proteinaceous secretions, and fungus can also generate high signal intensity on T1WI.<sup>12,14</sup> In some respects, sinonasal melanoma (SNM) is distinct from other malignant sinonasal tumors. First, the prognosis of SNM is reportedly much worse than other malignant sinonasal tumors,<sup>15-17</sup> with its overall 5-year survival rates being estimated at <30% in most series,<sup>3</sup> while those of other sinonasal malignancies range from 22% to 67%, with an average of 45.5%.<sup>16</sup> Since 2010, the American Joint Committee on Cancer has created a separate system for staging mucosal melanoma of the head and neck, in which a primary tumor limited to the mucosa is considered T3, which reflects the aggressive biologic behavior of the tumor.<sup>18</sup> Second, SNM

Received July 24, 2017; accepted after revision November 20.

From the Departments of Radiology (Y.-K.K., H.-J.K., H.Y.K., G.M.P., J.C., S.T.K.) and Pathology (Y.-H.K.), Samsung Medical Center, Sungkyunkwan University School of Medicine, Seoul, Korea; Department of Radiology (J.W.C.), Ajou University School of Medicine, Suwon, Korea; Department of Radiology (G.M.P.), Ulsan University Hospital, University of Ulsan College of Medicine, Ulsan, Korea; and Department of Radiology and Research Institute of Radiological Science (J.C.), College of Medicine, Yonsei University College of Medicine, Seoul, Korea.

Yi-Kyung Kim and Jin Wook Choi contributed equally to this work.

Please address correspondence to Hyung-Jin Kim, MD, Department of Radiology, Samsung Medical Center, Sungkyunkwan University School of Medicine, 81 Irwon-ro, Gangnam-gu, Seoul 135-710, Korea; e-mail: hyungkim@skku.edu

<http://dx.doi.org/10.3174/ajnr.A5539>

**Table 1: Visualization of a T1-SP on MR imaging in sinonasal melanomas and nonmelanomatous malignant sinonasal tumors based on consensus reading<sup>a</sup>**

	Total	Hyperintense Foci on T1WI		
		Present		
		T1-SP (+)	T1-SP (-)	Absent
Sinonasal melanoma <sup>b</sup>	31	23	4	4
Nonmelanomatous malignant tumor <sup>b</sup>	106	3	19	84
Squamous cell carcinoma	45	2	6	37
Lymphoma	22	1	2	19
Adenoid cystic carcinoma	10	0	4	6
Rhabdomyosarcoma	5	0	0	5
Neuroendocrine carcinoma	4	0	2	2
Adenocarcinoma	4	0	2	2
Malignant fibrous histiocytoma	3	0	1	2
Poorly differentiated carcinoma	3	0	0	3
Spindle cell sarcoma	3	0	0	3
Esthesioneuroblastoma	1	0	0	1
Small round cell sarcoma	1	0	1	0
Inflammatory myofibroblastic sarcoma	1	0	0	1
Malignant peripheral nerve sheath tumor	1	0	0	1
Ewing sarcoma	1	0	1	0
Chondrosarcoma	1	0	0	1
Myoepithelial carcinoma	1	0	0	1

**Note:**—+ indicates presence; —, absence.

<sup>a</sup> Data are presented as number of tumors.

<sup>b</sup> *P* value < .001 by the Fisher exact test.

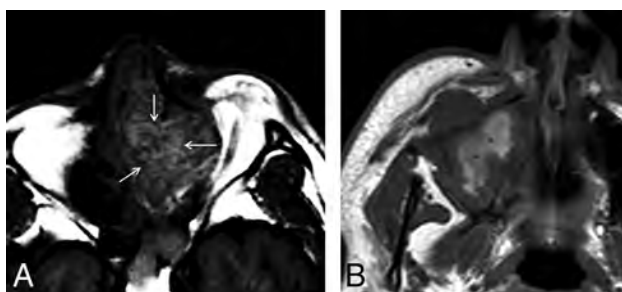


**FIG 1.** Two different types of SNM containing high signal intensity on T1WI with the presence (A) or absence (B) of a T1-SP. Although both tumors have intrinsic high signal intensity, only A demonstrates a regular pattern of the alternating hyperintense and hypointense striations, so-called T1-SP (arrows). In contrast, the high signal intensity in B appears amorphous without the alternating hyperintense and hypointense striations in a regular pattern (asterisks).

frequently presents as a mass with multicentric distribution.<sup>19</sup> Third, promising results are constantly being reported on the efficacy of targeted therapy for treating advanced SNMs, including biochemotherapy using cytotoxic chemotherapy and biologic immunomodulatory agents such as interferon  $\alpha$  and interleukin 2.<sup>3,20,21</sup> The purpose of this study was to evaluate the diagnostic value of the septate pattern on precontrast T1-weighted MR imaging (T1-SP) for distinguishing SNMs from nonmelanomatous malignant sinonasal tumors.

## MATERIALS AND METHODS

### Patients

This study was approved by the institutional review board at Samsung Medical Center, and informed consent was waived in accordance with the requirements of a retrospective study.

Between January 1998 and January 2015, a search of the electronic medical records of our hospital revealed 56 patients (male/female ratio = 34:22; mean age, 62 years; range, 21–88 years)

with histologically proved SNM, among whom MR imaging was performed in 35. Four patients were excluded from the study because no mass could be localized on MR images, resulting in 31 patients who were subjects of this study. There were 18 men and 13 women ranging in age from 37 to 88 years (mean age, 64 years).

To validate the role of T1-SP for diagnosing SNMs, we selected MR images of 106 adult patients with 16 different types of nonmelanomatous malignant sinonasal tumors through a search of the electronic data base of our institution between January 2010 and December 2014 using the keywords “malignant tumor of the nose and paranasal sinuses.” All tumors were diagnosed histologically by biopsy and/or an operation. These 106 patients consisted of 63 males and 43 females with ages ranging from 14 to 87 years (mean age, 56 years). Table 1 demonstrates the pathologic subtypes, of which squamous cell carcinoma was most common ( $n = 45$ ), followed by lymphoma ( $n = 22$ ), adenoid cystic carcinoma ( $n = 10$ ), and other sinonasal malignancies ( $n = 29$ ).

### MR Imaging

MR imaging examinations were performed on a 1.5T (Signa Advantage or Horizon; GE Healthcare, Milwaukee, Wisconsin) or 3T (Intera Achieva; Philips Healthcare, Best, the Netherlands) scanner. In all patients, precontrast spin-echo T1WI (TR/TE/NEX, 400–560 ms/10–14 ms/2) and fast spin-echo T2WI (TR/TE/NEX, 2500–4500 ms/80–110 ms/1) with or without fat saturation were obtained, followed by contrast-enhanced spin-echo T1WI with fat saturation after the intravenous injection of 0.1 mmol/kg of gadolinium-based contrast material. Images were obtained in at least 2 planes with 3- to 4-mm section thickness and 0- to 1-mm intersection gap.

### Image Analysis

All MR images were evaluated by 3 radiologists with 4, 2, and 2 years of experience in neuroradiology, respectively, in an anonymized and randomized manner. All reviewers were blinded to the final histologic diagnosis. We evaluated the general MR imaging features of SNMs, such as the signal intensity and enhancement pattern. We determined the presence or absence of a T1-SP on MR imaging in 31 SNMs and 106 nonmelanomatous malignant sinonasal tumors. A T1-SP was determined to be present if a regular pattern of the alternating hyperintense and hypointense striations was distributed partially or diffusely within the solid components of the tumor on unenhanced T1WI (Fig 1A). Hyperintense foci without a regular pattern of alternating striations were not considered a T1-SP (Fig 1B). Before image review, the observers were instructed and tested on the imaging appearance

**Table 2: Summary of the results of MR imaging interpretation by 3 observers<sup>a</sup>**

	Presence or Absence of T1-SP							
	Observer 1		Observer 2		Observer 3		Overall <sup>b</sup>	
	+	-	+	-	+	-	+	-
Sinonasal melanoma	22	9	26	5	20	11	23	8
Nonmelanomatous malignant sinonasal tumors	7	99	1	105	3	103	3	103

**Note:**—+ indicates presence; -, absence.

<sup>a</sup> Interobserver agreement between observers 1 and 2,  $\kappa = .69$ ; between observers 1 and 3,  $\kappa = 0.72$ ; between observers 2 and 3,  $\kappa = 0.71$ ; average,  $\kappa = 0.71$ .

<sup>b</sup> Data were obtained by consensus interpretation of 3 observers.

of a T1-SP. MR imaging interpretation proceeded in 2 ways: First, each observer independently reviewed the images in a randomized fashion; and second, the 3 observers reached a consensus by a joint interpretation that followed individual interpretation 1 month later to minimize recall bias.

### Histopathologic Evaluation

Histopathologic slides were available for review in 23 of 31 SNMs. A board-certified pathologist with 30 years of experience in head and neck pathology retrospectively re-examined the pathologic slides with special attention to the presence or absence of melanin, the presence or absence of intratumoral hemorrhage, and the predominant cell type. The tumors were grouped into melanotic and amelanotic tumors with the former being further categorized as those with abundant melanin when the melanin-containing cells exceeded 10% of tumor cells and those with a moderate amount of melanin when they composed <10%. Finally, we tried to identify the histopathologic features responsible for T1-SP.

### Statistical Analysis

On the basis of the observations made by each observer, interobserver agreement among 3 observers was evaluated by calculating  $\kappa$  statistics. A  $\kappa$  value  $\leq 0.20$  indicated positive but poor agreement; 0.21–0.40, fair agreement; 0.41–0.60, moderate agreement; 0.61–0.80, good agreement; and  $\geq 0.81$ , excellent agreement. On the basis of the results made by the 3 observers' consensus interpretations, the statistical difference of a T1-SP between SNMs and other malignant sinonasal tumors was analyzed using the Fisher exact test. We also determined the overall sensitivity, specificity, positive predictive value, negative predictive value, and accuracy of a T1-SP as the diagnostic indicator of SNM. The statistical differences in the prevalence of a T1-SP were sought according to the presence or absence of melanin, the presence or absence of hemorrhage, and the different cell types using the  $\chi^2$  test. During statistical analysis, differences of  $P < .05$  were considered statistically significant.

### RESULTS

Compared with the brain stem, 26 of 31 SNMs showed heterogeneous isointense and hyperintense signal intensity on T1WI, while 5 tumors demonstrated homogeneous hypointense ( $n = 1$ ) or heterogeneous isointense and hyperintense ( $n = 4$ ) signal intensity. Various signal intensities were demonstrated on T2WI, including heterogeneous isointense and hypointense signal intensity ( $n = 15$ ), heterogeneous isointense and hyperintense signal intensity ( $n = 9$ ), and heterogenous hypointense and hyperintense signal intensity ( $n = 7$ ). Twenty-seven tumors were generally well-enhanced on contrast-enhanced T1WI, while the re-

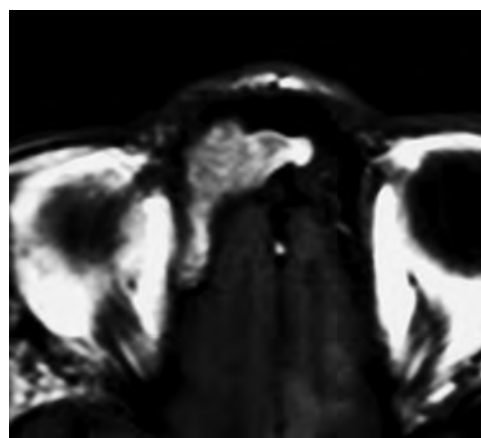


**FIG 2.** SNM in the right frontal sinus displaying a diffuse T1-SP. Pre-contrast T1WI demonstrates a mass with the alternating hyperintense and hypointense bands, the so-called T1-SP.

maining 4 tumors showed poor enhancement. Only 2 tumors demonstrated intratumoral necrosis.

### Comparison of the Prevalences of T1-SP between SNMs and Other Malignant Tumors

On the basis of the results of individual and consensus interpretations, we summarized the prevalences of a T1-SP in SNMs and other nonmelanomatous sinonasal malignant tumors in Tables 1 and 2. Interobserver agreement among 3 observers for the presence of a T1-SP was good, with an average  $\kappa$  value of 0.71.

According to a consensus reading by the 3 observers, there was a significant statistical difference in the prevalence of a T1-SP between SNMs and other malignant tumors ( $P < .001$ ). Twenty-seven (87.1%) of 31 SNMs showed hyperintense foci on T1WI, among which a T1-SP was seen in 23 (74.2%), either diffusely ( $n = 7$ , Fig 2) or partially ( $n = 16$ , Fig 3). In contrast, 22 (20.8%) of 106 nonmelanomatous malignant sinonasal tumors demonstrated hyperintense foci on T1WI, among which only 3 (2.8%) showed a T1-SP. These 3 tumors included 2 of 45 squamous cell carcinomas (Fig 4A) and 1 of 14 lymphomas (Fig 4B). Overall, the sensitivity, specificity, positive predictive value, negative predictive value, and accuracy of a T1-SP for the diagnosis of SNM were 74% (95% CI, 55%–88%), 97% (95% CI, 92%–99%), 88% (95% CI, 71%–96%), 93% (95% CI, 88%–96%), and 92% (95% CI, 83%–96%), respectively.

### Histopathologic Features of SNMs in Correlation with MR Imaging Features

Of 23 SNMs for which retrospective histopathologic analysis was available, 18 tumors were melanotic and 5 were amelanotic. Overall, intratumoral hemorrhage was present in 14 and absent in 9.

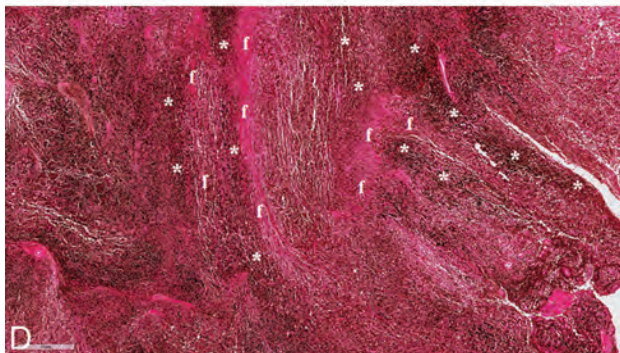
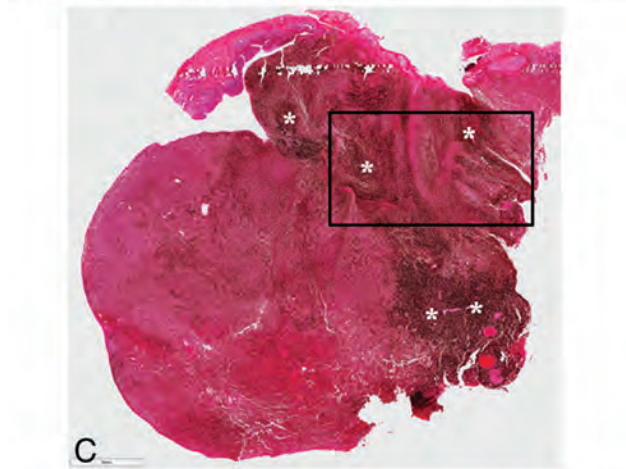
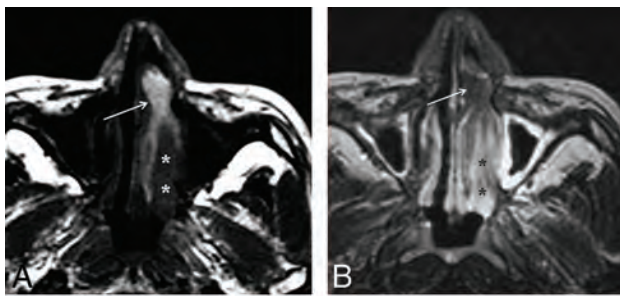


**FIG 3.** SNM displaying a partial T1-SP. *A*, Precontrast axial T1WI demonstrates an elongated mass with heterogeneous signal intensity in the left nasal cavity. While the anterior portion of the mass shows the alternating hyperintense and hypointense bands, the so-called T1-SP (arrow), the posterior portion is the soft-tissue component with the signal intensity isointense to the brain stem (asterisks). *B*, On fat-suppressed axial T2WI, the anterior portion of the mass appears isointense to the brain stem (arrow), while the posterior portion becomes hyperintense (asterisks). Insufficient facial and buccal fat suppression was caused by magnetic field inhomogeneity due to metallic dental hardware. *C*, Photomicrograph reveals an uneven distribution of melanin pigments (dark bands marked with asterisks). The bar on the left bottom indicates 3 mm (hematoxylin-eosin, original magnification  $\times 7$ ). *D*, Photomicrograph with higher magnification corresponding to the box in *C* shows the area of the alternating melanin (dark bands marked with asterisks) and fibrous (f) bands. The bar on the left bottom indicates 700  $\mu\text{m}$  (hematoxylin-eosin, original magnification  $\times 30$ ).

Various histologic cell types were seen, including 15 epithelioid cell, 3 spindle cell, and 5 mixed cell types. Correlation of the histopathologic features with the MR imaging features in these 23 SNMs in terms of the presence or absence of a T1-SP is summarized in Table 3. A T1-SP was found in 14 of 18 melanotic melanomas and 4 of 5 amelanotic melanomas. Twelve of 14 tumors

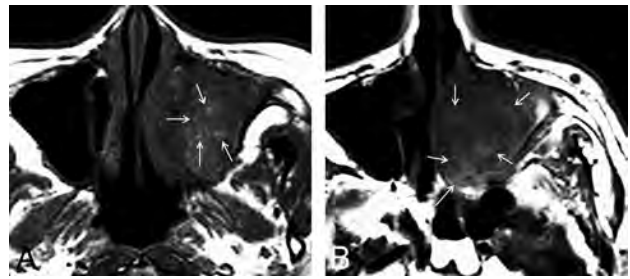


**FIG 4.** Examples of nonmelanomatous sinonasal tumors displaying a T1-SP (arrows). *A*, Squamous cell carcinoma. *B*, Lymphoma.

**Table 3: Correlation of histopathologic and MR imaging features of 23 sinonasal melanomas<sup>a</sup>**

	T1-SP (+)	T1-SP (-)	P Value <sup>b</sup>
Melanin			.915
Melanotic	14	4	.043 <sup>c</sup>
Abundant	9	0	
Moderate	5	3	
Amelanotic	4	1	
Hemorrhage			.280
Present	12	2	
Absent	6	3	
Cell type			.399
Epithelioid	12	3	
Spindle	3	0	
Mixed	3	2	

**Note:**—+ indicates presence; —, absence.

<sup>a</sup> Data are presented as numbers of tumors.

<sup>b</sup> Comparison of the prevalence of a T1-SP according to the presence of melanin, the presence of hemorrhage, and the different cell types using the  $\chi^2$  test.

<sup>c</sup> Comparison of the prevalence of a T1-SP between tumors with abundant melanin and the group of tumors with no and moderate melanin by the  $\chi^2$  test.

with intratumoral hemorrhage had a T1-SP, while 6 of 9 tumors without hemorrhage demonstrated it. There was no significant statistical difference in the prevalence of a T1-SP among tumors regarding the presence of melanin ( $P = .915$ ), the presence of hemorrhage ( $P = .280$ ), and the different cell types ( $P = .399$ ). Melanin pigments were abundant in 9 of 18 melanotic tumors and moderate in the remaining 9 tumors. If melanotic tumors with moderate melanin and amelanotic tumors were grouped together, there was a significant statistical difference in the prevalence of a T1-SP between the group of tumors with no and moderate melanin and melanotic tumors with abundant melanin ( $P = .043$  using the  $\chi^2$  test), suggestive of a close relationship between the amount of melanin and the presence of T1-SP. Hemorrhage was present in 10 of 18 melanotic tumors and 4 of 5 amelanotic tumors. T1-SP was demonstrated in 1 amelanotic melanoma that had no hemorrhage on histologic examination.

Although the retrospective nature of this study kept us from performing a side-by-side MR imaging–pathologic correlation, 4 cases revealed an uneven distribution of melanin with alternating melanin and fibrous bands, which might be considered one of the pathologic features responsible for a T1-SP on MR imaging (Fig 3C, -D).

## DISCUSSION

The results of the present study are promising in that a T1-SP might be a useful imaging marker for the diagnosis of SNM with high specificity (97%) and a moderate sensitivity (74%). While 23

(74.2%) of 31 SNMs showed a T1-SP, only 3 (2.8%) of 106 non-melanomatous malignant tumors demonstrated it. It also proved to be reproducible, shown by good interobserver agreement.

In this study, 14 of 18 melanotic SNMs and 4 of 5 amelanotic SNMs demonstrated a T1-SP. Although we failed to reveal a significant statistical difference in the prevalence of a T1-SP between melanotic and amelanotic tumors, our results showing a significant higher prevalence of a T1-SP in SNMs compared with other nonmelanomatous tumors may still be good evidence that melanin pigment is the important source for T1-SP. In their study with 7 melanotic SMMs and 5 amelanotic SMMs, Yousem et al<sup>11</sup> reported that all melanotic tumors were hyperintense to gray matter on T1WI regardless of the presence of hemorrhage, while the signal intensities of all amelanotic tumors were intermediate on T1WI. They suggested that the presence of melanin should be considered the main cause of hyperintensity.<sup>11</sup>

We also failed to find any statistical significance of the prevalence of a T1-SP between hemorrhagic and nonhemorrhagic tumors and among tumors of the different cell types as well. In their study with 6 melanotic SNMs and 5 amelanotic SNMs, Kim et al<sup>9</sup> suggested that the signal intensity of SNMs on MR imaging was affected mainly by melanin pigments but also, in part, by the hemorrhagic products. We speculate that intratumoral hemorrhage in addition to melanin should play a role in creating a T1-SP in a certain proportion of SNMs, as seen in 4 amelanotic SNMs and 3 nonmelanomatous sinonasal tumors demonstrating a T1-SP in this study. Most interesting, we found an intimate relationship between the amount of melanin and the presence of a T1-SP. Although no statistical difference in the prevalence of a T1-SP was found between melanotic and amelanotic tumors, the difference was significant between tumors with abundant melanin and the group of tumors with no and moderate melanin. This finding is in accordance with the results of the study by Kim et al,<sup>9</sup> who reported that the signal intensity pattern could vary on MR imaging depending on the amount and distribution of melanin within individual SNMs.

Previous studies also found intratumoral vessels and fibrous septa within malignant melanomas on histologic examination.<sup>9,22</sup> We suggest that a T1-SP may be attributed to an uneven distribution of melanin and hemorrhage within the tumors. In this study, 1 amelanotic tumor without evidence of hemorrhage demonstrated a T1-SP. Although unclear, it is possible that insufficient histopathologic examination might have overlooked the presence of melanin and/or hemorrhage in this case. Although an uneven distribution of melanin with the alternating melanin and fibrous bands within the tumors seen in 4 cases in this study might be considered one of the pathologic features responsible for a T1-SP, the retrospective nature of this study interfered with an exact 1:1 MR imaging–pathologic correlation; thus, the elucidation of the exact histopathologic basis for a T1-SP was difficult. We recommend a prospective study focusing on the MR imaging–pathologic correlation in a large cohort of patients with SNM in the near future.

A T1-SP seen in an SNM in the present study looks like the convoluted cerebriform pattern seen in inverted papillomas.<sup>23</sup> The only difference is that the former is best seen on T1WI, while the latter is seen on T2WI and contrast-enhanced T1WI. A “con-

voluted cerebriform pattern” is the term first used in the pathology literature by Barnes et al<sup>24</sup> to describe a distinctive gross mucosal morphology of inverted papilloma, created by the juxtaposed epithelial and stromal layers. This peculiar mucosal morphology results in a characteristic pattern on MR imaging (ie, the alternating hypointense and hyperintense bands on T2-weighted and contrast-enhanced T1-weighted images), making the imaging diagnosis of inverted papilloma possible.<sup>23,25</sup> Histologically, the convoluted cerebriform pattern seen in inverted papilloma is known to result from the alternation of highly cellular metaplastic epithelium and less cellular edematous stroma.<sup>25</sup>

This study has several limitations. First, the case series of SNMs is small, and the number of SNMs that underwent a histopathologic review is even smaller. Second, we used varying imaging parameters and different magnets in this study. These might alter the results of the prevalence of T1-SP because a higher magnetic field strength causes a greater sensitivity to T1 shortening. Third, the histopathologic features responsible for T1-SP were not exactly determined because the retrospective nature of this study prevented us from performing histopathologic re-examination in all cases of SNM, making an exact 1:1 MR imaging–pathologic correlation difficult. Fourth, the proportion of SNMs included in this study is roughly 23% (31 of 137), which is much higher than up to 4% reported among all sinonasal malignant tumors. The skewed composition of the patients due to the unusually high proportion with the disease of interest can have an unreliable impact on the calculations of the diagnostic index, such as specificity, positive and negative predictive values, and accuracy and thus may not reflect the true values encountered in clinical practice.

## CONCLUSIONS

Despite several limitations of this study, a T1-SP might be an adjunctive MR imaging finding for distinguishing SNM from various nonmelanomatous malignant sinonasal tumors with an overall accuracy of 92%. Although the exact histopathologic features responsible for a T1-SP are yet to be determined, we suggest that it may be attributed to an uneven distribution of melanin and hemorrhage within the tumors. A prospective study focusing on the MR imaging–pathologic correlation is highly recommended.

## REFERENCES

1. Chang AE, Karnell LH, Menck HR. **The National Cancer Data Base report on cutaneous and noncutaneous melanoma: a summary of 84,836 cases from the past decade: the American College of Surgeons Commission on Cancer and the American Cancer Society.** *Cancer* 1998;83:1664–78 Medline
2. Bachar G, Loh KS, O’Sullivan B, et al. **Mucosal melanomas of the head and neck: experience of the Princess Margaret Hospital.** *Head Neck* 2008;30:1325–31 CrossRef Medline
3. López F, Rodrigo JP, Cardesa A, et al. **Update on primary head and neck mucosal melanoma.** *Head Neck* 2016;38:147–55 CrossRef Medline
4. Moreno MA, Roberts DB, Kupferman ME, et al. **Mucosal melanoma of the nose and paranasal sinuses, a contemporary experience from the M. D. Anderson Cancer Center.** *Cancer* 2010;116:2215–23 CrossRef Medline
5. Lombardi D, Bottazzoli M, Turri-Zanoni M, et al. **Sinonasal mucosal melanoma: a 12-year experience of 58 cases.** *Head Neck* 2016; 38(suppl 1):E1737–45 CrossRef Medline

6. Marcus DM, Marcus RP, Prabhu RS, et al. **Rising incidence of mucosal melanoma of the head and neck in the United States.** *J Skin Cancer* 2012;2012:231693 Medline
7. Youssef D, Vasani S, Marquess J, et al. **Rising incidence of head and neck mucosal melanoma in Australia.** *J Laryngol Otol* 2017;131: S25–28 CrossRef Medline
8. Batra K, Chhabra A, Rampure J, et al. **CT and MRI appearances of primary sphenoid melanoma: a rare case.** *AJNR Am J Neuroradiol* 2005;26:2642–44 Medline
9. Kim SS, Han MH, Kim JE, et al. **Malignant melanoma of the sinonasal cavity: explanation of magnetic resonance signal intensities with histopathologic characteristics.** *Am J Otolaryngol* 2000;21: 366–78 CrossRef Medline
10. Xu QG, Fu LP, Wang ZC, et al. **Characteristic findings of malignant melanoma in the sinonasal cavity on magnetic resonance imaging.** *Chin Med J (Engl)* 2012;125:3687–91 Medline
11. Yousem DM, Li C, Montone KT, et al. **Primary malignant melanoma of the sinonasal cavity: MR imaging evaluation.** *Radiographics* 1996; 16:1101–10 CrossRef Medline
12. Escott EJ. **A variety of appearances of malignant melanoma in the head: a review.** *Radiographics* 2001;21:625–39 CrossRef Medline
13. Enochs WS, Petherick P, Bogdanova A, et al. **Paramagnetic metal scavenging by melanin: MR imaging.** *Radiology* 1997;204:417–23 CrossRef Medline
14. Woodruff WW Jr, Djang WT, McLendon RE, et al. **Intracerebral malignant melanoma: high-field-strength MR imaging.** *Radiology* 1987;165:209–13 CrossRef Medline
15. Turner JH, Reh DD. **Incidence and survival in patients with sinonasal cancer: a historical analysis of population-based data.** *Head Neck* 2012;34:877–85 CrossRef Medline
16. Khademi B, Moradi A, Hoseini S, et al. **Malignant neoplasms of the sinonasal tract: report of 71 patients and literature review and analysis.** *Oral Maxillofac Surg* 2009;13:191–99 CrossRef Medline
17. Bhattacharyya N. **Factors affecting survival in maxillary sinus cancer.** *J Oral Maxillofac Surg* 2003;61:1016–21 CrossRef Medline
18. Edge SB, Compton CC. **The American Joint Committee on Cancer: the 7th edition of the AJCC cancer staging manual and the future of TNM.** *Ann Surg Oncol* 2010;17:1471–74 CrossRef Medline
19. Stanimirov Rossi O, Vital D, Soyka MB, et al. **Multilocular sinonasal malignant melanoma: a poor prognostic subgroup?** *Eur Arch Otorhinolaryngol* 2015;272:123–29 CrossRef Medline
20. Bartell HL, Bedikian AY, Papadopoulos NE, et al. **Biochemotherapy in patients with advanced head and neck mucosal melanoma.** *Head Neck* 2008;30:1592–98 CrossRef Medline
21. Bedikian AY, Johnson MM, Warneke CL, et al. **Prognostic factors that determine the long-term survival of patients with unresectable metastatic melanoma.** *Cancer Invest* 2008;26:624–33 CrossRef Medline
22. Nazarian LN, Alexander AA, Kurtz AB, et al. **Superficial melanoma metastases: appearances on gray-scale and color Doppler sonography.** *AJR Am J Roentgenol* 1998;170:459–63 CrossRef Medline
23. Jeon TY, Kim HJ, Chung SK, et al. **Sinonasal inverted papilloma: value of convoluted cerebriform pattern on MR imaging.** *AJNR Am J Neuroradiol* 2008;29:1556–60 CrossRef Medline
24. Barnes L, Verbin RS, Gnepp DR. **Diseases of the nose, paranasal sinuses, and nasopharynx.** In: Barnes L, ed. *Surgical Pathology of the Head and Neck*. Vol 1. New York: Marcel Dekker; 1985:403–51
25. Ojiri H, Ujita M, Tada S, et al. **Potentially distinctive features of sinonasal inverted papilloma on MR imaging.** *AJR Am J Roentgenol* 2000;175:465–68 CrossRef Medline

# Intraoperative Conebeam CT for Assessment of Intracochlear Positioning of Electrode Arrays in Adult Recipients of Cochlear Implants

H. Jia, R. Torres, Y. Nguyen, D. De Seta, E. Ferrary, H. Wu, O. Sterkers, D. Bernardeschi, and I. Mosnier

## ABSTRACT

**BACKGROUND AND PURPOSE:** Intraoperative conebeam CT has been introduced into the operating room and provides quick radiologic feedback. This study aimed to investigate its utility in the assessment of the positioning of the electrode array after cochlear implantation.

**MATERIALS AND METHODS:** This was a retrospective study of 51 patients (65 ears) with intraoperative imaging by conebeam CT (O-arm) after cochlear implantation between 2013 and 2017. Correct placement into the cochlea was immediately identified. Positioning assessments were later analyzed with OsiriX software.

**RESULTS:** Intraoperative imaging was quickly performed in all cases. No misplacement into the vestibule or semicircular canals was found. A foldover of the implanted array was identified in 1 patient. Secondary analysis by 2 raters showed excellent agreement on insertion depth angle (intraclass correlation = 0.96,  $P < .001$ ) and length of insertion of the electrode array (intraclass correlation coefficient = 0.93,  $P = .04$ ) measurements. The evaluation of the number of extracochlear electrodes was identical between the 2 raters in 78% of cases (Cohen  $\kappa = 0.55$ ,  $P < .001$ ). The scalar position was inconsistent between raters. When we compared O-arm and high-resolution CT images in 14 cases, the agreement was excellent for insertion depth angle (intraclass correlation coefficient = 0.97,  $P < .001$ ) and insertion length (intraclass correlation coefficient = 0.98,  $P < .001$ ), good for the number of extracochlear electrodes (Cohen  $\kappa = 0.63$ ,  $P = .01$ ), but moderate for the scalar position (Cohen  $\kappa = 0.59$ ,  $P = .02$ ).

**CONCLUSIONS:** Intraoperative conebeam CT using the O-arm is a safe, rapid, easy, and reliable procedure to immediately identify a misplacement or foldover of an electrode array. The insertion depth angle, insertion length, and number of electrodes inserted can be accurately assessed.

**ABBREVIATIONS:** CBCT = conebeam CT; HRCT = high-resolution CT; ICC = intraclass correlation coefficient

The cochlear implant is an electronic medical device for rehabilitation of profound hearing loss. When implanted into the cochlea, the electrode array stimulates the spiral ganglion cells

with encoded electrical impulses; therefore, correct placement of the array is essential for a well-functioning cochlear implant. Imaging examination after implantation with, for example, radiography and fluoroscopy or high-resolution CT (HRCT) is mandatory in most centers to verify correct placement of the electrode array intra- or postoperatively, in particular, assessment of the insertion depth and the number of electrodes inserted.<sup>1,2</sup> Radiography and fluoroscopy, typically using a transorbital or modified Stenvers view, were initially applied to cochlear implantation,<sup>3,4</sup> but their major limitations were poor image resolution of the intracochlear structures and the lack of 3D views. Consequently, some cases of misplacement of the array into the semicircular canal or vestibule could not be distinguished intraoperatively.<sup>1,5,6</sup> Thus, in many medical centers, HRCT, which provides better resolution and presents sagittal, axial, and coronal views, became the routine imaging procedure after cochlear implantation and before discharge. Nevertheless, the HRCT platform is fixed, and this imaging cannot be performed in the operating room like radiography and fluoroscopy.

Received September 14, 2017; accepted after revision December 28.

From the Unité de Réhabilitation Chirurgicale Mini-Invasive Robotisée de l'Audition (H.J., R.T., Y.N., D.D.S., E.F., O.S., D.B., I.M.), Sorbonne Universités, Université Pierre et Marie Curie Paris 6, Institut National de la Santé et de la Recherche Médicale, Paris, France; Otologie, Implants Auditifs et Chirurgie de la Base du Crane (H.J., Y.N., D.D.S., E.F., O.S., D.B., I.M.), Paris Assistance Publique, GHU Pitié-Salpêtrière, Service ORL, Paris, France; Department of Otolaryngology-Head and Neck Surgery (H.J., H.W.), Shanghai Ninth People's Hospital, Shanghai Jiaotong University School of Medicine, Shanghai, China; and Shanghai Key Laboratory of Translational Medicine on Ear and Nose Diseases (H.J.), Jiaotong University School of Medicine, Shanghai, China.

Paper previously presented, in part, as preliminary results at: International Conference on Cochlear Implants and Other Implantable Technologies, May 11–14, 2016; Toronto, Ontario, Canada.

Please address correspondence to Isabelle Mosnier, MD, Unité Otologie, Implants Auditifs et Chirurgie de la Base du Crâne, GH Pitié-Salpêtrière-Bâtiment Castaigne, 47-83 Boulevard de l'Hôpital, 75651 Paris Cedex 13, France; e-mail: isabelle.mosnier@aphp.fr

<http://dx.doi.org/10.3174/ajnr.A5567>

**Table 1: Population characteristics (N = 51 patients)**

Demographics	
Age (mean ± SEM) (range) (yr)	53 ± 7.1 (20–87)
Sex (M/F)	24:27
Anatomy	
Normal	64 ears
Major aplasia	1 ear
Implanted side	
Left	18 patients
Right	19 patients
Bilateral	14 patients

Note:—SEM indicates standard error of the mean.

**Table 2: Device characteristics (N = 65 devices)**

Devices	Proprietary	O-arm	HRCT
	Name		
Advanced Bionics (16 electrodes)	Helix 1J	2	
	Mid-Scala	3	
Cochlear (22 electrodes)	Perimodiolar	CI 24, CI 512	12
		CI 532	1
	Straight	CI 422, CI 522	31
MED-EL (12 electrodes)	Flex 28	13	3
Oticon (20 electrodes)	Evo	2	
	Standard	1	

Conebeam CT (CBCT), which was primarily developed for dental and maxillofacial imaging, is now used in cochlear implantation.<sup>7,8</sup> In contrast to conventional spiral HRCT, which uses a narrow fan-shaped beam requiring multiple rotations around the patient to create a volume of data, CBCT only requires a single rotation of a cone-shaped beam that includes the whole FOV. The x-ray source and the flat panel detector rotate around a fixed point in the center of the ROI. CBCT can provide higher spatial resolution and dynamic range than HRCT. Other advantages of CBCT include less intense metallic artifacts and lower radiation exposure than conventional multislice HRCT.<sup>9</sup> During the past 10 years, CBCT has been developed as an alternative to HRCT in temporal bone imaging.<sup>10–13</sup> Several studies have shown high sensitivity and specificity of nonmobile CBCT in the assessment of the scalar position of the electrode array in temporal bone specimens from cadavers.<sup>14–17</sup> Furthermore, CBCT can be a mobile platform that can be used in the operating room. The purpose of this study was to assess the feasibility, reliability, and utility of mobile CBCT in the assessment of positioning of an electrode array in the operating room, immediately after cochlear implantation.

## MATERIALS AND METHODS

All participants provided written informed consent allowing retrospective analysis of their data (CNIL No. 2040854).

### Patients

A retrospective review was conducted on 51 patients (65 ears) who underwent cochlear implantation in a French tertiary medical center between July 2013 and March 2017 (Tables 1 and 2). An intraoperative radiologic evaluation (O-arm imaging system; Medtronic, Minneapolis, Minnesota) was performed after cochlear implantation and before the patients awoke from the anesthesia. Their medical records, including type of implant, surgical details, and radiologic images, were collected.

### Surgical Procedures

The operation was performed by the same senior otologist. Cochlear implantation was performed in all cases using a minimally invasive protocol,<sup>18</sup> with 4 brands of implant devices (Advanced Bionics, Valencia, California; Cochlear, Lane Cove, Australia; MED-EL, Innsbruck, Austria; and Oticon Medical, Vallauris, France).

### Radiologic Examinations and Analysis

In 14 patients who had implantation on their second side, the electrode position of the first side was assessed on preoperative HRCT images (0.6-mm thickness), performed in the neuroradiologic center, using a Discovery CT 750 HD scanner (GE Healthcare, Milwaukee, Wisconsin). This assessment allowed a comparison of the imaging between HRCT and CBCT for the same implant, without an additional radiologic examination. The mean CT dose index of HRCT for these 14 patients was  $91 \pm 10.4$  mGy, and the dose-length product was  $605 \pm 57.2$  mGy · cm<sup>2</sup>.

CBCT was performed immediately after closure of the incision using the O-arm. The tube voltage was 120 kV, with a 12-mA charge at the terminals. This intraoperative imaging platform provides 2D fluoroscopic imaging and a 360° scan resulting in 3D multiplanar views. Fluoroscopy must be performed before the 3D acquisitions to verify the optimum positioning of the targeted ear in the gantry. The 3D imaging volume was cylindrical (15-cm height × 20-cm diameter; 512 × 512 × 192 resolution), which was large enough to simultaneously detect both ears in 1 scan. After each scan, the 3D-MPR was automatically generated and 3 windows with planar images (coronal, sagittal, and axial) were immediately shown with free 3D rotation (Fig 1A). This process provided a slice thickness of 0.83 mm in the axial plane and 0.415 mm in the coronal and sagittal planes. One 360° rotation of the x-ray tube took 13 seconds. The CT dose index in the 51 patients was  $12 \pm 2.6$  mGy, and the dose-length product was  $200 \pm 53.4$  mGy · cm<sup>2</sup>.

The patients underwent the operation on a radiolucent carbon fiber surgical table in a dedicated operating room with x-ray protection. The installation and scanning with the O-arm were performed by the surgeon. The duration from the entrance of CBCT into the operating room to the completion of scanning was timed. The CBCT images were assessed by the surgeon immediately after scanning to eliminate a misplacement of the electrode array into the vestibule or semicircular canals or a foldover of the intracochlear array.

The radiologic images were later analyzed by 2 specialists experienced in cochlear implant imaging. The depth angle and the length of insertion, the number of extracochlear electrodes, and the scalar position of the array at 180° and 360° depth were assessed using OsiriX Imaging Software (<http://www.osirix-viewer.com>) as previously described.<sup>15,16</sup> Briefly, the reconstruction plane for the evaluation of the electrode position was the midmodiolar plane obtained with the curved multiplanar reconstruction (3D Curved MPR Viewer in OsiriX). This plane was defined as a 3D Bézier path along the electrode array. Once the path was defined by the selection of all the single electrodes, the array was straightened and visible in the Curved MPR Viewer window. Then, the electrode array can be visualized in a dynamic series of

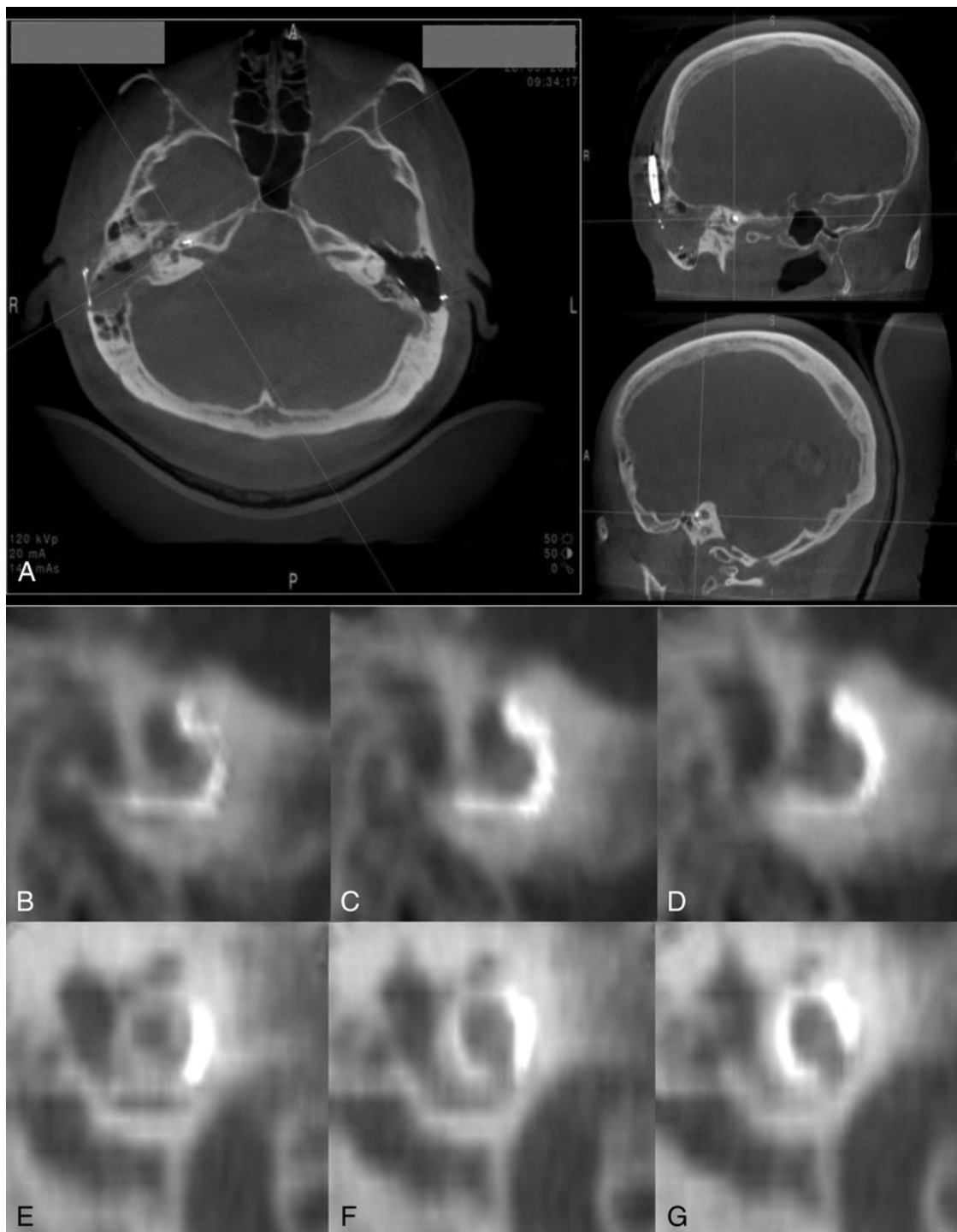


**FIG 1.** Output interface of the O-arm workstation and the case with foldover of the electrode array. The O-arm automatically shows the axial, sagittal, and coronal views on its screen after scanning and provides free 3D rotation (A). A foldover of the CI 532 electrode array was observed on the original and consecutive sagittal views (B–D). After a Cochlear CI 522 was re-implanted, the electrode array was verified in the correct position (E–G).

the midmodiolar section of the cochlea, and the raters estimated the localization, scala tympani, scala vestibuli, or intermediate position on the basis of the theoretic positions of the scala for electrodes positioned at 180° and 360°. Assessment was performed independently and was timed. In cases in which there was a discrepancy in the number of extracochlear electrodes or in the scalar position between independent analyses, a reassessment was

then performed by both raters to obtain a result with which they both agreed.

#### **Statistical Analysis**

Data are presented as mean  $\pm$  standard error of the mean. Interrater reliability was calculated using the intraclass correlation coefficient (ICC) for the quantitative variables insertion depth angle

**Table 3: Insertion depth angle and length of insertion of the electrode array—results from 2 raters using O-arm data<sup>a</sup>**

Implant	Rater	Depth Angle (°)	Length (mm)
Advanced Bionics (n = 5)	A	384 ± 28.8	19.5 ± 1.02
	B	389 ± 27.7	19.5 ± 0.96
Cochlear (perimodiolar) (n = 12)	A	357 ± 10.1	18.8 ± 0.71
	B	360 ± 9.5	18.6 ± 0.79
Cochlear (straight) (n = 31)	A	425 ± 12.9	22.1 ± 0.47
	B	427 ± 13.4	22.3 ± 0.47
MED-EL (n = 13)	A	500 ± 30.0	24.1 ± 0.90
	B	502 ± 30.0	24.4 ± 0.93
Oticon (n = 3)	A	370 ± 13.2	23.4 ± 0.30
	B	366 ± 21.7	23.4 ± 0.28

<sup>a</sup> Values are mean ± standard error of the mean.

and insertion length or the Cohen  $\kappa$  for the categorical variables electrode number and scalar position. The reliability of the electrode number with the total number of cases was calculated with the weighted data based on the electrode number of the implant device. Paired *t* tests or Fisher exact tests were applied for comparison of variables. The criterion for statistical significance was set at *P* < .05, 2-tailed. R statistical and computing software (<http://www.r-project.org>) was used.

## RESULTS

### Analysis of Intraoperative Electrode Positioning Using the O-Arm

The mean duration of installation and scanning was  $5.4 \pm 1.2$  minutes. In this series, misplacement into the vestibule or semicircular canals was eliminated intraoperatively. In 1 case with major aplasia of the ear, the difficulty of implantation was increased by malformation of the middle ear, but the intraoperative images confirmed the correct position of the array. In another case in which a novel design of the array (CI 532; Cochlear, Lane Cove, Australia) was implanted, a foldover of the inserted array was observed (Fig 1B–D). This patient was re-implanted with a CI 522 (Cochlear), and the new electrode array was inserted correctly with an insertion depth angle of  $399^\circ$  and insertion length of 22.4 mm (Fig 1E–G). The case of foldover was excluded from the OsiriX analysis.

### Assessment of Electrode Positioning

Independent assessments were performed by 2 raters for 64 ears with O-arm data, using the MPR viewer of OsiriX. The mean time for analysis was  $3.1 \pm 1.1$  minutes for one rater and  $3.7 \pm 0.4$  minutes for the other. There was an excellent agreement between raters for the depth angle of insertion (ICC = 0.96, *P* < .001) and insertion length (ICC = 0.93, *P* = .04), with a non-statistically significant difference between raters of  $8^\circ \pm 0.8^\circ$  for insertion depth angle and  $0.6 \pm 0.1$  mm for insertion length (Table 3).

Because the intracochlear electrodes were not clearly shown on O-arm images (Fig 2G, -H), apart from those of the MED-EL implant, which has only 12 electrodes (Fig 2E, -F), the extracochlear electrodes that were more clearly identified were counted. Their numbers were assessed identically between the 2 raters in 50 ears (78%, Cohen  $\kappa$  = 0.53, *P* < .001), and the identical rates among the different types of arrays did not show a statistically significant difference (Table 4). Regarding the scalar position of the electrodes, initial assessment was the same between raters in only 34/64 ears (53%) at  $180^\circ$  and 20/46 ears (43%) at  $360^\circ$ , with

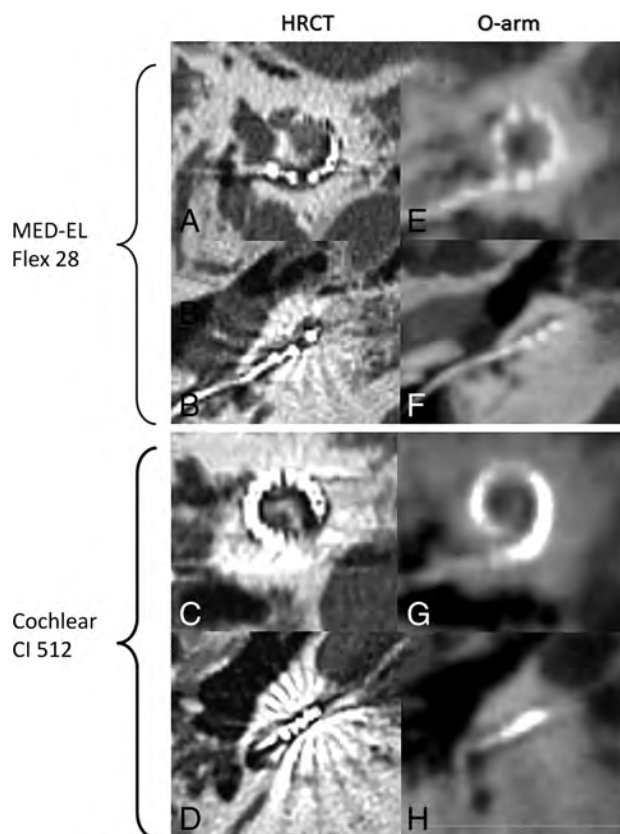


**FIG 2.** Examples of radiologic images of HRCT and the O-arm for 2 types of cochlear implants. MED-EL Flex 28 (A, B, E, F) and Cochlear CI 512 (C, D, G, H) electrode arrays were observed with both HRCT (A–D) and the O-arm (E–H), and with sagittal (A, C, E, G) and axial (B, D, F, H) views.

no significant consistency between the evaluations of the 2 raters (Cohen  $\kappa$  = 0.16, *P* = .10 at  $180^\circ$ ; and Cohen  $\kappa$  = 0.14, *P* = .05 at  $360^\circ$ ). After reassessment by the 2 raters, no significant difference was found for the various types of arrays, for the rate of extracochlear electrodes, or for the scalar position (Table 5).

### Concordance of the Electrode Assessment between HRCT and the O-Arm

When comparing reassessment results obtained by HRCT and O-arm in the 14 ears of patients who had implantation on their second side, we found an excellent agreement for the insertion depth angle (ICC = 0.97, *P* < .001) and the insertion length (ICC = 0.98, *P* < .001), with a non-statistically significant difference of  $11^\circ \pm 2.2^\circ$  for the insertion depth angle and of  $0.4 \pm 0.1$  mm for the insertion length. The number of extracochlear electrodes was identical in 13/14 ears (93%) and showed good agreement (Cohen  $\kappa$  = 0.63, *P* = .01). Analysis of the scalar position of the array still showed a moderate agreement at  $180^\circ$  (79%, Cohen  $\kappa$  = 0.59, *P* = .02) and a nonsignificant agreement at  $360^\circ$  (75%, Cohen  $\kappa$  = 0.44, *P* = .06) (Table 6).

## DISCUSSION

Misplacement of electrode arrays into the vestibule or semicircular canals or foldover of inserted arrays has been reported in about 0.2%–1% of patients<sup>4,19–21</sup> and needed to be surgically corrected. Electrophysiologic measurements, such as impedance or neural

**Table 4: Extracochlear electrode number and scalar position—difference in the results of 2 raters using O-arm data**

	Electrode No. Counting			Scalar Position at 180°		Scalar Position at 360° <sup>a</sup>	
	Rater A vs B			Rater A vs B		Rater A vs B	
	Same	±1	±2	Same	Different	Same	Different
Advanced Bionics ( <i>n</i> = 5)	3 (60%)	2 (40%)		4 (80%)	1 (20%)	2/3 (67%)	1/3 (33%)
Cochlear (perimodiolar) ( <i>n</i> = 12)	9 (75%)	2 (17%)	1 (8%)	6 (50%)	6 (50%)	5/9 (55%)	4/9 (45%)
Cochlear (straight) ( <i>n</i> = 31)	25 (80%)	3 (10%)	3 (10%)	14 (45%)	17 (55%)	6/21 (29%)	15/21 (71%)
MED-EL ( <i>n</i> = 13)	11 (85%)	2 (15%)		8 (62%)	5 (38%)	6/11 (55%)	5/11 (45%)
Oticon ( <i>n</i> = 3)	2 (67%)		1 (33%)	2 (67%)	1 (33%)	1/2 (50%)	1/2 (50%)
Total ( <i>n</i> = 64)	50 <sup>b</sup> (78%)	9 (14%)	5 (8%)	34 <sup>c</sup> (53%)	30 (47%)	20/46 <sup>c</sup> (43%)	26/46 (57%)

<sup>a</sup> Some electrode arrays did not pass 360° depth, so the number of measurable cases at 360° was less than at 180°. The number of cases is indicated.

<sup>b</sup> Cohen  $\kappa$  = 0.53 (*P* < .001). Among the different array types, the raters' concordance showed no significant difference.

<sup>c</sup> Cohen  $\kappa$  < 0.2 (not significant).

**Table 5: Extracochlear electrode number and scalar position—final results after coassessment using O-arm data**

	No. of Extracochlear Electrodes					Scalar Position at 180°			Scalar Position at 360° <sup>a</sup>		
	0	1	2	3	4	ST	Int	SV	ST	Int	SV
	Advanced Bionics ( <i>n</i> = 5)	2 (40%)	1 (20%)	2 (40%)			3 (60%)	1 (20%)	1 (20%)	2/3 (67%)	
Cochlear (perimodiolar) ( <i>n</i> = 12)	6 (50%)	3 (25%)	2 (17%)		1 (8%)	6 (50%)	5 (42%)	1 (8%)	3/9 (33%)	5/9 (56%)	1/9 (11%)
Cochlear (straight) ( <i>n</i> = 31)	26 (84%)	1 (3%)	1 (3%)	2 (6%)	1 (3%)	16 (52%)	12 (38%)	3 (10%)	5/21 (24%)	13/21 (62%)	3/21 (14%)
MED-EL ( <i>n</i> = 13)	10 (77%)	1 (8%)	2 (15%)			9 (69%)	4 (31%)		7/11 (64%)	4/11 (36%)	
Oticon ( <i>n</i> = 3)	1 (33%)	1 (33%)	1 (33%)			1 (33%)	2 (67%)		1/2 (50%)	1/2 (50%)	
Total ( <i>n</i> = 64)	45 (70%)	7 (11%)	8 (13%)	2 (3%)	2 (3%)	35 (55%)	24 (38%)	5 (7%)	18/46 (39%)	23/46 (50%)	5/46 (11%)

**Note:**—ST indicates scala tympani; Int, intermediate position; SV: scala vestibuli.

<sup>a</sup> Some electrode arrays did not pass 360° depth, so the number of measurable cases at 360° was less than at 180°. The number of cases is indicated.

**Table 6: Concordances of raters' coassessment between HRCT and O-arm—extracochlear electrode number and scalar position**

	No. of Extracochlear Electrodes		Scalar Position at 180°		Scalar Position at 360° <sup>a</sup>	
	HRCT vs O-Arm		HRCT vs O-Arm		HRCT vs O-Arm	
	Same	±1	Same	Different	Same	Different
Cochlear ( <i>n</i> = 11)	10 (91%)	1 (9%)	8 (73%)	3 (27%)	6/9 (67%)	3/9 (33%)
MED-EL ( <i>n</i> = 3)	3 (100%)		3 (100%)		3/3 (100%)	
Total ( <i>n</i> = 14)	13 (93%)	1 (7%)	11 (79%)	3 (21%)	9/12 (75%)	3/12 (25%)

<sup>a</sup> Some electrode arrays did not pass 360° depth, so the number of measurable cases at 360° was less than at 180°. The number of cases is indicated.

response telemetry, can be performed immediately after implantation to verify the normal function of the electrode array; however, some intraoperative electrophysiologic measurements have been reported to be normal or near-normal in cases of misplacement.<sup>5,22,23</sup> In the present study, 1 patient presented with a foldover of the array, but intraoperative electrophysiologic measurements did not indicate abnormalities, so imaging was the exclusive method used to diagnose this misplacement. In the absence of postoperative imaging or in the case of misdiagnosis by fluoroscopy, a misplacement outside the cochlea might only be suspected at the first mapping, generally about 2–4 weeks after implantation, and then confirmed by HRCT. These patients have lost the optimum timing for revision surgery because the delay between the first surgery and revision increases the importance of tissue repair and fibrosis around the round window or cochleostomy site and thus may provoke more bleeding or damage in the inner ear.<sup>20,24,25</sup> If HRCT or CBCT is performed as routine postoperative imaging and a misplacement is reported, an additional anesthetic procedure is required for the revision surgery. Furthermore, for recipients who are children, postoperative HRCT is not a routine imaging procedure in many centers and sometimes is a complex procedure requiring sedation and special care. Therefore, intraoperative imaging is very useful and could be indicated at least for individuals who present a risk for a challenging operation because of inner ear malformations and pathologic narrow-

ing or obstruction of the cochlear scalae in the case of meningitis, trauma, or otosclerosis.<sup>21</sup>

CBCT by the O-arm is designed for intraoperative use, with a radiolucent carbon fiber surgical table in a dedicated operating room with x-ray protection and can be performed before closing the incision using a sterile tube drape. Even though this version of the O-arm software could not realize a maximum intensity projection on its platform, which can rebuild the entire electrode array, a function of free 3D rotation was provided and was very helpful for careful assessment of array positioning. Because of the easy manipulation with the O-arm, the installation, scanning, and assessment of the electrode array can be performed by the surgeon when the protocol is established. In this study, the performance of the O-arm in the operating room was successfully and quickly realized in all cases. In addition, the lower radiation dose compared with HRCT makes it a safer imaging technique.<sup>26</sup>

With advanced software for DICOM such as OsiriX, which has been approved as a reliable and rapid method for assessing radiologic imaging,<sup>16</sup> a more detailed positioning assessment of the electrode array can be realized in the operating room and can give timely feedback to the surgeon. In this series, the insertion depth angle and the length of insertion of the electrode array were assessed promptly (~3–4 minutes) and showed excellent agreement between the raters' independent assessments. These results also showed excellent agreement with those based on HRCT im-

ages, which is the most common imaging procedure and is considered the criterion standard postoperative protocol for the evaluation of electrode arrays in adults. For electrode counting, there was also good agreement between raters, even though it was difficult to clearly distinguish the electrodes near the round window or cochleostomy on O-arm images, especially for arrays with a high number of electrodes (Fig 2); however, the accuracy of electrode counting by the O-arm was still acceptable compared with HRCT. Consequently, O-arm imaging can be considered a reliable tool for assessing the electrode array position in the cochlea in current practice.

Besides correct placement in the cochlea, translocation into the scala vestibuli is increasingly being studied because it might be associated with poor speech performance.<sup>27</sup> In this series, the scalar positioning was difficult to evaluate on O-arm images and a poor interrater agreement was found, whereas other studies have reported more accurate identification of the scalar position.<sup>16,17,28,29</sup> This difference might be explained by the technologic differences between mobile and fixed CBCT equipment, such as the i-CAT 3D Imaging System (Imaging Sciences International, Hatfield, Pennsylvania), ILUMA Ultra Cone Beam CT Scanner (IMTEC Imaging, Ardmore, Oklahoma), and NewTom 5G or NewTom VGI CBCT scanner (NewTom, Verona, Italy).<sup>13,14,16</sup> Furthermore, analysis by a senior neuroradiologist or with coregistration of preoperative and postoperative images could give a more accurate assessment of the scalar position,<sup>10,28,30-33</sup> but this takes a long time and is not feasible for current intraoperative use. Finally, up to now, lack of diagnosis of a translocation is not of primary importance because it is not an indication for re-insertion of the array.

## CONCLUSIONS

The O-arm is an imaging platform with mobility, rapid installation, quick scanning, intraoperative use, and low radiation dose. It provides reliable image quality for eliminating misplacement of electrode arrays into the vestibule or semicircular canals or foldover of the inserted array; for measuring the insertion depth angle and length of insertion; and for counting the number of electrodes inserted, which makes it a practical radiologic technique for assessment of electrode array positioning in the operating room. This is particularly useful for patients in a 1-day operation and in the case of a challenging operation. This device could potentially be combined with navigation or robotic systems. It could also be shared by different disciplines, such as neurosurgery and orthopedics; this feature makes it a valuable piece of equipment in the operating room.

## ACKNOWLEDGMENTS

We thank Haoyue Tan for her assistance with statistical analysis and Colin Woodham for language editing.

Disclosures: Olivier Sterkers—UNRELATED: Consultancy: Medtronic, Comments: monitoring of the facial nerve.

## REFERENCES

- Gnagi SH, Baker TR, Pollei TR, et al. **Analysis of intraoperative radiographic electrode placement during cochlear implantation.** *Otol Neurotol* 2015;36:1045–47 CrossRef Medline
- Xu J, Xu SA, Cohen LT, et al. **Cochlear view: postoperative radiography for cochlear implantation.** *Am J Otol* 2000;21:49–56 Medline
- Viccaro M, Covelli E, De Seta E, et al. **The importance of intra-operative imaging during cochlear implant surgery.** *Cochlear Implants Int* 2009;10:198–202 CrossRef Medline
- Ying YL, Lin JW, Oghalai JS, et al. **Cochlear implant electrode misplacement: incidence, evaluation, and management.** *Laryngoscope* 2013;123:757–66 CrossRef Medline
- Sun JQ, Sun JW, Hou XY, et al. **Electrode array misplacement into the superior semicircular canal: as a rare complication of cochlear implantation.** *Int J Pediatr Otorhinolaryngol* 2014;78:1537–40 CrossRef Medline
- Hassan AM, Patel R, Redleaf M. **Intra-operative skull X-ray for misdirection of the cochlear implant array into the vestibular labyrinth.** *J Laryngol Otol* 2015;129:923–27 CrossRef Medline
- Richter B, Aschendorff A, Lohnstein P, et al. **The Nucleus Contour electrode array: a radiological and histological study.** *Laryngoscope* 2001;111:508–14 CrossRef Medline
- Husstedt HW, Aschendorff A, Richter B, et al. **Nondestructive three-dimensional analysis of electrode to modiolus proximity.** *Otol Neurotol* 2002;23:49–52 CrossRef Medline
- Arweiler-Harbeck D, Mönninghoff C, Greve J, et al. **Imaging of electrode position after cochlear implantation with flat panel CT.** *ISRN Otolaryngol* 2012;2012:728205 CrossRef Medline
- Aschendorff A, Kubalek R, Turowski B, et al. **Quality control after cochlear implant surgery by means of rotational tomography.** *Otol Neurotol* 2005;26:34–37 CrossRef Medline
- Miracle AC, Mukherji SK. **Conebeam CT of the head and neck, part 2: clinical applications.** *AJNR Am J Neuroradiol* 2009;30:1285–92 CrossRef Medline
- Dahmani-Causse M, Marx M, Deguine O, et al. **Morphologic examination of the temporal bone by conebeam computed tomography: comparison with multislice helical computed tomography.** *Eur Ann Otorhinolaryngol Head Neck Dis* 2011;128:230–35 CrossRef Medline
- Stutzki M, Jahns E, Mandapathil MM, et al. **Indications of conebeam CT in head and neck imaging.** *Acta Otolaryngol* 2015;135:1337–43 CrossRef Medline
- Marx M, Risi F, Escudé B, et al. **Reliability of conebeam computed tomography in scalar localization of the electrode array: a radio histological study.** *Eur Arch Otorhinolaryngol* 2014;271:673–79 CrossRef Medline
- Kurzweg T, Dalchow CV, Bremke M, et al. **The value of digital volume tomography in assessing the position of cochlear implant arrays in temporal bone specimens.** *Ear Hear* 2010;31:413–19 CrossRef Medline
- De Seta D, Mancini P, Russo FY, et al. **3D curved multiplanar cone beam CT reconstruction for intracochlear position assessment of straight electrodes array: a temporal bone and clinical study.** *Acta Otorhinolaryngol Ital* 2016;36:499–505 CrossRef Medline
- Mosnier I, Célrier C, Bensimon JL, et al. **Conebeam computed tomography and histological evaluations of a straight electrode array positioning in temporal bones.** *Acta Otolaryngol* 2017;137:229–34 CrossRef Medline
- Nguyen Y, Mosnier I, Borel S, et al. **Evolution of electrode array diameter for hearing preservation in cochlear implantation.** *Acta Otolaryngol* 2013;133:116–22 CrossRef Medline
- Loundon N, Blanchard M, Roger G, et al. **Medical and surgical complications in pediatric cochlear implantation.** *Arch Otolaryngol Head Neck Surg* 2010;136:12–15 CrossRef Medline
- Lee J, Eddington DK, Nadol JB. **The histopathology of revision cochlear implantation.** *Audiol Neurootol* 2011;16:336–46 CrossRef Medline
- Jiang Y, Gu P, Li B, et al. **Analysis and management of complications in a cohort of 1,065 minimally invasive cochlear implantations.** *Otol Neurotol* 2017;38:347–51 CrossRef Medline
- Pijl S, Westerberg BD, Gustin C, et al. **Objective findings with malpositioning of a nucleus 24RE(CA) cochlear implant.** *J Am Acad Audiol* 2008;19:435–42 CrossRef Medline

23. Cosetti MK, Shapiro WH, Green JE, et al. **Intraoperative neural response telemetry as a predictor of performance.** *Otol Neurotol* 2010; 31:1095–99 CrossRef Medline
24. Tien HC, Linthicum FH. **Histopathological changes in the vestibule after cochlear implantation.** *Otolaryngol Head Neck Surg* 2002;127: 260–64 CrossRef Medline
25. Bas E, Goncalves S, Adams M, et al. **Spiral ganglion cells and macrophages initiate neuro-inflammation and scarring following cochlear implantation.** *Front Cell Neurosci* 2015;9:303 CrossRef Medline
26. Schulze R. **Radiation protection vs research interests.** *Dentomaxillofac Radiol* 2013;42:20120348 CrossRef Medline
27. Holden LK, Finley CC, Firszt JB, et al. **Factors affecting open-set word recognition in adults with cochlear implants.** *Ear Hear* 2013; 34:342–60 CrossRef Medline
28. Boyer E, Karkas A, Attye A, et al. **Scalar localization by cone beam computed tomography of cochlear implant carriers: a comparative study between straight and periomodiolar precurved electrode arrays.** *Otol Neurotol* 2015;36:422–29 CrossRef Medline
29. Theunisse HJ, Joemai RMS, Maal TJ, et al. **Cone-beam CT versus multi-slice CT systems for postoperative imaging of cochlear implantation: a phantom study on image quality and radiation exposure using human temporal bones.** *Otol Neurotol* 2015;36:592–99 CrossRef Medline
30. Skinner MW, Holden TA, Whiting BR, et al. **In vivo estimates of the position of advanced bionics electrode arrays in the human cochlea.** *Ann Otol Rhinol Laryngol Suppl* 2007;197:2–24 Medline
31. Schuman TA, Noble JH, Wright CG, et al. **Anatomic verification of a novel method for precise intrascalar localization of cochlear implant electrodes in adult temporal bones using clinically available computed tomography.** *Laryngoscope* 2010;120:2277–83 CrossRef Medline
32. Helbig S, Mack M, Schell B, et al. **Scalar localization by computed tomography of cochlear implant electrode carriers designed for deep insertion.** *Otol Neurotol* 2012;33:745–50 CrossRef Medline
33. Lane JI, Witte RJ, Driscoll CLW, et al. **Scalar localization of the electrode array after cochlear implantation: clinical experience using 64-slice multidetector computed tomography.** *Otol Neurotol* 2007; 28:658–62 Medline

# Modeling Early Postnatal Brain Growth and Development with CT: Changes in the Brain Radiodensity Histogram from Birth to 2 Years

 K.A. Cauley,  Y. Hu,  J. Och,  P.J. Yorks, and  S.W. Fielden



## ABSTRACT

**BACKGROUND AND PURPOSE:** The majority of brain growth and development occur in the first 2 years of life. This study investigated these changes by analysis of the brain radiodensity histogram of head CT scans from the clinical population, 0–2 years of age.

**MATERIALS AND METHODS:** One hundred twenty consecutive head CTs with normal findings meeting the inclusion criteria from children from birth to 2 years were retrospectively identified from 3 different CT scan platforms. Histogram analysis was performed on brain-extracted images, and histogram mean, mode, full width at half maximum, skewness, kurtosis, and SD were correlated with subject age. The effects of scan platform were investigated. Normative curves were fitted by polynomial regression analysis.

**RESULTS:** Average total brain volume was 360 cm<sup>3</sup> at birth, 948 cm<sup>3</sup> at 1 year, and 1072 cm<sup>3</sup> at 2 years. Total brain tissue density showed an 11% increase in mean density at 1 year and 19% at 2 years. Brain radiodensity histogram skewness was positive at birth, declining logarithmically in the first 200 days of life. The histogram kurtosis also decreased in the first 200 days to approach a normal distribution. Direct segmentation of CT images showed that changes in brain radiodensity histogram skewness correlated with, and can be explained by, a relative increase in gray matter volume and an increase in gray and white matter tissue density that occurs during this period of brain maturation.

**CONCLUSIONS:** Normative metrics of the brain radiodensity histogram derived from routine clinical head CT images can be used to develop a model of normal brain development.

**ABBREVIATIONS:** FWHM = full width at half maximum; ID = identification; LOOCV = leave-one-out cross-validation; RMSE = root-mean-square error; R<sup>2</sup> = coefficient of determination

The availability and speed of CT imaging, together with radiation dose reduction strategies, serve to maintain the role of CT in pediatric clinical care. CT is particularly amenable to quantitative measures because the Hounsfield unit, reported by the scanner, is directly related to a physical property of tissue—tissue radiodensity. The differences in tissue radiodensity between gray and white matter enable segmentation of these tissues and characterization of the products of segmentation. Segmentation per-

mits quantitative analysis of volumes and densities of tissue types, with the potential to further the diagnostic power of the CT scan. The risks of radiation exposure preclude prospective scanning of healthy children, however, and little research has been directed at quantitative measures of brain development using CT.

Retrospective analysis of imaging data from the clinical archive provides a data base from which to develop a model of normal brain development using CT. We used a total brain radiodensity histogram method to investigate brain tissue changes as a function of subject age. This total brain histogram approach has the advantage of being objective and reproducible, is amenable to automation, and enables the development of a model of early brain maturation. Such a model could serve as a normative baseline for quantitative assessment of normal and abnormal brain development.

## MATERIALS AND METHODS

### Study Cohort

All children 2 years of age and younger presenting for evaluation by a CT imaging system at Geisinger Health System from May

Received October 2, 2017; accepted after revision December 11.

From the Department of Radiology (K.A.C., S.W.F.), Biomedical & Translational Informatics (Y.H.), and Department of Medical & Health Physics (J.O., P.J.Y.), Geisinger Health System, Danville, Pennsylvania; and Department of Imaging Science & Innovation (S.W.F.), Geisinger Health System, Lewisburg, Pennsylvania.

Previously presented as a scientific paper at: Annual Meeting of The Eastern Neuroradiological Society, August 24–27, 2017; Toronto, Ontario, Canada.

Please address correspondence to: Keith A. Cauley, MD, PhD, Department of Radiology, Div Neuroradiology, Geisinger Medical Center, Danville, PA 17822; e-mail: keithcauley@hotmail.com

 Indicates article with supplemental on-line appendix and table.

 Indicates article with supplemental on-line photos.

<http://dx.doi.org/10.3174/ajnr.A5559>

2010 to May 2016 were retrospectively reviewed after approval by the institutional review board. The study cohort included patients from neonate to 2 years of age with no known neurologic, neurocognitive, or developmental deficits, who had normal-appearing head CT findings. All head CT studies with normal findings were additionally reviewed and confirmed by a neuroradiologist with a Certificate of Added Qualification with 6 years of attending pediatric neuroradiology experience (K.A.C.). Patients who had any focal abnormal findings on the head CT study or any subsequent brain MR imaging with any abnormal focal intensity on FLAIR or other sequences, cysts, or other nonspecific structural appearances were excluded. Patients with metal artifacts or motion-degraded or non-diagnostic-quality imaging were also excluded.

A thorough chart review was performed (K.A.C.) to identify any disease history. Most cases were of minor trauma without traumatic findings, isolated seizure, apnea, and tremor. Other cases included scalp nevus and isolated facial and neck lesions without associated syndromes or intracranial extension. Patients with any systemic or noncentral nervous system diseases (eg, diseases of the renal, gastrointestinal, cardiac systems), cancers, history of prematurity, phakomatoses, genetic or syndromic conditions, epilepsy, fracture, hemorrhage, vascular lesions (aneurysm, AVM, fistula, or steno-occlusive disease of the CNS or elsewhere), acute or recent infection and fever of unknown origin, chronic medical therapy, or endocrine symptoms/laboratory abnormal results were excluded.

One hundred twenty healthy subjects from birth to 2 years (60 males and 60 females) met the inclusion criteria and were included in the study. Cases were drawn from 3 different scan platforms and were analyzed separately. The resulting cohort consisted of 45 cases (21 female) scanned on scanner 1 (described below), 51 cases (29 female) scanned on scanner 2, and 24 cases (12 female) scanned on scanner 3.

### Imaging Methods

To assess the variation in image histogram metrics due scan platform, we collected images from 3 different scan platforms within our health care system.

- Scanner 1 serves a community medical center, is a Brilliance 64 (Philips Healthcare, Best, the Netherlands) with helical acquisition and pediatric head CT protocol with 120 kV(peak) and fixed 192 mA (rotation time = .781 seconds, pitch = 0.64, effective milliamperes-second = 234.3).
- Scanner 2 primarily serves the emergency department of a level 1 trauma center, is a LightSpeed VCT (GE Healthcare, Milwaukee, Wisconsin) with an axial acquisition and pediatric head CT protocol with 120 kVp and modulated milliamperes, minimum 20 and maximum 75mA (rotation time = 0.5 seconds).
- Scanner 3 serves a second community medical center, is a Discovery 690 (GE Healthcare) with axial acquisition and pediatric head CT protocol with 120 kVp and fixed 240 mA (rotation time = 0.5 seconds).

Each scanner undergoes a daily quality assurance procedure, which assesses the radiodensity of water. This value must be within allowable limits, generally  $0 \pm 5$  HU. Drift or trending is rarely observed. In addition, scanners undergo an annual inspec-

tion by a medical physicist using the American College of Radiology phantom. Acceptable ranges of Hounsfield units for clinical scanners are broad ( $-7$ – $7$  for water, 110–135 for acrylic).<sup>1</sup> This testing is extended to all kilovolt(peak)s used by the scanner. Additionally, service engineers routinely test the calibration at preventive maintenance.

### Image Processing and Analysis

Images were thresholded, brain-extracted, and segmented in FSL ([www.fmrib.ox.ac.uk/fsl](http://www.fmrib.ox.ac.uk/fsl)),<sup>2-4</sup> as described in Cauley et al.<sup>5</sup> In brief, CSF was eliminated by setting a threshold minimum at 10 HU. The upper threshold value was set at 50 HU based on the pre-brain-extracted histogram and served to eliminate skull. The FSL Brain Extraction Tool (<http://fsl.fmrib.ox.ac.uk/fsl/fslwiki/BET>) standard brain extraction was used with a fractional intensity threshold of 0.01. All cases were carefully reviewed for integrity of brain extraction. No cases were eliminated on the basis of technical failure of the brain extraction protocol, and no manual masking was necessary. Brain volumes were computed in FSL from brain-extracted images.

Histograms and histogram analysis were performed in Matlab (Release 2009b; MathWorks, Natick, Massachusetts). The histogram of a normal brain follows the general appearance of the normal distribution. Matlab functions skewness and kurtosis were used to assess how far from this distribution each imaging dataset lay. In Matlab, the skewness of a distribution is defined as  $s = E(x - \mu)^3 / \sigma^3$ , where  $\mu$  is the mean of  $x$ ,  $\sigma$  is the SD of  $x$ , and  $E(t)$  represents the expected value of the quantity  $t$ . Kurtosis is defined as  $k = E(x - \mu)^4 / \sigma^4$ , where  $\mu$  is the mean of  $x$ ,  $\sigma$  is the SD of  $x$ , and  $E(t)$  represents the expected value of the quantity  $t$ . The kurtosis of the normal distribution is 3. Other histogram features, including histogram mean, mode, full width at half maximum (FWHM), and SD, were recorded.

For segmentation, a 2-tissue compartment segmentation strategy was used, with FAST at default settings and partial volume segmentation. Segmentations were confirmed by histogram (Fig 1) as previously described.<sup>5</sup>

### Statistical Analysis

For the brain volume growth curve, we first fitted the basic polynomial regression model, in which a third-degree polynomial of age was used to model the scaled brain volume growth curve.<sup>6</sup> Sex and scanner identification (ID) covariables were then added, and the model was refitted. For characteristics of the CT density histogram, a polynomial regression of the second-degree of age (basic model) was fitted first, and the additional covariates such as sex and scanner ID were considered. Dependent variables were scaled by SD. Models were selected on the basis of the adjusted coefficient of determination ( $R^2$ ). Models were evaluated using leave-one-out cross-validation (LOOCV), and root-mean-square error (RMSE) was computed for predictive accuracy. Curve fitting and statistical analysis were performed using GraphPad Prism software, Version 7.0c for Mac OS X (GraphPad Software, San Diego, California). The statistical significance of sex and scanner platform contribution were calculated in R statistical and computing software (<http://www.r-project.org/>).<sup>7</sup>

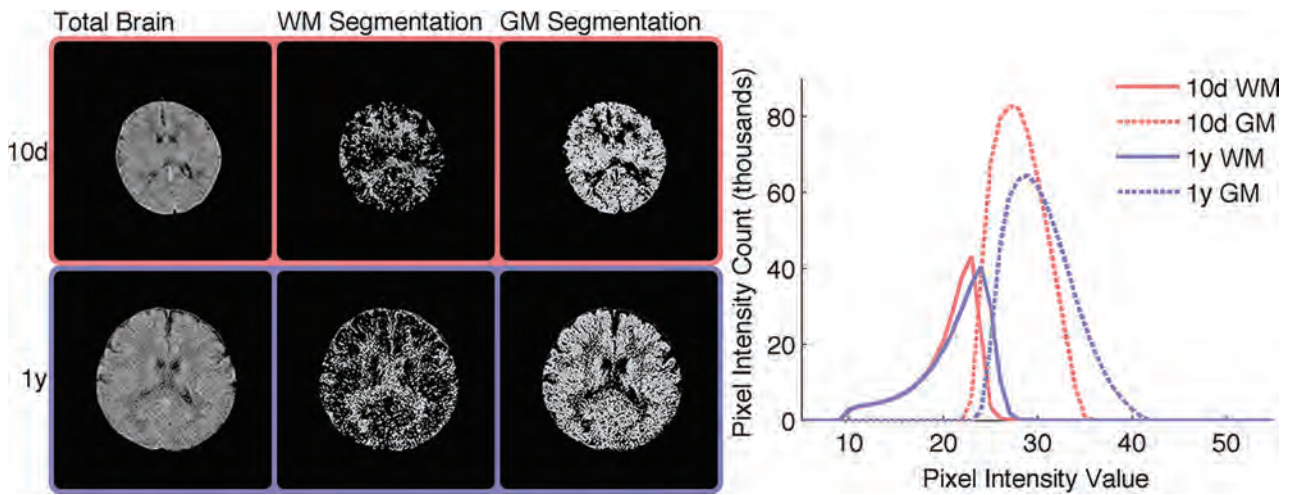


**FIG 1.** Brain-extracted head CT images with products of direct segmentation. Ten-day and 1-year-old brains were segmented. White matter segmentation is shown in the center panels, and gray matter segmentation is shown on the right. Histogram analysis of the products of segmentation shows a relative increase in the size of the gray matter peak and movement of the peak mode to a slightly higher density.

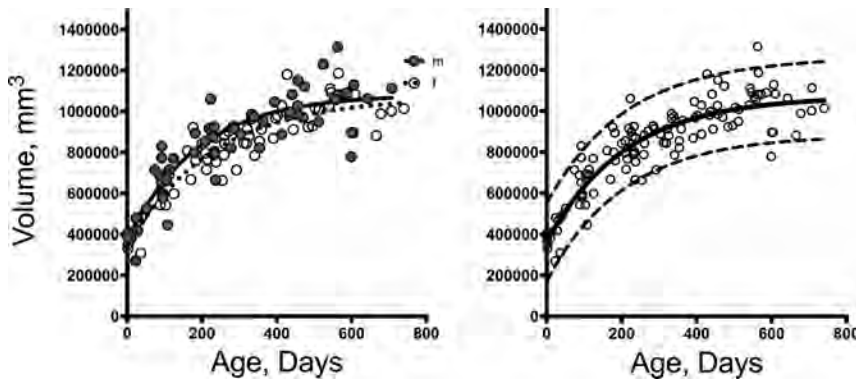


**FIG 2.** Nonlinear regression analysis of exponential growth of the brain in the first 2 years. *Curves (left) show boys (m, and solid trend line) and girls (f, and dotted trend line) with a small but statistically significant difference in absolute brain size (data not normalized to body weight). Curves (right) show 95% prediction bands. Prediction bands may be used to aid in the identification of clinical pathology.*

**Table 1: Model fitting and cross-validation results for scaled brain volume**

	Polynomial Regression			
	Polynomial (Age <sup>3</sup> )	Polynomial (Age <sup>3</sup> ) + Sex	Polynomial (Age <sup>3</sup> ) + Scanner	Polynomial (Age <sup>3</sup> ) + Sex + Scanner
$R^2$	0.828	0.841	0.831	0.844
Adjusted $R^2$	0.823	0.835	0.823	0.835
RMSE	0.927	0.891	0.919	0.884
Cross-validation (LOOCV)				
RMSE	0.954	0.925	0.962	0.932
RMSE increase <sup>a</sup>	2.9%	3.8%	4.7%	5.4%

<sup>a</sup> Percentage increase in RMSE after one performs LOOCV compared with the non-cross-validated model.

## RESULTS

### Brain Volume Curve Modeling

Brain volume as a function of age is shown in Fig 2, with trendlines and 95% predictive bands. From Table 1, adjusted  $R^2$  indicated that a third-degree polynomial of age with sex as a covariate performed the best in Equation 1, while adding the additional scanner did not improve the adjusted  $R^2$ .

1)

$$\begin{aligned} \text{Vol}/10,000 &= 7.97 + 20.63 \times \text{Age} \\ &\quad - 8.66 \\ &\quad \times \text{Age}^2 + 2.08 \times \text{Age}^3 + 0.52 \\ &\quad \times \text{Sex}(\text{boy}). \end{aligned}$$

At birth, the brain volume is between 300 and 400 cm<sup>3</sup>, greater than double in the first year of life (average volume at 1 year is 948 cm<sup>3</sup>), and growing an additional 19% in volume in the second year, to 1072 cm<sup>3</sup>. With a polynomial model with baseline volume at 0–30 days, brain volume increase is 150% in the first year (95% CI, 144%–150%) and 172% at year 2 (95% CI, 148%–197%) (Fig 2, Table 1, and Equation 1). Regression results for Equation 1 indicated a 5200 mm<sup>3</sup> significantly higher average brain volume for boys over girls ( $P < .01$ ), not adjusted for body weight.

Although adding both sex and scanner as covariates resulted in a smaller RMSE than adding sex only, the cross-validation (LOOCV) RMSE indicated that adding both covariates resulted in overfitting the data (5.4% versus 3.8% increase in RMSE, Table 1).

### Brain Density Histogram Analysis

The radiodensity of the brain changes as a function of age (Fig 3), and the changes can be quantified through analysis of the radiodensity histogram metrics (Fig 4, trendlines and 95% predictive bands are shown). Model-fitting results indicated that a sec-

ond-degree polynomial of age with an additional scanner ID performed the best for mean, mode, and kurtosis; first-degree of age with scanner ID performed best for FWHM; and  $\sigma$ , first-degree of log (age) with scanner ID performed best for skewness (Equation 2). Cross-validation (LOOCV) results on scaled dependent variables indicated that our models had good predictive power in CT histogram data because the RMSE from LOOCV demonstrated small differences (3%–7%) from the RMSE from the polynomial model (Table 2).

$$2) \text{ Radiodensity Histogram Characteristic} = \beta_0 + \beta_1$$

$$\times \text{Age} + \beta_2 \times \text{Age}^2.$$

Histogram mean and modal Hounsfield density curves parallel the brain volume changes that occur in the first 500 days of life (Fig 4). Mean brain tissue density increases from 25.6 HU to 30.6 HU during this period (Tables 2). The skewness of the brain tissue density histogram decreases logarithmically from the time of birth to a zero value at approximately 200 days. The total brain Hounsfield unit histogram kurtosis also decreases during this period to approach a value of 3, representing a normal distribution.

With concern that differences in scanner acquisition and calibration may impact the characteristics of the radiodensity histogram, data from the different scan platforms were analyzed separately. Histogram analysis showed similar trends from all 3 scan platforms (On-line Figs 1 and 2). A composite model inclusive of all 3 scan platforms was also derived (On-line Appendix and On-line Table).

#### Gray and White Matter Segmentation

Direct segmentation of images from a single scan platform (scanner 2) permits an analysis of gray and white matter changes as a function of brain develop-

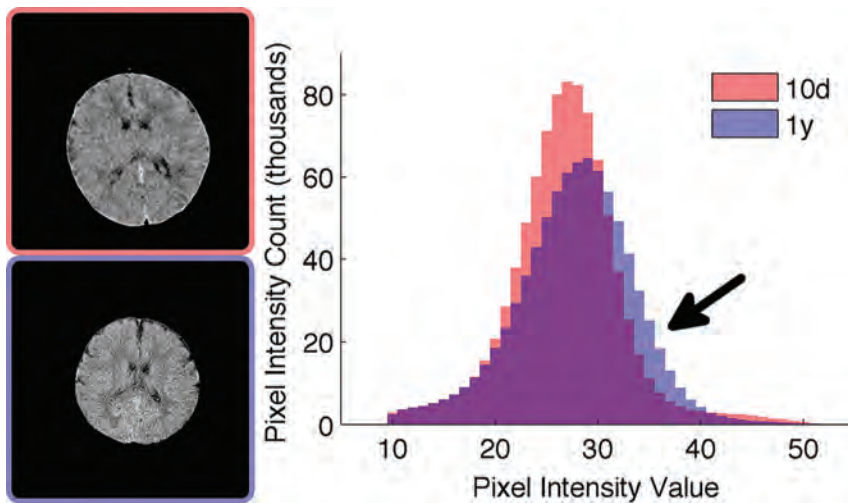


**FIG 3.** Histogram analysis of brain-extracted head CT images, at 10 days and 1 year. The histogram becomes more symmetric with age, and the leading edge at 1 year (arrow) reflects higher density voxels. y indicates year; d, day.

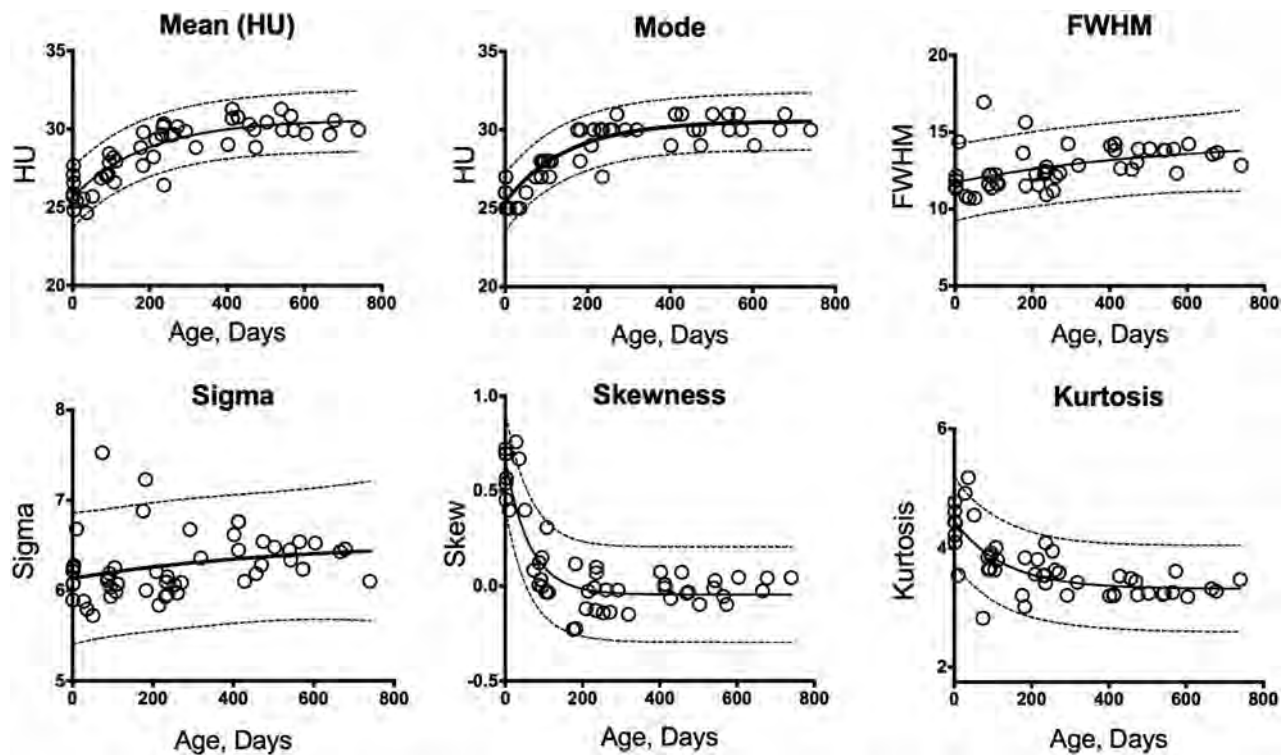


**FIG 4.** Total brain histogram analysis from 1 scan platform (scanner 2) shows total brain Hounsfield unit mean and Hounsfield unit histogram mode as well as FWHM, histogram SD ( $\sigma$ ), histogram skewness, and kurtosis as a function of subject age. Trendline and 95% predictive bands are shown.

**Table 2: Model fitting and cross-validation results for scaled CT radiodensity histogram (scanner 2)**

	CT Histogram					
	Mean (k = 2)	Mode (k = 2)	FWHM (k = 1)	Skewness (log [age]), (k = 1)	Kurtosis (k = 2)	$\sigma$ (k = 1)
Polynomial (age, k)						
$R^2$	0.77	0.80	0.22	0.70	0.54	0.068
RMSE	0.87	0.85	1.16	0.14	0.35	0.34
$\beta_0$	28.6	28.7	12.7	0.68	3.7	6.3
$\beta_1$	10.2	10.5	4.4	-0.12	-2.3	0.65
$\beta_2$	-5.3	-6.4	-	-	1.3	-
Cross-validation (LOOCV)						
RMSE	0.93	0.91	1.20	0.15	0.36	0.35
RMSE increase	6.9%	7.1%	3.4%	7.1%	5.3%	3.6%

Note:— k indicates order/degree of the polynomial.

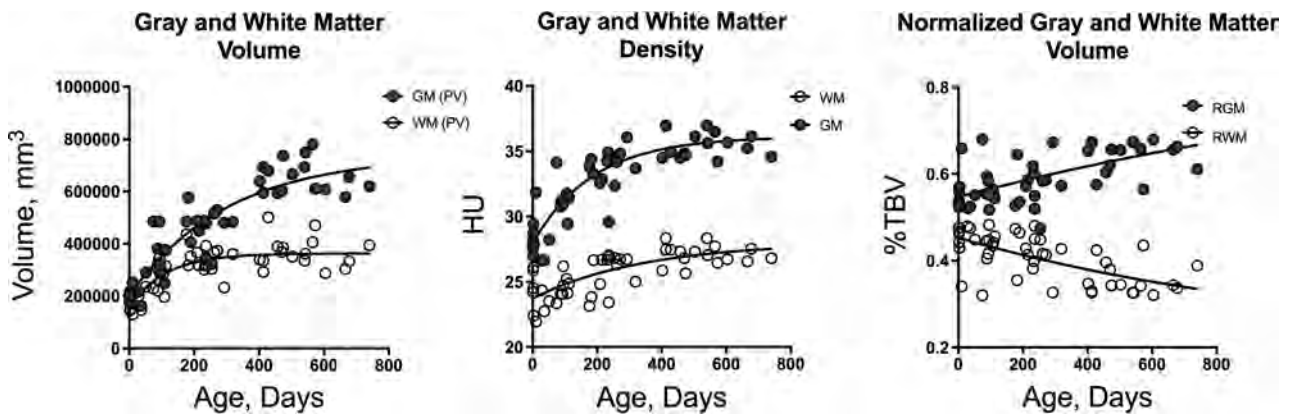


**FIG 5.** Direct segmentation into gray and white matter with nonlinear regression as a function of age. Tissue volumes (left), tissue densities (center), and tissue volumes normalized to total brain volume (right) are shown. PV indicates partial volume; RGM, relative gray matter volume; RWM, relative white matter volume.

ment (Figs 1 and 5). Both gray and white matter volumes increase in the perinatal period, with the greatest changes occurring in the first 200 days of life (Fig 5). Gray and white matter volumes appear nearly convergent at birth, at approximately 200 cm<sup>3</sup>. Gray matter volume increases dramatically in the first year, to approximately 500 cm<sup>3</sup>, a 150% increase, whereas white matter increases to approximately 350 cm<sup>3</sup>, a 75% increase. Segmented tissue volumes normalized to total brain volumes show a relative increase in gray matter volume from 55% of brain volume to 65% at 1 year, while the relative white matter volume decreases proportionally in the same period. Concurrent with these changes, both gray and white matter densities increase, with gray matter from 28 HU at birth to 36 HU at 1 year and WM from 23.7 HU at birth to 26 HU at 1 year.

## DISCUSSION

Although several studies of quantitative imaging of brain growth and development have focused on the immediate perinatal period,<sup>8-10</sup> few studies have focused on the first years of life.<sup>11-13</sup> This time window is important in brain development because the largest changes in brain maturation occur in the first 2 years.<sup>14,15</sup> Subtle abnormalities of brain size and abnormal gray and white matter volumes and growth trajectories have been associated with diseases such as attention deficit/hyperactivity disorder,<sup>6,16</sup> autism,<sup>17,18</sup> and schizophrenia.<sup>19</sup> Reference data in this time window are also needed because neonates and toddlers can pose a challenge for diagnostic medicine in the clinical setting, where

history and physical examination may be limited. Most in vivo studies are based on MR imaging data, with the few studies based on CT imaging having been performed before the wide use of MR imaging.<sup>10,13,20</sup> To our knowledge, this is the first study to investigate the changes in brain development by digital analysis of head CT data. The logistics of MR imaging of toddlers can limit investigation into brain development in this period of childhood, and additional data derived from head CT images serve to support and augment data obtained from MR imaging studies.

Our CT-derived brain volumes are overall consistent with reported MR imaging findings, though no true curve fitting has yet been reported for brain growth in this period of brain development, to our knowledge. In an early MR imaging study with emphasis on brain development of premature and mature neonates, Hüppi et al<sup>9</sup> found a near-linear growth curve in the immediate perinatal period and a birth volume at maturity of approximately 400,000 mm<sup>3</sup> at full-term. Also using MR imaging, Holland et al<sup>8</sup> investigated brain growth trajectories and rates of change in the first 3 months of infant brain development, finding a near-linear growth curve in the first 90 days of life and a birth volume of 347,388 mm<sup>3</sup>, similar to our finding of 361,494 mm<sup>3</sup>. Choe et al<sup>11</sup> studied infant brain development from 3 to 13 months, recruiting 27 full-term and developing neonates, some scanned more than once, with scans at 3, 6, and 12 months. Although the emphasis of that study was on relative growth of segmented brain structures,

the study recorded total brain volumes at approximately 650 cm<sup>3</sup> at 16 weeks, 800 cm<sup>3</sup> at 30 weeks, and 950 cm<sup>3</sup> at 52 weeks, similar to our findings, and with individual variation (data scatter) similar to the variation that we report.<sup>11</sup>

Studies by Knickmeyer et al<sup>12</sup>, and Shi et al<sup>21</sup> are of similar design and offer the most complete MR imaging data regarding brain growth during the first 2 years of life, with cohorts scanned in the neonatal period (at 2–4 weeks) and at 1 and 2 years. This study design with clustering of the data at discrete time points does not permit generation of a detailed growth curve but does show comparable brain volumes with approximately 400 cm<sup>3</sup> at 2–4 weeks and 800–900 cm<sup>3</sup> at 12 months, with a plateau at approximately 1000 cm<sup>3</sup> at 24 months seen in both studies, with a qualitative growth curve and intersubject variation (data scatter) similar to those in the current study.

Previous studies have investigated sex differences in perinatal brain volume with mixed conclusions, likely due to differences in the ages of the children being evaluated and small sample sizes.<sup>8,12</sup> Similar to the prospective MR imaging findings of Shi et al,<sup>21</sup> we found a small but statistically significant difference in brain growth curves between boys and girls, with boys being consistently larger, approximately 5.5% larger at 1 year and 5% larger at 2 years. These numbers were not normalized to body size. Statistical analysis also revealed that the use of different scan platforms does not contribute significantly to the volume estimate or the fitted growth curve.

Our study investigated the correlation between the parametric measures of the brain density histogram and subject age. Although whole-brain histogram analysis has been explored in a number of different MR imaging techniques, histogram analysis of head CT images has not been widely investigated, to our knowledge. Histogram analysis offers objective, quantitative evaluation of parameters beyond those seen at routine diagnostic image interpretation and lends itself to automated analysis of head CT imaging. The clear age-dependent trends of the data motivated the concept of a statistical model. Our retrospective study design resulted in a continuous age distribution, which enabled curve fitting, which is not possible with prospective studies with discrete age cohorts.<sup>11,16</sup>

Total brain density histogram analysis as a function of age yields several findings. The overall brain tissue density (mean density) increases in the neonatal period, consistent with early reports using single-slice brain CT ROI methods.<sup>13</sup> The shape of the density histogram also changes, with rapidly decreasing histogram skewness in the first 200 days of life, reflecting a shift of the histogram toward higher density and an increasing percentage of higher density voxels during this period (Fig 3). Major changes in brain tissue known to occur in this time include an overall decrease in the percentage of water in the tissue,<sup>22</sup> and a relative increase in gray matter volume.<sup>9,12,23</sup> Both factors would be expected to contribute to the increase in density and the changes in the attenuation histogram.

Direct segmentation of brain CT yields gray and white matter maps, which can be characterized for density and volume, showing a relative increase in gray matter in the first 2 years, with steeper changes in the first 200 days, as well as an increase in both gray and white matter density during early brain development.

Previous studies based on MR imaging have shown that rapid changes in brain volume occurring in the immediate postnatal period relate to an increase in gray matter volume,<sup>9,12,23,24</sup> which, in turn, is thought to reflect synapse formation and the development of the neuropil.<sup>12</sup> Decreases in water diffusion seen in brain tissue during this time may reflect, in part, myelination and a decreasing tissue-water fraction.<sup>15,22</sup>

Although clinical CT machines are subject to routine calibration, with an accepted margin of error,<sup>25</sup> the effect of variations between machines becomes important in quantitative studies. Our curve fitting represents a feasibility study rather than a true predictive, universal, or optimal model, however, because various alternative statistical models were not evaluated and the contributions of small differences in scan platform and data acquisition were not fully explored. Rather our goal was to illustrate the feasibility of such model development based on digital analysis of head CT images. Appreciation of the possibility of such modeling serves to emphasize the value of quantitative imaging and underscore the value of higher standards in image acquisition and hardware calibration.

## CONCLUSIONS

Changes in brain radiodensity are highly correlated with developmental age, and normative metrics of the brain radiodensity histogram derived from routine clinical head CT images can be used to develop a model of normal brain development. Histogram analysis is amenable to automation, and digital analysis together with normative metrics derived from head CT images may be used to improve the sensitivity of head CT in the detection of subtle brain injury and neurodevelopmental disorders.

## REFERENCES

1. **CT Accreditation Program: Testing Instructions.** Revised January 6, 2017. <https://www.acraccreditation.org/~media/ACRAccreditation/Documents/CT/CT-Accreditation-Testing-Instructions.pdf>, Accessed August 15, 2017
2. Zhang Y, Brady M, Smith S. **Segmentation of brain MR images through a hidden Markov random field model and the expectation-maximization algorithm.** *IEEE Trans Med Imaging* 2001;20:45–57 CrossRef Medline
3. Jenkinson M, Beckmann CF, Behrens TE, et al. **FSL.** *Neuroimage* 2012;62:782–90 CrossRef Medline
4. Muschelli J, Ullman NL, Mould WA, et al. **Validated automatic brain extraction of head CT images.** *Neuroimage* 2015;114:379–85 CrossRef Medline
5. Cauley KA, Och J, Yorks PJ, et al. **Automated segmentation of head computed tomography images using FSL.** *J Comput Assist Tomogr* 2018;42:104–10 CrossRef Medline
6. Castellanos FX, Lee PP, Sharp W, et al. **Developmental trajectories of brain volume abnormalities in children and adolescents with attention-deficit/hyperactivity disorder.** *JAMA* 2002;288:1740–48 CrossRef Medline
7. R Core Team. *R: A Language and Environment for Statistical Computing.* Vienna, Austria: R Foundation for Statistical Computing; 2014. <http://www.R-project.org/>. Accessed January 3, 2015
8. Holland D, Chang L, Ernst TM, et al. **Structural growth trajectories and rates of change in the first 3 months of infant brain development.** *JAMA Neurol* 2014;71:1266–74 CrossRef Medline
9. Hüppi PS, Warfield S, Kilkinis R, et al. **Quantitative magnetic resonance imaging of brain development in premature and mature newborns.** *Ann Neurol* 1998;43:224–35 CrossRef Medline
10. Brant-Zawadzki M, Enzmann DR. **Using computed tomography**

- of the brain to correlate low white-matter attenuation with early gestational age in neonates. *Radiology* 1981;139:105–08 CrossRef Medline
11. Choe MS, Ortiz-Mantilla S, Makris N, et al. **Regional infant brain development: an MRI-based morphometric analysis in 3 to 13 month olds.** *Cereb Cortex* 2013;23:2100–17 CrossRef Medline
  12. Knickmeyer RC, Gouttard S, Kang C, et al. **A structural MRI study of human brain development from birth to 2 years.** *J Neurosci* 2008;28:12176–82 CrossRef Medline
  13. Penn RD, Trinko B, Baldwin L. **Brain maturation followed by computed tomography.** *J Comput Assist Tomogr* 1980;4:614–16 CrossRef Medline
  14. Pfefferbaum A, Mathalon DH, Sullivan EV, et al. **A quantitative magnetic resonance imaging study of changes in brain morphology from infancy to late adulthood.** *Arch Neurol* 1994;51:874–87 CrossRef Medline
  15. Zhang L, Thomas KM, Davidson MC, et al. **MR quantitation of volume and diffusion changes in the developing brain.** *AJNR Am J Neuroradiol* 2005;26:45–49 Medline
  16. Proal E, Reiss PT, Klein RG, et al. **Brain gray matter deficits at 33-year follow-up in adults with attention-deficit/hyperactivity disorder established in childhood.** *Arch Gen Psychiatry* 2011;68:1122–34 CrossRef Medline
  17. Petropoulos H, Friedman SD, Shaw DW, et al. **Gray matter abnormalities in autism spectrum disorder revealed by T2 relaxation.** *Neurology* 2006;67:632–36 CrossRef Medline
  18. Courchesne E, Karns CM, Davis HR, et al. **Unusual brain growth patterns in early life in patients with autistic disorder: an MRI study.** *Neurology* 2001;57:245–54 CrossRef Medline
  19. Lei W, Deng W, Li M, et al. **Gray matter volume alterations in first-episode drug-naive patients with deficit and nondeficit schizophrenia.** *Psychiatry Res* 2015;234:219–26 CrossRef Medline
  20. Hamano K, Iwasaki N, Kawashima K, et al. **Volumetric quantification of brain volume in children using sequential CT scans.** *Neuroradiology* 1990;32:300–03 CrossRef Medline
  21. Shi F, Yap PT, Wu G, et al. **Infant brain atlases from neonates to 1- and 2-year-olds.** *PLoS One* 2011;6:e18746 CrossRef Medline
  22. Dobbing J, Sands J. **Quantitative growth and development of human brain.** *Arch Dis Child* 1973;48:757–67 CrossRef Medline
  23. Gilmore JH, Lin W, Prastawa MW, et al. **Regional gray matter growth, sexual dimorphism, and cerebral asymmetry in the neonatal brain.** *J Neurosci* 2007;27:1255–60 CrossRef Medline
  24. Matsuzawa J, Matsui M, Konishi T, et al. **Age-related volumetric changes of brain gray and white matter in healthy infants and children.** *Cereb Cortex* 2001;11:335–42 CrossRef Medline
  25. Allen JS, Damasio H, Grabowski TJ. **Normal neuroanatomical variation in the human brain: an MRI-volumetric study.** *Am J Phys Anthropol* 2002;118:341–58 CrossRef Medline

# MRI Features of Aquaporin-4 Antibody–Positive Longitudinally Extensive Transverse Myelitis: Insights into the Diagnosis of Neuromyelitis Optica Spectrum Disorders

C.G. Chee, K.S. Park, J.W. Lee, H.W. Ahn, E. Lee, Y. Kang, and H.S. Kang

## ABSTRACT

**BACKGROUND AND PURPOSE:** Longitudinally extensive transverse myelitis is a well-documented spinal manifestation of neuromyelitis optica spectrum disorders, however, other forms of nontumorous myelopathy can also manifest as longitudinally extensive transverse myelitis. Our aim was to evaluate the MR imaging features of aquaporin-4 antibody–positive longitudinally extensive transverse myelitis, which is strongly associated with neuromyelitis optica spectrum disorders.

**MATERIALS AND METHODS:** We evaluated cervicomedullary junction involvement, cord expansion ratios, bright spotty lesions, the number of involved segments, skipped lesions, enhancement patterns, and axial distribution patterns using spinal MR imaging of 41 patients with longitudinally extensive transverse myelitis who underwent aquaporin-4 antibody testing. Univariate logistic regression analysis was performed to identify factors associated with aquaporin-4 antibody seropositivity, which were then used to develop a scoring system for diagnosing aquaporin-4 antibody–positive longitudinally extensive transverse myelitis. Interrater reliability for cord expansion ratio measurement and bright spotty lesions was determined using intraclass correlation coefficients and  $\kappa$  values, respectively.

**RESULTS:** Fifteen patients with longitudinally extensive transverse myelitis were aquaporin-4 antibody–positive. Sex (female), cervicomedullary junction involvement, a cord expansion ratio of  $>1.4$ , and bright spotty lesions were significantly associated with aquaporin-4 antibody seropositivity. The sensitivity and specificity of the scoring system were 73.3% and 96.2%, respectively. The interclass correlation value for the cord expansion ratio was 0.78, and the  $\kappa$  value for bright spotty lesions was 0.61.

**CONCLUSIONS:** Our scoring system, based on cervicomedullary junction involvement, higher cord expansion ratio, bright spotty lesions, and female sex, can facilitate the timely diagnosis of neuromyelitis optica spectrum disorders.

**ABBREVIATIONS:** AQP4 = aquaporin-4; LETM = longitudinally extensive transverse myelitis; NMO = neuromyelitis optica; NMOSD = neuromyelitis optica spectrum disorders

Longitudinally extensive transverse myelitis (LETM) is a well-documented spinal manifestation of neuromyelitis optica (NMO) that presents as a hyperintense spinal cord lesion extending over  $\geq 3$  vertebral levels on sagittal T2-weighted spinal MR imaging.<sup>1</sup> NMO is an inflammatory central nervous system disorder that differs from multiple sclerosis and is associated with the presence of the serum aquaporin-4 (AQP4) antibody as a highly specific feature.<sup>1–3</sup> It is currently understood as a spectral disorder, and the International Panel for NMO Diagnosis has re-

defined the disease entity as NMO spectrum disorders (NMOSD). NMOSD is stratified further according to the presence of the AQP4 antibody. LETM is a diagnostic criterion for NMOSD<sup>4</sup>; however, other forms of nontumorous myelopathy, such as acute transverse myelitis (idiopathic) or viral myelitis, can also manifest as LETM. There is limited clinical or laboratory information regarding the initial presentation of LETM, which is crucial for diagnosing NMOSD. A long turnaround time (days to weeks) for serologic assay results for the AQP4 antibody further delays the diagnosis of NMOSD. Yet, recent studies demonstrating the beneficial effects of rituximab, plasma exchange, or lymphocytapheresis combined with steroid therapy<sup>5–9</sup> have emphasized the importance of early diagnosis and timely treatment of NMOSD.

A recent report by Pekcevik et al<sup>10</sup> has suggested that characteristic MR imaging findings may help differentiate NMOSD from other pathologies associated with LETM. Yet, the study by Pekcevik et al used criteria-based diagnosis, excluded acute

Received July 19, 2017; accepted after revision November 29.

From the Departments of Radiology (C.G.C., J.W.L., H.W.A., E.L., Y.K., H.S.K.) and Neurology (K.S.P.), Seoul National University Bundang Hospital, Gyeonggi-do, Korea.

Choong Guen Chee and Kyung Seok Park contributed equally to this work.

Please address correspondence to Joon Woo Lee, MD, PhD, Department of Radiology, Seoul National University Bundang Hospital, 82 Gumi-ro, 173 Beon-gil, Bundang-gu, Seongnam-si, Gyeonggi-do, 13620, Korea; e-mail: joonwoo2@gmail.com

<http://dx.doi.org/10.3174/ajnr.A5551>

transverse myelitis and seronegative NMOSD, and included certain diagnoses based on MR imaging and the clinical setting, such as spinal arteriovenous fistula and acute spinal infarction.

The purpose of our study was to evaluate the imaging features of AQP4-positive LETM, which is highly associated with NMOSD, and to develop a scoring system for diagnosing AQP4-positive LETM on the basis of MR imaging findings. Furthermore, we investigated quantitatively measurable image characteristics and provided interobserver agreement for subjective MR imaging interpretation.

## MATERIALS AND METHODS

### Study Overview

This retrospective observational study was conducted in an urban teaching hospital. The institutional review board approved the study and waived the requirement for informed consent.

### Patients

We retrospectively reviewed adult (16 years of age or older) patients who had undergone spinal MR imaging between December 2004 and September 2014 and who had initially presented with myelopathy. Patients with MR imaging findings or a clinical course consistent with spinal dural arteriovenous fistula or spinal infarction were excluded. We identified 43 consecutive patients with hyperintense spinal cord lesions extending over  $\geq 3$  vertebral levels on sagittal T2-weighted spinal MR imaging. All patients' sera were tested for the presence of the AQP4 antibody at the Weatherall Institute of Molecular Medicine (John Radcliffe Hospital, Oxford, UK) using a cell-based assay.<sup>11</sup> One patient's MR imaging findings were determined to be artifactual after short-term follow-up MR imaging. One patient who had undergone the initial MR imaging outside the hospital had not undergone axial imaging. After we excluded these 2 patients, 41 patients were included in our analysis. When available, we also reviewed any brain MR imaging results obtained within an 8-week interval of spinal MR imaging.

### MR Image Acquisition

MR imaging was performed using a 1.5T or 3T scanner (Achieva; Philips Healthcare, Best, the Netherlands) with a 16-channel neurovascular coil for the 3T imager and a head neck coil for the 1.5T imager. Parameters for individual sequences were as follows: for sagittal T1-weighted TSE images: voxel size =  $0.5 \times 0.5 \times 3.0$  mm<sup>3</sup>; TR = 480–550 ms; TE = 10–15 ms; echo-train length = 6; slice thickness = 3.0 mm; slice gap = 0.3 mm; NEX = 1–2; for sagittal T2-weighted TSE images: voxel size =  $0.5 \times 0.5 \times 3.0$  mm<sup>3</sup>; TR = 2700–3500 ms; TE = 120 ms; echo-train length = 28–32; slice thickness = 3.0 mm; slice gap = 0.3 mm; NEX = 2–3; for axial T2-weighted TSE images: voxel size =  $0.7 \times 0.7 \times 6.0$  mm<sup>3</sup>; TR = 2700–3500 ms; TE = 120 ms; echo-train length = 25–32; slice thickness = 6.0 mm; slice gap = 2.0 mm; NEX = 2. For selected cases, additional thin-section axial TSE images were obtained with the following parameters: voxel size =  $0.7 \times 0.7 \times 3.0$  mm<sup>3</sup>; TR = 2700–3500 ms; TE = 120 ms; echo-train length = 25–32; slice thickness = 3.0 mm; slice gap = 0.3 mm; NEX = 2. For patients who underwent the initial MR imaging outside our



**FIG 1.** Sagittal T2-weighted spinal MR imaging of a 36-year-old woman with LETM. The lesion extends beyond the imaginary line (*dashed line*) connecting the inferior cortex of the C1 anterior and posterior arches. Cervicomedullary junction involvement is present.

hospital, images were imported into our PACS system. These imported MR images had been obtained at diverse hospitals using various MR imaging scanners and different protocols.

### MR Image Assessment

Radiologists were blinded to all patient and clinical data. Cervicomedullary junction involvement was defined as the main or separate lesion involving the uppermost cervical spinal cord at the level of the medulla oblongata. An imaginary line connecting the inferior cortex of the C1 anterior and posterior arches on sagittal T2WI was used as the lower border (Fig 1), and the pontomedullary junction was used as an upper border. Cord expansion was independently measured on sagittal T2WI by 2 radiologists with 5 and 3 years of experience, respectively. Values were averaged for the analysis. Only MR images obtained during the acute/early stage of disease (within 2 months of onset)<sup>12</sup> were used for measurement. The ratio of cord expansion was measured as the anteroposterior diameter of the most swollen spinal cord segment to the anteroposterior diameter of the noninvolved spinal cord in the cranial direction on sagittal T2WI (Fig 2). The diameters were measured in millimeters to an accuracy of 1 decimal digit. If LETM extended to the level of the foramen magnum, the ratio was not useful for representing cord expansion due to an anatomic



**FIG 2.** Sagittal T2-weighted spinal MR imaging of a 43-year-old man with LETM. Cord expansion ratio is measured as the anteroposterior diameter of the most swollen spinal cord segment (*solid line*) to the anteroposterior diameter of the noninvolved spinal cord in the cranial direction (*dotted line*). Two independent readers measured the cord expansion ratio as 1.65 and 1.71.

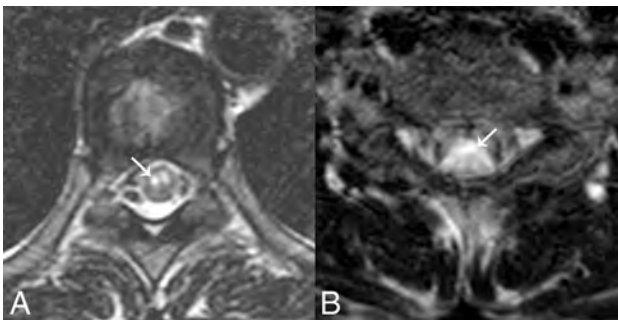


**FIG 3.** Two examples of bright spotty lesions (*white arrows*) in axial T2-weighted spinal MR imaging. Two independent readers judged the lesions as positive.

increase in the anteroposterior diameter of the medulla oblongata; thus, ratios were not measured in such cases. Ratio values were dichotomized with a cutoff value to maximize the sum of the sensitivity and specificity.

Bright spotty lesions were defined as lesions that were visually hyperintense or of equal signal intensity to the surrounding CSF on axial T2WI (Fig 3).<sup>13</sup> Two radiologists independently judged the presence of bright spotty lesions. Suspicious or indeterminate cases were interpreted as having negative findings. In cases of discordance, a consensus reading was performed and used for further statistical analyses. The number of involved segments and the presence of skipped lesions were evaluated. If available, enhancement patterns were assessed by visual inspection and graded as involving >50%, involving <50%, or showing no enhancement. Axial distribution was classified as centrally lo-

cated, peripherally located, or both. Whether the cord involvement was greater or less than 50% of the cord in the axial plane was evaluated.

### Statistical Analysis

A univariate logistic regression analysis was performed to identify factors associated with the presence of confirmed AQP4 antibody-positive status. Key factors for the logistic regression analysis were predefined in accordance with previous studies (brain stem involvement, cord expansion, and bright spotty lesions).<sup>10,12,14</sup> We did not perform a multivariable logistic regression analysis, given the small sample size. Factors that were significantly associated with AQP4 seropositivity were used to generate a scoring system for predicting AQP4 antibody status. Optimal cutoff values that maximized the sum of sensitivity and specificity were used as a threshold. Sensitivity and specificity of the scoring system were measured; interobserver reliability for the measurement of cord expansion was evaluated by using the intraclass correlation coefficient derived from a 2-way mixed-effects model, while interobserver agreement for judging the presence of bright spotty lesions was evaluated using  $\kappa$  values. A 2-sided *P* value < .05 was considered statistically significant. All statistical analyses were performed using STATA 13.1 (StataCorp, College Station, Texas).

### RESULTS

Of the 41 patients with LETM, 18 were female and 23 were male. The mean age of the patients at the time the spinal MR imaging was obtained was 45 years (age range, 16–72 years). Fifteen patients (15/41, 36.6%) were seropositive for AQP4 antibodies. If we excluded 4 patients who did not undergo tests for an oligoclonal band, all 37 patients were negative for oligoclonal band test. According to the recent diagnostic criteria by Wingerchuk et al,<sup>4</sup> all 15 patients in the AQP4 antibody-positive group could be diagnosed as having NMOSD, while only 3 of 26 patients (11.5%) in AQP4 antibody-negative group had it. Seventeen patients underwent 1.5T spine MR imaging, and 24 patients underwent 3T spine MR imaging. Imaging in 9 patients was performed at outside institutions. The ethnicity of the study population was exclusively Asian. The median time interval between the initial symptom to MR imaging study was 14 days (interquartile range, 3–30 days). Patient characteristics in each group are summarized in Table 1. Thirty-six patients completed brain MR imaging within 2 months after the first attack of myelitis symptoms. Sixteen patients showed suspected demyelinating lesions, and 2 patients had findings suspicious for meningitis. Five patients had a history of optic neuritis preceding the initial symptoms of suspected myelopathy.

Spinal MR imaging findings in the AQP4 antibody-positive and AQP4 antibody-negative groups are shown in Table 2. The cord expansion ratio was measured in 32 patients, excluding 5 patients with dates of onset of >2 months before the MR imaging and 4 patients with medulla oblongata involvement. The mean value of the cord expansion ratio was not different whether symptom onset was within 2 months or 15 days (Table 2). Cord expansion ratios were dichotomized using a cutoff value of 1.4. Regression analysis showed that female sex, cervicomedullary junction involvement, a cord expansion ratio of >1.4, and the presence of bright

**Table 1: Patient characteristics (n = 41)<sup>a</sup>**

Characteristic	AQP4 Antibody-Positive Group (n = 15)	AQP4 Antibody-Negative Group (n = 26)
Age (mean) (yr)	48 ± 13	42 ± 12
Female	13 (87%)	5 (19%)
Ethnicity	Asian (100%)	Asian (100%)
Time interval from first attack to MRI study (median) (interquartile range) (days)	10 (3–21)	14 (5–30)
1–15 days	10 (67%)	14 (54%)
16–30 days	3 (20%)	6 (23%)
31–60 days	1 (1%)	2 (8%)
>60 days	1 (1%)	4 (15%)
Brain involvement	8 (53%)	10 (38%)
Preceding optic neuritis	4 (27%)	1 (4%)

<sup>a</sup> Data are number and percentage unless otherwise indicated.

**Table 2: Spinal MRI findings in AQP4 antibody-positive and -negative groups<sup>a</sup>**

Imaging Features	AQP4 Antibody-Positive Group (n = 15)	AQP4 Antibody-Negative Group (n = 26)
Cervicomedullary junction involvement	9 (60%)	6 (23%)
Medulla oblongata involvement	4 (27%)	1 (4%)
Cord expansion ratio (mean) (onset ≤2 months) <sup>b</sup>	1.35 ± 0.15	1.24 ± 0.15
Cord expansion ratio (mean) (onset ≤15 days) <sup>c</sup>	1.34 ± 0.17	1.24 ± 0.17
Bright spotty lesion		
Negative	1 (7%)	18 (69%)
Positive	14 (93%)	8 (31%)
Involved segment		
Cervical	5 (33%)	7 (27%)
Cervicothoracic	8 (53%)	5 (19%)
Thoracic	2 (13%)	10 (38%)
Thoracolumbar	0 (0%)	1 (4%)
Holocord	0 (0%)	3 (12%)
No. of segments involved (mean)	9 ± 4	7 ± 4
Axial distribution		
Central	10 (67%)	21 (81%)
Peripheral	4 (27%)	4 (15%)
Both	1 (7%)	1 (4%)
>Half of the cord area	12 (80%)	24 (92%)
Enhancement		
No enhancement	4 (27%)	6 (23%)
<50% enhancement	9 (60%)	17 (65%)
>50% enhancement	0 (0%)	0 (0%)
Not available	2 (13%)	3 (12%)

<sup>a</sup> Data are number and percentage unless otherwise indicated.

<sup>b</sup> Cord expansion ratio was measured only for 32 patients.

<sup>c</sup> Cord expansion ratio was measured only for 22 patients.

**Table 3: Univariable logistic regression analysis**

Variable	OR (95% CI)	P Value
Sex		
Male	Reference	
Female	3.3 (1.5–5.1)	<.001
Cervicomedullary involvement		
Absent	Reference	
Present	1.6 (0.2–3.0)	.02
Bright spotty lesion		
Negative	Reference	
Positive	3.4 (1.3–5.6)	.002
Cord expansion ratio		
≤1.4	Reference	
>1.4	2.1 (0.5–3.7)	.01

spotty lesions on T2WI were significantly associated with AQP4 antibody seropositivity (Table 3). Age, the number of involved segments, the presence of skipped lesions, the enhancement pattern, and the axial distribution pattern of >50% involvement in the axial plane were not significantly associated with AQP4 antibody status.

A scoring system was developed on the basis of the above results (Table 4). Equal scores were assigned for parameters associated with AQP4 antibody seropositivity, except for cervicomedullary junction involvement. Additional points were given if the lesion involved the medulla oblongata. The area under the receiver operating curve for the scoring system was 91.7 (95% confidence interval, 82.9–100.0). With a score threshold of ≥3, the sensitivity of the scoring system was 73.3% (11/15) and the specificity was 96.2% (25/26). The sensitivity and specificity of each parameter are as follows: female sex (sensitivity, 87%; specificity, 81%), cervicomedullary junction involvement (sensitivity, 60%; specificity, 77%), cord expansion ratio >1.4 (sensitivity, 40%; specificity, 82%), and bright spotty lesions (sensitivity, 93%; specificity, 69%). The interclass correlation value for measuring the cord expansion ratio was 0.78 (95% confidence interval, 0.61–0.88). The κ value for interobserver agreement in judging bright spotty lesions was 0.61 (95% confidence interval, 0.37–0.85).

## DISCUSSION

In our study, we identified characteristic spinal MR imaging features in Asian patients with AQP4-positive LETM (ie, probable NMOSD) compared with those with AQP4-negative LETM. Cervicomedullary junction involvement, cord expansion in the acute/early stage, the presence of bright spotty lesions, and female sex were significantly associated with AQP4 seropositivity in patients with LETM.

An important factor distinguishing our study from previous work is the use of serum AQP4 antibody status, rather than disease diagnostic criteria, as a reference standard. Although criteria-based diagnosis is clinically necessary, it was not appropriate to use this approach as a reference standard in our study because the aim of our study was to predict the AQP4 antibody status for the patients with LETM with unknown AQP4 antibody status. The concept of NMO as a disease has recently been expanded to a spectrum of disorders (NMOSD) based on the International Panel for NMO Di-

agnosis criteria. The use of serum AQP4 antibody status as a reference standard is clinically necessary, it was not appropriate to use this approach as a reference standard in our study because the aim of our study was to predict the AQP4 antibody status for the patients with LETM with unknown AQP4 antibody status. The concept of NMO as a disease has recently been expanded to a spectrum of disorders (NMOSD) based on the International Panel for NMO Di-

**Table 4: Scoring system**

Parameters	Points
Sex	
Male	0
Female	1
Cervicomedullary involvement	
Absent	0
Present	1
Medulla oblongata involvement	+1 = 2
Bright spotty lesion	
Absent or suspicious	0
Definite	1
Cord expansion ratio for acute or early-stage MRI	
≤1.4	0
>1.4	1

agnosis criteria, and this definition may continue to evolve in the future. Additionally, LETM is not specific for NMOSD and may be representative of other disease states that cannot be further classified using the current diagnostic criteria.

Female predilection, extension of cervical lesions to brain stem lesions,<sup>15–17</sup> spinal MR imaging findings of cord swelling,<sup>14,18</sup> and bright spotty lesions<sup>13</sup> have previously been reported in patients with NMO; however, the aforementioned characteristics were mostly descriptive data without statistical inference. Although Yonezu et al<sup>13</sup> reported bright spotty lesions as statistically discriminative findings with a sensitivity and specificity of 54% and 97%, the comparison was done within patient groups with NMO and MS.<sup>13</sup> Recently, Pekcevik et al<sup>10</sup> reported that only bright spotty lesions on T2WI are highly specific findings that can be used to differentiate NMO from other etiologies that could manifest as LETM. In contrast to a previous study by Pekcevik et al,<sup>10</sup> we found that cervicomedullary junction involvement and a high cord expansion ratio in the acute/early stage of disease were statistically associated with AQP4 antibody seropositivity. This discrepancy might be attributed to several factors. First, the study of Pekcevik et al excluded idiopathic acute transverse myelitis or possible AQP4-negative NMOSD, which would be most cases of the AQP4-negative group in our study. Second, cord swelling is a subjective judgment of the radiologist, and few studies have addressed the degree of cord swelling. In contrast, we quantitatively measured cord swelling and showed good interobserver agreement when measurements were performed by 2 independent radiologists. Third, we have defined cervicomedullary junction involvement, a broader concept than brain stem extension, and suggested a clear margin for judging the presence of cervicomedullary junction involvement. Last, our study excluded potential cases of spinal dural arteriovenous fistula and spinal infarction, which could be diagnosed on the basis of MR imaging findings and the clinical setting.

Our study provides confirmation that bright spotty lesions on axial T2WI are highly specific for AQP4 antibody-positive LETM, in keeping with a previous study.<sup>10</sup> The interobserver agreement for the judgment of bright spotty lesions was substantial ( $\kappa = 0.61$ )<sup>19</sup> and was higher than the minimal  $\kappa$  value of 0.55 suggested for classification systems.<sup>20</sup> Therefore, our scoring system (sensitivity, 73.3%; specificity, 96.2%) provides an accurate and reliable tool for diagnosing AQP4 antibody-positive LETM and possible NMOSD. The presence or history of optic neuritis was more fre-

quent in the AQP4 antibody-positive group. It did not reach statistical significance ( $P$  value = .051) and was not incorporated in our scoring system, though it showed potential as a discriminative feature of the AQP4 antibody-positive patient group. However, the interpretation should be made with caution because the reported sensitivity and specificity of the AQP4 antibody for NMO are 58%–76% and 85%–99%; thus, a positive AQP4 antibody result does not necessarily indicate NMO.<sup>1,21–23</sup>

The present study had several limitations mainly related to its retrospective design and small sample size. First, we were unable to prepare a validation set for the scoring system. Additionally, we were unable to perform a multivariable logistic regression analysis due to our sample size. Therefore, in building the scoring system, we could only assign equal scores for each parameter. Second, our study population was exclusively of Asian descent. Future studies are necessary to determine the generalizability of our findings to other populations. Third, the influence of different protocols, such as section thickness, on the presence of bright spotty lesions on axial T2WI is unknown. The use of thin-section MR imaging (which is less influenced by partial averaging effects in the cranio-caudal direction) might increase the sensitivity for judging the presence of bright spotty lesions. Fourth, our study only included adult patients; therefore, our study results should not be extended for usage in the pediatric population, for which a differential diagnosis of acute disseminated encephalomyelitis with NMOSD might be important.

## CONCLUSIONS

Cervicomedullary junction involvement, a higher cord expansion ratio, bright spotty lesions, and female sex are highly indicative of AQP4 antibody seropositivity in patients with LETM and may predict a diagnosis of NMOSD.

## REFERENCES

1. Wingerchuk DM, Lennon VA, Pittock SJ, et al. **Revised diagnostic criteria for neuromyelitis optica.** *Neurology* 2006;66:1485–89 CrossRef Medline
2. Wingerchuk DM, Lennon VA, Lucchinetti CF, et al. **The spectrum of neuromyelitis optica.** *Lancet Neurol* 2007;6:805–15 CrossRef Medline
3. Jarius S, Wildemann B. **Aquaporin-4 antibodies (NMO-IgG) as a serological marker of neuromyelitis optica: a critical review of the literature.** *Brain Pathol* 2013;23:661–83 CrossRef Medline
4. Wingerchuk DM, Banwell B, Bennett JL, et al; International Panel for NMO Diagnosis. **International consensus diagnostic criteria for neuromyelitis optica spectrum disorders.** *Neurology* 2015;85:177–89 CrossRef Medline
5. Cree BA, Lamb S, Morgan K, et al. **An open label study of the effects of rituximab in neuromyelitis optica.** *Neurology* 2005;64:1270–72 CrossRef Medline
6. Aguilera AJ, Carlow TJ, Smith KJ, et al. **Lymphocytapheresis in Devic's syndrome.** *Transfusion* 1985;25:54–56 CrossRef Medline
7. Weinschenker BG, O'Brien PC, Petterson TM, et al. **A randomized trial of plasma exchange in acute central nervous system inflammatory demyelinating disease.** *Ann Neurol* 1999;46:878–86 Medline
8. Keegan M, Pineda AA, McClelland RL, et al. **Plasma exchange for severe attacks of CNS demyelination: predictors of response.** *Neurology* 2002;58:143–46 CrossRef Medline
9. Nozaki I, Hamaguchi T, Komai K, et al. **Fulminant Devic disease successfully treated by lymphocytapheresis.** *J Neurol Neurosurg Psychiatry* 2006;77:1094–95 Medline

10. Pekcevik Y, Mitchell CH, Mealy MA, et al. **Differentiating neuromyelitis optica from other causes of longitudinally extensive transverse myelitis on spinal magnetic resonance imaging.** *Mult Scler* 2016;22:302–11 CrossRef Medline
11. Waters P, Jarius S, Littleton E, et al. **Aquaporin-4 antibodies in neuromyelitis optica and longitudinally extensive transverse myelitis.** *Arch Neurol* 2008;65:913–19 Medline
12. Cassinotto C, Deramond H, Olindo S, et al. **MRI of the spinal cord in neuromyelitis optica and recurrent longitudinal extensive myelitis.** *J Neuroradiol* 2009;36:199–205 CrossRef Medline
13. Yonezu T, Ito S, Mori M, et al. **“Bright spotty lesions” on spinal magnetic resonance imaging differentiate neuromyelitis optica from multiple sclerosis.** *Mult Scler* 2014;20:331–37 CrossRef Medline
14. Kitley JL, Leite MI, George JS, et al. **The differential diagnosis of longitudinally extensive transverse myelitis.** *Mult Scler* 2012;18:271–85 CrossRef Medline
15. Wingerchuk DM, Hogancamp WF, O’Brien PC, et al. **The clinical course of neuromyelitis optica (Devic’s syndrome).** *Neurology* 1999;53:1107–14 CrossRef Medline
16. Asgari N, Skejoe HP, Lillevang ST, et al. **Modifications of longitudinally extensive transverse myelitis and brainstem lesions in the course of neuromyelitis optica (NMO): a population-based, descriptive study.** *BMC Neurol* 2013;13:33 CrossRef Medline
17. Kim W, Park MS, Lee SH, et al. **Characteristic brain magnetic resonance imaging abnormalities in central nervous system aquaporin-4 autoimmunity.** *Mult Scler* 2010;16:1229–36 CrossRef Medline
18. Qiu W, Wu JS, Zhang MN, et al. **Longitudinally extensive myelopathy in Caucasians: a West Australian study of 26 cases from the Perth Demyelinating Diseases Database.** *J Neurol Neurosurg Psychiatry* 2010;81:209–12 CrossRef Medline
19. Landis JR, Koch GG. **The measurement of observer agreement for categorical data.** *Biometrics* 1977;33:159–74 CrossRef Medline
20. Sanders RW. **The problem with apples and oranges.** *J Orthop Trauma* 1997;11:465–66 CrossRef
21. Lennon VA, Wingerchuk DM, Kryzer TJ, et al. **A serum autoantibody marker of neuromyelitis optica: distinction from multiple sclerosis.** *Lancet* 2004;364:2106–12 CrossRef Medline
22. Jarius S, Franciotta D, Bergamaschi R, et al. **NMO-IgG in the diagnosis of neuromyelitis optica.** *Neurology* 2007;68:1076–77 CrossRef Medline
23. Nakashima I, Fujihara K, Miyazawa I, et al. **Clinical and MRI features of Japanese patients with multiple sclerosis positive for NMO-IgG.** *J Neurol Neurosurg Psychiatry* 2006;77:1073–75 CrossRef Medline

# Normal Values of Magnetic Relaxation Parameters of Spine Components with the Synthetic MRI Sequence

M. Drake-Pérez, B.M.A. Delattre, J. Boto, A. Fitsiori, K.-O. Lovblad, S. Boudabbous, and M.I. Vargas



## ABSTRACT

**BACKGROUND AND PURPOSE:** SyMRI is a technique developed to perform quantitative MR imaging. Our aim was to analyze its potential use for measuring relaxation times of normal components of the spine and to compare them with values found in the literature using relaxometry and other techniques.

**MATERIALS AND METHODS:** Thirty-two spine MR imaging studies (10 cervical, 5 dorsal, 17 lumbosacral) were included. A modified multiple-dynamic multiple-echo sequence was added and processed to obtain quantitative T1 (millisecond), T2 (millisecond), and proton density (percentage units [pu]) maps for each patient. An ROI was placed on representative areas for CSF, spinal cord, intervertebral discs, and vertebral bodies, to measure their relaxation.

**RESULTS:** Relaxation time means are reported for CSF (T1 = 4273.4 ms; T2 = 1577.6 ms; proton density = 107.5 pu), spinal cord (T1 = 780.2 ms; T2 = 101.6 ms; proton density = 58.7 pu), normal disc (T1 = 1164.9 ms; T2 = 101.9 ms; proton density = 78.9 pu), intermediately hydrated disc (T1 = 723 ms; T2 = 66.8 ms; proton density = 60.8 pu), desiccated disc (T1 = 554.4 ms; T2 = 55.6 ms; proton density = 47.6 ms), and vertebral body (T1 = 515.3 ms; T2 = 100.8 ms; proton density = 91.1 pu). Comparisons among the mean T1, T2, and proton density values showed significant differences between different spinal levels (cervical, dorsal, lumbar, and sacral) for CSF (proton density), spinal cord (T2 and proton density), normal disc (T1, T2, and proton density), and vertebral bodies (T1 and proton density). Significant differences were found among mean T1, T2, and proton density values of normal, intermediately hydrated, and desiccated discs.

**CONCLUSIONS:** Measurements can be easily obtained on SyMRI and correlated with previously published values obtained using conventional relaxometry techniques.

**ABBREVIATIONS:** PD = proton density; pu = percentage units

MR imaging provides excellent soft-tissue contrast. However, this information is qualitative; on T1WI or T2WI, the absolute intensity has no physical unit and diagnosis relies on relative contrast differences between adjacent tissues in the image.<sup>1</sup> Nevertheless, quantitative imaging is rapidly gaining importance

as a complement to qualitative sequences, such as diffusion-based sequences, perfusion imaging, and MR spectroscopy.

Relaxometry is a quantitative method that allows the absolute quantification of MR imaging parameters such as T1 and T2 relaxation times as well as proton density (PD). This technique is nevertheless very time-consuming and requires T1 and T2 quantifications to be performed separately through different types of sequences that were not feasible from a practical point of view in a clinical routine setup.<sup>2</sup> These sequences included inversion recovery<sup>3</sup> for T1 measurements or techniques derived from modifications to the Carr-Purcell Meiboom-Gill sequence, considered the criterion standard for the measurement of T2 relaxation time.<sup>4,5</sup>

Several methods are currently being developed to perform quantitative MR imaging techniques in a more efficient manner. MR fingerprinting consists of a pseudorandomized variation of the sequence parameters (flip angle, TR, and *k*-space trajectory), thus producing a unique signal evolution or “fingerprint” for each tissue.<sup>6</sup> Following acquisition, the process involves a pattern-

Received August 28, 2017; accepted after revision December 12.

From the Division of Diagnostic and Interventional Neuroradiology (M.D.-P., J.B., A.F., K.-O.L., M.I.V.), Geneva University Hospitals and Faculty of Medicine of Geneva, Geneva, Switzerland; Department of Radiology (M.D.-P.), University Hospital Marqués de Valdecilla-Instituto de Investigación Sanitaria Valdecilla, Santander, Spain; and Division of Radiology (B.M.A.D., S.B.), Geneva University Hospitals, Geneva, Switzerland.

Please address correspondence to Maria Isabel Vargas, MD, Geneva University Hospitals, Division of Diagnostic and Interventional Neuroradiology of Geneva University Hospitals, Department of Radiology and Medical Informatics, Rue Gabrielle-Perret-Gentil 4, 1211 Genève 14, Switzerland; e-mail: maria.i.vargas@hcuge.ch

Indicates article with supplemental on-line tables.

<http://dx.doi.org/10.3174/ajnr.A5566>

identification algorithm to link the obtained fingerprints to those stored in a predefined dictionary.<sup>7</sup> Recent studies aim to differentiate common types of adult intra-axial brain tumors<sup>8</sup> or to perform quantitative abdominal imaging<sup>9</sup> using this method.

Another MR imaging quantitative method is the SyntAc sequence (based on the QRAPMASTER sequence,<sup>1</sup> SyntheticMR, Linköping, Sweden). This is the technique we have chosen for our study because it is more readily available and is already approved by the Conformité Européenne (CE) and FDA. In this method, physical properties (PD, longitudinal [T1] and transverse [T2] relaxation rates, and correction for B1-inhomogeneities) are calculated using a single, multiecho, saturation recovery TSE sequence.<sup>10</sup> Subsequently, any “synthetic” T1WI or T2WI can be achieved from the absolute parameters.<sup>1</sup>

Common advantages of these 2 methods for brain imaging are reduced acquisition time<sup>6</sup> and the possibility of performing automatic tissue segmentation and volume estimation.<sup>11</sup> This has already been used for the evaluation of demyelinating diseases.<sup>10,12</sup>

The recent study published by Tanenbaum et al<sup>13</sup> compared synthetic-versus-conventional MR imaging for routine neuroimaging, concluding that synthetic MR imaging quality was comparable with conventional sequences despite artifacts being more common in the synthetic FLAIR sequence, as previously reported.<sup>10,14</sup> This shortcoming was also reported with MR fingerprinting methodology.<sup>15</sup>

The goal of this study was to measure T1 and T2 relaxation times, as well as PD values, of normal structures included in normal spine MR imaging (CSF, spinal cord, healthy-versus-desiccated intervertebral disc, and vertebral body) using Synthetic MRI (SyMRI) 8.0 software (SyntheticMR) (this method has already been used for quantifying relaxation times in the brain, but, as far as we know, it has not been used in the spinal region). Furthermore, we aimed to compare our values with those found in the literature from studies using relaxometry.

## MATERIALS AND METHODS

### Participants

Thirty-two nonconsecutive patients (17 males; 15 females; mean age, 55.47 years; range, 17–85 years) undergoing spine MR imaging studies (10 cervical, 5 dorsal, 17 lumbosacral) at our institution (Geneva University Hospitals) in 2016 were included in this study.

All subjects met the following criteria: 1) a synthetic MR image added to our standard imaging protocol when time constraints allowed it, and 2) no history of neoplastic conditions, radiation therapy, or multiple sclerosis.

The study was approved by our institutional review board, and informed consent was waived.

### Image Acquisition

All studies were performed on a 1.5T Ingenia scanner (Philips Healthcare) using a 52-channel spine coil. The imaging protocol included quantitative sagittal MR imaging and the conventional MR imaging sequences used in our center, which include at least conventional 2D sagittal spin-echo T1-weighted, FSE T2-weighted, and STIR sequences.

A multiple-dynamic multiple-echo sequence (SyntAc) was

modified<sup>1</sup> for spine imaging. Parameters were the following: sagittal orientation, FOV = 200 × 321 mm, acquisition (reconstruction) voxel size = 0.89 × 1.48 mm<sup>2</sup> (0.71 × 0.72 mm<sup>2</sup>), 15 contiguous slices of 4-mm thickness, TE = 11/100 ms, TR = 2485 ms, TSE factor = 12, sensitivity encoding acceleration factor = 2. The acquisition time of the synthetic sequence was 5 minutes 40 seconds.

This sequence generates 8 different contrasts (2 different TEs and 4 different TIs), which are then processed by SyMRI 8.0 software to obtain quantitative T1 (millisecond), T2 (millisecond), and PD (pu) maps. The PD maps are measured in percentage units (pu), in which 100% is the value of brain CSF that is used for calibration. Because fat has a higher signal intensity than CSF, it is displayed with a PD value above 100 pu (0–108 pu if T1 > 1100 ms and 0–120 pu if T1 < 1100 ms). The dynamic ranges of T1 and T2 values are 300–4300 and 20–2000 ms, respectively (this information was extracted from the software manual<sup>16</sup>).

These maps were then saved in DICOM format and analyzed in OsiriX Imaging Software (Version 7.0.3; <http://www.osirix-viewer.com>).

### Radiologic Assessment

All images were analyzed by a neuroradiologist and a fellow in neuroradiology on standard radiologic workstations connected to the PACS. A consensus was reached in the choice of representative normal-intensity areas for CSF, spinal cord, intervertebral disc, and vertebral body on each study (based on the conventional MR imaging sequences). We subsequently placed an ROI on these areas and measured representative T1 (millisecond), T2 (millisecond), and PD (pu) of each spinal element, carefully avoiding partial volumes (Figs 1 and 2).

The cervical cord was assessed at the C2 and C7 levels. The dorsal spinal cord was assessed on an upper and lower level around T2 and T10, respectively. In the lumbar spine, a single ROI was placed on the conus medullaris. We placed the ROI in the center of the spinal cord, including both gray and white matter, to elude a possible partial volume effect.

Two ROIs were placed in each spinal region for CSF, also on the highest and lowest possible positions, carefully avoiding descending nerve roots and flow artifacts. In the cervical studies, the upper ROI was placed in the cisterna magna, and the lower one, at the level of C7. In the dorsal studies, ROIs were placed at levels similar to the ones used for the spinal cord. In the lumbar studies, one ROI was placed at the level of the conus medullaris, and another, around S1.

All cervical, dorsal, and lumbar vertebrae fully within the FOV were included, as well as the first sacral vertebra. ROIs were placed on the anterior part of the vertebral body to avoid vascular artifacts, cortical bone, partial volume effects, and areas with signal abnormalities (eg, hemangiomas) on conventional MR imaging sequences. We excluded 3 fractured vertebrae and 2 with metallic artifacts.

All cervical, dorsal, and lumbar discs that were completely visualized were evaluated, excluding 1 with artifacts secondary to instrumentation. Intervertebral discs were measured and assigned a status of clearly normally hydrated (equivalent to a grade I of the Pfirrmann scoring<sup>17</sup>), intermediate signal (grades II or

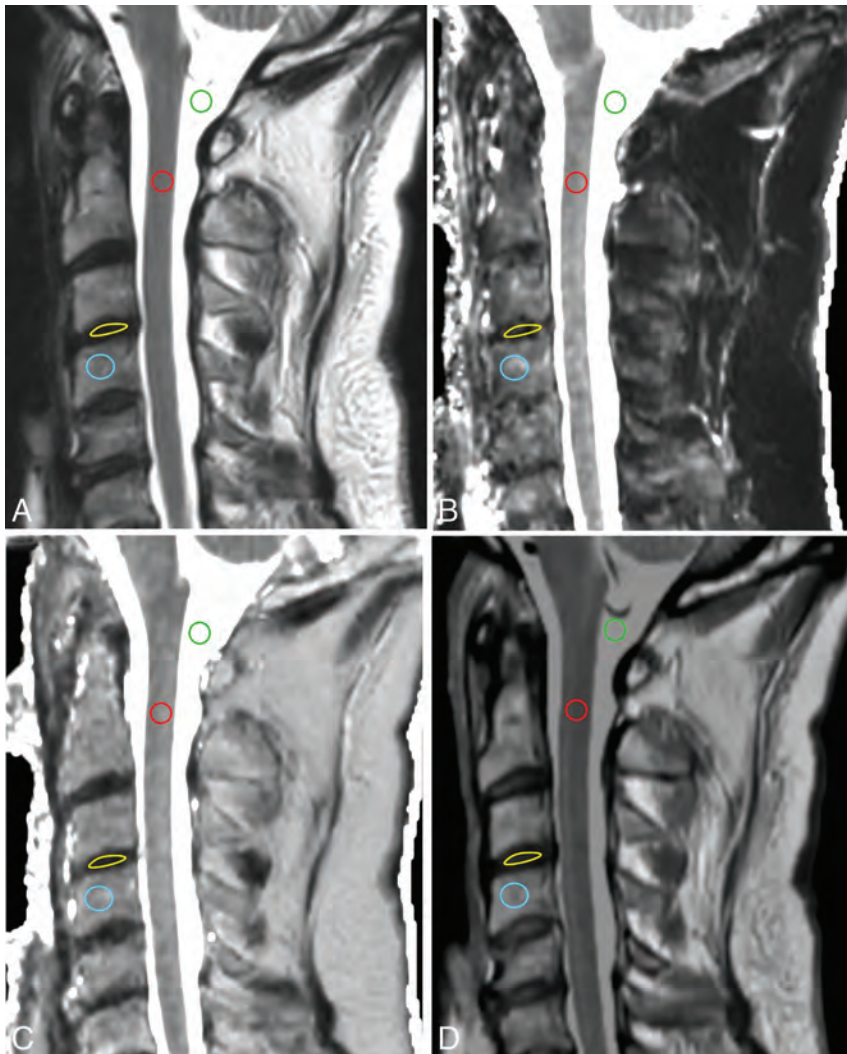


**FIG 1.** Conventional T2WI (A) and quantitative T1 (B), T2 (C), and PD (D) maps in a cervical study. ROIs are placed in the CSF (green), spinal cord (red), intervertebral disc (yellow), and vertebral body (blue).

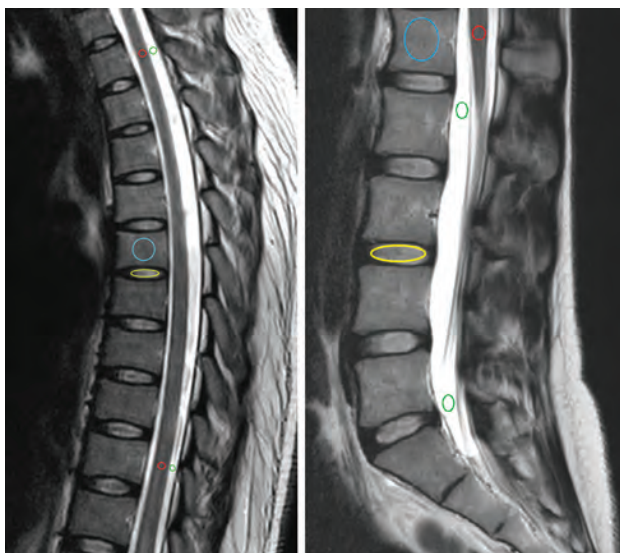


**FIG 2.** Conventional T2WI in a dorsal and lumbar study, showing how ROIs are placed in the CSF (green), spinal cord (red), intervertebral disc (yellow, only 1 example), and vertebral body (blue, only 1 example).

III), or desiccated (grades IV or V) by visual assessment. The intermediate signal status included discs that were neither clearly normally hydrated nor clearly desiccated. Discs showing complete loss of height were not included.

These ROIs were originally placed on the sagittal T2-weighted image and copied and pasted into the sagittal synthetic T1, T2, and PD maps; their mean value, SD, and area were calculated.

#### **Validity of Quantification Measurements**

To verify whether the quantification with our modified SyMRI sequence with a relatively low TR (2485 ms) was correct, we compared the T1, T2, and PD values obtained on a set of gel tubes composed of different agar and gadolinium concentrations measured with the SyMRI sequence with a TR of 6000 ms (and we used this technique as the criterion standard). Apart from TR, all parameters were kept identical. The acquisition time of this sequence was 11 minutes 20 seconds, which precludes its use in clinical routine. We also added an idealized model with mineral water to the FOV to include a compartment with high T1 and T2 values.

#### **Statistical Analysis**

Means and standard errors of the mean of T1, T2, and PD values for CSF, spinal cord, discs (normal, desiccated, and intermediate hydration), and vertebral bodies across all spinal levels were calculated. A 1-sample Kolmogorov-Smirnov test was used to investigate whether continuous variables were normally distributed across groups (spinal region or disc hydration status). If normal distribution of the data was confirmed in all groups, differences between group mean values were investigated by 1-way ANOVA with age as a covariate using a model with type III sum of squares. Pair-wise comparisons were subsequently performed by the least significant difference method. If data were not normally distributed in at least 1 group, differences among group median values were investigated by the nonparametric Kruskal-Wallis H test. The Mann-Whitney *U* test was used for pair-wise comparisons in this case.

Correlation coefficients (*R*) were calculated, and linear regression was performed between the values obtained with the SyMRI sequence used in the study (TR = 2485 ms) and those obtained by the criterion standard (TR = 6000 ms).

A .05 two-tailed significance level was used for all tests. Statistical analysis was performed with the Statistical Package for the Social Sciences, Version 22 (IBM, Armonk, New York).<sup>18</sup>

## RESULTS

Table 1 shows the linear regression and the correlation coefficients obtained for T1, T2, and PD values measured with our SyMRI sequence and with a sequence with a long TR (6000 ms) used as the criterion standard. Correlation was high for T1 and T2 values ( $R = 1.00$  for both) and moderately high for PD values ( $R = 0.57$ ). The slope of the line of best fit was close to 1 in all 3 analyses (1.06, 0.96, and 0.94 for T1, T2, and PD, respectively).

Descriptive statistics with means and 95% confidence intervals of the mean of T1, T2, and PD measured values of CSF, spinal cord, normal discs, intermediately hydrated discs, desiccated discs, and vertebral bodies for all spinal levels are shown in Table 2.

### Comparison of Spinal Levels

The Kolmogorov-Smirnov test showed that only T1 and PD values for CSF were not normally distributed in any of the spinal levels (cervical, dorsal, lumbar, and sacral) ( $P < .05$ ). The non-parametric Kruskal-Wallis H test was therefore used to compare medians of spinal levels in these 2 variables. The distribution of

**Table 1: Validity of quantification measurements**

Range of Values (Water Bottle)	Linear Regression Equation	R
T1, 300–822 (2819)	$y = 1.06x - 40.1$	1.00
T2, 41–255 (1929)	$y = 0.96x - 4.72$	1.00
PD, 41.8–131.4 (100.9)	$y = 0.94x + 7.44$	0.57

**Note:**—Linear regression and correlation coefficients between T1, T2 and PD values measured with the SyntheticMR sequence with TR 6000 ms (criterion standard) and the sequence used in this study (TR 2385 ms). Range of values investigated is indicated in first column.

**Table 2: Normal values of CSF, spinal cord, discs and vertebral bodies**

	T1 (ms) 95% CI	T2 (ms) 95% CI	PD (pu) 95% CI
CSF ( $n = 64$ )	4273.4 (4263.8–4283.1)	1577.6 (1501.2–1654.0)	107.5 (107.2–107.8)
Spinal cord ( $n = 45$ )	780.2 (753.6–806.9)	101.6 (98.7–104.6)	58.7 (56.9–60.6)
Normal disc ( $n = 64$ )	1164.9 (1071.1–1258.7)	101.9 (94.2–109.5)	78.9 (76.0–81.9)
Intermediate disc ( $n = 29$ )	723 (677.3–768.6)	66.8 (62.6–71.1)	60.8 (58.2–63.4)
Desiccated disc ( $n = 144$ )	554.4 (536.7–572.0)	55.6 (54.2–57.0)	47.6 (46.2–49.0)
Vertebral body ( $n = 260$ )	515.3 (506.0–524.6)	100.8 (99.5–102.2)	91.1 (89.6–92.5)

**Note:**—Means and 95% CI of the mean of T1, T2 and PD measured values of CSF, spinal cord, discs, and vertebral bodies for all spinal levels.

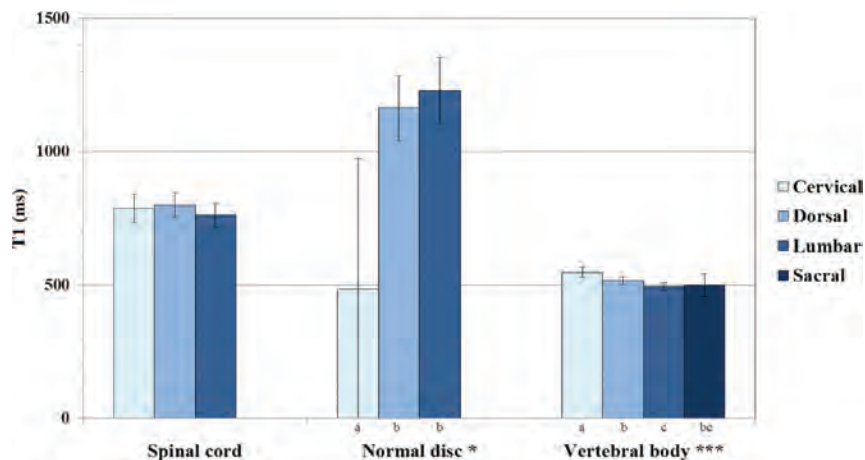


**FIG 3.** ANOVA results with comparison of estimated marginal means of T1 values for spinal cord, normal discs, and vertebral bodies across spinal levels, assuming fixed ages of 56.2, 36.9, and 56.4 years, respectively (single asterisk indicates  $P < .05$ ; double asterisks,  $P < .01$ ; triple asterisks,  $P < .001$ ). Significant pair-wise differences between spinal levels are indicated by a different letter assigned to each level.

all the other variables was not significantly different from normality in all spinal levels, which allowed comparison of means by ANOVA.

We did not find a significant difference among different spinal levels in spinal cord T1 values ( $P = .456$ ). The T1 value of normal discs across spinal levels was significantly different, with cervical spine discs showing the largest difference in relation to dorsal and lumbar discs ( $P < .05$ ). There was an even more significant effect of spinal level on the T1 value of vertebral bodies ( $P < .001$ ). These results are summarized in Fig 3.

Spinal level had a significant effect on T2 signal intensity of the spinal cord and normal discs ( $P < .05$  and  $P < .001$ , respectively). Overall, the T2 value of normal discs increased progressively from the cervical to the lumbar region. The T2 value of vertebral bodies was not significantly affected by spinal level ( $P = .370$ ) (Fig 4). Similarly, CSF T2 values did not show a significant difference among spinal levels ( $P = .081$ ) (Fig 5).

PD values of spinal cord, normal discs, and vertebral bodies were significantly affected by spinal level ( $P < .01$ ,  $P < .001$ , and  $P < .001$ , respectively). PD values of the spinal cord and vertebral bodies tended to decrease from cervical to lumbar, whereas PD values of discs tended to increase (Fig 6).

Medians of CSF T1 values were not significantly different across spinal levels ( $P = .234$ ). Despite the noticeable similarity of CSF PD values in the 4 different spinal levels, a significant difference was found among medians ( $P < .05$ ) (Table 3).

### Comparison of Disc Hydration Statuses

Means of disc T1 values were strongly affected by disc hydration status ( $P < .001$ ), with progressively lower values as the disc water content decreased (Fig 7). The same trend was found on the non-parametric test results with disc T2 and PD values significantly decreasing as disc hydration declined ( $P < .001$ ) (Table 4).

## DISCUSSION

### CSF

Our results for CSF mean relaxation times are comparable with those found in the literature. Krauss et al<sup>19</sup> showed T1, T2, and PD values very similar to ours on the charts displaying their phantom measurements with the QRAPMASTER technique. Using the same technique, Warntjes et al<sup>1</sup> obtained T1 and T2 values of 3940 ms and 1910 ms, respectively, and PD values of 1029 pu, specifying that “the PD of pure water at 37°C corresponds to 1000” and arguing that the proton density of CSF appeared “somewhat high, possibly due to flow-effects or diffusion.” In a review article from 2017, Bojorquez et al<sup>4</sup> reported the following CSF T1 values in

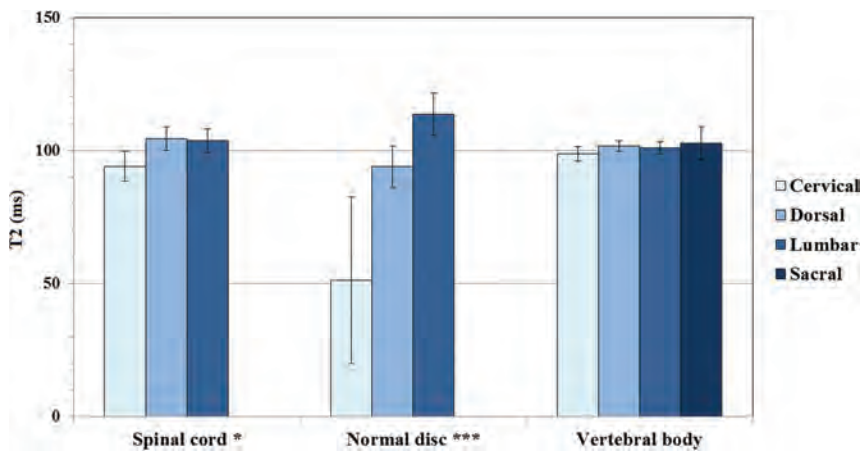


**FIG 4.** ANOVA results with comparison of estimated marginal means of T2 values for spinal cord, normal discs, and vertebral bodies across spinal levels, assuming fixed ages of 56.2, 37.2, and 56.4 years, respectively (single asterisk indicates  $P < .05$ ; double asterisks,  $P < .01$ ; triple asterisks,  $P < .001$ ). Significant pair-wise differences between spinal levels are indicated by a different letter assigned to each level.

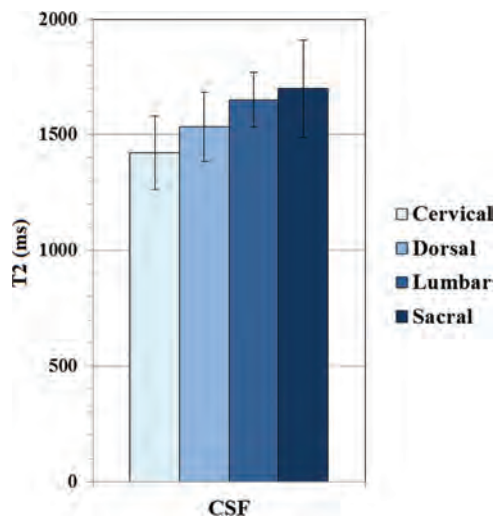


**FIG 5.** ANOVA results with comparison of estimated marginal means of T2 values for CSF across spinal levels assuming a fixed age of 55.5 years. There was no significant difference among spinal levels.

the literature:  $4391 \pm 545$  ms,<sup>20</sup>  $3817 \pm 424$  ms,<sup>5</sup>  $4522 \pm 417$  ms,<sup>20</sup>  $6873$  ms, and  $4184$  ms.<sup>21</sup>

We found significant differences in CSF values among spinal levels only in PD, despite the medians being very similar. This finding was unexpected and could potentially represent a false-positive result. However, another possible explanation for this difference is that, due to our slice thickness (4 mm), partial volume could have been introduced from the nerve roots of the cauda equina at the sacral level, therefore lowering the measured CSF PD values. Because this second explanation is not immediately apparent from the analysis of the median values, we provide means of PD CSF values by spinal level:  $107.86 \pm 0.36$  for the cervical spine,  $107.97 \pm 0.09$  for the dorsal spine,  $107.35 \pm 1.31$  for the lumbar spine, and  $106.67 \pm 2.06$  for the sacral spine.

T1 and PD values for CSF were not normally distributed. As mentioned in the “Materials and Methods” section, we found an upper limit of 108 for PD and 4300 for T1 with this technique, which was produced by the software and could be considered a

systematic bias, as we further discuss in the limitations in the “Discussion.” Conversely, all T2 values were within the dynamic range of measurement.

Limitations to CSF measurements were the presence of flow artifacts, which are slightly more prominent than those usually encountered in routine imaging, especially in the T2 and PD maps, as previously reported.<sup>10</sup>

### Spinal Cord

T1 relaxation times in the spinal cord reported by Smith et al<sup>22</sup> were  $863 \pm 23$  ms and  $972 \pm 36$  ms for white matter and gray matter using a 3T MR imaging system. Massire et al<sup>23</sup> reported  $1189 \pm 42$  ms for white matter and  $1313 \pm 51$  ms for gray matter. Both publications reported higher values than

our mean of  $780 \pm 26.6$  ms. This difference is probably because their study was performed at 3T and 7T and relaxometry measures (especially T1) are dependent on field strength.

T2 relaxation times reported in the literature are 73 ms for white matter and 76 ms for gray matter,<sup>22</sup> which differ from our T2 mean value of  $101.6 \pm 2.9$  ms. Lu et al<sup>5</sup> reported T2 values for brain gray matter at 1.5T, ranging from 81 (putamen) to 99 ms (cortex). We did not find any previously reported PD values for the spinal cord.

Although the absolute values did not show large variations, we found that the cervical region had a significantly different T2 value from the thoracic and lumbar regions (94.1 versus 104.4 and 103.6 ms, respectively). The same difference was found in PD values (63.3 versus 58.7 and 55.7 pu, respectively). No significant differences were found for T1 values. This may relate to the normal anatomy of the spinal cord because the configuration of the gray matter and gray/white matter ratio varies along spinal cord regions, depending on the neural requirements of a given region.<sup>24</sup> There is also variation in the total number of tracts (which decreases from cervical to lumbar, as more and more nerve projections arise), as well as in the cross-sectional area of the cord (which increases at the cervical and lumbar enlargements). These 2 features determine variations in the density of spinal tracts along different segments of the cord.

We believe SyMRI could prove to be a good quantitative MR imaging technique for the assessment of the spinal cord. T1, T2, and PD measurements have the potential to be used as biomarkers of both myelin and axonal integrity. A promising application could therefore be to evaluate the degree of spinal cord integrity in posttraumatic or demyelinating lesions. Further studies would be needed to corroborate the variations we found among spinal levels and clarify the possible causes. Recently, the role of T1, T2, PD, and myelin measurements has been analyzed in different neurologic conditions in the brain,<sup>25</sup> and we believe it could potentially be directly translated into spinal cord conditions. Moreover, although outside of the scope of this study, myelin water fraction can be extracted from SyMRI T2 measures.<sup>26</sup> Preliminary studies

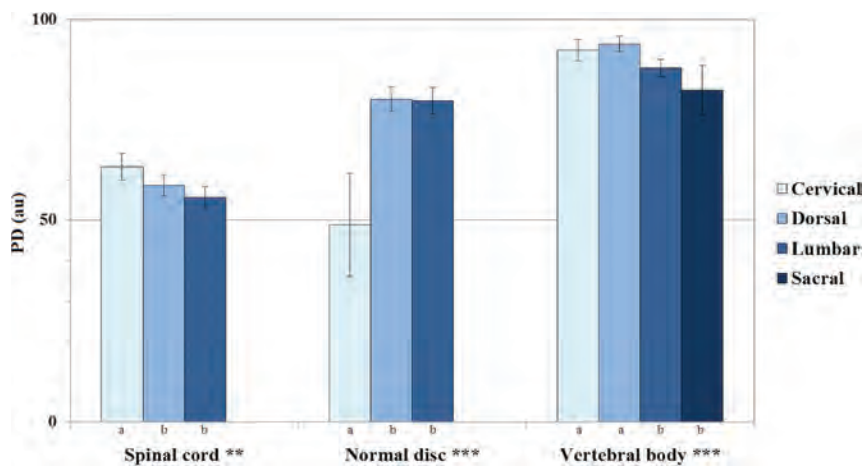


**FIG 6.** ANOVA results with comparison of estimated marginal means of PD values for spinal cord, normal discs, and vertebral bodies across spinal levels, assuming fixed ages of 56.2, 37.2, and 56.4 years, respectively (single asterisk indicates  $P < .05$ ; double asterisks,  $P < .01$ ; triple asterisks,  $P < .001$ ). Significant pair-wise differences between spinal levels are indicated by a different letter assigned to each level.

**Table 3: Results of the Kruskal-Wallis H test with T1 and PD median values for CSF across spinal levels**

	Cervical	Dorsal	Lumbar	Sacral	P
T1 CSF	4287.7	4285.5	4289.6	4294.3	.234
PD CSF	108.0 <sup>a,b</sup>	108.0 <sup>a</sup>	108.0 <sup>b</sup>	108.0 <sup>a,b</sup>	<.05

**Note:**—Significant pairwise differences between spinal levels are indicated by a different letter (a, b) assigned to each level.

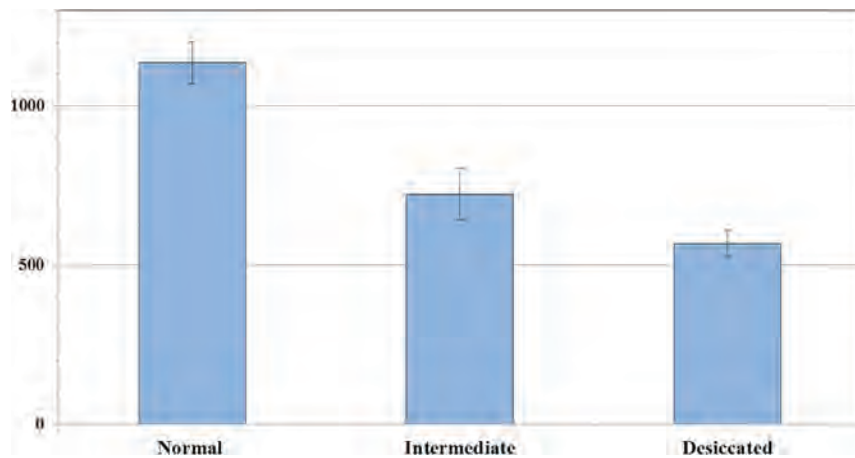


**FIG 7.** ANOVA results with comparison of estimated marginal means of T1 values for normal, intermediately hydrated, and desiccated discs, assuming a fixed age of 55.9 years, which shows a significant effect of hydration status ( $P < .001$ ). All pair-wise comparisons also show a significant difference among groups.

**Table 4: Results of the Kruskal-Wallis H test with median T2 and PD values for discs across the 3 hydration status**

	Normal	Intermediate	Desiccated	P
T2 disc	95.5 <sup>a</sup>	66.2 <sup>b</sup>	54.0 <sup>c</sup>	<.001
PD disc	80.9 <sup>a</sup>	58.0 <sup>b</sup>	47.8 <sup>c</sup>	<.001

**Note:**—Significant pairwise differences between hydration status are indicated by a different letter (a, b, c) assigned to each level.

applied to multiple sclerosis have already shown interesting results with this technique, which seems to be more sensitive than longitudinal and transverse relaxation rates (R1 and R2, respectively) and PD for plaque assessment, even though some changes are already seen with these parameters.<sup>27</sup>

## Discs

We have found significant differences among mean T1, T2, and PD values of normal, intermediately hydrated, and desiccated discs, confirming the formerly described negative relationship between relaxation time (T1, T2) and disc-degenerative grade.<sup>28</sup> T1 relaxation time has been shown to decrease with disc degeneration<sup>29</sup> and herniation.<sup>30</sup> T2 relaxation times are related to disc biochemical composition in that decreased T2 values represent decreased disc water content and proteoglycan loss<sup>31</sup> or replacement of the nucleus by degenerative tissue, which has lower T2 values.<sup>32</sup>

Our results also showed significant differences in disc values among different spinal levels, with lower T1, T2, and PD values in the cervical spine compared with the thoracic or lumbar levels. This finding agrees with previous biochemistry reports of lower water content in cervical discs compared with lumbar discs.<sup>33</sup>

Another possible explanation for our significantly lower values in cervical discs could be related to the ROI areas, which were smaller in that region. This feature may have affected the proportion of annulus fibrosus or its analogous fibrous structure, the intranuclear cleft versus the nucleus pulposus. As reported by Stelzeneder et al in 2012,<sup>34</sup> the annulus fibrosus has significantly lower values compared with the nucleus pulposus. Because the reduction in cervical disc areas is mainly at the expense of nucleus pulposus, this finding could be another reason for their decreased T1, T2, and PD values.

Limitations to our conclusions in disc analysis could be because we established disc hydration status by agreed visual assessment and the age

range is wide in our population (17 to 81 years), possibly explaining the large variability of the values obtained for discs (and vertebral bodies).

Disc degeneration is a condition reported daily on spine examinations, and SyMRI could help establish universal cutoffs (settled by spinal level) for staging it.

## Vertebral Bodies

Our mean values of T1 and T2 mean relaxation times are consistent with those found in the literature. In the Bojorquez et al review,<sup>4</sup> the values obtained for T1 vary between  $106 \pm 4$  ms<sup>35</sup> and

586 ± 73 ms,<sup>3</sup> and from 40 to 160 ms for T2.<sup>36</sup> Le Ster et al<sup>37</sup> reported T1 values of 621 ms.

T2 relaxation times did not show significant differences among spinal levels, but T1 values significantly decreased from cervical to lumbar (from 547.1 to 495.1 ms) as did PD values (from 92.3 to 82.4 pu). Because bone marrow is characterized by large variations in T1 relaxation times between water and fat compartments,<sup>38</sup> the differences found may be due to normal anatomic changes in the proportion of fatty marrow along the spine (which increases from C3 to L5).<sup>39</sup>

A potential application of determining T1, T2, and PD values of vertebral bodies could be in the detection of bone marrow infiltrative conditions, such as hematologic malignancies, by providing a quantitative tool for imaging assessment in situations in which it is difficult to visually confirm and demarcate pathologic changes. However, consideration must be given to the high variability relating to vertebral body composition among healthy individuals because it depends on different factors such as age, with conversion from red to yellow marrow, or the effect of hematocrit levels.

The On-line Table outlines previously published measured values with conventional relaxometry techniques for CSF, spinal cord, disc, and bone marrow.

Our study has some limitations, some of which have already been mentioned above. Another limitation is the potential bias introduced by manually performing some operations such as ROI selection. For spinal cord measurements, atlas-based techniques are available that could potentially have allowed gray-white matter distinction.

Nonconsecutive selection of patients may have introduced some bias. We nevertheless believe that this is minimized because there were no criteria in selecting patients for the study other than time constraints allowing the synthetic sequence to be performed. Taking this into account, all patients in whom this sequence was performed, within the time considered, took part in the study; this feature made the selection consecutive in this subgroup of patients.

We probably also have some limitations in accurately quantifying elements with high T1 and PD because our sequence has a relatively low TR (2485 ms). This limitation means that complete relaxation of high T1 structures is not fulfilled during the sequence; therefore, signal can be somehow saturated. Our attempt to verify the validity of quantification due to our short TR showed a high correlation of values for a T1 range of 300–822 ms as well as in the idealized model with T1 of 2819 ms. However, we did not compare the validity of the measurements with higher T1 as is the case with CSF; this difference may have biased the results obtained in this compartment due to the low TR.

Moreover, when we analyzed structures with small dimensions, such as the spinal cord, our quantitative values could have partial volume effects due to our slice thickness of 4 mm. This could be an explanation for the higher T2 values found in the spinal cord compared with previously published values in the literature.

Another limitation of our study is the lack of comparison among the values obtained with an internal criterion standard. These values would be more meaningful if compared with quan-

titative measures using conventional techniques in the same patients. Unfortunately, it is difficult in practice to add conventional sequences to the imaging protocol due to the additional acquisition time needed. Similarly, conventional T1 and T2 quantitative mapping techniques were not used for the agar phantom experiments. We are aware that SyMRI with a TR of 6000 is not a true criterion standard. However, quantification with SyMRI (TR ranging from 2900 to 5000 ms) has been validated in several previous publications.<sup>1,11,19,40-42</sup>

## CONCLUSIONS

T1, T2, and PD measurements can be easily and rapidly obtained with SyMRI, a tool that could be readily available as a quantitative method in the spinal region, retrieving results comparable with those made previously by other quantitative techniques.

It is likely that the use of quantitative MR imaging will be implemented as part of the radiologist's every day work. Setting the reference range for relaxation times of CSF, spinal cord, vertebral bodies, and discs in healthy individuals will therefore have a straightforward application. These measurements could be used in our future daily practice as a quantitative extra aid in the radiologic assessment of spinal conditions, such as infiltration of bone marrow in hematologic disease, demyelinating disease, and spondylodiscitis. They could also play a role in the classification of disc degeneration and the choice of treatment.

## ACKNOWLEDGMENTS

M.D.-P. is supported by a research contract (Contrato post-MIR López Albo 2016) from the Instituto de Investigación Sanitaria Valdecilla (IDIVAL).

## REFERENCES

1. Warnrjes JB, Leinhard OD, West J, et al. **Rapid magnetic resonance quantification on the brain: optimization for clinical usage.** *Magn Reson Med* 2008;60:320–29 CrossRef Medline
2. Bottomley PA, Foster TH, Argersinger RE, et al. **A review of normal tissue hydrogen NMR relaxation times and relaxation mechanisms from 1–100 MHz: dependence on tissue type, NMR frequency, temperature, species, excision, and age.** *Med Phys* 1984;11:425–48 CrossRef Medline
3. de Bazelaire CM, Duhamel GD, Rofsky NM, et al. **MR imaging relaxation times of abdominal and pelvic tissues measured in vivo at 3.0 T: preliminary results.** *Radiology* 2004;230:652–59 CrossRef Medline
4. Bojorquez JZ, Bricq S, Acquitter C, et al. **What are normal relaxation times of tissues at 3 T?** *Magn Reson Imaging* 2017;35:69–80 CrossRef Medline
5. Lu H, Nagae-Poetscher LM, Golay X, et al. **Routine clinical brain MRI sequences for use at 3.0 Tesla.** *J Magn Reson Imaging* 2005;22:13–22 CrossRef Medline
6. Ma D, Gulani V, Seiberlich N, et al. **Magnetic resonance fingerprinting.** *Nature* 2013;495:187–92 CrossRef Medline
7. European Society of Radiology (ESR). **Magnetic resonance fingerprinting: a promising new approach to obtain standardized imaging biomarkers from MRI.** *Insights Imaging* 2015;6:163–65 CrossRef Medline
8. Badve C, Yu A, Dastmalchian S, et al. **MR fingerprinting of adult brain tumors: initial experience.** *AJNR Am J Neuroradiol* 2017;38:492–99 CrossRef Medline
9. Chen Y, Jiang Y, Pahwa S, et al. **MR fingerprinting for rapid quantitative abdominal imaging.** *Radiology* 2016;279:278–86 CrossRef Medline
10. Granberg T, Uppman M, Hashim F, et al. **Clinical feasibility of syn-**

- thetic MRI in multiple sclerosis: a diagnostic and volumetric validation study. *AJNR Am J Neuroradiol* 2016;37:1023–29 CrossRef Medline
11. West J, Warntjes JB, Lundberg P. Novel whole brain segmentation and volume estimation using quantitative MRI. *Eur Radiol* 2012;22:998–1007 CrossRef Medline
  12. Vågberg M, Lindqvist T, Ambarki K, et al. Automated determination of brain parenchymal fraction in multiple sclerosis. *AJNR Am J Neuroradiol* 2013;34:498–504 CrossRef Medline
  13. Tanenbaum LN, Tsiouris AJ, Johnson AN, et al. Synthetic MRI for clinical neuroimaging: results of the Magnetic Resonance Image Compilation (MAGiC) prospective, multicenter, multireader trial. *AJNR Am J Neuroradiol* 2017;38:1103–10 CrossRef Medline
  14. Blystad I, Warntjes JB, Smedby O, et al. Synthetic MRI of the brain in a clinical setting. *Acta Radiol* 2012;53:1158–63 CrossRef Medline
  15. Deshmane A, McGivney D, Badve C. Accurate synthetic FLAIR images using partial volume corrected MR fingerprinting. In: *Proceedings of the Annual Meeting and Exhibition of International Society for Magnetic Resonance in Medicine*, Singapore. May 7–13, 2016
  16. *User Manual*, Version 8.0.1, SyMRI 8. Linköping: SyntheticMR AB; 2016–10-26
  17. Pfirmann CW, Metzendorf A, Zanetti M, et al. Magnetic resonance classification of lumbar intervertebral disc degeneration. *Spine (Phila Pa 1976)* 2001;26:1873–78 CrossRef Medline
  18. *IBM SPSS Statistics (for Windows)* [computer program]. Version 22.0. Armonk, New York: IBM Corp; 2013
  19. Krauss W, Gunnarsson M, Andersson T, et al. Accuracy and reproducibility of a quantitative magnetic resonance imaging method for concurrent measurements of tissue relaxation times and proton density. *Magn Reson Imaging* 2015;33:584–91 CrossRef Medline
  20. Shin W, Gu H, Yang Y. Fast high-resolution T1 mapping using inversion-recovery Look-Locker echo-planar imaging at steady state: optimization for accuracy and reliability. *Magn Reson Med* 2009;61:899–906 CrossRef Medline
  21. Liberman G, Louzoun Y, Ben Bashat D. T<sub>1</sub> mapping using variable flip angle SPGR data with flip angle correction. *J Magn Reson Imaging* 2014;40:171–80 CrossRef Medline
  22. Smith SA, Edden RA, Farrell JA, et al. Measurement of T1 and T2 in the cervical spinal cord at 3 Tesla. *Magn Reson Med* 2008;60:213–19 CrossRef Medline
  23. Massire A, Taso M, Besson P, et al. High-resolution multi-parametric quantitative magnetic resonance imaging of the human cervical spinal cord at 7T. *Neuroimage* 2016;143:58–69 CrossRef Medline
  24. Diaz E, Morales H. Spinal cord anatomy and clinical syndromes. *Semin Ultrasound CT MR* 2016;37:360–71 CrossRef Medline
  25. Hagiwara A, Hori M, Yokoyama K, et al. Utility of a multiparametric quantitative MRI model that assesses myelin and edema for evaluating plaques, periplaque white matter, and normal-appearing white matter in patients with multiple sclerosis: a feasibility study. *AJNR Am J Neuroradiol* 2017;38:237–42 CrossRef Medline
  26. Warntjes M, Engström M, Tisell A, et al. Modeling the presence of myelin and edema in the brain based on multi-parametric quantitative MRI. *Front Neurol* 2016;7:16 CrossRef Medline
  27. Hagiwara A, Warntjes M, Hori M, et al. SyMRI of the brain: rapid quantification of relaxation rates and proton density, with synthetic MRI, automatic brain segmentation, and myelin measurement. *Invest Radiol* 2017;52:647–57 CrossRef Medline
  28. Hwang D, Kim S, Abeydeera NA, et al. Quantitative magnetic resonance imaging of the lumbar intervertebral discs. *Quant Imaging Med Surg* 2016;6:744–55 CrossRef Medline
  29. Chatani K, Kusaka Y, Mifune T, et al. Topographic differences of 1H-NMR relaxation times (T1, T2) in the normal intervertebral disc and its relationship to water content. *Spine (Phila Pa 1976)* 1993;18:2271–75 CrossRef Medline
  30. Boos N, Wallin A, Schmucker T, et al. Quantitative MR imaging of lumbar intervertebral disc and vertebral bodies: methodology, reproducibility, and preliminary results. *Magn Reson Imaging* 1994;12:577–87 CrossRef Medline
  31. Marinelli NL, Haughton VM, Muñoz A, et al. T2 relaxation times of intervertebral disc tissue correlated with water content and proteoglycan content. *Spine (Phila Pa 1976)* 2009;34:520–24 CrossRef Medline
  32. Grunert P, Hudson KD, Macielak MR, et al. Assessment of intervertebral disc degeneration based on quantitative magnetic resonance imaging analysis: an in vivo study. *Spine (Phila Pa 1976)* 2014;39:E369–78 CrossRef Medline
  33. Driscoll SJ, Zhong W, Torriani M, et al. In-vivo T2-relaxation times of asymptomatic cervical intervertebral discs. *Skeletal Radiol* 2016;45:393–400 CrossRef Medline
  34. Stelzeneder D, Welsch GH, Kovács BK, et al. Quantitative T2 evaluation at 3.0T compared to morphological grading of the lumbar intervertebral disc: a standardized evaluation approach in patients with low back pain. *Eur J Radiol* 2012;81:324–30 CrossRef Medline
  35. Wang G, El-Sharkawy AM, Edelstein WA, et al. Measuring T2 and T1, and imaging T2 without spin echoes. *J Magn Reson* 2012;214:273–80 CrossRef Medline
  36. Pai A, Li X, Majumdar S. A comparative study at 3 T of sequence dependence of T2 quantitation in the knee. *Magn Reson Imaging* 2008;26:1215–20 CrossRef Medline
  37. Le Ster C, Lasbleiz J, Kannengiesser S, et al. A fast method for the quantification of fat fraction and relaxation times: comparison of five sites of bone marrow. *Magn Reson Imaging* 2017;39:157–61 CrossRef Medline
  38. Schick F, Bongers H, Jung W, et al. Proton relaxation times in human red bone marrow by volume selective magnetic resonance spectroscopy. *Appl Magn Reson* 1992;3:947–63 CrossRef
  39. Baum T, Yap SP, Dieckmeyer M, et al. Assessment of whole spine vertebral bone marrow fat using chemical shift-encoding based water-fat MRI. *J Magn Reson Imaging* 2015;42:1018–23 CrossRef Medline
  40. Warntjes JB, Engström M, Tisell A, et al. Brain characterization using normalized quantitative magnetic resonance imaging. *PLoS One* 2013;8:e70864 CrossRef Medline
  41. Engström M, Warntjes JB, Tisell A, et al. Multi-parametric representation of voxel-based quantitative magnetic resonance imaging. *PLoS One* 2014;9:e111688 CrossRef Medline
  42. West J, Blystad I, Engström M, et al. Application of quantitative MRI for brain tissue segmentation at 1.5 T and 3.0 T field strengths. *PLoS One* 2013;8:e74795 CrossRef Medline
  43. Chen L, Bernstein M, Huston J, et al. Measurements of T1 relaxation times at 3.0 T: implications for clinical MRI. In: *Proceedings of the International Society for Magnetic Resonance in Medicine 9th Scientific Meeting & Exhibition*, Glasgow, Scotland. April 21–27, 2001
  44. Chen C, Huang M, Han Z, et al. Quantitative T2 magnetic resonance imaging compared to morphological grading of the early cervical intervertebral disc degeneration: an evaluation approach in asymptomatic young adults. *PLoS One* 2014;9:e87856 CrossRef Medline

## “Delayed Pial Vessels” in Multiphase CT Angiography Aid in the Detection of Arterial Occlusion in Anterior Circulation

We read the article by Byrne et al, “Improved Detection of Anterior Circulation Occlusions: The ‘Delayed Vessel Sign’ on Multiphase CT Angiography” with great interest.<sup>1</sup> However, we would like to point out other important aspects of multiphase CT angiography (mCTA) to the readers of the *American Journal of Neuroradiology*. Multiphase CTA is a useful recent addition to neurovascular imaging in acute stroke, providing information on the degree and extent of pial arterial filling in the whole brain in a time-resolved manner.<sup>2</sup> It was designed to assess pial vessel asymmetry in terms of delayed contrast filling and/or delayed contrast washout compared with the contralateral side. The time-resolved imaging acquisition additionally enables judgment on either antegrade or retrograde pial vessel contrast filling and thus gives the reader information on clot permeability, collateral circulation, and possible response to thrombolytic therapy.

A recent study from our group was able to show an increase in the detection of anterior circulation intracranial occlusion with mCTA, especially for distal occlusions.<sup>3</sup> In the presence or absence of obvious large-vessel occlusion, pial vessel asymmetry in the second and third phase added to the yield of mCTA for occlusion detection. The “delayed vessel sign” mentioned in the study by Byrne et al<sup>1</sup> is one but not the only component of pial vessel asymmetry as explained above. Both low-flow (upstream stenocclusive lesions) and high-flow (recanalization) states could cause pial vessel asymmetry as proposed in our article.<sup>3</sup>

Our study also established that mCTA is a user-friendly imaging tool that can improve the diagnostic accuracy for anterior

circulation occlusions, even when used by relatively inexperienced readers and when occlusions are more distal. Thus, inclusion of multiphase CTA in acute ischemic stroke imaging protocols has the potential to allow non-radiology trained physicians and trainees to rapidly and accurately determine anterior circulation occlusions, a crucial point in clinical management when considering patients for revascularization procedures.<sup>3</sup> Furthermore, pial vessel dynamics captured on mCTA can also be quantified to provide information similar to that of perfusion CT and can be used to predict tissue fate regionally in patients with acute ischemic stroke.<sup>4</sup>

### REFERENCES

1. Byrne D, Sugrue G, Stanley E, et al. **Improved detection of anterior circulation occlusions: the “delayed vessel sign” on multiphase CT angiography.** *AJNR Am J Neuroradiol* 2017;38:1911–16 CrossRef Medline
2. Menon BK, d’Esterre CD, Qazi EM, et al. **Multiphase CT angiography: a new tool for the imaging triage of patients with acute ischemic stroke.** *Radiology* 2015;275:510–20 CrossRef Medline
3. Yu AY, Zerna C, Assis Z, et al. **Multiphase CT angiography increases detection of anterior circulation intracranial occlusion.** *Neurology* 2016;87:609–16 CrossRef Medline
4. d’Esterre CD, Trivedi A, Pordeli P, et al. **Regional comparison of multiphase computed tomographic angiography and computed tomographic perfusion for prediction of tissue fate in ischemic stroke.** *Stroke* 2017;48:939–45 CrossRef Medline

 R.-J. Singh

 C. Zerna

 B.K. Menon

Calgary Stroke Program, Department of Clinical Neuroscience  
University of Calgary  
Calgary, Alberta, Canada

<http://dx.doi.org/10.3174/ajnr.A5529>

**REPLY:**

**W**e thank Drs Singh, Zerna, and Menon for their interest in our study,<sup>1</sup> and we are grateful for the opportunity to address their comments. First, we would like to acknowledge the utility and value of multiphase CT angiography as a development in the assessment of acute stroke, first described by the Calgary Stroke Program. It is a dynamic, versatile, and multipurpose tool,<sup>2</sup> with benefit in the detection of distal intracranial arterial occlusions as previously described by Yu et al.<sup>3</sup> The purpose of our study was to demonstrate the effectiveness of an easily communicated imaging sign on multiphase CTA, “the delayed vessel sign,” which we have found to be intuitively understood even by junior trainees. It is a reliable indicator of an intracranial arterial occlusion, providing a rapid method to identify the precise site of occlusion. The sign is distinct from “asymmetric pial enhancement,” which we separately evaluated in our article; in clinical practice, we have found it to be a subtler imaging feature, especially when associated with distal vessel occlusions. We have recently developed a new postprocessing technique “subtraction multiphase CT angiography,” which increases the conspicuity of the delayed vessel sign by suppressing normally enhancing vessels

<http://dx.doi.org/10.3174/ajnr.A5536>

(including pial vessels), enabling faster detection of intracranial arterial occlusions.<sup>4</sup>

**REFERENCES**

1. Byrne D, Sugrue G, Stanley E, et al. **Improved detection of anterior circulation occlusions: the “delayed vessel sign” on multiphase CT angiography.** *AJNR Am J Neuroradiol* 2017;38:1911–16 CrossRef Medline
2. Menon BK, d’Este CD, Qazi EM, et al. **Multiphase CT angiography: a new tool for the imaging triage of patients with acute ischemic stroke.** *Radiology* 2015;275:510–20 CrossRef Medline
3. Yu AY, Zerna C, Assis Z, et al. **Multiphase CT angiography increases detection of anterior circulation intracranial occlusion.** *Neurology* 2016;87:609–16 CrossRef Medline
4. Byrne D, Walsh JP, Sugrue G, et al. **Subtraction multiphase CT angiography: a new technique for faster detection of intracranial arterial occlusions.** *Eur Radiol* 2017 Nov 13. [Epub ahead of print] CrossRef Medline

 **D. Byrne**

 **J.P. Walsh**

Department of Radiology  
Mater Misericordiae University Hospital  
Dublin, Ireland

 **P.J. MacMahon**

Department of Radiology  
Mater Misericordiae University Hospital  
Dublin, Ireland  
School of Medicine  
University College Dublin  
Dublin, Ireland

## Neuroradiology Fellowship Case Requirements Need Reform

**P**ediatric radiology and neuroradiology have long been radiology subspecialties certified by the American Board of Radiology (ABR), and both pathways have been Accreditation Council for Graduate Medical Education (ACGME)-accredited for many years. The discipline of pediatric neuroradiology, however, remains unaccredited by the ACGME despite increased interest in postgraduate year 7–level pediatric radiology fellowships in recent years. Pediatric neuroradiologists who complete a pediatric neuroradiology fellowship must thus practice as neuroradiology faculty at an accredited program for at least 2 years before the subspecialty examination can be taken. Pediatric neuroradiologists in private practice unaffiliated with accredited training environments are ineligible for the neuroradiology subspecialty certificate even though they have completed a year of dedicated training.

Neuroradiologists were not long ago entrenched in interventional procedures, but noninvasive angiography using CT and MR imaging has greatly supplanted catheter-based cerebral angiography. The rise of endovascular surgical neuroradiology as a distinct ACGME-accredited fellowship—which can be undertaken by neurologists and neurosurgeons—has further reduced the volume of direct cerebral angiography performed by radiologists. Despite this reduction, ACGME requirements still mandate participation in 50 catheter-based angiographic procedures and 50 image-guided invasive procedures.<sup>1</sup> Programs with as many as 8 fellows must thus have 400 catheter-based angiographic procedures available. Many neuroradiology programs now struggle to meet this requirement, and others report that participation is very loosely defined.

Case log requirements also include interpretation of 1500 neuroradiologic CT scans and 1500 neuroradiologic MR images. Review of a recent pediatric neuroradiology graduate's case log indicated 1321 CT scans and 2920 MR images interpreted. Exposure to CT examinations in the pediatric population is challenging, given the need to limit radiation, but pediatric CT examinations are often greater in complexity due to variable maturation of pediatric osseous structures and/or complicated craniofacial/temporal bone anomalies. ACGME neuroradiology case log require-

ments also include exposure to plain radiography, transcranial Doppler sonography, and fetal sonography. Pediatric neuroradiologists are more likely to be involved in these types of examinations than adult neuroradiologists.

The ABR requires that a fellowship or employment take place at an ACGME-accredited institution before the experience can be applied to a training requirement for a subspecialty examination. Of the 14 domestic pediatric neuroradiology fellowship programs advertised by the American Society of Pediatric Neuroradiology,<sup>2</sup> all take place at facilities that train ACGME-accredited fellows.

I posit that the ACGME should consider altering its case log requirements to allow greater flexibility. A reasonable solution would be to have 3 available pathways, including a general neuroradiology curriculum that includes the current number of diagnostic neuroradiology examinations but fewer required procedures; a neurointerventional radiology pathway that is more focused on procedural neuroradiology but may have slightly fewer diagnostic requirements; and a pediatric neuroradiology option that requires more MR imaging examinations but fewer CTs.

A procedure-focused neuroradiology pathway would allow neuroradiology programs to concentrate these cases among individuals likely to perform these procedures in practice while giving them an excellent foundation should they opt to pursue advanced neurointerventional training. It would allow those less interested in procedures to focus more on advanced diagnostic neuroradiology skills (eg, functional MR imaging, diffusion tensor imaging, perfusion imaging, and so forth) that are becoming more relevant. A pediatric-focused neuroradiology pathway would provide pediatric neuroradiologists an avenue to acquire recognition of their training while broadening employment opportunities for pediatric radiologists who have this extra year of training.

The time has come to reassess the objectives and goals of neuroradiology fellowship training with respect to the state of the art in modern neuroradiology practice. By allowing variations to case log requirements, we can train future neuroradiologists to adapt their training to fit their own interests as well as the needs of modern employers.

<http://dx.doi.org/10.3174/ajnr.A5553>

## REFERENCES

1. Accreditation Council for Graduate Medical Education. ACGME Program Requirements for Graduate Medical Education in Neuroradiology. [https://www.acgme.org/Portals/0/PFAssets/ProgramRequirements/423\\_neuroradiology\\_2017-07-01.pdf](https://www.acgme.org/Portals/0/PFAssets/ProgramRequirements/423_neuroradiology_2017-07-01.pdf). Accessed November 1, 2017
2. American Society of Pediatric Neuroradiology. Pediatric Neuroradiology Fellowships and Training. <http://aspnr.org/pediatric-neuroradiology-fellowships/>. Accessed November 1, 2017

 **C.M. Pfeifer**

Department of Radiology  
University of Texas Southwestern Medical Center  
Dallas, Texas

# Relationship between Ischemic Injury and Patient Outcomes after Surgical or Endovascular Treatment of Ruptured Anterior Communicating Artery Aneurysms



Heit et al<sup>1</sup> retrospectively investigated the relationship between ischemic injury and patient outcomes after surgical or endovascular treatment of ruptured anterior communicating artery (AcomA) aneurysms. Their method chiefly consisted of reviewing neuroimaging studies to examine the frequency of frontal lobe and striatum ischemic injury and reviewing patient data to examine mortality and clinical outcome at discharge and at 3 months. They showed that patients whose aneurysms were clipped exhibited higher incidences of frontal lobe infarction and recurrent artery of Heubner (RAH) infarction than those whose aneurysms were coiled and were more likely to be functionally dependent at discharge. We agree that their results could be plausible. However, we cannot help but mention a few problems in their methodology.

Recent studies, both of which are cited by Heit et al,<sup>1</sup> reported infarction in the subcallosal artery (the largest unpaired perforator of the AcomA) territory in addition to infarctions of the frontal lobe and RAH territory.<sup>2,3</sup> In our study examining patients with amnesia diagnosed using formal neuropsychological testing after clipping for AcomA aneurysms, all 10 patients had subcallosal artery infarction and 5 had additional infarcts in the RAH territory, as observed by 3D-MR imaging.<sup>2</sup> These subcallosal artery infarcts inevitably involved the columns of the fornix. In a different study by Mortimer et al,<sup>3</sup> in which they used CT or 2D-MR imaging but not neuropsychological assessment, infarcts of the fornix and septal/subcallosal region (both structures are supplied by the subcallosal artery) were observed in 5 (7.6%) and 12 (18.1%), respectively, of the patients with clipped aneurysms following treatment for AcomA rupture. In contrast, fornix and septal/subcallosal infarcts were found in 1 (1.1%) and 1 (1.1%), respectively, of the patients with coiled aneurysms.<sup>3</sup>

However, Heit et al<sup>1</sup> completely disregarded subcallosal artery infarction, though it could cause postoperative memory deficits and thus largely affect clinical outcomes or quality of life. Their neuroimaging studies may have failed to reveal lesions as small as

subcallosal artery infarctions, but this failure should have been mentioned in their article as a limitation of their study.

Their study lacked formal neuropsychological testing for evaluating clinical outcome, which they mentioned as a limitation. We have previously discussed the association of orbitofrontal area or RAH infarcts with memory deficits,<sup>2,4</sup> and we suggest that memory loss following AcomA repair is rare when ischemic injury is limited to the orbitofrontal area or RAH territory without any involvement of the subcallosal artery territory. However, simultaneous involvement of the RAH and subcallosal artery territories might affect the frontostriatal circuits, resulting in frontal dysfunction, and is associated with poor long-term prognosis of patients with amnesia.<sup>4</sup>

Thus, we believe that the study by Heit et al<sup>1</sup> is largely limited by the inadequacy in the evaluation of ischemic injury by neuroimaging as well as the evaluation of patient outcomes by neuropsychological testing. To clarify the clinical significance of the ischemic injury that might develop after surgical or endovascular treatment of ruptured AcomA aneurysms, detailed prospective neuroimaging and neuropsychological assessments would be mandatory. For neuroimaging, we recommend the use of diffusion-weighted imaging in the acute phase (immediately after treatment) as well as 3D-MR imaging (not just CT or 2D-MR imaging) in the chronic and stable phases following injury, to visualize small foci of subcallosal artery infarction.<sup>2</sup> For evaluation of patient outcomes, formal neuropsychological assessments would be desirable after confusion, disorientation, and intellectual deficits during the acute phase have subsided.<sup>2</sup> Moreover, evaluating long-term outcomes would also be important.<sup>4</sup>

Disclosures: Shunji Mugikura—RELATED: Grant: JSPS Kakenhi Grant Number JP15K10290\*; UNRELATED: Grants/Grants Pending: Philips Healthcare\*; Payment for Lectures Including Service on Speakers Bureaus: Daiich Sankyo, Bayer, Fuji Pharma. \*Money paid to the institution.

This work was supported by JSPS KAKENHI grant number 15K10290.

## REFERENCES

1. Heit JJ, Ball RL, Telischak NA, et al. **Patient outcomes and cerebral infarction after ruptured anterior communicating artery aneurysm treatment.** *AJNR Am J Neuroradiol* 2017;38:2119–25. CrossRef Medline

Indicates open access to non-subscribers at [www.ajnr.org](http://www.ajnr.org)

<http://dx.doi.org/10.3174/ajnr.A5564>

2. Mugikura S, Kikuchi H, Fujii T, et al. **MR imaging of subcallosal artery infarct causing amnesia after surgery for anterior communicating artery aneurysm.** *AJNR Am J Neuroradiol* 2014;35:2293–301 CrossRef Medline
3. Mortimer AM, Steinfert B, Faulder K, et al. **Rates of local procedural-related structural injury following clipping or coiling of anterior communicating artery aneurysms.** *J Neurointerv Surg* 2016;8:256–64 CrossRef Medline
4. Mugikura S, Kikuchi H, Fujimura M, et al. **Subcallosal and Heubner artery infarcts following surgical repair of an anterior communicat-**

**ing artery aneurysm: a causal relationship with postoperative amnesia and long-term outcome.** *Jpn J Radiol* 2017 Nov 23. [Epub ahead of print] CrossRef Medline

 **S. Mugikura**

 **S. Takahashi**

 **K. Takase**

Department of Diagnostic Radiology  
Graduate School of Medicine  
Tohoku University  
Sendai, Japan

## REPLY:

We thank Dr Mugikura and colleagues for their comments regarding our recent article “Patient Outcomes and Cerebral Infarction after Ruptured Anterior Communicating Artery Aneurysm Treatment.”<sup>1</sup> Patients who undergo ruptured anterior communicating (AcomA) aneurysm treatment by microsurgical clipping have been shown to have worse clinical outcomes compared with coil embolization,<sup>2</sup> and these worse outcomes include reduced levels of functional independence and more severe neurocognitive outcomes. In our study, we found that ischemic infarction was more common after microsurgical clipping compared with coil embolization. Our observation that cerebral infarction in the recurrent artery of Heubner (RAH) territory was much more common in patients who underwent microsurgical clipping compared with coil embolization (33% versus 2%) does suggest an interesting mechanism by which surgical clipping might result in worse outcomes compared with coil embolization. We agree that the limitations of retrospective analyses result in much difficulty in discerning the exact causes of patient dependency after such a neurologically complicated event as rupture of a cerebral aneurysm.

In response to the first question raised by our colleagues, we did not detect any subcallosal artery infarctions in our study population, as they note in their letter. Patients in our study underwent posttreatment imaging evaluation by both CT and MR imaging, and the reduced sensitivity of CT to cerebral infarction, especially with subarachnoid and intraventricular hemorrhages, may limit the detection of subcallosal artery infarctions (including the fornix) in our study. This limitation is perhaps more pronounced because more patients who underwent surgical clipping had imaging follow-up by CT rather than MR imaging, and these were the patients more likely to have an RAH infarction and possibly a subcallosal artery infarction, as our colleagues argue. We agree that a more thorough discussion of these (and other) limitations could have been mentioned in our discussion. However, as any author of a retrospective study must do, we chose to list the most important limitations to our overall results; the lack of randomization, lack of blindness to treatment technique on follow-up imaging, and limited patient follow-up were deemed more important to emphasize to our readers.

We would like to further highlight the important methodologic and patient population differences between our colleagues' prior study<sup>3</sup> and our study.<sup>1</sup> The prior study of Mugikura et al<sup>3</sup> that identified subcallosal infarctions was performed in patients who developed amnesia following ruptured or elective AcomA aneurysm clipping, and the imaging evaluation of these patients was performed several months after treatment using only MR imaging. By contrast, our study<sup>1</sup> and another study<sup>4</sup> included all patients who underwent ruptured AcomA treatment, patients treated by both clipping and coiling, and no specific posttreatment symptom (ie, amnesia) was required for subsequent analysis. We would argue that these differences in patient populations limit direct comparison between these studies when attempting to

compare the frequency of infarctions related to the various perforating vessels that arise from the anterior communicating artery complex. We would also advise caution in directly applying the results from Mugikura et al to the population in our study, given these differences.

In response to the second point raised by our colleagues, reduced functional independence may be due to memory loss and amnesia, which is the focus of the prior study of Mugikura et al.<sup>3</sup> However, there are many other causes of patient dependency after rupture of a cerebral aneurysm. As they note in their letter and we note in our limitations, we do not routinely perform neuropsychological testing after AcomA aneurysm rupture and treatment. We are therefore unable to comment on the specifics of memory loss, decision-making, and other executive function deficits. As we discussed in our article, striatum infarction has been linked to all these deficits,<sup>5-7</sup> whereas subcallosal artery infarction may be more specific for memory deficits.<sup>3</sup> Thus, we would argue that RAH infarction may be an overall more important contributor to patient outcome in patients with ruptured AcomA aneurysms.

Last, we agree with our colleagues that a prospective study of patients with ruptured AcomA aneurysms is necessary to understand better the cause of worse neurologic outcomes after surgical treatment compared with coil embolization. Clearly, detailed MR imaging evaluation before and after treatment (at several time points) in concert with detailed neuropsychological evaluation would provide the best data to answer these questions.

## REFERENCES

1. Heit JJ, Ball RL, Telischak NA, et al. **Patient outcomes and cerebral infarction after ruptured anterior communicating artery aneurysm treatment.** *AJNR Am J Neuroradiol* 2017;38:2119–25 CrossRef Medline
2. Molyneux AJ, Kerr RSC, Yu LM, et al. **International subarachnoid aneurysm trial (ISAT) of neurosurgical clipping versus endovascular coiling in 2143 patients with ruptured intracranial aneurysms: a randomised comparison of effects on survival, dependency, seizures, rebleeding, subgroups, and aneurysm occlusion.** *Lancet* 2005;366:809–17 CrossRef Medline
3. Mugikura S, Kikuchi H, Fujii T, et al. **MR imaging of subcallosal artery infarct causing amnesia after surgery for anterior communicating artery aneurysm.** *AJNR Am J Neuroradiol* 2014;35:2293–301 CrossRef Medline
4. Mortimer AM, Steinfors B, Faulder K, et al. **Rates of local procedural-related structural injury following clipping or coiling of anterior communicating artery aneurysms.** *J Neurointerv Surg* 2016;8:256–64 CrossRef Medline
5. Mendez MF, Adams NL, Lewandowski KS. **Neurobehavioral changes associated with caudate lesions.** *Neurology* 1989;39:349–54 CrossRef Medline
6. Mizuta H, Motomura N. **Memory dysfunction in caudate infarction caused by Heubner's recurring artery occlusion.** *Brain Cogn* 2006;61:133–38 CrossRef Medline
7. Martinaud O, Perin B, Gérardin E, et al. **Anatomy of executive deficit following ruptured anterior communicating artery aneurysm.** *Eur J Neurol* 2009;16:595–601 CrossRef Medline

© J.J. Heit

Department of Radiology, Interventional Neuroradiology Section  
Stanford University Medical Center  
Stanford, California